ASPECTS OF MAGNETISATION AND IRON LOSS CHARACTERISTICS IN SWITCHED-RELUCTANCE AND PERMANENT-MAGNET MACHINES

Jill Alison Walker

A Thesis
Submitted To
The Department of Electronics and Electrical Engineering
Of the Engineering Faculty of
The University Of Glasgow
For The Degree of
Doctor Of Philosophy

March 2006

Abstract

This thesis discusses the measurement and analysis of magnetisation and loss characteristics. The work contained in the thesis can be summarised in three sections.

In the first section, the magnetisation characteristics of the switched-reluctance motor are examined. Measurements have been carried out using both static and dynamic test methods. The test data has been compared with simulation results from analytical design programs and finite element models. The effects of mutual coupling on the magnetisation characteristics are investigated through measurement and simulation. Results show that the degree of mutual coupling is strongly dependent on the winding arrangement of the machine.

In the next section, the difficulties in measuring the properties of permanent-magnet machines are discussed in detail, and solutions to common problems proposed. The measurement and analysis methods used for the switched-reluctance motor are further developed for analysis of permanent magnet machines. Techniques for determining the variation in synchronous reactances and permanent magnet flux are presented. Finite element simulations are used to show the variation of magnet flux under loading, a condition ignored in classical analysis methods.

The final section discusses the analysis of magnetisation characteristics of electrical sheet steels. Comparison is made between measurements carried out on single sheet tester and Epstein square test rigs. The iron losses of a typical non-grain-orientated steel are measured under both sinusoidal and nonsinusoidal flux density conditions. The iron losses are shown to increase significantly when higher harmonic components are introduced to the flux density waveform. The difficulties in modelling the nonlinear iron loss characteristics of electrical steels are considered.

Acknowledgements

Over the period of my doctoral studies, I have received much support and encouragement from those around me. I have been supervised by Prof. TJE Miller, Dr. David Dorrell and Mr Calum Cossar. The support and encouragement shown by each of them has helped me enormously. I am greatly indebted to a number of other staff in the department who helped me during my studies. In the SPEED Laboratory I would like to thank Saffron Pearce, Malcolm McGilp and Dr. Mircea Popescu for answering my numerous queries, and the technicians both in the SPEED Laboratory and in the department's mechanical workshop for their help with many test set-ups. I must also thank Dr. Karen McIlvaney, whose door was always open when I needed someone to listen.

During the course of my PhD, I was given the opportunity to spend some time at the Institute of Energy Technology at Aalborg University, Denmark. I would like to thank the department at Aalborg, particularly Prof. Ewen Ritchie for his hospitality and guidance. I would also like to thank the Dept. of Electrical Engineering at the University of Sheffield, who were kind enough to lend me a single sheet tester for use in the iron loss measurements.

Thank you to both the SPEED Consortium and Robert Bosch GmbH, who supplemented my EPSRC funding, for their financial support. Thanks also to Electrolux Compressors, Italy, for providing prototype IPM motors and material samples for testing.

Lastly, I thank my friends and family, and in particular my parents, for bearing with me through the last three and a half years. I think at some points they despaired that I would ever finish. Most importantly, I thank my partner James for his patience, understanding and love. I could not have succeeded without him.

Thank you all.

List of Contents

List of Figures

List of Tables

Nomenclature

SYMBOLS

A	magnetic vector potential	
A_{path}	cross-section area of eddy current path	m^2
A_{sample}	cross-section area of sample	m^2
A_{w2}	cross-section area of secondary winding	m^2
A_{wall}	area of domain wall	m^2
B	flux density	T
$\hat{B}$	peak flux density	T
B_1	fundamental component of flux density	T
$\hat{B}_{air}$	air flux component of flux density	T
B_{adj}	adjusted flux density	T
B_e	effective field in ferromagnet	T
B_{meas}	measured flux density	T
B_r	remnant flux density	T
B_{rr}	radial component of remnant flux density	T
B_{tt}	tangential component of remnant flux density	T
B_x	component of flux density in x-direction	T
B_y	component of flux density in y-direction	T
dL	end turn inductance	H
dM/dt	microscopic remagnetisation rate	
D	bore diameter	m
E	magnet effective voltage phasor	
E_0	open-circuit EMF from permanent magnet	V
E_{loss}	energy loss	J
E_p	average pinning energy per site	J
E_v	energy loss per remagnetisation cycle	J
f	frequency	Hz
f_{eq}	equivalent frequency	Hz
$f(t)$	output of hysteresis transducer model	
$f^+_{u(t)}$	output value of ascending hysteresis branch	
$f^-_{u(t)}$	output value of descending hysteresis branch	
H	applied magnetic field	A/m
H_c	coercive field	A/m
$\hat{H}$	peak applied field	A/m
h	lamination height	m

H_x	applied field in x-direction	A/m
H_y	applied field in y-direction	A/m
$\boldsymbol{I}$	current vector	
i	current	A
I_0	reference current	A
i_a	current in phase a	A
i_b	current in phase b	A
i_c	current in phase c	A
i_d	direct axis current	A
I_d	direct axis current vector	A
I_{eddy}	eddy current	A
I_{max}	current limit	A
i_{ph1}	current in phase 1	A
i_{ph2}	current in phase 2	A
I_{RMS}	Root Mean Square current	A
i_q	quadrature axis current	A
I_q	quadrature axis current vector	A
J	magnetic polarisation	T
$j, j+1$	successive iterations of current	
k	empirical Steinmetz parameter	
k_a	Steinmetz coefficient of anomalous loss	
k_e	Steinmetz coefficient of eddy current loss	
k_h	Steinmetz coefficient of hysteresis loss	
k_i	empirical iGSE parameter	
k_{wl}	fundamental winding factor	
$k_{winding}$	material constant (=234.5 for copper winding)	
L	self-inductance	H
L_{au}	end turn inductance (aligned position)	H
L_{dd}	direct axis self-inductance	H
L_{dq}	direct axis mutual inductance	H
l_{eff}	effective path length of SST	m
L_M	motor winding inductance	H
l_m	toroid core magnetic path length	m
l_{path}	eddy current path length	m
L_{qd}	quadrature axis mutual inductance	H
L_{qq}	quadrature axis self-inductance	H
l_{SST}	measured path length of SST	m
L_{stack}	stack length	m
L_u	end turn inductance (unaligned position)	H
m	number of phases	

M	magnetisation	A/m
M_L	mutual inductance	H
M_s	spontaneous magnetisation within domain	A/m
n	intensity of pinning sites per unit volume	
N	number of turns in winding	
N_1	number of turns in primary winding	
N_2	number of turns in secondary winding	
N_e	number of laminations in stack	
N_{ph}	number of phases	
N_r	number of rotor poles	
p	number of pole pairs	
P_a	anomalous loss	W
P_d	power dissipation function	
P_e	eddy current loss	W
P_h	hysteresis loss	W
P_s	specific loss of sample	W/kg
P_{sE}	power loss measured on Epstein square	W
P_{SST}	power loss measured on single sheet tester	W
P_v	power loss per unit volume	W/m^3
R_1, R_2	balancing resistances in inductance bridge	Ω
R_e	eddy current loss resistance	Ω
R_{ep}	eddy current path resistance	Ω
R_{inner}	inner radius of toroid core	m
R_M	motor winding resistance	Ω
R_{outer}	outer radius of toroid core	m
R_p	primary winding resistance	Ω
R_{ph}	phase resistance	Ω
R_T	phase resistance under ambient temperature	Ω
R_{test}	phase resistance during test	Ω
R_{VAR}	variable resistance in inductance bridge	Ω
S	strokes per revolution	
$ScPsi$	scaling factor for flux-linkage	
Sci	scaling factor for current	
T	torque	Nm
T	period of waveform	secs
t	time	secs
T_{ave}	average torque	Nm
T_e	electromagnetic torque	Nm
T_{ON}	turn-on angle of controller	°elec
T_{OFF}	turn-off angle of controller	°elec

t_T	ambient temperature	°C
t_{test}	winding temperature during test	°C
U	no-load voltage	V
$u(t)$	input to hysteresis transducer model	
$U_{compensation}$	compensating voltage for single sheet tester	V
$U_{leakage}$	equivalent leakage voltage in single sheet tester	V
$U_{resultant}$	resultant voltage in single sheet tester	V
U_{sample}	sample voltage in single sheet tester	V
v	voltage	V
V	volume of laminations	m^3
v_1	voltage in primary winding	V
v_2	voltage in secondary winding	V
v_d	direct axis voltage	V
v_{dc}	DC supply voltage	V
v_{m1}	mutual induced voltage in phase 1	V
v_{m2}	mutual induced voltage in phase 2	V
v_{mhc}	mutual voltage (soft chopping control)	V
v_{msc}	mutual voltage (hard chopping control)	V
v_q	quadrature axis voltage	V
V_{R2}	voltage across resistor R_2	V
V_{RMS}	RMS voltage	V
w	lamination thickness	m
W'	coenergy	J
x	distance moved by domain wall	m
X_d	direct axis synchronous reactance	Ω
X_Lstk	adjustment factor for stack length	
X_{md}	direct axis mutual reactance	Ω
X_{mq}	quadrature axis mutual reactance	Ω
X_q	quadrature axis synchronous reactance	Ω
Z	impedance	Ω

GREEK SYMBOLS

α	empirical material parameter for Steinmetz-type equations	
α	magnetising switching operator of Preisach model	
β	empirical material parameter for Steinmetz-type equations	
β	demagnetising switching operator of Preisach model	
γ	torque angle (between *E* and *I*)	deg.
δ	load angle (between *E* and *V*)	deg.
η	empirical material parameter for Steinmetz-type equation	
θ	rotor position	°elec.
θ_{ph2}	rotor position of phase 2	°elec.
μ_0	permeability of free space (= 1.257E-06)	H/m
μ_r	relative permeability of material	H/m
ρ	resistivity of lamination	Ω-m
ρ_{sample}	density of sample	Kg/mm^3
σ_v	Von Mises stress	Kg/mm^2
σ_1	principal stress from direction 1	Kg/mm^2
σ_2	principal stress from direction 2	Kg/mm^2
σ_3	principal stress from direction 3	Kg/mm^2
τ	lamination thickness	m
φ	power factor angle (between *I* and *V*)	deg.
Φ	flux	W
ψ	flux-linkage	V-s
ψ_0	zero sequence component of flux-linkage	V-s
Ψ_1	peak of fundamental component of flux-linkage	V-s
ψ_a	flux-linkage in phase a	V-s
ψ_{adj}	adjusted flux-linkage	V-s
ψ_b	flux-linkage in phase b	V-s
ψ_c	flux-linkage in phase c	V-s
ψ_d	direct axis flux-linkage	V-s
ψ_{did}	direct axis flux-linkage due only to d-axis current	V-s
ψ_m	flux-linkage due to permanent magnets	V-s
ψ_{orig}	original flux-linkage	V-s
ψ_{ph2}	flux-linkage in phase 2	V-s
ψ_q	quadrature axis flux-linkage	V-s
ω	angular frequency	rad/sec

ACRONYMS & ABREVIATIONS

2D	Two-dimensional
3D	Three-dimensional
AC	Alternating Current
AlNiCo	Aluminium Nickel Cobalt
ASTM	American Society of Testing and Materials
d-axis	Direct Axis
DC	Direct Current
DSO	Digital Storage Oscilloscope
EMF	Electro Motive Force
FE	Finite Element
FEA	Finite Element Analysis
GO	Grain Orientated
GPIB	General Purpose Interface Bus
GSE	General Steinmetz Equation
IEC	International Electrotechnical Commission
iGSE	Improved Generalised Steinmetz Equation
IPM	Interior Permanent Magnet
MC	Magnetising Current
MMF	Magneto Motive Force
MSE	Modified Steinmetz Equation
Nd-Fe-B	Neodinium Iron Boron
NGO	Non-grain-orientated
PD	Proportional Differential
PI	Proportional Integral
PM	Permanent Magnet
PWM	Pulse Width Modulation
q-axis	Quadrature Axis
RPM	Rotations Per Minute
Sm-Co	Samarium Cobalt
SR	Switched-reluctance
SST	Single Sheet Tester
THD	Total Harmonic Distortion

Chapter 1

Introduction

This thesis describes the measurement and analysis of the magnetisation characteristics of switched-reluctance and interior permanent-magnet machines, and investigates the assessment of iron losses in electrical steels. In this chapter, a brief introduction is provided for both motor topologies. From there, a reasoning of the work contained in the thesis is given. The chapter concludes with an outline of the thesis structure and original contributions.

1.1. Switched-reluctance motor

Principle of operation

The switched-reluctance motor is a doubly-salient, variable-speed machine. It is also known in the United States by the term 'variable reluctance'. The motor is energised via stator windings formed from short-pitched coils wound round individual poles to form separately-excited phases. The winding may also be fully-pitched, although this is not common. There is no rotor winding. Some typical types of switch reluctance machine are shown in Fig. 1.1.

The operation of the switched-reluctance motor is based on the principle of reluctance torque. Reluctance torque is produced by the tendency of the rotor poles to align with the stator at the position of minimum reluctance (when the inductance is maximised, due to the minimised airgap between rotor and stator). When the rotor is at intermediate positions between an aligned and unaligned position, the direction of the torque produced is towards the closest aligned position. Positive torque is only produced at those rotor positions between an unaligned position and the closest aligned position in the forward direction of rotation. As such, for torque production over a full rotation of 360

degrees, it is necessary to have more than one phase. Fig. 1.2 shows typical inductance and current profiles. The aligned and unaligned positions are marked for reference.

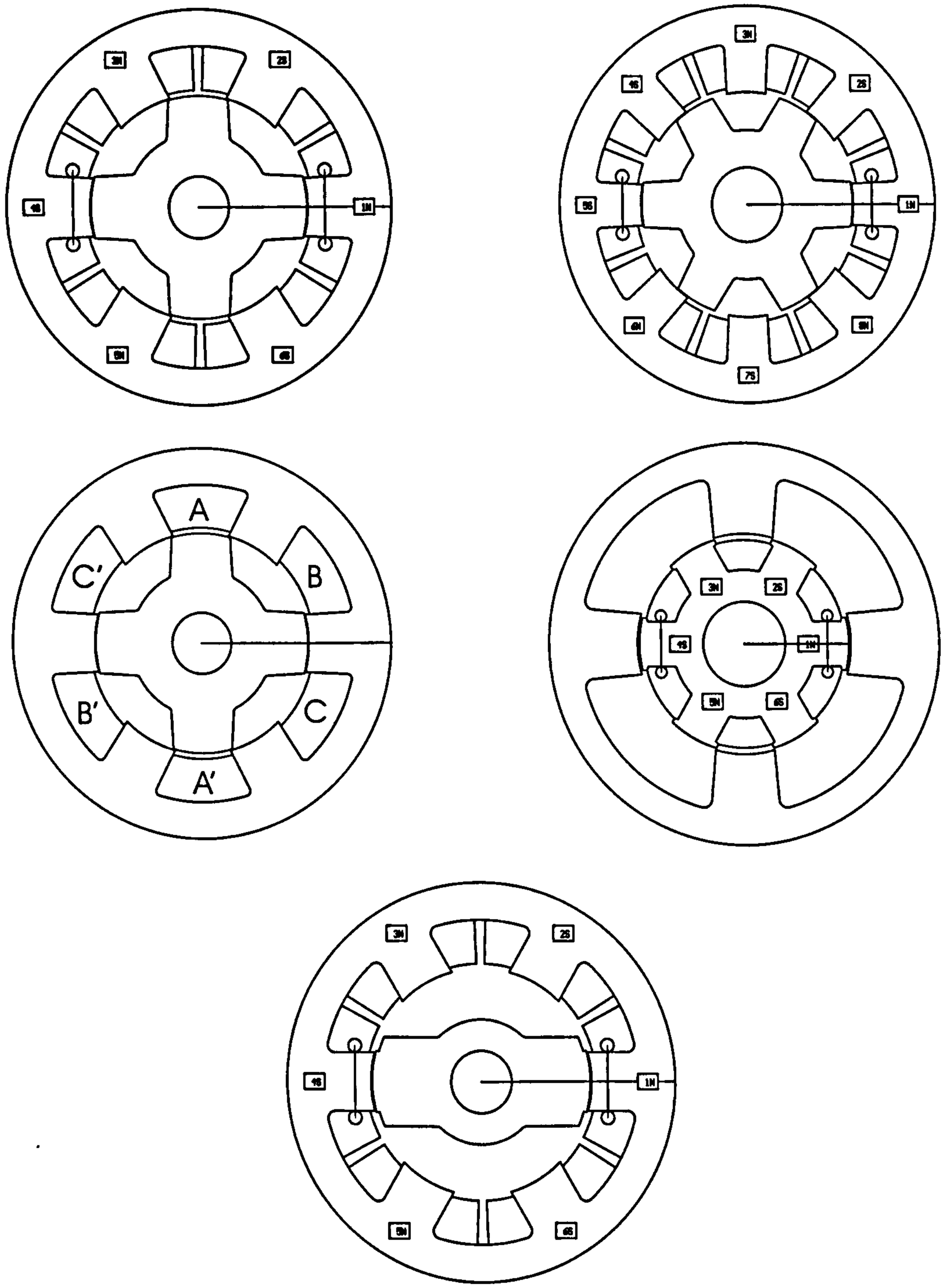

Fig. 1.1. Cross-sections of different switched-reluctance motor types.
From top left: 3-phase 6/4 pole motor, 4-phase 8/6 pole motor, 3-phase 6/4 pole motor with fully-pitched winding, 3-phase 6/4 pole motor with outer rotor, 3-phase 6/2 pole motor with stepped airgap.

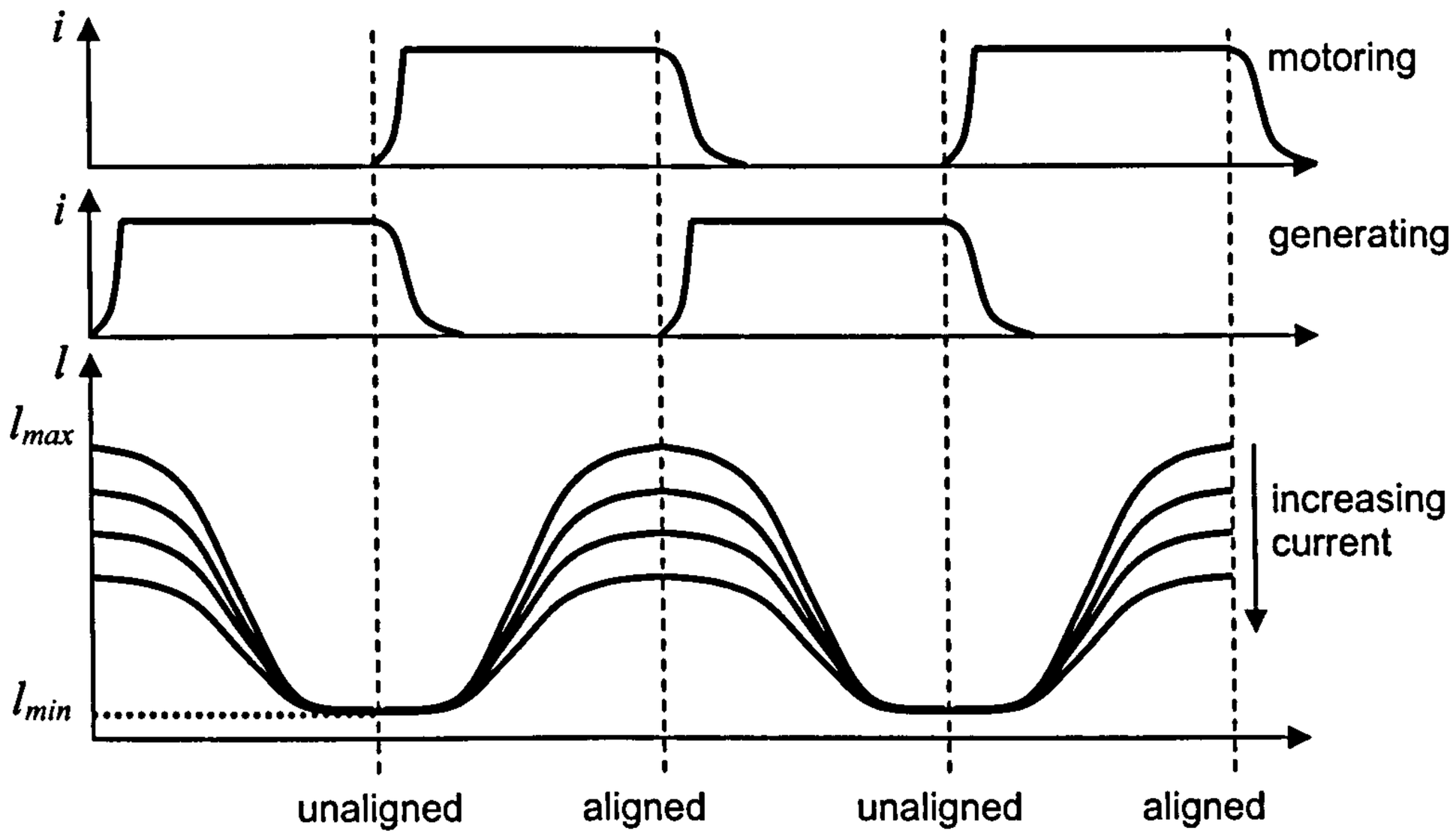

Fig. 1.2. Inductance and current profiles of switched-reluctance motor

The phase currents are synchronised with rotor position to optimise torque production. The rotor position is normally determined from a shaft position sensor, although schemes exist for sensorless control. The torque produced is a non-linear function of both the phase currents and rotor position. The switched-reluctance machine commonly operates under saturated conditions.

It is not possible to calculate the properties of the switched-reluctance motor using classical theory such as the phasor diagram, and so alternative methods must be considered. Most commonly, the motor is analysed in terms of the per-phase static magnetisation curves and the energy conversion loop.

History of the Switched-reluctance Motor

The earliest recorded switched-reluctance motor was produced by Davidson in 1838, for use in locomotive propulsion. The motor was rather unsuccessful, resulting in low power output and capable of speeds of only a few miles per hour. Development of the switched-reluctance motor did not begin in earnest until the 1960s, by which time electronic commutation was achievable due to the development of solid-state switching

devices. The term *switched-reluctance* was coined by Nasar in a journal article of 1969, to describe a DC motor without commutator [1]. In the early 1970s, Bedford patented a system that synchronised the commutation of the phase currents with rotor position using simple control circuits using only 2 or 3 solid-state switches [2,3].

A number of papers by Byrne et al. in the 1970s considered improvements to the control of the switched-reluctance motor. Of particular importance was the development of control strategies utilising advanced switching angles to improve the per-phase i-ψ trajectories [4].

It was not until the 1980s that the switched-reluctance motor became a viable choice for commercial production, thanks largely to development work at the University of Leeds and later at Switched-reluctance Drives Ltd [5,6]. Lawrenson et al. provided a comprehensive discussion of energy conversion principles and suitable stator/rotor pole ratios for self-starting operation, and highlighted many of the useful design characteristics of the switched-reluctance machine [5].

Further developments have included switched-reluctance motors with fully-pitched windings, developed at the University of Newcastle [7]. Comprehensive discussions on switched-reluctance motor design and previous literature can be found in either [8] or [9].

Today, commercial projects involving switched-reluctance motors are still relatively limited. Commercial motors have been designed for use in domestic appliances such as washing machines; in actuators, where the degree of rotation is limited; and in aerospace applications. For example, the test motor used in this thesis is used in aeroplane landing gear.

1.2. Brushless interior permanent-magnet motor

Principle of operation

Broadly speaking, there are two main types of brushless permanent-magnet machines: brushless permanent-magnet DC motors and brushless permanent-magnet AC motors. As with all brushless motors, there are no brushes or slip rings. The absence of a rotor winding removes any need for mechanical commutation. Many brushless permanent-magnet motors can be run under either AC or DC control strategies.

In the brushless DC machine, the back EMF waveform is designed to be approximately trapezoidal; the motor is sometimes known as a *trapezoidal* or *squarewave* permanent-magnet motor. The brushless permanent-magnet DC machine can be considered equivalent to an inverted DC commutator motor, where the mechanical commutation is replaced by electronic switching of the current polarity, by means of power electronics [10]. The polarity of each phase current is switched in synchronism with the motor back-EMF. The rotor position is determined from a shaft position sensor such as a resolver or Hall-effect transducer.

DC control is commonly used in power drive applications; although higher power densities can be achieved, there is often torque ripple and the position control is less precise than that of AC control.

The brushless synchronous permanent-magnet AC motor can be considered a development of the wound-field synchronous motor, whereby the rotor field winding is replaced by permanent magnet pieces. The motor is excited by a stator winding with sinusoidally-distributed conductors. The induced back-EMF is ideally sinusoidal. The phase currents may be either sinusoidal or pulse width modulated (PWM) and are synchronised to rotor position using position feedback sensors such as encoders or Hall sensors. The permanent magnets can either be mounted on the rotor surface or embedded within the rotor structure. Embedding the permanent magnets within the rotor

steel simplifies construction and improves the mechanical integrity of the rotor. The control strategies commonly require knowledge of the rotor position, determined by a rotary shaft encoder, although sensorless control strategies also exist.

The synchronous permanent-magnet AC machine is commonly analysed using the classical phasor diagram, where the phase quantities are translated into polar and interpolar axis phasor quantities. The electromagnetic properties of motors with surface-mounted and embedded permanent magnets are quite distinct. Motors with surface-mounted permanent magnets are non-salient-pole machines, meaning that the reluctances (and thus synchronous reactances) of the polar and interpolar axes are equal. When the permanent magnets are buried within the rotor structure, the machine is salient pole, with different reluctances in the polar and interpolar axis paths. As such, distinct sets of equations exist to describe the electromagnetic properties of motors with surface-mounted and buried permanent magnets.

The work contained in this thesis focuses primarily on rotors with embedded magnet pieces, commonly known as *interior permanent-magnet* (IPM) motors; however, the measurement and analysis methods used can easily be applied to synchronous AC motors with surface-mounted permanent magnets. A number of different types of IPM motor exist, a selection of which are shown in Fig. 1.3.

History of the Permanent-magnet Motor

A number of designs for brushless permanent-magnet motors can be found from the 1940s onwards. In 1951, Saunders and Weakley presented a qualitative approach to the design of permanent-magnet alternators, focussing on the behaviour of the permanent-magnet materials and demagnetisation effects [11]. The Westinghouse Electric Corporation patented a number of designs from the mid-1950s onwards; the motors were designed for use with Aluminium-Nickel-Cobalt (AlNiCo) and later ceramic (ferrite) magnets [12,13,14].

By the 1970s, new designs were being produced to maximise the electromagnetic and mechanical properties of permanent-magnet machines. Binns et al. described various existing rotor structures and proposed a punched-lamination rotor incorporating a squirrel cage for line-start operation. The use of punched laminations simplifies rotor construction and improves mechanical robustness. The authors also provide useful discussion on leakage flux paths [15,16].

In the 1980s, Honsinger produced two comprehensive papers on the performance and calculation of synchronous permanent-magnet machines. The first calculates the steady-state operation using the phasor diagram method [17]. The phasor diagram and machine equations are adjusted to include iron-loss components. The second includes a discussion on the validity of the phasor diagram and the calculation of magnet flux under the full range of load characteristics [18].

Commercial applications for IPM motors include domestic electrical appliances such as washing machines and refrigerators; industrial electrical applications such as pumps and compressors; traction drives; and servo drives, where smooth and precise control is needed. In recent years there has been particular interest in the use of synchronous permanent-magnet motors in hybrid electric vehicle systems [19].

The development of permanent-magnet motors would not have been possible without the development of the permanent-magnet materials themselves. When the earliest motors were being developed in the 1940s and 50s, the most common magnet material was AlNiCo, which has a low energy product (maximum *B-H* product) and was susceptible to demagnetisation due to a low coercivity. AlNiCo magnets were quickly replaced by ferrite materials, which have a higher energy product and linear demagnetisation characteristics. Ferrite magnets have remained a popular cost-effective choice for many motor designs, and their use is still widespread in automotive applications.

The first rare-earth magnets to be developed were Samarium-Cobalt (Sm-Co). Sm-Co5 was developed in 1966. Although it was thermally stable and had an energy product of around 150 kJ/m^3, it was much more expensive than previous materials. In the 1970s a variant, Sm2-Co17, was developed. Although cheaper than Sm-Co5, and with a larger energy product (240 kJ/m^3), it was more difficult to manufacture. Sm-Co magnets are often used in machines developed for aerospace applications.

By the mid-1980s, a new type of rare-earth magnet, Neodinium-Iron-Boron (Nd-Fe-B), had been developed. The Nd2-Fe14-B variant has an energy product of 300 kJ/m^3. It is less expensive than Samarium-Cobalt but also less stable. Nd-Fe-B magnets are susceptible to corrosion, but can be treated to limit such effects.

Comprehensive discussions on permanent-magnet materials, including extensive information on the methods of production of permanent magnets, can be found in References [20-22]. A summary of the properties of some common permanent-magnet materials can be found in table 1.1.

Magnet type	Materials	Date first developed	Max BH product	Max working temperature
AlNiCo	Aluminium Nickel Cobalt	1940s	20 – 110 kJ/m^3	500 – 550 °C
Ferrite	Ceramic Ferrite	1960s	40 kJ/m^3	250 °C
SmCo	Samarium Cobalt	1966	150 – 240 kJ/m^3	250 – 350 °C
NdFeB	Neodinium Iron Boron	1980s	300 kJ/m^3	80 – 200 °C

Table 1.1. Properties of permanent-magnet materials

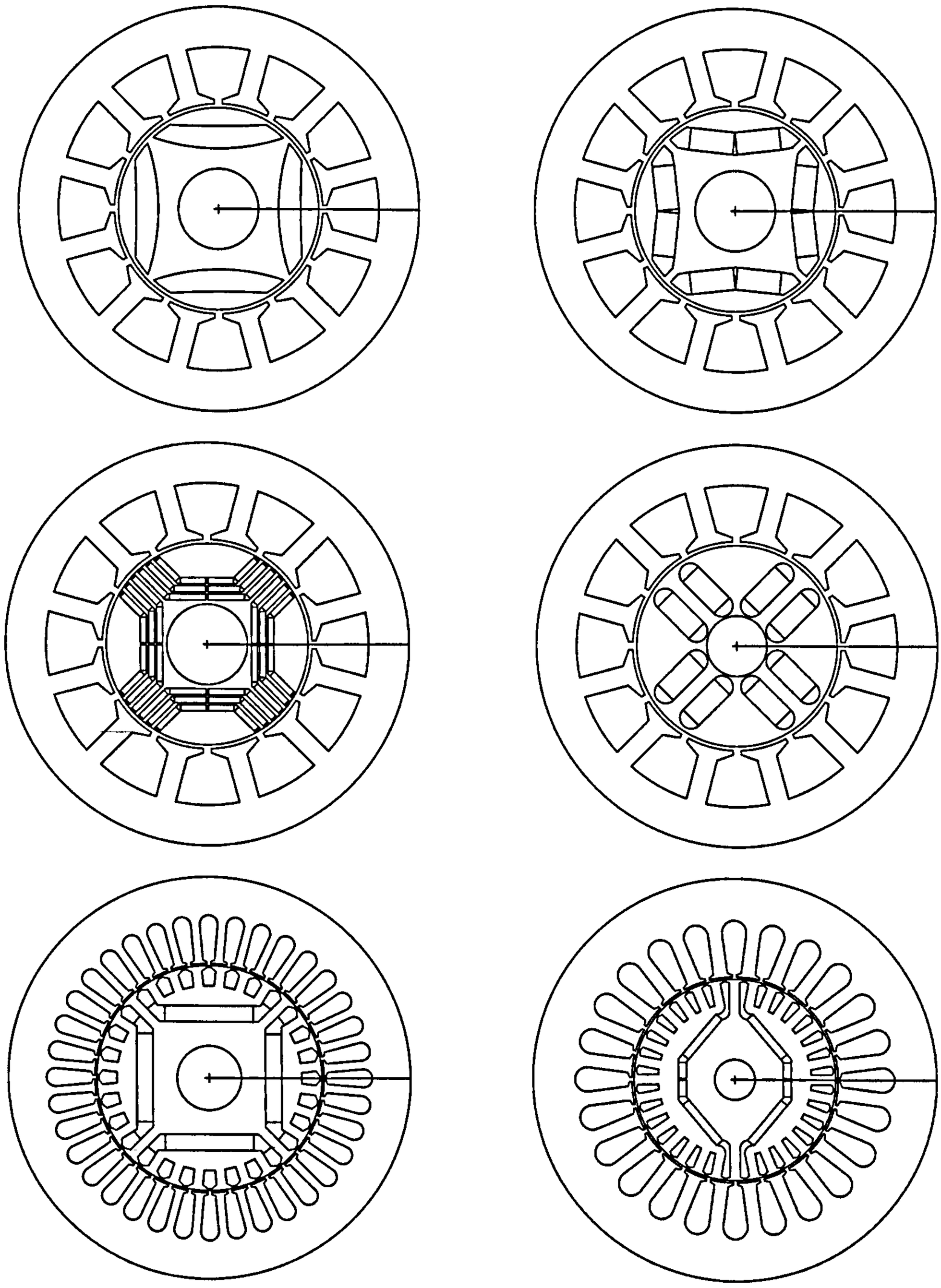

Fig. 1.3. Cross-sections of different interior permanent-magnet motor types.
From top left: 4 pole motor with shaped pole pieces, 4 pole motor with 2 magnet segments per pole, 4 pole motor with 3 magnet layers per pole, 4 pole motor with parallel-magnetised magnets, 4 pole motor with squirrel cage to enable line-start operation, 2 pole motor with squirrel cage and 4 magnet pieces per pole.

1.3. Problem definition

In recent years, advances in the design of personal computers have led to significant increases in computational and data storage ability. This has allowed the development of fast and powerful software packages for use in the design and analysis of electric machines. Analytical and finite element computer programs are now an essential part of the design process, and are used to create optimised designs ready for prototyping. As more sophisticated programs are developed, more computationally-intensive analysis methods are possible. For those motor topologies whose properties cannot easily be calculated by equivalent circuits or the classical phasor diagram, the use of software such as finite element analysis programs is essential.

While modelling and simulation are an essential part of the design process, the performance of the machine must be verified by measurement of its electrical and mechanical properties. The measured properties of the machine should be used to make adjustments to the prototype design and may be used as an input to further design calculations; they are also useful as a tool for calibration of the motor model.

Although there is a wealth of literature concerning the measurement of magnetisation characteristics of both switched-reluctance and permanent-magnet motors, there are no internationally recognisable standards (such as those of the IEC or the ASTM) at present. This raises a number of key questions:

- What are the most suitable ways of defining the magnetisation characteristics of each type of motor?
- Can the same measurement methods be applied to permanent-magnet motors as to other motor topologies?
- What is the best way to model the motors in analytical or finite element design programs?
- How can the properties of the lamination materials, as measured from sheet steel samples, be used in calculations of motor characteristics?

The main objectives of this thesis are to examine the existing methods of measurement and analysis of the magnetisation characteristics of both switched-reluctance and permanent-magnet motors, and of the lamination materials used in the construction of such machines. The aims of the work can be considered under three main headings:

Switched-reluctance Motor:

- To examine existing measurement and analysis methods for the magnetisation characteristics of the switched-reluctance motor and to highlight any sources of error
- To improve existing methods and develop alternative techniques
- To examine the influence of mutual coupling and end-turn effects on the characterisation of magnetic properties

Interior Permanent-magnet Motor:

- To determine whether the measurement methods used for the switched-reluctance motor can be successively applied to motors containing permanent magnets
- To develop new methods of both measurement and analysis, designed specifically for the permanent-magnet motor
- To examine the influence of rotor design on the magnetic characteristics of the motor, particularly the torque production and synchronous reactances

Lamination steel samples:

- To compare the most common methods of measurement of sheet steel samples
- To measure the magnetisation curves and losses of steel samples using an Epstein square and single sheet tester
- To find relationships between the magnetising waveforms and losses using measured data, for use in an iron loss model
- To examine the effects of nonsinusoidal flux density waveforms on the iron losses

Limitations of the project:

The measurement of magnetisation characteristics has been limited to two types of motor, the switched-reluctance and interior permanent-magnet motor. Details of the test motors used in the thesis, which were designed in conjunction with the SPEED Laboratory, can be found in Appendix 1. Methods presented in the thesis have been verified as far as is possible using the test motors.

Measurements of electrical sheet steel have been limited to samples of the non-grain-orientated (NGO) lamination material of the interior permanent-magnet test motor 1. The test results are indicative of trends only for NGO materials. Testing of grain-orientated (GO) materials was outwith the scope of thesis, as all test motors were constructed with NGO lamination material.

1.4. Thesis structure and original contributions

Fig. 1.4 shows the structure of the thesis. Chapter information is given below, along with details of the original contributions. A number of publications have arisen from the original contributions; details of these can be found in Appendix 9.

Chapter 2 describes the methods for measurement and analysis of magnetisation characteristics of both the switched-reluctance and interior permanent-magnet motor. In particular, the measurement of static magnetisation curves and i-ψ trajectories is discussed. The disadvantages of current measurement methods are described and a number of improvements suggested. Common methods of simulating such properties are discussed and a special finite element analysis method, the *frozen permeability* method, is presented.

Chapter 3 presents results of both measurements and simulations of magnetisation characteristics. Static and dynamic measurements have been made on a commercial switched-reluctance motor and a prototype interior permanent-magnet motor.

Comparison has been made between a number of different simulation methods, with reference to measured data.

In *Chapter 4*, the magnetisation characteristics of the switched-reluctance motor are examined in greater detail. The chapter focuses on the effects of mutual coupling between phases on the torque production and phase flux-linkages. The *frozen permeability* method is used to determine the self and mutual flux-linkages of each phase of the motor, for cases with muliple-phase excitation. Results from finite element simulations illustrate the dependence of mutual coupling on phase polarity arrangement.

The properties of the interior permanent-magnet motor are discussed in more detail in *Chapter 5*. Methods for measuring and calculating the synchronous reactances of permanent-magnet motors are explained. The major drawbacks of existing methods are highlighted. The *frozen permeability* method is used to calculate the flux-linkage contributions from the phase currents and from the permanent magnets. The simulation results illustrate the errors that can arise from the assumption that the flux-linkage attributed to the permanent magnets is constant. Included in this chapter is an investigation into how the design of the rotor can affect the flux-linkage contributions from each source, and also the production of torque.

Chapter 6 presents an overview of the current state-of-the-art of iron loss modelling, including methods based on the Steinmetz equation and on microscopic changes in magnetisation. Following on from this is a description of the methods commonly used to measure the iron losses of sheet steels. Details of the test equipment used are provided.

Chapter 7 shows results from measurements made on a single sheet tester and an Epstein square test rig of non-grain-orientated electrical steel samples. It highlights the differences that may occur when using different methods to measure the iron loss. It also discusses the difficulties in accurate prediction of the iron losses when the flux

density is non-sinusoidal, a condition which is shown to occur in different parts of the motor cross-section.

Some conclusions are presented in *Chapter 8*, along with suggestions for further work.

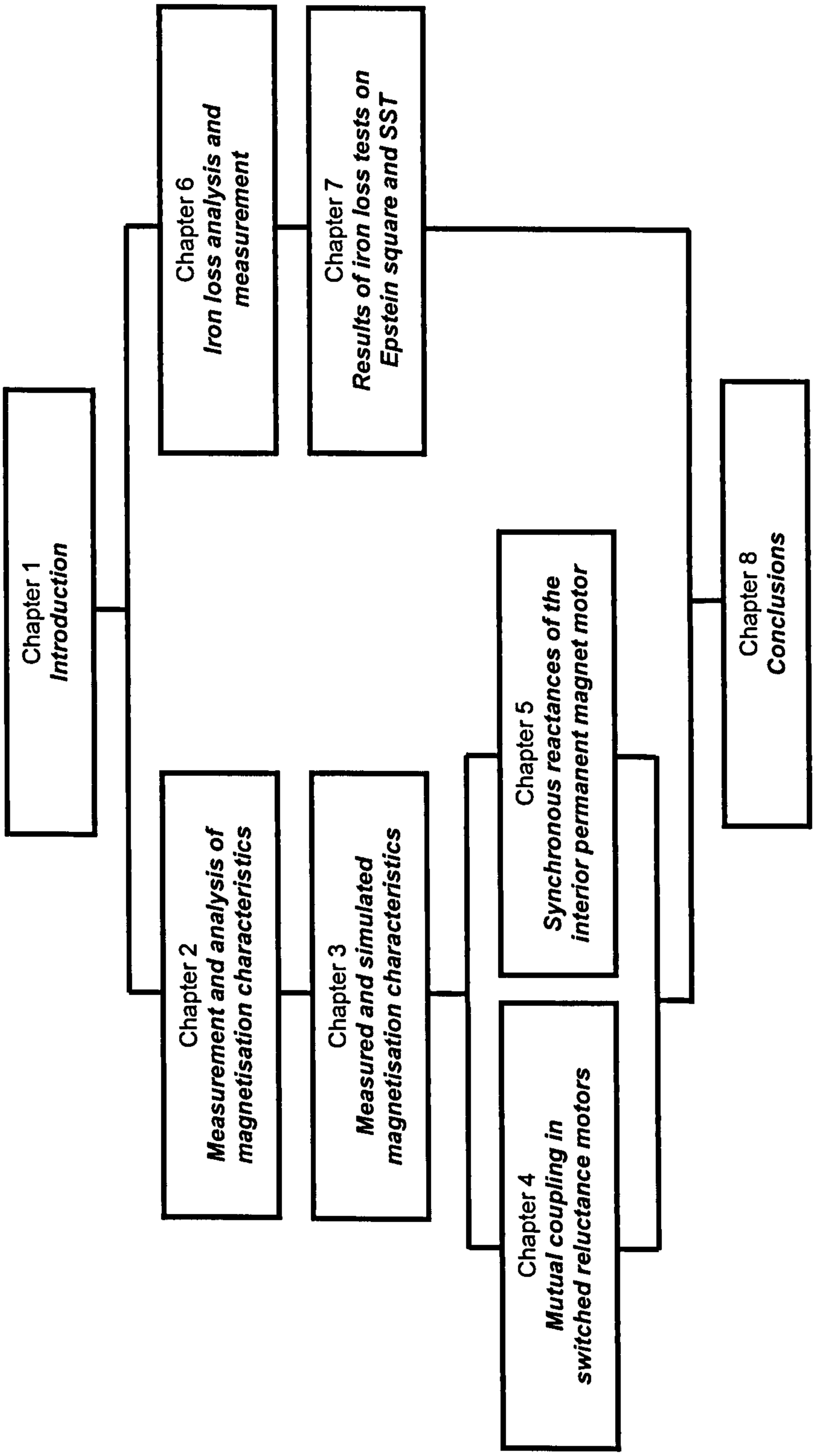

Fig. 1.4. Diagram of thesis structure

Chapter 2

Calculation and Measurement of Magnetisation Characteristics of Switched-Reluctance and Interior Permanent-Magnet Motors

In this chapter, common methods of defining and calculating motor magnetisation characteristics of permanent-magnet and switched-reluctance motors are discussed. The differences in application of such methods to the different motor types are described, and suggestions for improvements to current methods are given. Whilst they represent two different types of machine in terms of design and operation, they can be investigated using similar techniques, which are compared and contrasted here.

2.1. Static Magnetisation Curves

It is not possible to analyse the switched-reluctance motor using equivalent circuits and analytical functions due to the nonlinear relationship between the current and torque. Unlike most other machine topologies, the primary torque is a reluctance torque rather than an excitation torque. The magnetic characteristics of the switched-reluctance motor can be represented by magnetisation curves of flux-linkage versus current for successive rotor positions between the unaligned and aligned rotor positions. Such magnetisation curves form an essential part of switched-reluctance motor analysis; the data can be used as a basis for calculation in analytical simulation packages. As well as indicating levels of saturation in the steel laminations, they can be used to calculate both inductance levels and electromagnetic torque. In this section, previous work on the simulation and measurement of the static magnetisation curves is evaluated. A method of measuring the magnetisation curves is discussed and updated.

Magnetisation curves can also be used to assess the magnetisation and level of saturation in permanent-magnet motors. The magnetisation curves can be used in

analytical models of motor performance. In this chapter, the measurement and modelling of magnetisation curves for both switched-reluctance and permanent-magnet machines is reviewed. The problems arising from constant field excitation from the permanent magnets are discussed, and improvements to the existing measurement methods are suggested.

2.1.1. Measurement of magnetisation curves of SR motor

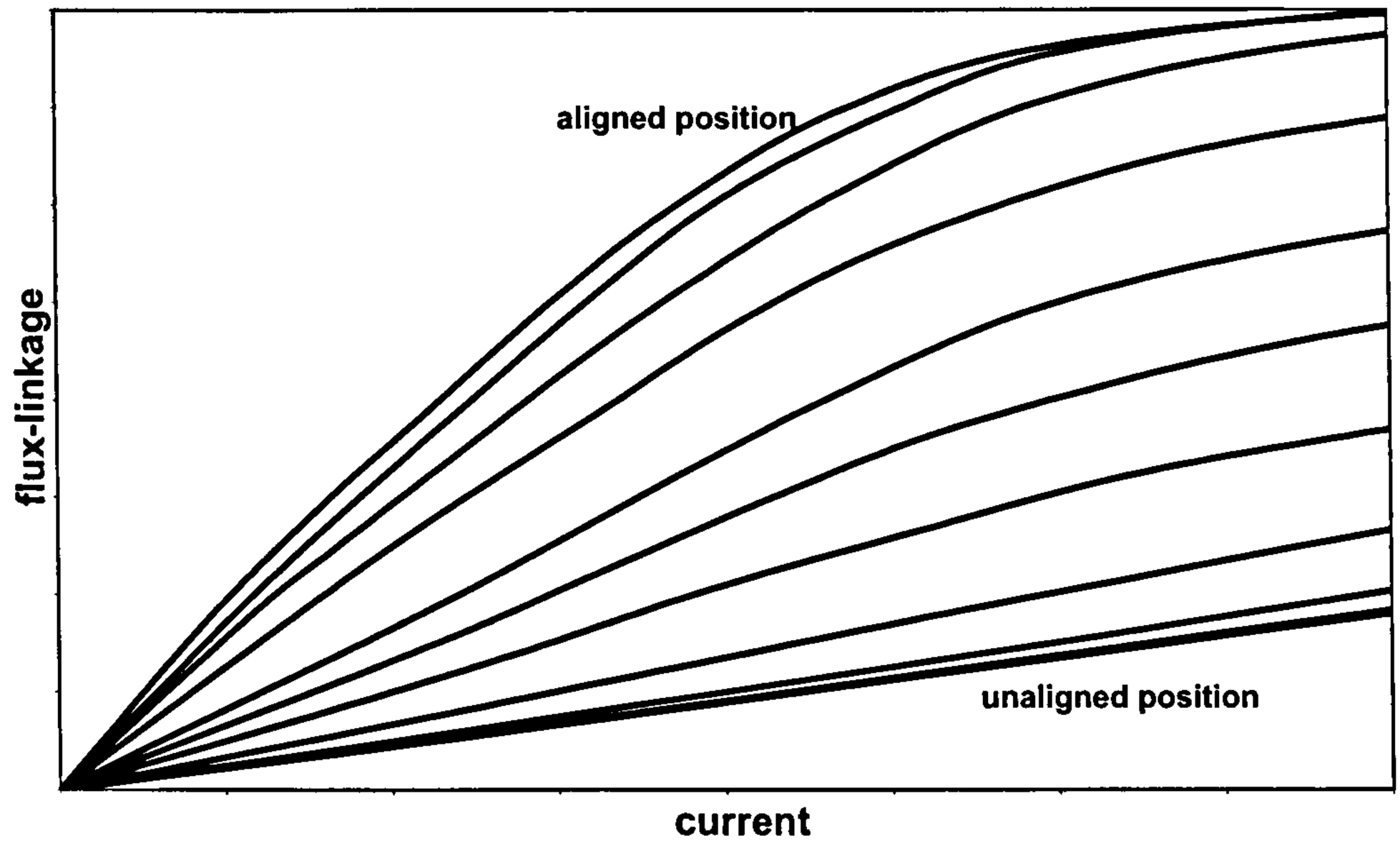

Fig. 2.1. Magnetisation curves of a switched-reluctance motor

The static magnetisation curves of flux-linkage versus current, at successive rotor angles between the unaligned and aligned positions, for one phase of a switched-reluctance motor are shown in Fig. 2.1. The aligned and unaligned positions have been labelled. The effects of iron loss in the steel have been neglected. The presented magnetisation curves assume single-phase excitation. Cross-coupling effects produced by overlapping phase excitations are investigated in Chapter 4.

The magnetisation curves cover only one quadrant of operation, due to unidirectional phase current excitation and the selection of the commutation interval. The inductance is

a function of the phase current at each rotor position and is given by the slope of each magnetisation curve

$$L = \frac{\psi}{i} \tag{2.1}$$

The unaligned position is the point of minimum inductance (maximum airgap) and the linear characteristic of the magnetisation curve indicates little or no saturation. Maximum inductance occurs in the aligned position (minimum airgap). The nonlinear characteristic of the aligned magnetisation curve indicates saturation in the lamination steel.

The measurement of magnetisation curves for the switched-reluctance motor is covered in detail in the literature. Lovatt and Stephenson [23] compare a number of methods of measuring the magnetisation curves and conclude that the most accurate method is a "transformer" method, whereby the main winding is energised and the resulting voltage on a secondary search winding integrated to give the flux-linkage. The method is only suitable for bifilar-wound stators, where there is more than one winding per pole.

Cossar and Miller [24] proposed two methods discounted by Lovatt and Stephenson, the direct and indirect methods of measuring magnetisation curves. The direct method measures the phase voltage and current, which are used to compute the phase flux-linkage using the equation

$$\psi = \int [v(t) - i(t) R_{ph}] dt \tag{2.2}$$

Lovatt and Stephenson argue that the method is unworkable due to variation in time of the phase resistance due to the increasing temperature of the winding. However, [24] proposes that the resistance is determined graphically; when there is no current, the flux-linkage value will rest at zero if the resistance value used in the integration is correct. This method can be used to "fine tune" the resistance. The method is also used

in [25] as part of an automated measurement system created in the LabVIEW environment.

The indirect method uses the static torque curves to reconstruct the magnetisation curves. The static torque curves can only be used to calculate incremental flux-linkages between successive rotor positions, and so one magnetisation curve must be calculated using another method. The unaligned magnetisation curve is essentially linear, with constant inductance, and so can be determined from an AC test using Eq. (2.3) and (2.4)

$$V_{RMS} = I_{RMS}|Z| \tag{2.3}$$

$$|Z|^2 = R_{ph}{}^2 + \omega L^2 \tag{2.4}$$

Reference [23] assumes that the effects of hysteresis and residual magnetism can be neglected. Work by Pulle [26] shows that hysteresis effects are such that there are in fact two current/flux-linkage trajectories, corresponding to rising and falling currents, and suggests that an average of the two curves be taken as the true static magnetisation curve. These results are confirmed by Manzer et al. [27].

2.1.2. Modelling of magnetisation curves of SR motor

The magnetisation curves can be modelled using either analytical design software such as PC-SRD, or finite element software. Much of the literature concentrates on simulation using measured magnetisation curve data as a basis for the calculations.

Stephenson and Corda [28] used tables of magnetisation data in the form $\psi(\theta,i)$, which was then inverted to give the input table $i(\theta,\psi)$. Points at intermediate flux-linkage values on each $i(\theta,\psi)|_{\theta=const}$ curve are found by quadratic interpolation. The output data points

are integrated to create a table of coenergies $W'(\theta,i)$ that can be used in transient torque calculations. Manzer et al. [27] model the ψ-i-θ relationship using piece-wise polynomials by splitting the operating plane of the motor into nine distinct operating regions, each defined by a different bicubic polynomial.

Pulle [26] describes a database that can be used in computer-aided design to determine the base functions $\psi(i,\theta)|_{i\ =\ \text{const}}$, $i(\psi,\theta)|_{\psi\ =\ \text{const}}$ and $T(i,\theta)|_{i\ =\ const}$ from cubic-spline interpolated representations of the flux-linkage/current curves. Coenergy data is derived from the flux-linkage base function using analytical methods rather than numerical integration; the coenergies are represented by three analytical functions corresponding to different current regions. The torque base function is determined by differentiating the coenergy data and interpolating in θ the resulting data. The method is advantageous as it eliminates the coenergy and torque tables used in the Stephenson and Corda method.

Miller and McGilp [29] modelled the nonlinear magnetisation characteristics analytically using piecewise functions of flux-linkage versus rotor position, rather than current. The method is based on time-stepping integration of the voltage equation (2.2). The magnetisation data is based on interpolations between the aligned and unaligned magnetisation curves. The aligned magnetisation curve is modelled in two sections – below the saturation region the unsaturated inductance is calculated and used as the gradient of the line. At higher levels of flux density, the curve is modelled by a second-order polynomial determined analytically using known points on the curve. Points on the unaligned curve are calculated using a linear relationship between the flux-linkage and unaligned inductance (calculated with the dual energy method). Curves at intermediate rotor positions are modelled using piecewise gauge curves. The resulting magnetisation characteristics assume that all phases are equal and that there is no mutual coupling between adjacent phases. The method also assumes no hysteresis, so that the rising current and falling current trajectories are identical. Similar curves can be constructed for the static torque characteristics. The method is useful for its speed in approximating the

motor waveforms, and gives reasonable accuracy in determining the average torque[1], though not comparable to that calculated by cubic spline interpolation of measured magnetisation curves.

The magnetisation curves can also be calculated from finite element analysis (in this case, PC-FEA supplied by the SPEED Laboratory, University of Glasgow). Using a script automatically generated by the finite element GoFER[2] of the SPEED Laboratory's switched-reluctance motor package PC-SRD, the flux-linkage at each rotor position can be calculated over a range of current values, up to a current limit specified by the user. The script computes a nonlinear simulation with one phase excited. The resulting magnetisation curves are single-valued (neglecting the hysteresis effects that can be seen in the measured data) and neglect the mutual coupling between phases. Magnetisation curves that include mutual coupling effects are multi-dimensional (a function of the currents in all phases) and thus computationally-intensive.

2.1.3. Measurement of magnetisation curves of PM motor

The magnetisation curves of the permanent-magnet motor are of a different form to those of the switched-reluctance motor. In a permanent-magnet motor, the current may be either positive or negative, as may the flux-linkage. As such, the magnetisation curves cover all four quadrants of operation. Due to the separate excitation from the permanent magnets, there is flux-linkage even when there is no current, leading to an offset in the magnetisation curves. The flux-linkage due to the permanent magnets varies with rotor position (because at each rotor position the flux from the permanent magnets is linked by a different number of turns). For sine-distributed windings, the flux-linkage from the permanent magnets varies sinusoidally with rotor position. The open-circuit magnet flux-linkage can be calculated by integration of the open-circuit back EMF

---

[1] Example given calculates electromagnetic torque to within 7.7% of the measured values compared to 4.3% using cubic spline fitting.
[2] The SPEED finite element link program ("GO to Finite Elements and Return")

waveform. Typical magnetisation curves of one phase of a permanent-magnet motor are given in Fig. 2.2.

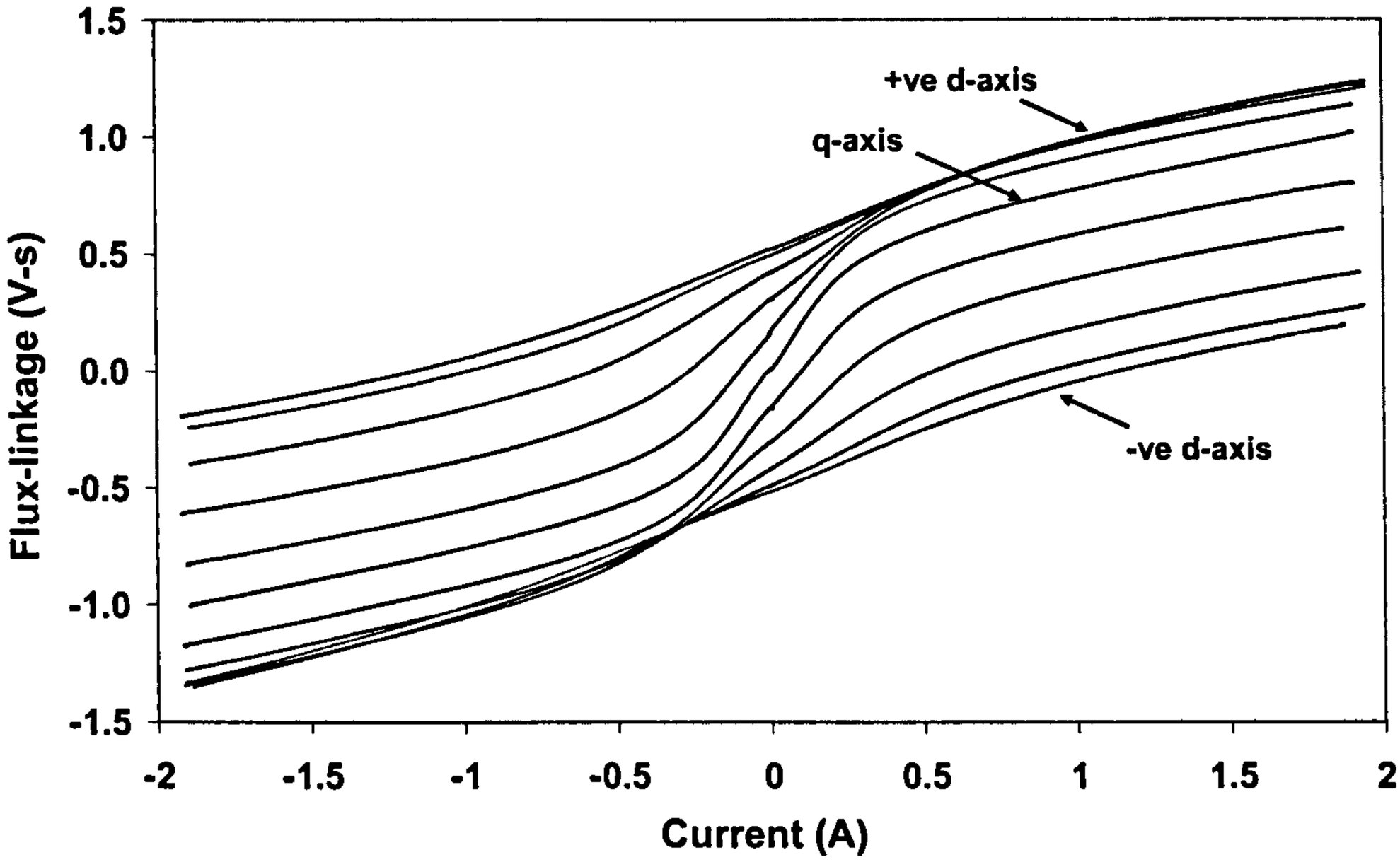

Fig. 2.2. Magnetisation curves of one phase of a permanent-magnet motor

Using the measurement methods described by Cossar and Miller in [24], the change in flux-linkage generated by the application of phase currents can be obtained. However, the method does not take into account the flux-linkage due to the permanent magnets. Making the assumption that the flux-linkage from the permanent magnets remains constant at the open-circuit value even under loading, static magnetisation curves can be constructed by adding the flux-linkage due to the phase currents, calculated from the locked rotor tests described by Cossar and Miller, to the open-circuit magnet flux-linkage at the required rotor position.

The validity of the assumption of constant magnet flux cannot be easily confirmed, as there is no way of directly measuring the flux due to the permanent magnets under load conditions [30]. As such, the magnetisation curves should be measured using a method that avoids any assumption or measurement of the magnet flux-linkage under load. The solution is to measure the total flux-linkage, rather than separate components of flux due to the permanent magnets or the phase currents. Such measurement requires rotation

of the motor under load conditions, and so the resulting magnetisation curves are not static. The rotation of the motor produces time-varying effects, which have been investigated using a dynamometer test rig. The results are reported below.

The motor was mounted on a dynamometer test rig, as shown in Fig. 2.3, and controlled using the SPEED FCIII flexible controller. The flux-linkage under load can be determined from Eq. (2.2). With constant current in the phase winding, it was possible to determine the change in total flux-linkage over a period of time or angle of rotation, but not an absolute value of flux-linkage at any point. At certain rotor positions, high field strengths can act in opposition to the fields from the permanent magnets, leading to partial demagnetisation (the risk is greater if ferrite magnets are used). To determine absolute values of flux-linkages, a reference point is needed whereby the flux-linkage is known for at least one rotor position. If the motor phases are independent of each other, there is no flux-linkage from the permanent magnets at the quadrature axis position. Calculating the flux-linkage for each phase current level at this rotor position (from a switching test) would then provide a reference point for the rotational test results. It is unlikely that there would be no cross-saturation effects between phases, especially at high current levels.

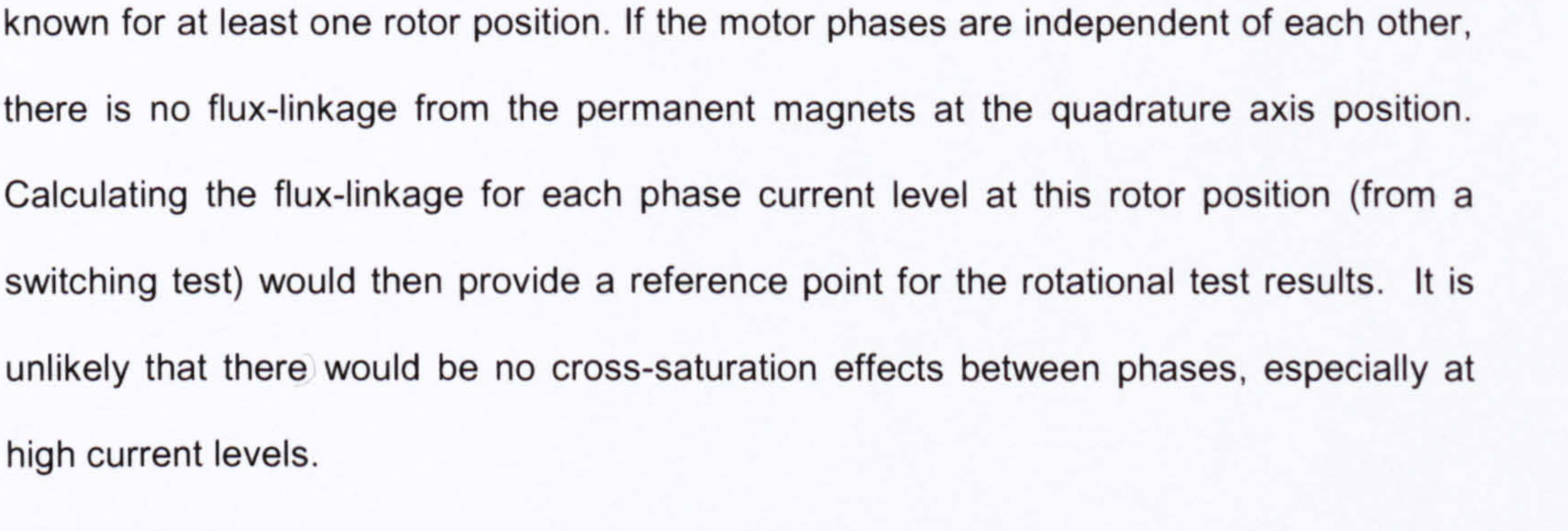

Fig. 2.3. Dynamometer test rig for magnetisation curve measurement.

One solution is to run the tests using the excitation waveform of the motor during normal operation. Using either a sinusoidal or trapezoidal excitation waveform, there are two rotor positions per revolution where there is no current in the phase windings. The flux-

linkage at these points is therefore the open-circuit magnet flux-linkage, which is known from measurement of the open-circuit back EMF waveform. The flux-linkage at all other rotor positions can then be calculated with reference to the two open-circuit rotor positions.

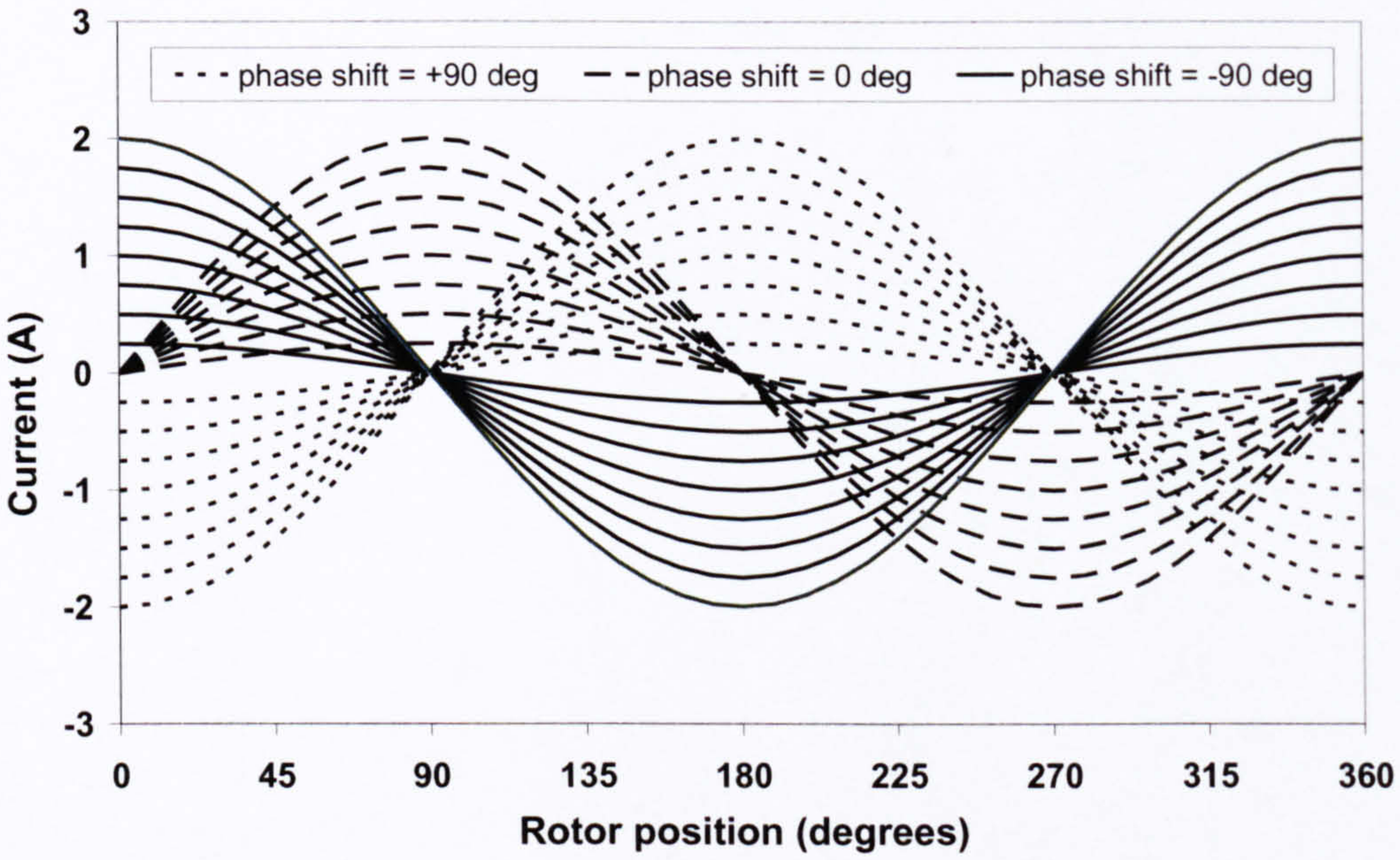

Fig. 2.4. Excitation waveforms for magnetisation curve measurements – changing current levels

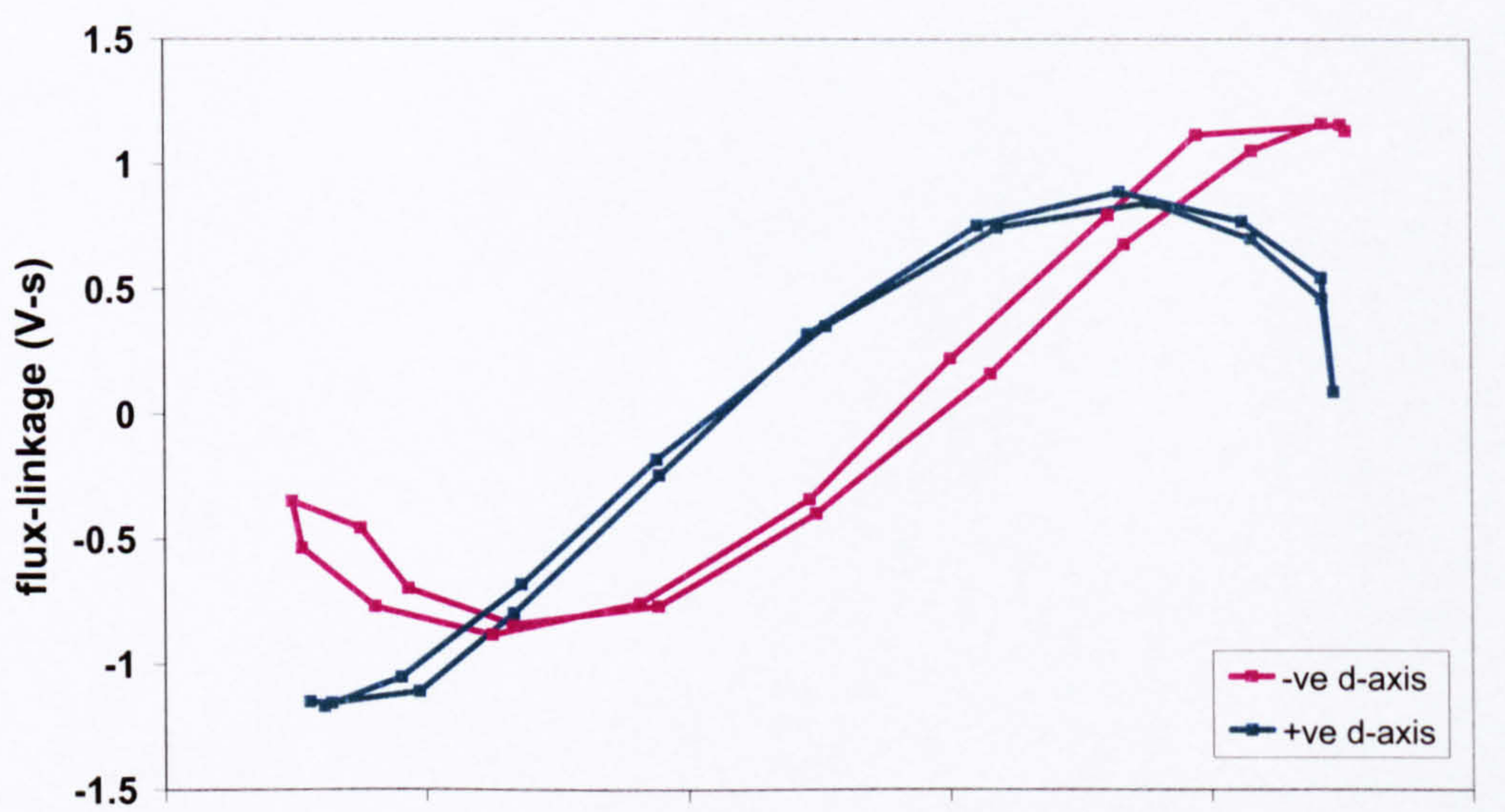

Fig. 2.5. Magnetisation curves resulting from dynamic tests with sinusoidal excitation

A number of problems arise if the tests are run with sinusoidal excitation. To achieve a range of current levels at all rotor positions, the test must either be run at a large number of torque angle values at one current level, which once again risks the partial demagnetisation of the permanent magnets, or at two or three 'safe' γ values over a range of currents (Fig. 2.4). Using the results, curves of flux-linkage versus current at each rotor position can be constructed, as shown in Fig. 2.5.

For each rotor position, there is not one unique magnetisation curve; there are two flux-linkage values for each current value. The lack of uniqueness results from the way in which the magnetisation curves are constructed. For each rotor position, each point on the magnetisation curve is the result of a separate test. Two separate tests can provide the same current at the same rotor position, even though the tests may be run with different γ values or peak currents. Taking Fig. 2.4 as an example, at 135 degrees there will be two different flux-linkage points for each required current level, corresponding to the two different γ values of 0 degrees and -90 degrees. For γ = 0 the current is decreasing at 135 degrees, whereas for γ = -90 it is increasing. The rate of change of current is also different for the different γ values. In effect, the curves at each rotor position exhibit hysteresis effects. With no current in the winding, the flux-linkage should be equal to the open-circuit magnet flux-linkage (0.448 V-s at 0°), but due to hysteresis effects the flux-linkage on open-circuit is reduced, as shown in Fig. 2.5. The hysteresis effects are most significant when the rotor interpolar axis is aligned with the excited phase winding, as there is no presaturation of the magnetic circuit.

The tests must be run using a waveform that eliminates the rate of change of current to obtain single-valued magnetisation curves, whilst fulfilling the criteria of a periodic, zero-crossing excitation waveform to provide reference flux-linkage values. Using ideal squarewave excitation, the current would switch instantaneously between maximum negative and maximum positive levels. Under test conditions, the change in current is not instantaneous due to the limitations of the controller and the inherent properties of the motor. This is illustrated in Fig. 2.6. Test points must be taken at two or more

different torque angle (γ) values to obtain full current and flux-linkage information at all rotor positions. The resulting magnetisation curves are single-valued and analogous to the static magnetisation curves of the switched-reluctance motor.

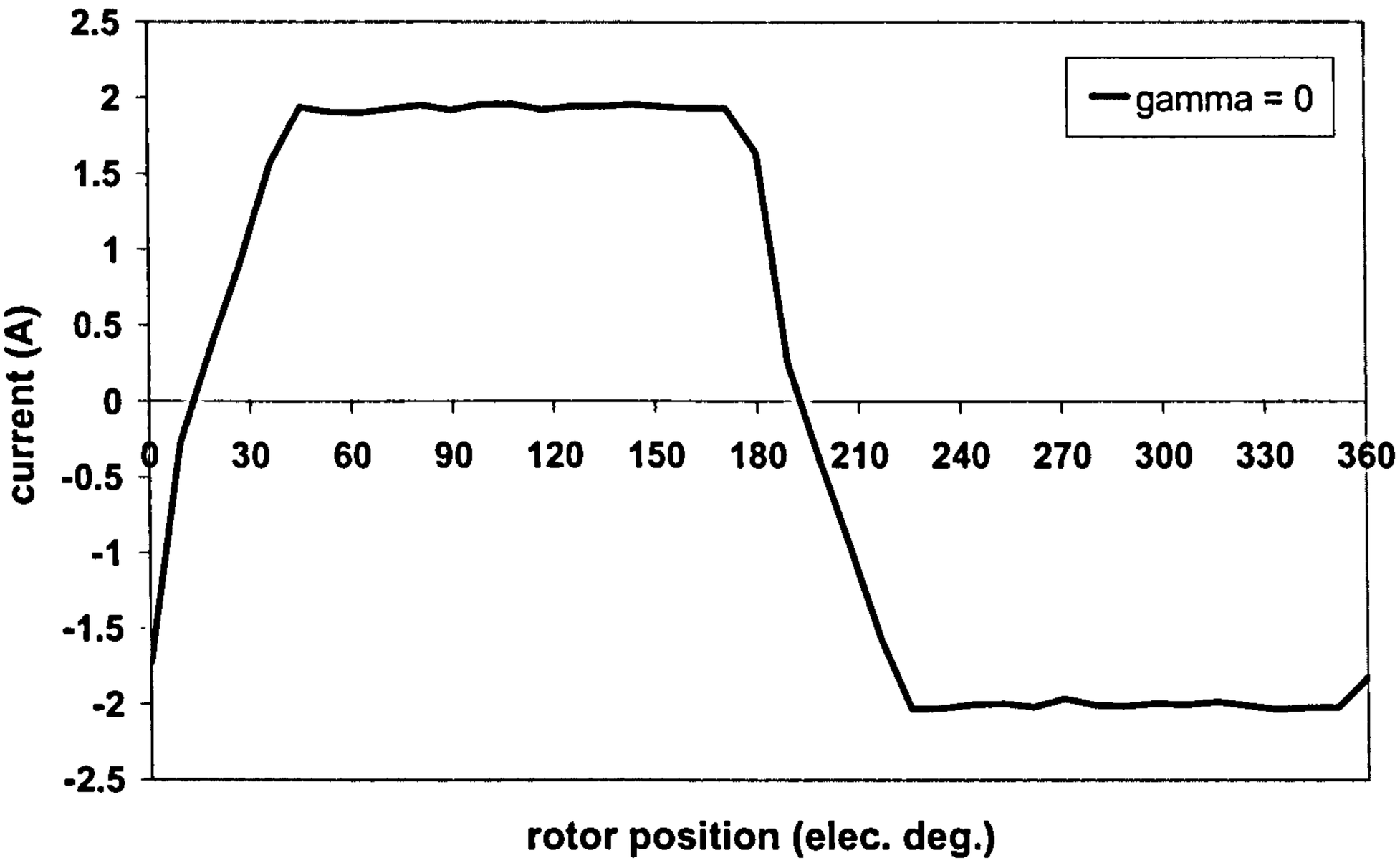

Fig. 2.6. Trapezoidal excitation waveform for dynamic magnetisation curve measurement

2.1.4. Modelling of magnetisation curves of PM motor

Due to the complexity of the magnetic circuit of the permanent-magnet motor, the magnetisation curves cannot be modelled in the same way as those of the switched-reluctance motor. Whereas the magnetisation curves of the switched-reluctance motor are used as an input and the basis for design calculations, the curves of the permanent-magnet motor are generally calculated as part of the design solution and form an output from design simulations. The magnetisation curves of the PM motor are easily calculable using finite element analysis. In PC-FEA, the automatically generated i-ψ loop script can be modified to calculate the magnetisation curves, by changing the phase currents from sinusoidally-varying to DC, and running the simulations over a number of current levels. The magnetisation curves are normally calculated for each phase individually and so do not include the effects of mutual coupling between phases. The resulting curves also neglect hysteresis effects.

In [31], the authors propose a circuit simulation model based on measured or simulated magnetisation curves, represented in the rotor reference frame. The model uses the differential circuit equations to calculate values of ψ_d and ψ_q at each time step. For each value of ψ_d and ψ_q, there is a range of possible values of i_d and i_q that can be found from the stored magnetisation curve data of flux-linkage against phasor current, Fig. 2.7. When the two ranges of current values are plotted on the complex d-q plane, they overlap at one point, which characterises the unique solution to the calculation.

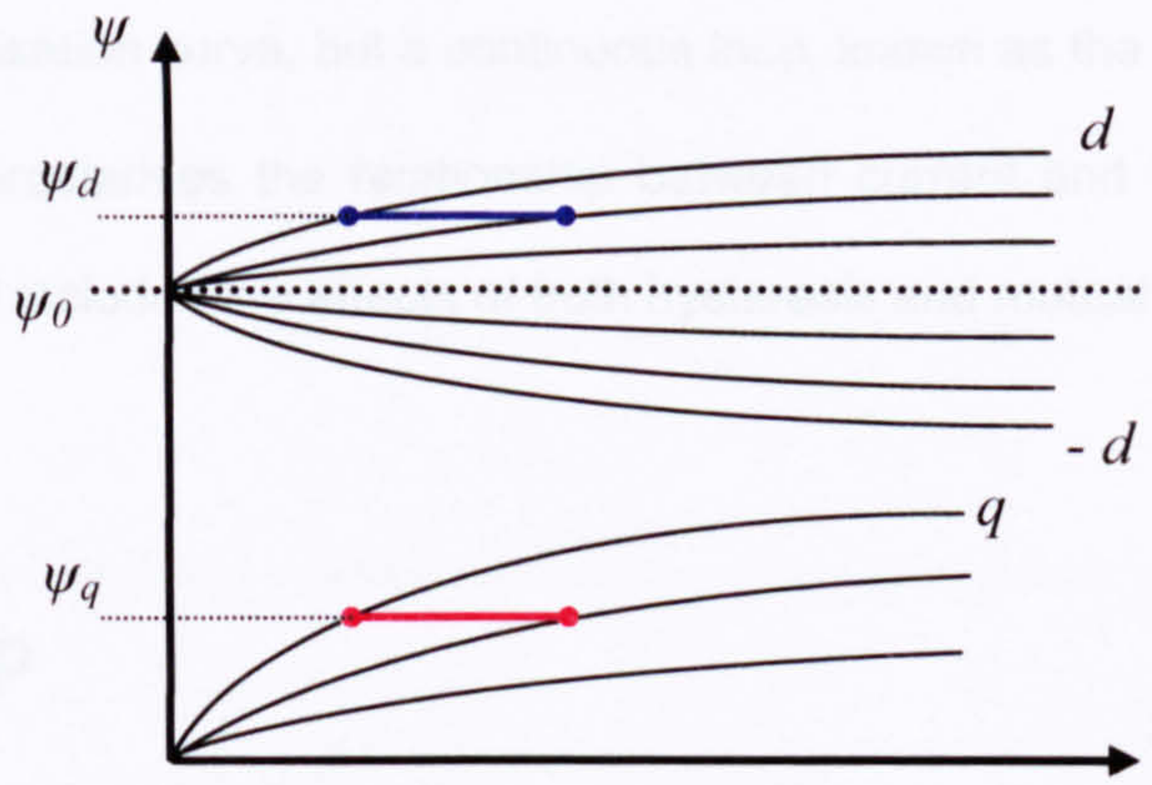

Fig. 2.7. Magnetisation curves represented with phasor currents, showing solution boundaries.

A significant benefit of the model is that the magnetisation curves are represented in terms of a phasor current, rather than the phase or axis currents. As such, cross-magnetisation and mutual coupling effects are considered. However, the model is of limited accuracy, as it uses the static magnetisation curves rather than dynamic characteristics.

The results from the magnetisation curve tests and simulations raise the question as to how accurately the permanent-magnet motor can be represented by static magnetisation curves. Although it is possible to produce single-valued magnetisation curves, they are a result of tests with constant current for most rotor positions. The curves characterise a current/flux-linkage relationship for a specific case of excitation, but such curves do not characterise the normal operation of the motor, where hysteresis

is a factor that must be considered. The flux-linkage at a certain rotor position is dependent not only on the magnitude of the phase current at that instant, but also on the polarity of the current and the rate at which it is changing. Under synchronous operation, the phase currents vary sinusoidally with rotor position and the magnetisation characteristics will not be the same as the static magnetisation curves.

To characterise the current/flux-linkage characteristic at each rotor position during normal operation, the flux-linkage must be calculated from a dynamic test. When the current/flux-linkage trajectory is the then plotted, the result is not a single-valued curve such as a magnetisation curve, but a continuous loop, known as the i-ψ or ipsi loop. The loop uniquely characterises the relationship between current and flux-linkage at each rotor position, and includes the effects of both hysteresis and mutual coupling.

2.2. i-ψ loop

Fig. 2.8(a) gives an example of a magnetisation curve; the stored field energy and coenergy are shown. At any rotor position, the coenergy is defined as the area under the magnetisation curve; this can be calculated using

$$W' = \int_0^{i_1} \psi di \tag{2.5}$$

The area enclosed by two adjacent magnetisation curves, shown in Fig. 2.8(b), represents the change in co-energy required to move between adjacent rotor positions. The instantaneous torque at any rotor position can be calculated from the change in co-energy (which is equivalent to the work done) using

$$T = \left.\frac{\partial W'}{\partial \theta}\right|_{i=const} \tag{2.6}$$

where $\partial\theta$ represents the change in rotor position and W' the coenergy.

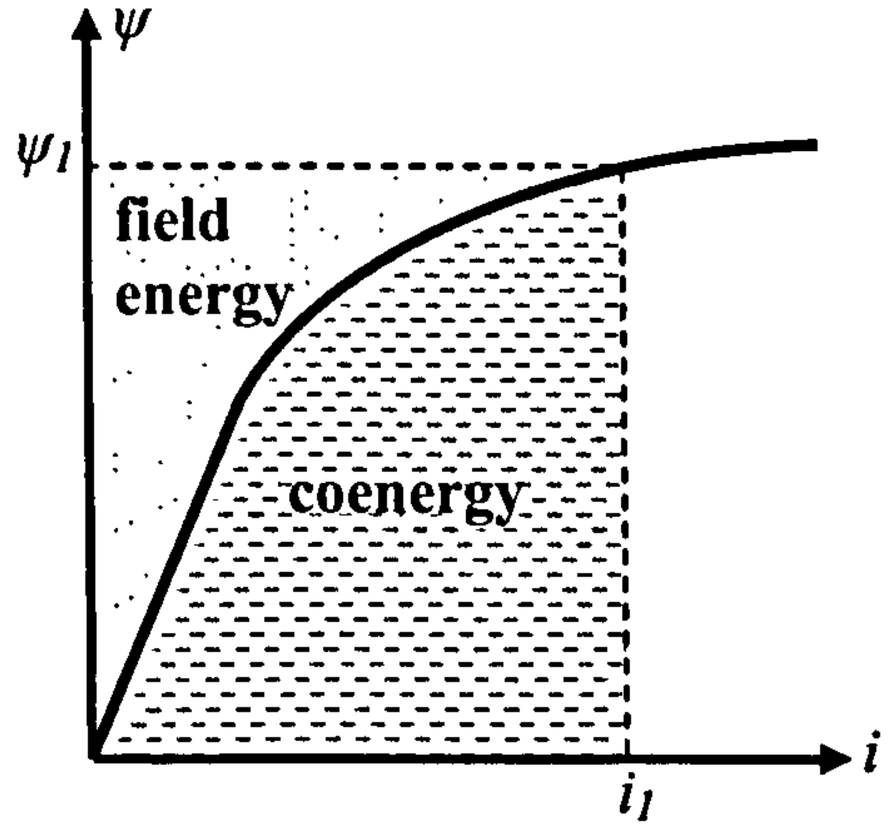

Fig. 2.8(a) aligned magnetisation curve with stored field energy and coenergy marked.

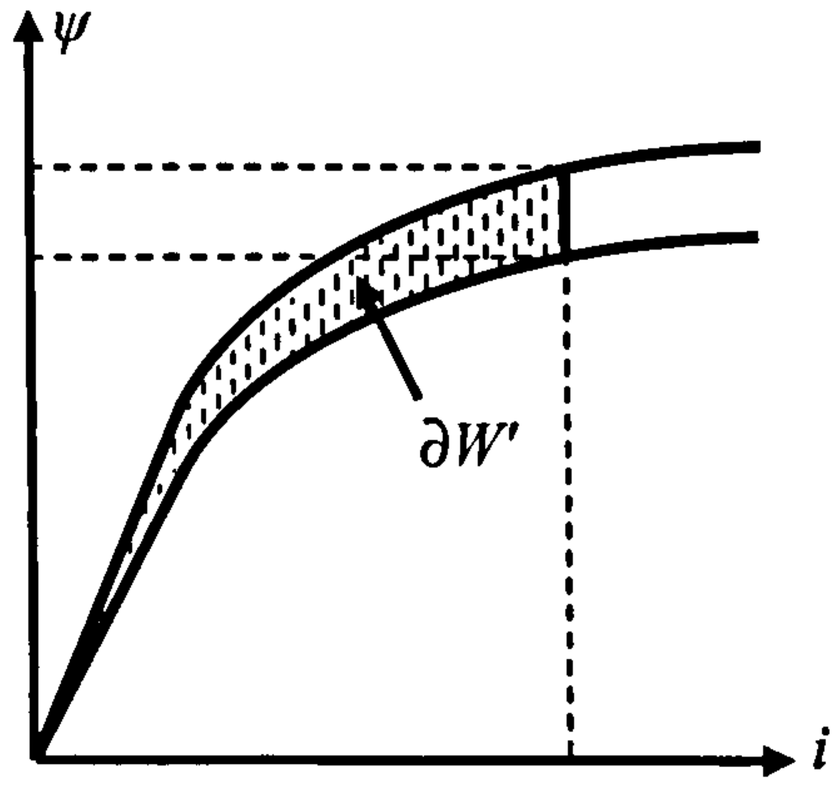

Fig. 2.8(b) change in coenergy between adjacent magnetisation curves.

If W is defined as the loop area over one complete stroke, or displacement from the unaligned to aligned position, then the average electromagnetic torque (which excludes friction and windage and iron loss) is

$$T_{ave} = \frac{SW}{2\pi} \tag{2.7}$$

(where S is the number of strokes per revolution, equal to the number of phases *m* multiplied by the number of rotor poles N_r). From Eq. (2.5) and (2.6), if the phase current and flux-linkage are known, the average electromagnetic torque produced by the energised phase (neglecting friction, windage and core losses) can be calculated. This principle forms the basis of the i-ψ loop for the switched-reluctance machine.

If the phase current is multiplied by the number of turns in series per phase, the magneto motive force (MMF) is found. By dividing the flux-linkage by the number of turns, the effective flux per turn is found[3]. If MMF is then plotted against the effective flux, a loop is produced with an area the same as the ipsi loop, and thus the same torque value can be computed. If each phase is equal and not magnetically coupled with the other phases, the average torque value obtained for the first phase can be multiplied by the number of phases to give the total torque produced by the motor. If the phases are unbalanced, or if there is mutual coupling between phases, then the ipsi loop should be calculated for each phase separately, and the values added to give the total electromagnetic torque over one cycle.

The Flux-MMF diagram makes the number of turns in series per phase an arbitrary constant, and so comparison between different machine types can thus be made. In general, if a machine is driven by sinusoidal currents then the i-ψ or Flux-MMF loops will be elliptical. For motors with squarewave excitation, the loops will be rectangular (see Fig. 2.9). In the case of the switched-reluctance motor, the ipsi loop is contained entirely within the 1st quadrant (positive current and flux-linkage); for other types of motor, the loop covers all four quadrants. This suggests that to produce a given torque, a switched-reluctance motor would need to produce much higher MMF and flux than other types of motor. The i-ψ loop is especially useful in torque calculations for the switched-reluctance motor, as the phasor diagram cannot be used (because it is not possible to perform d-q axis transformations).

---

[3] The effective flux can be thought of as the flux that links the winding to produce torque. It is not the same as the actual flux [33]

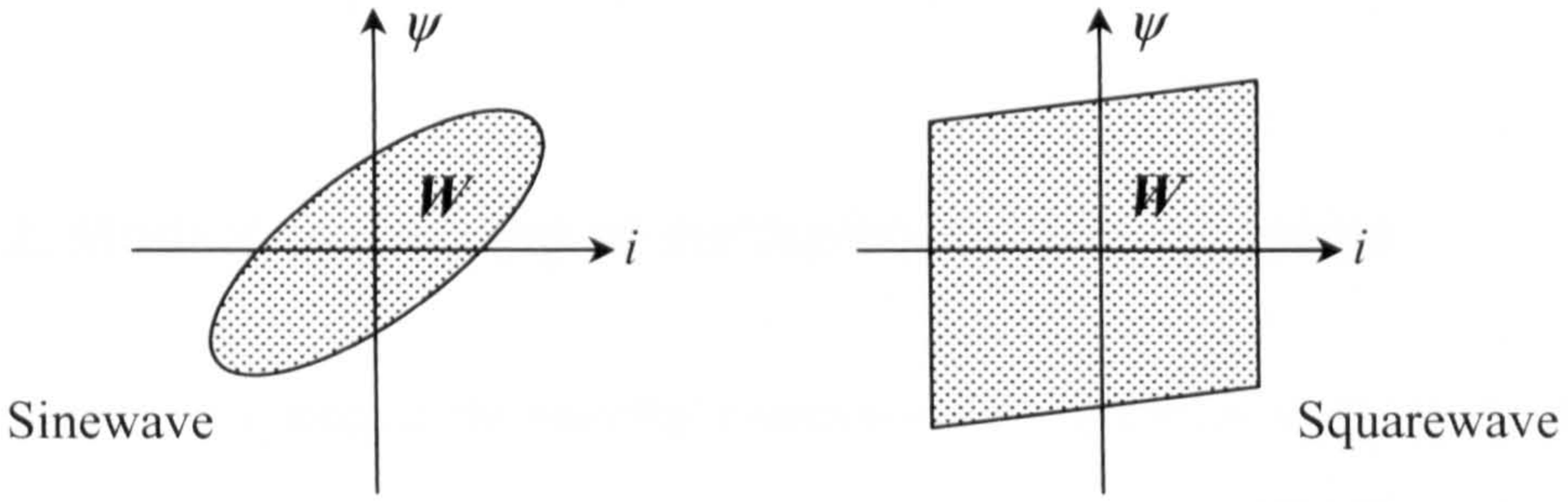

Fig. 2.9. ipsi loops for sinewave and squarewave driven motors

2.2.1. Measuring the *i*-ψ loop of a switched-reluctance motor

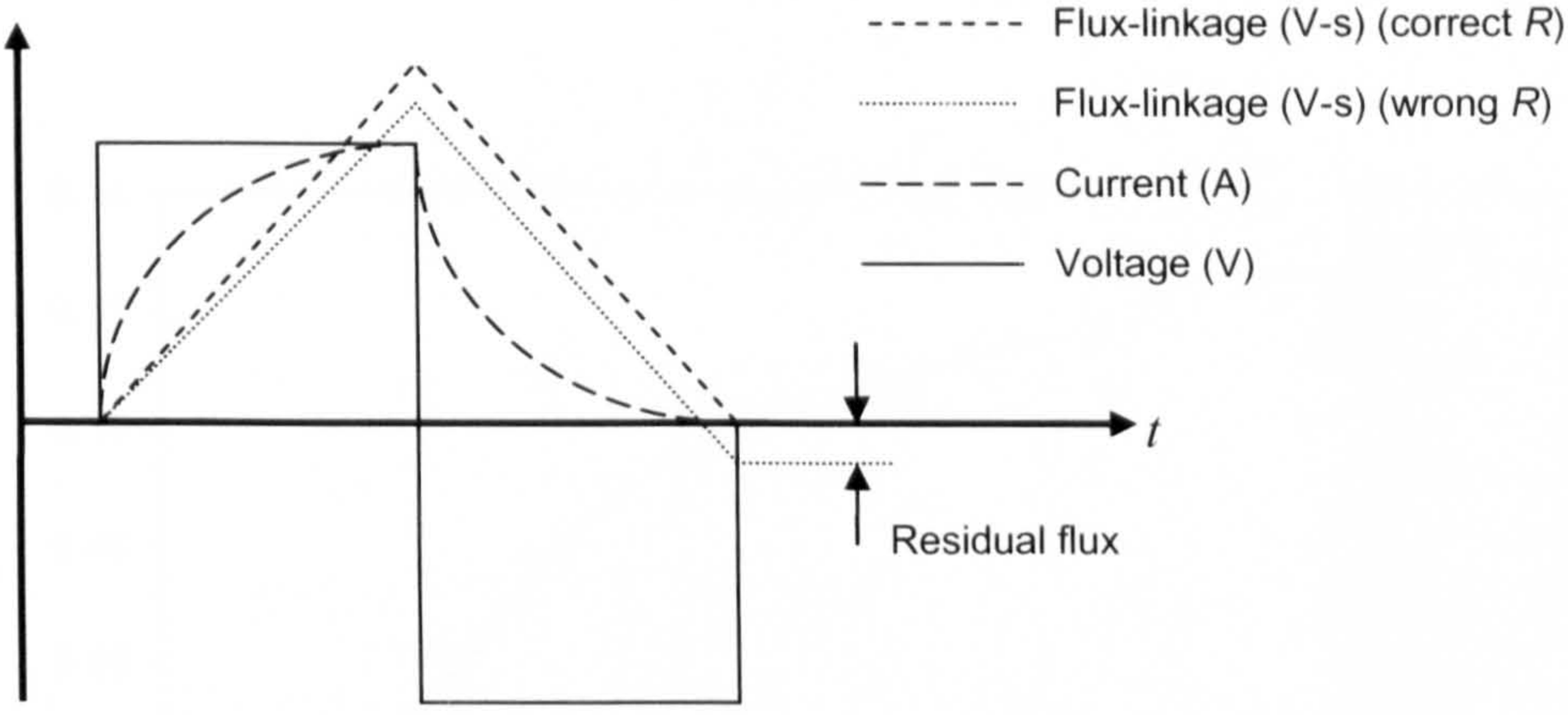

Fig. 2.10. Typical waveforms for single shot operation of SR motor, showing effect of erroneous resistance value.

To calculate the electromagnetic torque from the energy conversion loop, the dynamic flux-linkage and current waveforms are needed. The phase current is measured directly, while the flux-linkage is calculated from the phase voltage using Eq. (2.2). The voltage and current waveforms can be stored using a digital oscilloscope, then imported into Matlab for calculation of the flux-linkage. The phase resistance can be measured on a multimeter, but is subject to variation as the winding temperature increases. As discussed for the magnetisation curve measurements, the correct value of resistance can be determined by inspection of the resultant flux-linkage waveform. Typical

waveforms for single-shot operation are shown in Fig. 2.10. The area of the measured loop is calculated using an internal Matlab command.

2.2.2. Modelling i-ψ loop of switched-reluctance motor

The measured i-ψ loops of the switched-reluctance test motor have also been modelled, in three different ways – from a Simulink model of the motor characteristics, using the analytical design package PC-SRD and from two-dimensional finite element calculations (using PC-FEA). A basic Simulink model of the motor has been developed[4]; details of the model are given in Appendix 2. The model calculates the phase currents in single-phase operation from a two-dimensional look-up table, based on measured magnetisation curves. The model is fast, but does not take mutual coupling effects into account.

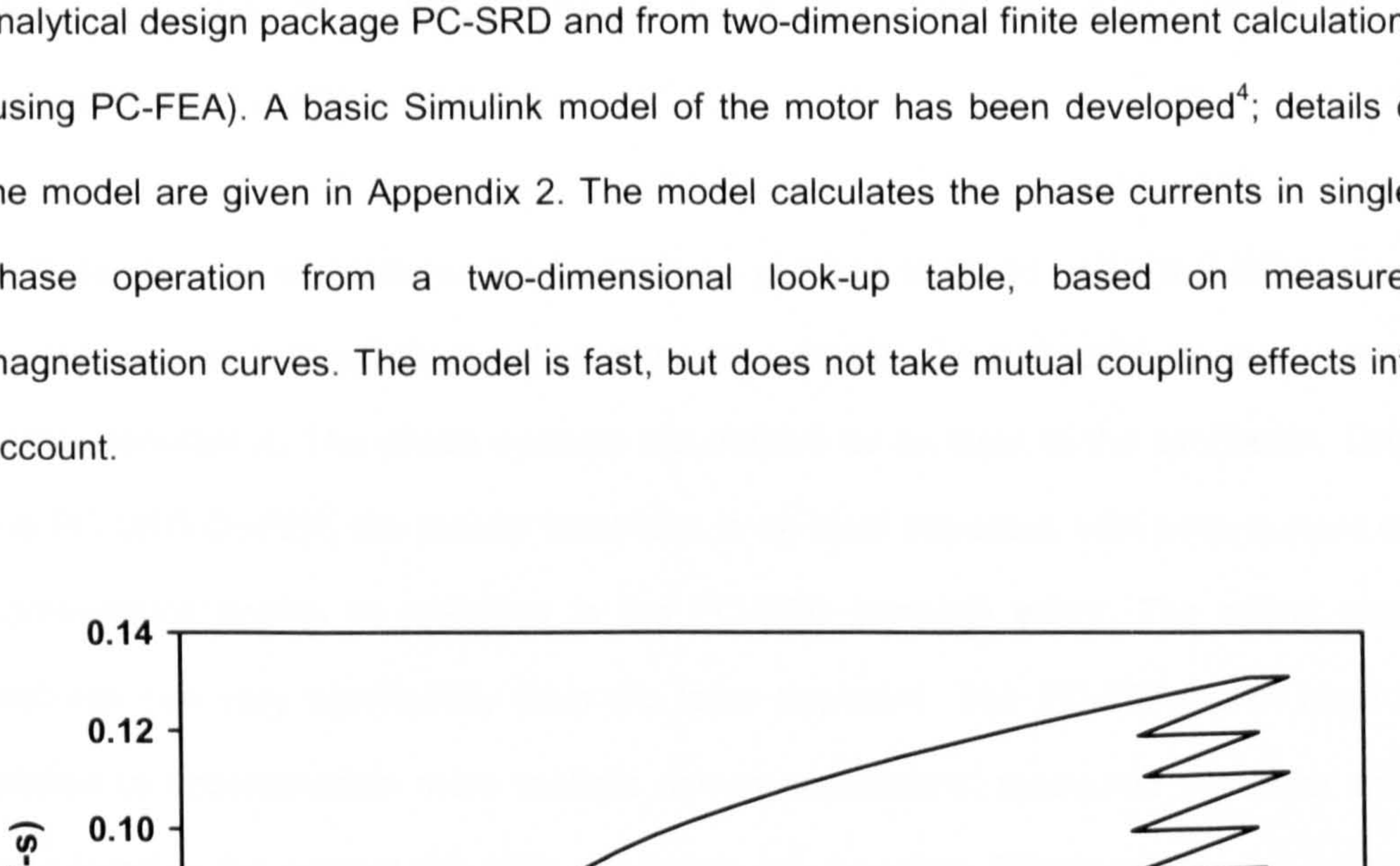

Fig. 2.11. Example i-ψ trajectory calculated from PC-SRD, showing chopping due to current limit

In PC-SRD, the i-ψ loop can be calculated from internally-calculated magnetisation curves or from measured magnetisation data (by setting the type of magnetisation curve

[4] Model developed by Mr. Calum Cossar, manager of the SPEED Laboratory.

calculation to 'external'). Each point on the i-ψ trajectory is calculated by integration of the voltage equation. The magnetisation characteristics are calculated using the method described in [29]. As with the modelling of the magnetisation curves, the calculation of the current/ flux-linkage trajectory ignores any mutual coupling effects between phases. If the peak current is limited, the i-ψ loop may show chopping within the hysteresis band limits set by the user. An example is shown in Fig. 2.11, where the current limit has been set to 20 A, with a 2 A hysteresis band. As soon as the current limit is reached, the soft-chopping begins. The chopping keeps the current within the range of 18 (I_{max} – hysteresis band width) to 20 A.

In finite element simulations, the flux-linkage per turn is found using the difference in weighted average flux-linkage between the two coil sides, calculated from the magnetic vector potential A. The phase currents are defined as an input to the simulation. Using the PC-SRD GoFER, the current waveform is an ideal trapezoid, with peak current and commutation angles as specified in the PC-SRD template editor. The actual phase currents can vary significantly from the ideal trapezoid. The PC-FEA script must be altered to accommodate more realistic current waveforms; measured values or those calculated in the original PC-SRD simulation can be used. The finite element i-ψ loop will include mutual coupling effects for those rotor positions where there is current in more than one phase.

There are errors in the two-dimensional finite element simulation results, because end effects are neglected. [32] advocates 'realignment' of the finite element magnetisation curves to account for three-dimensional effects. The 2D FEA magnetisation curves can be realigned using end-effect adjustment factors, such as those calculated in SPEED PC-SRD, then used in the analytical software to calculate a new i-ψ trajectory that takes into account both 3D effects and mutual coupling between phases. Simulated i-ψ loops calculated from realigned magnetisation curves are given in Chapter 3.

Extensive information on simulation of the i-ψ loop using finite element analysis can be found in a number of works by the University of Glasgow SPEED Laboratory [33-35]. These include information on skew effects and cogging torque calculations (in permanent-magnet machines). The works also include comparison between different motor types including switched-reluctance and permanent-magnet motors.

2.2.3. Measuring the i-ψ loop of a permanent-magnet motor

The i-ψ loop of the permanent-magnet motor can be measured from rotational tests on a dynamic test rig, using the same method as for the switched-reluctance motor. Typical current and flux-linkage waveforms are shown in Fig. 2.12. The PWM voltage signal is omitted from the graph for clarity. As each phase of the motor may be excited by a different current waveform (especially in the case of split-phase motors) and have a different number of turns, the i-ψ loops for each phase must be measured individually.

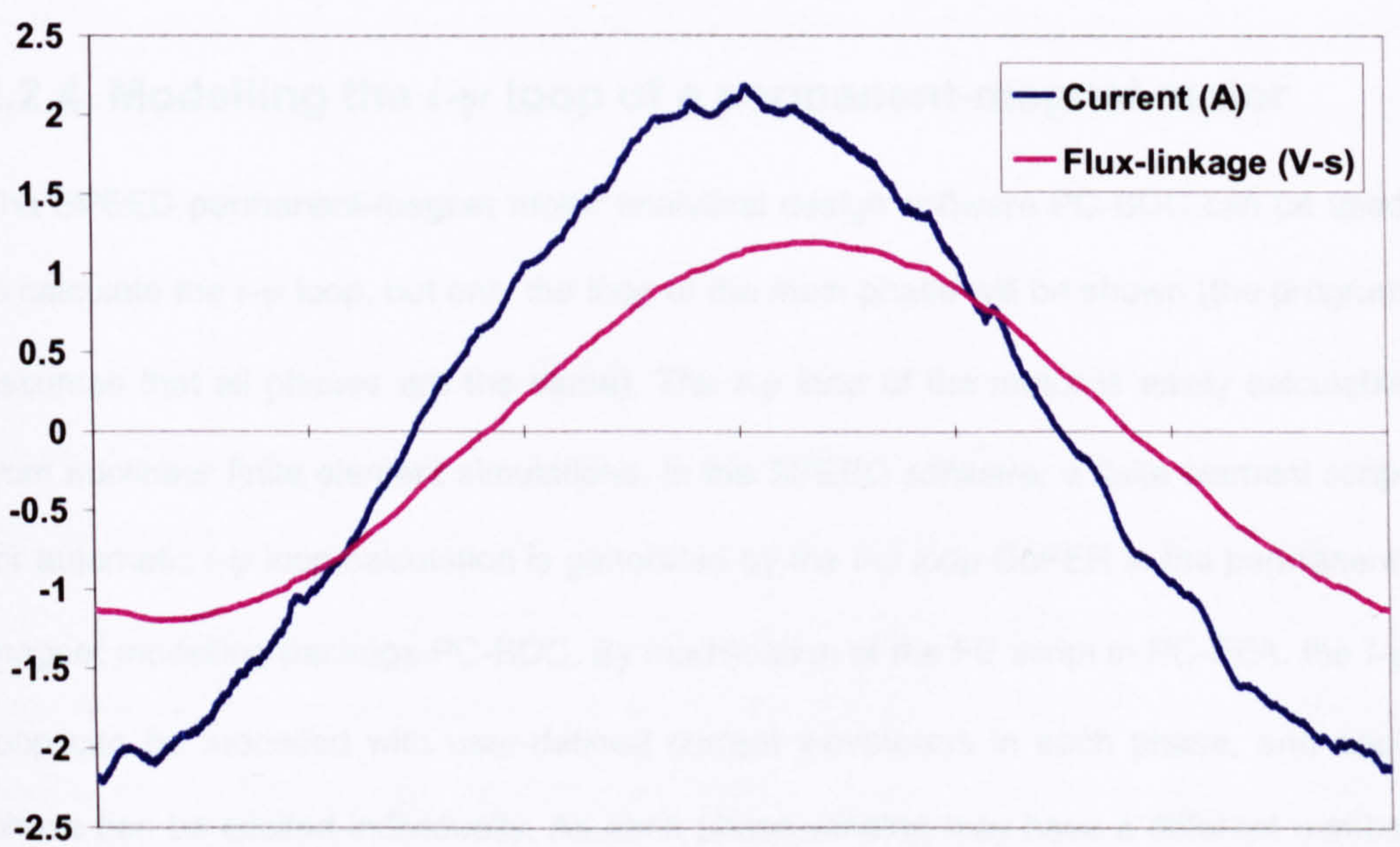

Fig. 2.12. Typical waveforms from rotation test for i-ψ loop measurement on dynamic test rig

The Matlab program used to compute the i-ψ loop of the switched-reluctance motor can be edited to compute the i-ψ loop of the permanent-magnet motor (see Appendix 3). In the case of switched-reluctance motor, the initially-calculated flux-linkage waveform was

plotted, then the value of phase resistance adjusted until the sections between pulses were zero. For the case of the permanent-magnet motor, the flux-linkage waveforms are sinusoidal and continuous, so this method is no longer valid. Instead, the value of phase resistance can be measured at ambient temperature, and then adjusted according to the temperature variation under test. The winding temperature is measured using a thermocouple embedded in the phase winding. The winding resistance under test can be determined from Eq. (2.18) and then used to calculate the flux-linkage. The value of resistance used in the tests can be confirmed by running a dynamic test with current in the winding for only 180 electrical degrees. If the value of resistance is correct, the resultant calculated flux-linkage waveform will return to zero (no residual flux-linkage, as in the switched reluctance tests).

$$R_{test} = \frac{R_T\left(t_{test} + k_{winding}\right)}{\left(t_T + k_{winding}\right)} \tag{2.18}$$

2.2.4. Modelling the i-ψ loop of a permanent-magnet motor

The SPEED permanent-magnet motor analytical design software PC-BDC can be used to calculate the i-ψ loop, but only the loop of the main phase will be shown (the program assumes that all phases are the same). The i-ψ loop of the motor is easily calculable from nonlinear finite element simulations. In the SPEED software, a finite element script for automatic i-ψ loop calculation is generated by the i-ψ loop GoFER in the permanent-magnet modelling package PC-BDC. By modification of the FE script in PC-FEA, the i-ψ loop can be modelled with user-defined current waveforms in each phase, and each phase can be excited individually. As each phase winding may have a different number of turns, the peak current in each phase can vary accordingly. The i-ψ loops generated by finite elements include mutual coupling between phases but ignore dynamic effects.

2.3. Finite element frozen permeability method

The frozen permeability technique is a finite element method for apportioning the total flux-linkage, determined from the magnetic vector potential, into contributions from each individual field source. The method can be used to calculate the self and mutual flux-linkages from each source, for any given excitation waveforms. The method can also be used to solve permanent-magnet motors. A complete nonlinear solution is run for each required rotor position and excitation, and the permeabilities for each element in the mesh are stored. Using these "frozen" permeabilities, a linear solution is then calculated for each field source in turn. These linear solutions provide the self flux-linkage due to the excited field source, and also the mutual flux-linkages generated in each of the unexcited phases.

The principle behind the method can be explained using Figs. 2.13 and 2.14. Fig. 2.13 shows a typical *B-H* curve of electrical steel laminations as would be used in simulation of an IPM motor. Running a nonlinear simulation calculates the total applied field in each element of the finite element mesh. With all field sources applied, the operating point of the steel is moved along the *B-H* (or *H* v μ_r curve).

Taking as an example Fig. 2.13, assume the total field in the element is 40 kA/m, the corresponding flux density is 2.15 T and the relative permeability 42.77. The field from the first source is 15 kA/m, corresponding to a relative permeability of 102.39 (from Fig. 2.14). If the flux density is calculated from the first source alone, as in the nonlinear simulation with one phase excited, the flux density is 1.93 T. Using the same calculation for the second field source, using the permeability of 65.25, the flux density is 2.05 T. Adding the flux densities calculated with each phase singly excited gives a result of 3.98T, which is almost double the total flux-linkage calculated from the nonlinear solution with all phases simultaneously excited.

However, if the permeability from the nonlinear simulation (42.77) is used, the flux density due to the first field source is 0.806 T and from the second source is 1.344 T. Together the sources give a total flux density of 2.15 T, which is exactly the same as that calculated from the nonlinear solution with all phases simultaneously excited.

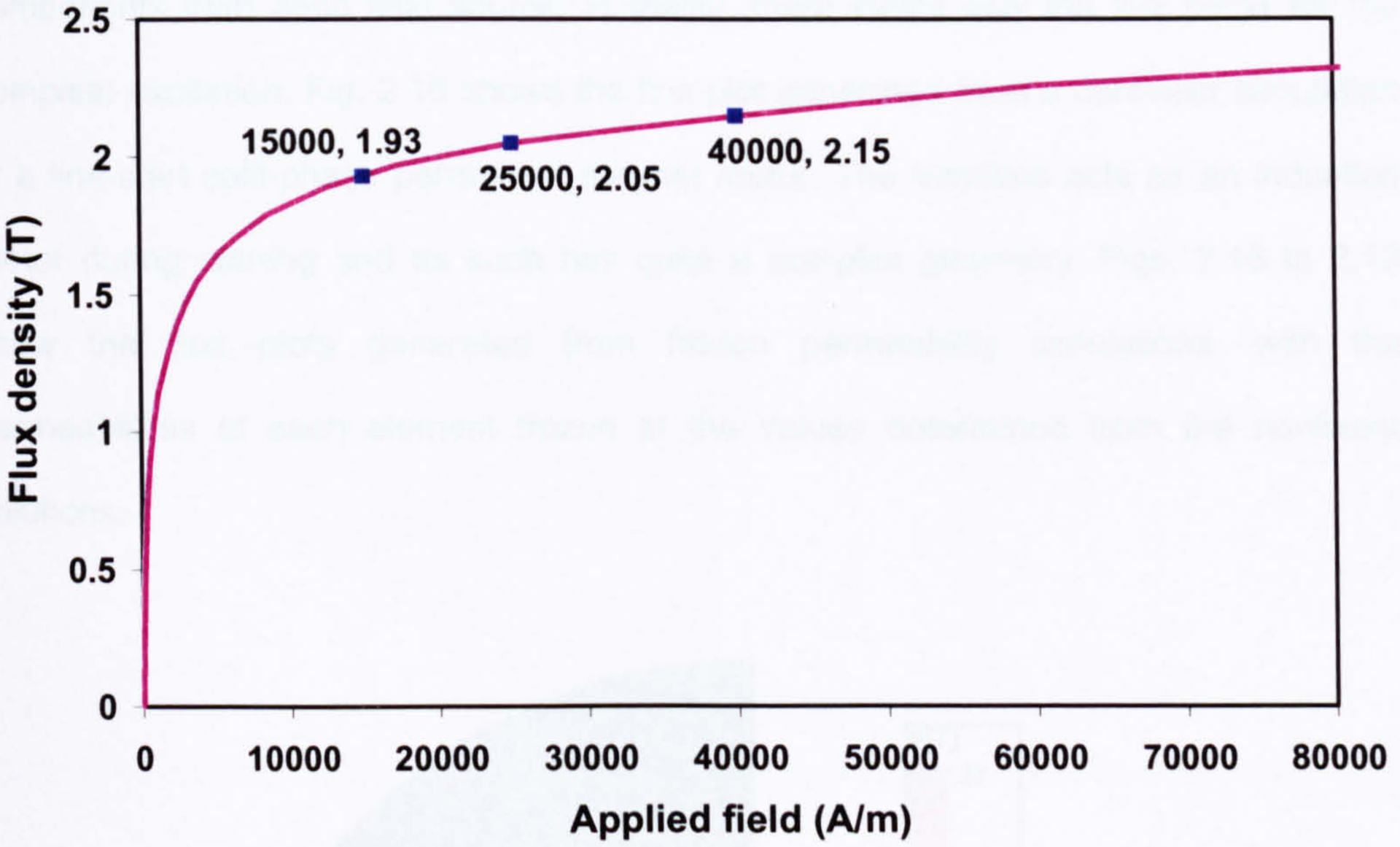

Fig. 2.13. Typical *B-H* curve of IPM motor lamination steel.

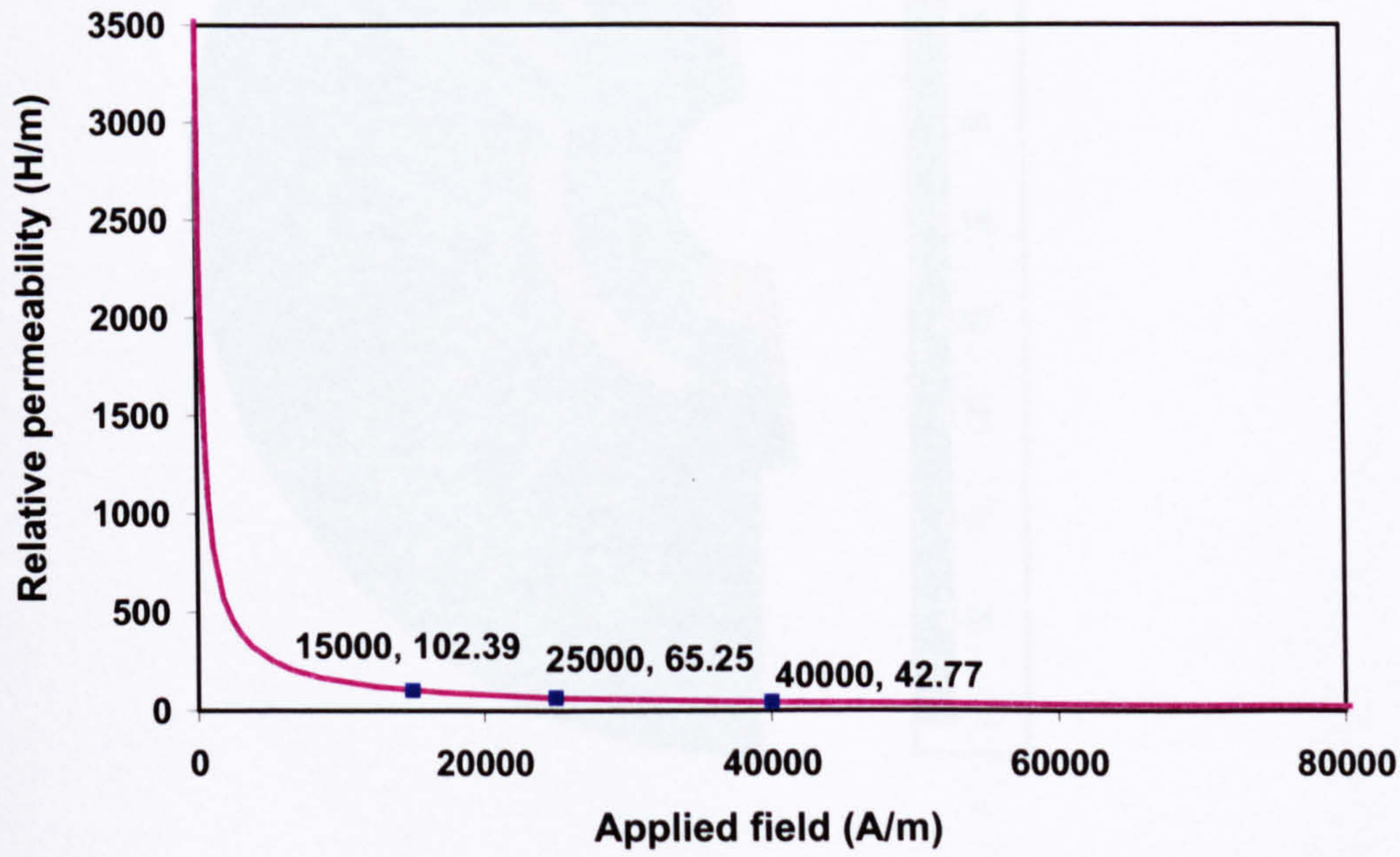

Fig. 2.14. Corresponding *H*-μ_r characteristic of IPM motor lamination steel.

For each frozen permeability solution, a flux plot is produced showing the flux lines that would exist in the case of the given permeabilities and single-source excitation. For each phase, the sum of the individual frozen permeability flux contributions from each field source will equal the total flux-linkage calculated from the initial nonlinear solution. These flux plots are conceptual and represent the circuit breakdown of the flux into components from each field source; in reality, there exists only the flux paths for the complete excitation. Fig. 2.15 shows the flux plot generated from a nonlinear simulation of a line-start split-phase permanent-magnet motor. The machine acts as an induction motor during starting and as such has quite a complex geometry. Figs. 2.16 to 2.18 show the flux plots generated from frozen permeability simulations, with the permeabilities of each element frozen at the values determined from the nonlinear solutions.

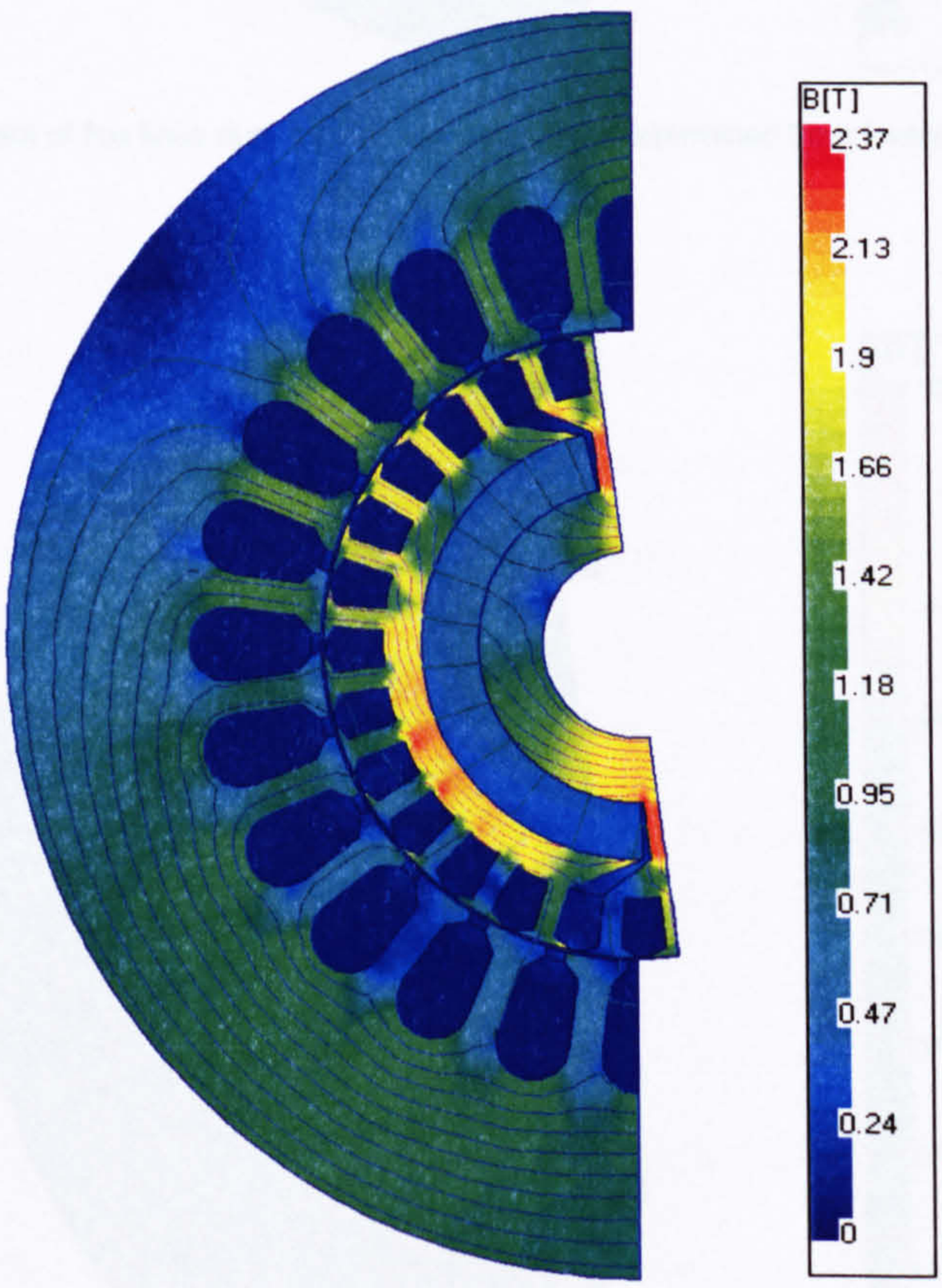

Fig. 2.15. Flux plot showing total flux, generated from complete nonlinear solution

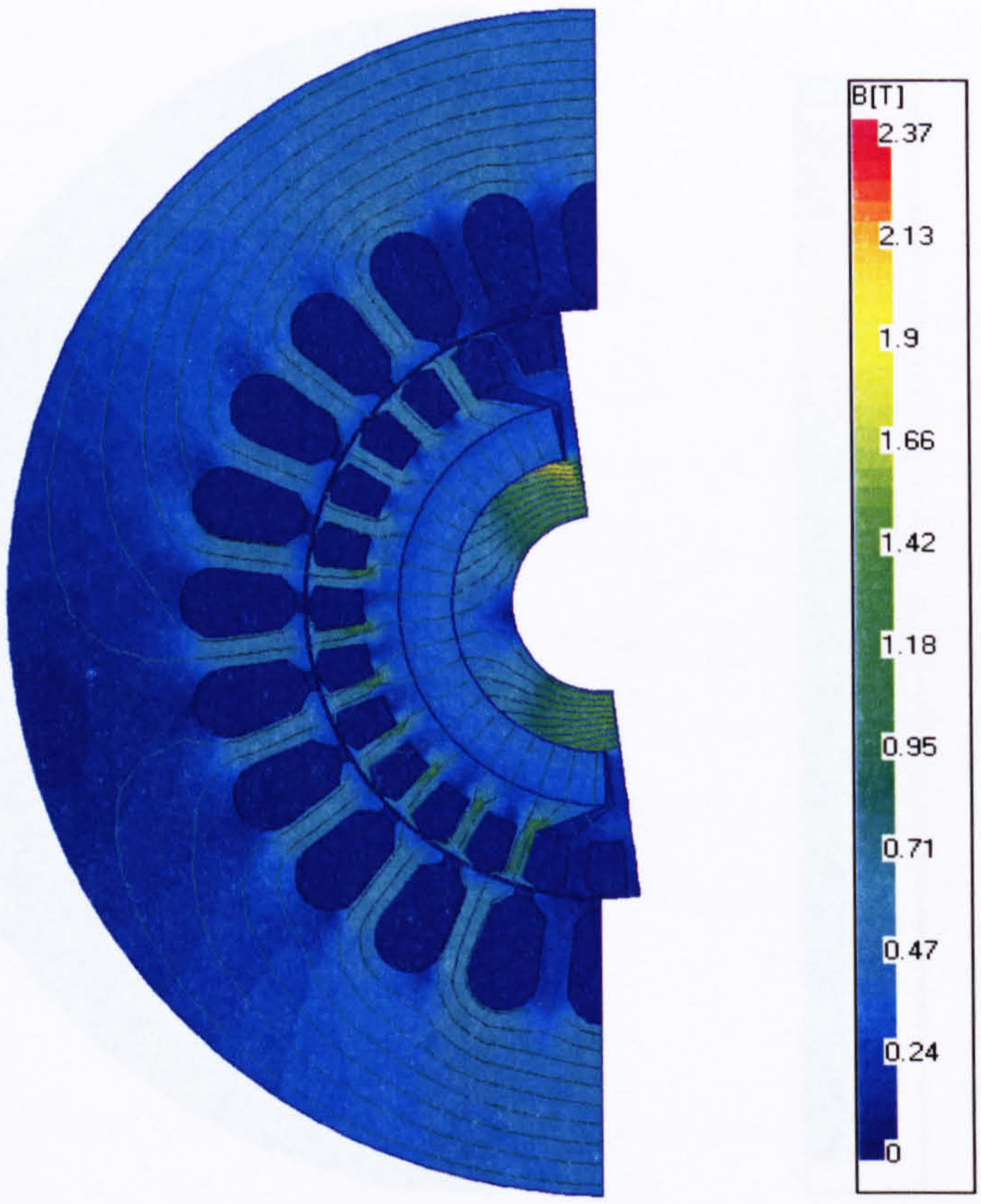

Fig. 2.16. Flux plot of flux lines due to permanent magnets, determined from frozen permeability solution

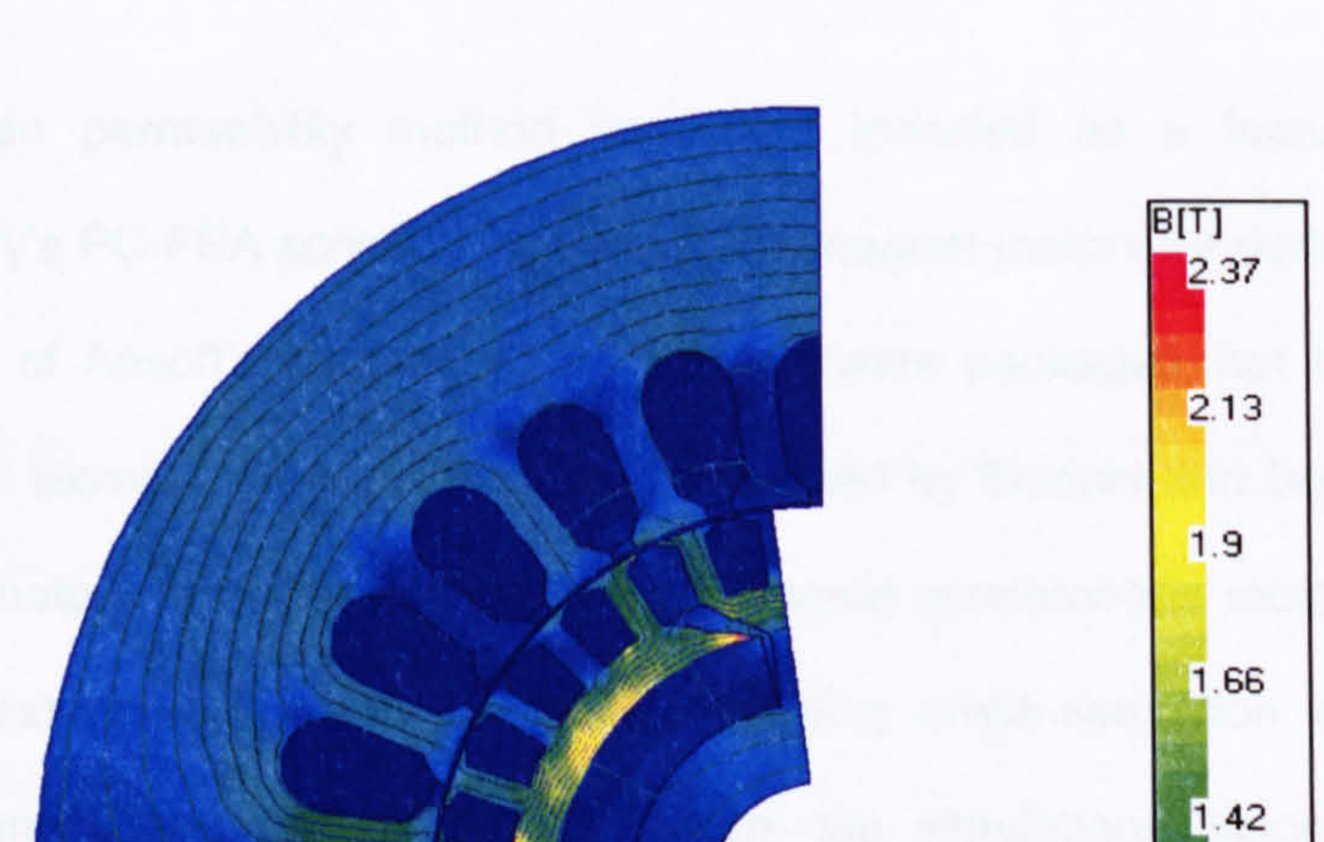

Fig. 2.17. Flux plot of flux lines due to current in phase 1, determined from frozen permeability solution

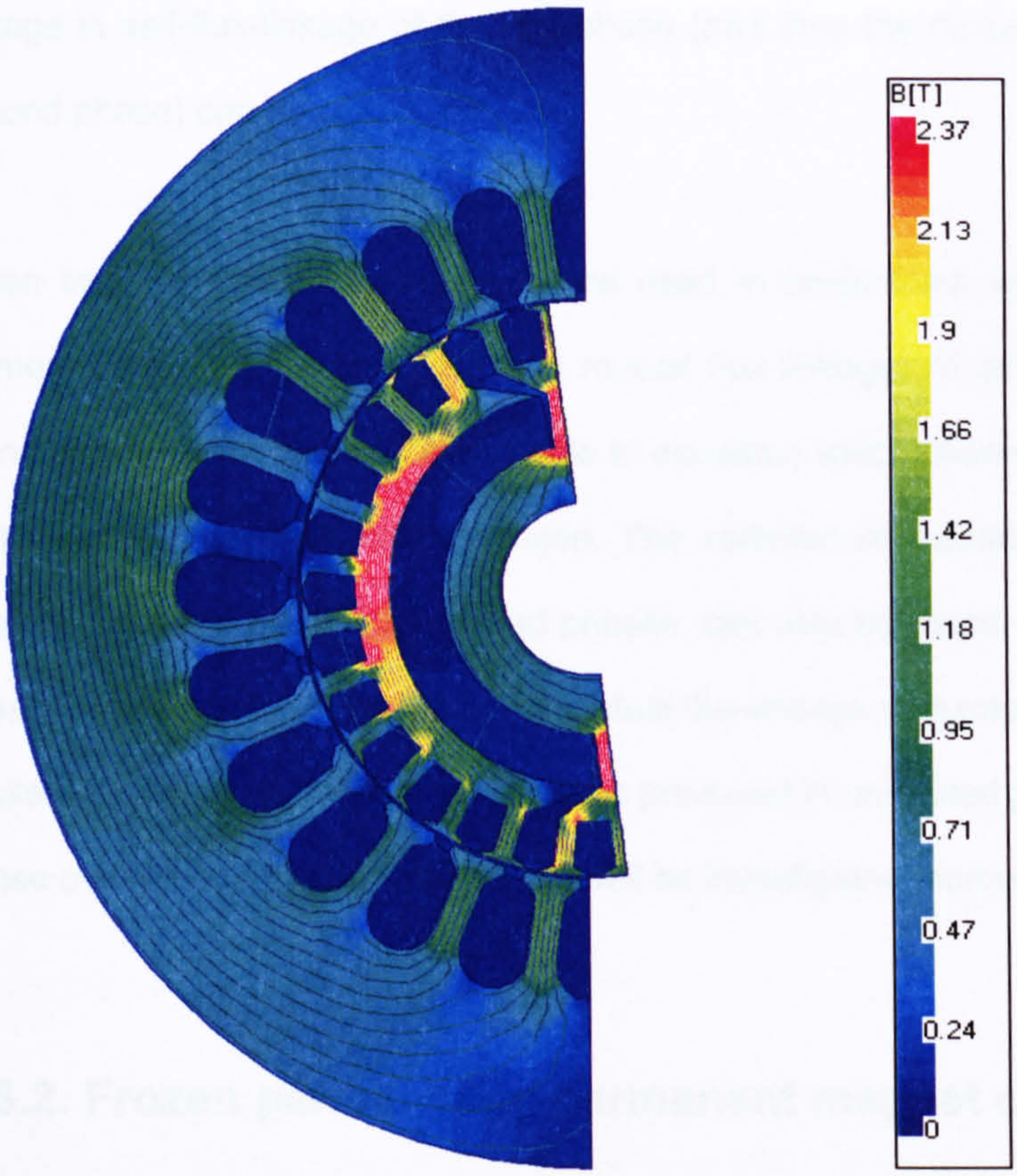

Fig. 2.18. Flux plot of flux lines due to current in phase 2, determined from frozen permeability solution

The frozen permeability method has been included as a feature in the SPEED Laboratory's PC-FEA scripting for permanent-magnet motors for some years, and is now a feature of Ansoft's Magnet 2D and 3D software packages, but there is little on the method in literature. The method has been used by Bianchi and Bolognani to calculate the parameters of an interior permanent-magnet synchronous motor [36]. The authors present extensive simulation results, including cross-saturation effects, but do not include any measurement data to confirm the simulations, since there is no direct method of verification.

2.3.1. Frozen permeability switched-reluctance calculations

The frozen permeability method is useful for calculation of mutual coupling between phases of the switched-reluctance motor. While the change in the total flux-linkage in an excited phase due to the excitation of a second phase can be calculated from the standard nonlinear simulation, it is only with the frozen permeability method that the

change in self-flux-linkage of the first phase (and thus the mutual flux-linkage from the second phase) can be calculated.

When frozen permeability solutions are used in conjunction with the nonlinear finite element solutions, the total, self and mutual flux-linkages of all phases can easily be found. From these results, it is possible to ascertain which phases produce the greatest mutual effects for each excited phase. The variation of mutual flux-linkage with rotor position, with any number of excited phases, can also be found. Previously, it was only possible to determine the variation of mutual flux-linkage with rotor position with only one excited phase (i.e. the mutual flux-linkage produced in unexcited phases). The effects of phase overlap and mutual inductances will be investigated thoroughly in Chapter 4.

2.3.2. Frozen permeability permanent magnet calculations

The frozen permeability method can also be used to calculate the self and mutual flux-linkages of the permanent-magnet motor, as for the switched-reluctance motor. In addition, the method also enables the calculation of the individual components of flux-linkage due to current and the permanent magnets in each phase, where previously it was not possible to determine the magnet flux-linkage under load conditions from finite element solutions.

The permanent magnets are treated exactly like an additional current source. To calculate the flux-linkage from the permanent magnets, the frozen permeabilities from the nonlinear solution are used in a linear solution, with the current sources 'switched off'. The magnet properties remain the same. To calculate the flux-linkage from the phase current, the permanent magnets are 'switched off' for the linear solution, by setting the remnant flux densities B_{rr} and B_{tt} to zero. The use of the frozen permeability method to measure the synchronous reactances of the permanent-magnet motor is discussed in detail in Chapter 5.

2.4. Conclusions

This chapter has discussed the two main methods of measuring the magnetisation characteristics of both switched reluctance and permanent-magnet motors – per-phase magnetisation curves and i-ψ loops.

The measurement of per-phase magnetisation curves of permanent-magnet motors is more complicated than for switched-reluctance machines, due to the additional excitation from the permanent-magnets. It has been shown that to accurately define the magnetisation characteristics of permanent-magnet machines, the magnetisation curves can no longer be measured using static test methods. The method of measurement of i-ψ loops is similar for both types of machine.

This chapter has also discussed how to determine the magnetisation characteristics of both motor types analytically, using spreadsheet-type and finite element motor design packages. In the next chapter, the above-mentioned methods are used to compare measured and simulated magnetisation characteristics.

Chapter 3

Measured and Simulated Magnetisation Characteristics

3.1. Measured and simulated magnetisation curves of SR motor

In this chapter the simulation results from both a commercial spreadsheet-type analytical design package (SPEED PC-SRD) and a two-dimensional finite element package (SPEED PC-FEA) are presented, and their shortcomings discussed.

The measurement of the magnetisation curves is based on the direct method described by Cossar and Miller in [24]. Only the phase under test was excited. The initial rotor position was found by energising the test phase, which causes the rotor to move into alignment with the test phase (the position of minimum reluctance). The rotor was then clamped into position using a dividing head, as shown in Fig. 3.1. The dividing head allows rotation of the shaft in small increments. A pin and disk configuration on the side of the dividing head allows varying degrees of accuracy to be selected, by selecting tracks at different radii from the centre of the disk (as illustrated in Fig. 3.1). The disk was set to allow measurement of magnetisation curves at three degree intervals, with a resolution of 0.33 mechanical degrees.

A resolver was used to confirm the rotor position at each test point. The phase winding was energised with a pulsed voltage waveform; the peak current was controlled by variation of the pulse duration. The voltage and current waveforms at each rotor position were stored and used to calculate the flux-linkage using Eq. (2.2). The phase resistance was determined graphically. The resulting magnetisation curves from the unaligned to the aligned position are shown in Fig. 3.2.

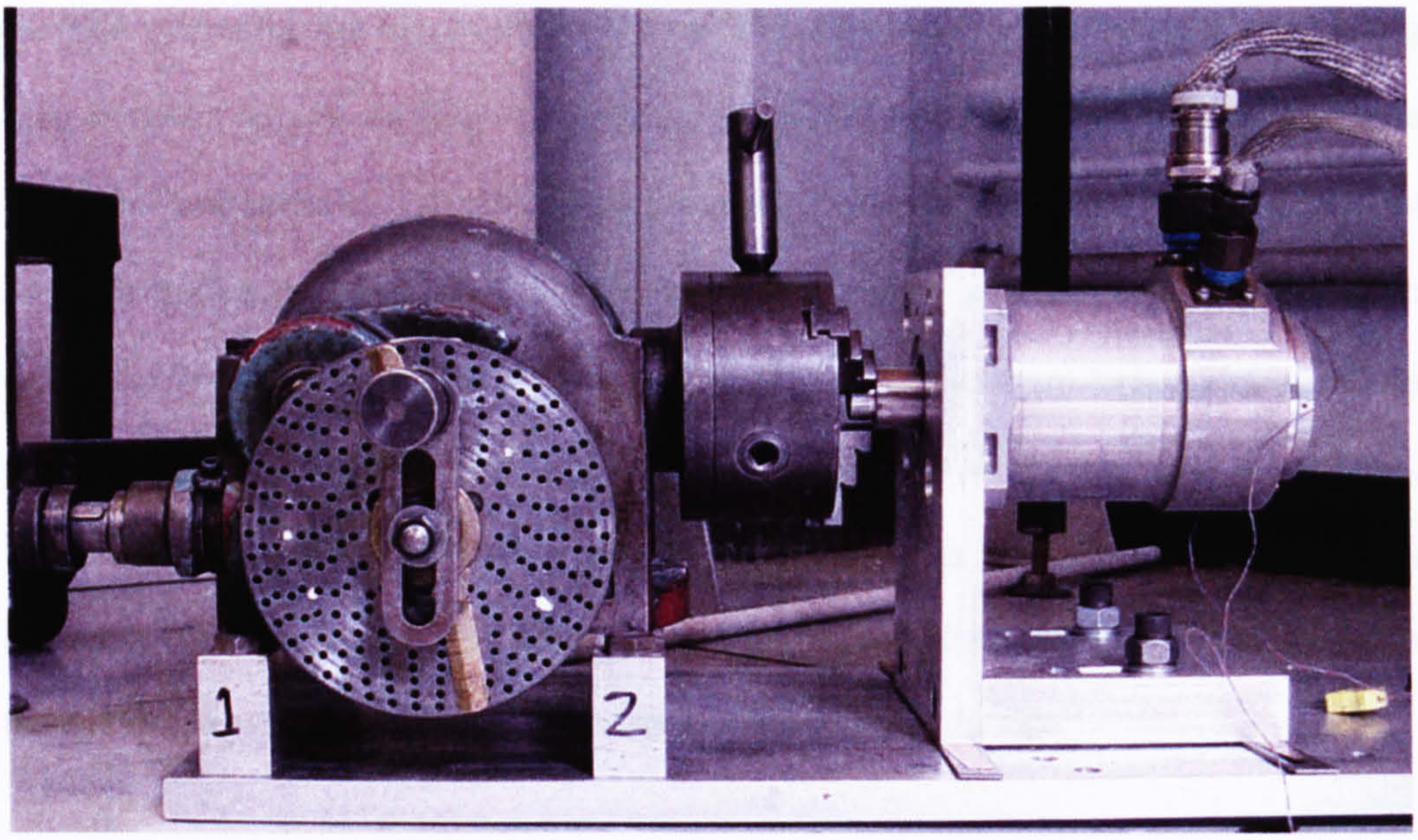

Fig. 3.1. Switched-reluctance motor mounted on dividing head test rig

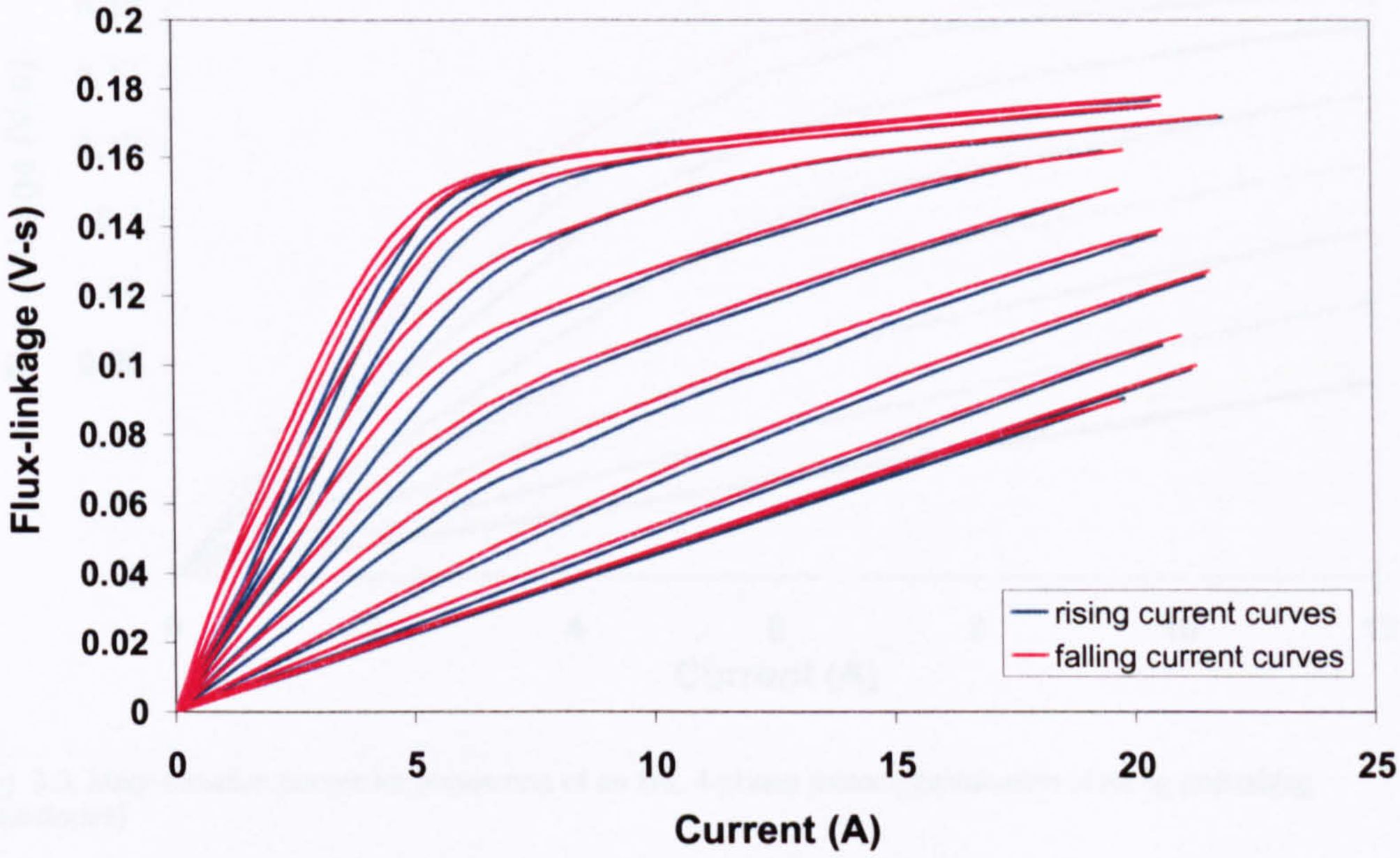

Fig. 3.2. Measured magnetisation curves of the Switched-Reluctance test motor

Fig. 3.2 shows that the rising and falling trajectories of the magnetisation curve differ, due to hysteresis effects in the steel. The difference between the two trajectories is smallest at the unaligned position, and increases as the rotor moves towards the aligned position (due to the reduced airgap). Ref. [23] ignores these effects entirely, while Ref. [26] suggests finding the average flux-linkage value at each point and using these

average points for the magnetisation curve. This would, however, result in misleading magnetisation curves, as any measured i-ψ loops may fall outside the boundaries of the 'average' magnetisation curves. Using average magnetisation curves in analytical software packages (such as PC-SRD) to calculate the i-ψ loops would also lead to erroneous results. The curves determined from the falling current trajectories could be used for all rotor positions, to ensure that the i-ψ loop falls inside the curve boundaries; however, although the difference between the two sets of curves is least at the unaligned position, using the falling current trajectories for rotor positions before the turn-off angle will introduce errors into the loop torque calculations.

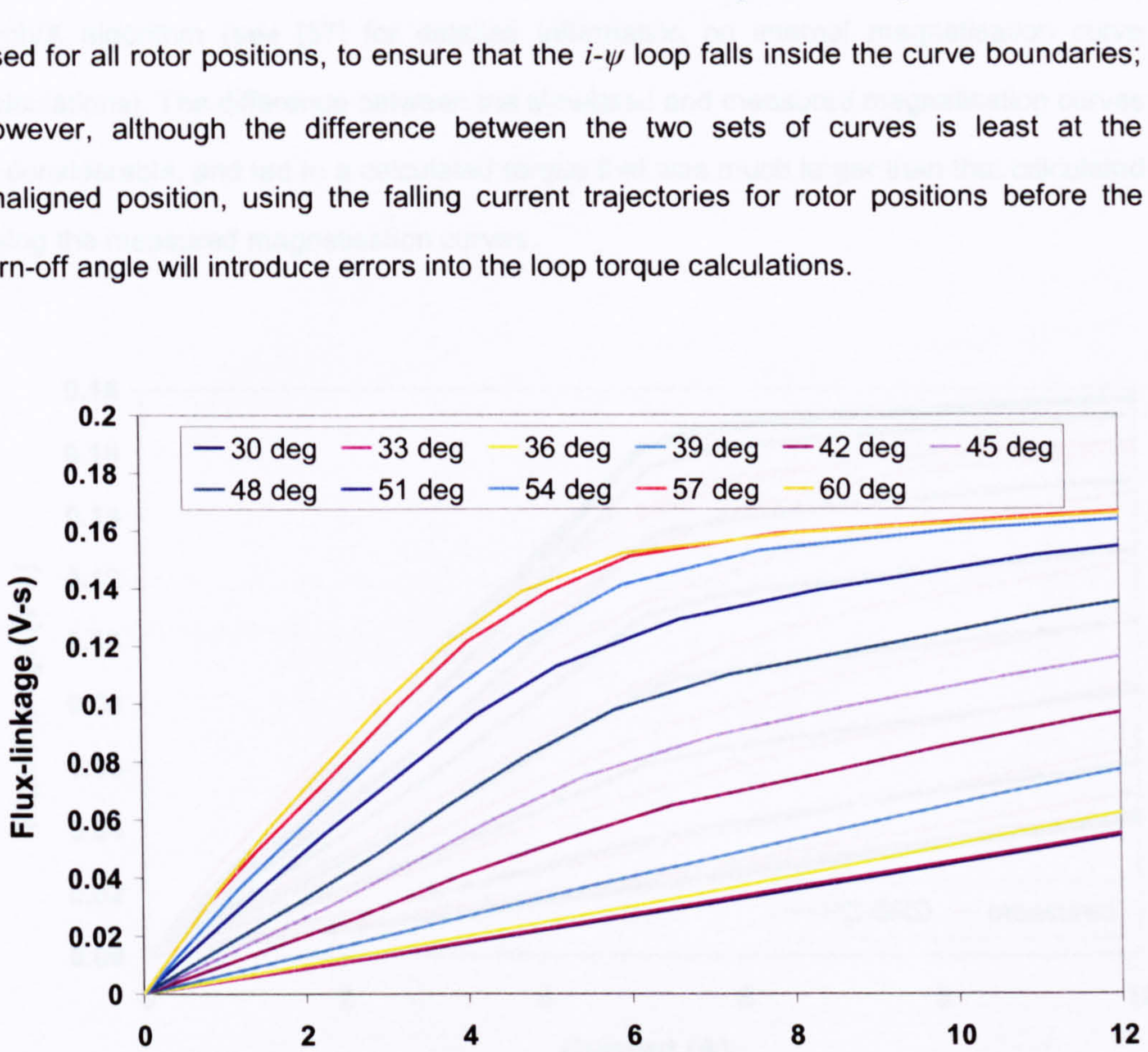

Fig. 3.3. Magnetisation curves for phase one of an 8/6, 4-phase motor (combination of rising and falling trajectories)

A suitable solution for use in the software is to use the rising magnetisation curves for all rotor positions up to the current turn-off angle, and the falling trajectories for all rotor positions after the turn-off angle. The rising and falling current trajectories must be selected manually and used to construct the flux-linkage (.psi) file required for the PC-SRD simulations. A complete set of measured magnetisation curves is given in Fig. 3.3, for the test point T_{ON} = 35 degrees and T_{OFF} = 51 degrees. The magnetisation curves for the rotor positions of 30 to 51 degrees using the rising current trajectory, while the

curves for rotor positions 54 to 60 degrees use the falling current trajectory. The magnetisation curves agree with i-ψ loop measurements and also with previous experimental data.

Fig. 3.4 shows the magnetisation curves calculated internally by PC-SRD, using the Froh/X algorithm (see [37] for detailed information on internal magnetisation curve calculations). The difference between the simulated and measured magnetisation curves is considerable, and led to a calculated torque that was much larger than that calculated using the measured magnetisation curves.

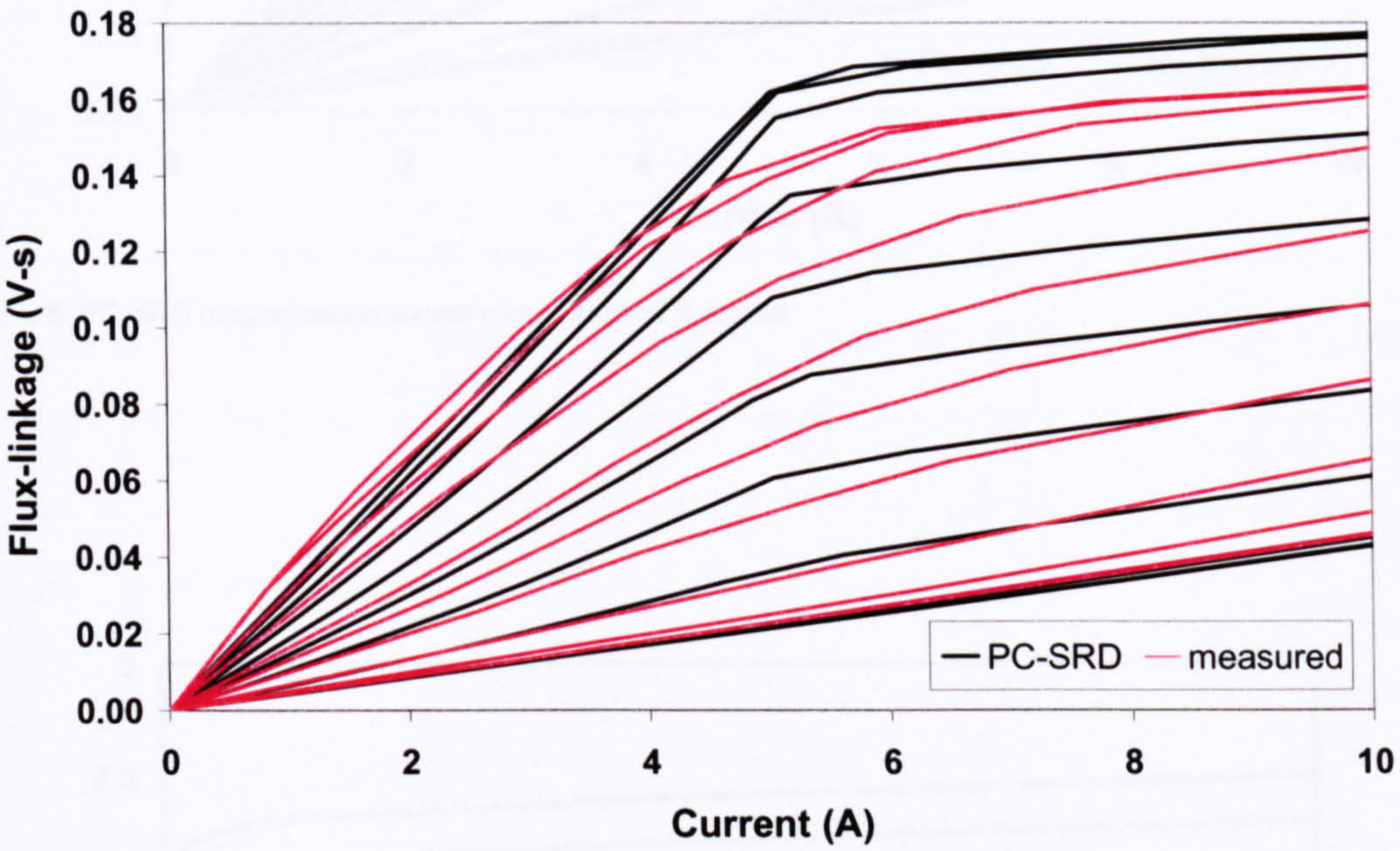

Fig. 3.4. PC-SRD magnetisation curves using original *B-H* data

The discrepancy between results is thought to be due to the material data used in the simulations. The lamination material of the motor was a Rotalloy composite, but no sample laminations were available for measurement of the *B-H* characteristic. It is thought that the heat treatment of the steel used in the test motor was not successful, leading to lower flux density values. The measured magnetisation curves of the motor were believed to be accurate, as the resulting torque calculation compared well with the torque as measured on the dynamometer test rig, and so the *B-H* curve was modified until the PC-SRD magnetisation curves correlated with the measured curves, as shown

in Fig. 3.5. The new *B-H* curve was used for all further simulations. The original and modified *B-H* curves are shown in Fig. 3.6. The linear region is shown in Fig. 3.7.

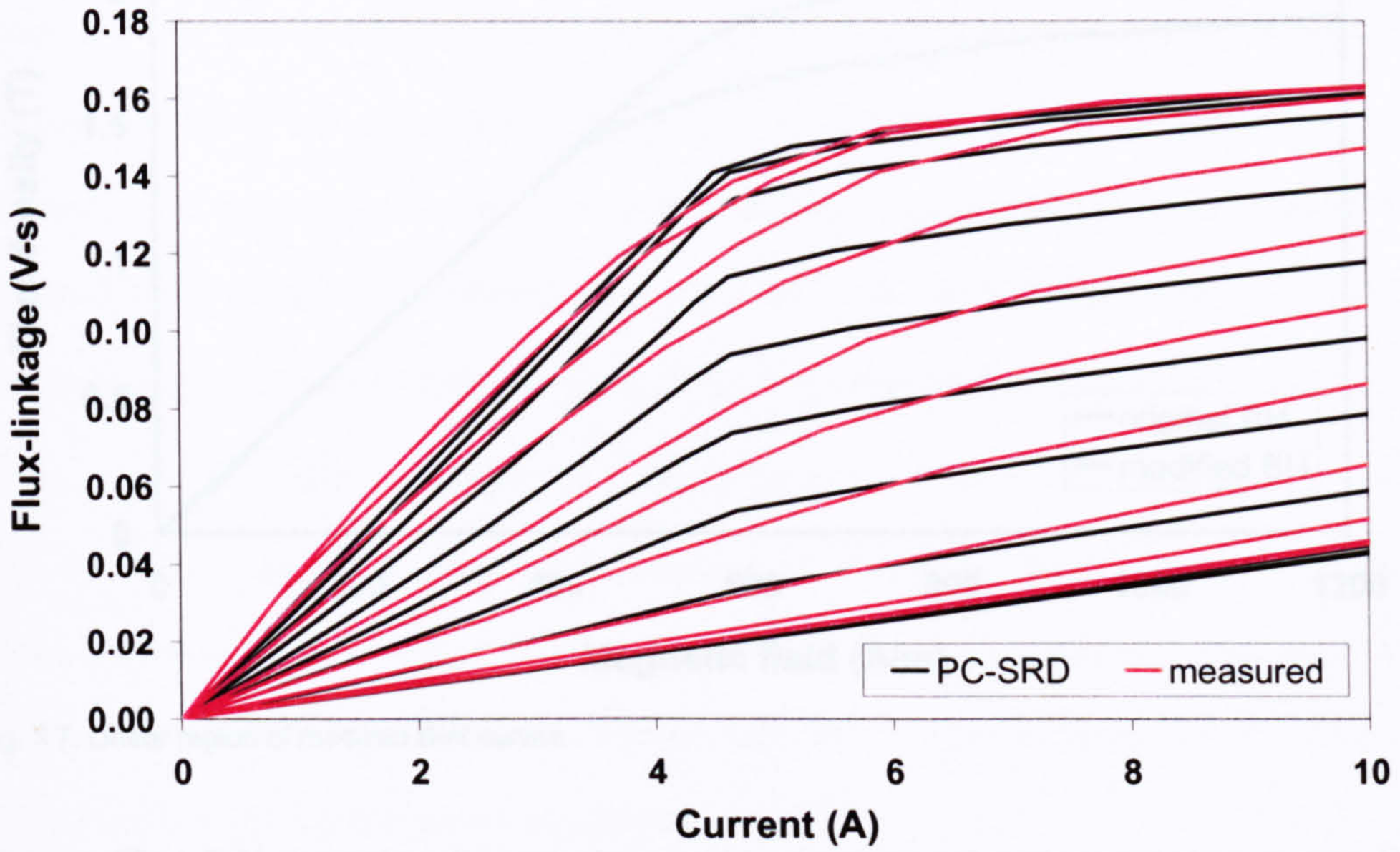

Fig. 3.5. PC-SRD magnetisation curves using modified *B-H* data

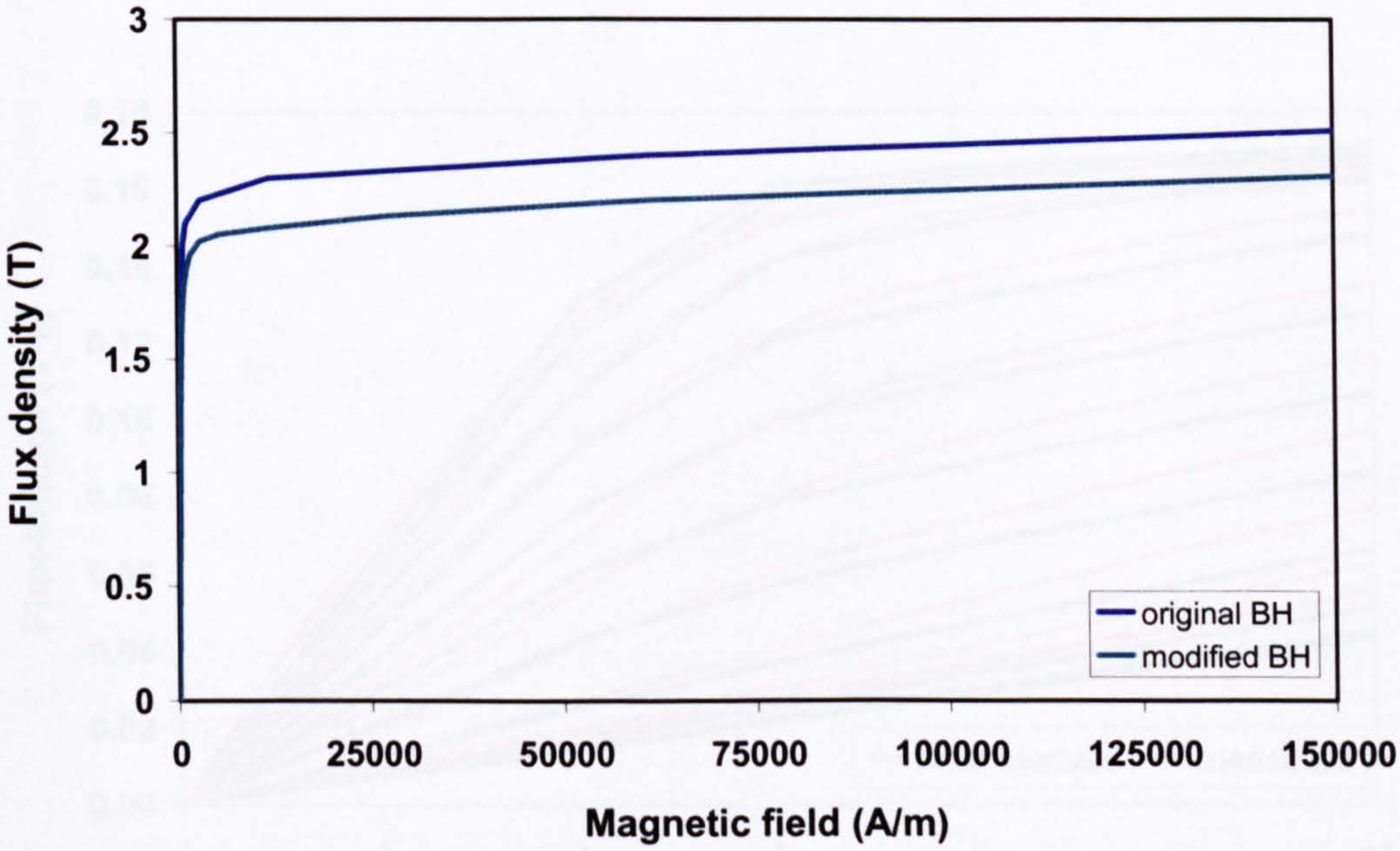

Fig. 3.6. Original and modified *B-H* curves of SR test motor lamination steel

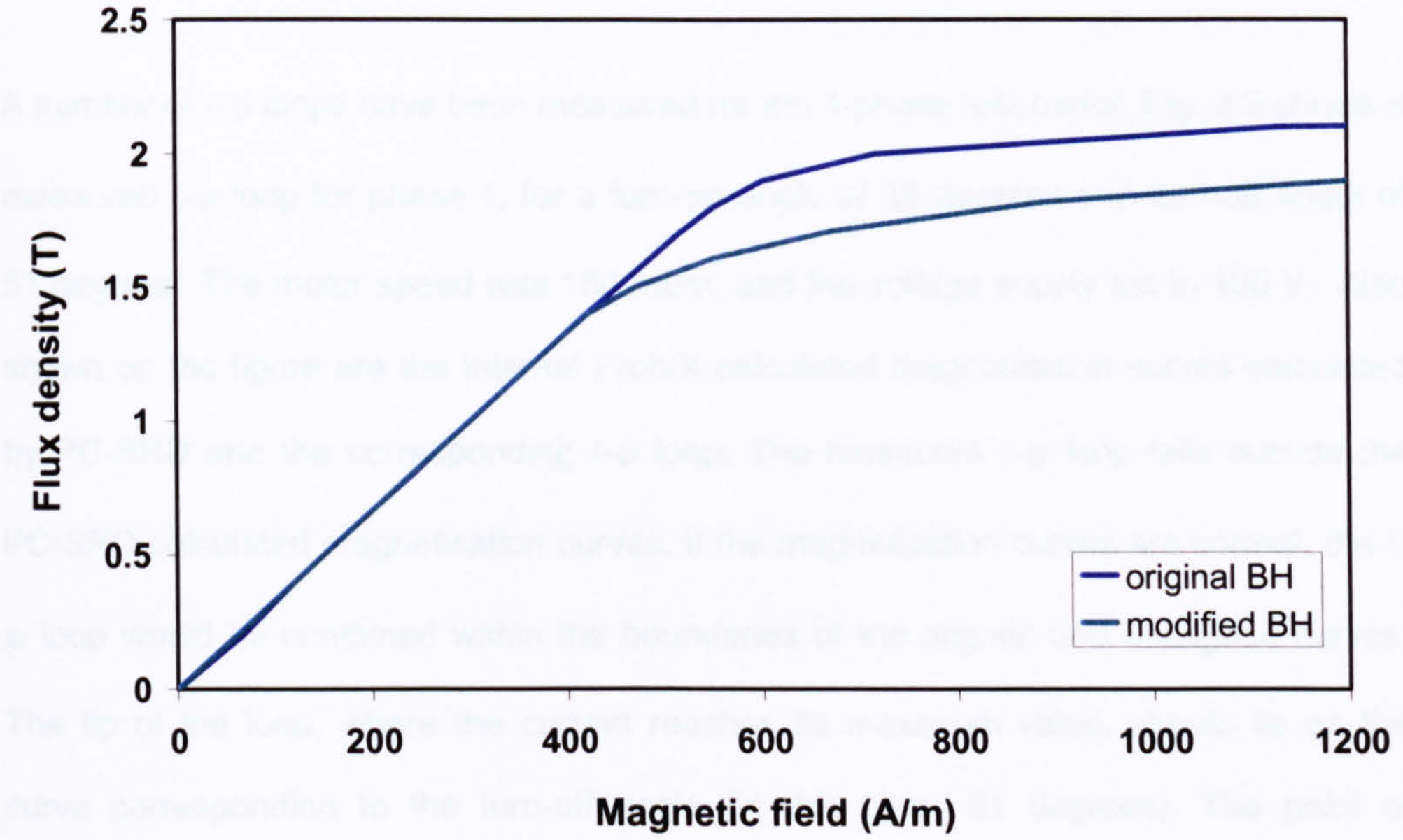

Fig. 3.7. Linear region of modified *B-H* curves.

The modified *B-H* characteristic was also used to determine the magnetisation curves in the two-dimensional finite element simulations, as shown in Fig. 3.8. There are discrepancies between the measured magnetisation curves and the finite element results, since the simulations are two-dimensional and do not take into account end-effects. This is discussed in section 3.3.

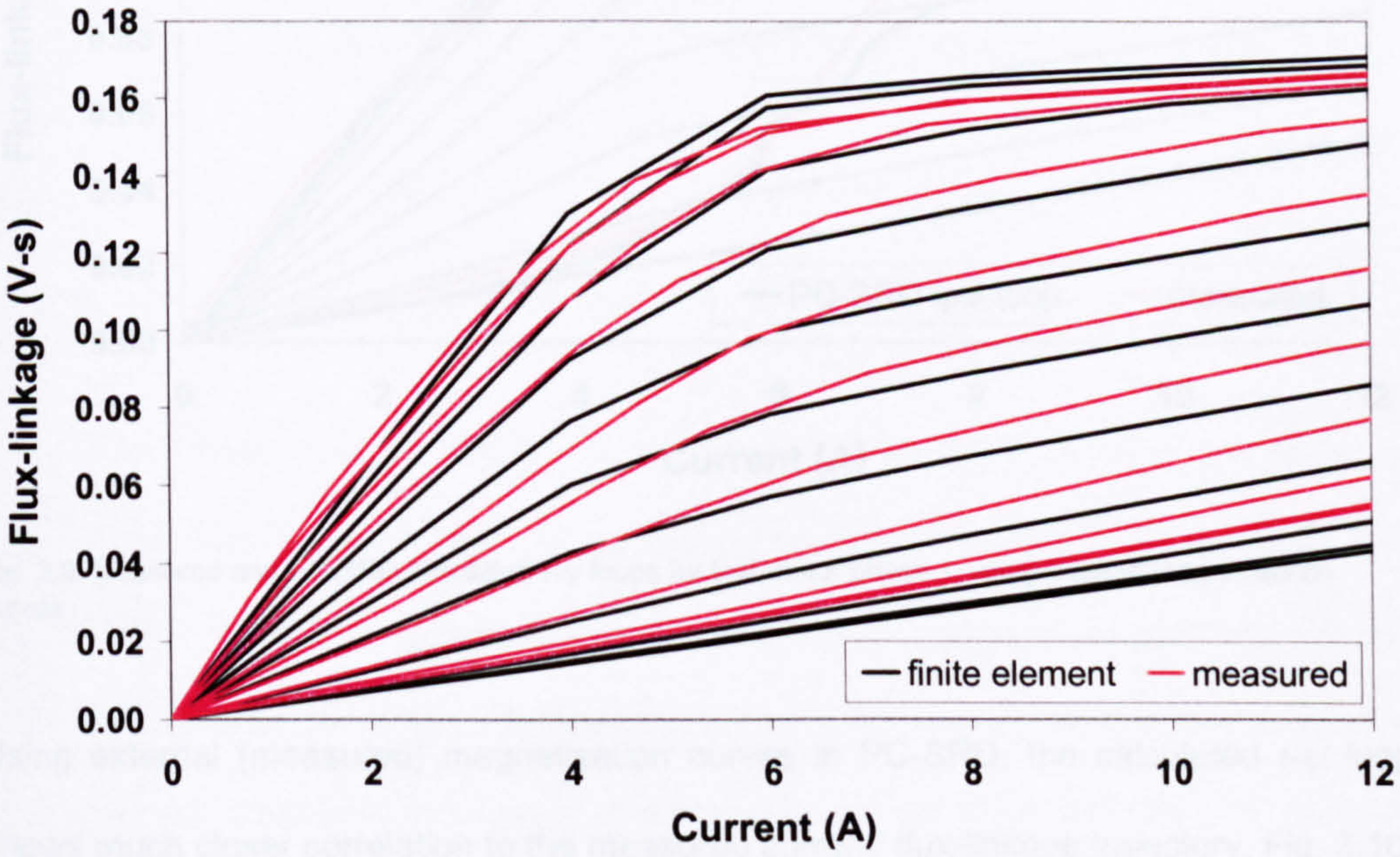

Fig. 3.8. Magnetisation curves calculated from two-dimensional finite element analysis

3.2. Measured and simulated i-ψ loops of SR motor

A number of i-ψ loops have been measured for the 4-phase test motor. Fig. 3.9 shows a measured i-ψ loop for phase 1, for a turn-on angle of 35 degrees and turn-off angle of 51 degrees. The motor speed was 1500 rpm, and the voltage supply set to 100 V. Also shown on the figure are the internal Froh/X calculated magnetisation curves calculated by PC-SRD and the corresponding i-ψ loop. The measured i-ψ loop falls outside the PC-SRD calculated magnetisation curves. If the magnetisation curves are correct, the i-ψ loop would be contained within the boundaries of the aligned and unaligned curves. The tip of the loop, where the current reaches its maximum value, should lie on the curve corresponding to the turn-off angle (in this case, 51 degrees). The point of maximum current lies above the 51 degree magnetisation curve, further illustrating the inaccuracies in the internal curve calculation.

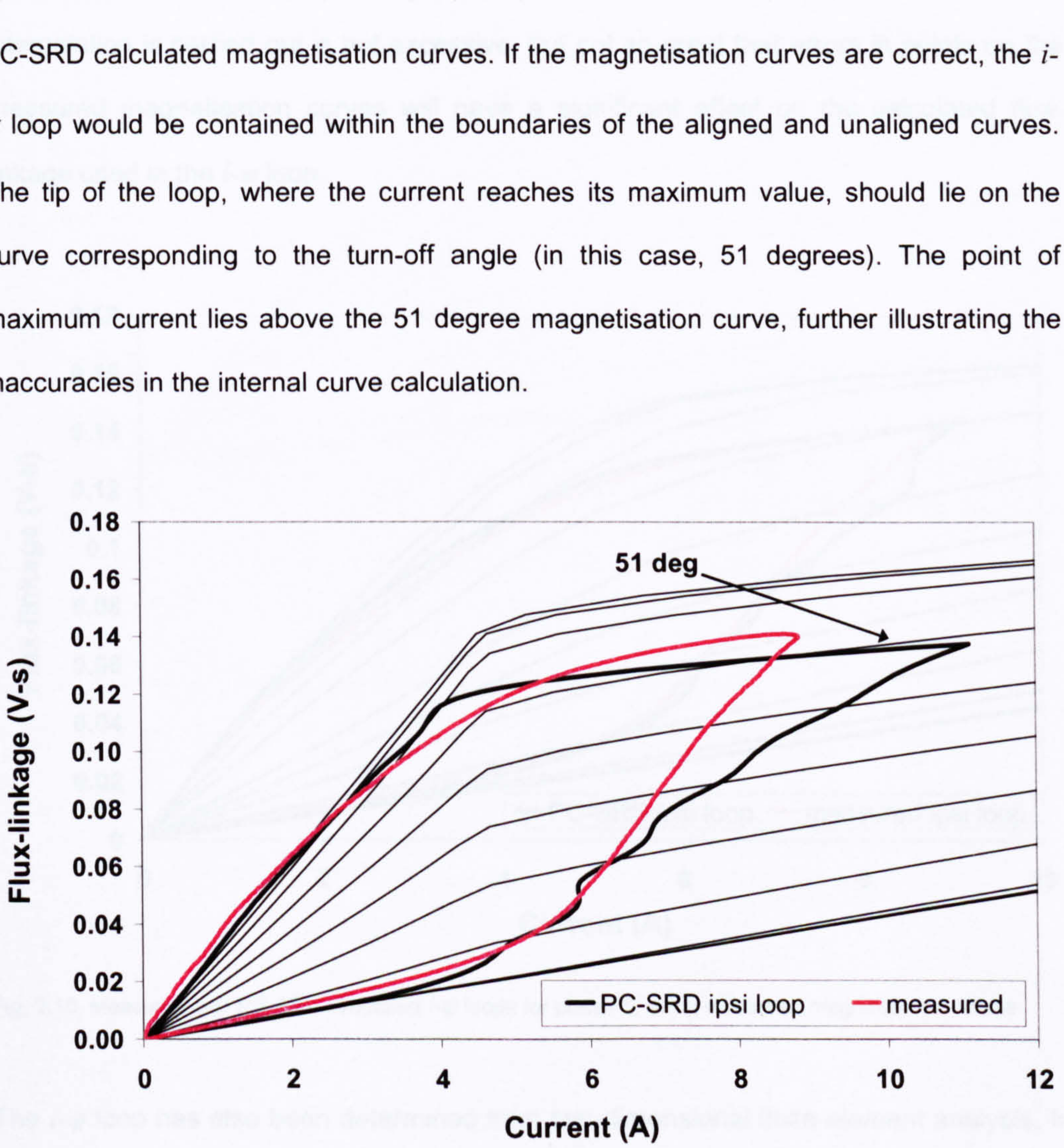

Fig. 3.9. Measured and PC-SRD simulated i-ψ loops for test motor phase 1, using internal magnetisation curves

Using external (measured) magnetisation curves in PC-SRD, the calculated i-ψ loop shows much closer correlation to the measured current/ flux-linkage trajectory, Fig. 3.10. The peak current is similar to that of the measured loop. The simulated i-ψ loop lies

within the boundaries of the measured magnetisation curves. The simulated loop is constrained by the known current points of the magnetisation curves. At the intermediate rotor positions, the current values are determined by cubic spline interpolation, which gives rise to the non-linear rippling in the flux-linkage between the measured points of the magnetisation curves. This rippling effect can be reduced by increasing the number of magnetisation curves (minimising the angular distance between curves). The number of magnetisation curves should be high enough that the angular distance over which the interpolation is carried out is not excessive, but not so great that errors in points on the measured magnetisation curves will have a significant effect on the calculated flux-linkage used in the i-ψ loop.

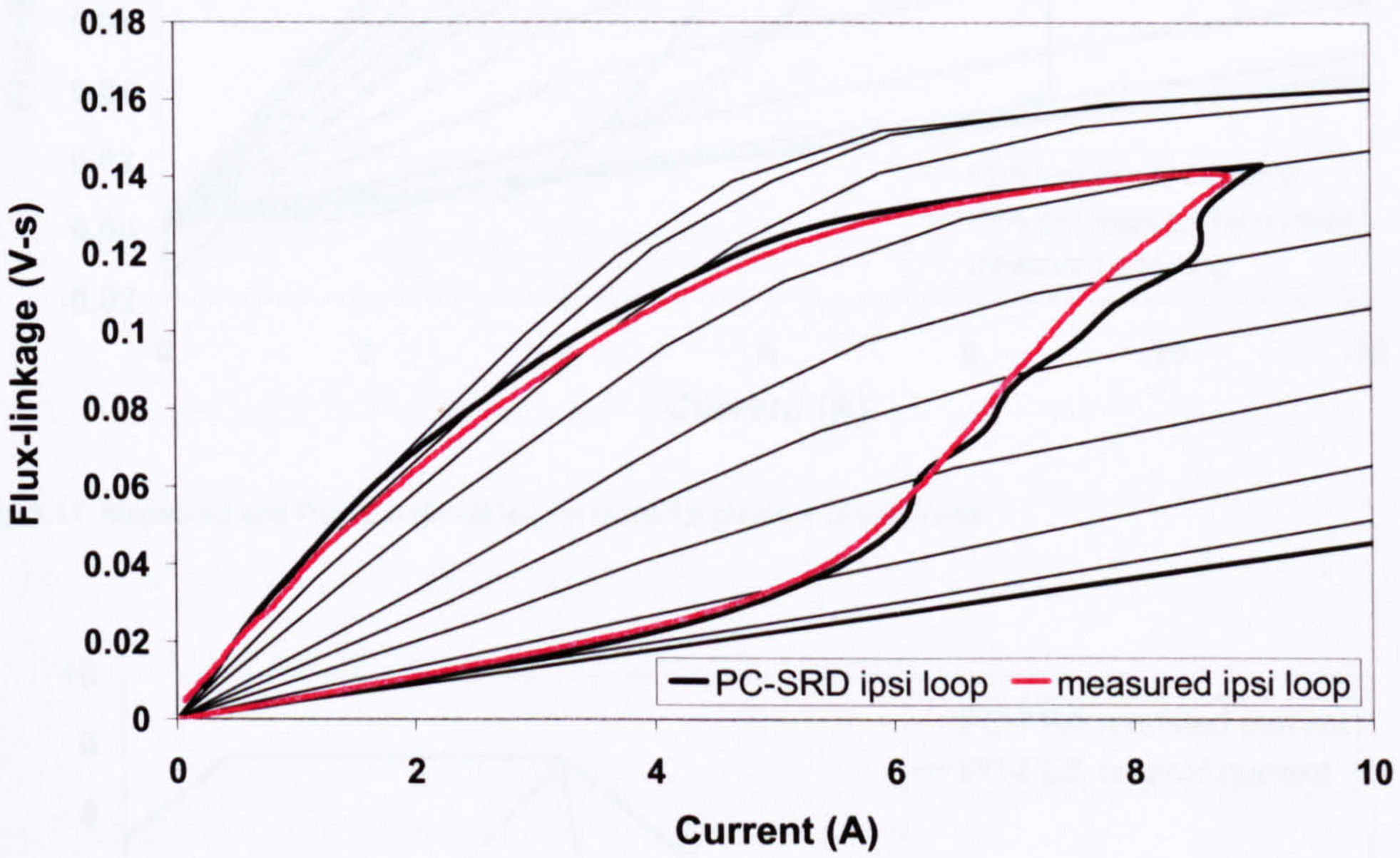

Fig. 3.10. Measured and PC-SRD simulated i-ψ loops for phase 1, using measured magnetisation curves

The i-ψ loop has also been determined from two-dimensional finite element analysis. In Fig. 3.11, the i-ψ loop calculated using the original current waveform, as determined by the PC-SRD GoFER, is compared with the loop that is calculated by the finite element software for a user-defined current waveform. For reference, the measured i-ψ loop and finite element magnetisation curves are included. Large discrepancies can be seen between the original finite element loop and the measured loop. The reasons for this are

two-fold. Firstly, the current waveform generated by the GoFER is an ideal trapezoid, as explained in section 2.2.2., and varies considerably from the actual waveforms that occur in the motor (as shown in Fig. 3.12). Secondly, the default setting of the finite element software is to excite all phases, whereas the measured i-ψ loop was determined from tests with only 1 phase excited.

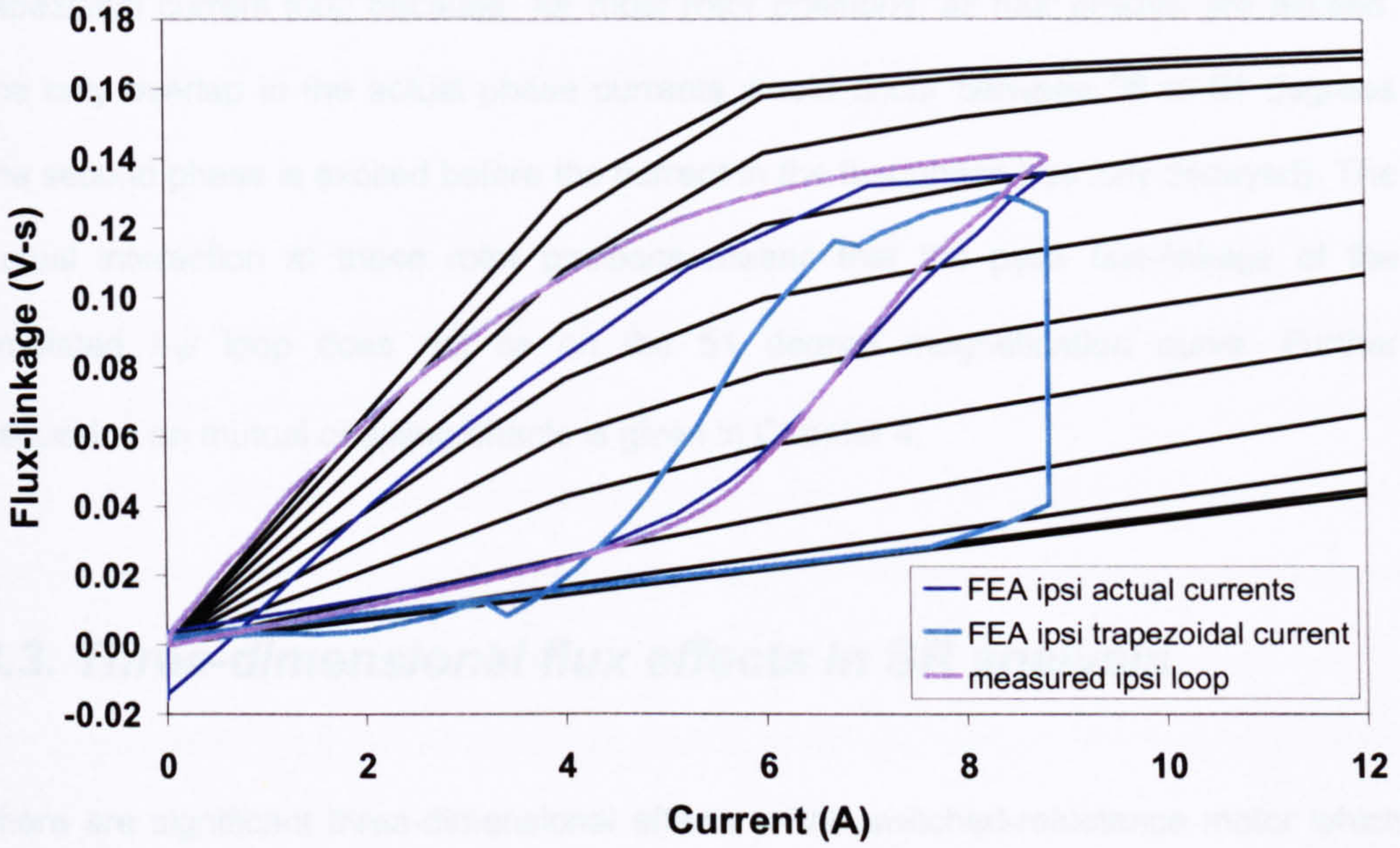

Fig. 3.11. Measured and PC-FEA simulated i-ψ loops for phase 1 of test motor

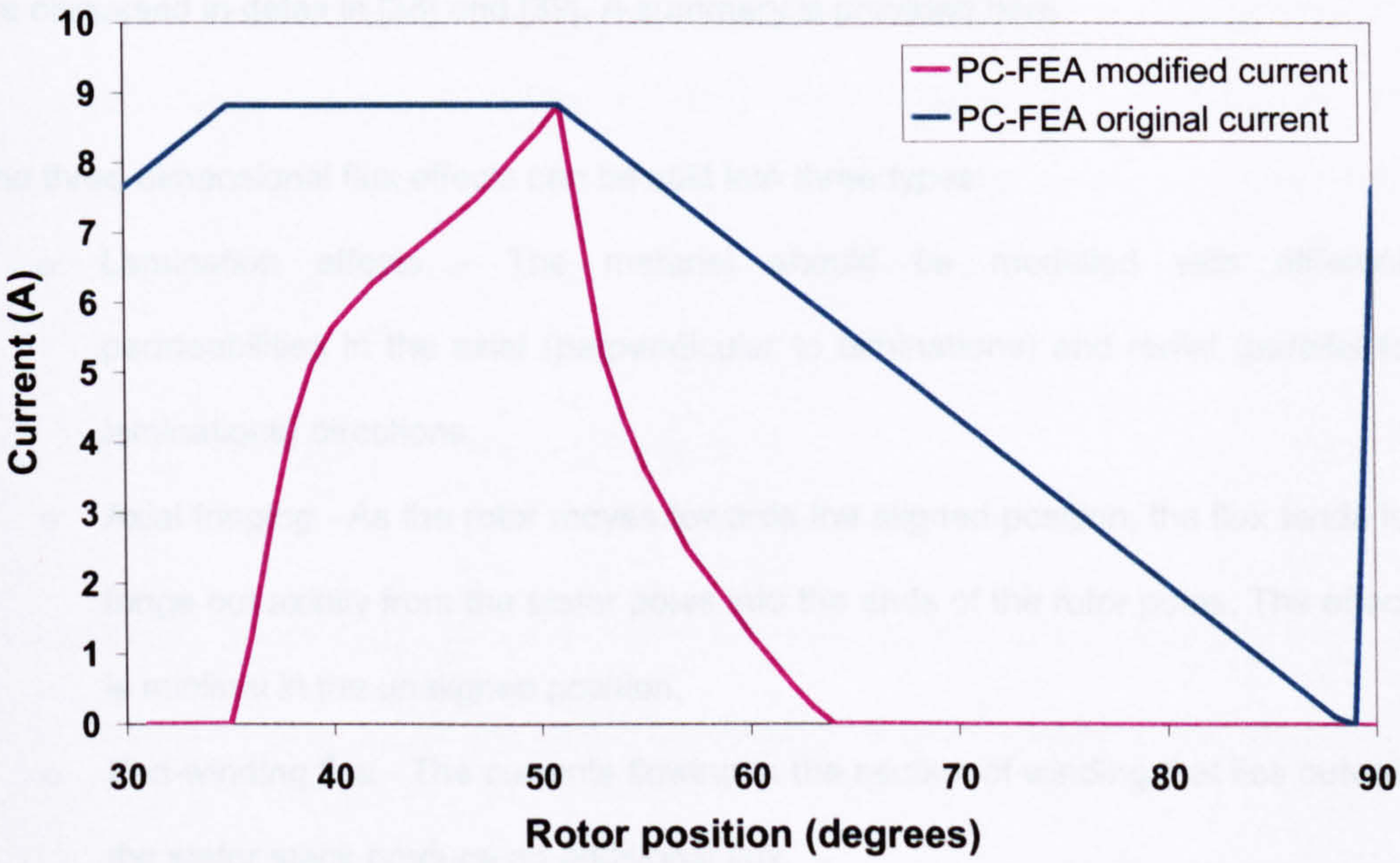

Fig. 3.12. Original and modified PC-FEA current waveforms

Figs. 3.11 and 3.12 clearly show the errors in the original i-ψ loop calculated by PC-FEA, due to the trapezoidal phase current trajectories. The repeated PC-FEA simulations (using the measured phase current profile) gave results much closer to the measured i-ψ loop. Both loops calculated in PC-FEA lie outside the expected boundaries of the finite element magnetisation curves. The loops are distorted, due to the mutual interaction between phases. The distortion is more noticeable on the trapezoidal current loop because, for most rotor positions, all four phases are excited. The only overlap in the actual phase currents would occur between 50 to 51 degrees (the second phase is excited before the current in the first phase has fully decayed). The mutual interaction at these rotor positions means that the peak flux-linkage of the simulated i-ψ loop does not lie on the 51 degree magnetisation curve. Further discussion on mutual coupling effects is given in Chapter 4.

3.3. Three-dimensional flux effects in SR analysis

There are significant three-dimensional effects in the switched-reluctance motor which are not taken into account in the two-dimensional finite element simulations - anisotropy in the laminations, axial fringing and end-winding flux. These three-dimensional effects are discussed in detail in [38] and [39]. A summary is provided here.

The three-dimensional flux effects can be split into three types:

- Lamination effects - The material should be modelled with different permeabilities in the axial (perpendicular to laminations) and radial (parallel to laminations) directions.
- Axial fringing - As the rotor moves towards the aligned position, the flux tends to fringe out axially from the stator poles into the ends of the rotor poles. The effect is minimal in the unaligned position.
- End-winding flux - The currents flowing in the section of winding that lies outwith the stator stack produce an additional flux.

The three-dimensional flux effects are most significant when the stack is short, as the length of the end turns is a greater proportion of the stack length. End effects can be calculated using three-dimensional finite element analysis, but construction and simulation of the 3D model is extremely time-consuming. It is possible to adjust 2D finite element results to take into account the 3D effects. The additional flux-linkage due to these 3D effects will vary depending on rotor position and current levels. The errors in 2D finite element simulations are greater at the unaligned position than the aligned; the end effects are more prominent in the unaligned position, due to the increased airgap.

A method was proposed in [38] to adjust two-dimensional finite element simulation results to account for end effects. To account for the anisotropy effects, the authors suggest scaling either the field values (by the product of the stack length and packing factor) or flux density values (by the packing factor). To determine the remaining end-effects, the authors have compared results from 2D and 3D simulations on the same lamination design, using motors with different stack lengths, and compiled the results into a correction factor chart that can be used to determine the end effects for any motor.

The PC-SRD software package automatically calculates two end-effect adjustment factors as part of the initial simulations, for the aligned and unaligned positions [40]. At the intermediate rotor positions, an exponential roll-off between the two values is used. The sharpness of the roll-off can be adjusted using an additional roll-off factor. The calculated values can then be used to adjust the magnetisation curves calculated from two-dimensional finite element software. The adjusted flux-linkage is calculated using

$$\psi_{adj} = \left(\psi_{orig} \times ScPsi \times X\_Lstk\right) + \left(dL(Sci \times i)\right) \tag{3.1}$$

where the adjustment factor dL varies from a minimum value L_u at the unaligned position to a maximum value L_{au} at the aligned position. Using the realignment adjustment

factors L_{au} and L_u[5], the finite element magnetisation curves of the switch reluctance test motor can be recalculated. The resulting curves are plotted in Fig. 3.13. There is greater correlation with the measured magnetisation curves, although there are still discrepancies near the aligned position. The results suggest that the realignment adjustment factor for the unaligned position is accurate but that for the aligned position there is some error in the calculated alignment factor.

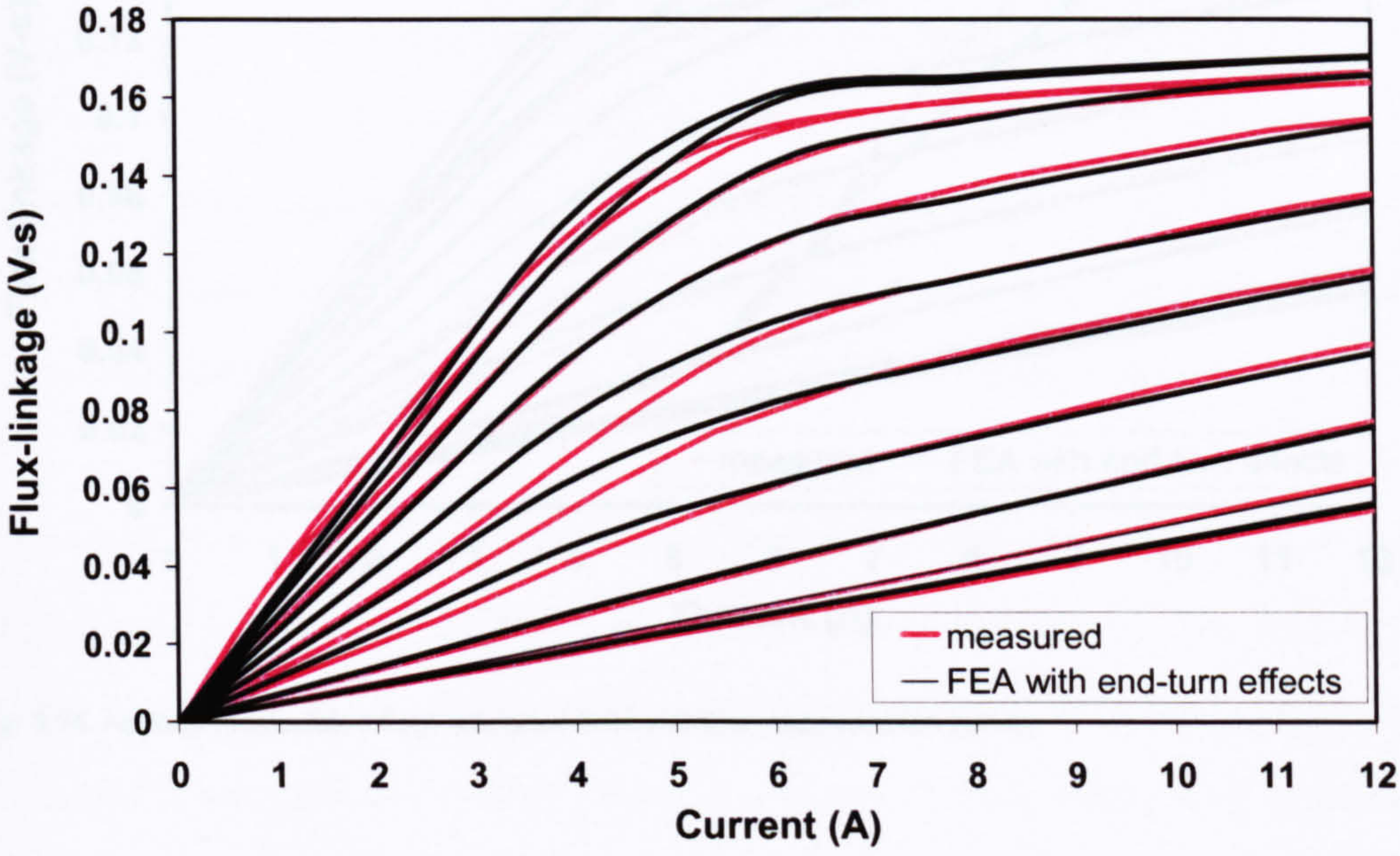

Fig. 3.13. Realigned magnetisation curves of switched-reluctance test motor, using PC-SRD realignment parameters

The i-ψ loop of the motor can be recalculated using the realigned finite element magnetisation curves, as shown in Fig. 3.14. Although the loops vary at the turn-off point (where the current is still overestimated by around 1 A in the loop calculated from the finite element magnetisation curves), overall there is much greater correlation between the measured and simulated results. The accuracy of the calculated i-ψ loop is dependent on the external magnetisation curves used (whether measured or taken from finite element simulations), so it is vital that the realignment factors allow for correct adjustment of the two-dimensional finite element magnetisation curves to account for any three-dimensional effects. Even with accurate magnetisation curve data, the degree

[5] Values of L_u and L_{au} (the adjustment factors of the unaligned and aligned inductances respectively) are calculated in the initial simulation in the PC-SRD software. More information can be found in [37].

of accuracy in the torque calculated from the simulated i-ψ loops is dependent on other factors in the model, such as the phase voltage (which can differ from the supply voltage due to the voltage drop across the power semiconductor switching devices).

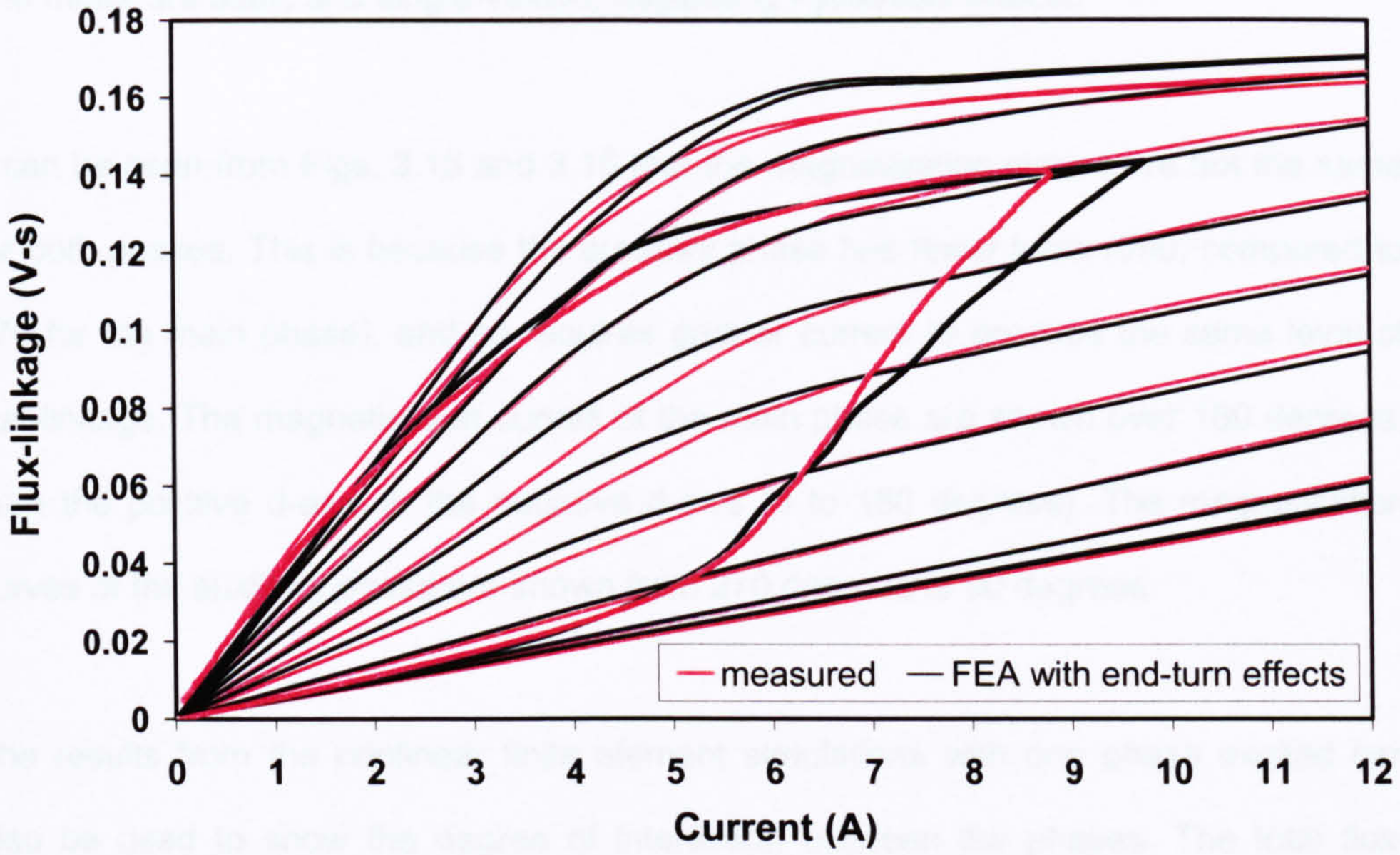

Fig. 3.14. i-ψ loop recalculated from realigned finite element magnetisation curves

3.4. Measured and simulated magnetisation curves of IPM motor

As discussed in Chapter 2, the magnetisation curves of the permanent-magnet motor cannot be easily determined from the simple analytical software simulations due to the complexity of the magnetic circuit. However, the complete set of curves can be calculated from nonlinear finite element simulations. The nonlinear finite element solver calculates the total nonlinear flux-linkage; it allows for variation in the magnet flux-linkage with load.

Nonlinear finite element simulations were carried out for IPM test motor 1 using measured B-H data for the motor laminations. The remnant flux of the permanent magnets has been adjusted in the finite element script (by adjusting parameters B_{rr} and B_{tt}), so that the peak of the open-circuit flux-linkage waveform corresponds to that

derived from the measured open-circuit back EMF waveform. Fig. 3.15 shows magnetisation curves of the main phase, (with excitation only in the main phase); the magnetisation curves of the auxiliary phase (with excitation only in the auxiliary phase) are shown in Fig. 3.16. As for the switched-reluctance motor, the simulated curves of the IPM motor are static and single-valued, neglecting hysteresis effects.

It can be seen from Figs. 3.15 and 3.16 that the magnetisation curves are not the same for both phases. This is because the auxiliary phase has fewer turns (690, compared to 970 for the main phase), and so requires greater current to produce the same level of flux-linkage. The magnetisation curves of the main phase are shown over 180 degrees, from the positive d-axis to the negative d-axis (0 to 180 degrees). The magnetisation curves of the auxiliary phase are shown from 270 degrees to 90 degrees.

The results from the nonlinear finite element simulations with one phase excited can also be used to show the degree of interaction between the phases. The total flux-linkage in the main phase, due to current in the auxiliary phase, is shown in Fig. 3.17. The total flux-linkage in the auxiliary phase, due to current in the main phase, is shown in Fig. 3.18.

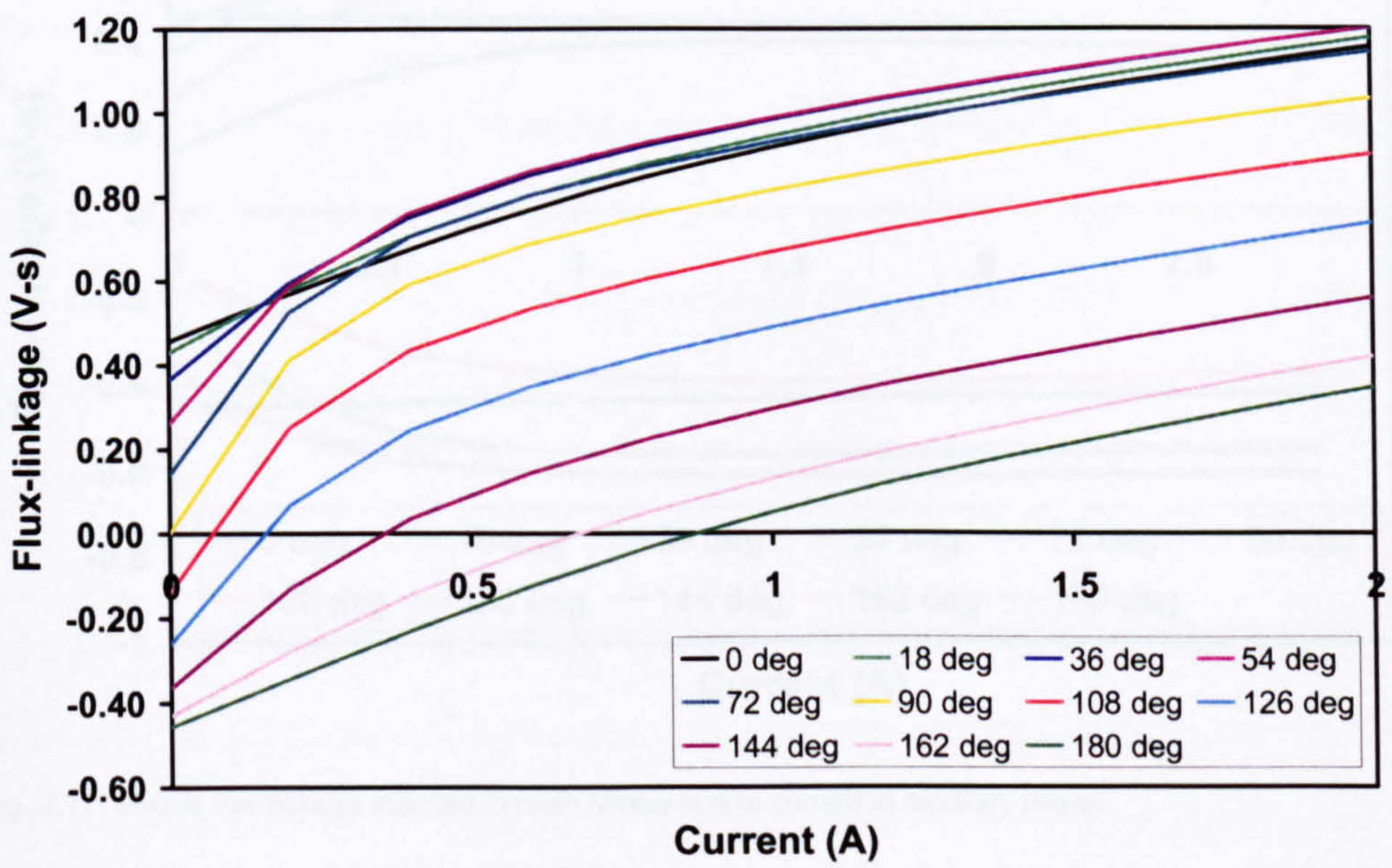

Fig. 3.15. Simulated magnetisation curves of main phase of IPM test motor 1.

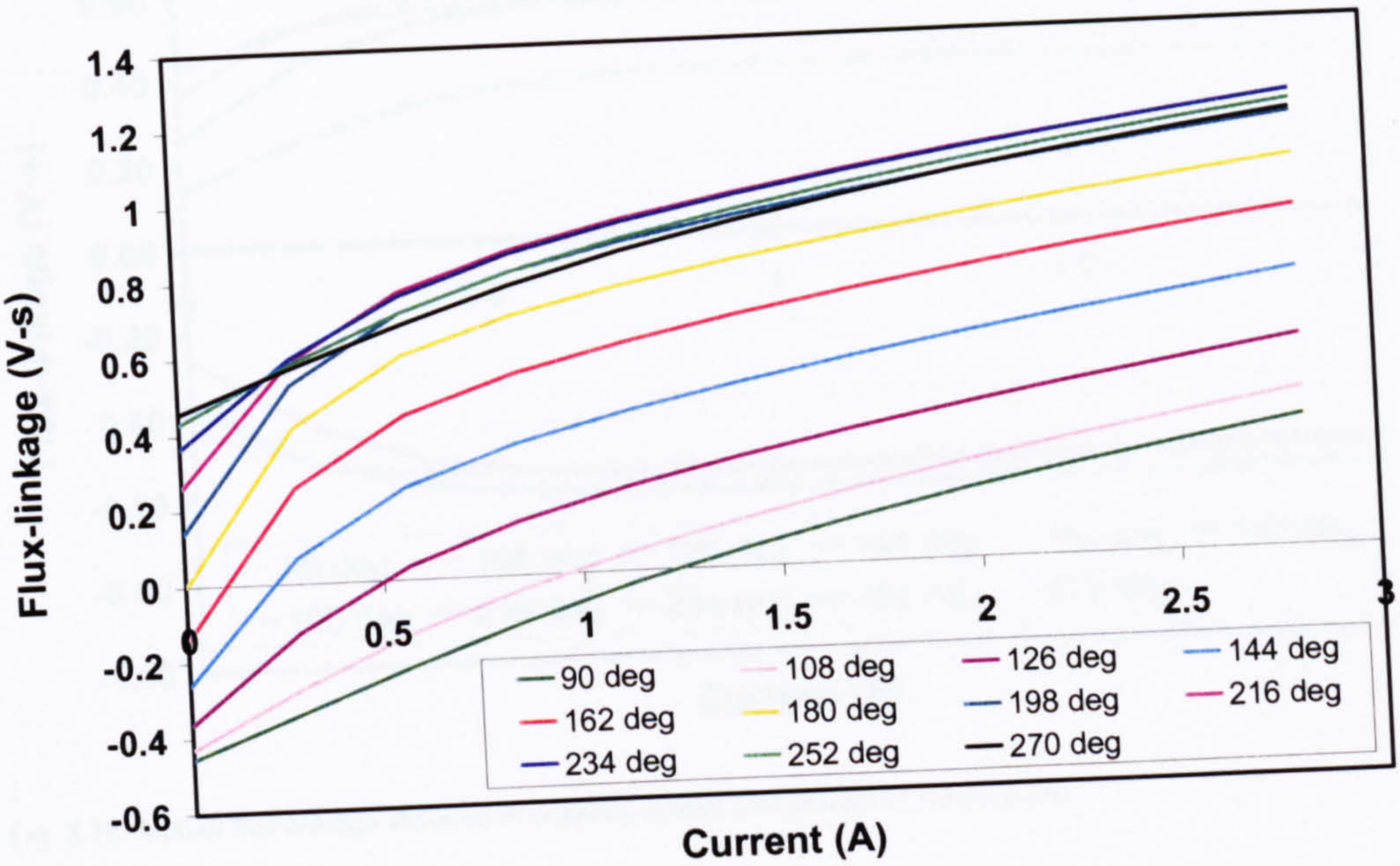

Fig. 3.16. Simulated magnetisation curves of auxiliary phase of IPM test motor 1.

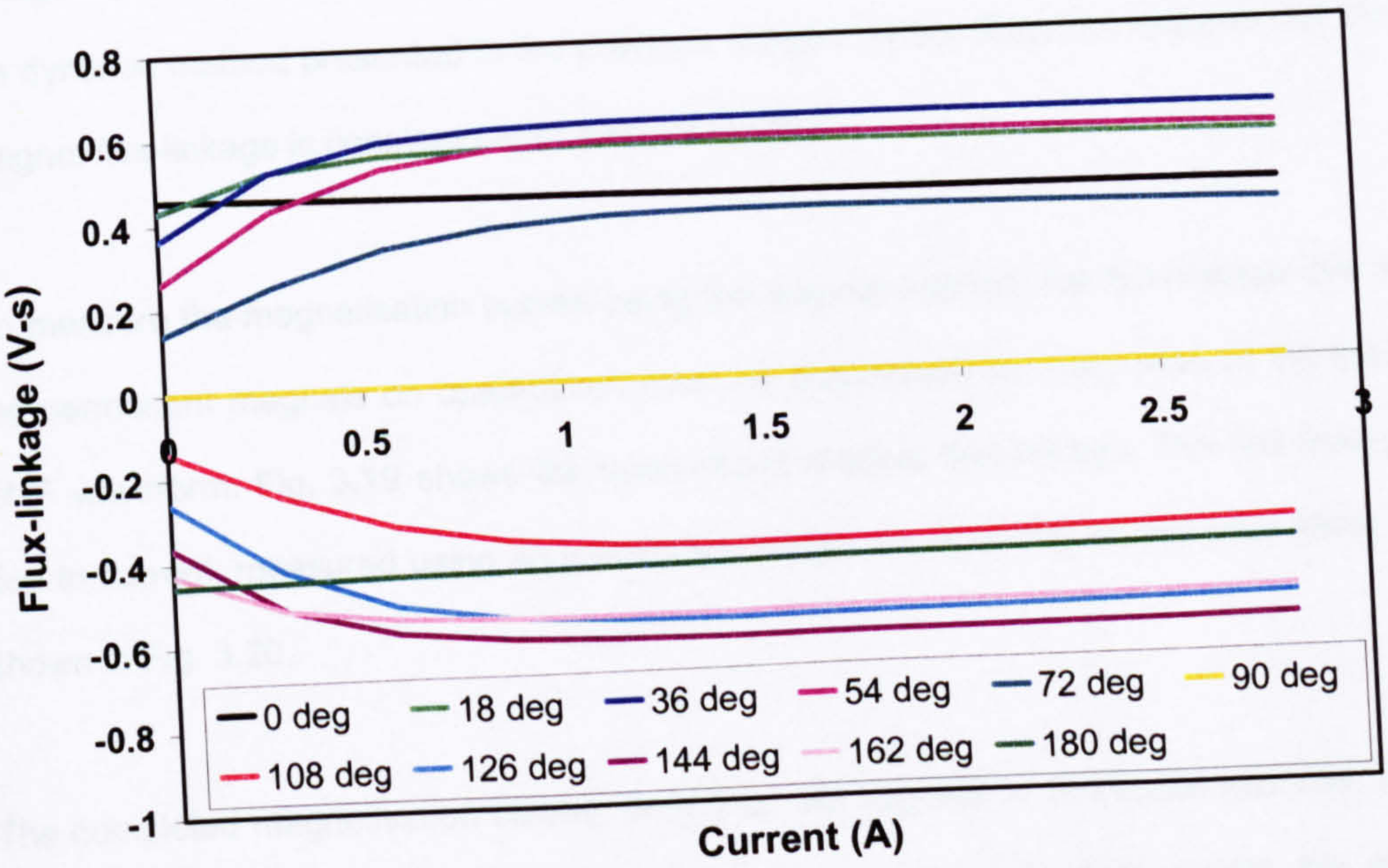

Fig. 3.17. Mutual flux-linkage induced in main phase due to current in auxiliary phase

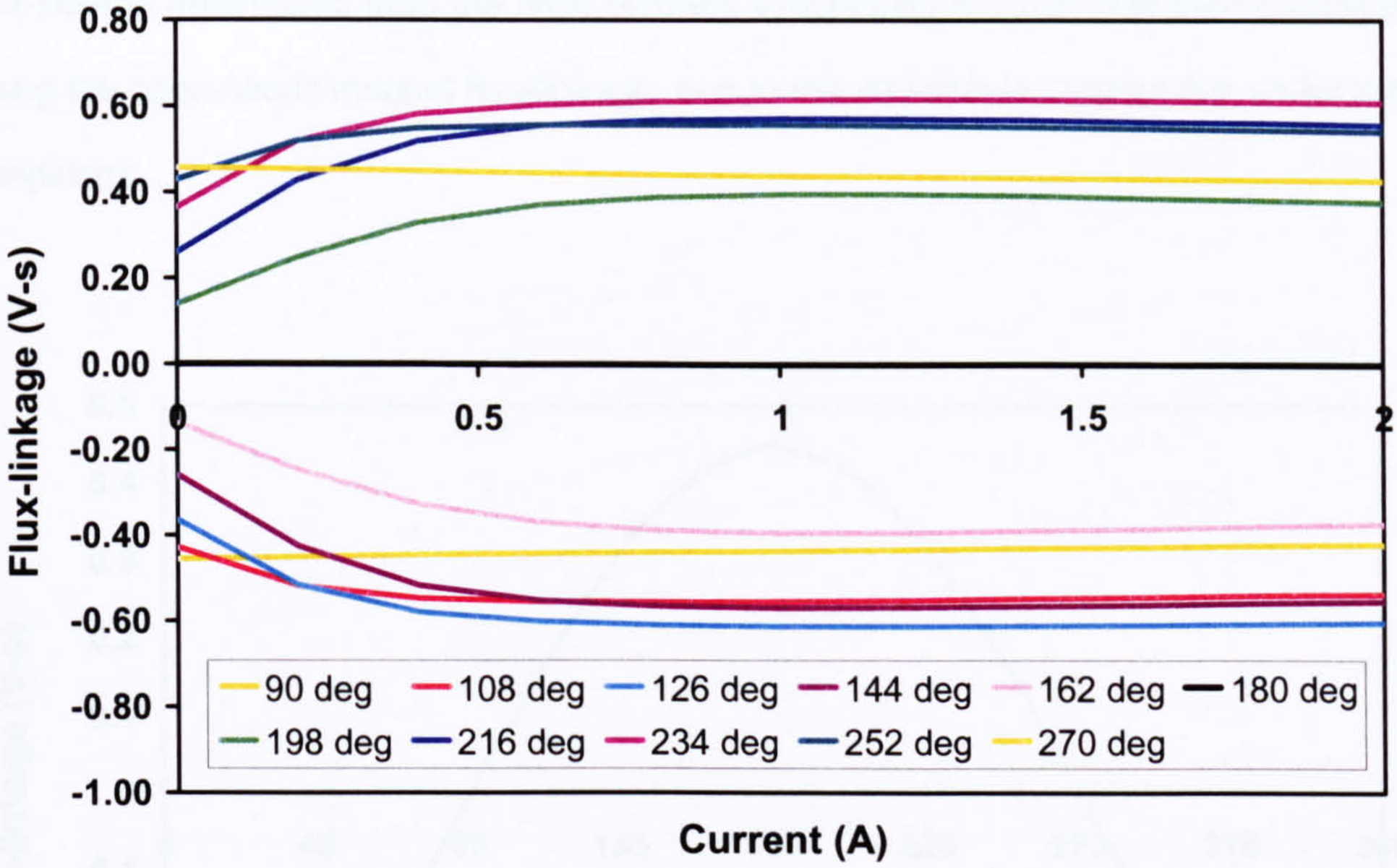

Fig. 3.18. Mutual flux-linkage induced in auxiliary phase due current in main phase

The magnetisation curves of the motor were also measured. Results are presented below for measurements of the main phase. The magnetisation curves have been measured using two methods – the previously established method whereby the flux-linkage due to the phase currents is added to the open-circuit magnet flux-linkage, and the dynamic method presented in the previous chapter (which does not assume that the magnet flux-linkage is constant under load conditions).

To measure the magnetisation curves using the original method, the flux-linkage due to the permanent magnets on open-circuit must be determined by integration of the back EMF waveform. Fig. 3.19 shows the open-circuit magnet flux-linkage. The flux-linkage due to current, measured using an inductance bridge circuit during locked rotor tests, is shown in Fig. 3.20.

The completed magnetisation curves, from 0 to 180 degrees in 18 degree intervals, are given in Fig. 3.21; the corresponding finite element magnetisation curves are also plotted for comparison. There is good agreement between the magnetisation curves for some rotor positions. At those rotor positions where the magnetic circuit is saturated, the

flux-linkage determined from the finite element simulations is much less than calculated using the open-circuit magnet flux-linkage, due to the variation in magnet flux under load conditions.

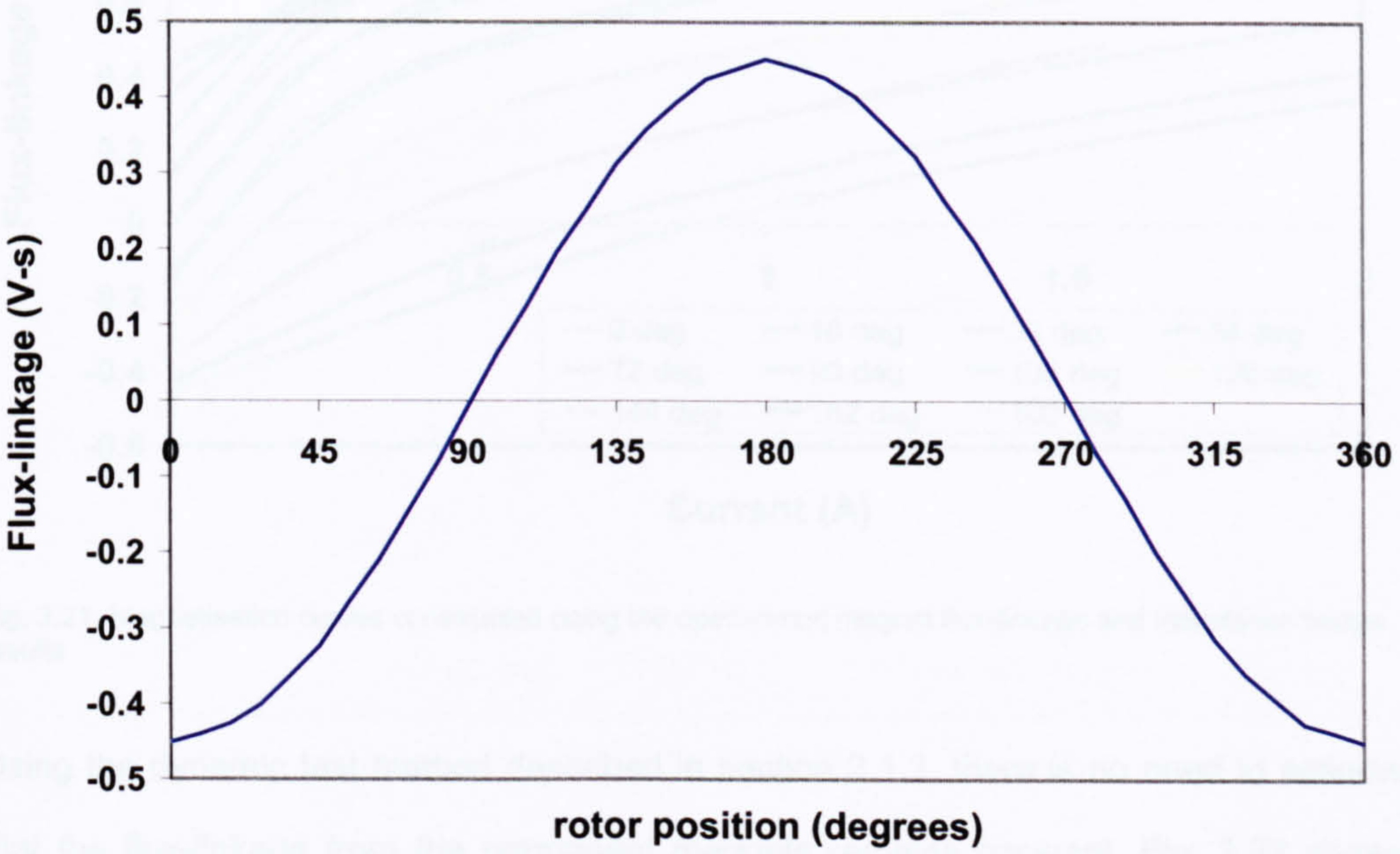

Fig. 3.19. Open-circuit magnet flux-linkage

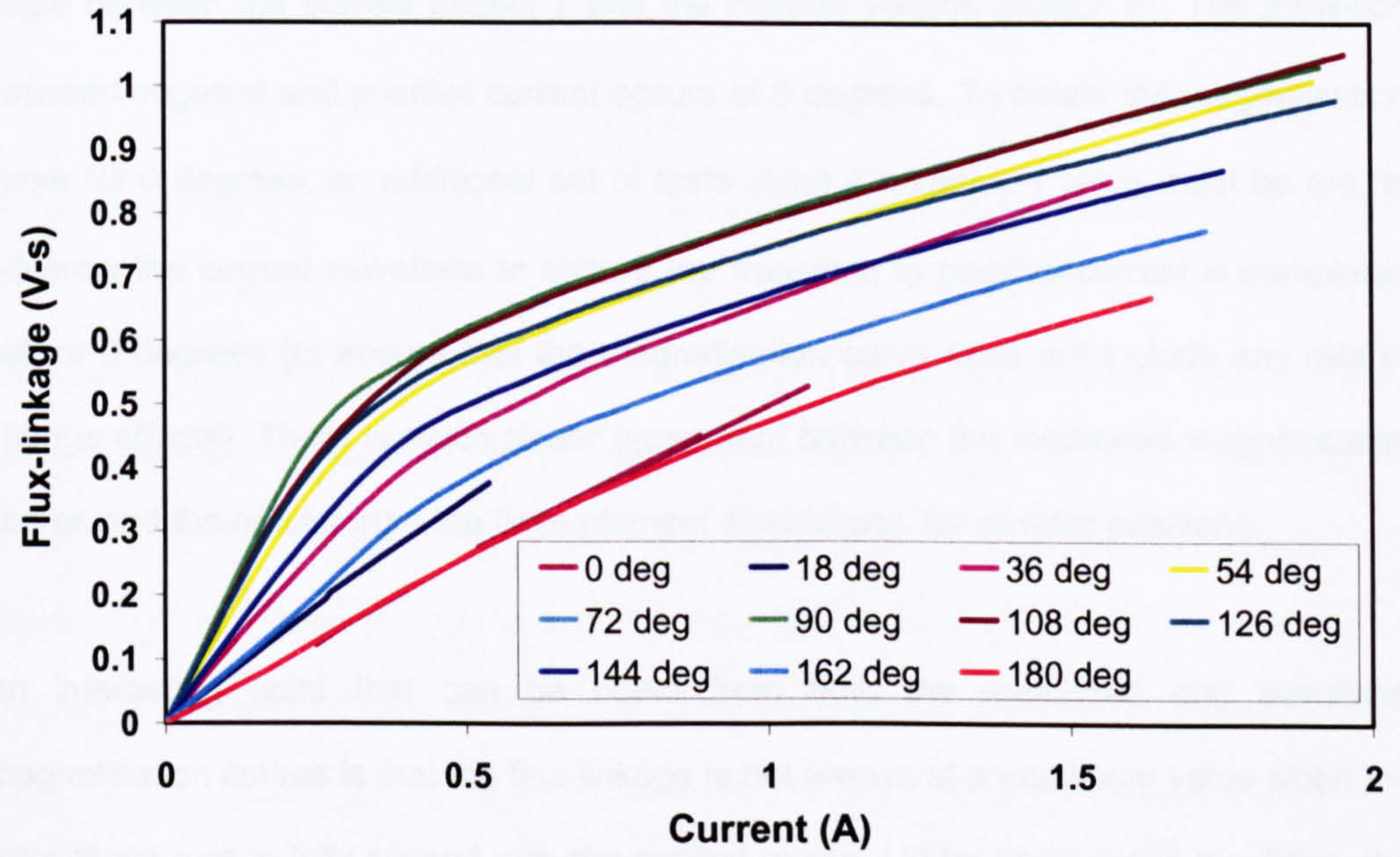

Fig. 3.20. Flux-linkage due to current, measured from inductance bridge tests

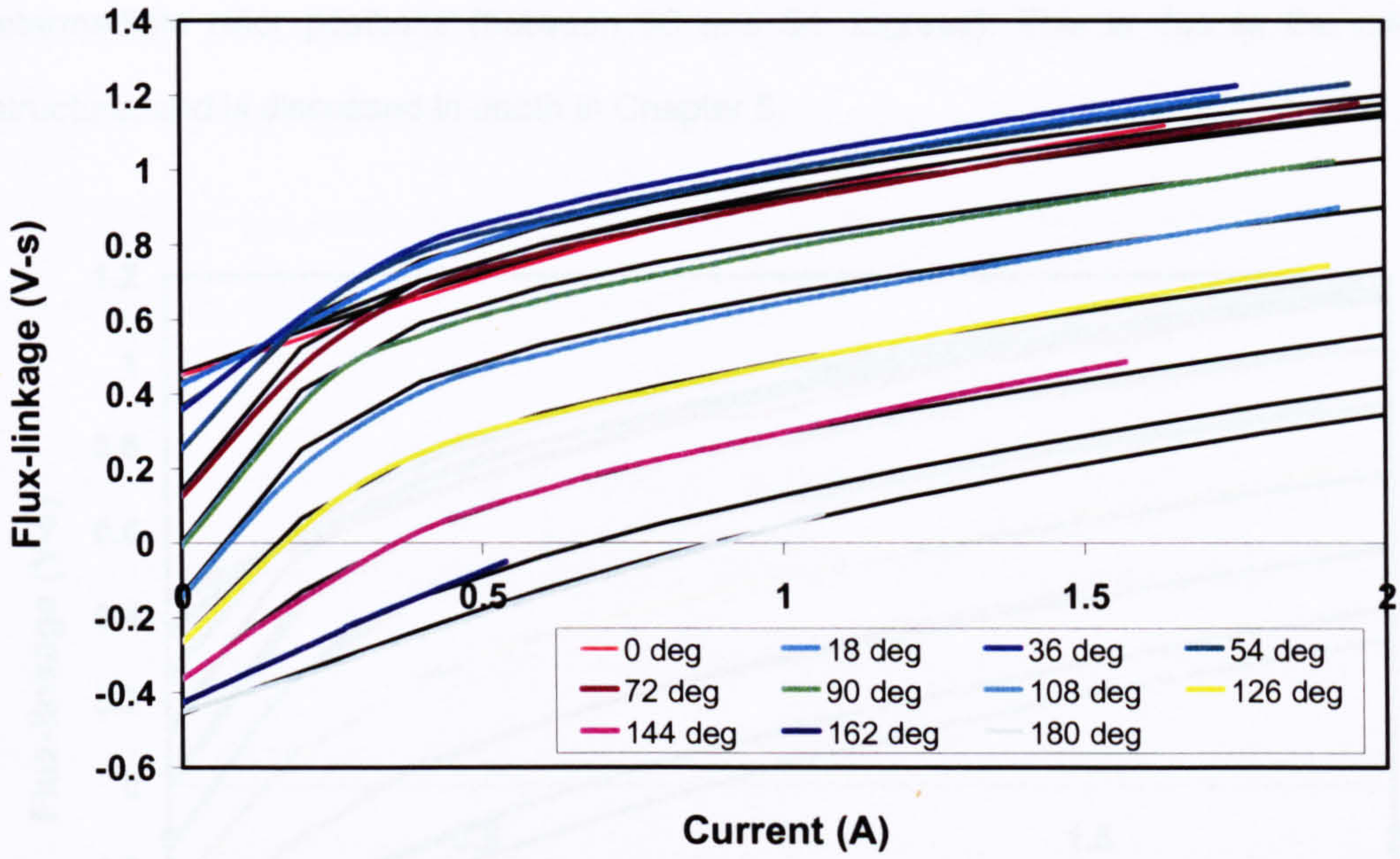

Fig. 3.21. Magnetisation curves constructed using the open-circuit magnet flux-linkage and inductance bridge results

Using the dynamic test method described in section 2.1.3, there is no need to assume that the flux-linkage from the permanent magnets remains constant. Fig. 3.22 shows magnetisation curves measured on the dynamometer test rig, for excitation waveforms similar to those given in Fig. 2.6. The tests were run for one γ value, $\gamma = 0$ (where γ is the angle between the current phasor $\boldsymbol{I}$ and the magnet voltage phasor $\boldsymbol{E}$). The transition between negative and positive current occurs at 0 degrees. To obtain the magnetisation curve for 0 degrees, an additional set of tests using a negative γ value must be run, to advance the current waveform to ensure the transition to positive current is completed before 0 degrees (to ensure that the magnetisation curve does not include any rate of change effects). There is much closer agreement between the measured magnetisation curves and the results from the finite element simulations, for all rotor positions.

An interesting point that can be noted from both the measured and simulated magnetisation curves is that the flux-linkage is not always at a maximum value when the rotor direct axis is fully aligned with the excited phase. Under open-circuit condition, the greatest flux-linkage is seen when the rotor direct axis is fully aligned with the phase

under test. However, under load conditions, the maximum flux-linkage occurs at intermediate rotor positions (between 36 and 54 degrees). This is due to the rotor structure, and is discussed in depth in Chapter 5.

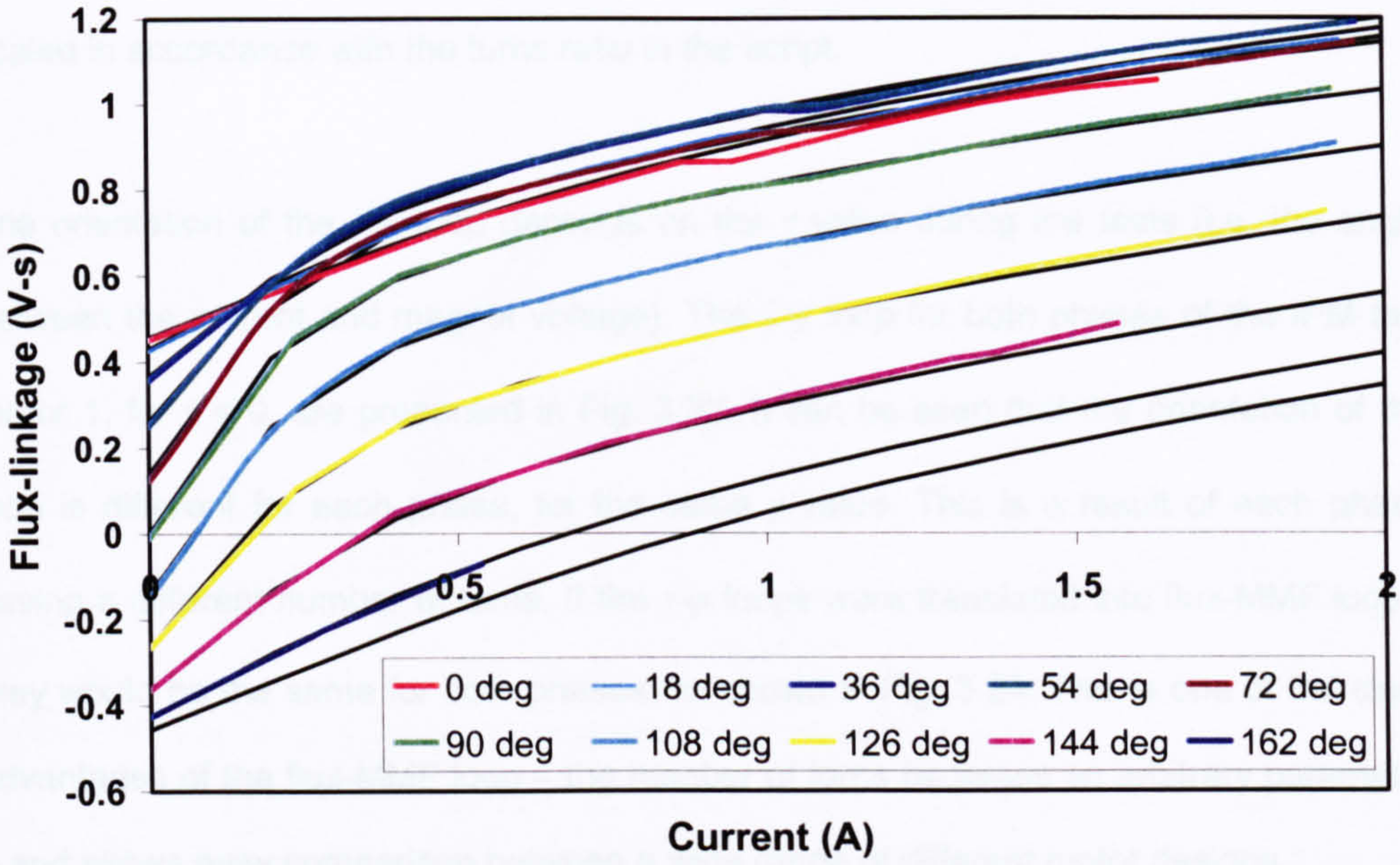

Fig. 3.22. Magnetisation curves determined from dynamic tests with squarewave currents

3.5. Measured and simulated i-ψ loops of IPM motor

The i-ψ loop of the interior permanent-magnet motor can be measured using the same dynamic test rig and controller as is used for measurement of the magnetisation curves. The SPEED Flexible Controller FCIII was again used to provide the current reference waveforms. The motor was run under normal conditions so that the current reference waveforms were sinusoidal. The controller tracks the reference current by adjusting the duty cycle of the PWM voltage signal used as an input to the motor. The reference current is scaled according to the number of turns per phase so that normal operation of the motor is observed; the current in the auxiliary phase is 1.41 times greater than that of the main phase. The i-ψ loops of both phases are measured simultaneously, thus including any mutual interactions that may occur between the phases.

The i-ψ loops generated from the static design in the PC-BDC software have been discounted, since the loops are different for the main and auxiliary phases, and the analytical software assumes phase independence. The i-ψ loops were also simulated using PC-FEA. To replicate the test conditions, the current in the second phase i_b was scaled in accordance with the turns ratio in the script.

The orientation of the i-ψ loop depends on the γ value during the tests (i.e. the angle between the current and magnet voltage). The i-ψ loop for both phases of the IPM test motor 1, for γ = 0, are presented in Fig. 3.23. It can be seen that the orientation of the loop is different for each phase, for the same γ value. This is a result of each phase having a different number of turns. If the i-ψ loops were translated into flux-MMF loops, they would be the same for both phases, as shown in Fig. 3.24. This is one of the clear advantages of the flux-MMF loop – the number of turns becomes an arbitrary parameter – and allows easy comparison between a wide range of different motor designs.

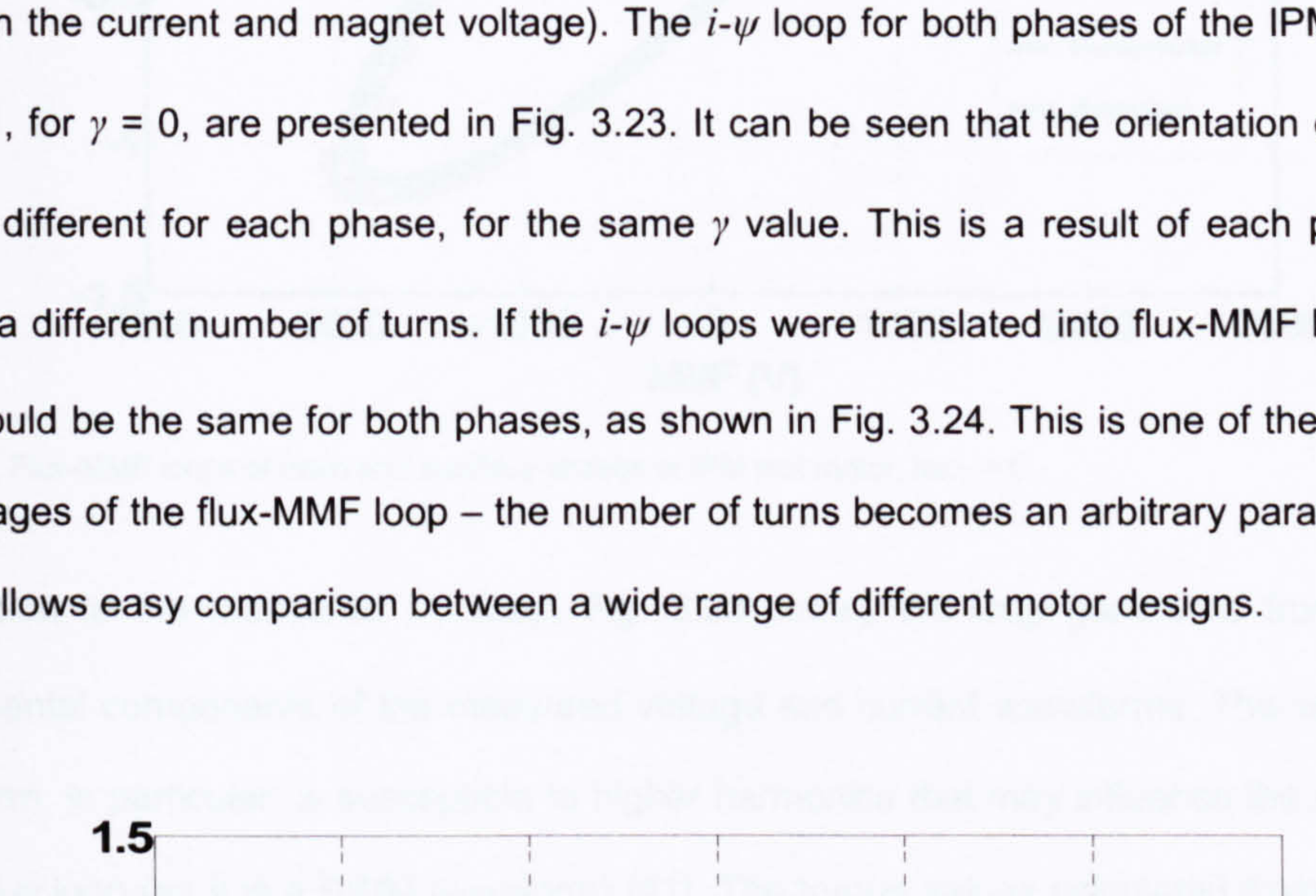

Fig. 3.23. i-ψ loops of main and auxiliary phases of IPM test motor, for γ = 0

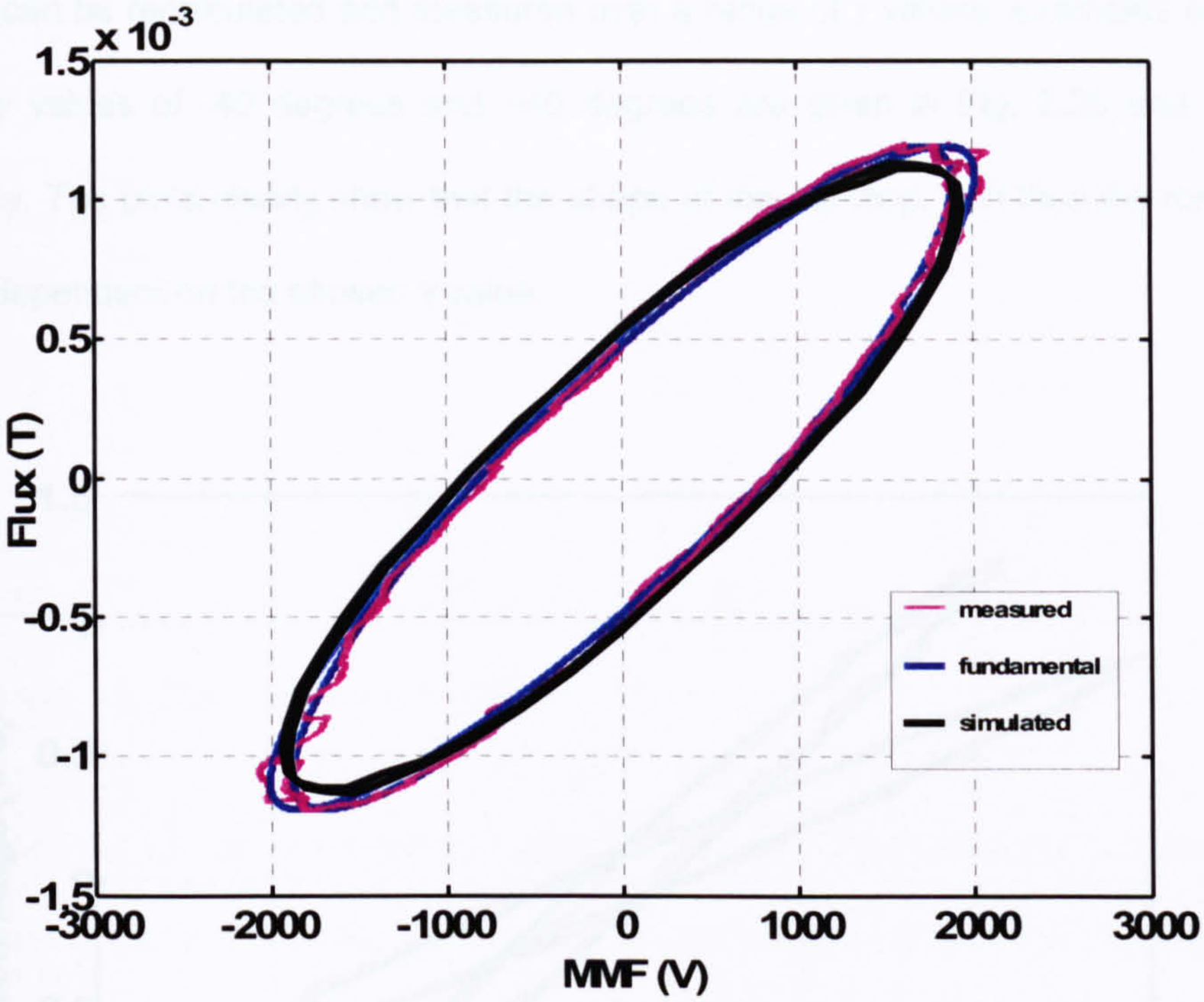

Fig. 3.24. Flux-MMF loops of main and auxiliary phases of IPM test motor, for $\gamma = 0$

In addition to the measured i-ψ loop, Fig. 3.23 shows the loop generated from the fundamental components of the measured voltage and current waveforms. The voltage waveform, in particular, is susceptible to higher harmonics that may influence the shape of the i-ψ loop (as it is a PWM waveform) [41]. The torque values calculated from each loop, for the three methods, are presented in Table 3.1. It is clear that, for this case, the use of the PWM voltage waveform has little effect on the area of the i-ψ loop. Although there is some discrepancy between the measured and simulated i-ψ loops, the calculated torques show reasonable agreement.

Method	Torque calculated from loop area (Nm)			% change in torque
	Main	***Auxiliary***	***Total***	
PC-FEA	0.5135	0.5108	1.0243	+ 3.97
Measured	0.4906	0.4946	0.9852	—
Fundamental	0.4860	0.4909	0.9766	- 0.87%

Table 3.1. Torque values calculated from i-ψ loop at $\gamma = 0$

The loops can be recalculated and measured over a range of γ values. Examples of i-ψ loops for γ values of -40 degrees and +40 degrees are given in Fig. 3.25 and 3.26 respectively. The plots clearly show that the shape of the i-ψ loop, and thus the torque, is heavily dependent on the chosen γ value.

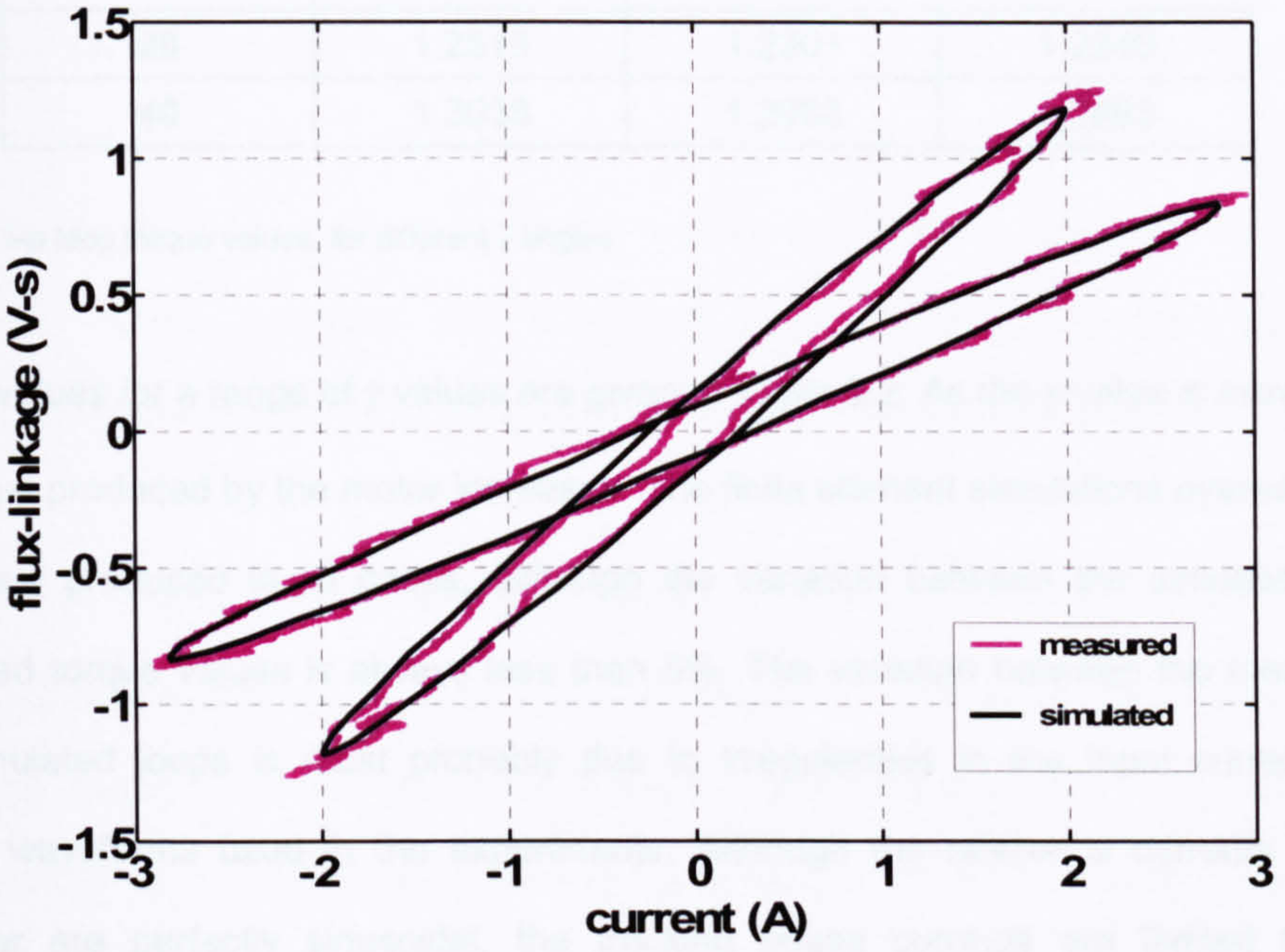

Fig. 3.25. i-ψ loop of IPM test motor, for γ = -40 degrees

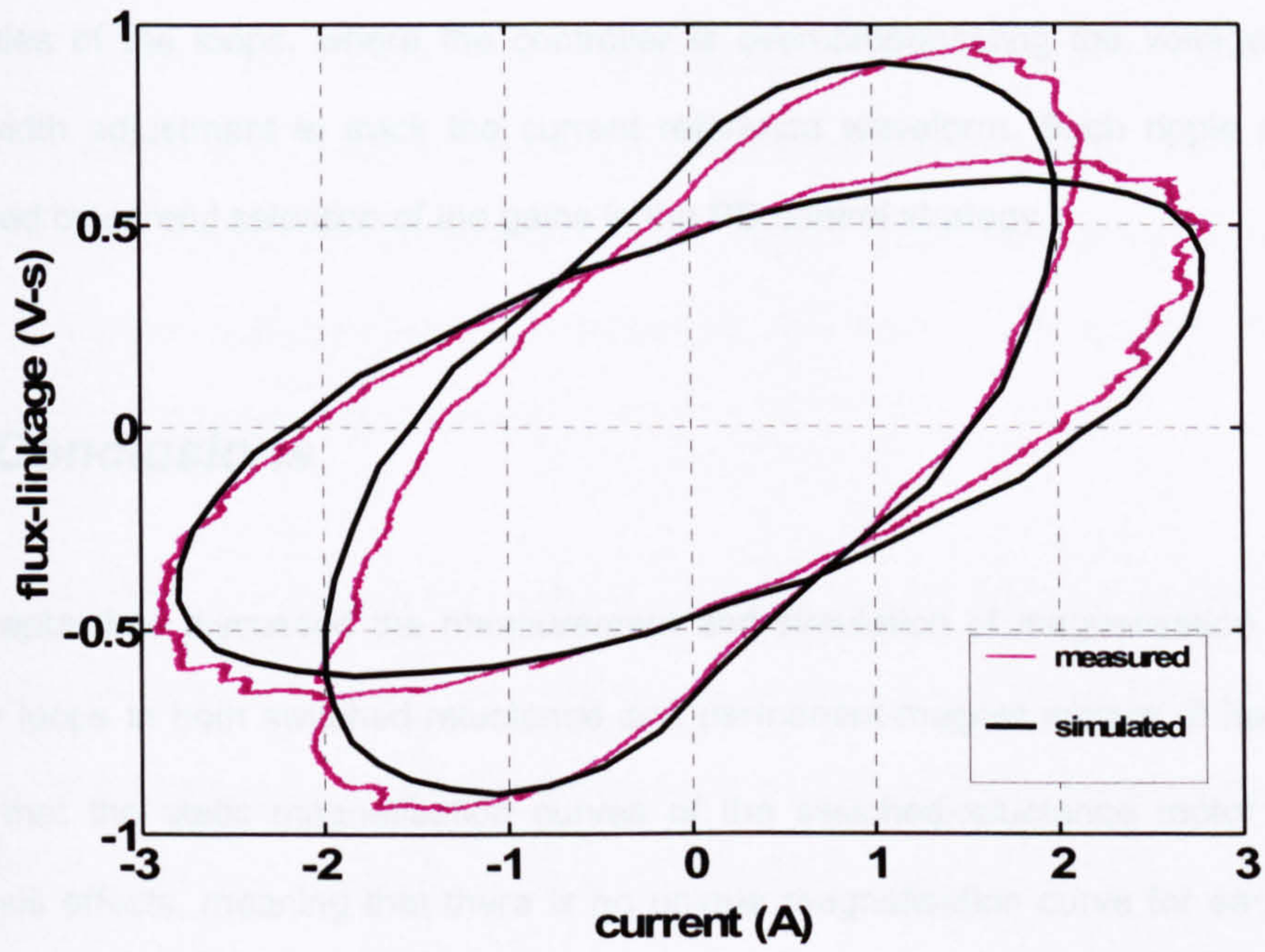

Fig. 3.26. i-ψ loop of IPM test motor, for γ = +40 degrees

γ	Torque calculated from loop area (Nm)		
	PC-FEA	*Measured*	*Fundamental*
- 40	0.2688	0.2722	0.2654
- 20	0.6872	0.6606	0.6553
- 10	0.8709	0.8401	0.8337
0	1.0243	0.9852	0.9766
10	1.1530	1.1230	1.2117
20	1.2516	1.2301	1.2240
40	1.3038	1.2953	1.2893

Table 3.2. *i-ψ* loop torque values, for different γ angles

Torque values for a range of γ values are given in Table 3.2. As the γ value is increased, the torque produced by the motor increases. The finite element simulations overestimate the torque produced in all cases, although the variation between the simulated and measured torque values is always less than 5%. The variation between the measured and simulated loops is most probably due to irregularities in the input current and voltage waveforms used in the experiments. Although the reference currents to the controller are perfectly sinusoidal, the tracking phase currents are limited by the response of the controller. Any deviation from the purely sinusoidal waveforms results can be seen in the orientation of the *i-ψ* loop. Current ripple can be seen at the extremities of the loops, where the controller is overcompensating the voltage PWM pulse width adjustment to track the current reference waveform. Such ripple can be minimised by careful selection of the gains in the PD control strategy.

3.6. Conclusions

This chapter has discussed the measurement and simulation of magnetisation curves and *i-ψ* loops in both switched-reluctance and permanent-magnet motors. It has been shown that the static magnetisation curves of the switched-reluctance motor exhibit hysteresis effects, meaning that there is no unique magnetisation curve for each rotor position. Instead, there are two possible magnetisation curves, corresponding to cases

of rising and falling current. From the results presented, the common method of determining an averaged magnetisation curve has been discounted. Instead, it is proposed that the magnetisation curves corresponding to rising current are used at all rotor positions before the turn-off angle, and the falling current magnetisation curve used for all rotor positions after the turn-off angle.

Tests have shown errors in the magnetisation curves of the SR motor determined from finite element solutions, because end-effects are not considered. Although the magnetisation curves can be realigned to include end-effects, there was still some discrepancy when compared with measured curves. Where possible, measured magnetisation curve data should be used as an input to design calculations.

The i-ψ loops of the SR motor have been measured on a dynamic test rig and simulated in finite element analysis. The most accurate simulation method of the per-phase i-ψ loops was found to be the analytical software, used in conjunction with measured magnetisation curve data. Errors were once again found in the results from finite element simulation, due to the neglecting of end-effects.

The measurement of magnetisation curves of the interior permanent-magnet motor was discussed in detail. Construction of the magnetisation curves using the results from the locked rotor tests and the magnet flux-linkage determined from open-circuit was found to give erroneous results. An alternative method, which does not assume a constant magnet flux under load conditions, was presented. The method, using a dynamometer test rig, was found to be straightforward.

The dynamometer test rig was also used to measure the i-ψ loops of the IPM motor. The measured loops of the main and auxiliary phase were shown to be different, due to the different number of turns on each phase. This result highlights the advantage of the flux-MMF diagram over the i-ψ loop, as in the flux-MMF loop the number of turns-per-phase is arbitrary. The area of the i-ψ loop, and thus the electromagnetic torque, was

shown to vary considerably as a function of the phase angle between the phase current I and magnet voltage E.

The i-ψ loops were also simulated using two-dimensional finite element analysis. When compared to measured data, the simulated loops showed good correlation; calculated torque was accurate to within 5% for all test points.

Chapter 4

Effect of Mutual Coupling on Magnetisation Characteristics

When two or more phases are conducting simultaneously, the flux paths from each phase may overlap, leading to saturation and lower permeabilities in some sections of the steel. When the phases share saturated sections of the flux paths, the phase flux-linkage is a function of all currents, not just the current of that phase [42,43]. This magnetic coupling between phases affects the per-phase magnetisation curves.

In most switched-reluctance motors, each winding is wound around a single tooth, and there is only one winding per tooth. Although there is some magnetic coupling between phases, it is often ignored in design calculations. The flux-linkage is assumed to be a function of the rotor position and the current in that phase alone; the magnetisation curves of each phase are assumed independent of any current in other phases. However, any such coupling between phases will affect the per-phase torque produced. By comparing the static torque waveforms with one phase and multiple phases excited, the effects of mutual coupling between phases can be determined. In motors with fully-pitched windings, there is far greater interaction between the phases, and the flux-linkage must be considered a function of not just the current in the test winding, but of all other excited windings as well. The mutual coupling is due to slot leakage and saturation of the steel in the core back [7].

The degree of mutual coupling is dependent on the polarity arrangement of the phases – whether adjacent phases are of the same or opposite polarity. Fig. 4.1. shows the flux paths of an 8/6, four phase motor with two phases conducting. On the left of the picture, both phases are the same polarity (NN configuration). For three quarters of the stator back iron, the fluxes are additive. In these sections of the back iron, the steel is most likely to saturate, leading to reduced permeability and lower flux-per-phase. In the

remaining quarter of the back iron, the fluxes are in opposition, and saturation is unlikely. On the right of the picture, the phases have opposite polarity (NS configuration) and the fluxes are in opposition for three quarters of the stator back iron. As such, one would expect the mutual effects to be less prominent in the case of NS polarities.

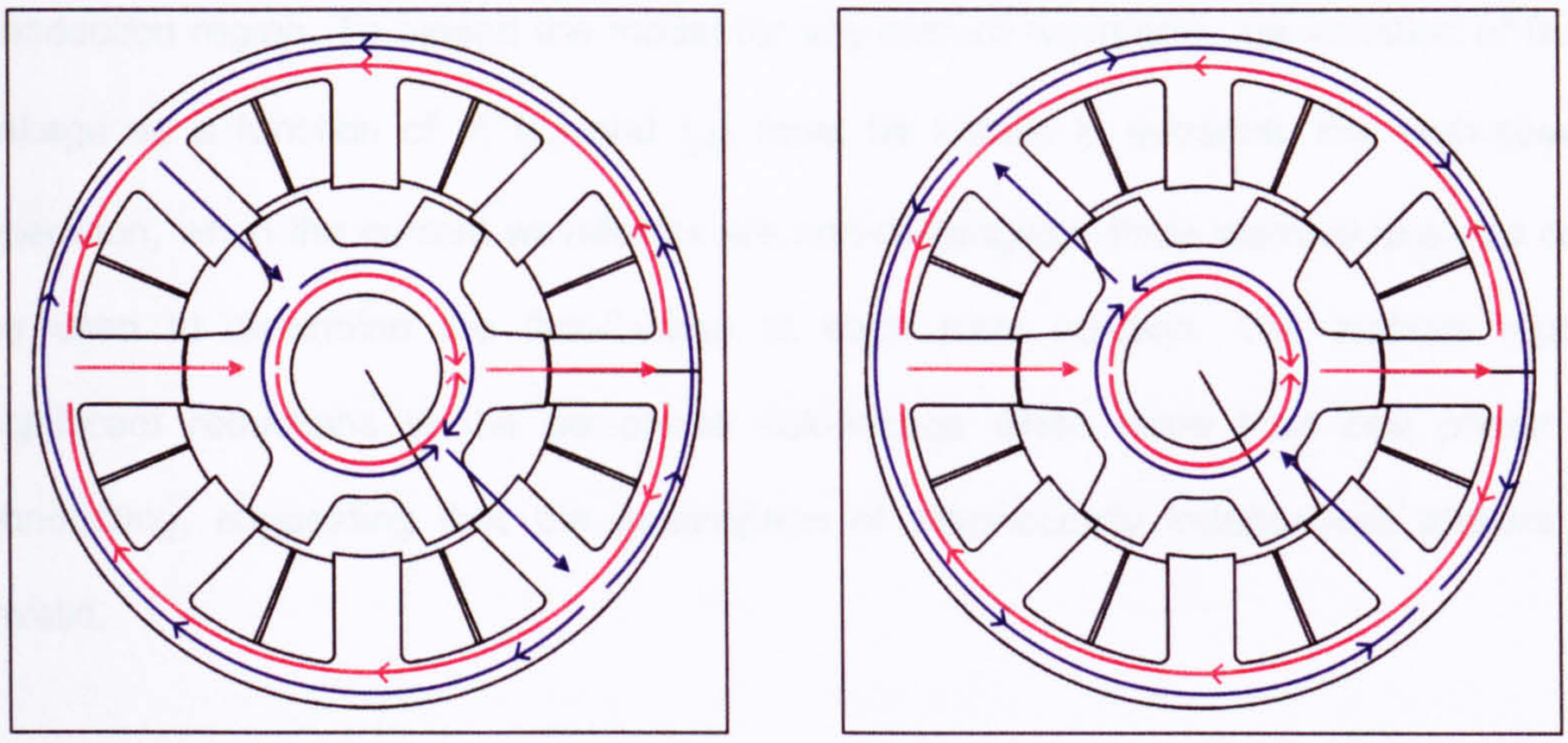

Fig. 4.1. Flux paths of 8/6 motor with two phases conducting simultaneously, showing NN and NS polarities.

4.1. Analytical determination of the effects of mutual coupling

The effects of mutual coupling on the magnetisation characteristics of the motor can be modelled using analytical and finite element techniques. With the exception of fully-pitched windings, the analytical design program PC-SRD assumes no mutual coupling between phases when calculating either the magnetisation curves or the i-ψ loop of each phase. For certain geometries there are minimal mutual effects and the per-phase magnetisation curves can be calculated independently of the currents in the other phases, but this is by no means the case for all motors. Motors with thin stator back irons, in particular, are susceptible to greater mutual effects, as the levels of saturation in the back iron are likely to be high. A number of papers discuss the calculation and modelling of mutual effects in switched-reluctance motors.

In [42], Michaelides and Pollock discuss the effects of mutual coupling on the per-phase i-ψ loops. The average torque output is found from calculation in the change in coenergy

over one excitation cycle. The coenergy integral is evaluated in steps, by calculating the coenergy associated with the excitation of the first phase, then calculating the coenergy in the second phase in the presence of the first excitation. The method is restricted to ideal rectangular current waveforms, which limits the scope of the model to low-speed operation. The model assumes both phases carry maximum current for the entire conduction region. To extend the model for any current waveform, the variation of flux-linkage as a function of θ, i_{ph1} and i_{ph2} must be known in advance. For high-speed operation, when the current waveforms are non-rectangular, finite element analysis can be used to determine the flux-linkage at each rotor position. The authors report significant reductions in the per-phase flux-linkage when more than one phase is conducting, suggesting that the assumption of magnetically independent phases is invalid.

Panda and Ramanarayanan presented results of a four phase 8/6 motor, claiming to take mutual effects into account [44]. While the authors measure the induced voltage in secondary phases when the initial phase is excited at different current levels, the results do not include mutual flux measurements with currents in both phases. The authors erroneously use the mutual effects calculated with only one phase excited in instances when there is current in both phases; such superposition is invalid in the nonlinear system. Simulation results show that, without mutual effects, the energy conversion loops of all the phases are equal. The methods presented in the paper should be expanded to account for current in more than one phase.

[45] describes a model of two-phase excitation, utilising the motor symmetry to reduce the number of measurements or simulations needed. The model assumes normal operation, with only two phases are conducting at any one time. Measured values as used to create a three-dimensional look-up table for use in a Simulink model, where the phase currents are a function of the rotor position and the flux-linkages in both excited windings.

4.2. Finite element modelling of mutual effects

De Paula et al. suggest modelling mutual effects using a combination of two dimensional magnetostatic finite element simulations and the magnetic circuit equations [46]. Coupling of the FEA and circuit equations uses a circuit model and leads to a system of equations solved by a time-stepping Newton Raphson method. The authors report differences in the peak values of each phase current due to the mutual coupling effects, which in turn leads to uneven peaks in the torque waveform.

Cao and Tseng present a model that accounts for mutual coupling, with two phases excited. Finite element simulations are run to determine flux-linkage/ current characteristics in the second excited phase, resulting in look-up tables of $i_{ph2}/\psi_{ph2}/\theta_{ph2}$ for discrete values of current in phase 1 [47]. These look-up tables form the basis of the model. When the current in phase 1 falls between two values with existing look-up tables, the authors propose a linear interpolation to determine the flux-linkage value at the intermediate point. The flux-linkages at the lower and higher current levels (j and j+1) are found from Eq. (4.1) and (4.2), respectively. The flux-linkage at the intermediate current point is found from Eq. (4.3).

$$\lambda_{ph2}(1) = \lambda_{ph2}\left(i_{ph2}, i_{ph1}(j), \theta_{ph2}\right) \tag{4.1}$$

$$\lambda_{ph2}(2) = \lambda_{ph2}\left(i_{ph2}, i_{ph1}(j+1), \theta_{ph2}\right) \tag{4.2}$$

$$\lambda_{ph2} = \lambda_{ph2}(1) + \frac{\lambda_{ph2}(2) - \lambda_{ph2}(1)}{i_{ph1}(j+1) - i_{ph1}(j)}\left(i_{ph1} - i_{ph1}(j)\right) \tag{4.3}$$

The method needs a large amount of simulation data to construct the look-up tables used in the model. If the interval between successive i_{ph1} values is large, the accuracy of

the model will be compromised, because it relies on linear interpolation between two flux-linkage values in a nonlinear system.

As reported in [44], the i-ψ loops are not equal for all phases when more than one phase is excited. The effects can be illustrated using results from finite element simulations. The current/ flux-linkage trajectories can be calculated for normal operation (with all phases excited in turn) and with only one phase excited (by turning off the currents in all other phases). Differences between the resulting i-ψ loops are due to the mutual interaction between the excited phase and the other phases.

From a design viewpoint, it is necessary only to determine the per-phase i-ψ loops during normal operation, though it may also be of interest to calculate the mutual coupling between adjacent phases with a view to improving the overall design. At some rotor positions, when there are two phases simultaneously excited and there will be mutual flux effects of varying strengths in every phase. The change in the i-ψ loop due to the mutual effects of all the phases is easily determined from nonlinear finite element solutions, but not the mutual effects of each phase individually. This can, however, be determined using the frozen permeabilities method. With small changes to the automatically generated script, the frozen permeabilities method can be implemented for the SR motor in PC-FEA (see Appendix 3).

4.3. Mutual coupling for sensorless control

For correct commutation of the phase currents in switched-reluctance machines, the rotor position must be known. In most cases a shaft position sensor such as an encoder or resolver is used, but for some applications there may be reliability or cost issues and so sensorless control is required. Sensorless control techniques based on mutually-induced voltage have been presented in a number of papers.

Husain and Ehsani present a control strategy based on measured mutual flux-linkage waveforms in either the adjacent or opposite phases of four-phase machines [48]. The mutually induced voltage in the phase opposite to the excited phase is measured during either magnetising or freewheeling operation. Either induced voltage can be used to calculate the rotor position, using Eq. (4.4) and (4.5) for magnetising and freewheeling operation respectively. In the opposite phase, the mutually induced voltage exhibits sine-like variation over one electrical cycle. The control algorithm compares the mutually induced voltage with a threshold level for commutation; when a predetermined voltage level is reached, a microcontroller generates the required gating signals for commutation.

$$v_{m1} = \frac{M_L(\theta)}{L(\theta)} V - \frac{M_L(\theta) I_0}{L(\theta)} \frac{dL}{d\theta} \omega - I_0 R_{ph} \frac{M_L(\theta)}{L(\theta)} + I_0 \frac{dM_L}{d\theta} \omega \tag{4.4}$$

$$v_{m2} = -\frac{M_L(\theta) I_0}{L(\theta)} \frac{dL}{d\theta} \omega - I_0 R_{ph} \frac{M_L(\theta)}{L(\theta)} + I_0 \frac{dM_L}{d\theta} \omega \tag{4.5}$$

The voltage equations include speed-dependent terms, which are negligible under low-speed operation but can have significant effect at higher speeds. The method relies on accurate knowledge of a number of parameters.

A similar method using the magnetising and freewheeling voltages is proposed by Chi et al. [49]. The mutually induced voltages from both magnetising and freewheeling operation in the hysteresis current band are measured, close to the point of maximum current. By subtracting the voltage induced during freewheeling operation from the voltage measured during magnetising operation, the resulting voltage can be represented in terms of the ratio between self and mutual inductance. For soft chopping control, the resulting mutual voltage is given by Eq. (4.6). For hard chopping, a factor of 2 is introduced, as shown in Eq. (4.7). The ratio M_L/L is calculated from Eq. (4.6) and (4.7) and used to determine the rotor position from a look-up table. The M_L/L versus θ

data is found by measurement. The authors present results from a Simulink model of the control system, showing prediction of the rotor position to within 3.3 electrical degrees.

$$v_{msc} = \frac{M_L}{L} v_{dc} \tag{4.6}$$

$$v_{mhc} = 2\frac{M_L}{L} v_{dc} \tag{4.7}$$

The model is not specifically limited to operation with current in only phase at each rotor position, but operation with current in more than one phase will result in complex M_L/L inductance ratios, which cannot be characterised easily in terms of multiple currents. The subtraction used to determine the resulting mutual voltage relies on the assumption that the current is the same at both measurement points. In the example given in the paper, the current is a near ideal squarewave pulse, with current variation only within the hysteresis band limits. In normal operation at high speeds, the current rise and fall times are limited by the power electronics and there is no instantaneous rise. During the rise times, the currents may be changing considerably and this would lead to errors in the rotor position sensing.

4.4. Measuring the effects of mutual coupling

The effects of mutual coupling can be measured in two ways – either by modelling the *i*-ψ loops or the static torque waveforms. If there is no mutual coupling between phases, then the resultant *i*-ψ loop of a phase under single-phase excitation will be the same as the loop generated in a test with all phases excited.

The static torque waveforms can be used to determine the influence of mutual effects on torque production in the motor, as described in [50]. If there is no mutual coupling

between phases, the total torque waveform can be constructed by superposition of the static torque waveforms of each phase singly excited. In [50], the authors suggest measurement of the static torque waveform of only the first phase, then shifting the waveform by (360/($N_{ph}N_r$)) for each subsequent phase. This approach will produce erroneous results; it is unlikely that there will be no mutual coupling effects (and for saturated conditions, the mutual coupling will lead to significant differences between the i-ψ loops for each phase).

The i-ψ loops of each phase can also be used to determine the effects of mutual coupling. Comparison of the i-ψ loops generated under normal operation, and generated when each phase is separately excited, will suggest the extent to which mutual coupling affects the motor performance. The mutual voltages induced in each unexcited phase can also be measured.

4.4.1. Mutual coupling from static torque measurements

Figs. 4.2 and 4.3 compare measured static torque waveforms for two phases conducting, with constant and equal current in both phases. Fig. 4.2 corresponds to the total torque values when the adjacent phases have the same polarity (e.g. NN). Fig. 4.3 gives the torque values when the adjacent values have opposite polarities (e.g. NS). The total torque is clearly higher when the adjacent phases have opposing polarities (NS rather than NN). The effect is more noticeable at higher current values, due to increased saturation levels in the steel. Table 4.1 compares the measured torque curves at a current of 10 amps with the constructed torque waveform. It is clear that there is some mutual coupling between phases, and that the effect is more prominent when the adjacent phases have the same polarities.

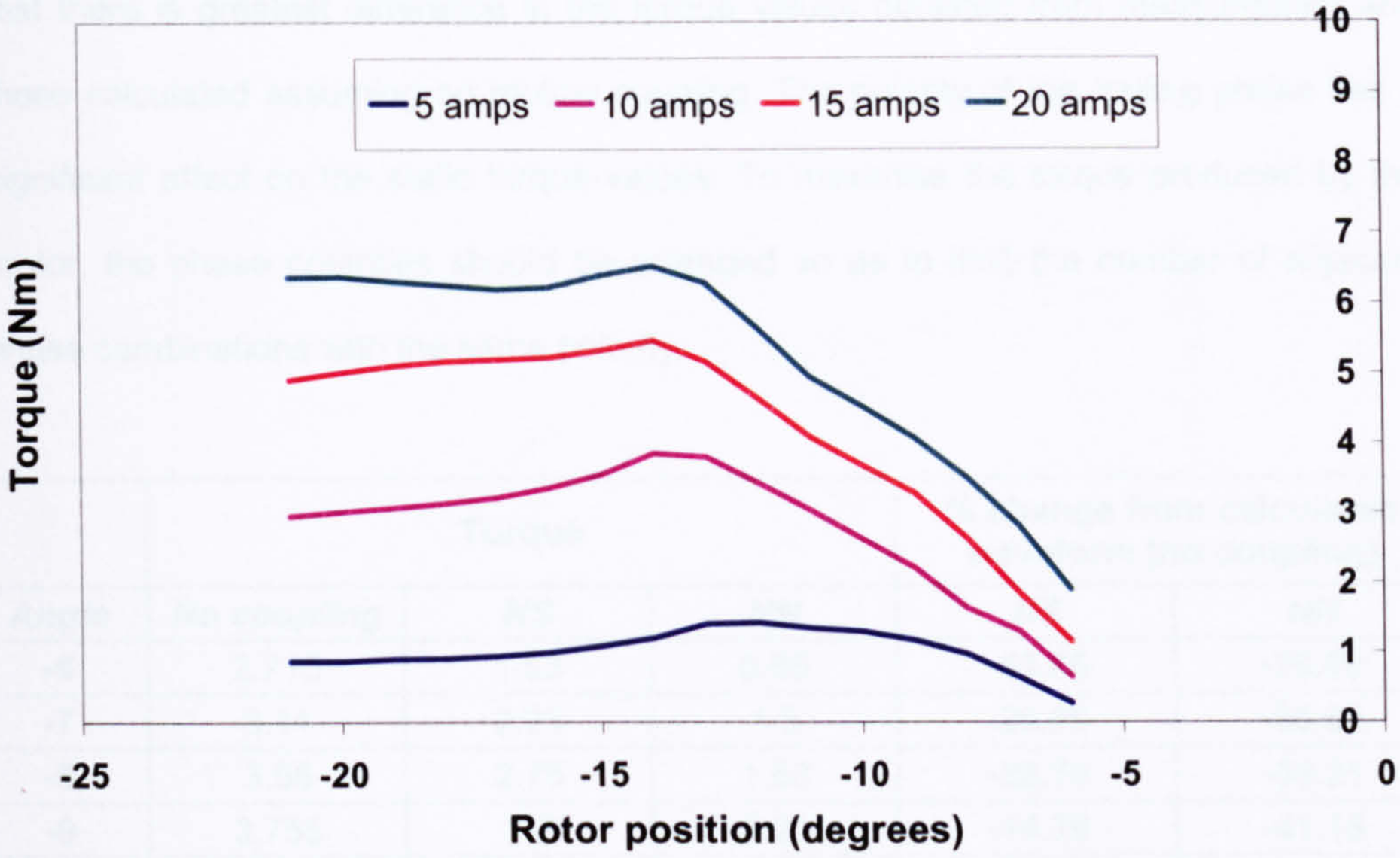

Fig. 4.2. Measured static torque waveforms with two phases conducting (same polarities - NN)

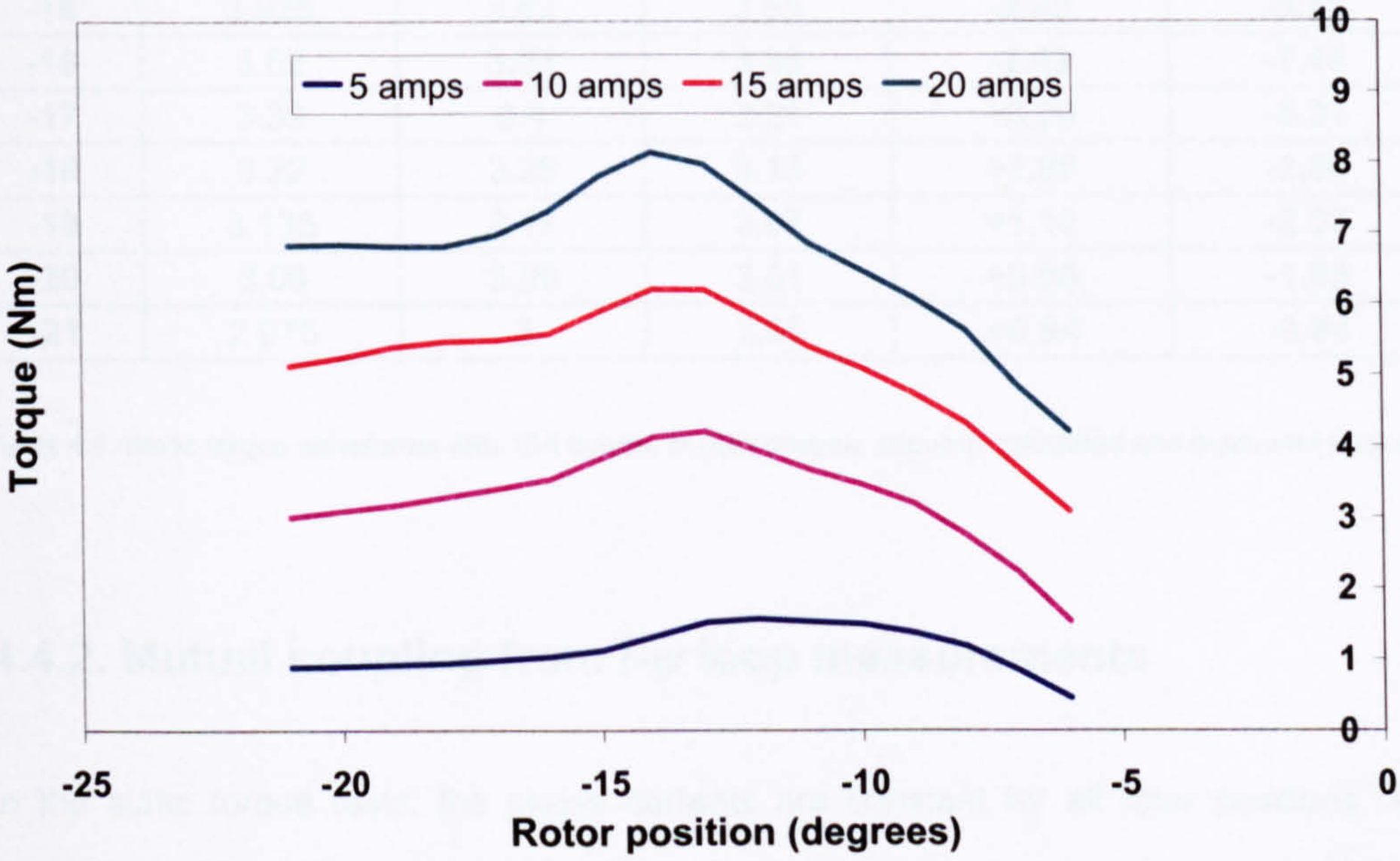

Fig. 4.3. Measured static torque waveforms with two phases conducting (opposite polarities - NS)

From Table 4.1, it can be seen that the mutual coupling effects are greater at -6 degrees than at -21 degrees. As the rotor position changes from -21 to -6 degrees, the level of torque in the second phase gradually increases until, at -6 degrees, when the rotor is in the aligned position, the torque in the second phase is at a maximum. It is at this point

that there is greatest difference in the torque values obtained from measurement and those calculated assuming no mutual coupling. The polarity of the trailing phase has a significant effect on the static torque values. To maximise the torque produced by the motor, the phase polarities should be arranged so as to limit the number of adjacent phase combinations with the same polarity.

	Torque			% change from calculated waveform (no coupling)	
Angle	***No coupling***	***NS***	***NN***	***NS***	***NN***
-6	2.715	1.53	0.65	**-43.65**	**-76.06**
-7	3.14	2.23	1.3	**-28.98**	**-58.60**
-8	3.56	2.75	1.63	**-22.75**	**-54.21**
-9	3.755	3.2	2.21	**-14.78**	**-41.15**
-10	3.93	3.47	2.62	**-11.70**	**-33.33**
-11	4.28	3.68	3.04	**-14.02**	**-28.97**
-12	4.38	3.94	3.43	**-10.05**	**-21.69**
-13	4.615	4.21	3.8	**-8.78**	**-17.66**
-14	4.48	4.13	3.85	**-7.81**	**-14.06**
-15	3.925	3.83	3.55	**-2.42**	**-9.55**
-16	3.62	3.53	3.35	**-2.49**	**-7.46**
-17	3.39	3.4	3.21	**+0.29**	**-5.31**
-18	3.22	3.28	3.13	**+1.86**	**-2.80**
-19	3.135	3.17	3.07	**+1.12**	**-2.07**
-20	3.06	3.09	3.01	**+0.98**	**-1.63**
-21	2.975	3	2.95	**+0.84**	**-0.84**

Table 4.1. Static torque waveforms with 10A current in both phases, showing calculated and measured torque.

4.4.2. Mutual coupling from i-ψ loop measurements

In the static torque tests, the phase currents are constant for all rotor positions. To replicate this in the rotational i-ψ loop tests, a current-limiting controller is used to provide trapezoidal current waveforms with a peak current of 12 A. Figs. 4.4 and 4.5 show measured i-ψ loops for phases 1 and 4, under the conditions given in Table 4.2.

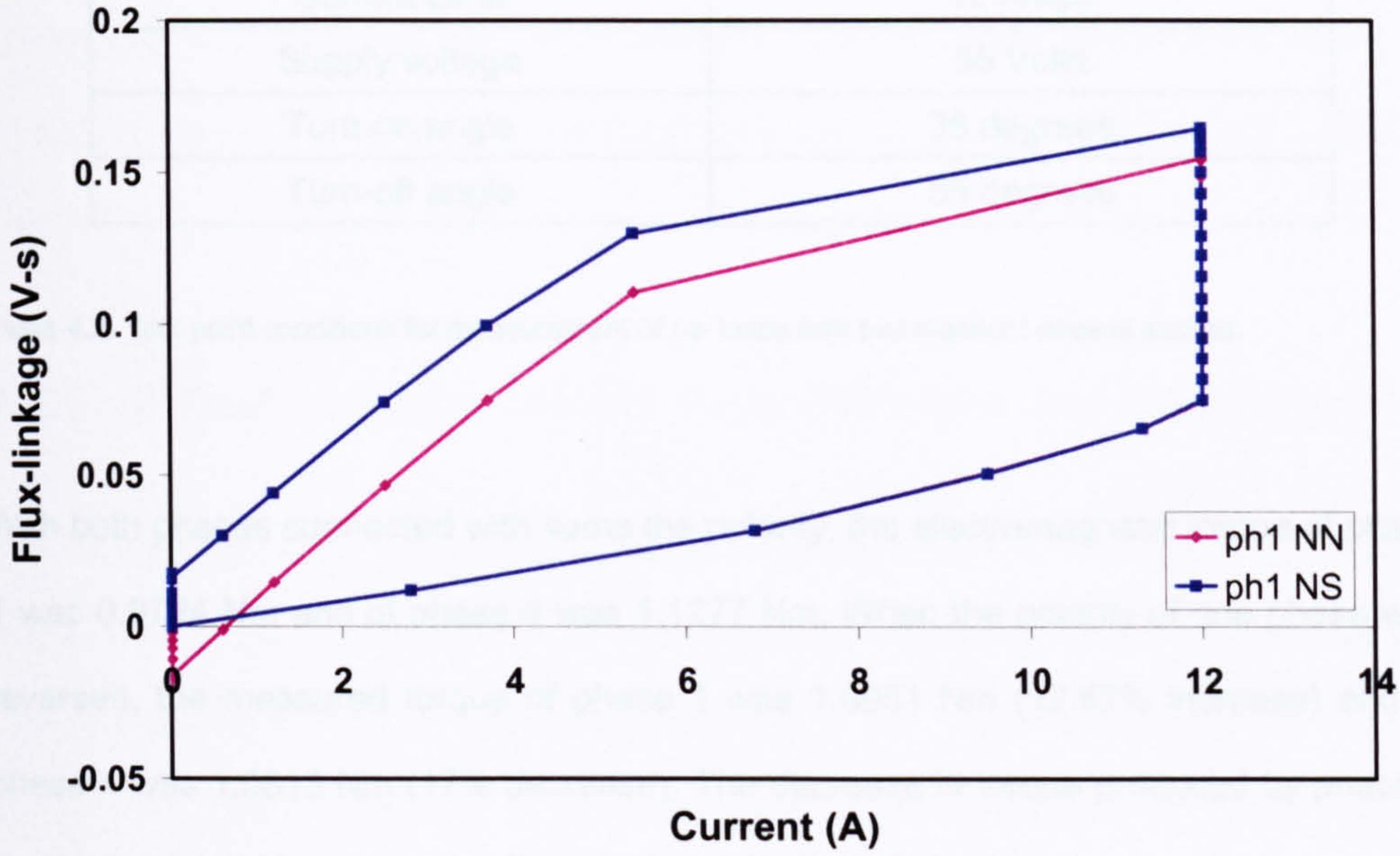

Fig. 4.4. Measured *i-ψ* loops for test motor phase 1 for NN and NS cases

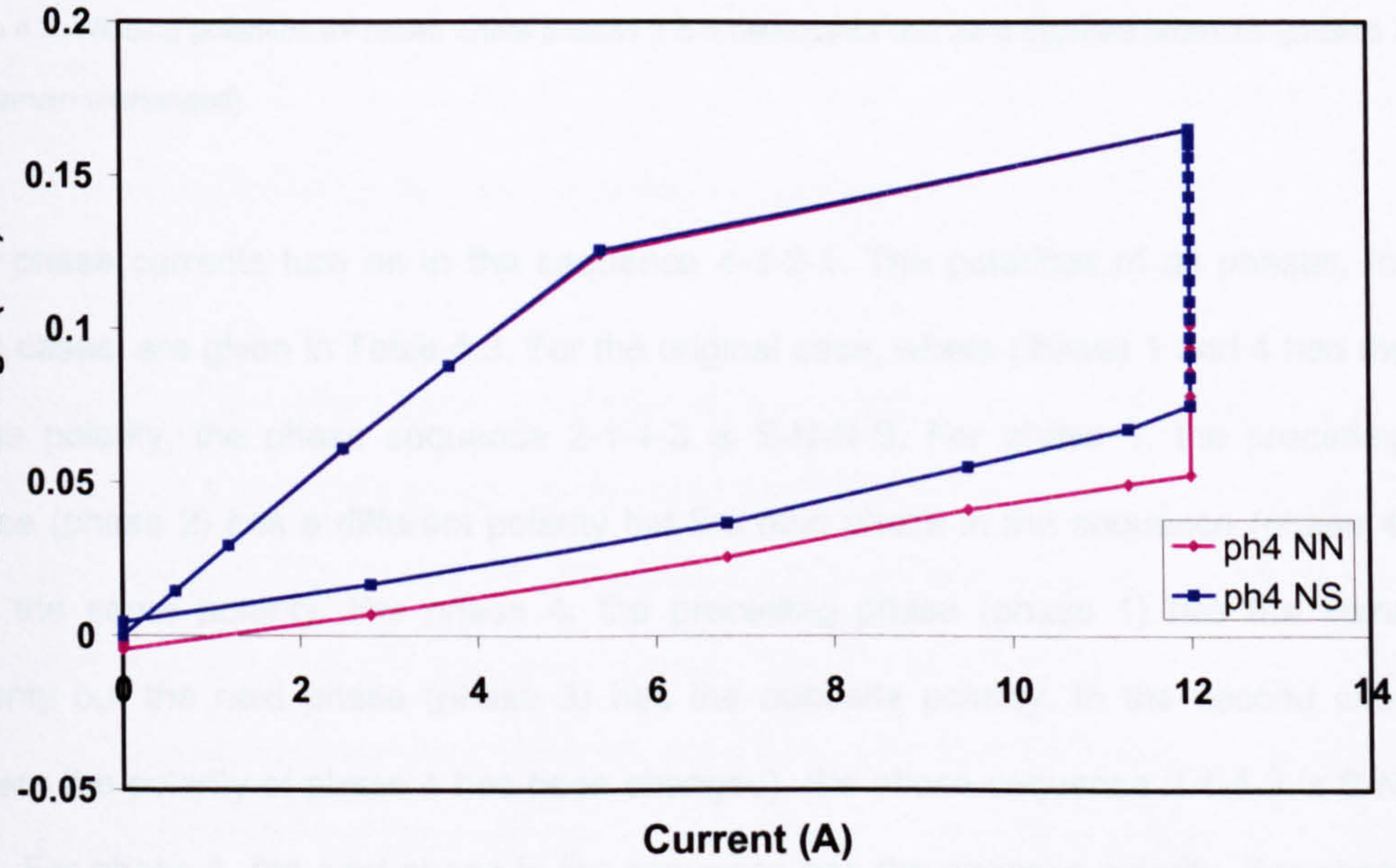

Fig. 4.5. Measured *i-ψ* loops for test motor phase 4 for NN and NS cases.

Parameters	Settings
Speed	200 rpm
Current Limit	12 Amps
Supply voltage	55 Volts
Turn-on angle	35 degrees
Turn-off angle	55 degrees

Table 4.2. Test point conditions for measurement of *i-ψ* loops with two adjacent phases excited.

With both phases connected with same the polarity, the electromagnetic torque of phase 1 was 0.9724 Nm and of phase 4 was 1.1277 Nm. When the polarity of one phase was reversed, the measured torque of phase 1 was 1.0951 Nm (12.62% increase) and of phase 4 was 1.0813 Nm (17% decrease). The decrease in torque produced by phase 4 can be explained by examining the winding polarities of all phases.

Pole (Phase)	**1** (1)	**2** (2)	**3** (3)	**4** (4)	**5** (1)	**6** (2)	**7** (3)	**8** (4)
Same	N	S	N	S	S	N	S	N
Opposite	N	S	N	N	S	N	S	S

Table 4.3. Winding polarities for cases where phases 1 & 4 have same and have opposite polarities (phases 2 & 3 remain unchanged).

The phase currents turn on in the sequence 4-3-2-1. The polarities of all phases, for both cases, are given in Table 4.3. For the original case, where phases 1 and 4 had the same polarity, the phase sequence 2-1-4-3 is S-N-N-S. For phase 1, the preceding phase (phase 2) has a different polarity but the next phase in the sequence (phase 4) has the same polarity. For phase 4, the preceding phase (phase 1) has the same polarity but the next phase (phase 3) has the opposite polarity. In the second case (where the polarity of phase 4 has been changed), the phase sequence 2-1-4-3 is S-N-S-S. For phase 1, the next phase in the sequence has the opposite polarity. For phase 4, the next phase in the sequence has the same polarity.

There is a correlation between the phase polarity patterns and the shape of the i-ψ loop produced. When the next phase in the sequence has the same polarity as the current phase, the i-ψ trajectory of the current phase will not be a single loop, but will exhibit as crossover, as shown in Fig. 4.4. This ultimately reduces the area of the loop and thus the torque.

4.4.3. Mutual coupling results from finite element simulations

The original tests were carried out with only two phases excited, to replicate the existing test data from the static torque tests. This data is insufficient to determine if the leading phase also affects the per-phase torque produced. As such, the conditions of the test point have been replicated in nonlinear and frozen permeability finite element simulations with all four phases excited. Three separate winding arrangements have been modelled, with polarities as given in Table 4.4.

Pole (Phase)	**1** (1)	**2** (2)	**3** (3)	**4** (4)	**5** (1)	**6** (2)	**7** (3)	**8** (4)
Case 1	N	S	N	S	S	N	S	N
Case 2	N	S	N	N	S	N	S	S
Case 3	N	N	N	N	S	S	S	S

Table 4.4. Winding polarities for the 3 cases simulated in nonlinear and frozen permeability finite element simulations.

The results from the measurements with two phases excited suggest that cases 1 and 2 should produce the same total torque (because for 3 of the 4 phases, the next phase is of the opposite polarity). Case 3 should produce significantly lower torque, as for 3 of the 4 phases, the next phase is the same polarity. This is confirmed by the results of the nonlinear finite element simulations, which show the total torque for cases 1, 2 and 3 as 3.5912 Nm, 3.5903 Nm and 3.4151 Nm respectively. The effect of reducing the number of NS combinations from 3 to 1 is a reduction of almost 4.9% in the torque produced. From the nonlinear solutions, it is possible to determine the per-phase torque for each of the cases given above. Results are shown in Table 4.5.

	Case 1	Case 2	Case 3
Phase 1	0.6931 Nm	0.9195 Nm	1.0583 Nm
Phase 2	0.9198 Nm	0.9198 Nm	0.8319 Nm
Phase 3	0.9198 Nm	1.0585 Nm	0.8323 Nm
Phase 4	1.0586 Nm	0.6925 Nm	0.6925 Nm
Total torque	**3.5912 Nm**	**3.5903 Nm**	**3.4151 Nm**

Table 4.5. Results from nonlinear finite element simulations

Table 4.5 shows a variation in the per-phase loop torque from 0.6925 to 1.0586 Nm, depending on the polarity of the phases. The polarities of the preceding and following phases have been examined for each phase, for all 3 cases. There is a strong relationship between the phase polarities and the per-phase torque produced, Table 4.6. Maximum torque is achieved when the preceding phase has the same polarity as the current phase, but the next phase in the sequence has the opposite polarity, e.g. for phase 1, the maximum torque is produced when phases 2 and 1 are the same polarity and phase 4 is the opposite polarity (phase sequence is 4-3-2-1-4).

Phase combination (Preceding/Current/Next)	Average torque produced
SNN , NSS	0.6927 Nm
NNN , SSS	0.8321 Nm
NSN , SNS	0.9197 Nm
NNS , SSN	1.0585 Nm

Table 4.6. Relationship between phase polarities and electromagnetic torque

The arrangement of phase polarities affects the torque produced in each phase, as different polarity combinations produce varying levels of mutual flux-linkage. The induced mutual flux-linkages in all phases can be determined by running frozen permeability finite element simulations for each phase in turn. The simulations have been run using a current waveform that replicates the actual operation of the motor; the current waveform is that used in the i-ψ loop calculations of Chapter 3 (as shown in Fig.

3.12). The mutual, self and total flux-linkages for each phase (determined from a combination of nonlinear and frozen permeability solutions) are given in Figs. 4.6 to 4.9.

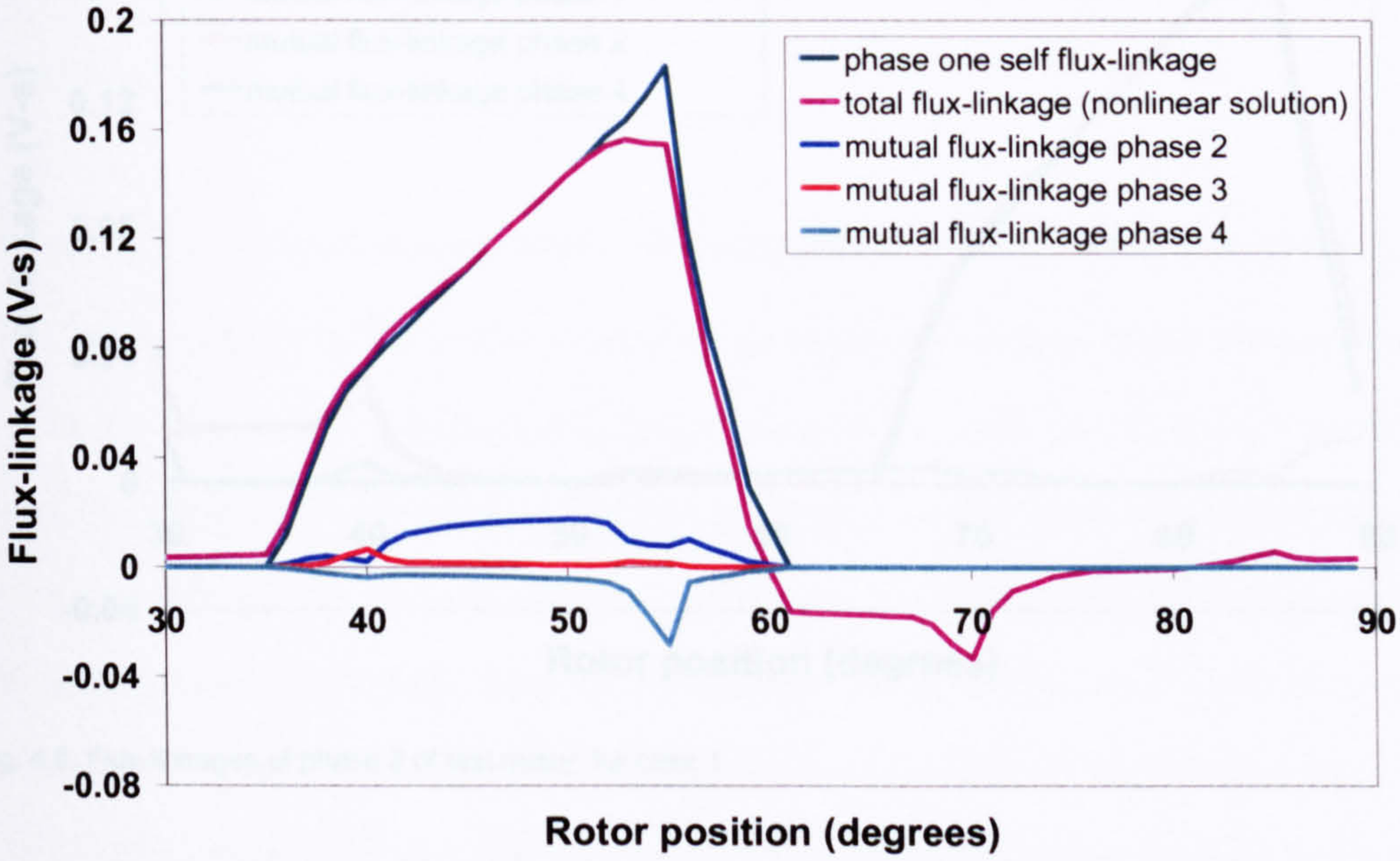

Fig. 4.6. Flux-linkages of phase 1 of test motor, for case 1.

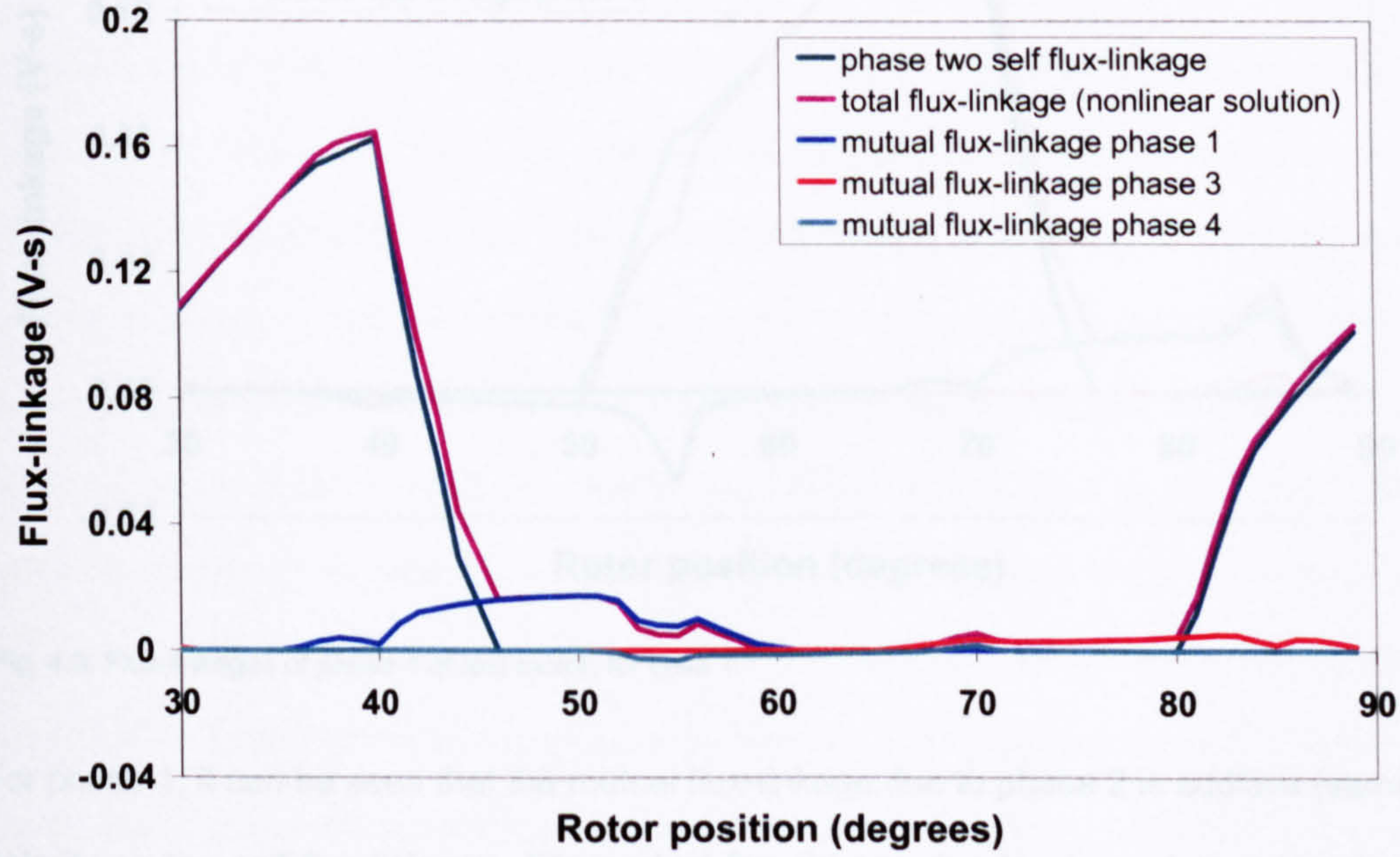

Fig. 4.7. Flux-linkages of phase 2 of test motor, for case 1.

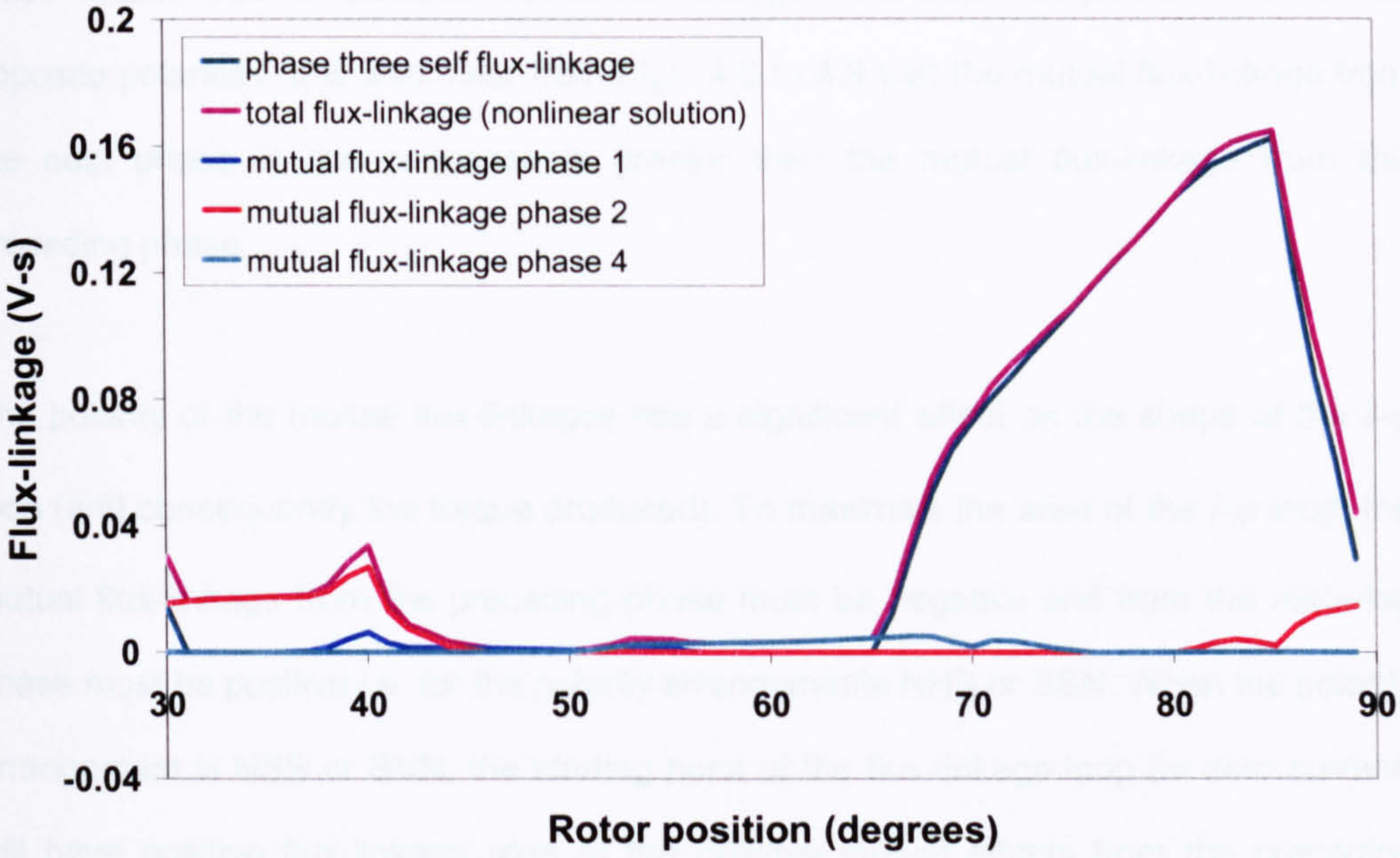

Fig. 4.8. Flux-linkages of phase 3 of test motor, for case 1.

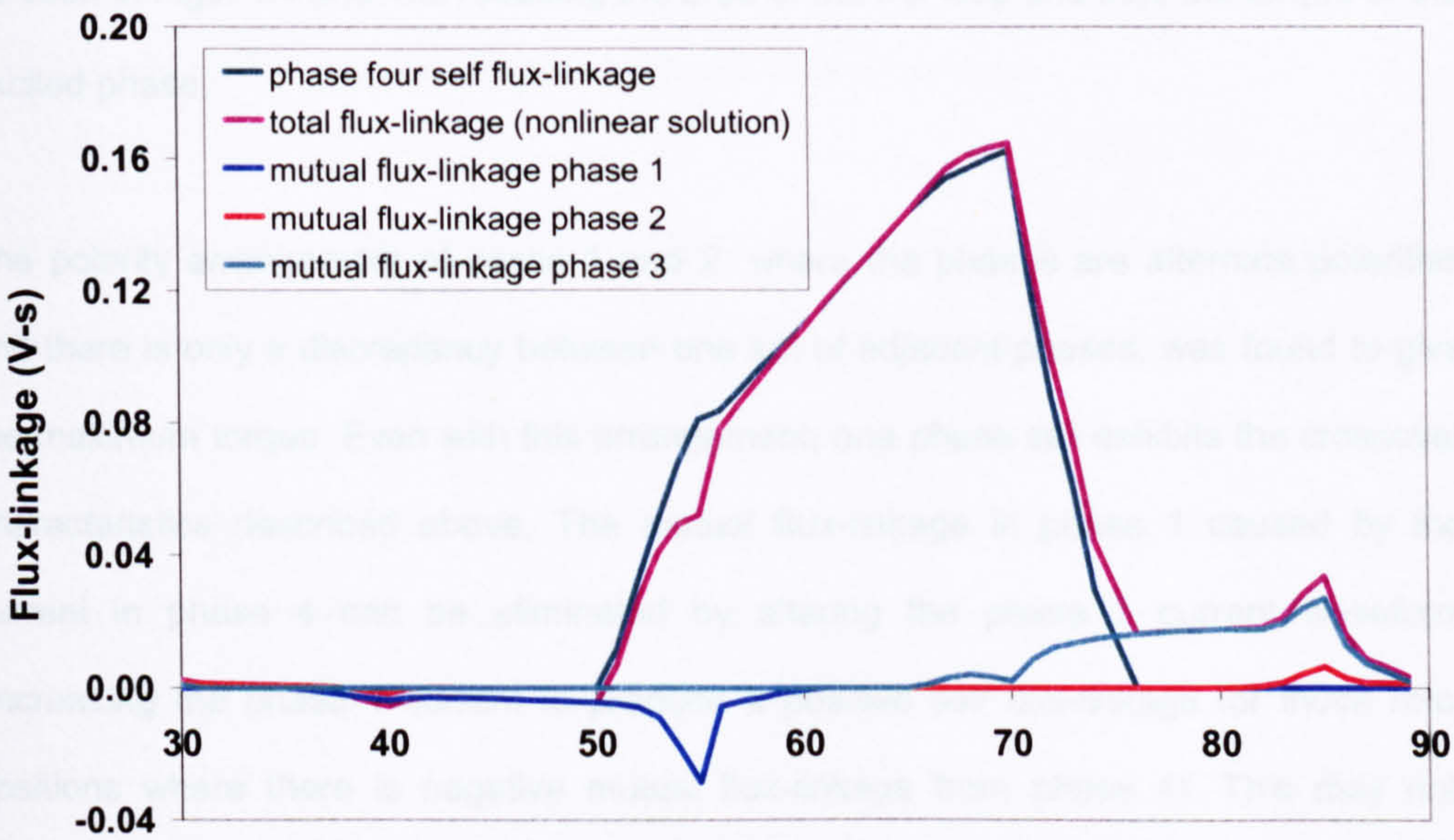

Fig. 4.9. Flux-linkages of phase 4 of test motor, for case 1.

For phase 1, it can be seen that the mutual flux-linkage due to phase 2 is additive (same polarity as the self flux-linkage). The mutual flux-linkage due to phase 4 is subtractive (opposite polarity to the self flux-linkage). For phases 2 and 3, the mutual flux-linkages from both the previous and next phases are additive. In the case of phase 4, the mutual

flux-linkage due to phase 1 is subtractive and from phase 3 is additive. It is clear from these results that for additive mutual flux-linkages, the adjacent phases must be of opposite polarities. It is also clear from Figs. 4.6 to 4.9 that the mutual flux-linkage from the next phase in the sequence is greater than the mutual flux-linkage from the preceding phase.

The polarity of the mutual flux-linkages has a significant effect on the shape of the i-ψ loop (and consequently the torque produced). To maximise the area of the i-ψ loop, the mutual flux-linkage from the preceding phase must be negative and from the following phase must be positive i.e. for the polarity arrangements NNS or SSN. When the polarity arrangement is NSS or SNN, the starting point of the flux-linkage loop (at zero current) will have positive flux-linkage (due to the positive mutual effects from the preceding phase) and the end point will have negative flux-linkage (due to the negative mutual effects from the next phase in the sequence). This causes the crossover point that can be seen in Figs. 4.4 and 4.5, reducing the area of the i-ψ loop and thus the torque of the excited phase.

The polarity arrangement of cases 1 and 2, where the phases are alternate polarities and there is only a discrepancy between one set of adjacent phases, was found to give the maximum torque. Even with this arrangement, one phase still exhibits the crossover characteristics described above. The mutual flux-linkage in phase 1 caused by the current in phase 4 can be eliminated by altering the phase 1 current waveform (increasing the phase 1 current to produce a positive self flux-linkage for those rotor positions where there is negative mutual flux-linkage from phase 4). This may not, however, lead to an increase in the average torque, as increasing the phase 1 current increases saturation, leading to lower permeabilities and thus lower self flux-linkage in phase 4. The frozen permeability solutions should be used in conjunction with nonlinear solutions to optimise the area of the i-ψ loops in each phase.

4.5. Conclusions

This chapter has discussed in detail the effects of mutual coupling in the switched-reluctance motor. Mutual coupling occurs when two or more phases are excited simultaneously. The degree of mutual coupling depends on the arrangement of the phase coil polarities and the design of the motor cross-section.

The effects of mutual coupling can be measured using either the static torque characteristics or the i-ψ loops of the motor. The static torque characteristic of two adjacent phases singly-excited can be added to determine the total torque that would occur if there were no mutual coupling effects present. This composite waveform can then be compared with the measured static torque characteristic of the motor will two phases excited simultaneously, when the phases are the same and of opposite polarities, to determine the effects of mutual coupling. Results from measurements on the switched-reluctance test motor showed that the mutual coupling effects were more prominent when the adjacent phases were of the same polarity.

The polarity of the phase coils affects the shape of the i-ψ loop under multiple-phase excitation, due to the mutual coupling effects from the adjacent phases. The area of the i-ψ loop, and thus the phase torque, is maximum when the polarity of the preceding phase is the same, and from the next phase in the sequence is opposite. For motors with an even number of phases, it is not possible for every phase to have the coil polarity arrangement which results in maximum torque.

Using the frozen permeability finite element method, the self and mutual flux-linkage of each phase can be determined under multiple-phase excitation for the first time. The simulation results show that when the adjacent phases are of the same polarity, the mutual flux-linkage produced is negative; when the adjacent phases are of opposite polarity, the mutual flux-linkage of the phase under test is positive.

Chapter 5

Synchronous Reactances of IPM Motor

In AC synchronous machines, the field produced by the stator phase currents rotates in synchronism with the rotor during steady state operation. To simplify analysis of such motors, a number of authors worked in the early twentieth century to develop methods whereby the calculation of field parameters is transformed from the stator to the rotor reference frame [51,52]. The transformation from three-phase stator quantities to two-axis rotor quantities (relating to the rotor direct and quadrature axis) is achieved using

$$\begin{bmatrix} \psi_d \\ \psi_q \\ \psi_0 \end{bmatrix} = \frac{2}{3}\begin{bmatrix} \cos\theta & \cos(\theta-120^\circ) & \cos(\theta+120^\circ) \\ \sin\theta & -\sin(\theta-120^\circ) & -\sin(\theta+120^\circ) \\ 1/2 & 1/2 & 1/2 \end{bmatrix}\begin{bmatrix} \psi_a \\ \psi_b \\ \psi_c \end{bmatrix} \tag{5.1}$$

ψ_0 is the zero-sequence component of flux-linkage. Under balanced 3-phase operation, the zero sequence component is zero. The electromagnetic torque is calculated using

$$T_e = \frac{mp}{\omega}\left(E_0 I_q + I_d I_q \left(X_d - X_q\right)\right) \tag{5.2}$$

where I_d and I_q are the direct and quadrature axis components of current, X_d and X_q are the direct and quadrature axis synchronous reactances, m is the number of phases, p is the number of pole pairs, $\omega=2\pi f$ is the frequency in radians per second and E_0 is the open circuit EMF per phase. The $E_0 I_q$ term in (5.2) represents the torque produced by the permanent magnets, while the second term represents the reluctance torque. The maximum torque produced is proportional to the difference between the direct and quadrature axis synchronous reactances, whereas the maximum power is proportional to the ratio of X_d to X_q [53]. Due to its salient pole structure, the quadrature axis

synchronous reactance of the interior permanent-magnet motor is much greater than the direct axis synchronous reactance. In non-salient pole machines (such as the surface-mounted permanent-magnet motor), the direct and quadrature axis synchronous reactances are equal.

The direct and quadrature axis properties can be graphically represented by the phasor diagram. The use of the phasor diagram in calculation of machine parameters is limited to certain machine types, due to the inherent restrictions of the method. The direct and quadrature axis parameters represented in the diagram are phasor quantities, and so the method is only valid for motors driven with sinusoidal current waveforms and with sine-distributed windings. Examples of simplified phasor diagrams of a salient pole permanent-magnet motor, for magnetising and demagnetising currents are given in Figs. 5.1 and 5.2 respectively. Demagnetising operation is often described as phase advance or field weakening, and is used for operation above the motor base speed. It can been seen in Fig. 5.2 that for demagnetising operation, the direct axis current produces a voltage drop that reduces the voltage requirement V.

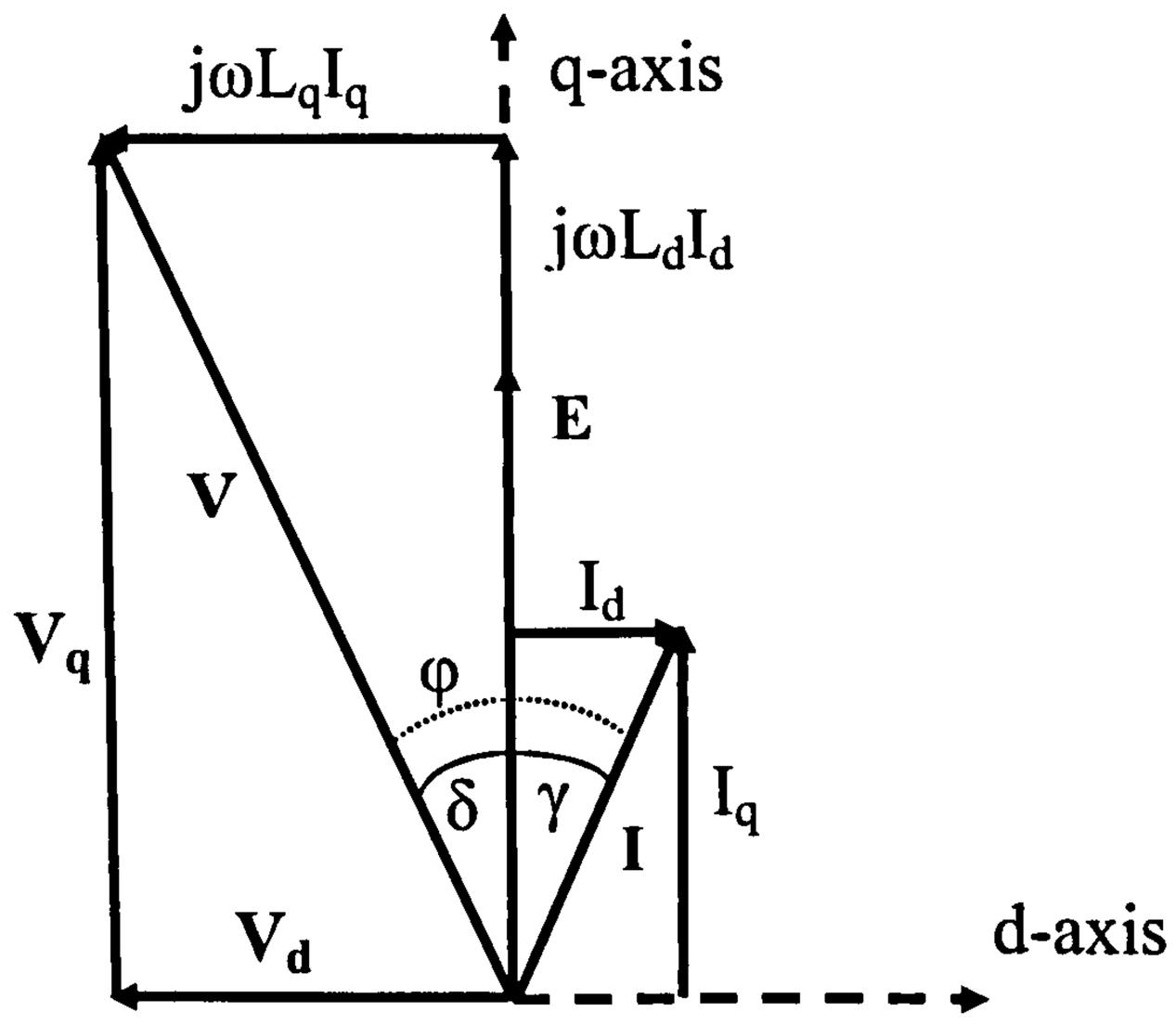

Fig. 5.1. Simplified phasor diagram of IPM motor (magnetising current)

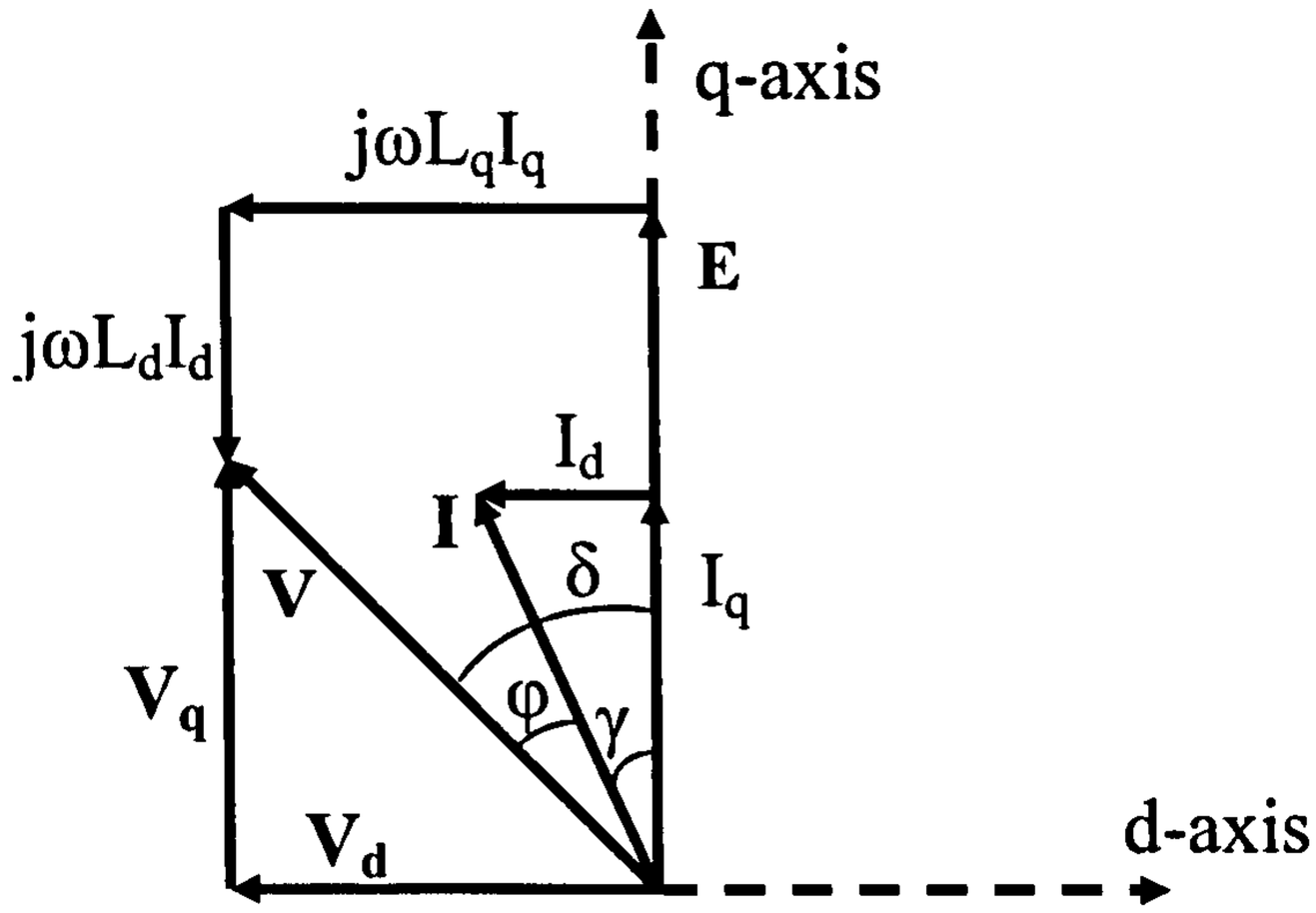

Fig. 5.2. Simplified phasor diagram of IPM motor (demagnetising current)

In the phasor diagram, the flux due to the permanent magnets is represented by an equivalent voltage phasor E, which lies on the quadrature axis. The voltage representing the permanent magnets is assumed to remain constant at the open-circuit value (E = E_0), as it is not possible to measure the flux-linkage from the permanent magnets directly under load conditions. The use of the constant magnet voltage E can lead to inaccuracies in the torque calculation, as the flux-linkage from the permanent magnets may vary under load conditions due to saturation [18,54-56]. In addition to variations in E, the synchronous reactances vary with both load current and rotor position, due to localised saturation in the motor laminations. It is important that the correct values of the motor parameters are used in the phasor diagram to ensure as accurate a torque prediction as possible under saturated conditions.

5.1. Measurement and analysis of Synchronous Reactances

The synchronous reactances of the permanent-magnet motor vary with both rotor position and load current. As such, the values of X_d (= ωL_d) and X_q (= ωL_q) used in the phasor diagram should be either calculated or measured under all operating conditions,

including cases of saturation. The synchronous reactances can be measured using locked rotor tests, dynamic load tests, or a combination of both methods.

5.1.1. Static rotor tests: Inductance Bridge

The most common method of measuring the synchronous reactances of the permanent-magnet motor is locked rotor tests using an inductive bridge circuit. The circuit is based on a Wheatstone bridge. The motor phase under test is connected into one leg of the circuit and the bridge balanced under load by means of a variable resistor in the opposite phase leg. The phase current is then switched off and the resulting change in flux-linkage or voltage across the centre of the bridge determined by means of a flux meter or digital storage oscilloscope. The circuit should be supplied from a constant source such as a battery, as any variations in the supply voltage affect the readings taken at the centre of the bridge. Detailed information on the circuit design and equations is given in Appendix 4.

The inductance bridge circuit was first proposed as a method for measurement of synchronous reactances by Jones [57]. Around the same time, Prescott and El-Kharashi independently published work proposing a similar method [58]. One of the main problems found with the original circuits was the use of either an integrating voltmeter or a Grassot flux meter, both of which are rather susceptible to drift. If a flux meter is used it is necessary to determine the meter time constant before any testing is carried out. To increase the accuracy of the results, the flux meter can be replaced with a digital storage oscilloscope (DSO). This allows the waveforms to be stored as up to 2 million samples each and then directly integrated to give a value proportional to the change in flux-linkage.

The static bridge method was first applied to permanent-magnet motors by Miller [55]. The method is used to measure self and mutual flux-linkages of a three-phase IPM motor. The results from the bridge tests show that while the self flux-linkage of the

quadrature axis is independent of the current polarity, the direct axis flux-linkage is different for magnetising and demagnetising currents, due to the saturation of the rotor bridge sections [18, 55, 59]. This is discussed further in section 5.5.2. Although the paper acknowledges that the flux-linkage produced by the permanent magnets is not constant, no attempt is made to calculate or measure it under load conditions.

Štumberger et al. [60] carried out a number of locked rotor tests with currents in both the direct and quadrature axis, to determine complete magnetisation characteristics of each axis including cross-magnetisation, i.e. $\psi_d(i_d, i_q)$ and $\psi_q(i_q, i_d)$. The machine equations can be expanded to include such cross-magnetisation effects, so that

$$v_d = Ri_d + L_{dd}\frac{di_d}{dt} + L_{dq}\frac{di_q}{dt} - \frac{d\theta}{dt}\psi_q \tag{5.3}$$

$$v_q = Ri_q + L_{qq}\frac{di_q}{dt} + L_{qd}\frac{di_d}{dt} - \frac{d\theta}{dt}\psi_d \tag{5.4}$$

$$\psi_d = \psi_{d\,id} + \psi_m \tag{5.5}$$

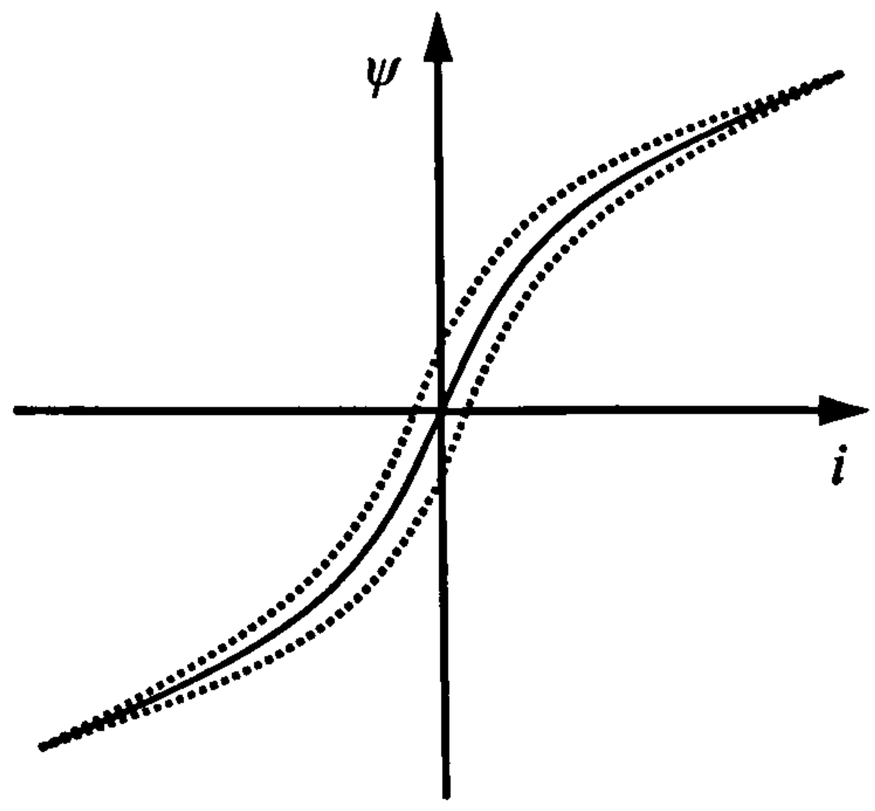

Fig. 5.3. Multiple quadrature axis current/flux-linkage trajectories

The test results show that for each rotor position the magnetisation characteristic is nonlinear due to hysteresis effects in the lamination material, as shown in Fig. 5.3. This is similar in principle to the hysteresis effects that can be seen in the magnetisation curves of the switched-reluctance motor, as discussed in Chapter 3. The authors take an average value of current for each flux-linkage point to produce a single-valued flux-linkage curve. Results from the bridge tests are used in differential equations to determine the self and mutual inductances of each axis. Again, the authors discuss the variation of magnet flux-linkage under load conditions; the dependence of the magnet flux-linkage on quadrature axis current is modelled, but it is assumed to be independent of direct axis current. Any direct axis current will alter the localised permeabilities of the motor laminations, resulting in a change in the flux-linkage contributions from the permanent magnets.

5.1.2. Load tests

A number of authors have suggested using a combination of locked rotor and load tests to determine saturated values of both the synchronous flux-linkages and the flux-linkage from the permanent magnets.

Mellor et al. propose the use of static, no load and load tests, but simplify the methods by neglecting cross-magnetisation effects; E and X_q are assumed independent of I_d, while X_d is assumed independent of I_q [54]. The open-circuit EMF associated with the permanent magnets is found from a no load test. The authors propose measurement of the direct axis synchronous reactance from the no load test. The synchronous reactances are also measured from locked rotor tests using the method described by Jones in [57].

Nee et al. also combine the locked rotor and load tests [61]. The authors measure the flux-linkage from the permanent magnets at no load and assume that this value remains constant so long as the motor does not exhibit high levels of saturation. The value of

magnet flux-linkage is then used in Eq. (5.6) to calculate the direct axis synchronous reactance, using the voltage measured on a no load test (where the load angle between E and U and the current in the quadrature axis are both assumed to be zero). The calculated values of E and X_d can then be used in Eq. (5.7) to calculate the load angle, the value of which can be used to calculate the quadrature axis flux-linkage under load conditions using Eq. (5.8). The method is useful for test set-ups where there is no rotor position sensor, as the method relies on calculation of the load angle rather than measurement. However, the method is limited by the assumption that both the flux-linkage from the permanent magnets and the direct axis flux-linkage are independent of the quadrature axis current. The calculated values of E and X_d are only valid if the flux paths remain unsaturated, but localised saturation is common in interior permanent-magnet motors. As in [55], results show that X_d is discontinuous, due to assumption of constant EMF due to the permanent magnets.

$$X_d = \frac{U - E}{I_d} \tag{5.6}$$

$$E + X_d I_d + R_s I_q = U\cos(\delta) \tag{5.7}$$

$$X_q I_q = U\sin(\delta) + R_s I_d \tag{5.8}$$

Zhou et al. discount the use of static bridge tests entirely and propose measurements that only use load tests [56]. The permanent magnet EMF E and both synchronous reactances are considered dependent on both the direct and quadrature axis currents. There is no need to assume that the flux-linkage produced by the permanent magnets is the same under load conditions as at open-circuit. An initial test is run at a certain load point and the voltage and load angle measured. Using the information in the test point, the following relationships can be expressed:

$$E_i \cos\delta_i = E_0 + I_1 \cos\beta X_{md} \tag{5.9}$$

$$E_i \sin\delta_i = I_1 \sin\beta X_{mq} \tag{5.10}$$

and β can be calculated from the torque angle δ and power factor angle φ using Eq. (5.11).

$$\beta = \frac{\pi}{2} + \delta - \varphi \tag{5.11}$$

A second test point is then run at a slightly different load level (an increment in the load current ΔI_1 is applied). The resulting governing equation at the second test point is:

$$E_i' \cos\delta_i = E_0 + I_1' \cos\beta' X_{md} \tag{5.12}$$

Eq. (5.9) and (5.12) can be solved as simultaneous equations to give saturated values of X_d and E. Results from the load measurements show that the direct axis synchronous reactance is no longer discontinuous, as the method allows for variation of the magnet EMF with load. The main drawback to the method is that the accuracy of the results is dependent on the size of the load current increment. The authors propose that the method could be applied to finite element simulations. This is discussed further in the following section.

5.2. Finite element analysis of Synchronous reactances

The synchronous reactances and flux-linkage from the permanent magnets can also be calculated from finite element simulations. There are three main methods which can be used to calculate the synchronous reactances of permanent-magnet motors from simulation results. These are:

- from the fundamental component of the airgap flux density distribution, calculated using analytical or finite element models
- from nonlinear finite element simulations, assuming that the flux-linkage from the permanent magnets remains constant under load
- from frozen permeability finite element simulations

5.2.1. Calculation based on the fundamental component of the airgap flux density

The direct and quadrature axis synchronous reactances can be calculated from the flux density distribution in the airgap [62]. The method is only applicable to motors running from sinusoidal current excitation and with sine-distributed phase windings. Only the fundamental component of the flux density distribution is considered; the distribution is assumed to be approximately sinusoidal. The peak fundamental flux-linkage can be calculated from

$$\Psi_1 = \frac{B_1 D L_{stk} N_{ph} k_{w1}}{p} \tag{5.13}$$

The direct and quadrature axis RMS synchronous reactances can be calculated from

$$X_d = \frac{\left[\frac{\Psi_1 \omega}{\sqrt{2}} - E_0\right]}{I} \tag{5.14}$$

$$X_q = \frac{\Psi_1}{I\sqrt{2}} \tag{5.15}$$

The flux-linkage calculated from Eq. (5.13) is the total flux-linkage from all field sources. To calculate the synchronous reactance using this fundamental flux-linkage value, it is

once again necessary to either determine the magnet EMF E in advance, or assume that the magnet flux remains constant for all load conditions so that $E = E_0$.

5.2.2. Calculations based on total flux-linkage calculated from finite element simulations

The total flux-linkage in each phase can be found from nonlinear finite element simulations. Multiple simulations should be run over the range of required current levels. Once the phase quantities have been determined, the direct and quadrature axis quantities can be calculated using the d-q axis transformation.

The direct axis flux-linkage calculated by nonlinear simulations is the total flux-linkage due to both the magnet and excitation current. To determine the direct axis synchronous reactance from the nonlinear solutions, it would be necessary to assume that the flux-linkage from the magnets remained constant under load. The direct axis synchronous reactance can then be found from

$$X_d = \frac{[\psi_d \omega - E_0]}{I_d} \tag{5.16}$$

5.2.3. Calculations based on results from frozen permeability finite element simulations

Both the methods presented above assume that the flux-linkage from the permanent magnets is independent of loading, which may lead to errors in the calculated synchronous reactance values under saturated conditions. An alternative is to use the frozen permeability method discussed in section 2.3.2.

Miller et al. suggest the method as a means of calculating the phase-current component of flux-linkage in permanent-magnet motor calculations [41]. The paper erroneously suggests that the permeabilities of each element in the mesh should be frozen at their open circuit values to determine the per-phase synchronous reactances. To accurately

determine the synchronous reactances using the frozen permeability method, it is the permeabilities from the complete nonlinear solution (with all phases excited) that should be used. The authors propose that interpretation of the frozen permeability results will lead to discontinuities in X_d around I_d = 0, but this is based on the assumption of constant flux-linkage being produced by the permanent magnets. Although this assumption is necessary for the phasor diagram method, there is no need to make such assumptions in frozen permeability calculations (in fact, the frozen permeability solutions confirm that the flux-linkage contribution from the permanent magnets varies under load conditions).

The principle behind the frozen permeability method is also suggested by Zhou et al. [56]. The authors suggest calculating the incremental load test data, for use in the proposed simultaneous equations model from finite element simulations (as a means of eliminating the dependence of the results on the size of the incremental current change ΔI). The initial load test point is simulated and the permeabilities from the nonlinear solution are frozen. The next load point is then calculated from a linear solution, using the frozen permeabilities. Using the permeabilities from the first load point to calculate the second load point will lead to erroneous results – the permeabilities are unique to the load point. The error in the calculations is still dependent on the size of the incremental change in current ΔI.

Using the frozen permeability method, there is no need to calculate the machine parameters from simultaneous equations. Each load point can be calculated without reference to other load points. The permeabilities stored from the nonlinear solution should be used to calculate linear solutions for each field source for the given load point (one linear solution for each phase current and one solution with no current excitation to determine the flux from the permanent magnets). In this way, there is no assumption that the permeabilities at each load point are the same (the calculation no longer depends on the incremental change in load that is necessary in the load tests).

5.3. Separation of flux-linkage into field source components, using the frozen permeability method.

Finite element frozen permeability tests have been run to determine the separation of flux-linkage in one phase of the split-phase interior permanent-magnet motor (IPM test motor 1) into contributions from the phase current and from the permanent magnets. The addition of the flux-linkage contributions from each field source gives the same total flux-linkage as is determined from the complete nonlinear solution. To verify whether the separation into individual flux-linkage components is correct, it is necessary to measure the flux-linkage contributions from each field source. The flux-linkage produced by the phase currents has been measured using the static inductance bridge synchronous reactance measurements outlined in section 5.1.1. The flux-linkage produced by the permanent magnets can only be measured directly on open-circuit (by integration of the open-circuit back EMF waveform). Under load conditions, the magnet flux-linkage is found by subtraction of the flux-linkage due to current from the total flux-linkage as determined from the motor magnetisation curves. The magnetisation curves are measured using the dynamic test method outlined in section 2.1.3 (thus avoiding assumption of constant magnet flux-linkage under load).

The total flux-linkage from the nonlinear finite element solution is compared with magnetisation curves of the main phase of the test motor, measured from dynamic tests, in Fig. 5.4. The close correlation between the two sets of results suggests that the material data used in the finite element solution is a reasonable approximation of the actual lamination *B-H* curve and permanent-magnet properties. The remnant flux of the permanent magnets has been adjusted in the finite element script to produce the same flux-linkage as was measured from open-circuit tests at the rated speed.

Using the inductive bridge circuit connected to the main phase of the test motor, the flux-linkage due to current has been measured at each rotor position, Fig. 5.5. These flux-linkages were then subtracted from the total flux-linkages of Fig. 5.4 to calculate the flux-linkage produced by the permanent magnets, Fig. 5.6.

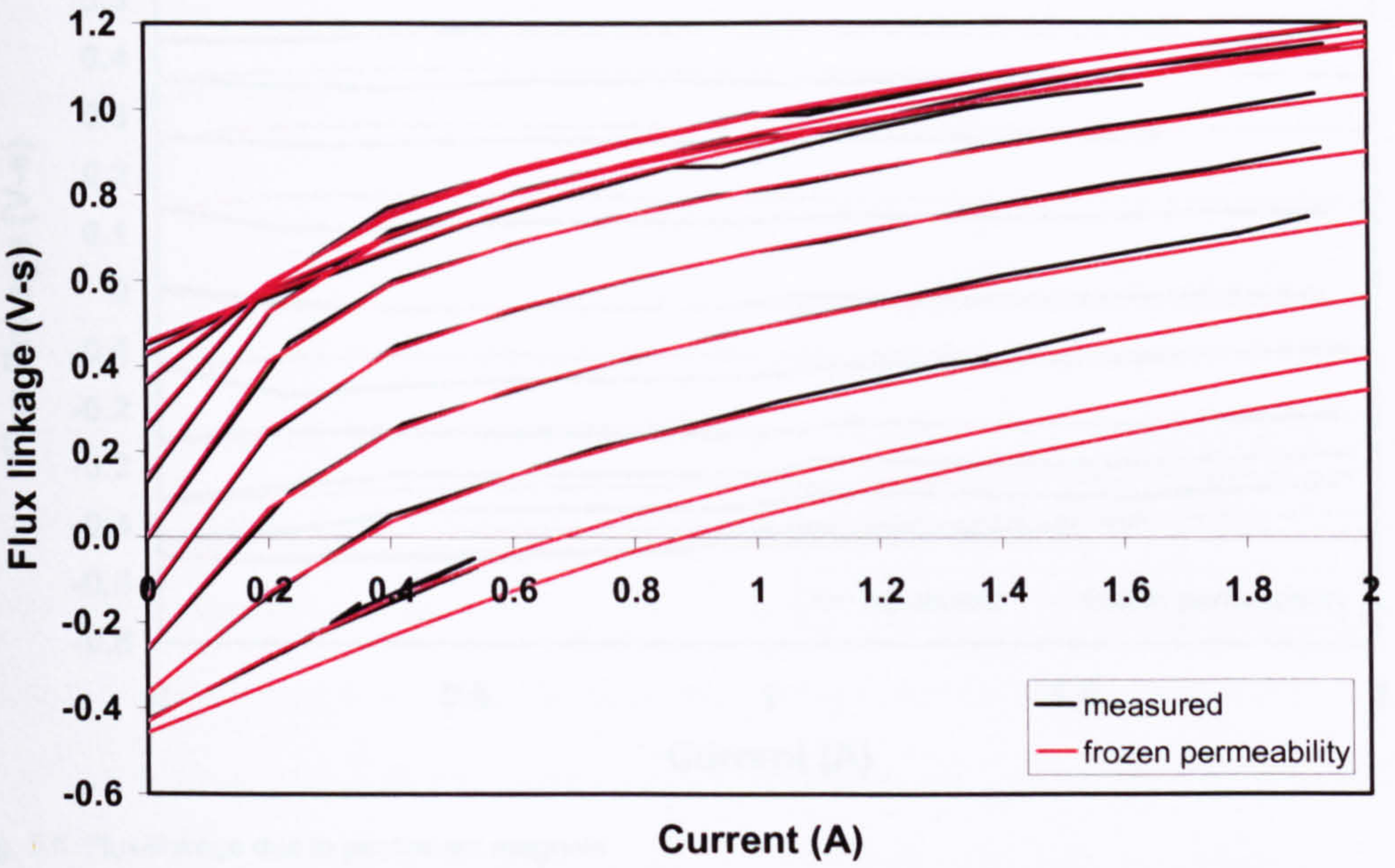

Fig. 5.4. Comparison between finite element simulated and measured magnetisation curves

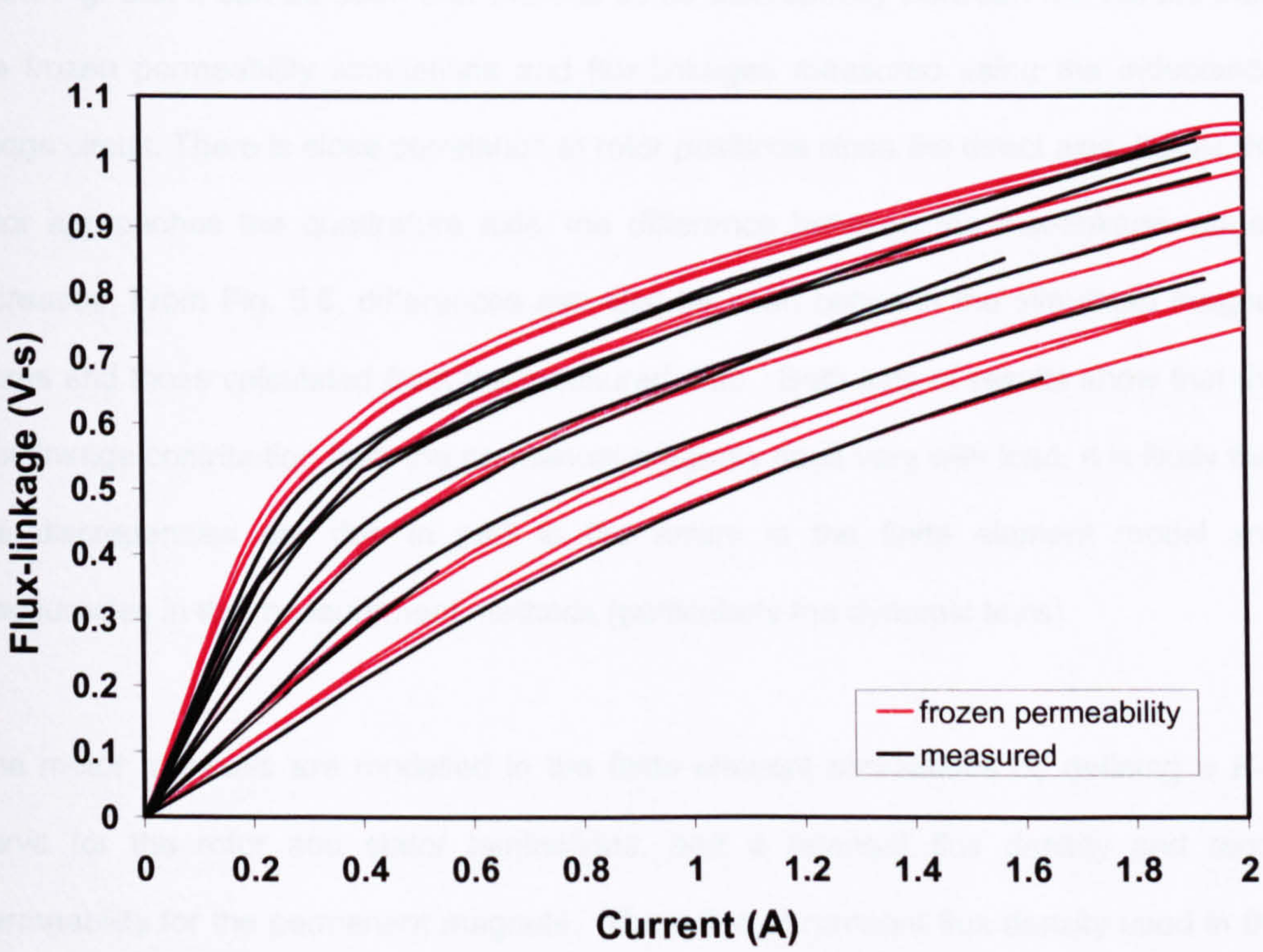

Fig. 5.5. Flux-linkage due to phase current

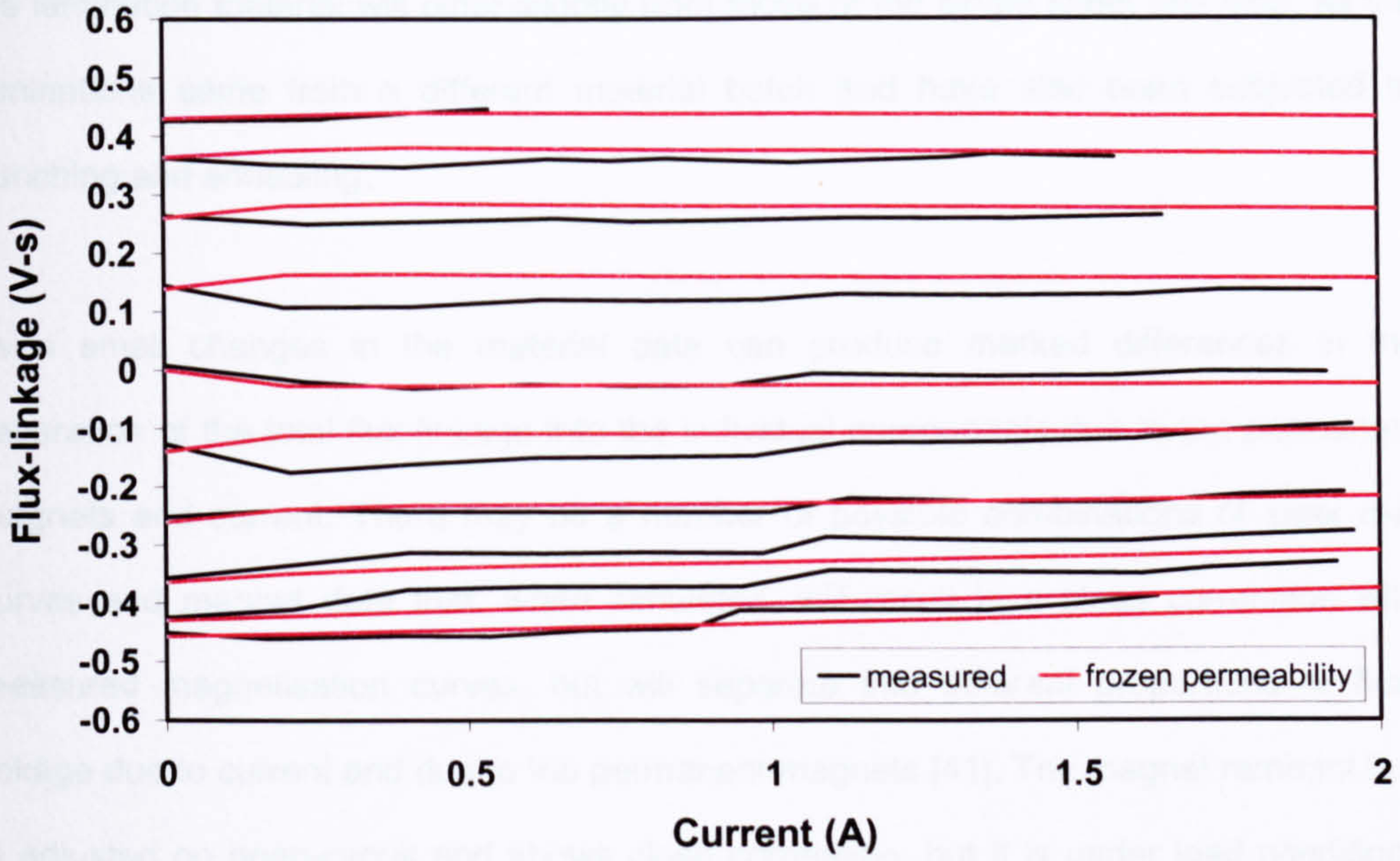

Fig. 5.6. Flux-linkage due to permanent magnets

From Fig. 5.5, it can be seen that there is some discrepancy between the results from the frozen permeability simulations and flux-linkages measured using the inductance bridge circuit. There is close correlation at rotor positions close the direct axis, but as the rotor approaches the quadrature axis, the difference between the flux-linkage values increases. From Fig. 5.6, differences can also be seen between the simulated magnet fluxes and those calculated from the measured data. Both sets of results show that the flux-linkage contribution from the permanent magnets does vary with load. It is likely that the discrepancies are due in part to the errors in the finite element model and inaccuracies in the measurement methods (particularly the dynamic tests).

The motor materials are modelled in the finite element simulations by defining a *B-H* curve for the rotor and stator laminations, and a remnant flux density and recoil permeability for the permanent magnets. The value of remnant flux density used in the simulations is adjusted to match measured data, but the recoil permeability is taken from the manufacturer's data sheets. It is thought that the permanent magnets may have been partially demagnetised during earlier tests and that the demagnetisation is not uniform over the magnet cross-section. The lamination *B-H* data is taken from measurements of steel strips made on a single sheet tester. The magnetic properties of

the lamination material will differ slightly from those of the single sheet test strip, as the laminations came from a different material batch and have also been subjected to punching and annealing.

Even small changes in the material data can produce marked differences in the separation of the total flux-linkage into the individual components due to the permanent magnets and current. There may be a number of possible combinations of steel *B-H* curves and magnet data that, when simulated, will result in a close correlation with measured magnetisation curves, but will separate into different proportions of flux-linkage due to current and due to the permanent magnets [41]. The magnet remnant flux is adjusted on open-circuit and shows close correlation, but it is under load conditions (when the magnets are subjected to an external field and the operating point is somewhere on the recoil line), that the discrepancies will arise.

The frozen permeability method has been discounted in some publications, which suggest that the separation of flux-linkage into individual components relies on the principle of superposition. Because the method uses the frozen permeabilities of the total nonlinear solution, the addition of flux-linkage contributions from each field source should not be considered as superposition. The method should be considered as means of attributing parts of a total flux to different field sources, rather than determining two separate flux-linkages (the field sources combine to produce a total flux that is not equal to the sum of flux-linkages from each field source excited separately).

The frozen permeability simulations have been rerun with modified material data, to illustrate the sensitivity of the model to inaccuracies in the material data. Fig. 5.7 shows the magnetisation curves corresponding to phase alignment with the direct and quadrature axis positions, for both the original material data and the modified data. The measured magnetisation curves are included for reference. It can be seen that both materials produce magnetisation curves that show a reasonable correlation with the measured data. Fig. 5.8 shows the *B-H* curves of both materials. In Figs. 5.9 and 5.10,

the separations into individual flux-linkage components are shown. The results show that care must be taken to ensure that the measured material data used as an input to the simulations is accurate.

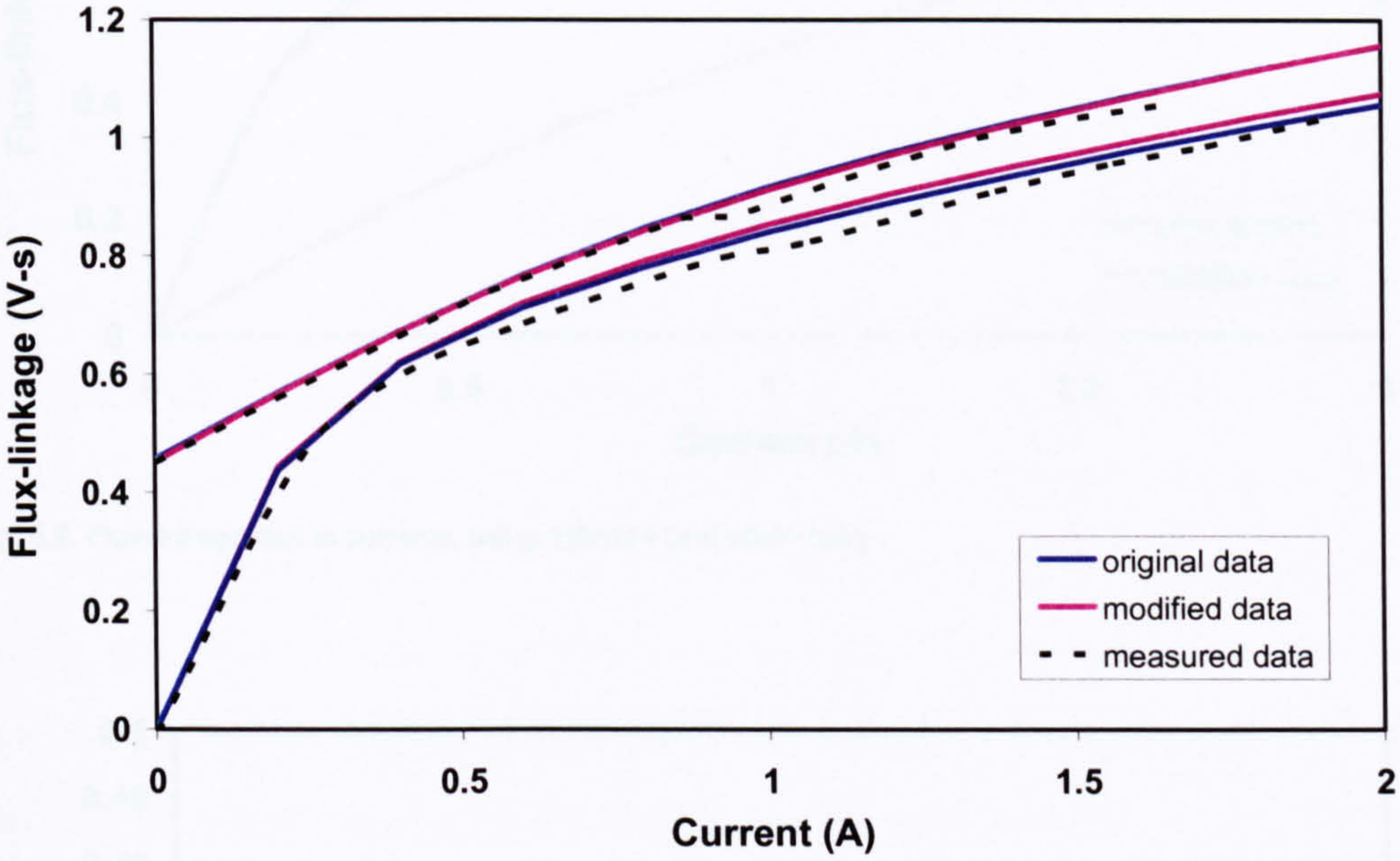

Fig. 5.7. Magnetisation curves of motor main phase for different lamination *B-H* curves

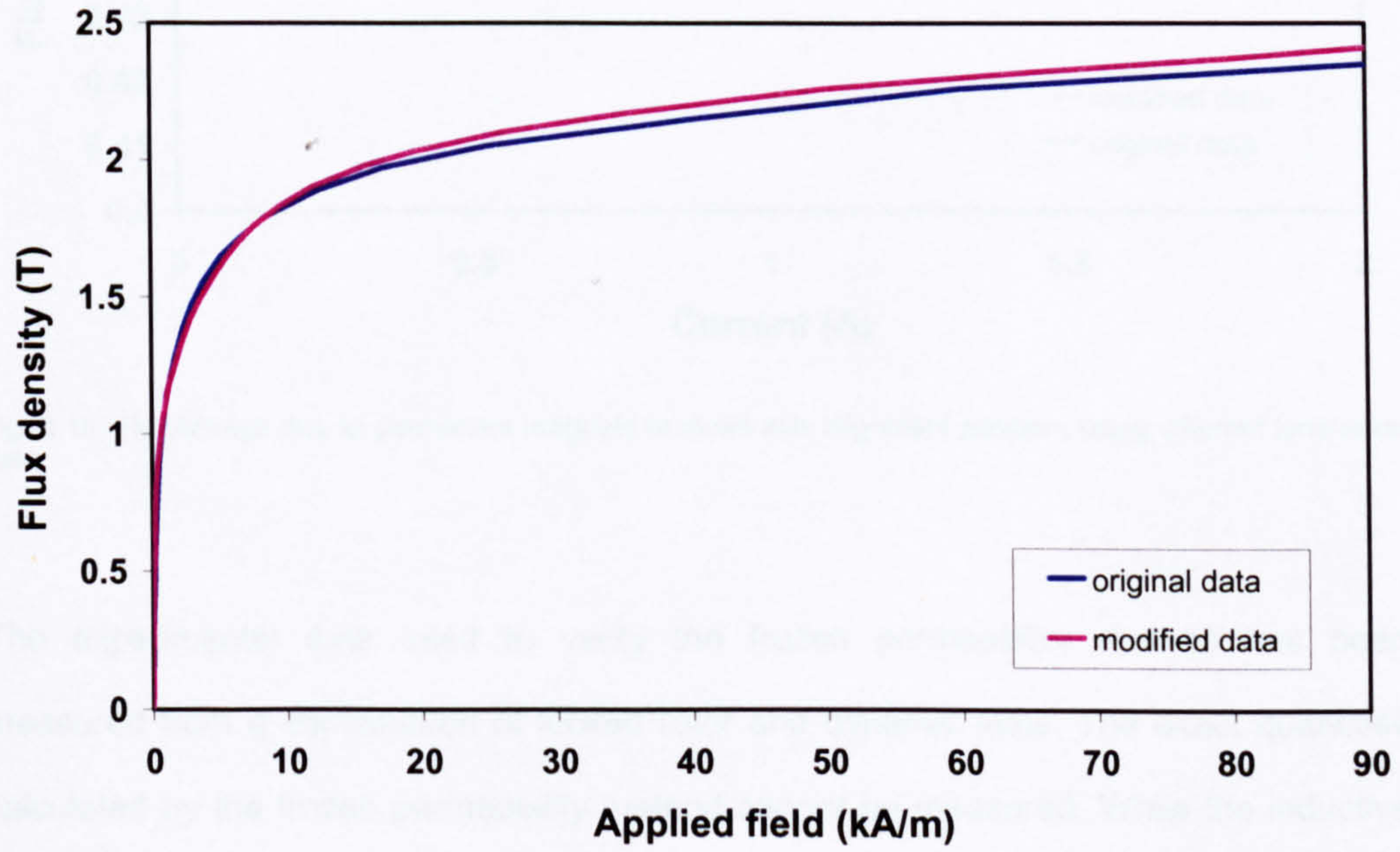

Fig. 5.8. *B-H* curves for lamination data

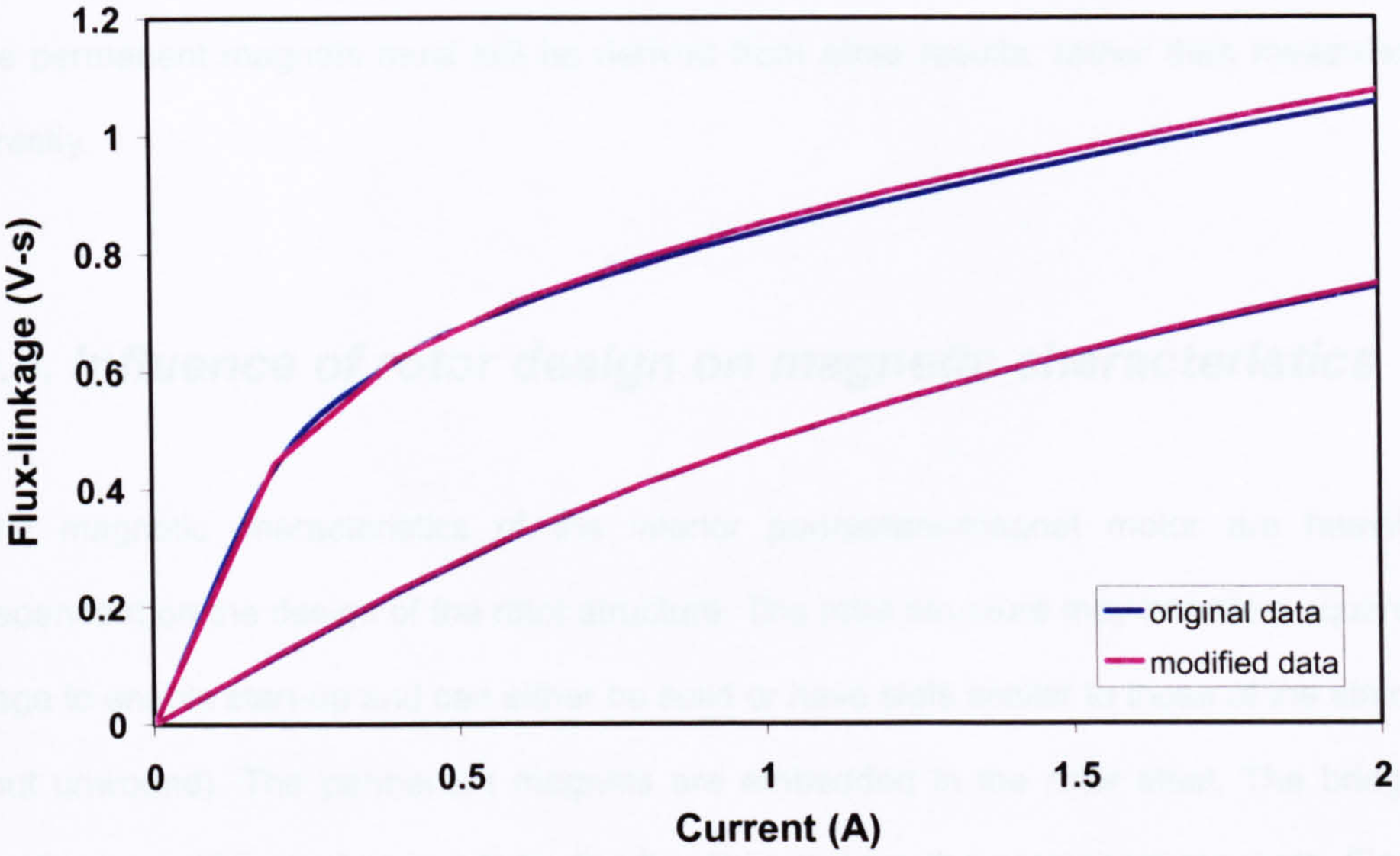

Fig. 5.9. Flux-linkage due to currents, using different lamination data

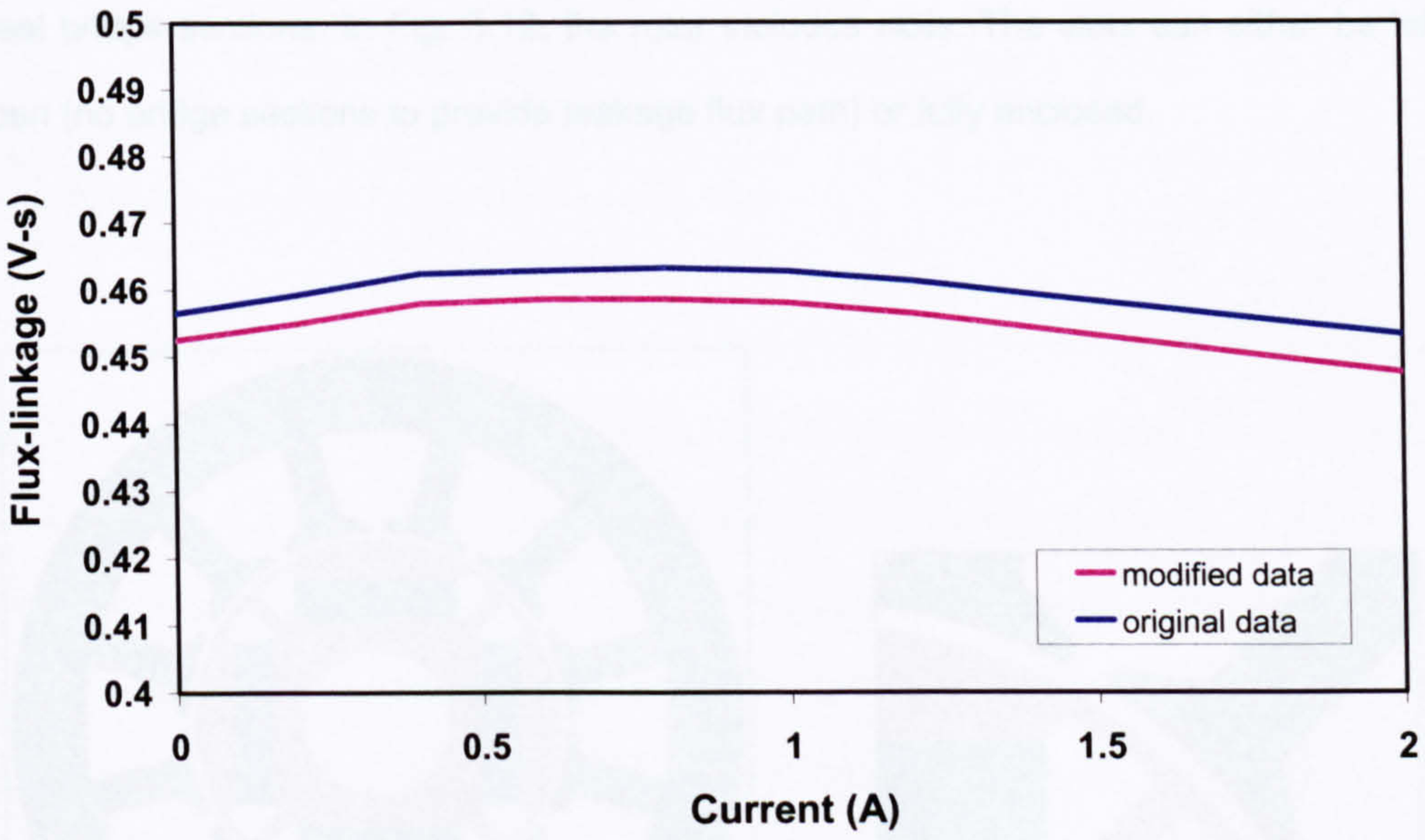

Fig. 5.10. Flux-linkage due to permanent magnets at direct axis alignment position, using different lamination data

The experimental data used to verify the frozen permeability method has been measured from a combination of locked rotor and dynamic tests. The exact quantities calculated by the frozen permeability method cannot be measured. While the inductive bridge test measures a change in flux-linkage due to an applied current, it gives no

indication as to how the magnets are affected by the applied field. The flux-linkage from the permanent magnets must still be derived from other results, rather than measured directly.

5.4. Influence of rotor design on magnetic characteristics

The magnetic characteristics of the interior permanent-magnet motor are heavily dependent on the design of the rotor structure. The rotor structure may include a squirrel cage to enable start-up and can either be solid or have slots similar to those of the stator (but unwound). The permanent magnets are embedded in the rotor steel. The bridge sections provide a leakage path for the flux-linkage from the permanent magnets. Figs. 5.11 and 5.12 show examples of rotor bridge sections for different rotor configurations. In Fig. 5.11, the permanent magnets are buried in the rotor and fully enclosed by the steel bridge sections. In Fig. 5.12, the rotor includes slots. The slots can either be left open (no bridge sections to provide leakage flux path) or fully enclosed.

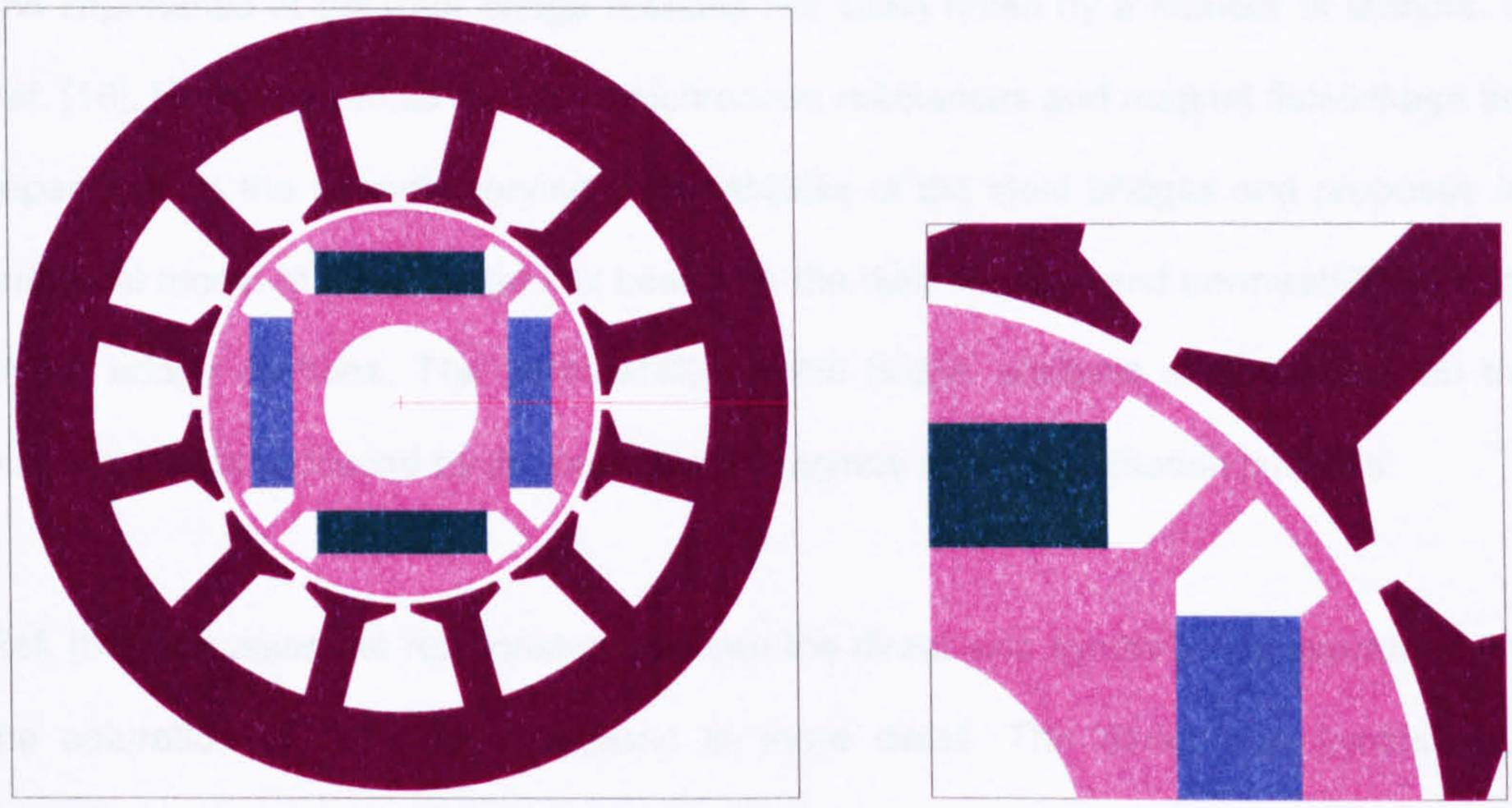

Fig. 5.11. Solid rotor structure showing magnetic bridge sections

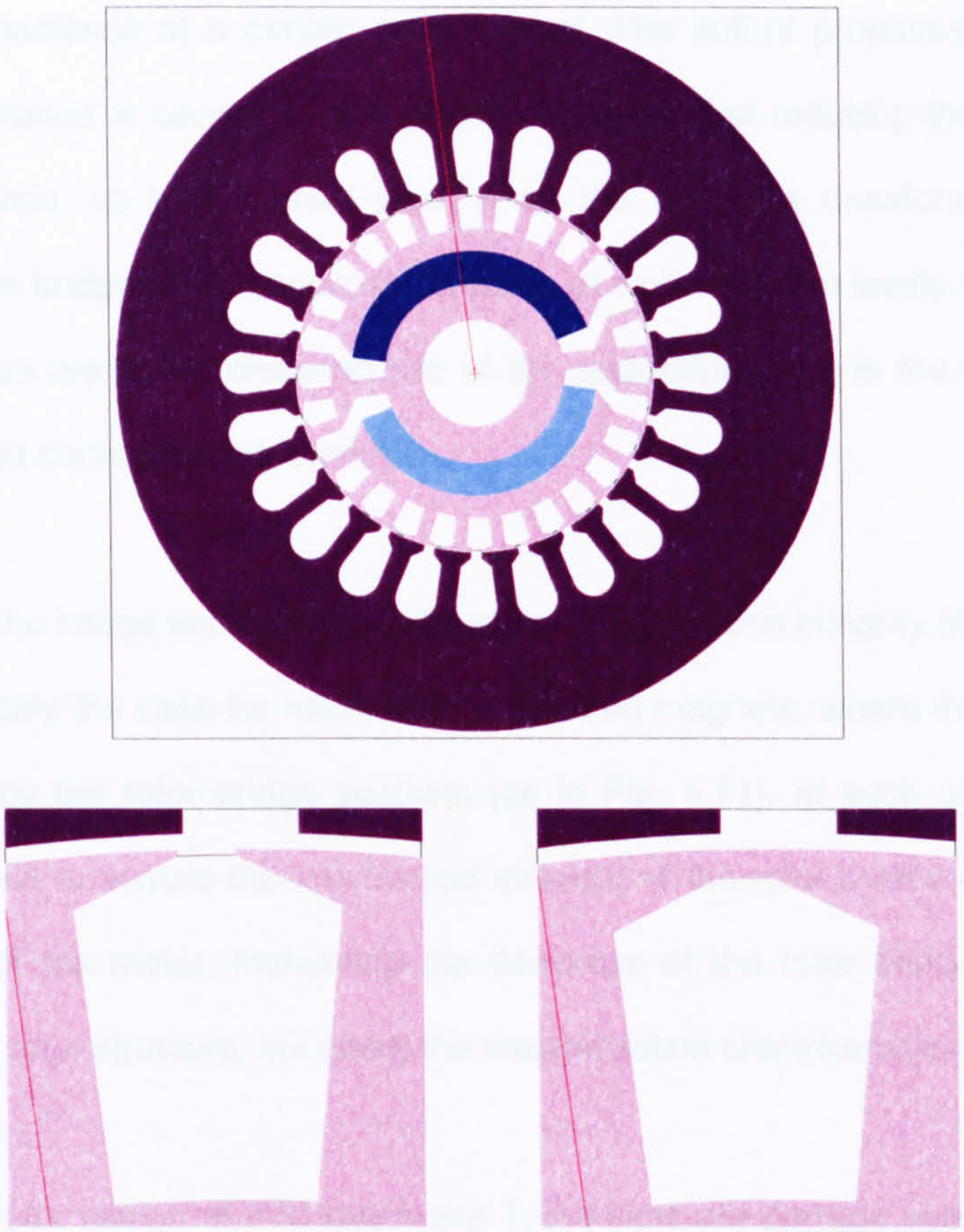

Fig. 5.12. Slotted rotor structure showing open and enclosed slots

The importance of the rotor bridge sections has been noted by a number of authors. In Ref. [18], Honsinger notes that the synchronous reactances and magnet flux-linkage are dependent on the strongly varying permeabilities of the steel bridges and proposes an analytical model of the leakage flux based on the field strength and permeability in each of the bridge sections. The permeability of the bridge sections is dependent on the magnetic fields produced by the permanent magnets and the excitation currents.

Ref. [55] discusses the relationship between the direct axis synchronous reactance and the saturation of the bridge sections in more detail. The direct axis synchronous reactance is shown through measurement to be different for magnetising and demagnetising currents. With demagnetising current in the winding, the synchronous reactance shows approximately linear characteristics over the range of load currents. With magnetising current in the winding, there is shown to be a step change in the

synchronous reactance at a certain current level. The author proposes that the step change in reactance is caused by the phase current at first reducing the saturation at low current levels, up to a current level when the bridge is unsaturated, and then saturation of the bridges in the opposite direction at higher current levels. It is noted that the synchronous reactance characteristic of the quadrature axis is the same for both magnetising and demagnetising currents.

The design of the bridge sections may also affect the structural integrity of the rotor. This is most commonly the case for rotors with embedded magnets, where the magnets are held in place by the rotor bridge sections (as in Fig. 5.11). In such cases, the rotor bridges are used to ensure the mechanical strength of the rotor over the full operating speed range of the motor. Increasing the thickness of the rotor bridge sections can strengthen the rotor structure, but alters the magnetisation characteristics of the motor.

In the slotted rotor design of IPM test motor 1, the slots are partially open and the rotor lamination is in fact made from 3 different sections of steel. The rotor pieces and permanent magnets are held in place by an epoxy-resin compound, which increases the robustness of the rotor. The resin binds the separate pieces of the rotor together without significantly affecting the electromagnetic properties of the rotor. Such methods allow optimised electromagnetic designs that are not constrained by mechanical considerations, but result in a more complicated (and thus more expensive) manufacturing process. A rotor cage can be included in the design as an alternative to a binding agent such as the epoxy resin. While a common feature in IPM motors for line-start applications, rotor cages can introduce unwanted harmonics and affect the electromagnetic properties of the motor.

Degner et al. [63] suggest burying the permanent magnets under magnetic bridge sections to improve the performance of surface-mounted permanent-magnet motors. The presented design is an interior permanent-magnet alternator, but utilises a high pole number to ensure that the chord length of the buried magnets is approximately equal to

the arc length of the surface-mounted magnets (ensuring that the buried magnet rotor has similar electromagnetic properties as the rotor with surface-mounted magnets). Burying the magnets simplifies the manufacturing process, as no additional measures are needed to hold the permanent magnets in place. Although the authors state that the calculation of the bridge thickness required to secure the permanent magnets is straightforward, no calculation is shown.

The structural implications of rotor bridge design are discussed in more detail by Lovelace [64]. A significant requirement of optimised mechanical design is to improve the structural integrity of the rotor, so as to prevent the forces experienced by the rotor exceeding the yield strength of the lamination material. The work presents a qualitative discussion on the centrifugal forces experienced by the rotor material. The centrifugal loading is concentrated on the rotor bridge sections, as these constrain the permanent-magnet material.

The author calculates the Von Mises stresses in each section of the rotor using 2D finite element analysis. The Von Mises stress is a scalar representation of complex loading (from more than one direction). The stress is calculated using

$$\sigma_v = \frac{\sqrt{(\sigma_1 - \sigma_2)^2 + (\sigma_2 - \sigma_3)^2 + (\sigma_3 - \sigma_1)^2}}{2} \tag{5.17}$$

where σ_1, σ_2 and σ_3 are the principal stresses from each direction. The Von Mises yield criterion states that yielding will occur if the Von Mises stress exceeds the yield stress (the maximum tensile strength).

The rotor outer diameter expands significantly, leading to a marked reduction in the airgap width. The stress levels are found to be highest in the thin rotor bridge sections. To reduce the peak stress, the rotor inner diameter can be constrained and the bridge

sections can be rounded. Reducing either the rotor speed or the mass per unit length of the magnets also leads to a significant reduction in the peak Von Mises stress.

Lee et al. provide a comprehensive analysis of all the forces experienced by the motor [65]. Whereas Ref. [64] deals only with centrifugal force, Lee et al. consider both electromagnetic and mechanical forces. The electromagnetic forces are determined by the Maxwell stress tensor method, while the mechanical forces are once again calculated using the Von Mises method. Three different types of force are considered:

1. Centrifugal Force – As the rotor rotates, the material experiences a centrifugal force in the radial direction, which increases as the rotor speed increases.
2. Airgap Force – There is an electromagnetic force across the airgap, the radial component of which contributes to the stress on the rotor material.
3. Magnet Force – The permanent magnets create a force due to the attraction between the magnets and the rotor lamination material.

The authors propose independent calculation of each component of the total force. The centrifugal force is calculated assuming the permanent magnets are unmagnetised. The attraction force from the permanent magnets counteracts the centrifugal force, leading to a lower calculated peak stress than if the attraction force from the permanent magnets is ignored. Taking the attractive force from the permanent magnets into account, the required bridge thickness is less. The results suggest that considering only the centrifugal force when analysing the rotor structure leads to thicker bridge sections than are required to maintain the mechanical integrity of the motor, resulting in a higher than necessary leakage flux.

5.5. Modelling the influence of the rotor bridge design on machine parameters

During the design stage, analytical and finite element modelling can be useful in determining the optimum cross-section design to maximise the motor parameters before building and testing of prototypes. The influence of the rotor design on the direct and quadrature axis synchronous reactances, and ultimately the torque produced by the motor, can be modelled.

5.5.1. Influence of rotor bridge design on airgap flux density distribution and total harmonic distortion

The method outlined in section 5.2.1 for calculation of the synchronous reactances requires knowledge of the fundamental component of the airgap flux density. It is possible to determine the airgap flux density distribution from a single load point nonlinear finite element simulation.

The open circuit airgap flux density distribution for IPM test motor 1, the two-pole split-phase IPM motor, has been calculated for four different rotor bridge designs – the original open rotor slot design, and with closed rotor slots with bridge thicknesses of 0.1 mm, 0.25 mm and 0.5 mm. The flux density distributions are shown in Fig. 5.13. When the rotor slots are fully enclosed, the rotor bridges provide a leakage path for the flux from the permanent magnets, which leads to the reduction in airgap flux density seen in Fig. 5.13. In Fig. 5.13, the rotor position (azimuth) is given with respect to the rotor negative d-axis.

The airgap flux density of a sinewave permanent-magnet motor should ideally be sinusoidal but in this case there are significant higher harmonic components, due to the slotting effects of the permanent magnets passing under the open stator slots. Additional slotting effects can be seen in the flux density distribution of the rotor designed with

open slots, due to interaction between the rotor and stator slots. The harmonic content can be greatly reduced by enclosing the rotor slots with solid bridge sections, creating a smooth rotor surface. Increasing the initial thickness of the rotor bridge sections will continue to reduce the total harmonic content of the flux density distribution, but to a less significant amount than the initial closing of the rotor slots. The fundamental component of the flux density is significantly reduced as the bridge thickness is increased. A summary is given in Table 5.1.

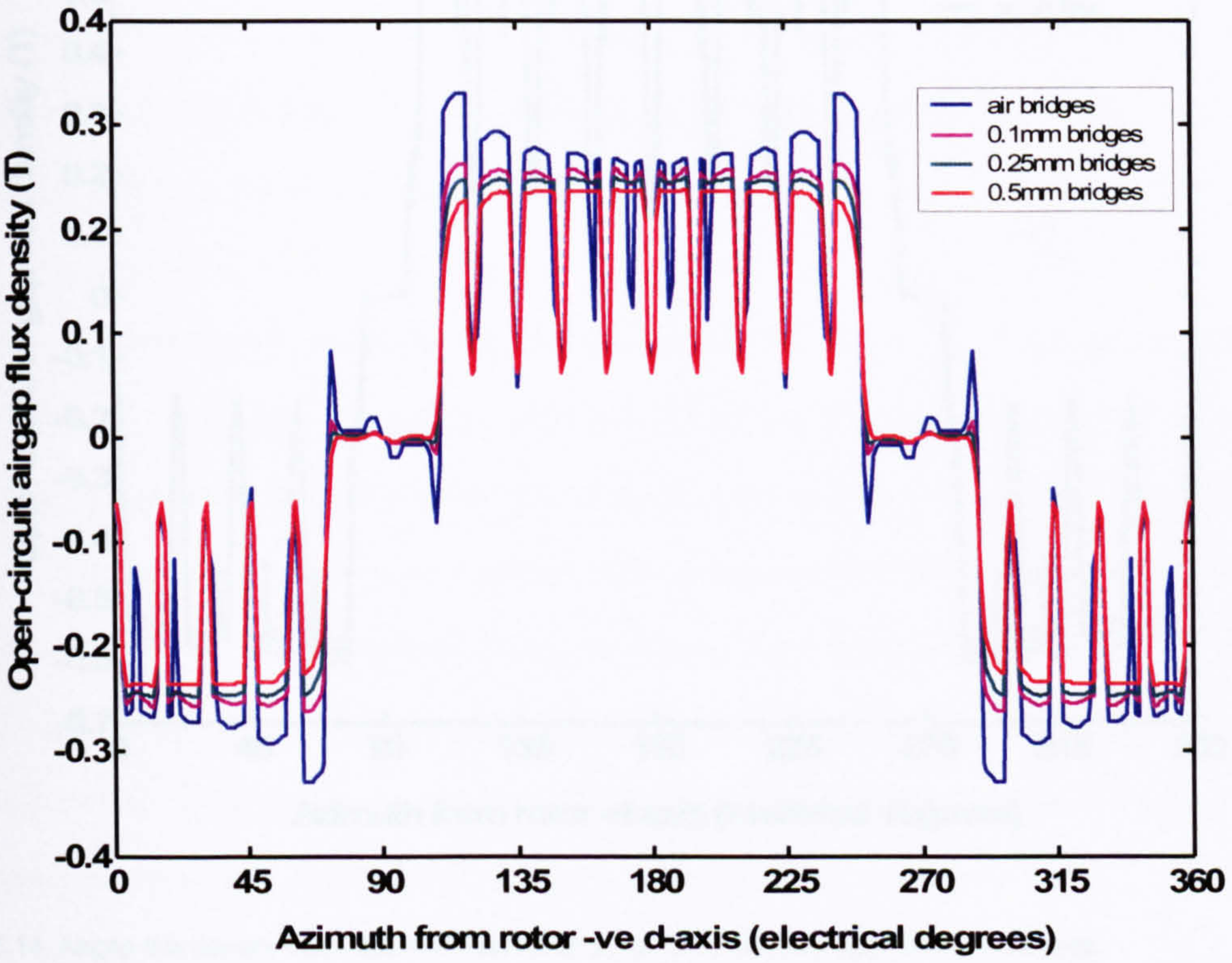

Fig. 5.13. Airgap flux density distributions of test motor 1, for four different rotor bridge designs

Bridge design	THD %	ΔTHD (%)	B_1 (T)	ΔB_1 (%)
Open rotor slots	56.65	-	0.263	-
0.10 mm	45.09	11.56	0.259	**1.52**
0.25 mm	43.67	12.98	0.251	**4.56**
0.50 mm	41.99	14.66	0.240	**8.75**

Table 5.1. Summary of results from airgap flux density distribution simulations of test motor 1

Similar simulations have been run for the four-pole, three phase IPM test motor 2, for open rotor slots, and closed rotor slots with bridge thicknesses of 0.25 mm and 0.5 mm. The open-circuit airgap flux density distributions are shown in Fig. 5.14. Initially closing the rotor slots results in the greatest reduction in total harmonic distortion, but once again reduces the fundamental flux density. The simulation results are summarised in Table 5.2.

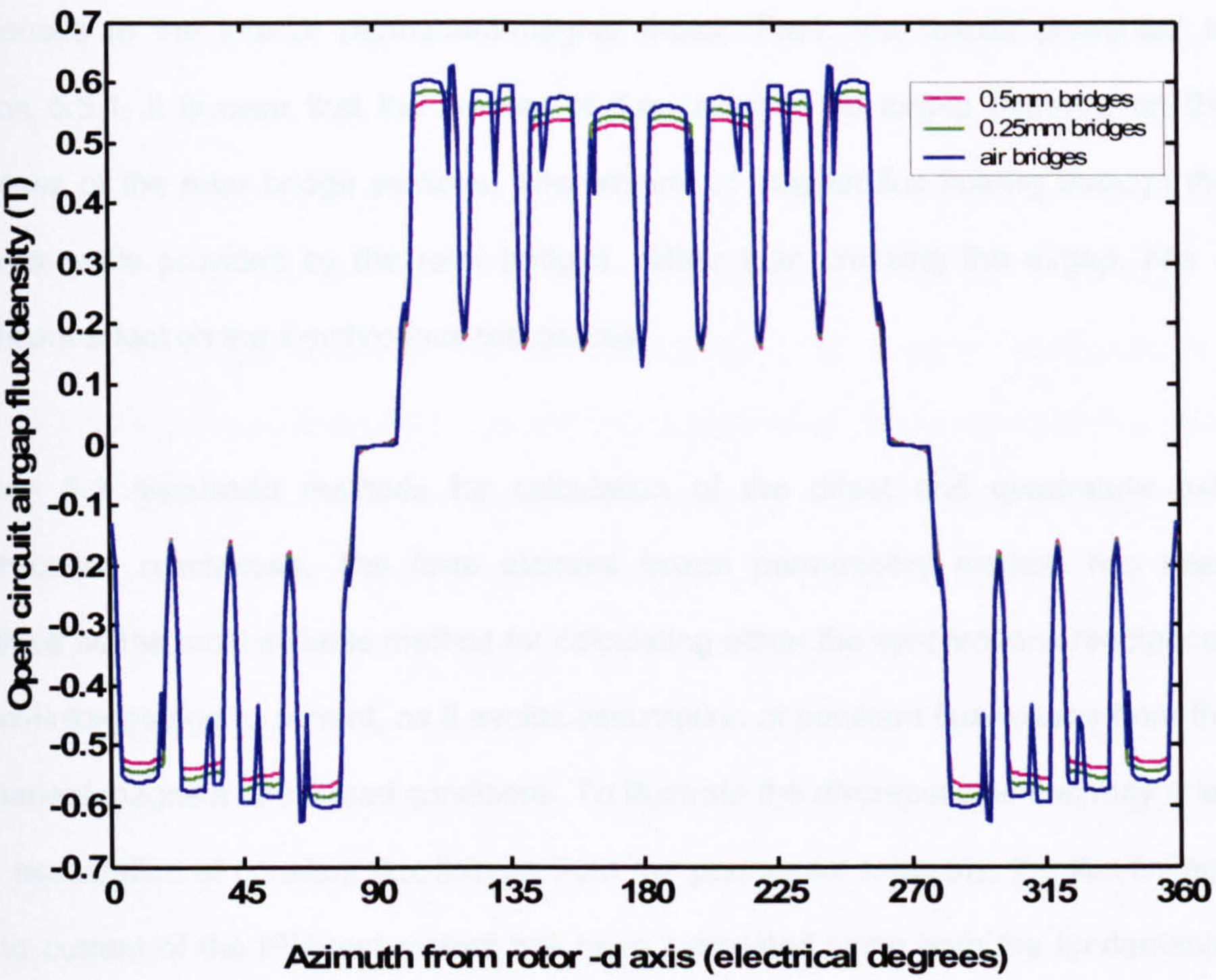

Fig. 5.14. Airgap flux density distributions of test motor 2, for three different rotor bridge structures

Bridge design	**THD %**	**ΔTHD (%)**	**B_1 (T)**	**ΔB_1 (%)**
Open rotor slots	51.38	-	0.633	-
0.25 mm	50.92	0.46	0.627	**0.98**
0.50 mm	50.70	0.68	0.612	**3.32**

Table 5.2. Summary of results from airgap flux density distribution simulations of test motor 2

The results show that although the total harmonic distortion is decreased when the rotor slots are fully enclosed by solid bridge sections, the fundamental flux density is also

reduced. A trade-off must be reached whereby unwanted harmonics are minimised without significant reduction of the airgap flux density.

5.5.2. Influence of rotor bridge design on flux-linkages and synchronous reactances

The design of the rotor bridge sections has a significant effect on the synchronous reactances in the interior permanent-magnet motor. From the results presented in section 5.5.1, it is clear that the amount of flux crossing the airgap depends on the thickness of the rotor bridge sections. The amount of magnet flux flowing through the leakage paths provided by the rotor bridges, rather than crossing the airgap, has a significant effect on the synchronous reactances.

Section 5.2 discussed methods for calculation of the direct and quadrature axis synchronous reactances. The finite element frozen permeability method has been identified as the most suitable method for calculating either the synchronous reactances or flux-linkages due to current, as it avoids assumption of constant flux-linkage from the permanent magnets under load conditions. To illustrate the discrepancies that may arise from assumption of constant flux-linkage from the permanent magnets, the flux-linkage due to current of the IPM test motors has been calculated using both the fundamental flux density and frozen permeability methods. The results are presented below.

5.5.2.1. Synchronous reactances from fundamental flux density

Synchronous reactance calculations have been carried out for IPM test motors one and two, using the fundamental flux density method outlined in section 5.2.1. The results were presented by the author in Ref. [59]. The direct and quadrature axis flux-linkages due to current and synchronous reactances of test motor 1 were calculated for the four different rotor bridge designs (open rotor slots, and closed slots with bridge thicknesses of 0.1 mm, 0.25 mm and 0.5 mm). Full results are presented in Appendix 5. The direct

axis flux-linkage due to current is shown to be strongly dependent on the current polarity (the synchronous reactance trajectory is different for magnetising and demagnetising currents). The magnitude of flux-linkage due to current is the same for both magnetising and demagnetising currents at each load point.

The results from the fundamental flux density simulations of IPM test motor 1 partly confirm the experimental findings from [55], that the synchronous reactances are not the same for magnetising and demagnetising currents. The step change in flux-linkage noted in [55] from the demagnetising current test cannot be seen in any of the results for test motor 1. The results shown in Appendix 5 from the simulations of the three rotors with different bridge thicknesses show that at low current levels, the flux-linkage is greater for magnetising current than for demagnetising. At higher current levels, the flux-linkage is greater for demagnetising current than magnetising. The current level at which the flux-linkage from the demagnetising current becomes greater than the magnetising current depends on the thickness of the rotor bridges; the thinner the bridges, the lower the level of current required. The reason for the cross-over between the magnetising and demagnetising flux-linkage trajectories is that for magnetising current the bridges gradually become more saturated as the level of current is increased, whereas for demagnetising current, the saturation of the rotor bridges is first reduced before the bridges saturate in the opposite direction.

For all rotor designs, the maximum flux-linkage under load conditions does not occur in the d-axis rotor position, but at an intermediate position between the direct and quadrature axis. This is due to the construction of the rotor – the magnet arc is not fully 180 degrees and so there are certain rotor slots under which the magnets do not span (four rotor slots for each pole). The maximum total flux-linkage occurs at around 54 degrees from the rotor direct axis.

IPM test motor 2 has also been modelled with different rotor bridge designs – with open rotor slots, and with closed rotor slots with bridge thicknesses of 0.25 mm and 0.5 mm.

The direct axis flux-linkages are presented in Appendix 5. The results from the simulations of IPM test motor 2 confirm the step change in flux-linkage described in Ref. [55] (as would be expected, as the test motor model is based on the Reliance motor used in [55]). The step change in flux-linkage can be seen in the simulation results of the original rotor, where the bridge thickness is 0.5 mm. It can also be seen, to a lesser extent, in the simulation results for the rotor with bridges of thickness 0.25 mm. In the simulation results of the rotor with open slots, there is no step change in flux-linkage; however, a difference can still be seen between the flux-linkage trajectories for magnetising and demagnetising currents.

The results from test motors 1 and 2 suggest that the step change in flux-linkage is specific to the motor geometry of the rotor and is not a result that is common to all motor designs. The results presented have assumed that the flux-linkage associated with the permanent magnets remains constant under all load conditions. To accurately determine the influence of the rotor bridge designs on the synchronous reactances, it is necessary to carry out frozen permeability simulations, as the frozen permeability method is the only method which does not rely on the assumption that the magnet flux-linkage remains constant under load conditions.

5.5.2.2. Synchronous reactances from frozen permeability method

To determine the permanent-magnet component of flux-linkage under load conditions, frozen permeability simulations have been carried out for IPM test motor 2, for the three different rotor structures of open rotor slots and closed slots with bridge thicknesses of 0.25 mm and 0.5 mm. Calculated direct-axis flux-linkages for the three different rotor structures, for magnetising and demagnetising currents, are presented in Appendix 5. The individual flux-linkage components due to currents and permanent magnets, as calculated using frozen permeabilities, are also presented.

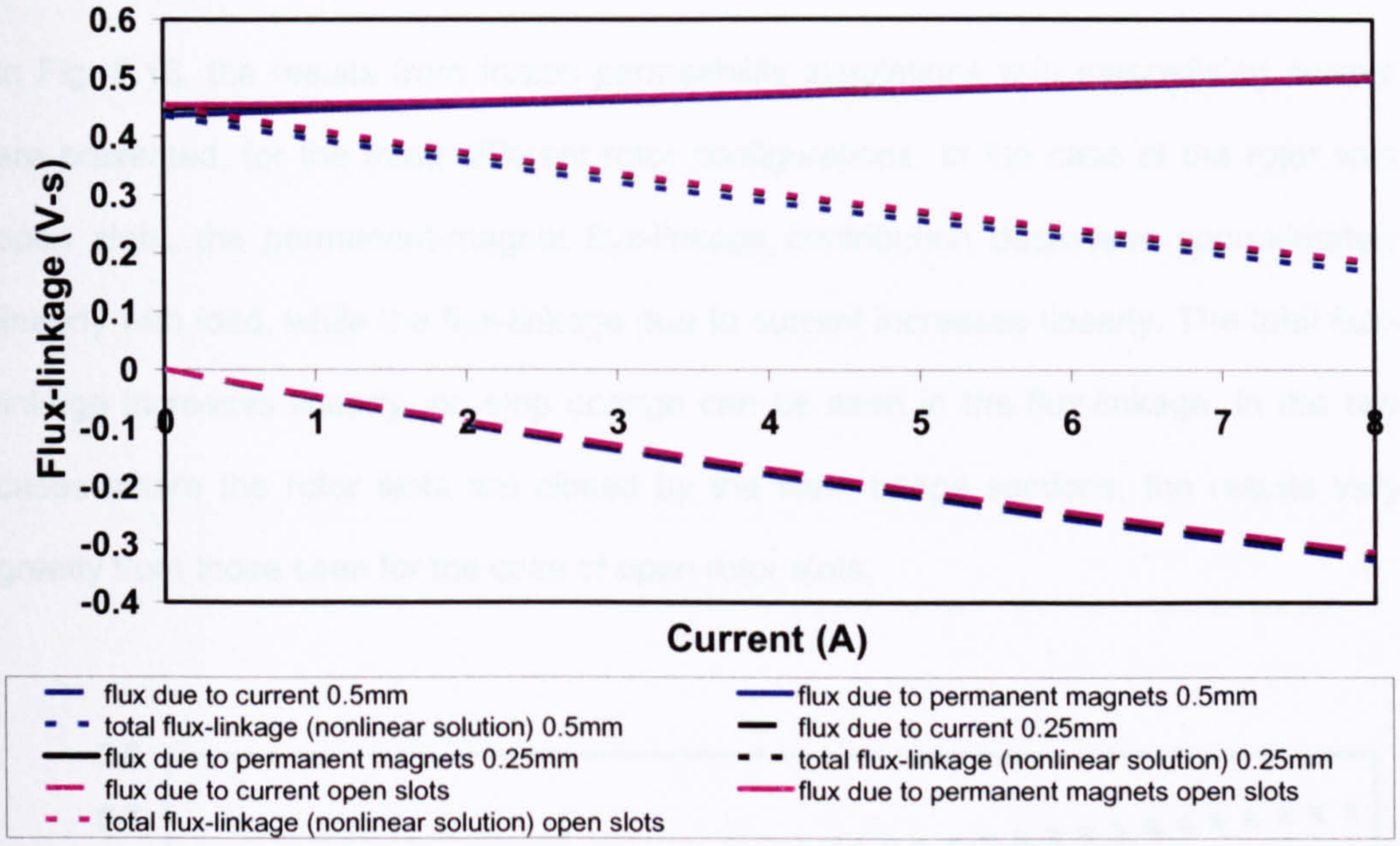

Fig. 5.15. Direct-axis flux-linkage of IPM test motor 2 due to demagnetising currents

Fig. 5.15 shows the individual flux-linkage contributions calculated for each of the three rotor designs using the frozen permeabilities method, for demagnetising currents. Although the total flux-linkage (calculated either from nonlinear simulations or by adding the individual flux-linkage components as determined from the frozen permeability simulations) is reduced as the load increases, the flux-linkage contribution from the permanent magnets increases slightly. This is due to the saturation of the rotor tooth tips, and occurs even when there are no rotor bridges (open rotor slots). In the two cases where the rotor slots are closed, the bridge sections are thin and so they saturate even under open circuit conditions. Due to the direction of the current, the bridges saturate even further as the load is increased, until the permeability in the bridges falls to such a level as to no longer make the bridges the preferred path of the magnetic flux. At this point, the flux will flow in the regions of air surrounding the rotor bridges, either across the airgap or in the rotor slots. The width of the slot opening is greater than that of the airgap, and so the flux crosses the airgap instead of flowing in the air regions between adjacent rotor teeth. This effect is also seen in the simulation results of the rotor with open slots; there is no iron between the rotor teeth to provide a high permeability preferred path for the magnetic flux, and so the flux flows across the airgap rather than between adjacent rotor teeth.

In Fig. 5.16, the results from frozen permeability simulations with magnetising current are presented, for the three different rotor configurations. In the case of the rotor with open slots, the permanent-magnet flux-linkage contribution decreases approximately linearly with load, while the flux-linkage due to current increases linearly. The total flux-linkage increases linearly; no step change can be seen in the flux-linkage. In the two cases where the rotor slots are closed by the steel bridge sections, the results vary greatly from those seen for the case of open rotor slots.

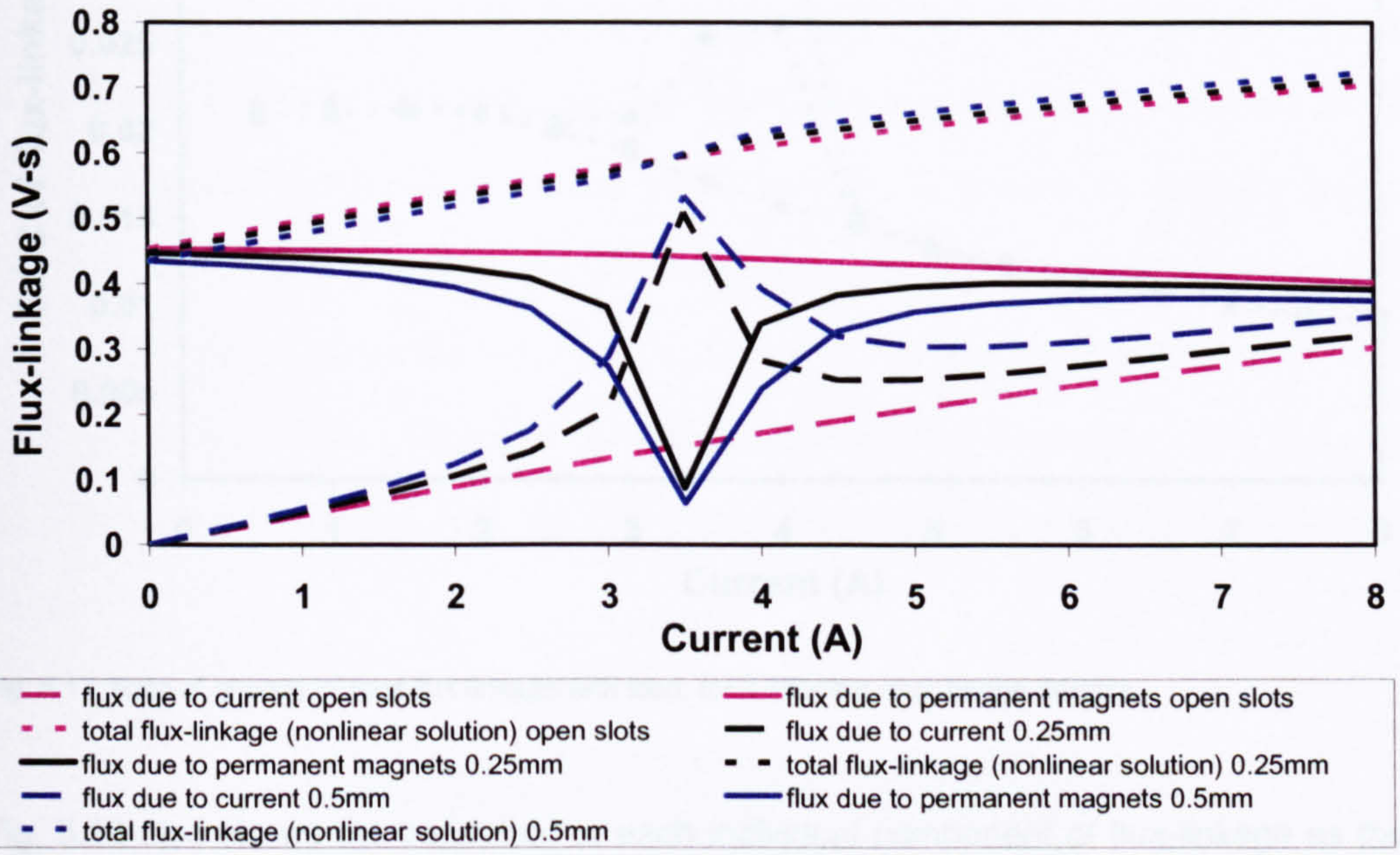

Fig. 5.16. Direct axis flux-linkage of IPM test motor 2 due to magnetising currents

Although the step change in total flux-linkage is not as prominent as is suggested in [55], a definite increase in flux-linkage can be seen in the results for both rotors with steel bridge sections. This is best illustrated by considering the rate of change of flux-linkage for different load current levels, as shown in Fig. 5.17. The results clearly show that for both rotors with closed slots, the rate of change of flux-linkage increases significantly at certain current loads. The rapid change in the rate of change of flux-linkage is due to changing saturation levels in the rotor bridge sections, caused by the addition of the magnetic field component from the phase currents. The current level at which the rate of change increases and decreases is dependent on the thickness of the rotor bridge

sections; the thicker the bridge section, the lower the level of current required to reduce the saturation and increase the rate of change of flux-linkage (and conversely, the higher the level of current required to saturate the bridges in the opposite direct). The results show that the rate of change of flux-linkage starts to rise at a lower current level for the rotor with 0.5 mm bridges than for the rotor with 0.25 mm bridges.

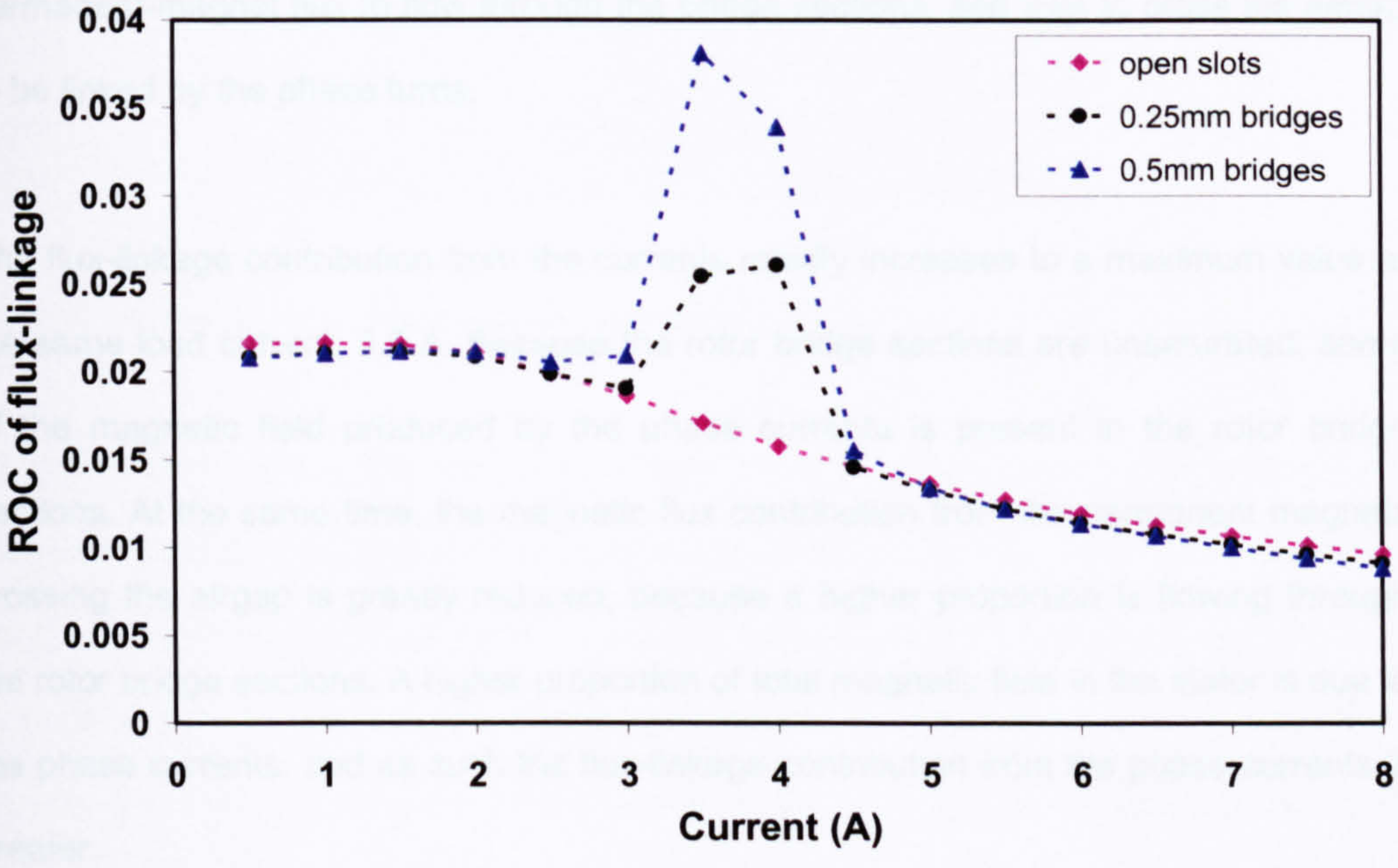

Fig. 5.17. Rate of change of total flux-linkage with load, for 3 different rotor bridge designs

Fig. 5.16 also shows the behaviour of each individual component of flux-linkage as the load is increased. The flux-linkages due to the currents and permanent magnets do not change linearly with current, as was the case for the demagnetising current tests. Instead, a spike can be seen in the flux-linkage trajectories, at around 3.5 A. From Fig. 5.16, the flux-linkage contribution from the permanent magnets can be seen to rapidly decrease to a minimum value at 3.5 A, then increases again as the load in increases further. The flux-linkage due to current rapidly increases to a maximum value at 3.5 A, and then decreases as the load is increased further.

The decrease in flux-linkage contribution from the permanent magnets suggests that the magnet flux-linkage crossing the airgap is reduced, because more of the flux due to the permanent magnets is flowing through the rotor bridges rather than crossing the airgap.

Fig. 5.18 shows the rotor bridge sections at open-circuit. The bridges are saturated by the flux produced by the permanent magnets. As the level of current is increased, some of the associated flux component flows through the magnetic bridge section. The minimum flux-linkage from the permanent magnets occurs when the opposing fields are balanced. At this point, the resultant flux density in the magnetic bridge sections is very low (the saturation is relieved), as shown in Fig. 5.19. This allows more of the permanent-magnet flux to flow through the bridge sections, and less to cross the airgap to be linked by the phase turns.

The flux-linkage contribution from the currents rapidly increases to a maximum value at the same load current, 3.5 A. Because the rotor bridge sections are unsaturated, some of the magnetic field produced by the phase currents is present in the rotor bridge sections. At the same time, the magnetic flux contribution from the permanent magnets crossing the airgap is greatly reduced, because a higher proportion is flowing through the rotor bridge sections. A higher proportion of total magnetic field in the stator is due to the phase currents, and as such the flux-linkage contribution from the phase currents is greater.

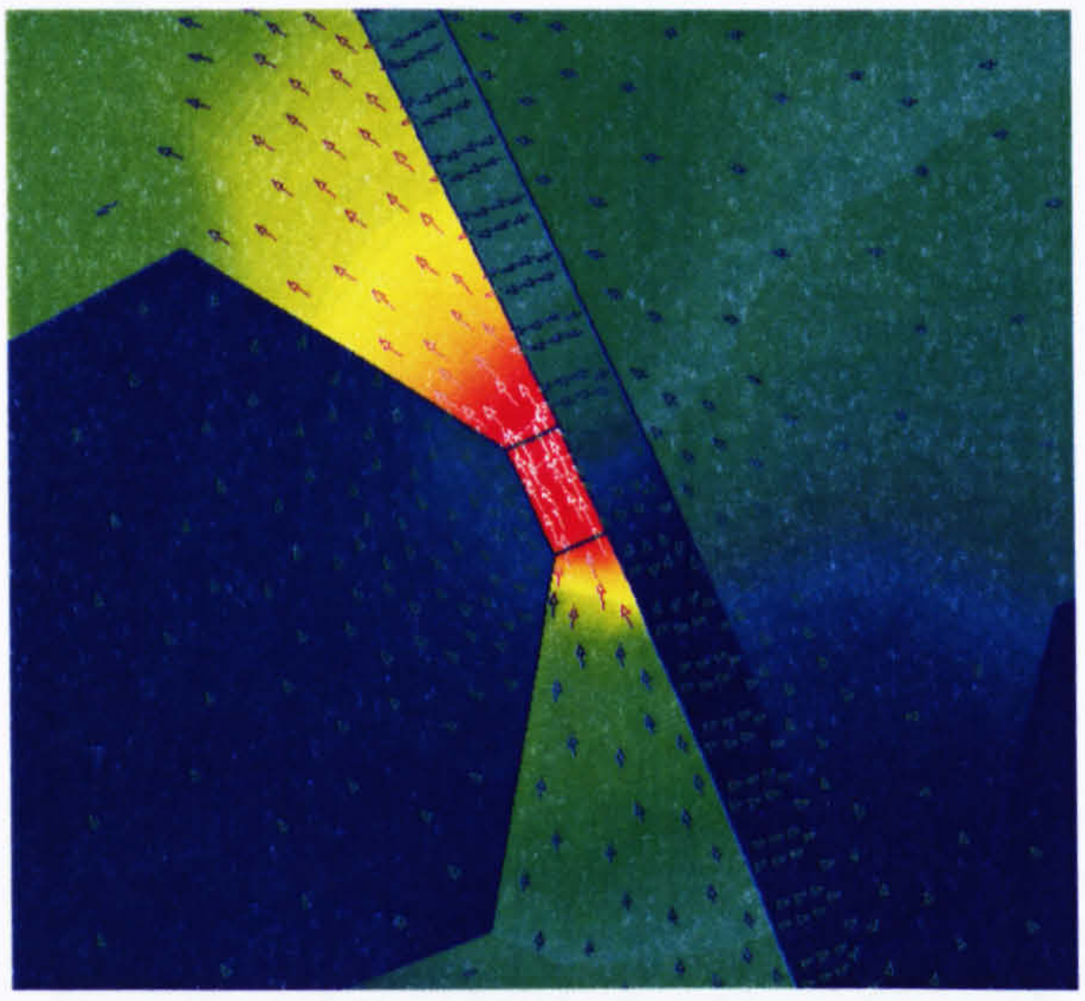

Fig. 5.18. Rotor bridge sections on open-circuit

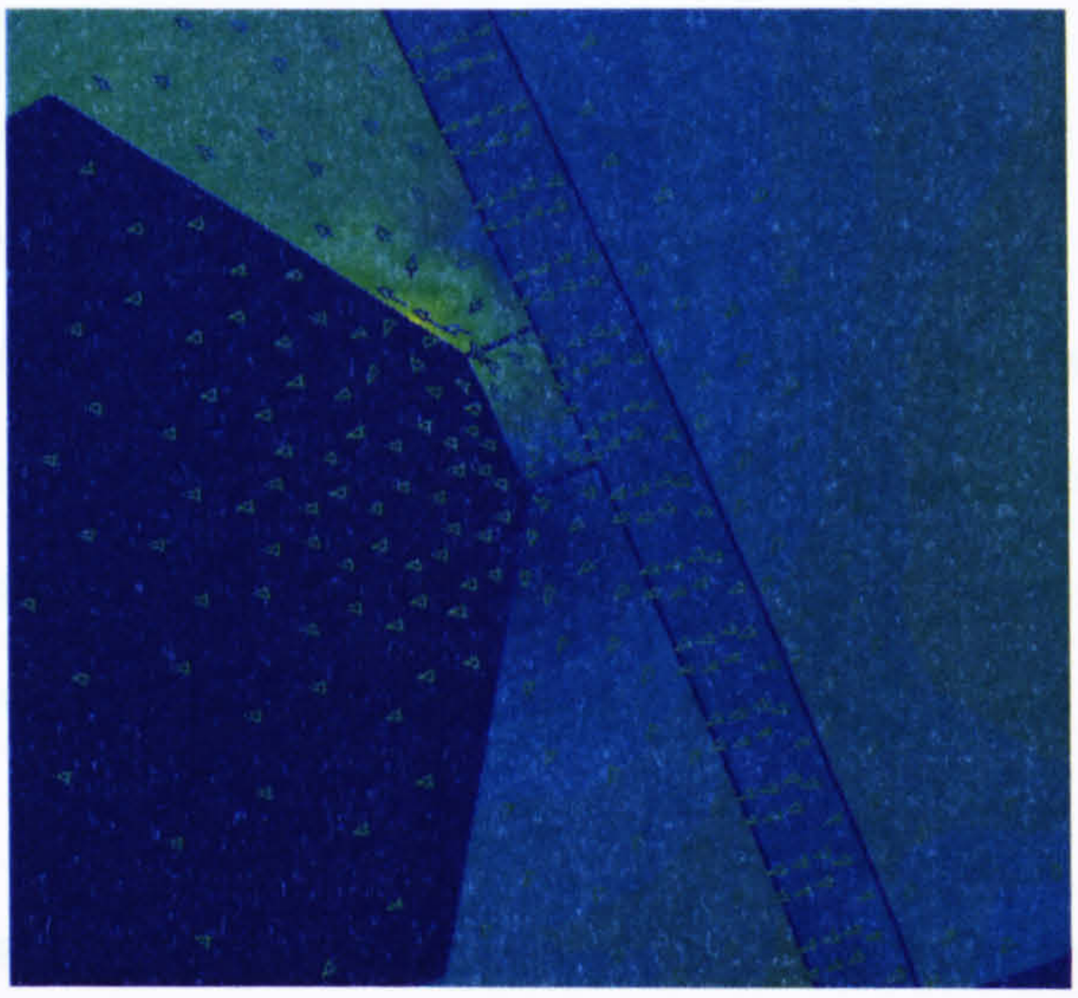

Fig. 5.19. Rotor bridge sections at load current of 3.5 Amps.

At higher load values, the magnetic bridges sections saturate in the direction of the magnetic field produced by the phase currents, as shown in Fig. 5.20. Once the bridge sections become saturated again, less flux from the permanent magnets can flow through them. As the saturation increases, more flux from the permanent magnets crosses the airgap, where it is linked by the phase coils. The permeability of the stator steel is reduced as the stator steel saturates and the flux-linkage contribution from the phase currents is once again reduced.

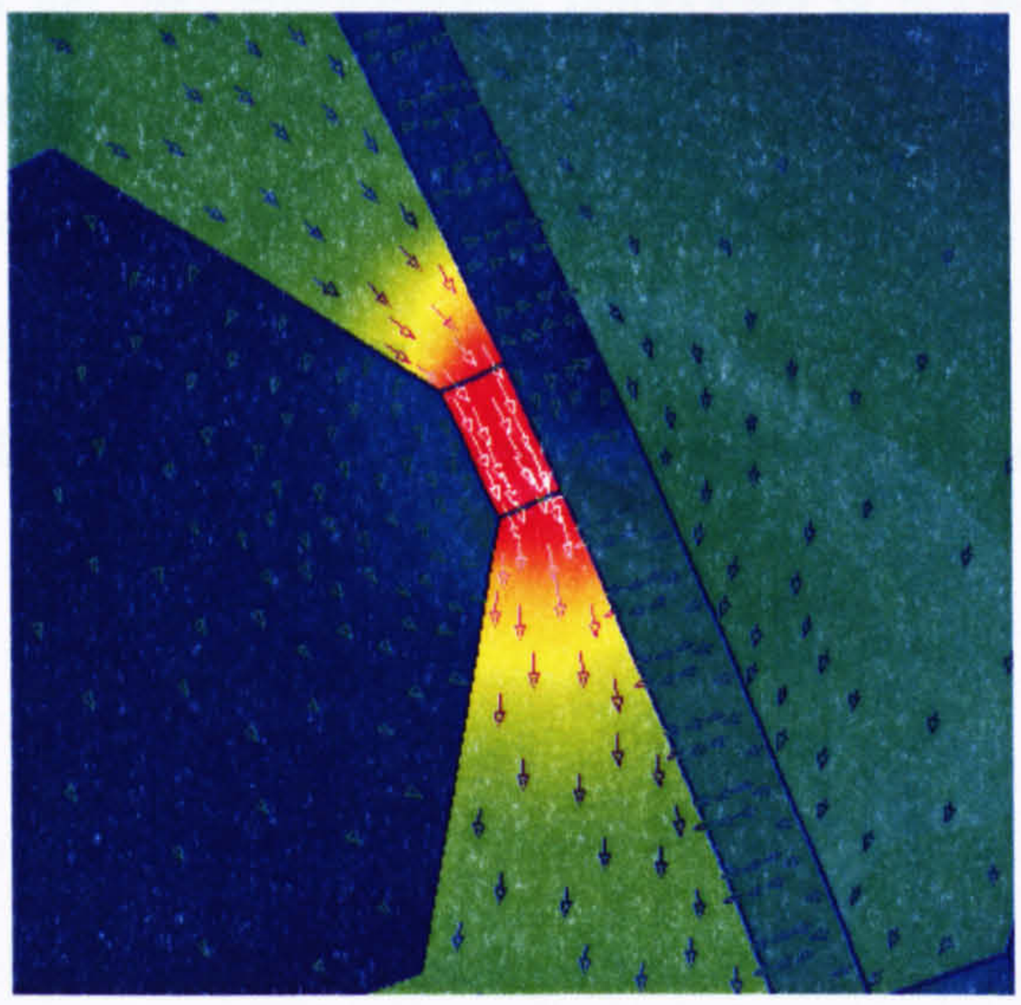

Fig. 5.20. Rotor bridge sections at load current of 8 Amps.

The presented results show that the calculation of flux-linkages and synchronous reactances using the fundamental flux density method is flawed. The frozen permeability simulations have shown that the flux-linkage due to the permanent magnets varies under load conditions, due to the changing levels of saturation in the rotor bridge sections. The flux-linkage due to current, and thus the synchronous reactances, can be accurately calculated using the frozen permeability method.

5.5.3. Influence of rotor bridge design on torque production

The different rotor bridge structures result in different flux-linkage versus current trajectories, which in turn can affect the instantaneous torque produced. The i-ψ loops for IPM test motor 1, for the different rotor bridge structures, are shown in Fig. 5.21. In each case, the motor has been excited with sinusoidal currents of 2 A peak magnitude. The loop trajectories show that the peak flux-linkage occurs for the rotor with the thickest bridge sections. At low current levels, the flux-linkage is higher for the rotor with open slots than all those with steel bridge sections. This confirms the results from Appendix 5, which show the direct-axis flux-linkage is higher at low load levels when the rotor slots are open, rather than fully closed. At low current levels, the bridge sections provide a leakage flux path for the permanent-magnet component of flux-linkage, reducing the amount of flux crossing the airgap in comparison to the rotor with open slots. It is only at high load levels, when the rotor bridge sections are saturated by the phase currents, that the flux-linkage from the magnets crosses the airgap. If the load currents were sufficiently high, the flux-linkages for all four rotor designs would be equal.

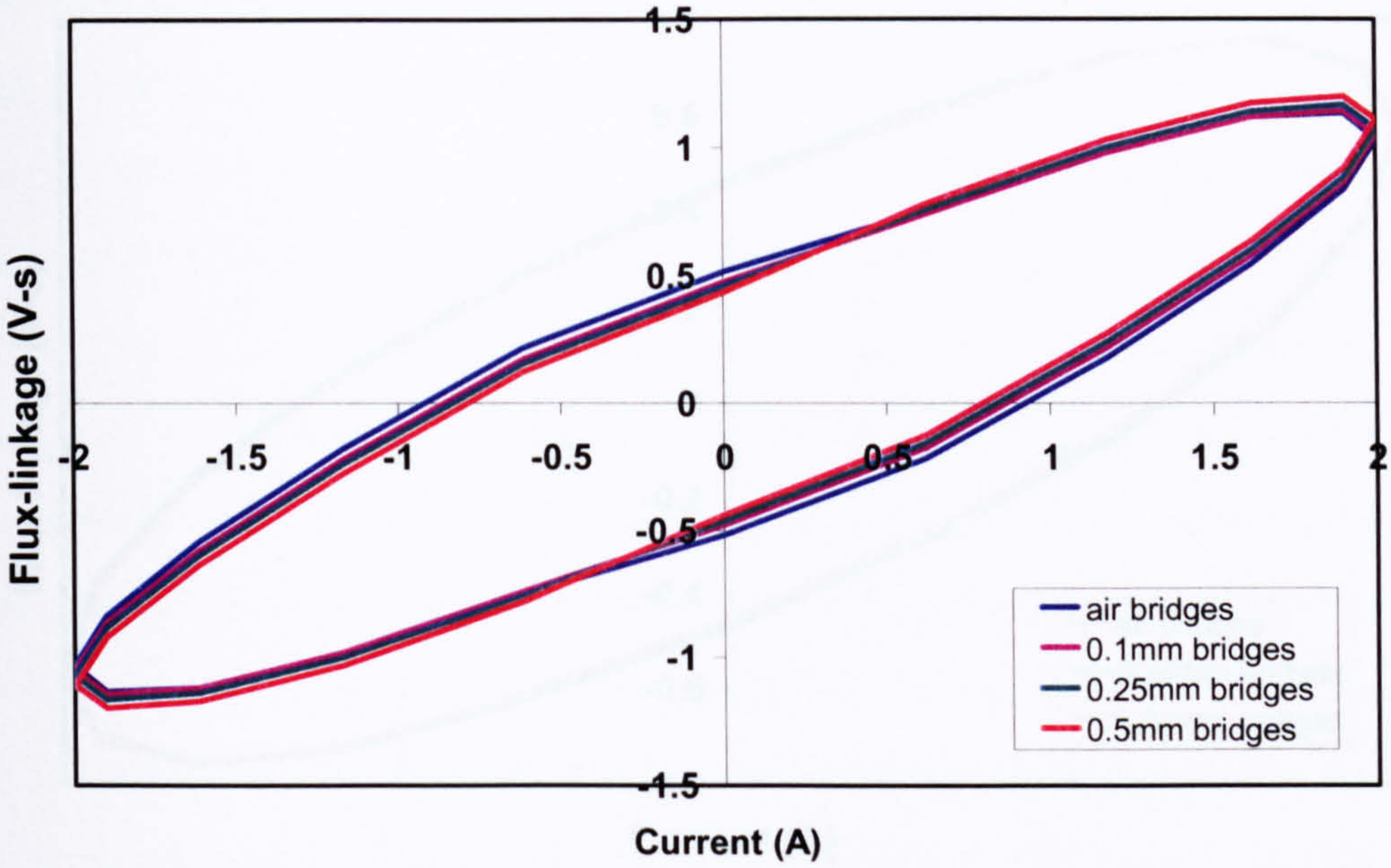

Fig. 5.21. *i*-ψ loops for test motor 1 for the four different bridge designs.

The average torque for each rotor design is shown in Table 5.3, for a rotational speed of 750 rpm. The torque produced is highest when the rotor slots are open, as there is no leakage flux path in the rotor. The difference in torque between the open slot and 0.1 mm bridge rotor designs is significant. As the thickness of the bridges is increases, the torque is reduced further, but the greatest decrease in torque is seen when the slots are initially closed.

Bridge design	Torque (Nm)	Change (%)
Open rotor slots	0.4955	-
0.10 mm	0.4646	**-6.27**
0.25 mm	0.4608	**-7.01**
0.51 mm	0.4538	**-8.42**

Table 5.3. Torque of IPM test motor 1 for each rotor design, for a rotational speed of 750 rpm.

Fig. 5.22 shows simulated *i*-ψ loops for IPM test motor 2, for a sinusoidal excitation current with maximum amplitude of 8 A. All three loops show close agreement, especially at higher current levels. At low current levels, the flux-linkage can once again be seen to be slightly higher in the case of the rotor with open rotor slots than those with steel bridge sections.

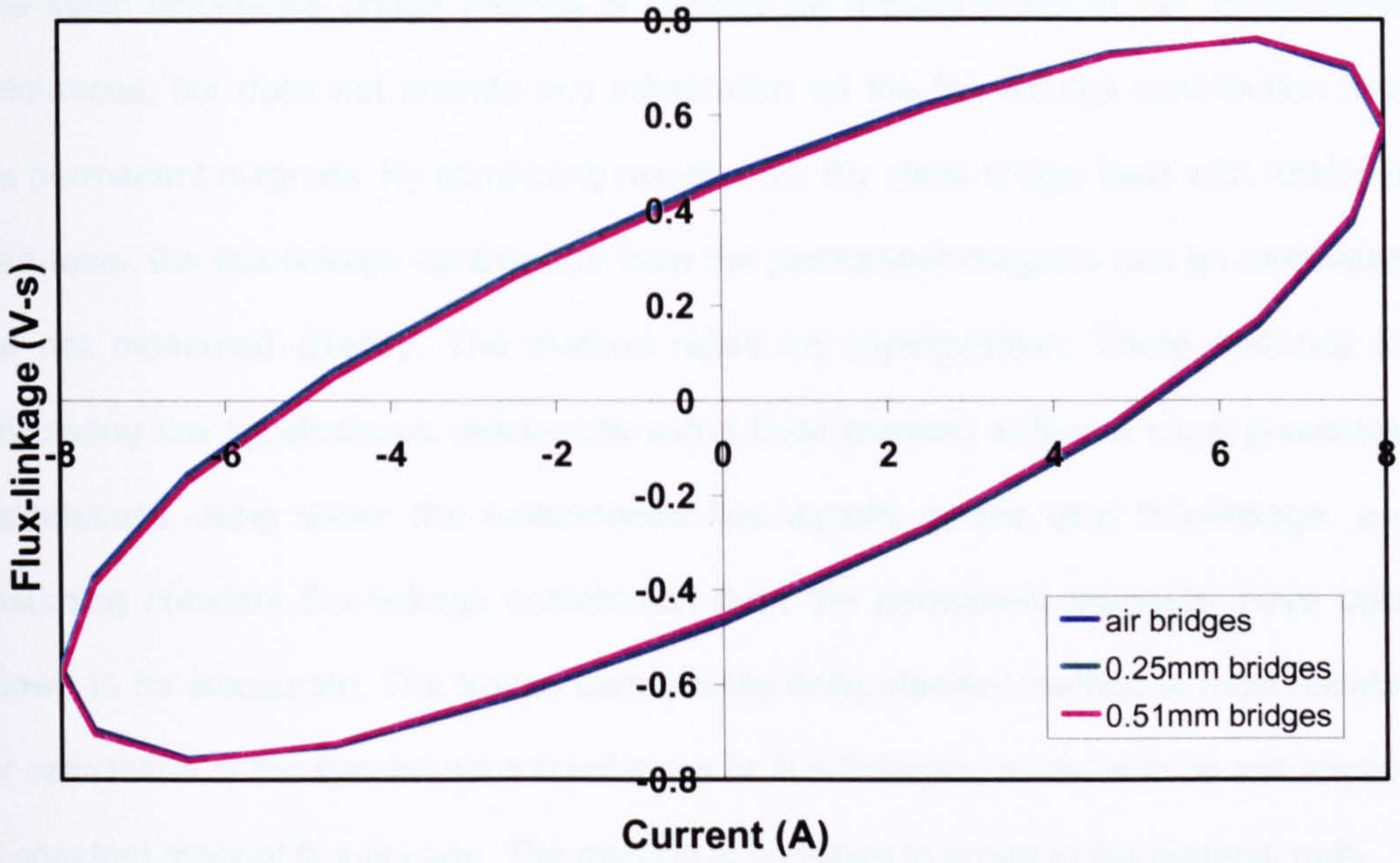

Fig. 5.22. *i-ψ* loops for test motor 2 for the three different bridge designs.

Bridge design	Torque (Nm)	Change (%)
Open rotor slots	1.9004	-
0.25 mm	1.8900	**-0.55**
0.51 mm	1.8499	**-2.66**

Table 5.4. Torque of IPM test motor 2 for each rotor design, for rotational speed of 1800 rpm

Table 5.4 shows the torque produced by each design, for a rotational speed of 1800 rpm. There is only a small difference in the torque produced by each rotor design. As with IPM test motor 1, the greatest torque is produced by the rotor with open slots; the greater the bridge thickness, the smaller the torque produced.

5.6. Conclusions

The phasor diagram method of calculating the interior permanent-magnet motor has been explained. Accurate torque calculation is only possible if saturated values of the magnet voltage *E* and synchronous reactances X_d and X_q are known for each load point.

The static inductance bridge method is suitable for measurement of the synchronous reactances, but does not provide any information on the flux-linkage contribution from the permanent magnets. By combining results from the static bridge tests with rotational load tests, the flux-linkage contribution from the permanent magnets can be calculated, but not measured directly. The method relies on superposition. Three methods for calculating the synchronous reactances using finite element software were presented. Calculations using either the fundamental flux density or the total flux-linkage, and assuming constant flux-linkage contribution from the permanent magnets, have been shown to be inaccurate. The frozen permeability finite element method is most suitable for calculation of the synchronous reactances or flux-linkages, as there is no assumption of constant magnet flux-linkage. The method is sensitive to errors in the material data.

Using finite element methods, the influence of rotor bridge design on the electromagnetic properties of the motor has been discussed. Rotor bridges are shown to reduce the flux density in the airgap, by providing a leakage path for the flux produced by the permanent magnets. The bridge sections reduce higher harmonics in the airgap flux density distribution. By design the rotor with thin bridge sections, the total harmonic distortion can be reduced with only a small reduction in airgap flux density.

Analysis of the flux-linkages due to current has shown that the direct axis synchronous reactance is different for magnetising and demagnetising currents, due to the saturation in the bridge sections. If the current is demagnetising, the total flux-linkage is greatest when the rotor slots are open, for all load levels. However, if the current is magnetising, the total flux-linkage is only greater for open rotor slots at low load levels. At higher currents, the flux-linkage is greater for rotors with steel bridge sections. This is caused by the reversed saturation in the bridge sections. The frozen permeability method also determines the flux-linkage contribution from the permanent magnets. The magnet flux linked by the stator coils varies greatly with load, due to the saturation in the rotor bridges being first reduced and then reversed. The results from the frozen permeability method were significantly different to those calculations made using the fundamental

component of the airgap flux density distribution, because no assumption was made of the flux-linkage contribution from the magnets.

Torque production is greatest for rotors with open slots, even though at high currents the flux-linkage may be greater for rotors with steel bridge sections. Simulation results have shown a reduction in torque due to closed rotor slots, but the amount of torque lost is dependent on a number of design factors, not just the thickness of the bridge sections.

Chapter 6

Iron Loss Analysis and Measurement

Electrical machines have improved in efficiency over the last twenty years largely due to advancements in materials science and manufacturing processes. Core losses in permanent-magnet machines are a significant component of the total electromagnetic losses (iron loss + copper loss) present in the machine, the remaining power loss being due to mechanical losses such as friction and windage. Core loss is normally described as the sum of hysteresis, classical eddy current and anomalous eddy current losses (often called stray load loss), with an additional term to describe losses due to rotational flux components sometimes included.

Although many methods have been developed to aid the understanding of core losses since Steinmetz, there is still no exact method of determining the core losses for non-sinusoidal excitation waveforms. With the advent of power electronic motor control, the need has arisen for an accurate method of determining iron losses generated by excitation waveforms with high levels of harmonics.

This chapter provides a brief overview of current methods for calculation of iron losses and discusses the advantages and drawbacks of each method. Suggestions are made for an improved iron loss model to simplify design calculations. Following on from this, the common methods of measuring the iron losses of lamination steel are described.

6.1. Iron loss prediction

A number of methods have been proposed for the calculation of iron losses in rotating machines. These methods can broadly be split into two groups: those based on the

classical Steinmetz equation and those based on the magnetisation characteristics of the lamination material, where the microscopic changes in magnetisation or energy are calculated. A brief introduction to the most pertinent methods is given below.

6.1.1. Methods based on the Steinmetz equation

Those methods based on the Steinmetz equation can be further categorised into two distinct groups. The first of these groups contains methods which follow the loss separation approach, where the loss is calculated as distinct components relating to eddy currents, hysteresis and 'excess' losses. The second group concerns methods that treat the losses as one complete phenomenon.

6.1.1.1. Steinmetz Calculations using Loss Separation Approach

Under the loss separation approach, the iron losses are split into contributions attributed to hysteresis, eddy currents and so-called excess or anomalous losses. Each loss component is thought to be the result of a specific physical occurrence in the magnetic moments and domains of the material. A brief overview of each loss component is given below, and models based on the loss separation method discussed.

Hysteresis losses

Hysteresis is caused by imperfections in the lamination material, which cause the material to hold some residual magnetisation when the applied field is removed. When a material is completely demagnetised, the domains will be randomly aligned. As a magnetic field is applied, the alignment of the domains changes until, under a high enough applied field, all the domains align in a uniform direction. If the applied field is then removed, some of the domains will be released from this alignment, but not all, and so the material will thus retain a certain level of magnetisation.

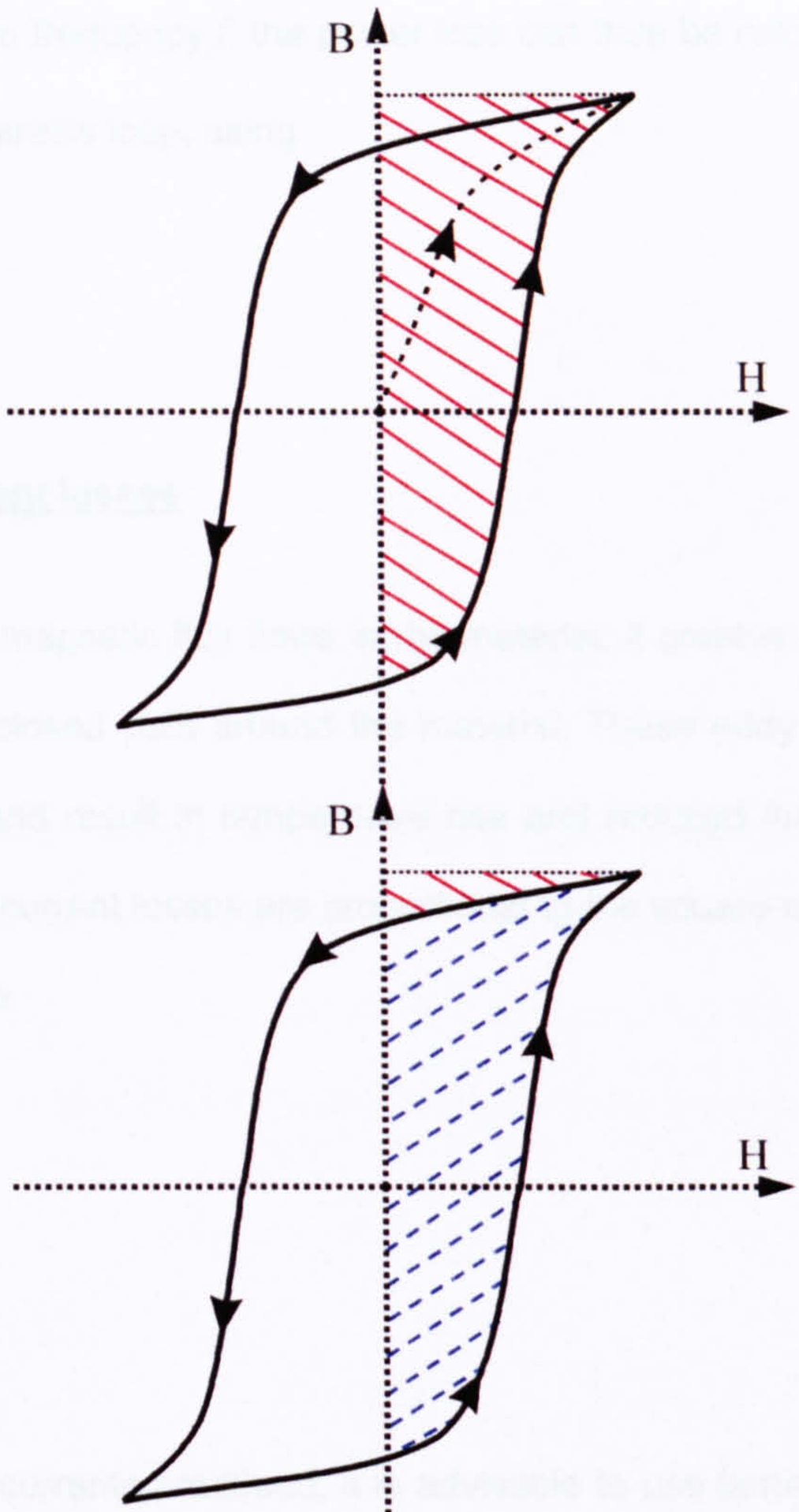

Fig. 6.1(a) and (b) Energy loss as a result of hysteresis effects

An example is shown in Fig. 6.1. In Fig. 6.1(a), a magnetic field *H* has been applied to the material. The shaded area depicts the energy required for each application of this field. The initial magnetisation curve is shown by the dotted line, for reference. When the applied field is removed, as in Fig. 6.1(b), the material retains some of its magnetisation. The energy returned by the removal of the field is thus less than the initial expended energy; it is proportional to the red shade area shown in Fig. 6.1(b). The energy lost is proportional to the blue shaded area. It can be seen that, for one complete magnetisation cycle, the difference between the expended energy required and that released when the field is removed will be equal to the area of the hysteresis loop traced out by the material. The energy loss is related to the power loss by the excitation

frequency. For a given frequency f, the power loss can thus be calculated from the area of the measured hysteresis loop, using

$$P_h = f \oint H.dB \tag{6.1}$$

Classical eddy current losses

When an alternating magnetic flux flows in the material, it creates eddy currents, which flow in an available closed path around the material. These eddy currents oppose the field inducing them and result in temperature rise and reduced flux capacity within the specimen. The eddy current losses are proportional to the square of the applied voltage, and vary according to

$$P_e \propto f^2 B^2 \tag{6.2}$$

To reduce the eddy currents produced, it is advisable to use lamination stacks in place of solid cores, as illustrated in Fig. 6.2. Fig. 6.2.(a) shows the eddy current paths in a solid core. The currents enclose large areas and the EMF induced in the material is high. When using laminated materials, as in Fig. 6.2.(b), the surface of the laminations is treated to create an insulating layer that prevents the flow of eddy currents between laminations. The eddy currents are then confined to rectangular paths within each lamination, resulting in smaller induced EMFs. Each lamination carries an equal proportion of the original flux but the power loss is reduced (because the power loss is proportional to the square of the rate of change of flux, which is inversely proportional to the number of laminations) [66].

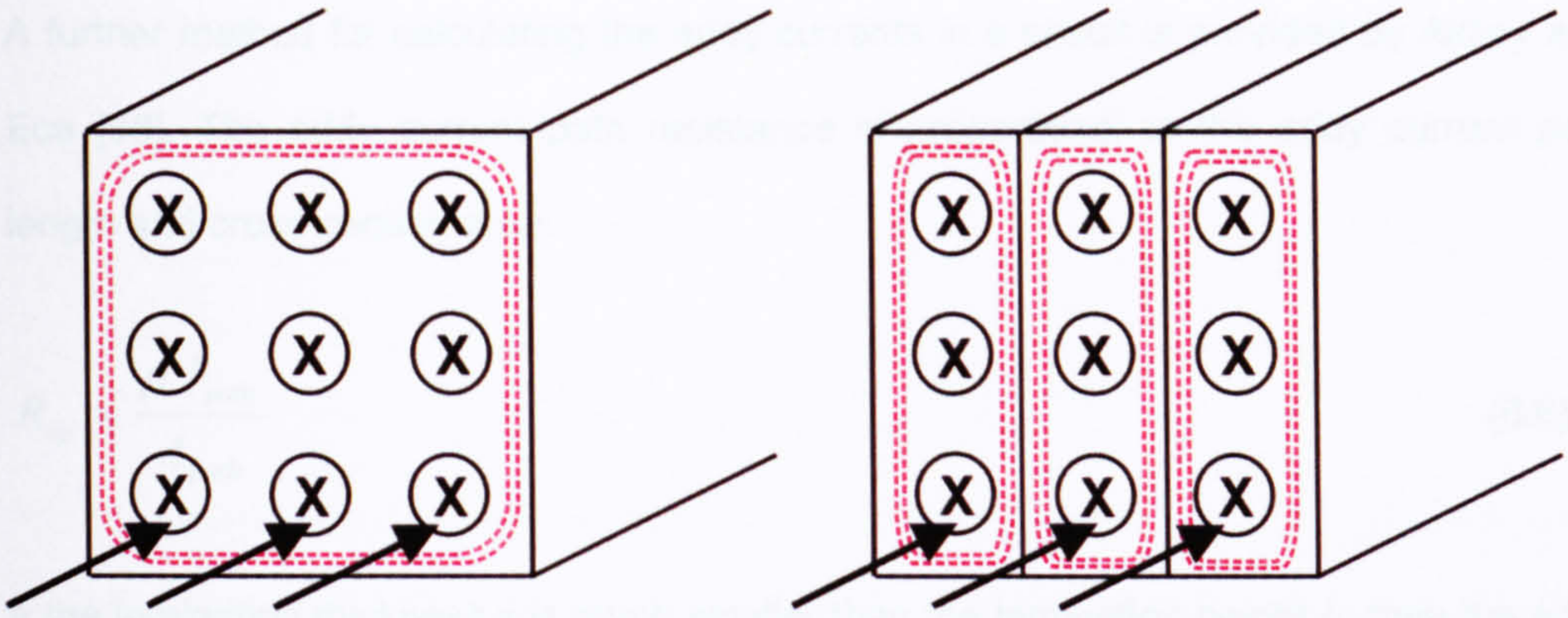

Fig. 6.2.(a) and (b) Reduction of eddy currents through use of laminated core

The eddy current losses can be calculated using either analytical calculations or finite element analysis. A useful equivalent circuit model of eddy current loss is provided by Udayagiri and Lipo [67]. The eddy current loss is shown to depend on the number of laminations and the volume, thickness and resistivity of the material of each lamination:

$$P_e(t) = \frac{Vw^2 N_e}{12\rho N^2 A^2 m} v(t) \tag{6.3}$$

The instantaneous voltage $v(t)$ is directly proportional to the rate of change of flux in the circuit. The power loss can then be proven to be proportional to the square of the rate of change of flux in the circuit:

$$P_e(t) = \frac{v(t)^2}{R_e} = \frac{\left(\frac{d\Phi}{dt}\right)^2}{R_e} \tag{6.4}$$

where R_e is the eddy current loss resistance calculable from:

$$R_e = \frac{12\rho N^2 A^2 m}{V\omega^2 N_e} \tag{6.5}$$

A further method for calculating the eddy currents in a circuit is provided by Akçay and Ece [68]. The eddy current path resistance is proportional to the eddy current path length and cross-section area:

$$R_{ep} = \frac{\rho\, l_{path}}{A_{path}} \tag{6.6}$$

If the lamination thickness τ is much smaller than the lamination height h, then the eddy current path length will be approximately $2h$ and the eddy current can be calculated from

$$I_{eddy} = \int_0^{\tau/2} dI_{eddy} = \frac{\omega \tau^2}{8\rho} \frac{dB}{dt} \tag{6.7}$$

Both the above methods illustrate the dependence of the eddy current losses on the properties of the lamination material, in particular the lamination thickness. The resistivity of the lamination material can be increased by heat treatment/ annealing methods.

Excess losses

The above hypothesis for eddy currents assumes that the field is homogeneous across the sample. Prediction of the iron loss by addition of the hysteresis and eddy current losses will give an answer somewhat smaller than the true losses in the material. The difference between calculated and measured values is often termed the 'excess' loss and can be explained if the material is considered in terms of domains. During the magnetisation process, the magnetic domains within the sample change shape and some will increase in size, leading to movement of the walls between such domains. Domain wall motion in turn leads to changes in the localised flux density, inducing localised eddy currents as shown in Fig. 6.3. The field is therefore not homogeneous at all; rather, it is localised around the areas of each domain wall.

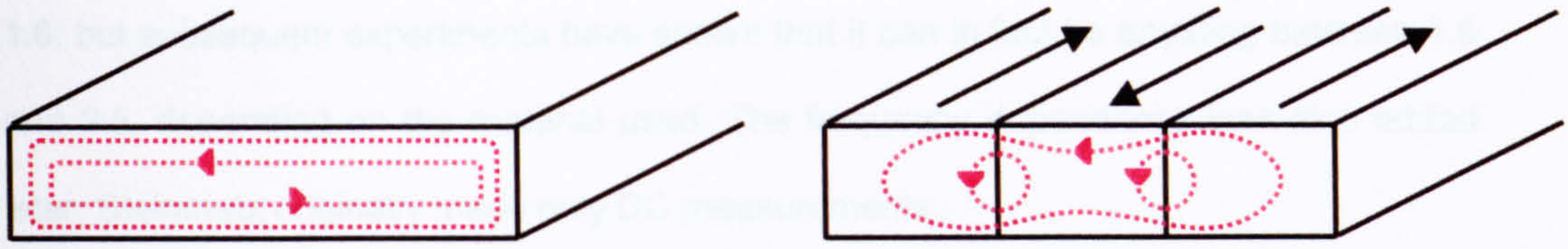

Fig. 6.3. Additional eddy currents created by domain wall motion

Although treatment of the losses is traditionally split into the hysteresis, classical eddy current and excess eddy current losses, it is easy to see from the above explanation that a more intuitive approach would be to examine the losses directly in terms of magnetisation or the interaction between domains. This is discussed further in following sections.

The above cases all consider an alternating flux density. In rotating electrical machines, the flux density vector may rotate in the plane of the lamination. This rotation will increase the total losses in the machine. Certain areas of the lamination will be more susceptible to rotational flux densities than others. For loss calculations in these sections, it is appropriate to calculate the radial and tangential loss components individually [69, 70]. The relationships presented above assume a sinusoidally-varying flux density, and do not take into account the increased losses that will be caused by any nested or minor hysteresis loops.

Steinmetz carried out pioneering work on the nature of core losses in the early 1900s, but the work was limited to static tests and low levels of flux density and the model is only truly accurate under these conditions. The hysteresis loss was found by Steinmetz to be proportional to the peak flux density [71]. Today, the equation

$$P_h = k_h f \hat{B}^n \tag{6.8}$$

is frequently used to determine the hysteresis loss in electrical machines. It should be noted that this equation is only truly accurate for sinusoidal flux density waveforms, and for low values of peak flux density. Steinmetz originally defined the parameter n to equal

1.6, but subsequent experiments have shown that it can in fact be anything between 1.5 and 2.5, depending on the material used. The frequency dependence was also added later; Steinmetz originally made only DC measurements.

The classical eddy current losses are produced by the alternating flux waveform. The currents flow in closed paths between the laminations. The eddy currents oppose the applied field and so reduce the overall flux capacity of the motor. The loss can be modelled in terms of the peak flux density, as shown in

$$P_e = k_e f^2 \hat{B}^2 \tag{6.9}$$

or in relation to the rate of change of the flux density, as in Eq. (6.10) [72,67].

$$P_e = k_{el}\left(\frac{dB}{dt}\right)^2 \tag{6.10}$$

For sinusoidal flux density, k_{el} simplifies to

$$k_{el} = \frac{k_e}{2\pi^2} \tag{6.11}$$

Anomalous eddy current losses are caused by non-uniform motion at the domain walls [50]. The anomalous losses can be determined approximately using

$$P_a = k_a\left(f\hat{B}\right)^{3/2} \tag{6.12}$$

The rotational losses are those losses generated by the rotation of the flux density vectors in the plane of the lamination. The effects of rotational losses on total losses are significant, but they remain very difficult to predict. Some progress has been made using

finite element analysis to determine the rotational and alternating components of the flux density. The rotational losses can be calculated from the measured applied field and flux density in the radial and tangential directions, using equation 6.13 [74].

$$P_t = \frac{1}{T}\int_T \left(H_x \frac{dB_x}{dt} + H_y \frac{dBy}{dt} \right) dt \qquad (6.13)$$

6.1.1.2. Calculations based on empirical Steinmetz equation

The above equations assume that each loss component is the result of a distinct physical effect. In fact, it has been shown that hysteresis and eddy current losses both result from motion of the domain walls [75]. Furthermore there is an assumption that the flux density waveforms are sinusoidal (or nearly sinusoidal), which is not the case for many permanent-magnet motors driven by power electronics. Some variations can be made to the original Steinmetz equation to allow use of non-sinusoidal flux density waveforms.

Reinert et al. first proposed the Modified Steinmetz Equation (MSE) in 1999 [76]. In the MSE, the core losses are not separated into eddy current and hysteresis components, but are treated together as the effect of local, non-uniform domain wall motion. The MSE is based on the empirical Steinmetz equation

$$P_v = k f^{\alpha} \hat{B}^{\beta} \qquad (6.14)$$

where P_v is the power loss per unit volume of the material, f is the remagnetisation frequency, $\hat{B}$ is the peak flux density and k, α and β are empirical material parameters. The remagnetisation frequency is replaced with the macroscopic remagnetisation rate dM/dt, which is proportional to the rate of change of induction dB/dt. The rate of change of induction is averaged over one cycle of remagnetisation to give

$$B = \frac{1}{\Delta B} \int_0^T \left(\frac{dB}{dt} \right)^2 dt \tag{6.15}$$

An equivalent frequency is determined from the averaged remagnetisation rate in Eq. (6.15) as

$$f_{eq} = \frac{2}{\Delta B^2 \pi^2} \int_0^T \left(\frac{dB}{dt} \right)^2 dt \tag{6.16}$$

and the total energy loss per remagnetisation cycle becomes

$$E_v = C_m f_{eq}^{\alpha-1} \left(\frac{\Delta B}{2} \right)^{\beta} \tag{6.17}$$

Tests carried out by Reinert et al. show good correlation for ferromagnetic materials with DC biased waveforms. Results show significant improvement on the original Steinmetz equation.

However, later work carried out at the University of Dartmouth [77, 78] highlights a number of discrepancies arising from use of the MSE. The results are shown to vary in some cases from those obtained with the Steinmetz equation. When the flux density waveform in question contains higher harmonics of similar amplitude to that of the fundamental, the calculated loss deviates greatly from measured values. In addition to this, the loss associated with minor loops must be determined separately, due to the dependence on the peak amplitude of the flux density waveform.

Instead, Abdallah et al. have developed a modified General Steinmetz Equation (GSE) [77], based on the generic power dissipation function

$$P_v(t) = P_d\left(\frac{dB}{dt}, B\right) \tag{6.18}$$

The Generalized Steinmetz Equation (GSE) improves on the MSE, but still deviates from measured data in cases where the flux density waveform contains a number of minor loops. Li et al. suggest an improved Generalised Steinmetz Equation (iGSE):

$$\overline{P_v} = \frac{1}{T}\int_0^T k_i \left|\frac{dB}{dt}\right|^{\alpha} (\Delta B)^{\beta-\alpha}\, dt \tag{6.19}$$

where the loss is once again dependent on the peak amplitude of the flux density waveform and is calculated separately for major and minor loops [78].

To give results consistent with the Steinmetz equation for sinusoidal flux density waveforms, k_i can be determined from the original Steinmetz coefficients using

$$k_i = \frac{k}{(2\pi)^{\alpha-1}\int_0^{2\pi} |\cos\theta|^{\alpha} 2^{\beta-\alpha}\, d\theta} \tag{6.20}$$

A weighted average of the loss in each loop is then taken to determine the average power loss per cycle. For flux density waveforms containing harmonics over a large frequency range, it may still be necessary to adjust the Steinmetz coefficients. Although it represents a significant improvement over previous loss calculation methods, the iGSE is still not ideal as the losses calculated are independent of any DC bias.

A model loosely based on the original Steinmetz equation has been developed at the University of Sheffield [79, 80]. In the model, the losses are split into hysteresis, classical eddy current and excess loss components. The loss is calculated for a known flux density waveform using the equation:

$$P_t = k_h f \hat{B}^{\alpha} K\left(\hat{B}\right) + \frac{\sigma}{12}\frac{d^2 f}{\rho}\int_1^f \left(\frac{dB}{dt}\right)^2 dt + k_e f \int_1^f \left(\frac{dB}{dt}\right)^{1.5} dt \qquad (6.21)$$

where the function $K(B_m)$ is used to account for the occurrence of minor loops within the major hysteresis loop, and can be calculated from the following equation:

$$K\left(\hat{B}\right) = \left(1 + \frac{0.65}{\hat{B}}\sum^{n}\Delta B\right) \qquad (6.22)$$

6.1.2. Methods based on prediction of magnetisation characteristics

Although the Steinmetz equation is the most common method for estimation of the core losses, methods based on the magnetisation properties of the lamination material have been developed in recent years. Two of these, the Preisach and Jiles-Atherton methods, are detailed below. Both models calculate the magnetisation of the material and use this to reproduce the dynamic hysteresis loop. Just as the static hysteresis loop represents the static (hysteresis) losses of the material, the dynamic loop represents the total dynamic losses (hysteresis, classical eddy current and excess losses combined) [69].

The Preisach method was first developed in early twentieth century [81]. The principle behind the method is that the magnetisation of a material can be determined from its known magnetisation history. The original Preisach model is given in by

$$f(t) = \iint_{\alpha \geq \beta} \mu(\alpha, \beta) \hat{\gamma}_{\alpha\beta} u(t) d\alpha d\beta \tag{6.23}$$

The current magnetisation $f(t)$ is determined from the magnetic field $u(t)$ and two switching operators α and β (corresponding to magnetising and demagnetising switching levels respectively). The function $\mu(\alpha, \beta)$ must be determined from transition curves of the material in question. $\hat{\gamma}_{\alpha\beta}$ is the hysteresis operator, where α and β are once again numbers corresponding to the input level at which the hysteresis operator switches output.

The Preisach model is denoted as 'static', as the current value of magnetisation is dependent only on the previous magnetisation history and not the speed at which the magnetisation is changing. An improvement to the model:

$$f(t) = \iint_{\alpha \geq \beta} \mu(\alpha, \beta, u(t)) \hat{\gamma}_{\alpha\beta} u(t) d\alpha d\beta + \frac{f^-_{u(t)} + f^+_{u(t)}}{2} \tag{6.24}$$

includes output values corresponding to branches on the hysteresis loop. However, this model is still static. To make the model dynamic, Mayergoyz [82] suggests the use of the power series expansion of the μ-functions. The dynamic Preisach model is then represented by

$$f(t) = \iint_{\alpha \geq \beta} \mu_0(\alpha, \beta, u(t)) \hat{\gamma}_{\alpha\beta} u(t) d\alpha d\beta + \frac{f^-_{u(t)} + f^+_{u(t)}}{2} + \frac{df}{dt} \iint_{\alpha \geq \beta} \mu_1(\alpha, \beta, u(t)) \hat{\gamma}_{\alpha\beta} u(t) d\alpha d\beta \tag{6.25}$$

As the variation in output tends to zero, the dynamic model will reduce to the original static case. As such, the μ_0 functions can be determined from the first- and second-order transition curves. The μ_1 function is related to the relaxation time of the material and must be determined from experimental data. Other improvements to the Preisach model have included the use of vector analysis to realise a dynamic solution. The main drawback to the method is the large number of parameters required and the need to determine the coefficients from experimental data.

Jiles and Atherton first proposed an alternative to the Preisach method during the mid-1980s [83 - 85]. Their model is based on characterisation of domain wall motion and on mean field approximation. The effective field in a ferromagnet can be expressed as

$$B_e = \mu_0 (H + \alpha M) \tag{6.26}$$

where H is the magnetic field and M is the magnetisation of the material. The effective field can then be substituted into the Weiss equation to give the mean field equation[6]

$$M = M_s \left[coth\left(\frac{\mu_0 m \bullet (H + \alpha M)}{kT} \right) - \frac{kT}{\mu_0 m \bullet (H + \alpha M)} \right] \tag{6.27}$$

The ferromagnetic material is structured in domains. If the material were without defects, these domains would be able to move freely from side to side. The defects restrict the domain wall motion, a phenomenon known as domain wall pinning. The domain walls remain restricted until sufficient field is applied to overcome the pinning effects.

Jiles and Atherton denote the intensity of pinning sites per unit volume as n and the average pinning energy per site as E_p. The total energy loss per unit volume due to pinning is thus nE_p and so the rate of change of energy loss can be expressed using

[6] Where M_s is the spontaneous saturation within the domain. For a detailed explanation see Ref. [59].

$$\frac{dE_{loss}}{dx} = nE_p A_{wall} \tag{6.28}$$

where A_{wall} is the area of the domain wall and x is the distant through which the domain wall moves. As the change in magnetisation is relative to the volume of movement in the domain wall, the energy loss can be expressed in terms of the change in magnetisation

$$\frac{dE_{loss}}{dM} = k \tag{6.29}$$

Using the Langevin function as a base, the model then becomes

$$M = f\left(\frac{M + \lambda H}{a}\right) - k\frac{dM}{dB_e} \tag{6.30}$$

where $\frac{\lambda}{a} = \frac{\mu_0 m}{kT}$ and $\frac{1}{a} = \frac{\alpha \mu_o m}{kT}$.

Early papers by Jiles and Atherton suggest it is possible to expand this model to deal with minor hysteresis loops. Other authors have contested this, with modifications being suggested by Carpenter and Lederer et al. [86, 87].

Although improvements to both of the above models have allowed determination of the magnetisation characteristics with reasonable accuracy, there is still scope for improvement. In both models, it is necessary to determine a number of parameters experimentally. A simpler model requiring parameters readily available from material manufacturers and requiring only minimal additional material testing would be a great improvement.

6.1.3. Methods based on the area of the dynamic hysteresis loop

As explained previously, the area of the dynamic hysteresis loop represents the total energy loss due to the hysteresis, eddy current and excess or anomalous loss components. The loss can be calculated from the closed loop integral

$$E_{loss} = \oint H.dB \tag{6.31}$$

The power loss in the sample is related to the energy loss by

$$P_v = fE_{loss} \tag{6.32}$$

The total specific loss of the sample can be found from

$$P_s = P_v \frac{1}{\rho_{sample}} \tag{6.33}$$

This method of loss calculation has been well documented [88 - 92]. Thottuvelil et al. discuss difficulties and possible sources of measurement error, with specific reference to higher frequency measurements [89]. References [90 - 92] propose systems for automated measurement of the hysteresis loops and specific losses. These papers restrict discussion to calculation of the losses from measured hysteresis loops and do not suggest any methods of predicting the loop shape or area.

A number of papers predict the hysteresis loop by treating it as a combination of the saturation curve characteristic of the material and a loss function that determines the shape and area of the loop. In Fig. 6.4, the saturation curve is shown by the line DJOG. The loss function is a reverse function of the normal magnetisation curve. The magnitude of the loss function at any point is illustrated by horizontal lines between the

static magnetisation curve and the outer edge of the loop, such as the lines EJ, JC, FO and OA. It is at a maximum when the saturation curve is at point O.

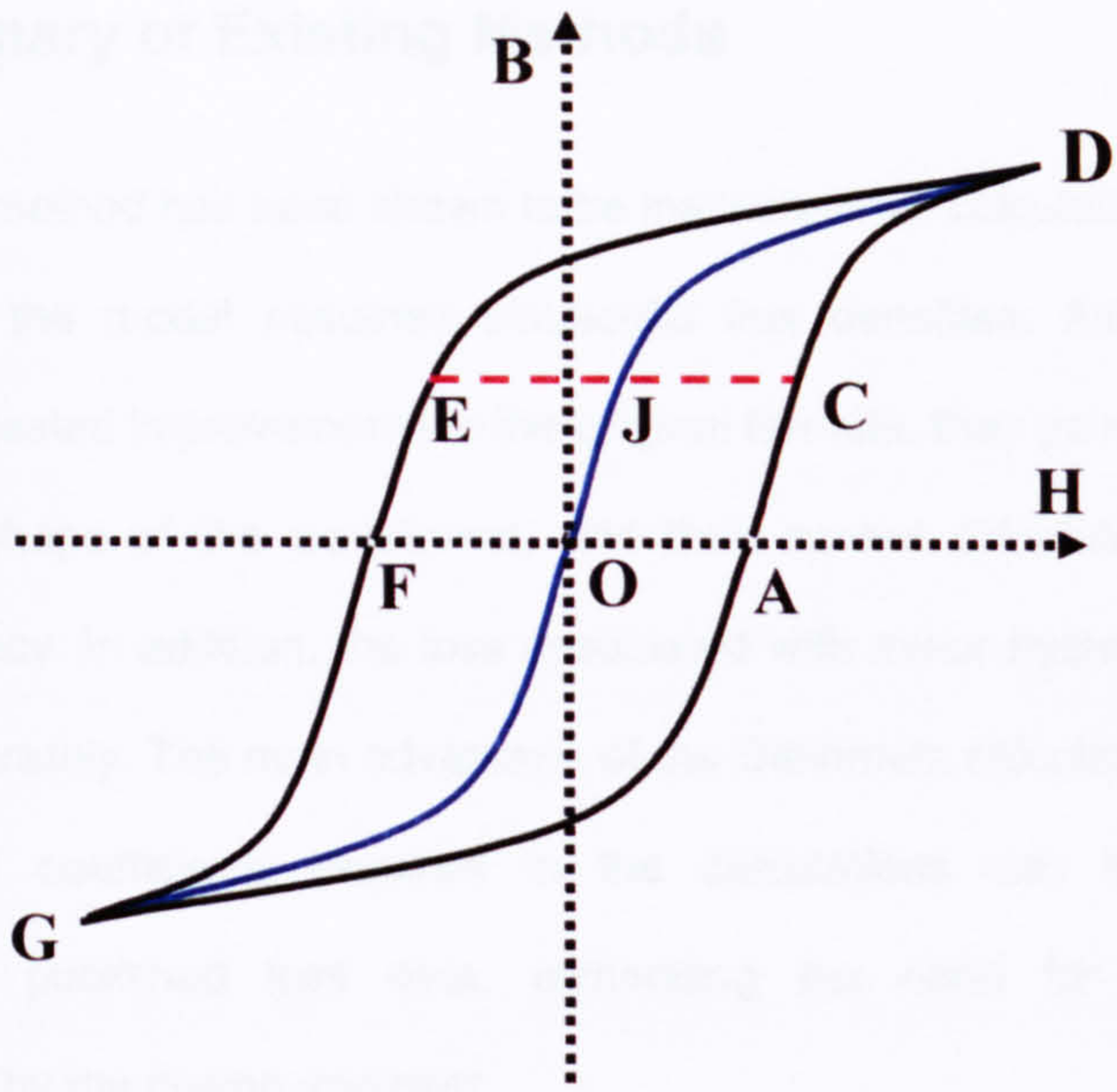

Fig. 6.4. Hysteresis loop showing saturation curve

Lin et al. have produced papers proposing a method of predicting the hysteresis loops of transformers using curve-fitting techniques [88,93]. Although the authors show good correlation between measured and calculated results, tests have been restricted to sinusoidal excitation and there is no indication as to the effects of increased harmonic content or the presence of minor loops. A similar method is proposed by Prusty and Rao [94]. The loss function is approximated using cubic- or quintic-order differential equations. Although the results show good correlation between predicted and measured results, a number of parameters must be determined by simultaneous equations using initial measurements of the saturation curve.

In [95], Del Vecchio discusses a possible method of determining the hysteresis loops using finite element analysis. The method uses two separate fields, *B* and *H*, rather than the single vector potential *A*. The relationship between *B* and *H* does not affect the solution of the differential equation as it is specified separately. Measurements must be

carried out to determine the saturated relationship between *B* and *H*. The method is applied to the nodes of a finite element mesh.

6.1.4. Summary of Existing Methods

The Steinmetz method has been shown to be inaccurate for calculations involving higher harmonics, as the model assumes sinusoidal flux densities. Although there are a number of suggested improvements to the original formula, they do not take into account the complete shape of the waveforms, and thus cannot calculate the loss with the required accuracy. In addition, the loss associated with minor hysteresis loops must be calculated separately. The main advantage of the Steinmetz calculation methods is that, in general, all coefficients required in the calculations can be found from the manufacturer's published loss data, eliminating the need for additional material measurements by the design engineer.

The models based on domain theory, such as the Preisach method, examine the instantaneous changes in magnetisation and produce accurate results regardless of the harmonic content of the waveforms. However, a large amount of experimental data is required to determine coefficient values, making the methods impractical for fast initial design calculations.

Determination of the losses from the dynamic hysteresis loop has a physical significance as the loop can be measured directly. The relationship between loop area and power loss is uncomplicated. Theoretical determination of the loop area is possible either through direct calculation of *B* and *H* (as described in [95]), or by defining a loss function from which to calculate the shape of the loop. Providing that the relationship between applied field and flux density is well defined, such methods should prove to be more accurate than the Steinmetz methods, as the loss computation is dependent only on the values of the waveforms, rather than additional coefficients. Current methods also

suggest some improvement over the Preisach and Jiles-Atherton methods, as the only experimental data required is measurements to confirm that the calculated *B-H* loops as the same as those measured.

There are important limitations to the current models based on determination of the dynamic hysteresis loop. There is no indication of how minor loops should be treated using the loss function approach. The loss function is added to the saturation curve of the motor, but in general minor loops will not be centred on the points of the saturation curve. Variation to the method, or indeed an entirely new method, would be needed to correctly determine the losses resulting from signals with high harmonic content.

6.2. Measurement of magnetisation characteristics

The model proposed uses the magnetisation characteristics of the material to determine the applied field from the given flux density. It is therefore important to have accurate data describing the magnetic properties of the material. In general, the data provided by steel manufacturers is limited to a DC magnetisation curve and graphs of specific losses versus frequency for different levels of flux density.

The saturation characteristics of the material are defined by the DC magnetisation curve. The curve is a measurement of the flux density created by the applied field. Measurements of flux density are taken at discrete increasing levels of applied field. Due to the test set-up employed, it has not been possible to measure the DC magnetisation curve. Instead, the normal magnetisation curve (essentially the same as the DC magnetisation curve but at low frequency) has been measured. The points for the normal magnetisation curve have been determined from hysteresis loops of the lamination material measured on a single sheet tester.

Although material manufacturers do not normally publish them in detail, the measured hysteresis loops can prove useful. Properties such as the remnant flux B_r and coercive force H_C (points E and F respectively in Fig. 6.4), determinable from hysteresis loops of the material, can vary greatly between material types. The shape of the hysteresis loop is dependent on the harmonic content of the flux density waveform. The presence of higher harmonics may generate minor loops inside the main hysteresis loop. The width of the loop (the coercive field of the material) will vary as a result of frequency. Losses are a function of the intrinsic characteristics of the material, the lamination thickness, applied field (and resulting flux density) and frequency. As such, hysteresis loop measurements should be made over the range of flux densities and power frequencies, for both sinusoidal and nonsinusoidal flux density characteristics.

The following sections describe the control systems and test apparatus used to measure the hysteresis loops and material characteristics of lamination steel.

6.2.1. Measurement System

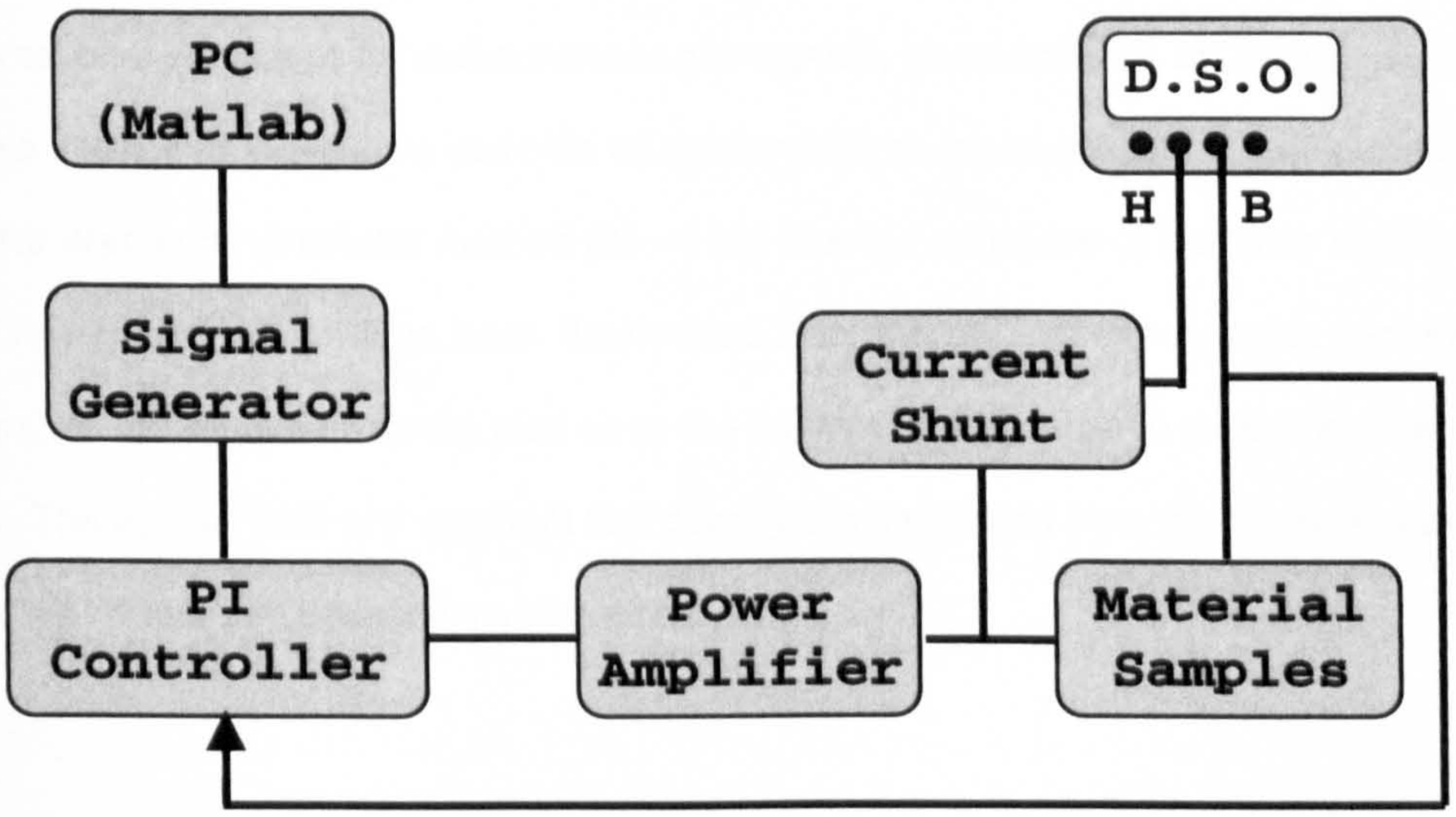

Fig. 6.5. System for measurement of magnetisation characteristics

Two types of measurements have been carried out – measurements with sinusoidal flux densities and tests with non-sinusoidal flux densities due to injected harmonic content. The measurement system is shown in Fig. 6.5. For measurements with sinusoidal flux density, the signal is taken directly from the signal generator. For other measurements, the input signal is generated by a Matlab program and downloaded from the PC via a GPIB (see Appendix 3).

Once the waveform shape has been downloaded to or selected on the signal generator, the amplitude and frequency of the signal can be altered. The signal generator acts as the input to a PI controller, the output of which is connected to an audio power amplifier connected in *bridge mono* mode [96]. The power amplifier feeds the primary winding of the selected test specimen. The secondary winding of the specimen is connected to a PI controller in a feedback loop. The PI controller was designed in collaboration with Grundfos AG and the University Of Aalborg Institute Of Energy Technology, for control of the single sheet tester; the gains must be altered for use with the Epstein square and toroid sample due to the difference in sample sizes. Information on the controller design can be found in [97].

International standards for measurement of magnetic characteristics on Epstein square, single sheet and toroid core samples all concentrate on measurement of the iron losses by the Wattmeter-Ammeter method [98 - 101]. For the purposes of the tests outlined in this report, the losses have been determined from the area of the dynamic hysteresis loops, as the proposed model also uses the hysteresis loop area to determine the iron loss. The applied field and resultant flux density are calculated from measurement of the primary current and secondary voltage respectively.

6.2.2. 25 cm Epstein square

The 25 cm Epstein square is the most established method of measurement of magnetic characteristics of electrical sheet steels and is covered by American Society of Testing and Materials (ASTM) and International Electrotechnical Commission (IEC) standards [98, 99]. It is suitable for measurements at power frequencies (between 25 and 400 Hz) for measurements up to 1.5 T on NGO steels and 1.8 T on GO steels.

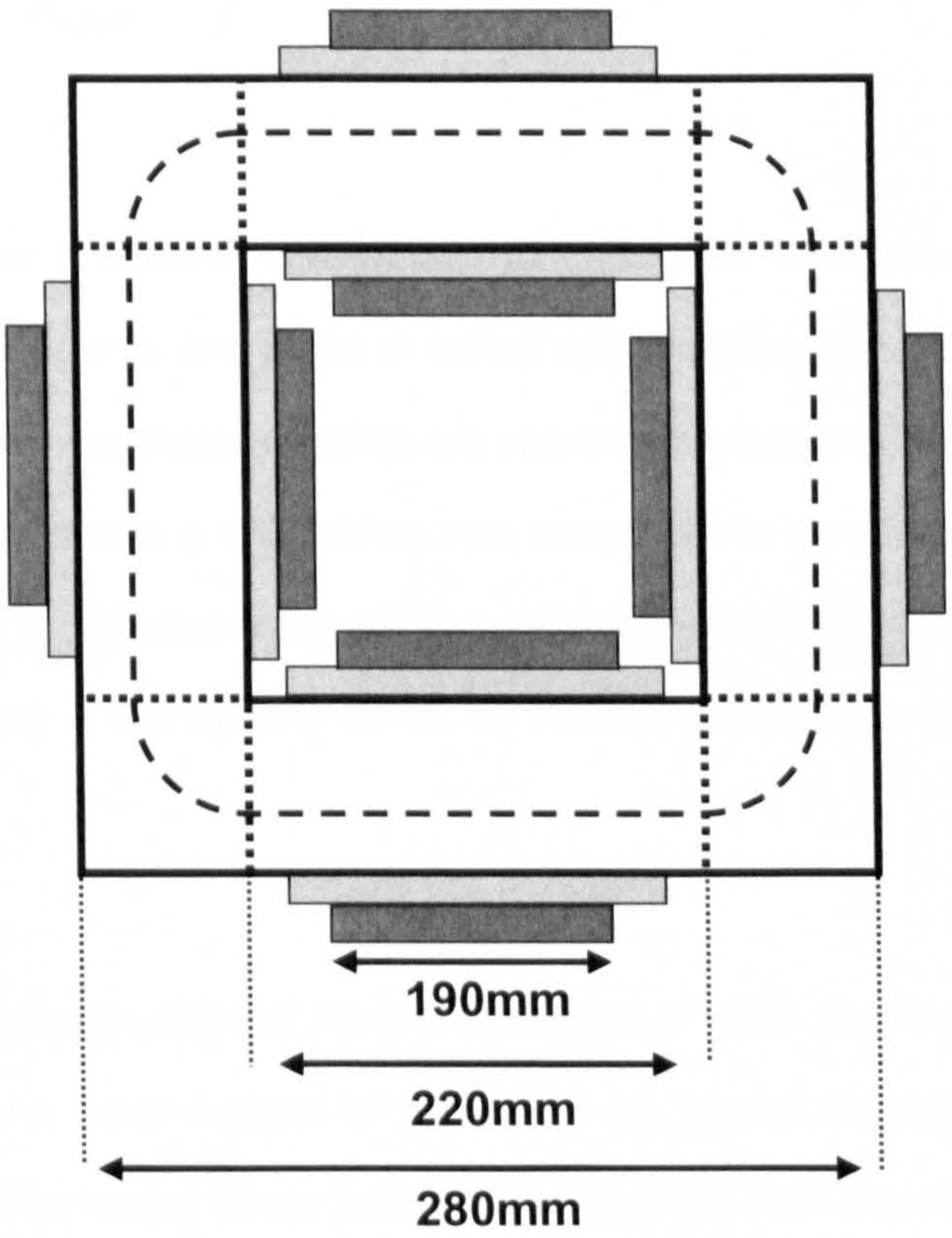

Fig. 6.6. Epstein square test frame

The test frame consists of four solenoids connected to form a square magnetic circuit, as shown in Fig. 6.6. The circuit has two windings, a primary (magnetising) winding and a secondary (potential) winding. The number of turns on each winding is distributed evenly between the four solenoids. Strips of the test specimen are inserted into the frame to form the magnetic core. The effective magnetic path length (illustrated by the dashed line in Fig. 6.6), used to calculate the applied field, is taken to be 0.94 m.

The cross-section area of the magnetising winding is determined by the solenoid formers. To allow for easy insertion of the material samples, this area is larger than the total cross-section of the samples. The voltage produced across the magnetising winding is not exactly proportional to the flux across the test specimen; there is an air flux component that must be subtracted. The air flux component can be calculated from

$$\hat{B}_{air} = \mu_0 \hat{H}\left(\frac{A_{w2} - A_{sample}}{A_{sample}}\right) \tag{6.34}$$

A mutual inductor is used to compensate for this error. The primary winding of the compensating inductor is connected in series with the primary winding of the Epstein frame while the two secondary windings are connected in series opposition. The value of compensating inductance is adjusted so that, when there is no sample in the frame, the voltage induced in the secondary winding will cancel out the voltage induced in the secondary winding of the Epstein frame. Air flux compensation is discussed further in Chapter 7.

The test frame requires strips of the test specimen, of width 30 mm and length no less than 280 mm. An equal number of test strips are placed on each side of the test specimen, with interleaved corner joints as shown in Fig. 6.7. The recommended mass of test specimen is between 0.5 and 2 kg, with the sample made up of at least 12 strips (3 strips each side of the Epstein square). If there is poor contact between the strips (caused by slight bending), a force of between 0.1 and 0.2 N can be applied to the corners. The Epstein square used in the measurements was manufactured by AEG [102]. Photographs are given in Appendix 6. Some important test parameters are given in Table 6.1.

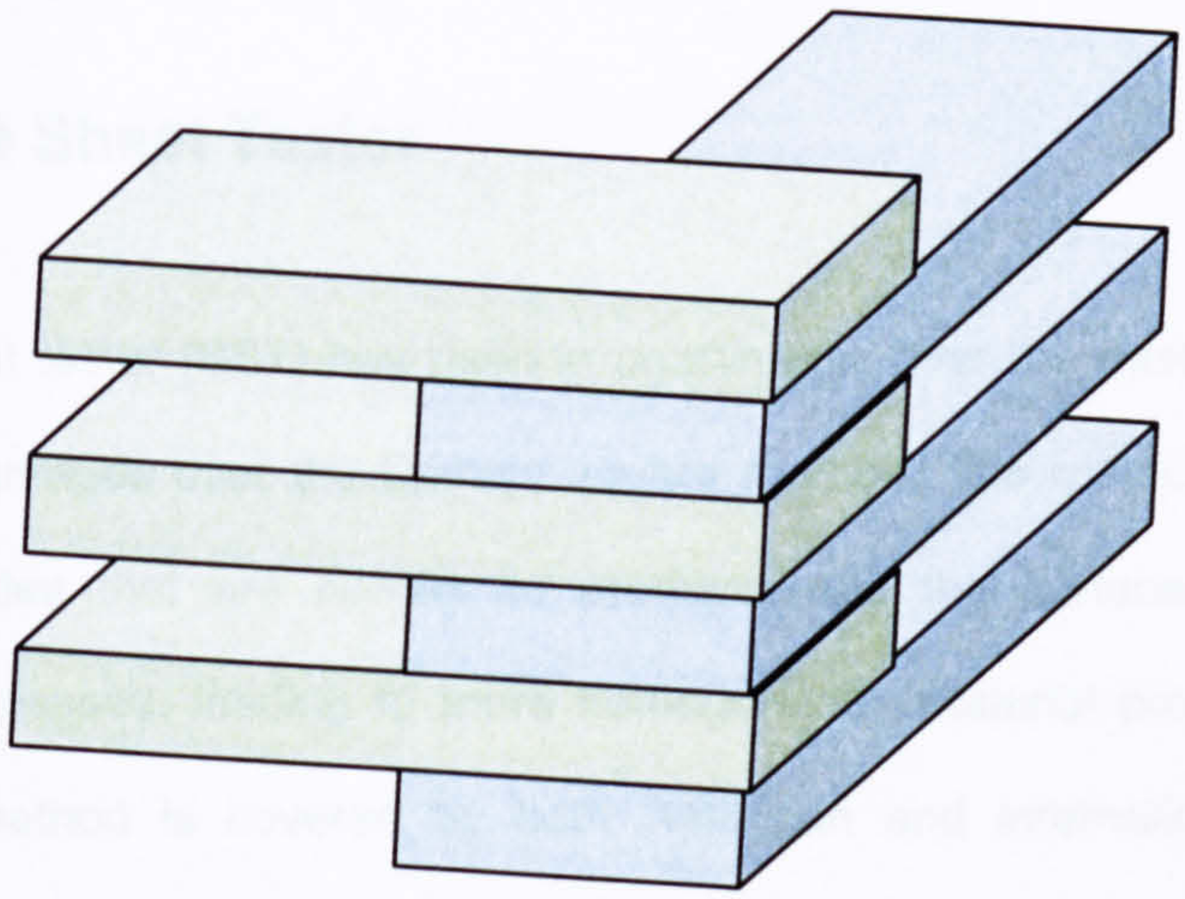

Fig. 6.7. Corner view of specimen showing interleaved joints

Parameter	***Setting***
Primary Winding	4 x 175 turns
Secondary Winding	4 x 175 turns
Mutual Inductor Primary	45 turns
Mutual Inductor Secondary	430 turns
Sample quantity	32 strips
Sample weight	1.027 Kg
Strip dimensions	280 x 30 mm
Corner force applied	0.1 N

Table 6.1. Parameters of Epstein Square

There are a number of drawbacks to the Epstein square. Preparation of the test samples is time consuming and a large volume of material is required compared to other test methods. When using samples of grain orientated steel, care must be taken to ensure that the samples are cut within the specified tolerances with respect to the rolling direction. By the very nature of the tester shape, the magnetic field will be inhomogeneous. The flux distribution is non-uniform around the sample; the overlap at the corners of the square leads to leakage flux and rotating flux vectors. Dissatisfaction with the Epstein square led to development of other sample testers, with the single sheet tester now the most popular alternative.

6.2.3. Single Sheet Tester

The single sheet tester (SST) has risen in prominence over the past decade, due to a number of advantages over the Epstein square method. The method requires smaller material quantities that are simpler to produce, and the surface area of the test specimen is increased, leading to more homogeneous material properties across the sample. The method is covered by both American and international measurement standards [100, 101] and is suitable for tests in the range 0.8 T to 1.6 T (NGO) and 0.8 T to 1.8 T (GO). In general, the peak permissible flux density will be limited by the heat rise in the magnetising winding due to the applied field; the maximum field will be in the region of 12 kA/m for a standard core.

Two main versions of the SST frame exist: the single yoke and the double yoke constructions. The single yoke geometry consists of a C-core, on top of which the material sample is positioned. The double yoke construction is made of two C-cores, with the material sample inserted across the middle, as shown in Fig. 6.8. The double yoke method is considered more accurate and as such has been used for the measurements reported in the following chapter.

The C-cores are made from either GO silicon steel or a nickel-iron alloy. The core can be constructed using either wound or stacked yokes, as shown in Fig. 6.9. It is recommended that wound laminations are used to minimise eddy current effects in the core. The laminations are wound around a former, then removed, annealed and impregnated with resin. It is common for the pole faces to be smoothed to provide good contact with the test specimen and minimise airgaps. This may cause short-circuits between adjacent core laminations, leading to increases in the core iron losses. Nakata et al. suggest cleaning the pole surfaces with acid to break the connections between laminations [103]. The recommended core dimensions vary between international

standards, from a length of 360 mm for the ASTM standard to dimensions of 500 mm by 500 mm, with pole faces of width no less than 25 mm, for the IEC standard.

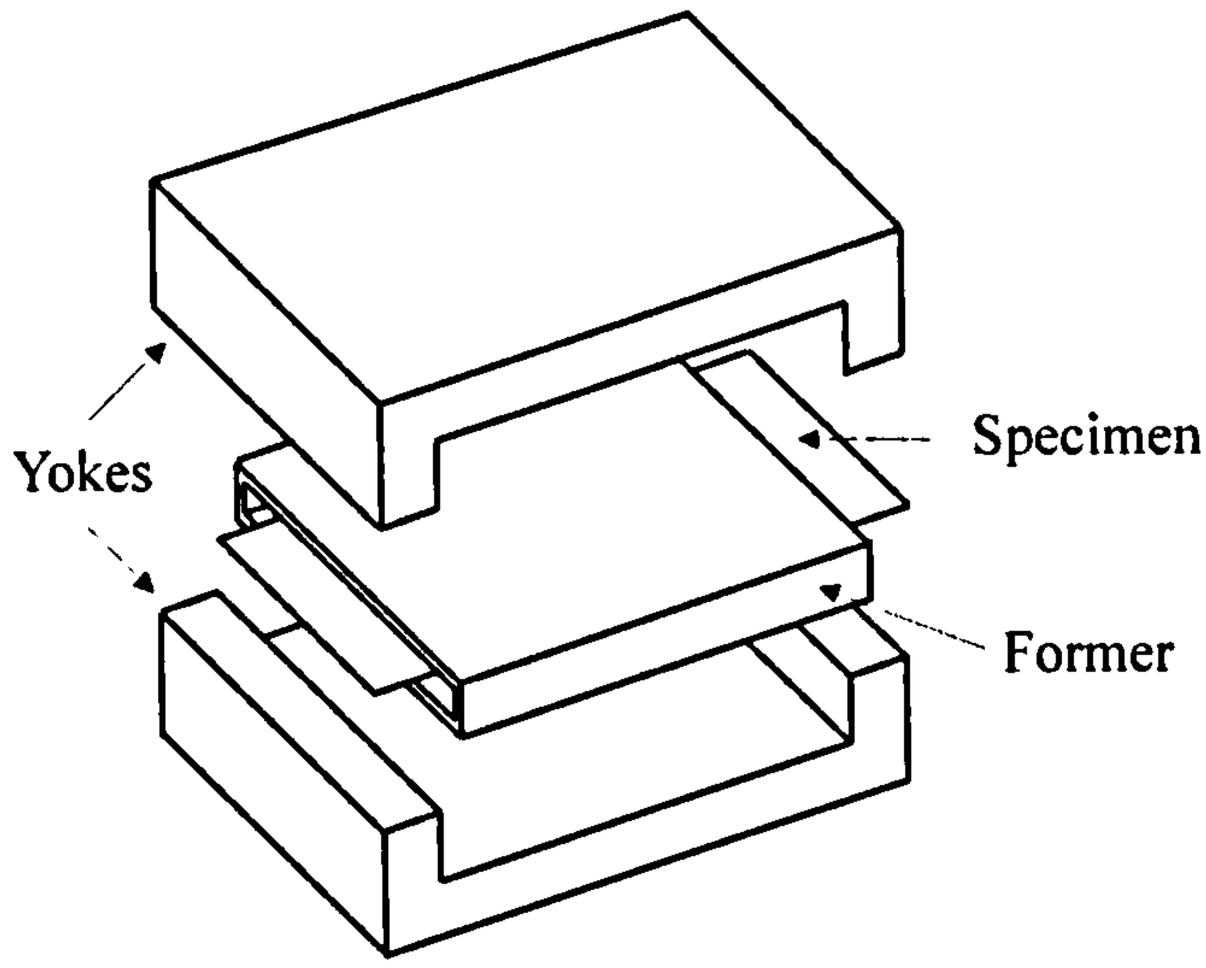

Fig. 6.8. Double-yoke single sheet tester

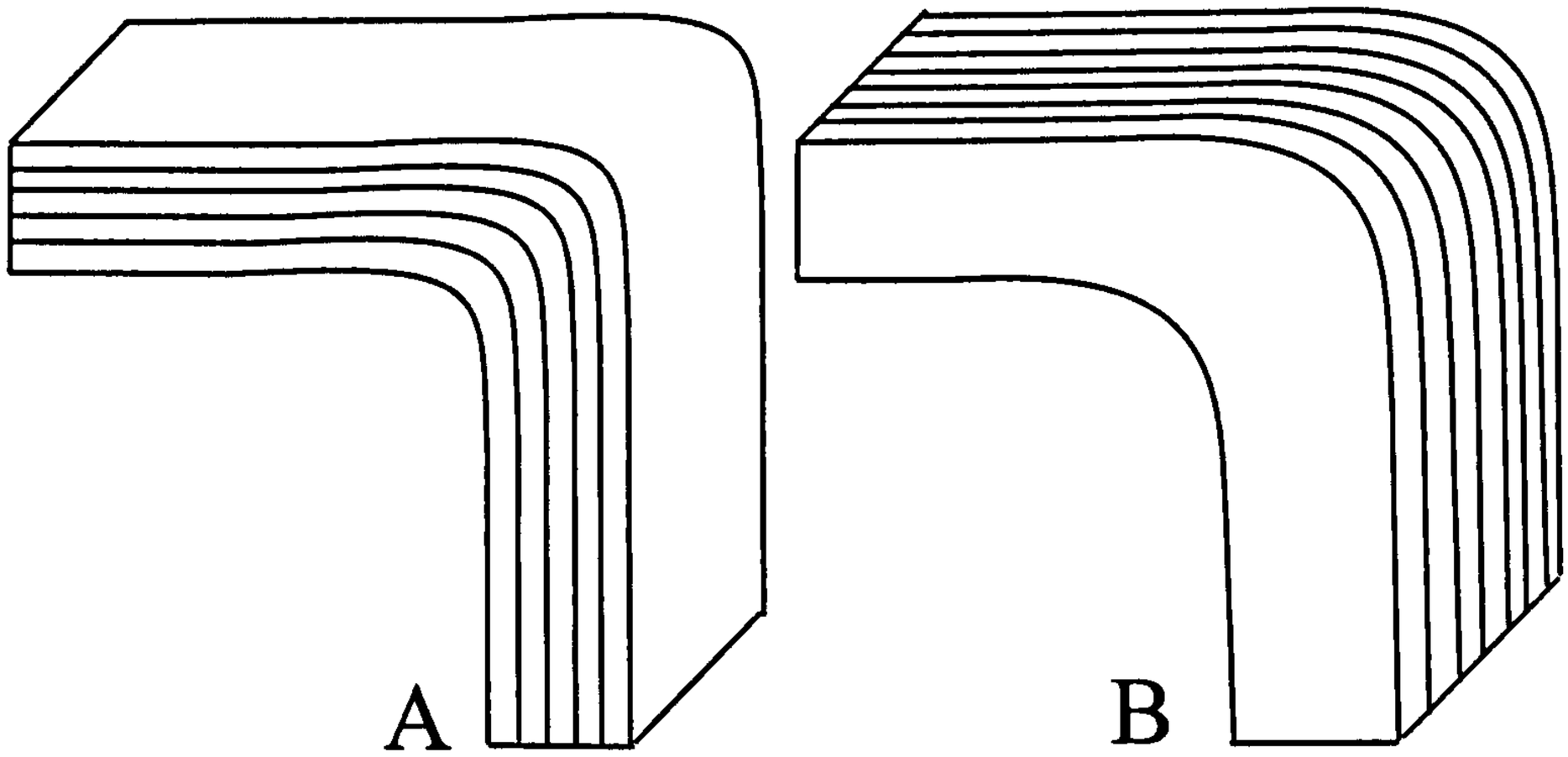

Fig. 6.9. SST Core sections showing wound laminations (A) and stacked laminations (B)

Similar to the Epstein square, there are two test windings; the outer winding is a primary (magnetising) winding and the inner the secondary (potential) winding. The primary may be wound over several layers, each connected in parallel. The secondary winding used to measure the voltage induced by the primary is wound as close to the material sample as possible. However, to allow for easier insertion of the material, it is necessary to place a non-magnetic former between the coil and sample. As with the Epstein square

test, this means that the voltage present in the secondary winding includes an air flux component and is not purely the result of flux flowing in the sample. It is once again possible to compensate for this leakage flux component using a mutual inductor [74]. This method has been implemented in the Grundfos SST system and is discussed further in Chapter 7.

There has been much discussion on measurement methods of the applied magnetic field in the SST. In Europe, the standard measurement method is the magnetising current (MC) method, using the primary winding current as in the Epstein square. This is the simplest form of measurement and is supported by IEC Standards, but can be lacking in accuracy. The effective magnetic path length is assumed to equal the inside width of the yokes (from pole face to pole face). In fact, the effective path length may vary depending on the material being tested and the level of induction [104].

Japanese and American standards favour the H-coil method. The method requires exact integration of the voltage induced in the coil and is susceptible to additional leakage and air flux components. Accuracy is dependent on positioning of the coil. In studies, the H-coil method has been proven to be up to 10 times more accurate, but difficulties involved in measurement have ensured that the MC method remains popular. To simplify experimental procedure, the MC method has been used for all measurements.

The single sheet tester requires one large sample sheet of material. The width of the sample must be at least 60 % of the yoke width. The sample should be at least as long as the yoke fixtures. A small amount of overhang is permissible but should not be more than is needed for easy insertion of the sample. To avoid undue stressing of the sample at the pole faces, it may be necessary to partially counterbalance the weight of the upper yoke section; the force on the sample should be between 100 and 200 N. The test specimen should be demagnetised before carrying out measurements. Parameter information for the single sheet tester used in the measurements is given in Table 1.2. A photograph of the test set-up is provided in Appendix 6.

Parameter	Value
Primary Winding	310 turns
Secondary winding	27 turns
Sample quantity	1 strip
Sample weight	0.1955 Kg
Strip dimensions	500 x 100 x 0.58 mm
Yoke lamination material	GO Silicon Steel
Yoke lamination thickness	0.3 mm
Yoke pole face dimensions	50 x 100 mm

Table 6.2. Parameters of SST

6.2.4. Toroid Sample

Toroid test samples are most commonly used for powdered core materials, where it would be difficult to produce samples suitable for the Epstein square or single sheet tester. The standard test can cover a much greater frequency range (from 20 Hz up to 20 kHz) but is not suitable for high levels of induction (when the sample is heavily saturated). The tests are covered by the American ASTM A927 standard and by IEC 60404 in Europe [105, 106].

Toroid sample tests do not require any specific test frame. The test set-up is shown in Fig. 6.10, and also in Appendix 6. The ring can be produced either from wound tape or from machined or chemically processed laminations. The sample should be constructed with a rectangular cross-section. The magnetic field is expected to vary across the cross-section, so it is necessary that the sample width be small. In general, the ratio of inner to outer diameter should be at least 0.82 and as close to unity as possible. With a ratio close to unity, it is permissible to use the average radius to determine the magnetic path length.

The coils may be wound directly onto the sample or, to avoid stressing, may be wound around a non-conducting case that fits over the sample. As with other sample types, two windings are required. The secondary, potential winding should be wound first to ensure close contact with the sample. Any looseness between the coil and the sample surface will introduce a leakage/ airgap flux component that will be picked up by the secondary winding. The primary coil can then be wound on top of the secondary. All turns should be evenly spaced around the sample perimeter. As thin a wire as possible should be chosen to ensure close contact with the sample, thus minimising errors in calculation of flux density (which is dependent on the cross-section area).

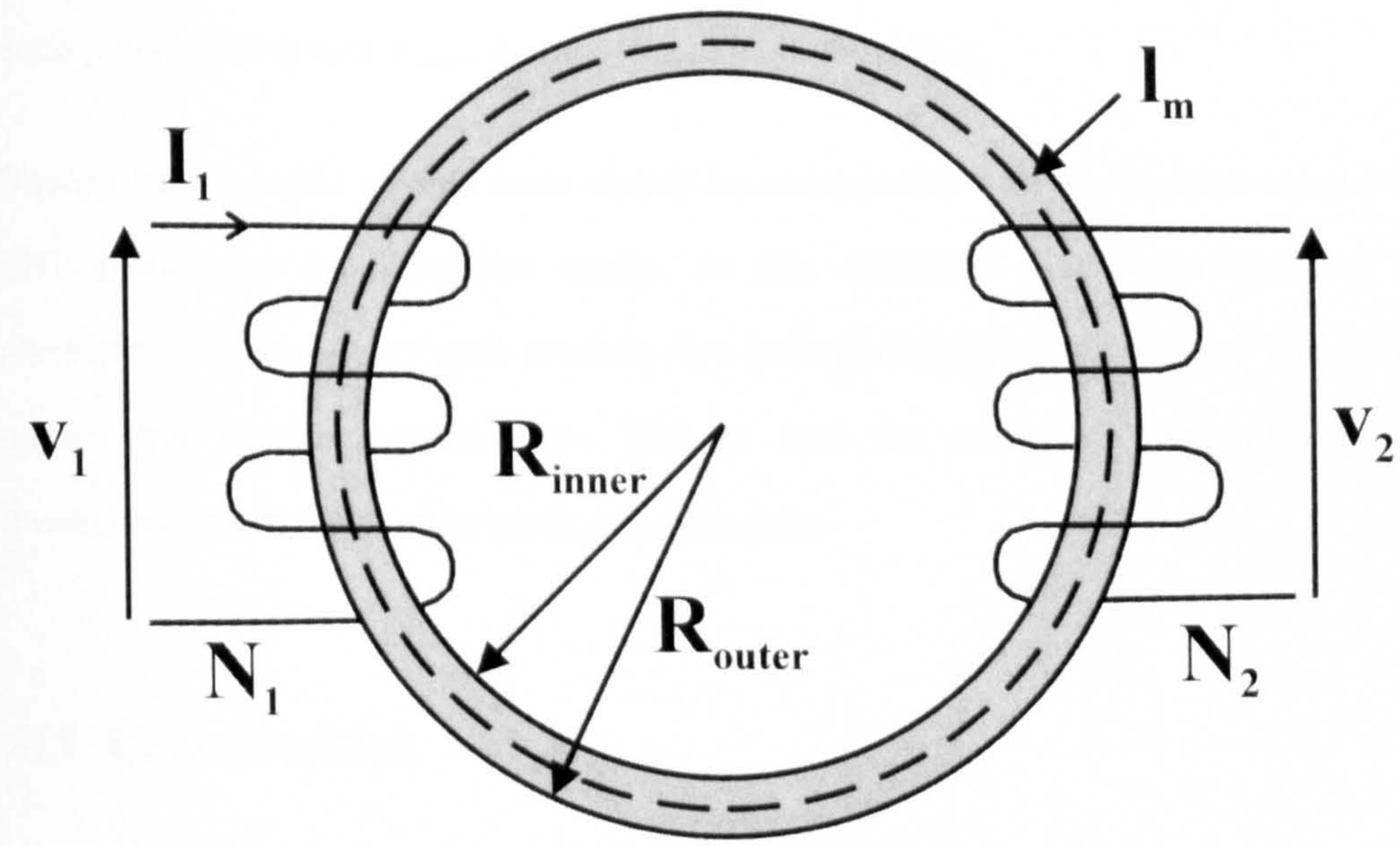

Fig. 6.10. Toroid Sample Test Set-up

As a rough estimate of the magnitude of the leakage flux, the voltages in the primary and secondary turns are integrated and compared. The difference between the two flux values is the air leakage flux component. In the primary, the voltage drop due to winding resistance must be considered:

$$V_1(t) = \left[i_1(t)R_p\right] + \frac{d\Psi_1(t)}{dt} \qquad V_2(t) = \frac{d\Psi_2(t)}{dt} \tag{6.35}$$

$$\Psi_1 = \int V_1(t) - [i_1(t) R_p] dt \qquad \Psi_2 = \int V_2(t) dt \tag{6.36}$$

If the air leakage flux component is large, it will be necessary to correct the measured flux density waveforms accordingly, using

$$B = B' - \mu_0 H \frac{(A_{w2} - A_{sample})}{A_{sample}} \tag{6.37}$$

where B' is the measured flux density, A_{w2} is the cross-section area enclosed by the secondary winding and A_{sample} is the specimen cross-section.

Results from toroidal sample tests should be comparable with the Epstein square and SST results for low induction levels. At flux densities above the knee of the magnetisation curve, saturation leads to non-uniform distribution of field and flux density across the sample cross-section. This in turn will affect the accuracy of any measurements made at such levels of flux density.

6.3. Conclusions

This chapter has discussed some of the most common methods used to determine the iron losses in electrical sheet steels. The methods fall into two categories – those based on the microscopic magnetic properties of the steel and those based on modified Steinmetz methods. Both types of method require large amounts of test data to determine the empirical parameters used in the models.

The steel samples can be measured using Epstein squares, single sheet testers or toroidal samples. The Epstein square is the most established test method and is commonly used by material manufacturers. The single sheet test method has gained

prominence in the last 15 to 20 years but is not used in industry to the same degree. Toroid test samples have a limited range of flux densities in which they can be considered accurate, but have the advantage that they are simple to construct and do not require complex test set-ups. With all types of measurements, it is necessary to take into account leakage flux components when calculating the flux density measured from the secondary windings of the test circuits. This is discussed further in the following chapter.

Chapter 7

Results from Electrical Steel Strip Tests Carried Out on Single Sheet and Epstein Square Test Yokes

The single sheet tester and Epstein square described in Chapter 6 have been used to measure the magnetic properties of samples of M340-50E, the material used for the rotor and stator laminations of the interior permanent-magnet test motor 1. Testing has been carried out over the frequency range 5 Hz to 150 Hz and for peak flux densities between 0.05 T and 2 T. The results from both test set-ups are presented below, with comparison between results.

7.1. Tests with sinusoidal flux density waveforms

The ASTM and IEC standards on testing of electrical steel specimens on both the Epstein square and single sheet tester state that a sinusoidal output flux density waveform should be maintained throughout the tests [98 - 101]. To ensure that the flux density remains sinusoidal under saturated conditions, feedback control has been used for all tests. The magnetising current and the secondary voltage waveform have been used to calculate the applied field and output flux density respectively.

7.1.1. Measurement of magnetisation curves

At each frequency, tests are made at increasing input current levels. The applied field and flux density waveforms from each test are used to plot the dynamic hysteresis loop. Hysteresis loops measured at 5 Hz using the single sheet tester are shown in Fig. 7.1. The measured loops show that as the input current is increased, the area of the dynamic hysteresis loop increases. Nested hysteresis loops such as these have been plotted for

each test frequency, for both the Epstein square and single sheet tester. The results can be found in Appendix 7. From the results in Appendix 7, it can be seen that the shape of the hysteresis loop is different at low levels of induction to when the motor is saturated. This is due to the phase difference between the applied field and flux density waveforms, and to the deviation from the ideal sinusoidal waveform shape [107, 108].

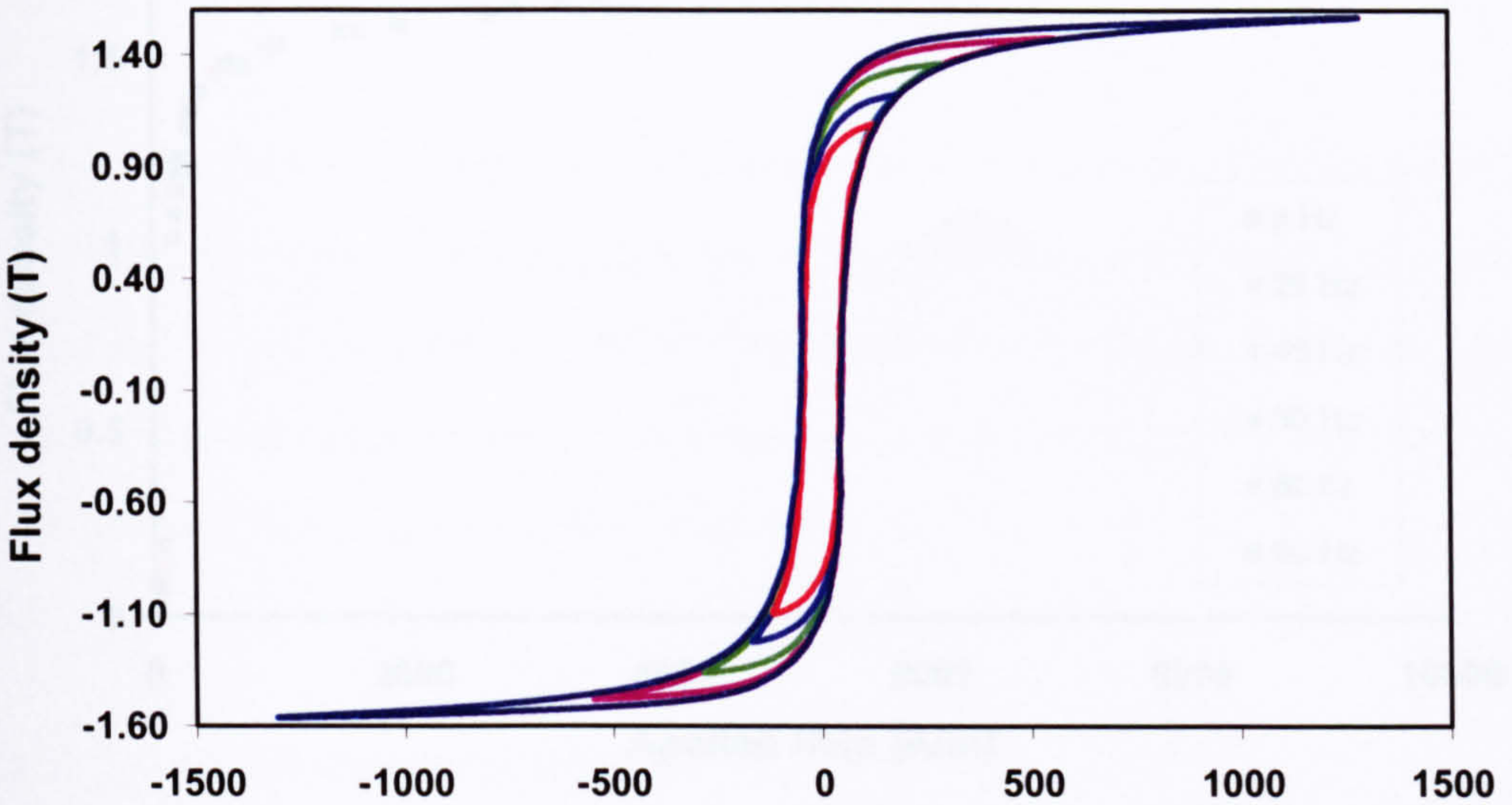

Fig. 7.1. Hysteresis loops measured at 5 Hz using single sheet tester

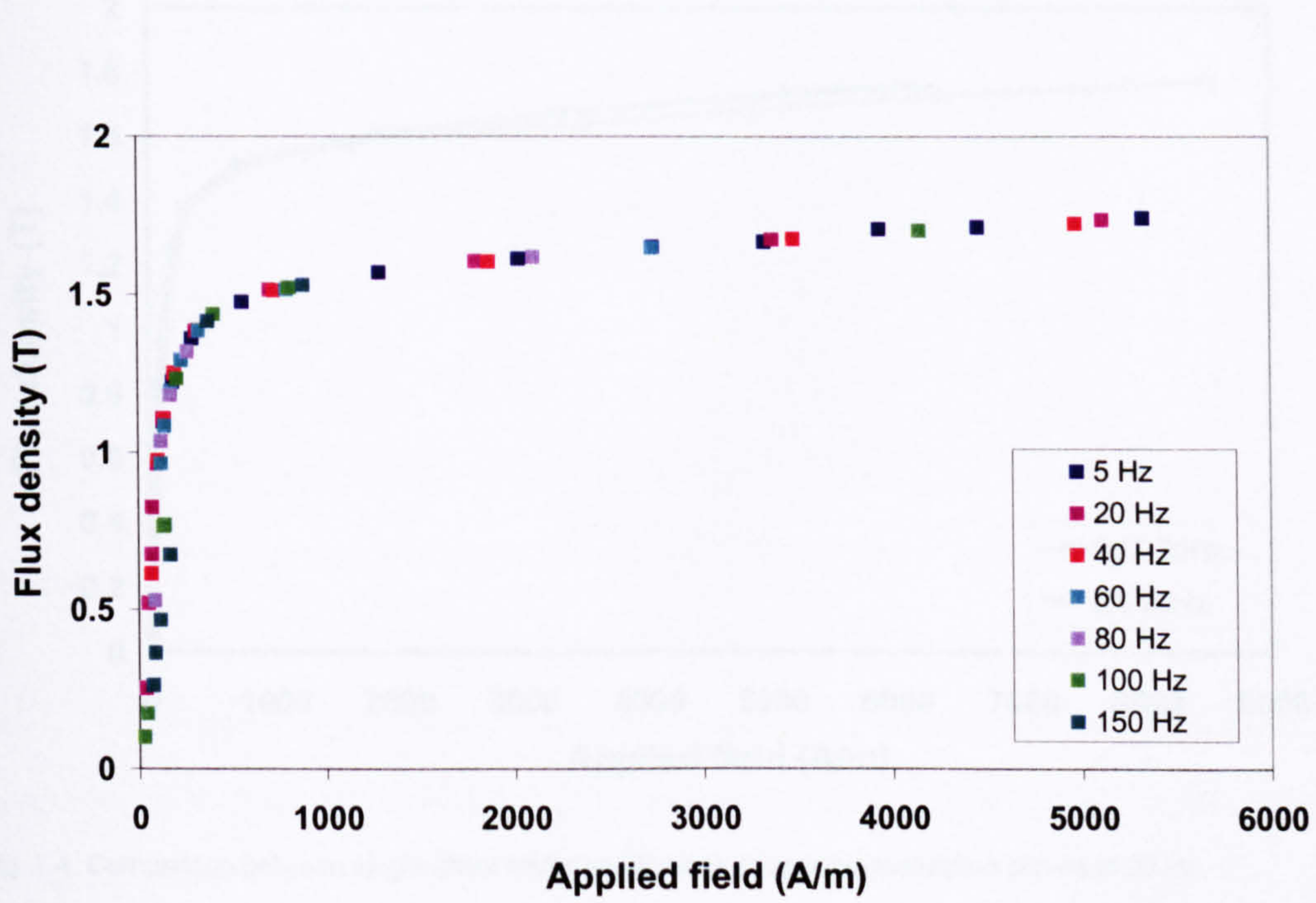

Fig. 7.2. Normal magnetisation curves as determined from results from the single sheet tester data

Using the data from the measured hysteresis loops, the normal magnetisation curves can be plotted at each frequency. Fig. 7.2 shows the normal magnetisation curve as determined from the single sheet tester results, while the results from the Epstein square tests are shown in Fig. 7.3.

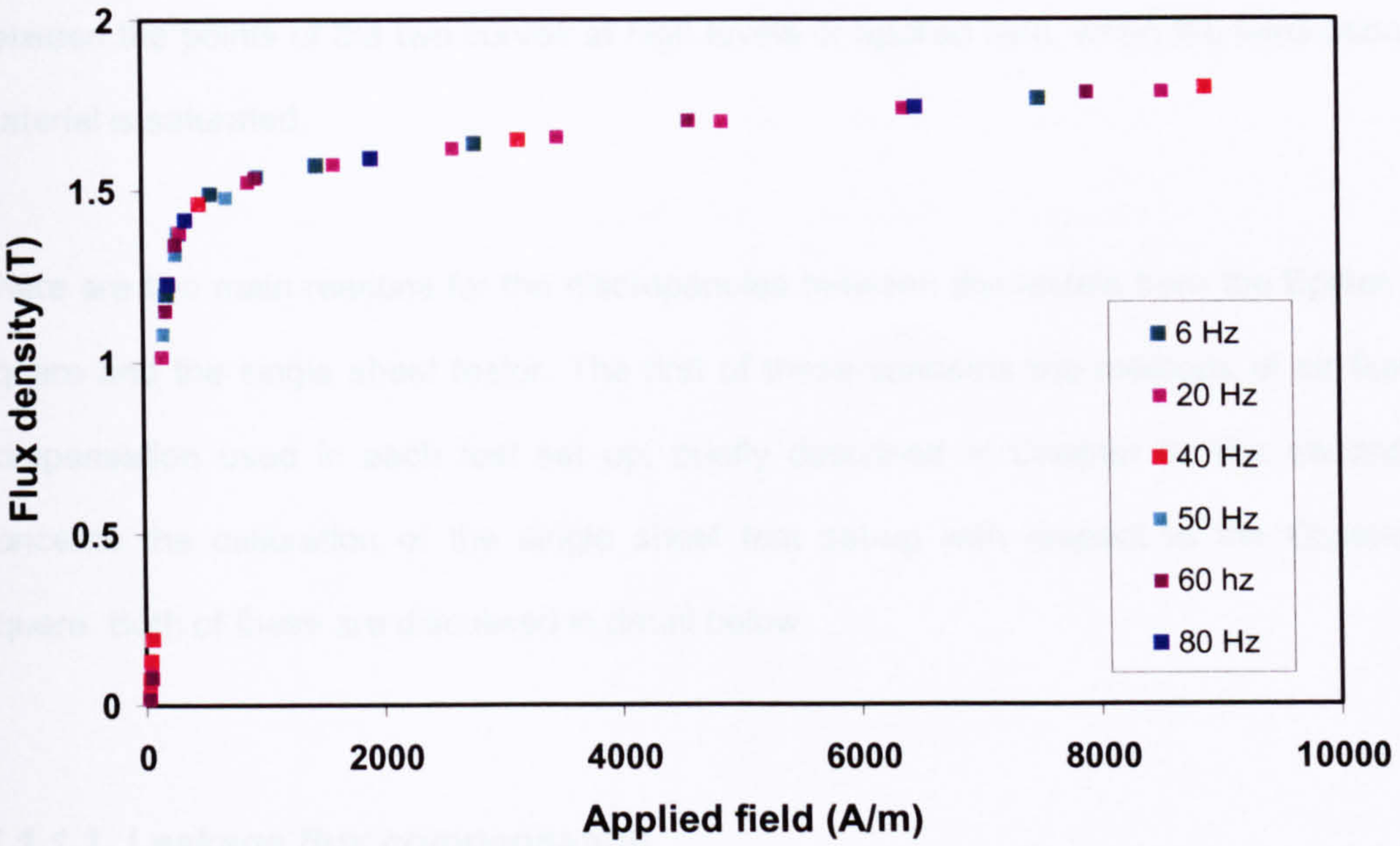

Fig. 7.3. Normal magnetisation curves as determined from results from the Epstein square data

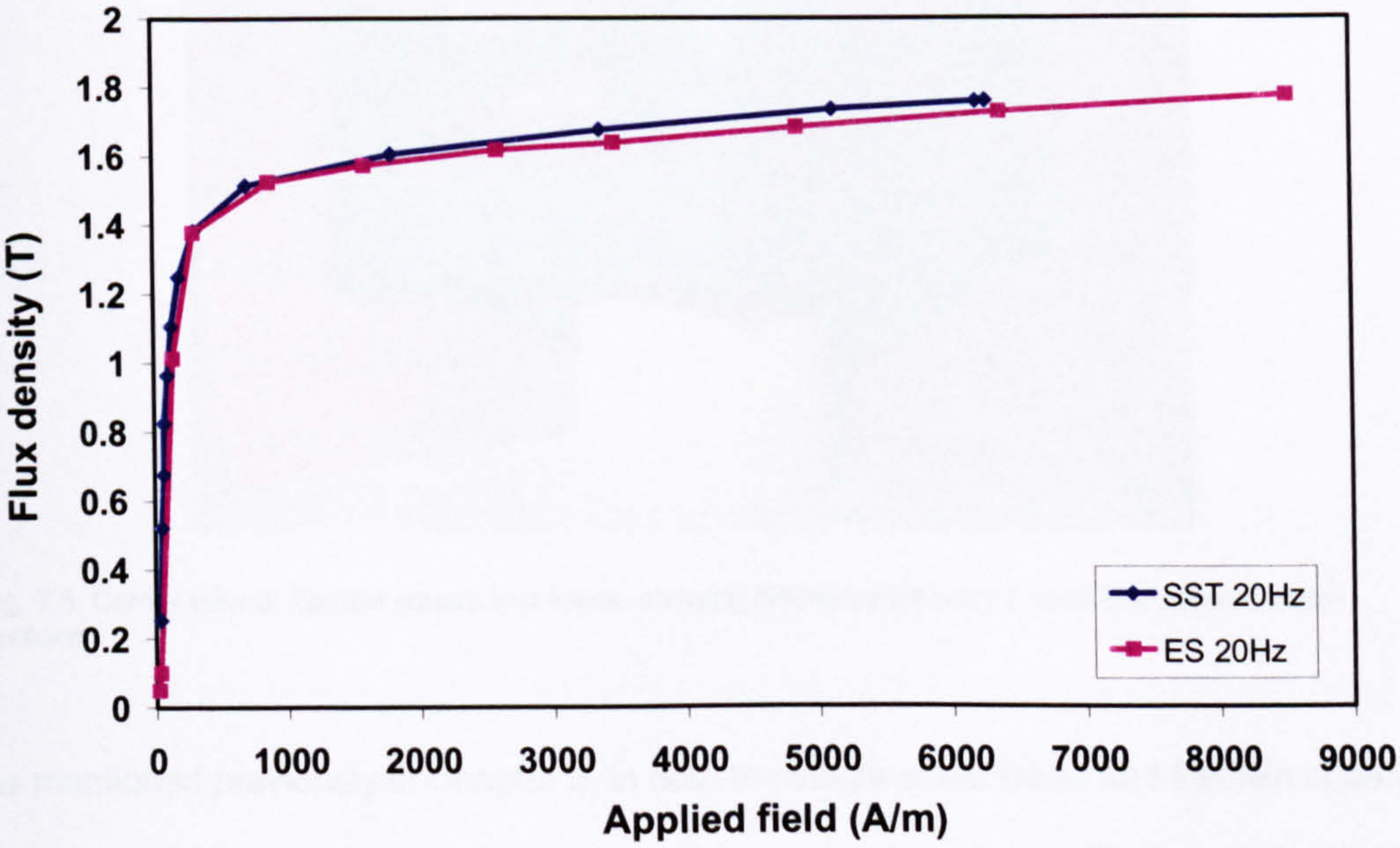

Fig. 7.4. Comparison between single sheet tester and Epstein square magnetisation curves at 20 Hz

The normal magnetisation curves determined from the single sheet tester and Epstein square experimental data can be compared for each test frequency. Fig. 7.4 shows one such comparison, for the normal magnetisation curves at 20 Hz operation. Further comparisons between the normal magnetisation curves at the other test frequencies can be found in Appendix 7. It can be seen from Fig. 7.4 that there are discrepancies between the points of the two curves at high levels of applied field, when the lamination material is saturated.

There are two main reasons for the discrepancies between the results from the Epstein square and the single sheet tester. The first of these concerns the methods of air flux compensation used in each test set up, briefly described in Chapter 6. The second concerns the calibration of the single sheet test set-up with respect to the Epstein square. Both of these are discussed in detail below.

7.1.1.1. Leakage flux compensation

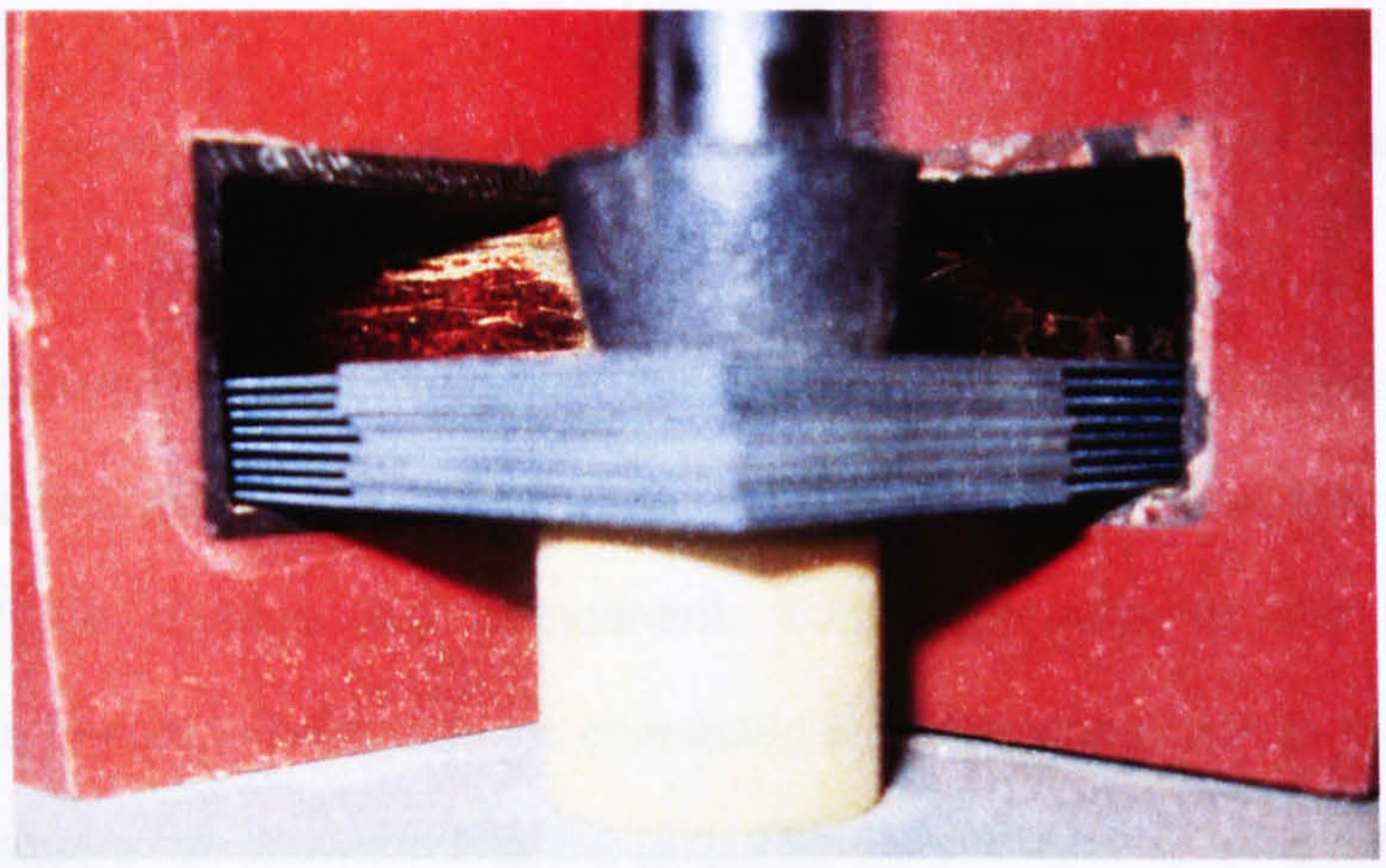

Fig. 7.5. Corner view of Epstein square test frame, showing difference between former and sample cross-sections

As mentioned previously in Chapter 6, in both the single sheet tester and Epstein square test rigs there may be a leakage flux component due to the design of the yoke structures, which must be taken into account in the measurement of the flux density waveforms of the lamination samples. In the Epstein square the air flux component

depends on the cross-section areas of the winding former and the lamination strips. The former cross-section may be significantly larger than the cross-section area of the lamination strips; a variable number of strips may be used in the tests, and the former is large to allow for easy insertion of the samples. The considerable difference between the former cross-section and the lamination cross-section can be seen in Fig. 7.5.

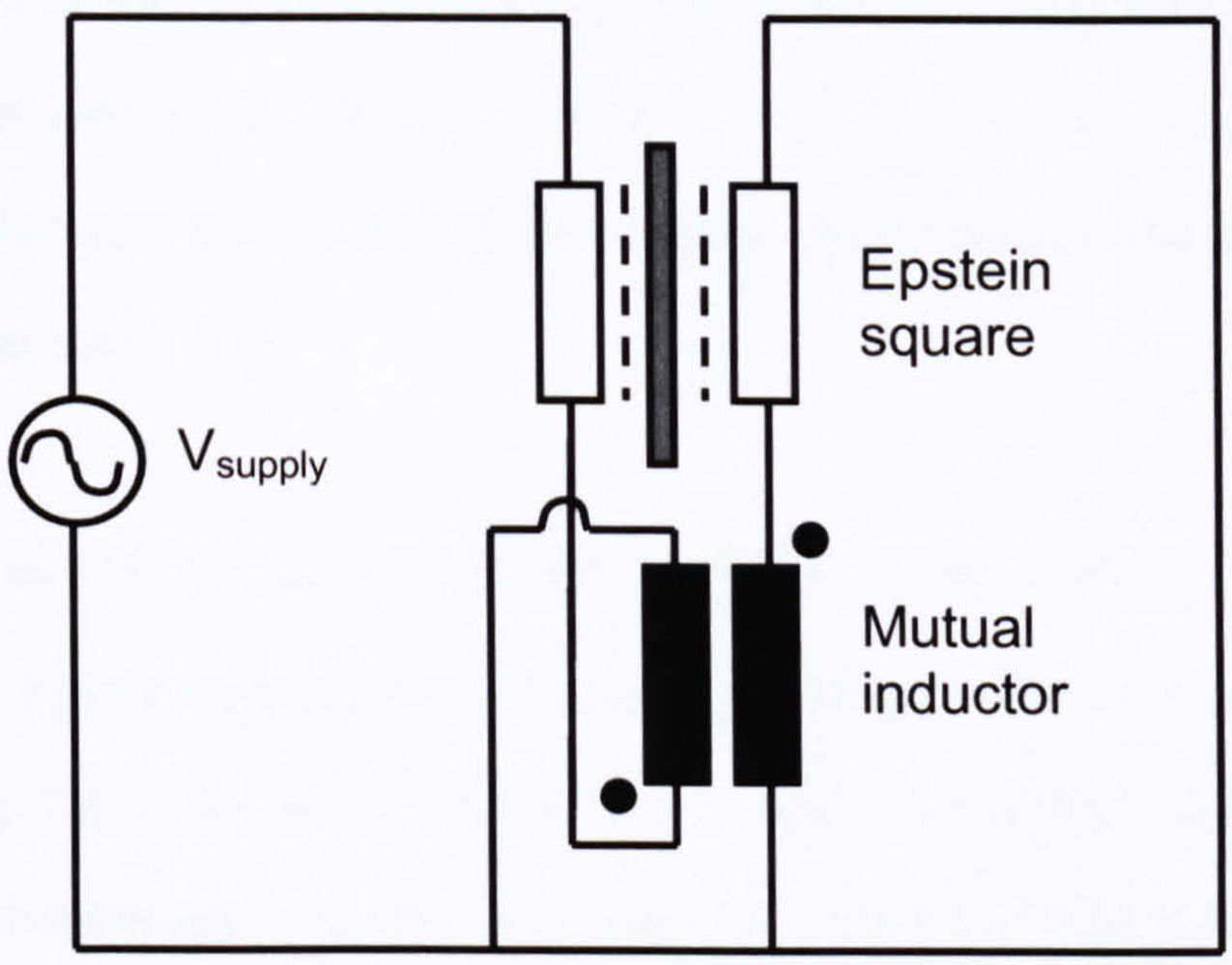

Fig. 7.6. Epstein square circuit diagram showing compensating mutual inductor in series opposition to windings

As the flux density is determined from the voltage induced in the secondary winding (wound round the former), the measured flux density includes both the flux density of the sample and the leakage flux component. To compensate for the leakage flux component, a mutual inductor can be connected in series opposition to the windings of the Epstein square, as shown in Fig. 7.6 [97]. The mutual inductor is tuned so that there is no secondary voltage when there is no sample inserted into the Epstein frame. With such tuning, the leakage flux component is eliminated. However, the resulting voltage induced in the secondary winding of the Epstein square is no longer proportional to the flux density B in the sample, but instead is proportional to J, the magnetic polarisation. Using the magnetising current waveform, the applied field can be calculated, and then used in

$$B = (\mu_0 H) + J \qquad (7.1)$$

to calculate the flux density in the sample from the magnetic polarisation.

From Eq. (7.1) it is clear that at low levels of applied field, the difference between magnetic polarisation and flux density in the sample will be negligible. Even at high fields, the difference will not be significant. For example, at an applied field of 10 kA/m the difference between *B* and *J* will be 0.0126 T, which is less than 1% of the probable flux density at that field for the lamination material used (the flux density at 10 kA/m would typically be over 1.8 T).

Fig. 7.7 compares the *B-H* and *J-H* curves of the lamination material, as determined from the Epstein square tests at 20 Hz. The corresponding *J-H* and *B-H* hysteresis loops are shown in Fig. 7.8. It can be seen from Figs. 7.7 and 7.8 that there will be some error in the normal magnetisation curve, and also the measured hysteresis loop, if the magnetic polarisation *J* is used in place of the magnetic flux density *B*.

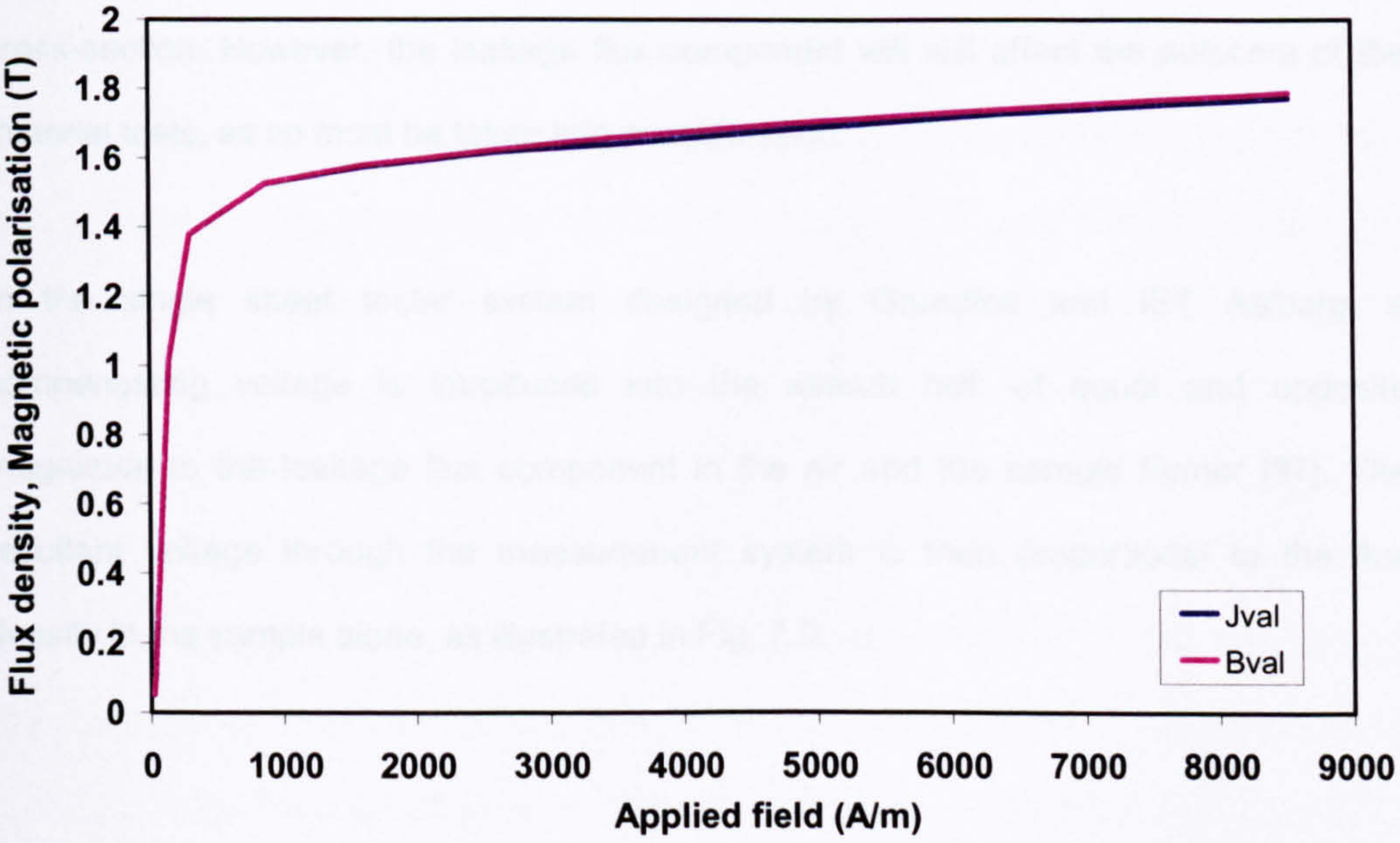

Fig. 7.7. *B-H* and *J-H* curves of lamination material at 20 Hz, as calculated from Epstein square tests

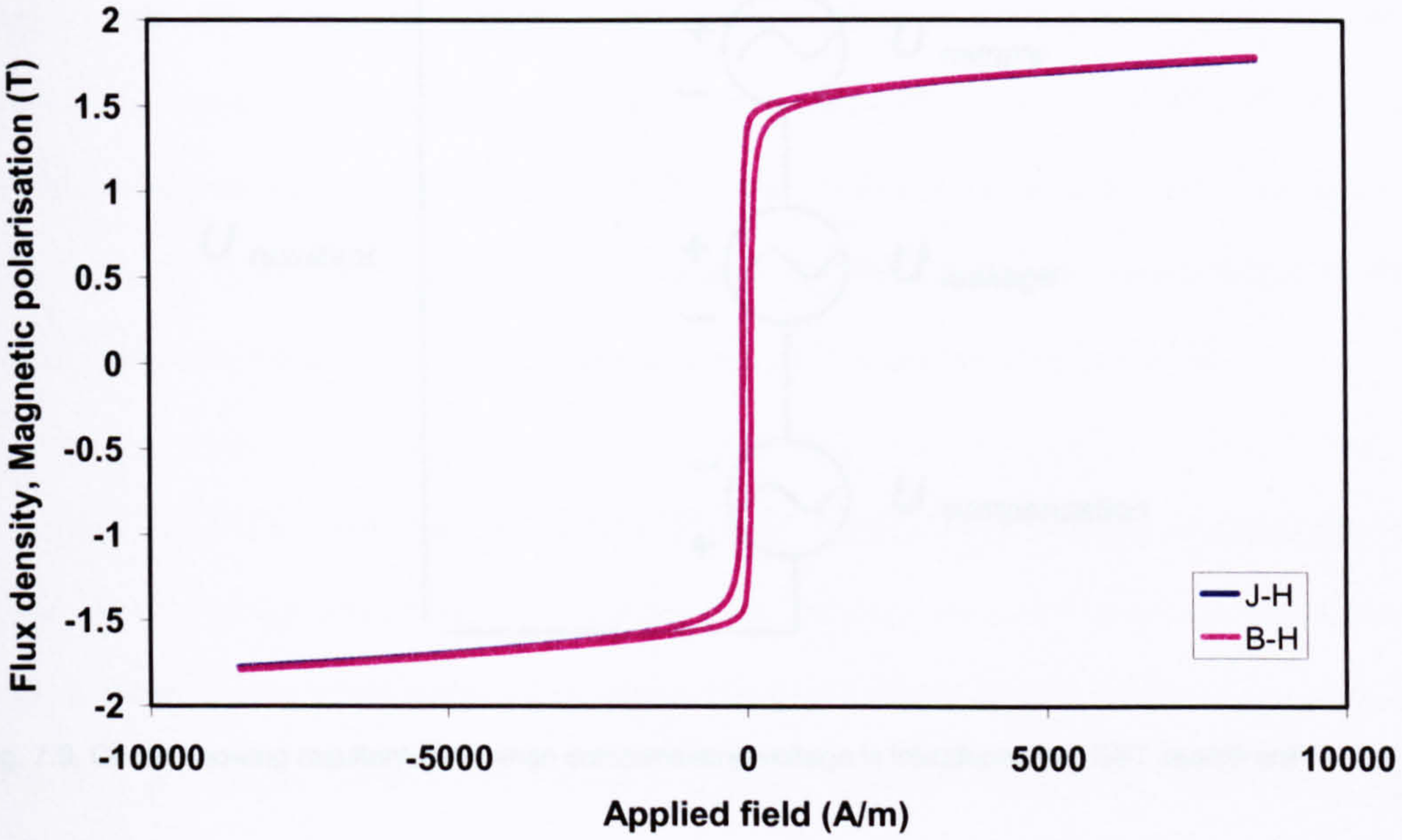

Fig. 7.8. *J-H* and *B-H* hysteresis loops of lamination material at 20 Hz, as calculated from Epstein square tests

It is also necessary to include leakage flux compensation in the single sheet tester experimental set-up. In the single sheet tester, the secondary winding search coil used to measure the induced voltage is wound around the sample former. The leakage flux component should be much less that that of the Epstein square, since the cross-section of the SST former is closer to the single sheet sample cross-section, whereas the cross-section of the Epstein square secondary winding is significantly larger than the sample cross-section. However, the leakage flux component will still affect the outcome of the material tests, as so must be taken into consideration.

In the single sheet tester system designed by Grundfos and IET Aalborg, a compensating voltage is introduced into the search coil, of equal and opposite magnitude to the leakage flux component in the air and the sample former [97]. The resultant voltage through the measurement system is then proportional to the flux density in the sample alone, as illustrated in Fig. 7.9.

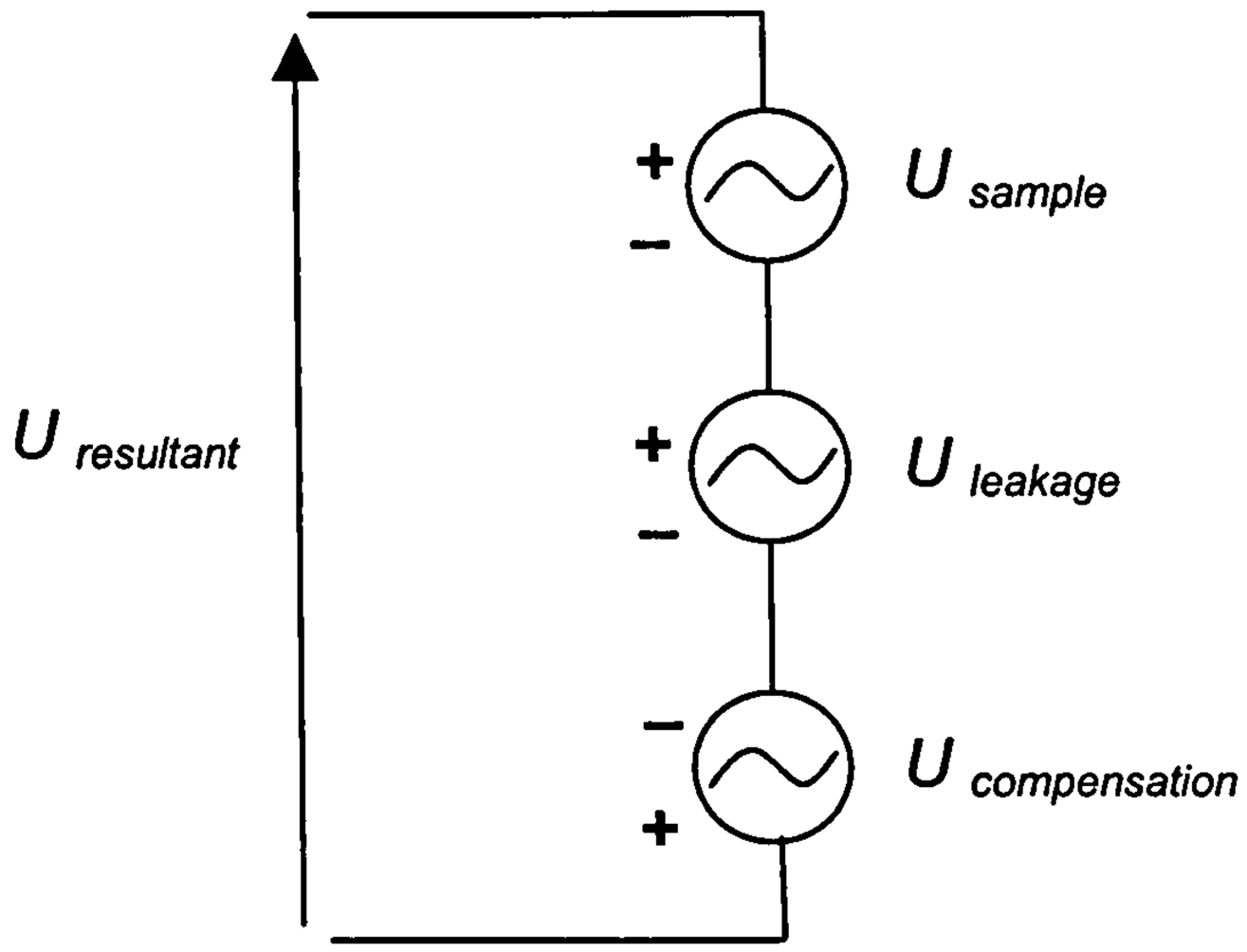

Fig. 7.9. Circuit showing resultant EMF when compensating voltage is introduced into SST search coil

7.1.1.2. Calibration of single sheet test set-up

In general, even taking into account the leakage flux components in the Epstein square and single sheet test set-ups, there will still be discrepancies between the results of each test system, which leads to some confusion as to which system is measuring the magnetic properties of the lamination materials with greatest accuracy.

The loss information found on steel manufacturer's data sheets is commonly taken from the results of tests using an Epstein square. As such, the Epstein square test has been established for some time as the standard method of testing for electrical steel samples, despite exhibiting an inhomogeneous field due to the interleaved sample strips at the corners of the square. In fact, the inhomogenities in the field become somewhat arbitrary, as all measurements made on an Epstein square are subject to the same inhomogeneous field [109].

The most significant drawback to the Epstein square method is that the material samples require significant preparation, particularly in the case of grain-orientated materials where the material strips must be cut both in the rolling direction and against it [99]. The single sheet tester was developed to allow easier testing of such materials, but

it now commonly used for both grain-orientated and non-grain-orientated materials. The original International Electrotechnical Commission (IEC) Standard for testing of steel sheet specimens using the single sheet tester required calibration, but such calibration is not essential in the latest version of the SST standard (although a method is provided for reference) [101]. However, the continued use of both test methods means that it is still useful to compare the single sheet tester and Epstein square measurements.

The revised IEC standard provides two different methods for relating measurements made on the single sheet tester to the Epstein square, for grain-orientated and non-grain-orientated materials [101]. For grain-orientated materials, a method is described for converting single sheet tester results to Epstein square results (and vice versa). For both non-grain-orientated and grain-orientated materials, a procedure for calibration of the SST results is also illustrated. Measurements of the specific total power losses are first made on the Epstein square test frame over a range of magnetic flux densities. Then, at least 12 strips from the Epstein square test frame are transferred to the single sheet tester and placed side by side. The losses are measured again over the same range of flux densities. The effective path length is calculated at each flux density level using

$$l_{eff} = \frac{P_{SST} l_{SST}}{m P_{sE}} \tag{7.2}$$

The effective path length thus varies over the range of flux density, although no mention is made of the effect of frequency on the length of the magnetic circuit.

The calibration of the single sheet tester to Epstein square test results is also discussed in literature. An extensive study into the correlation between Epstein square and single sheet tester results for a large collection of steels of various grades was made by Sievert et al. in 2000 [109]. The study concluded that the single sheet tester could only be

calibrated to results from an Epstein test frame if the same reference sample strips were used in both sets of tests.

De Wulf et al. also suggest calibration of the single sheet tester with Epstein square test results [110]. The losses measured on the single sheet tester are compared with the Epstein reference values at each flux density and frequency. The magnetic path length of the single sheet tester is then adjusted at each test point, until the power loss from the single sheet tester calculations is equal to the reference value of the Epstein square. No information is given as to the exact method of calculation of the adjusted path length at each test point. The authors suggest mapping the variation of adjusted path length with both frequency and flux density, and then calculating the average value to determine the correlated path length to be used in all future calculations. The paper states that the use of a constant path length, independent of frequency and flux density, is justified because the paths lengths are approximately constant for all points above $f = 30$ Hz and $B = 0.4$ T. However, there is significant variation in the path length of the presented test data within the specified range. This suggests that the adjusted path length should, in fact, be a function of both the frequency and flux density.

Comparison between single sheet tester and Epstein square test results has been made, and the effective magnetic circuit length of the single sheet tester for each test point has been calculated for a range of flux densities and frequencies. The results are presented in the following section.

7.1.2. Measurement of losses

Measurements have been taken of the specific loss using both the single sheet tester and Epstein square test frames, for a range of frequencies. The results from these measurements are presented in Appendix 8. For the Epstein square tests, the specific loss was calculated using both the magnetic polarisation J and the flux density B, and was found to be the same for both calculations at each test point. Although the

polarisation and flux density waveforms are different, they are related through Eq. (7.1). It was shown in Fig. 7.8 that the dynamic hysteresis loops of *B*-*H* and *J*-*H* follow slightly different trajectories due to the difference in the *J* and *B* waveforms. However, the area enclosed by the dynamic hysteresis loops is the same, and so the loss per unit volume will be the same regardless of whether *B* or *J* is used for the calculation. The loss per unit volume as measured by each test set-up can be compared by plotting loss versus flux density over the range of test frequencies. Fig. 7.10 compares the losses at 50 Hz. Plots of loss per unit volume at further frequencies can be found in Appendix 7.

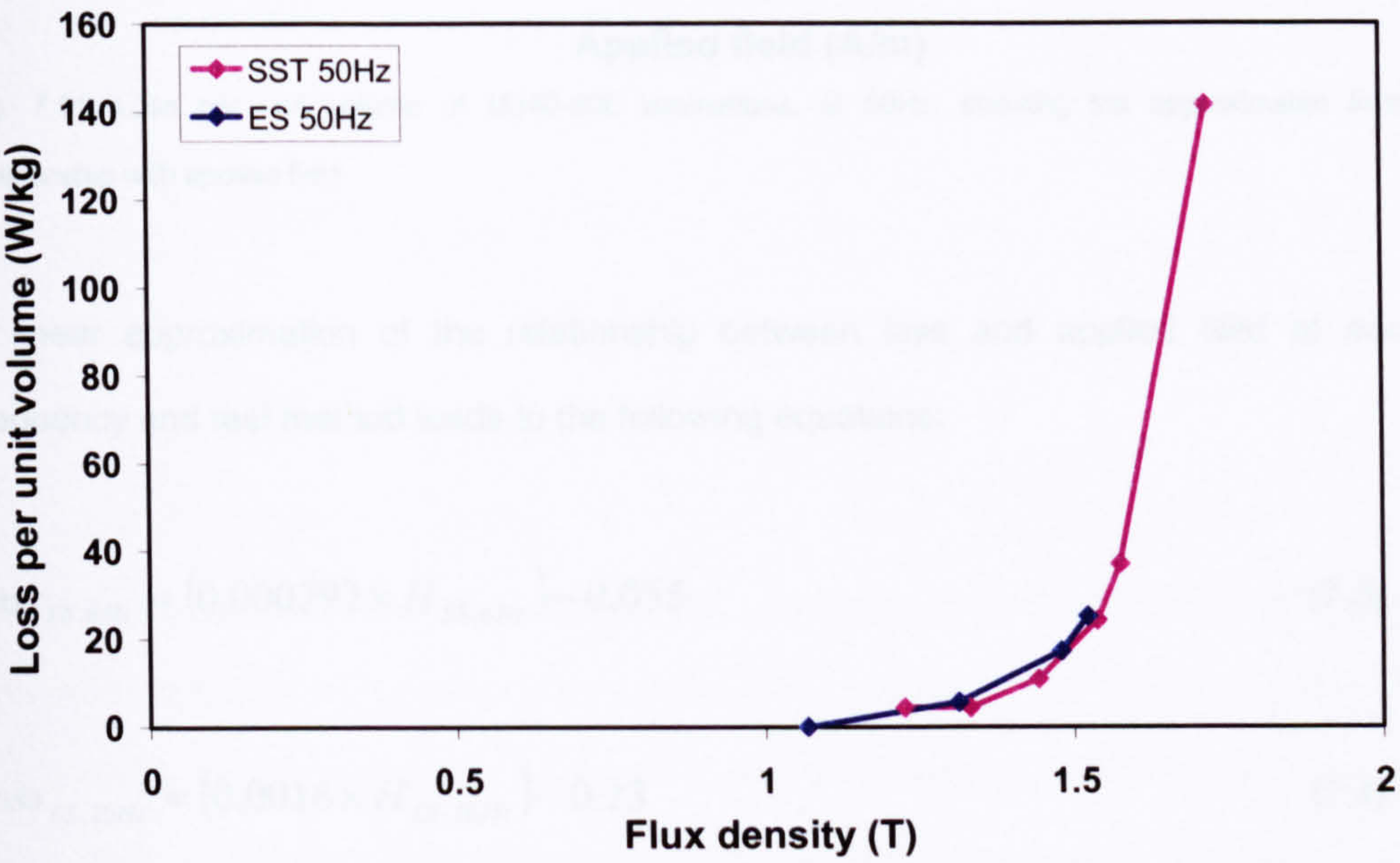

Fig. 7.10. Loss per unit volume of M340-50E laminations, at 50 Hz, as measured on Epstein square and single sheet tester

7.1.2.1. Linear approximation of loss as a function of applied field

It can be seen from Fig. 7.10 that there is a nonlinear relationship between the flux density and the specific loss of the sample. The loss per unit volume can also be plotted as a function of the applied field, shown in Fig. 7.11 for tests at 50 Hz. Results from tests at further frequencies are once again provided in Appendix 7. The relationship is approximately linear, suggesting that the losses may be better represented as a function of applied field rather than flux density, as is currently the norm.

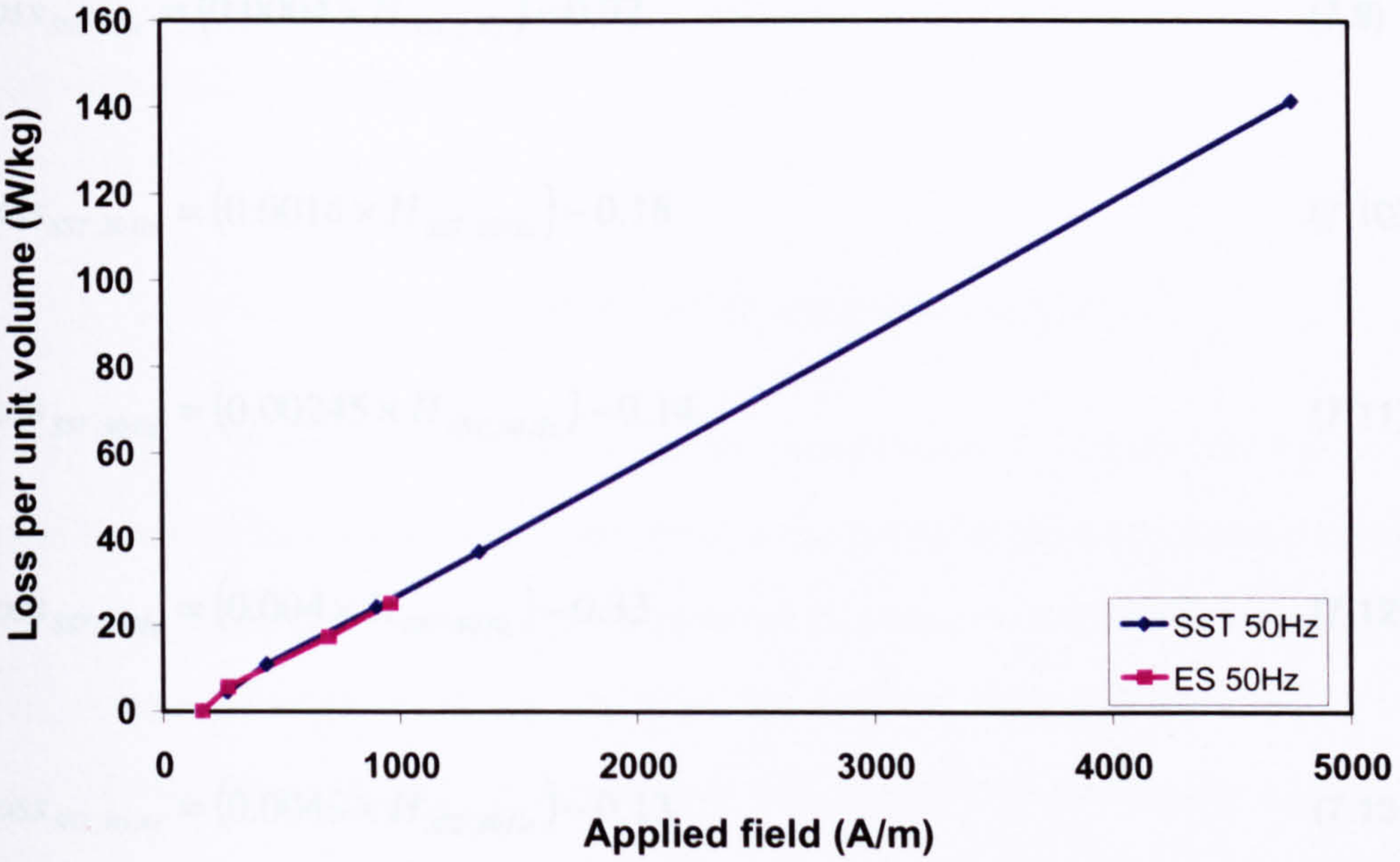

Fig. 7.11. Loss per unit volume of M340-50E laminations, at 50Hz, showing the approximated linear relationship with applied field

A linear approximation of the relationship between loss and applied field at each frequency and test method leads to the following equations:

$$loss_{ES,6Hz} = (0.000292 \times H_{ES,6Hz}) - 0.055 \quad (7.3)$$

$$loss_{ES,20Hz} = (0.0016 \times H_{ES,20Hz}) - 0.23 \quad (7.4)$$

$$loss_{ES,40Hz} = (0.00261 \times H_{ES,40Hz}) - 0.45 \quad (7.5)$$

$$loss_{ES,50Hz} = (0.0036 \times H_{ES,50Hz}) - 0.25 \quad (7.6)$$

$$loss_{ES,60Hz} = (0.0057 \times H_{ES,60Hz}) - 0.42 \quad (7.7)$$

$$loss_{ES,80Hz} = (0.0051 \times H_{ES,80Hz}) - 0.45 \quad (7.8)$$

$$loss_{SST,5Hz} = (0.0004 \times H_{SST,5Hz}) - 0.02 \quad (7.9)$$

$$loss_{SST,20Hz} = (0.0016 \times H_{SST,20Hz}) - 0.18 \quad (7.10)$$

$$loss_{SST,40Hz} = (0.00245 \times H_{SST,40Hz}) - 0.14 \quad (7.11)$$

$$loss_{SST,50Hz} = (0.004 \times H_{SST,50Hz}) - 0.33 \quad (7.12)$$

$$loss_{SST,80Hz} = (0.0049 \times H_{SST,80Hz}) - 0.13 \quad (7.13)$$

$$loss_{SST,100Hz} = (0.008 \times H_{SST,100Hz}) - 0.35 \quad (7.14)$$

$$loss_{SST,150Hz} = (0.0083 \times H_{SST,150Hz}) + 0.15 \quad (7.15)$$

Using these equations, the loss at each test point can be calculated from the applied field and compared with the measured losses. The results for the Epstein square and single sheet tester are given in Appendix 8. From the results in Appendix 8, it can be seen that using a linear approximation to characterise the relationship between specific loss and applied field results in high errors in loss calculation at low fields (in particular, at fields below 600 A/m), but provides a good approximation at applied fields above 600 A/m. The error in loss calculation at test points above 600 A/m is always less than 10% and in most cases the error is less than 5%. The results suggest that at higher fields, a linear approximation of the specific losses is adequate, but that a separate loss function may be required at low applied fields.

Further investigation is needed to determine the relationship between linear loss functions and the frequency of the applied field, and also the best method of modelling the specific losses at low fields. Although the initial test results suggest that there may

be a linear relationship between applied field and specific loss, further test data is required, particularly at low fields.

7.1.2.2. Calibration of single sheet tester magnetic path length

In both Figs. 7.10 and 7.11, differences can be seen between the results from the single sheet tester and Epstein square measurements. Such differences may be partly caused by variable accuracy in leakage flux compensation. However, it is more likely that the discrepancies between the results are due to the inherent differences between the two test methods, caused by the inhomogeneous field produced in the Epstein square. To correlate the two sets of results, the effective path length of the single sheet tester has been calculated at each test point, relative to the results from the Epstein square measurements, as described in section 7.1.1.2. The effective path length for 20, 40 and 80 Hz are shown at each flux density in Fig. 7.12.

The magnetic path length, used to calculate the applied field at each test point, was taken to have a nominal value of 0.4 m. The adjusted path length, calculated using Eq. (7.2), can be seen in Fig. 7.12 to vary with both flux density and frequency. Contrary to the suggestion by de Wulf et al. in [110], the variation in magnetic path length with flux density is significant and so to take an average value for use in all further calculations would lead to significant error in results. At high flux densities, the path length can be considered approximately constant, but at flux densities below 1 T, the path length varies considerably with frequency. That there is no simple adjustment factor for the SST magnetic path length highlights the difficulty in establishing the SST as a standard test method when much of industry still uses the Epstein square, and the difficulties in the comparison of magnetisation data that has been measured on different sets of equipment.

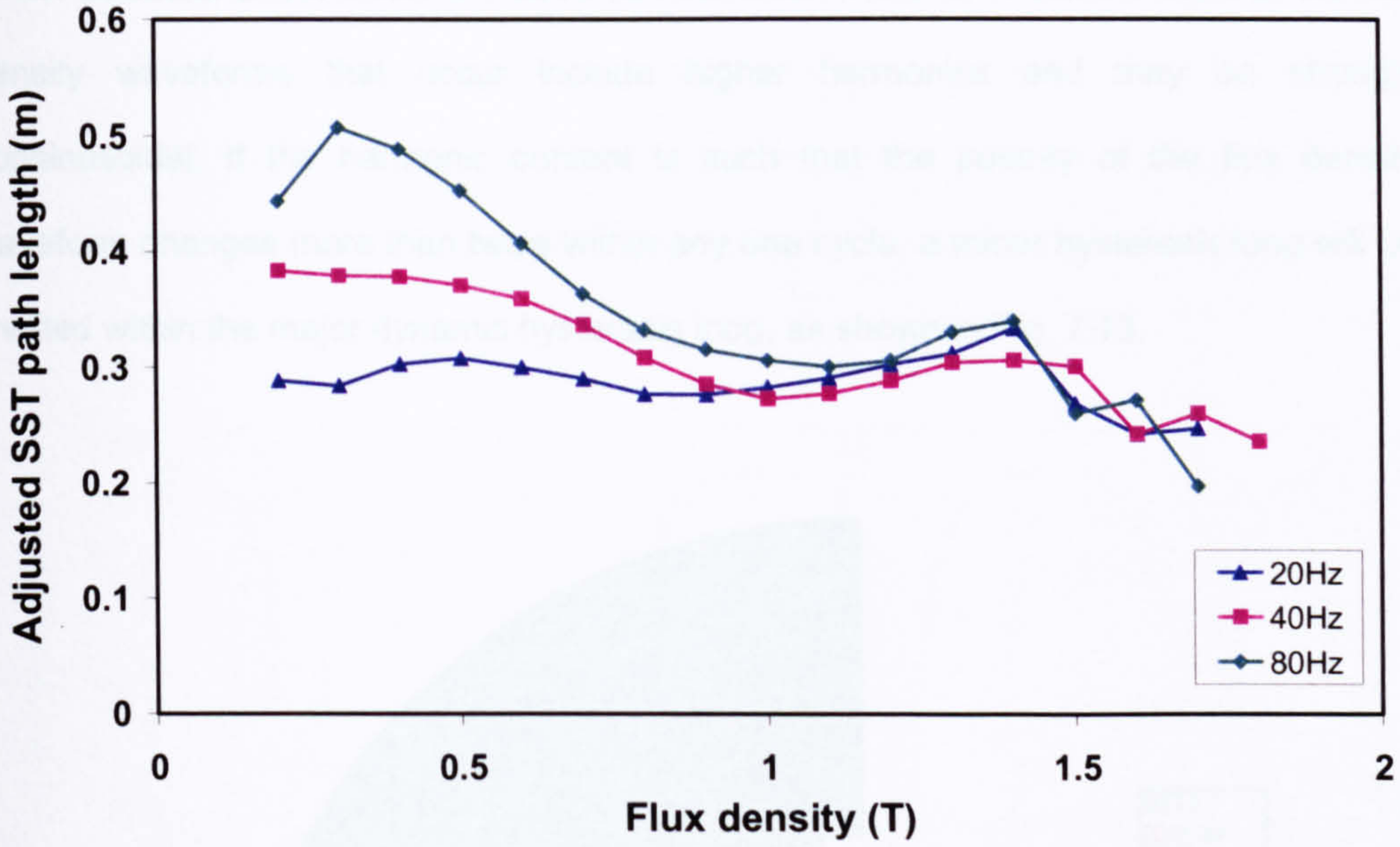

Fig. 7.12. Adjusted SST path length as a function of flux density

7.2. Tests with nonsinusoidal flux density waveforms

The common methods of testing sheet steels, described in the IEC and ASTM standards [98 - 101] all require sinusoidal flux density waveforms, which are normally enforced through some form of feedback control signal. All the results presented in section 7.1 have an approximately sinusoidal flux density output waveform.

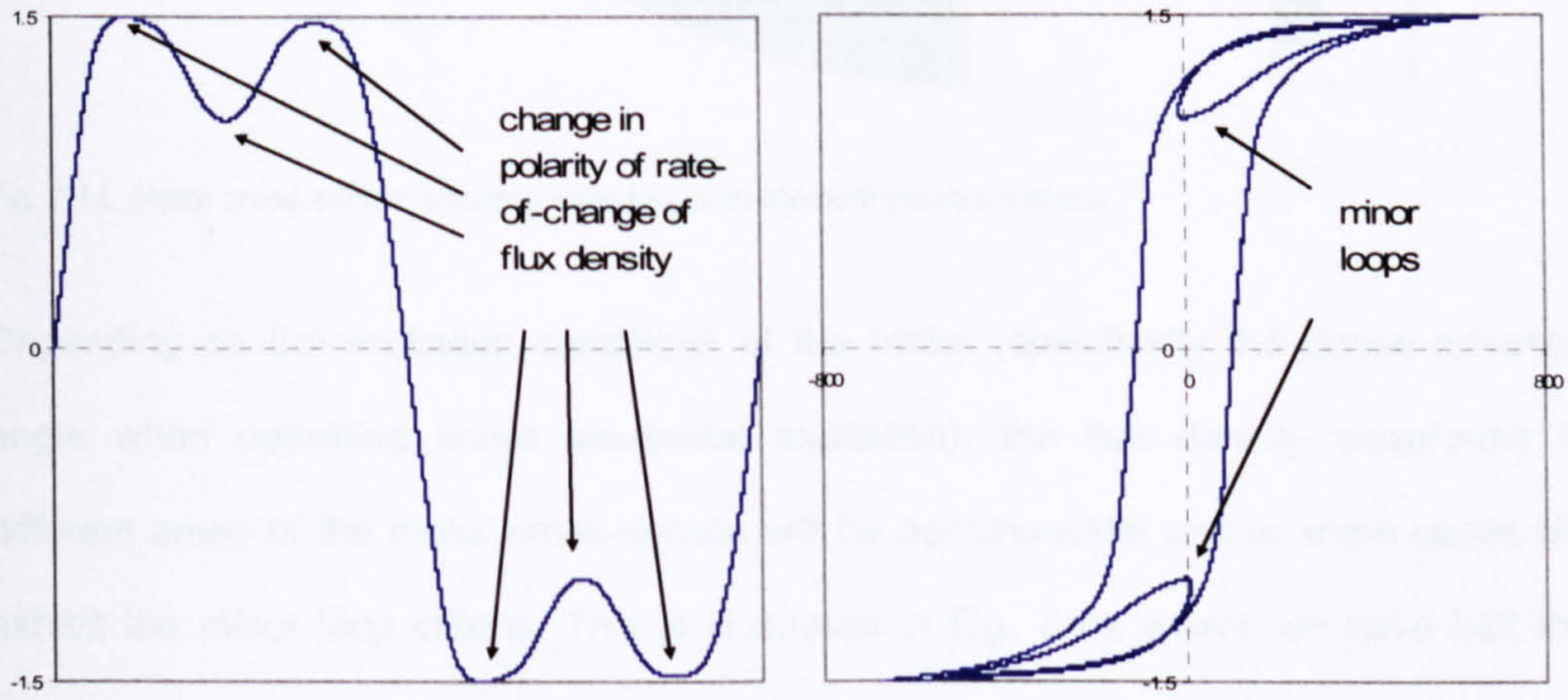

Fig. 7.13. Criteria for minor hysteresis loops

When electrical sheet steels are used as lamination material in electric motors, the flux density waveforms that occur include higher harmonics and may be strongly nonsinusoidal. If the harmonic content is such that the polarity of the flux density waveform changes more than twice within any one cycle, a minor hysteresis loop will be created within the major dynamic hysteresis loop, as shown in Fig. 7.13.

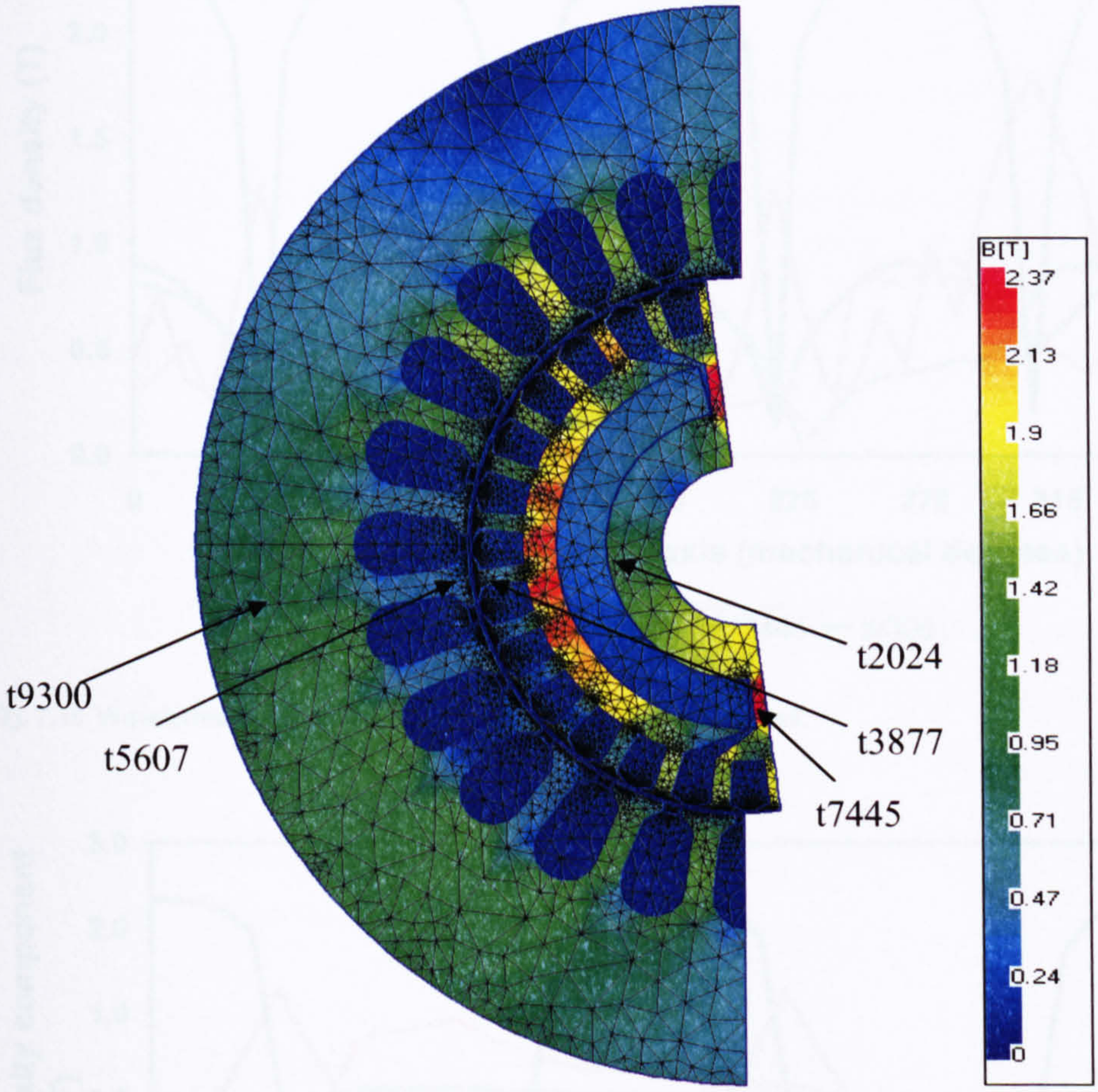

Fig. 7.14. Motor cross-section showing selected finite element mesh numbers

Depending on the excitation conditions of the motor (specifically the phase advance angle when operating under sinusoidal excitation), the flux density waveforms in different areas of the motor cross-section will be nonsinusoidal and in some cases will exhibit the minor loop criteria. This is illustrated in Fig. 7.14, where we have half the cross section of a line start permanent magnet motor. In this simulation we have two-phase excitation in the stator with the stator MMF rotating in the opposite direction to the rotor. This scenario could occur if plug reversal is used to stop the machine (although in

this instance we are omitting the rotor currents since we are simply illustrating the flux variation in the steel). Five elements from the finite element mesh are highlighted. The corresponding flux density (magnitude) waveforms can be seen in Fig. 7.15. For reference, the radial and tangential flux densities are shown in Figs. 7.16 and 7.17.

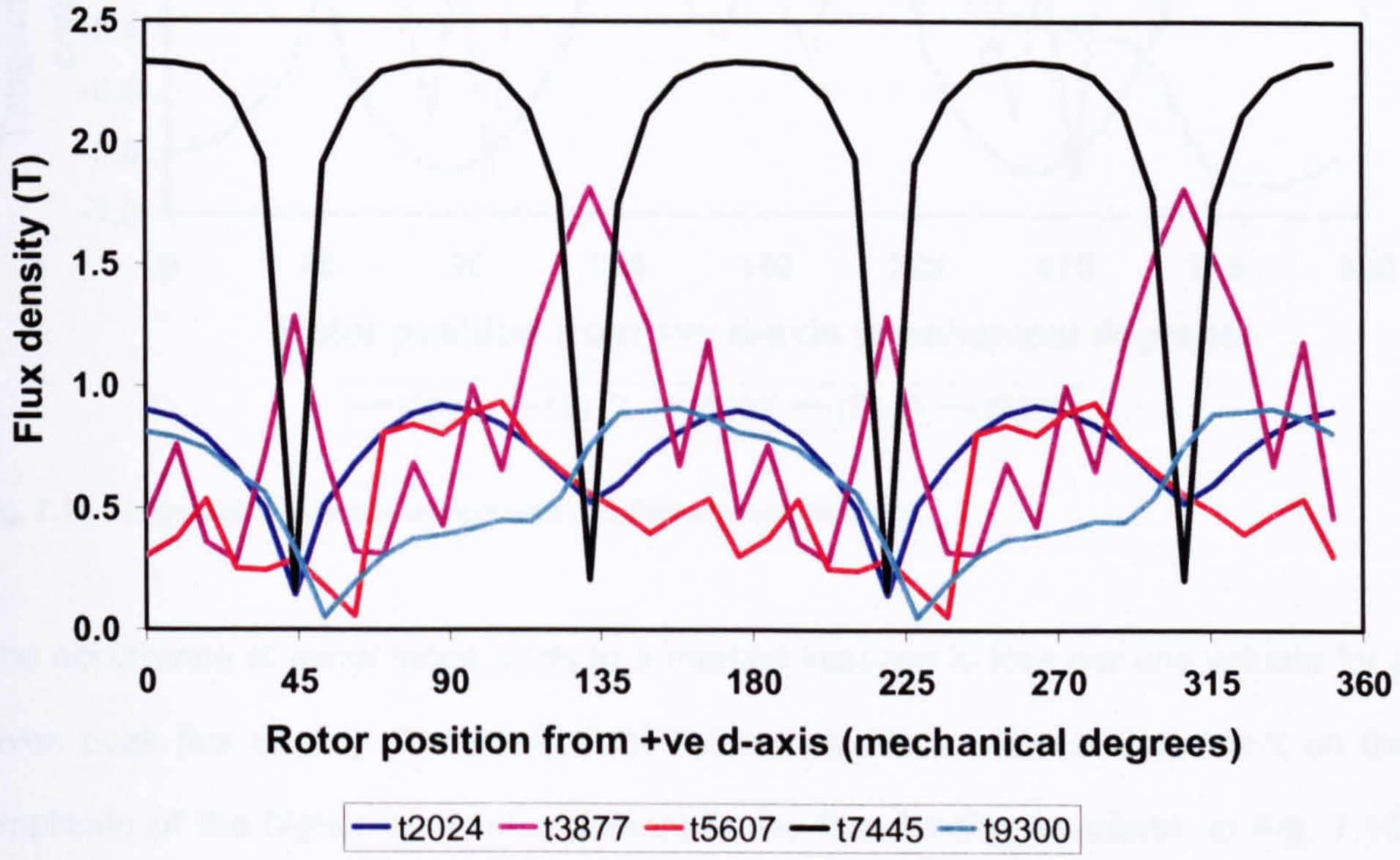

Fig. 7.15. Waveforms of flux density magnitude of each selected element

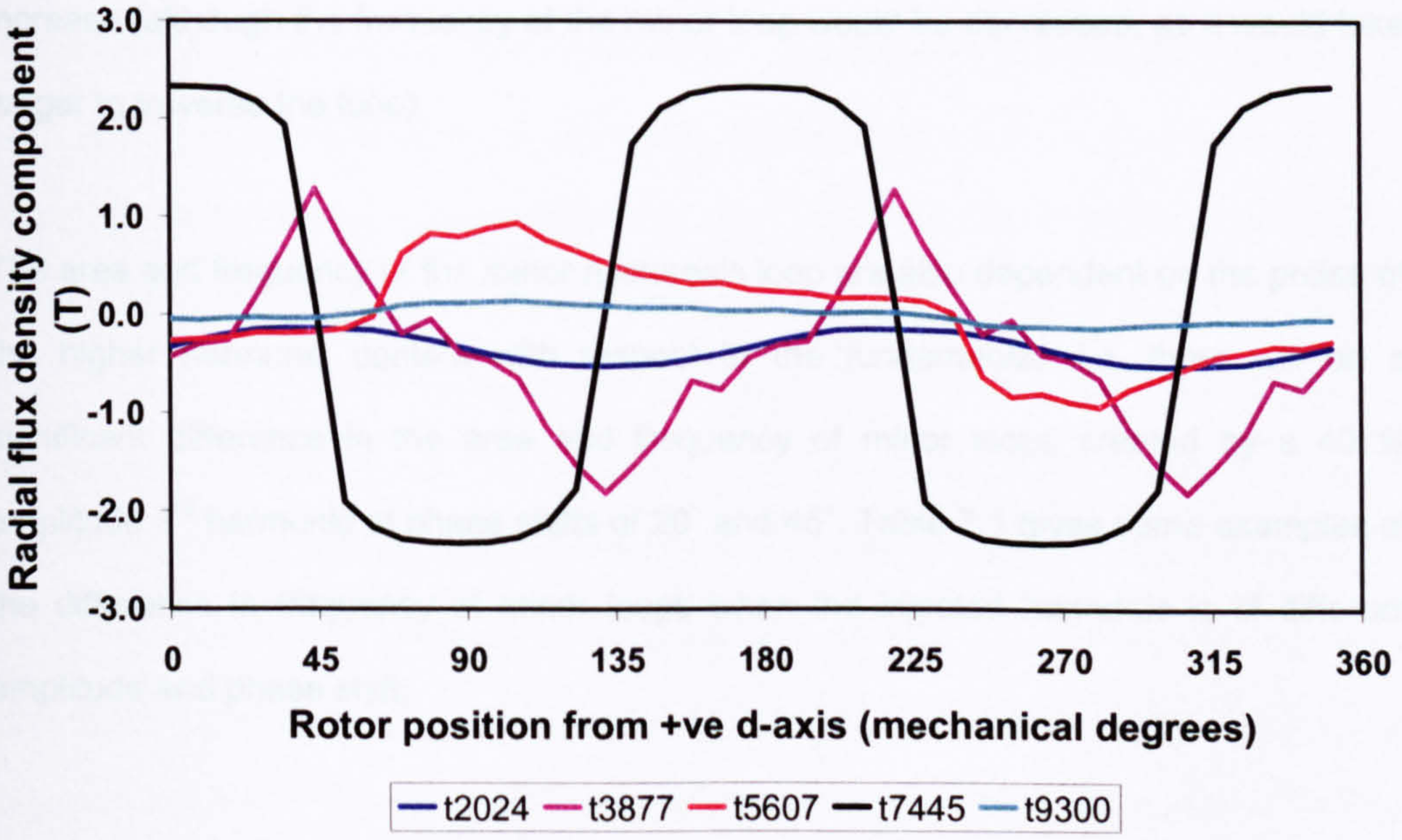

Fig. 7.16. Radial flux density components of selected mesh elements

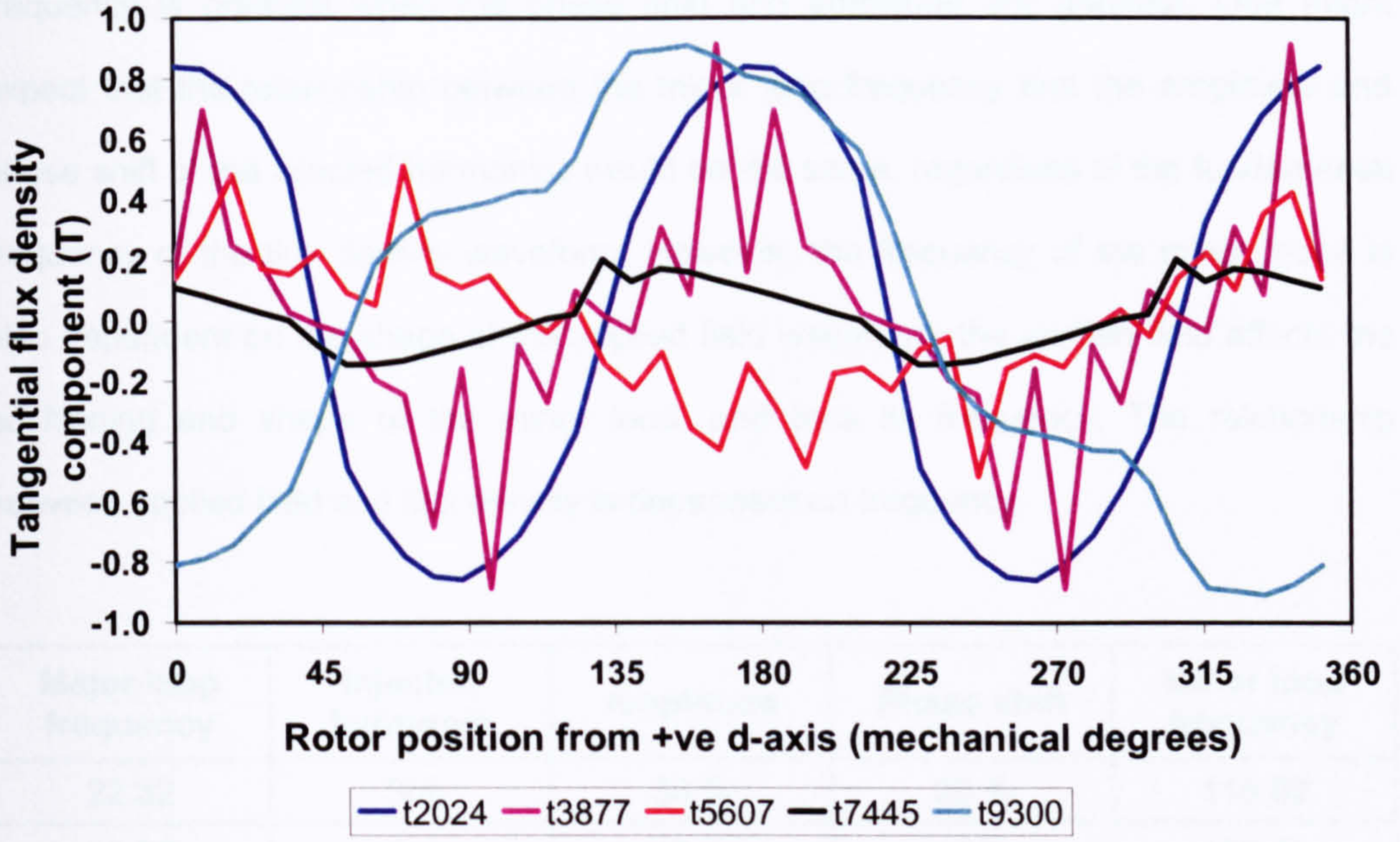

Fig. 7.17. Tangential flux density components of selected mesh elements

The occurrence of minor loops leads to a marked increase in loss per unit volume for a given peak flux density. The area of the minor hysteresis loops is dependent on the amplitude of the higher harmonics present in the flux density waveform. In Fig. 7.13, there is a dominant 3rd harmonic with amplitude of 40 % of the fundamental component. With a higher amplitude 3rd harmonic, the area of the minor hysteresis loop would increase (although the frequency of the minor loop would be decreased, as it would take longer to traverse the loop).

The area and frequency of the minor hysteresis loop are also dependent on the phase of the higher harmonic content with respect to the fundamental, i.e. there will be a significant difference in the area and frequency of minor loops created by a 40 % amplitude 3rd harmonic at phase shifts of 20° and 45°. Table 7.1 gives some examples of the difference in frequency of minor loops when the injected harmonic is of different amplitude and phase shift.

It can be noted from Table 7.1 that in the case of the 22.32 Hz tests, the frequency of the minor loops is greatest when the phase shift and amplitude of the injected 3rd harmonic are minimised. In the second test, the opposite is true; the minor loop

frequency is greatest when the phase shift and amplitude are greatest. One might expect that the relationship between the minor loop frequency and the amplitude and phase shift of the injected harmonics would be the same, regardless of the fundamental frequency of the flux density waveform. However, the frequency of the minor loops is also dependent on the shape of the applied field waveform; the applied field affects the positioning and shape of the minor loop, and thus its frequency. The relationship between applied field and flux density is dependent on frequency.

Major loop frequency	Injected harmonic	Amplitude	Phase shift	Minor loop frequency
22.32	3rd	30 %	20 %	116.82
22.32	3rd	30 %	45 %	103.41
22.32	3rd	40 %	20 %	93.02
22.32	3rd	40 %	45 %	86.96
52.08	3rd	30 %	20 %	245.09
52.08	3rd	30 %	45 %	284.09
52.08	3rd	40 %	20 %	206.61
52.08	3rd	40 %	45 %	257.73

Table 7.1. Minor loop frequencies for different amplitudes and phases of higher harmonic

The dependence on the applied field waveform, and thus the fundamental frequency, is best illustrated by examining the complete dynamic hysteresis loop, including minor loops, at different fundamental frequencies. Fig. 7.18 shows the dynamic hysteresis loop for a flux density waveform with injected 3rd harmonic of 30 % amplitude, at a phase shift of 20 degrees, for a fundamental frequency of 22.32 Hz. This can be compared with Fig. 7.19, which shows the dynamic hysteresis loop for a flux density waveform with the same additional harmonic component, but at a frequency of 52.08 Hz. The positioning of the minor loops can be seen to be different, and as such the area of the loops also differs. Differences between the dynamic hysteresis loops at the two test frequencies can also be seen for an increased harmonic phase shift of 45 degrees, as shown in Figs. 7.20 and 7.21 for fundamental frequencies of 22.32 Hz and 52.08 Hz respectively. The

area of the minor loops is thus a function of the fundamental frequency of the major loop, and both the magnitude and phase shift of the additional harmonic components.

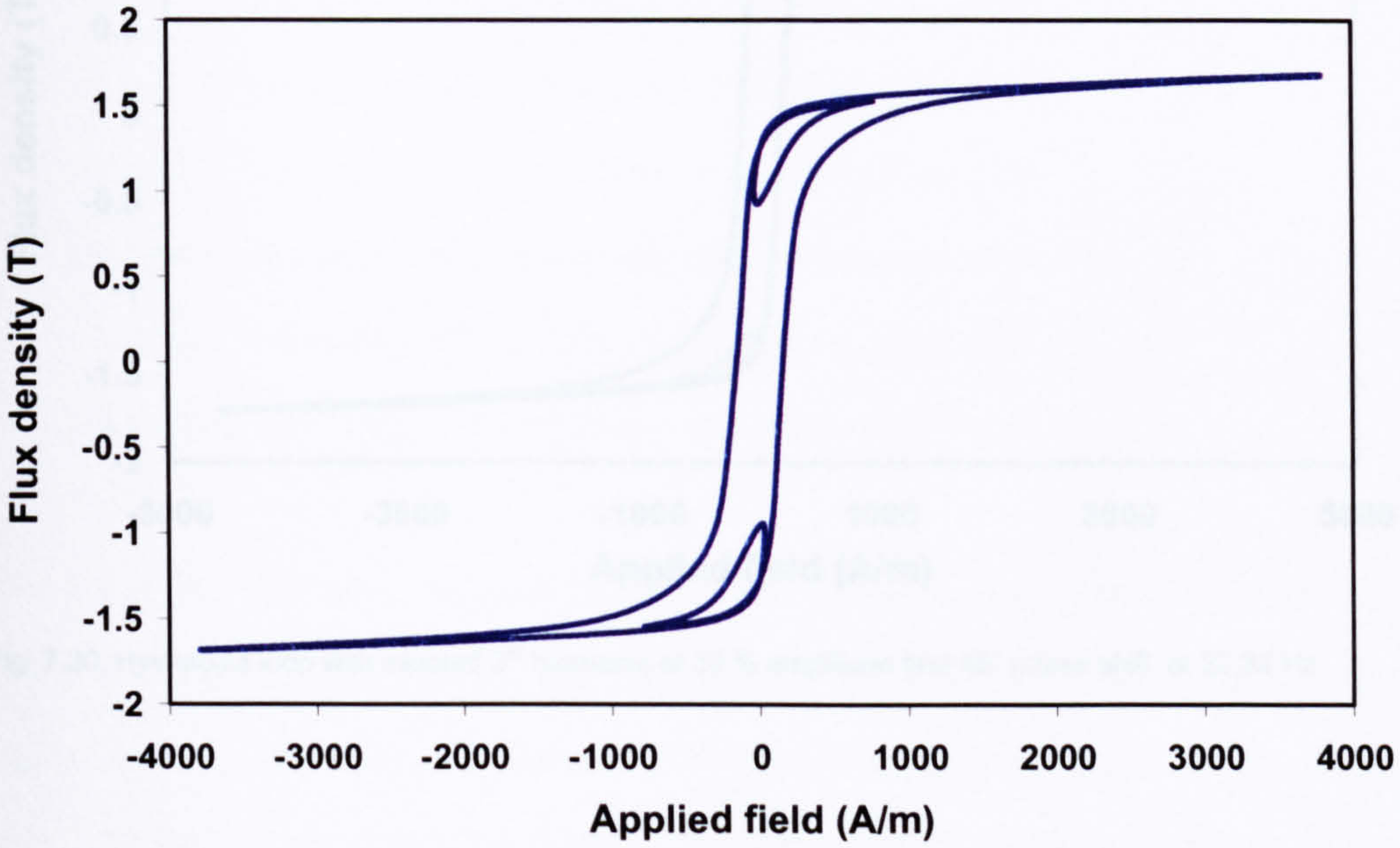

Fig. 7.18. Hysteresis loop with injected 3rd harmonic of 30 % amplitude and 20° phase shift, at 22.32 Hz

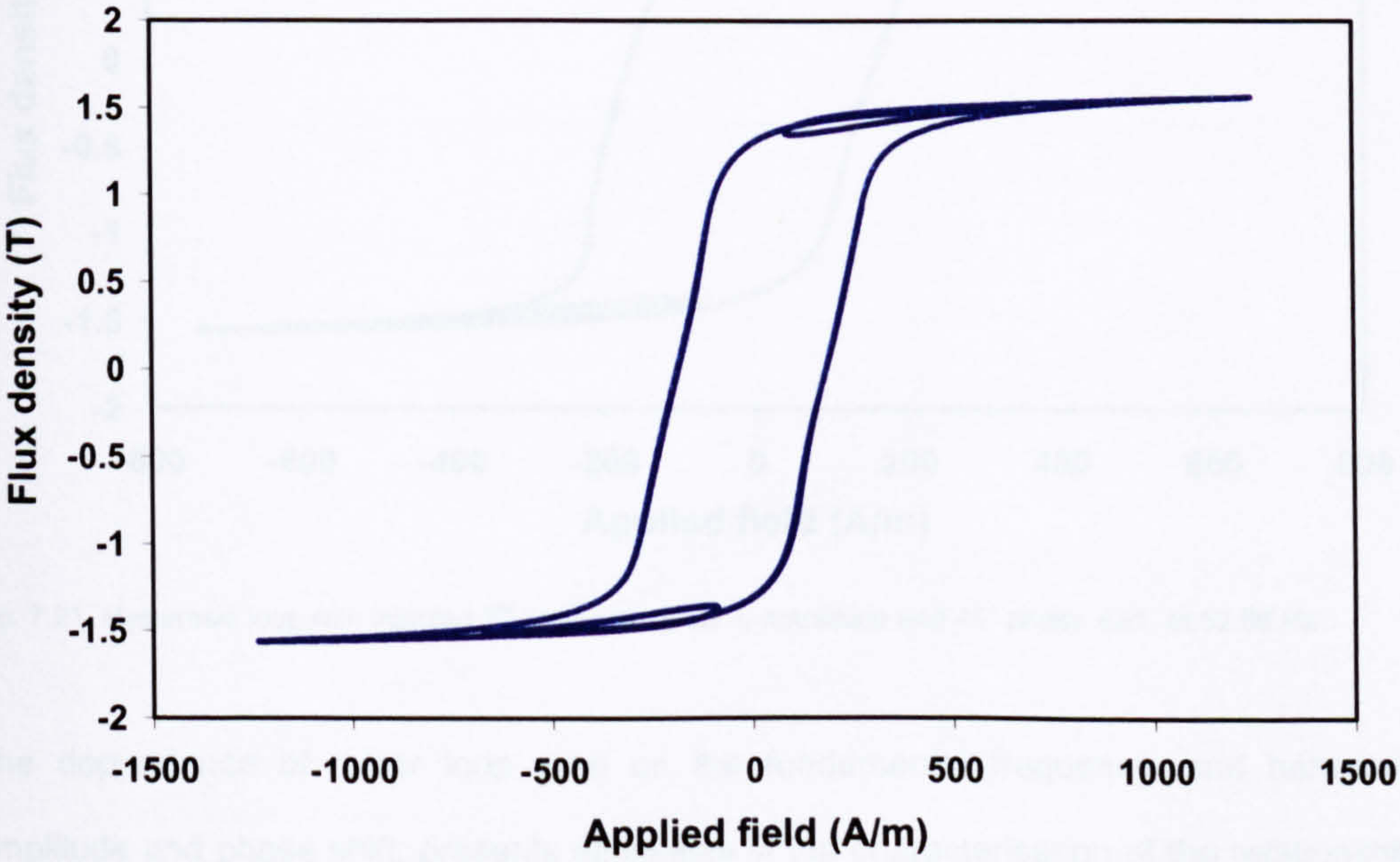

Fig. 7.19. Hysteresis loop with injected 3rd harmonic of 30 % amplitude and 20° phase shift, at 52.08 Hz

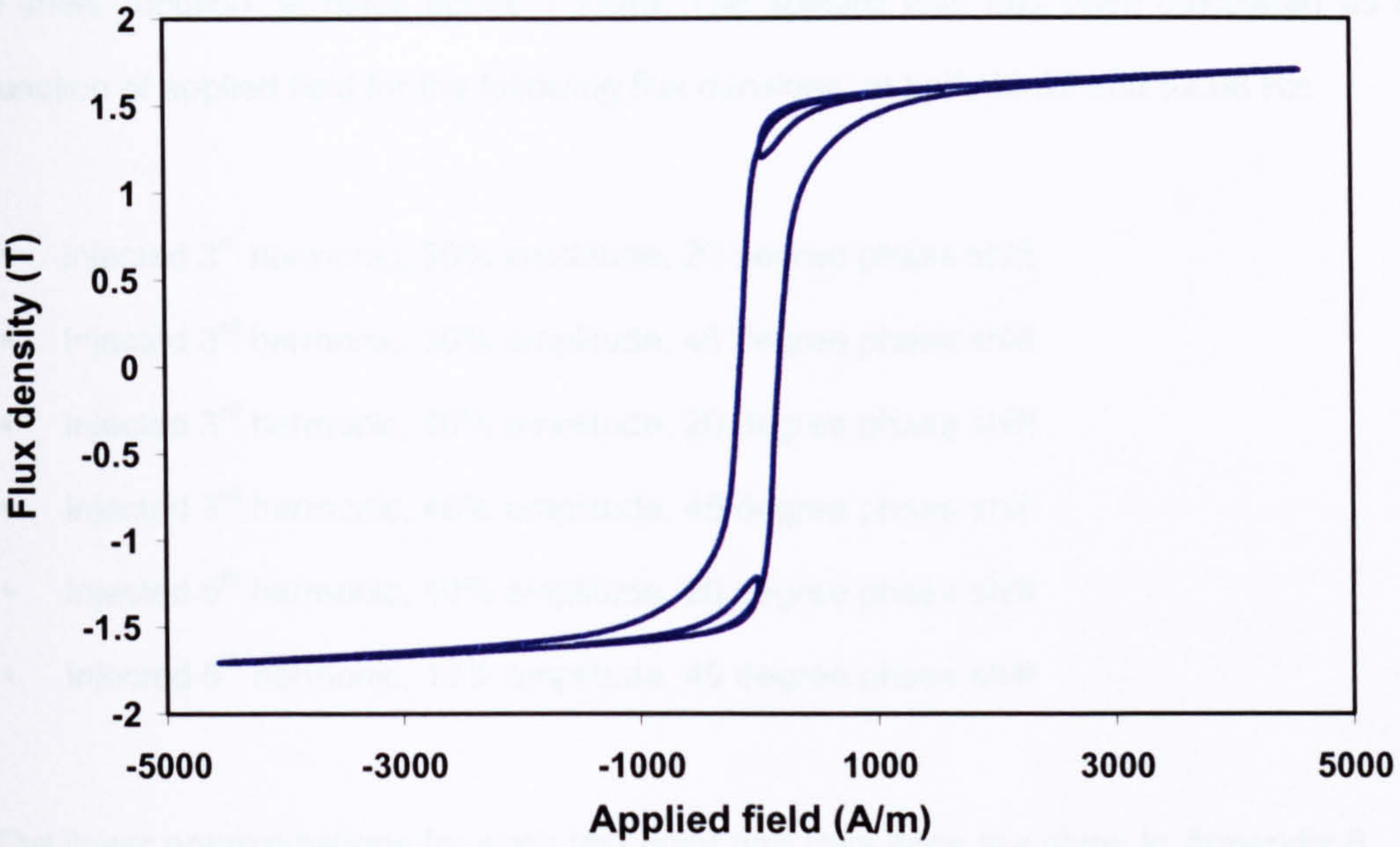

Fig. 7.20. Hysteresis loop with injected 3rd harmonic of 30 % amplitude and 45° phase shift, at 22.32 Hz

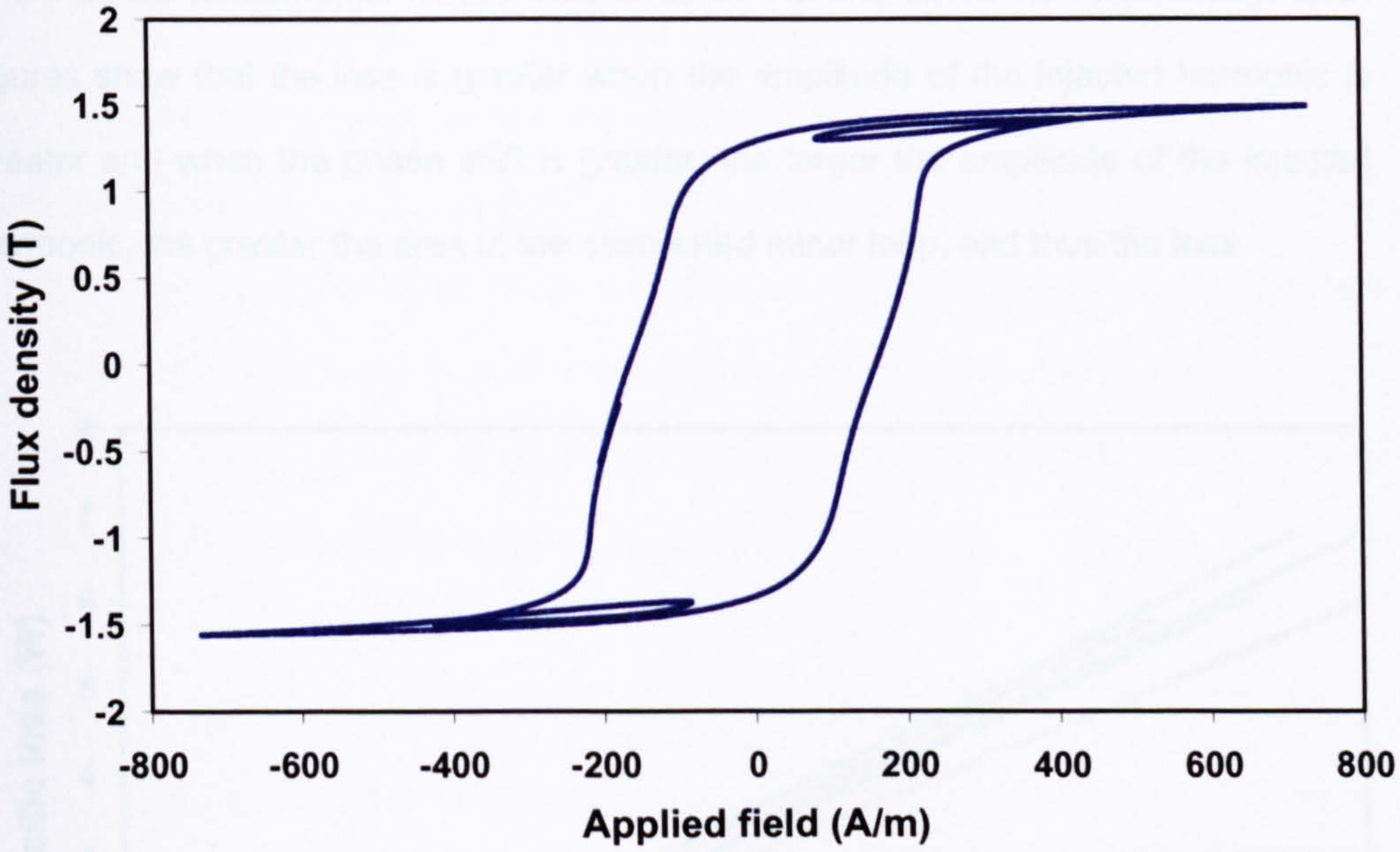

Fig. 7.21. Hysteresis loop with injected 3rd harmonic of 30 % amplitude and 45° phase shift, at 52.08 Hz

The dependence of minor loop area on the fundamental frequency, and harmonic amplitude and phase shift, presents difficulties in the characterisation of the relationship between the iron loss of a material and the flux density and frequency. The loss can again be plotted as a function of the flux density or applied field at different frequencies. The relationship between applied field and iron loss can once again be approximated by

a linear function, at fields above 1 kA/m. The specific loss has been calculated as a function of applied field for the following flux densities, at both 22.32 and 52.08 Hz:

- Injected 3rd harmonic, 30% amplitude, 20 degree phase shift
- Injected 3rd harmonic, 30% amplitude, 45 degree phase shift
- Injected 3rd harmonic, 40% amplitude, 20 degree phase shift
- Injected 3rd harmonic, 40% amplitude, 45 degree phase shift
- Injected 5th harmonic, 10% amplitude, 20 degree phase shift
- Injected 5th harmonic, 10% amplitude, 45 degree phase shift

The linear approximations for each test point and frequency are given in Appendix 8, along with the calculated losses and errors in the linear calculations. The losses at each harmonic amplitude and phase shift can be compared, as shown in Figs. 7.22 and 7.23 for fundamental frequencies of 22.32 Hz and 52.08 Hz respectively. Both figures show that the loss is greater when the amplitude of the injected harmonic is greater and when the phase shift is greater; the larger the amplitude of the injected harmonic, the greater the area of the associated minor loop, and thus the loss.

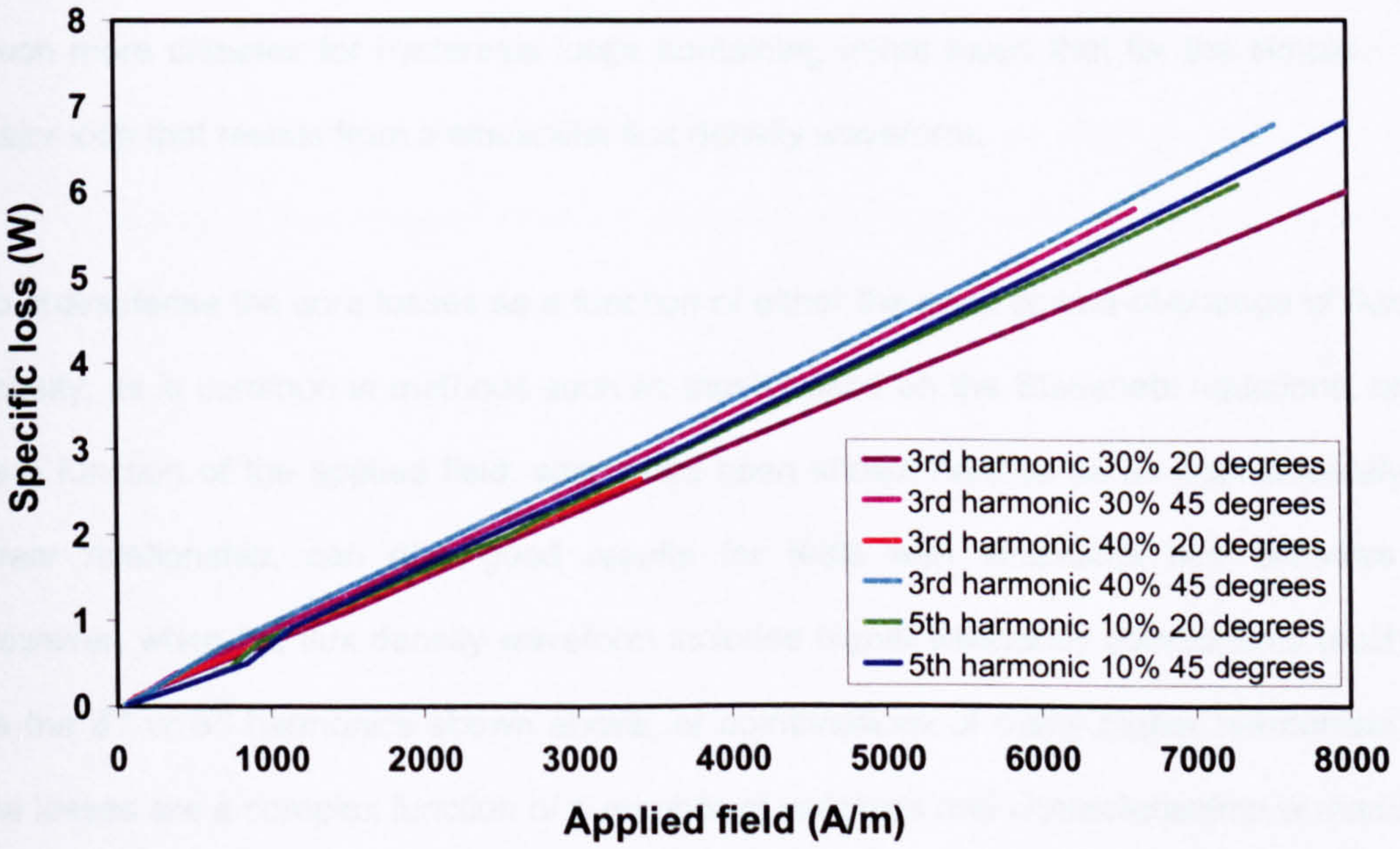

Fig. 7.22. Comparison of measured losses at 22.32 Hz

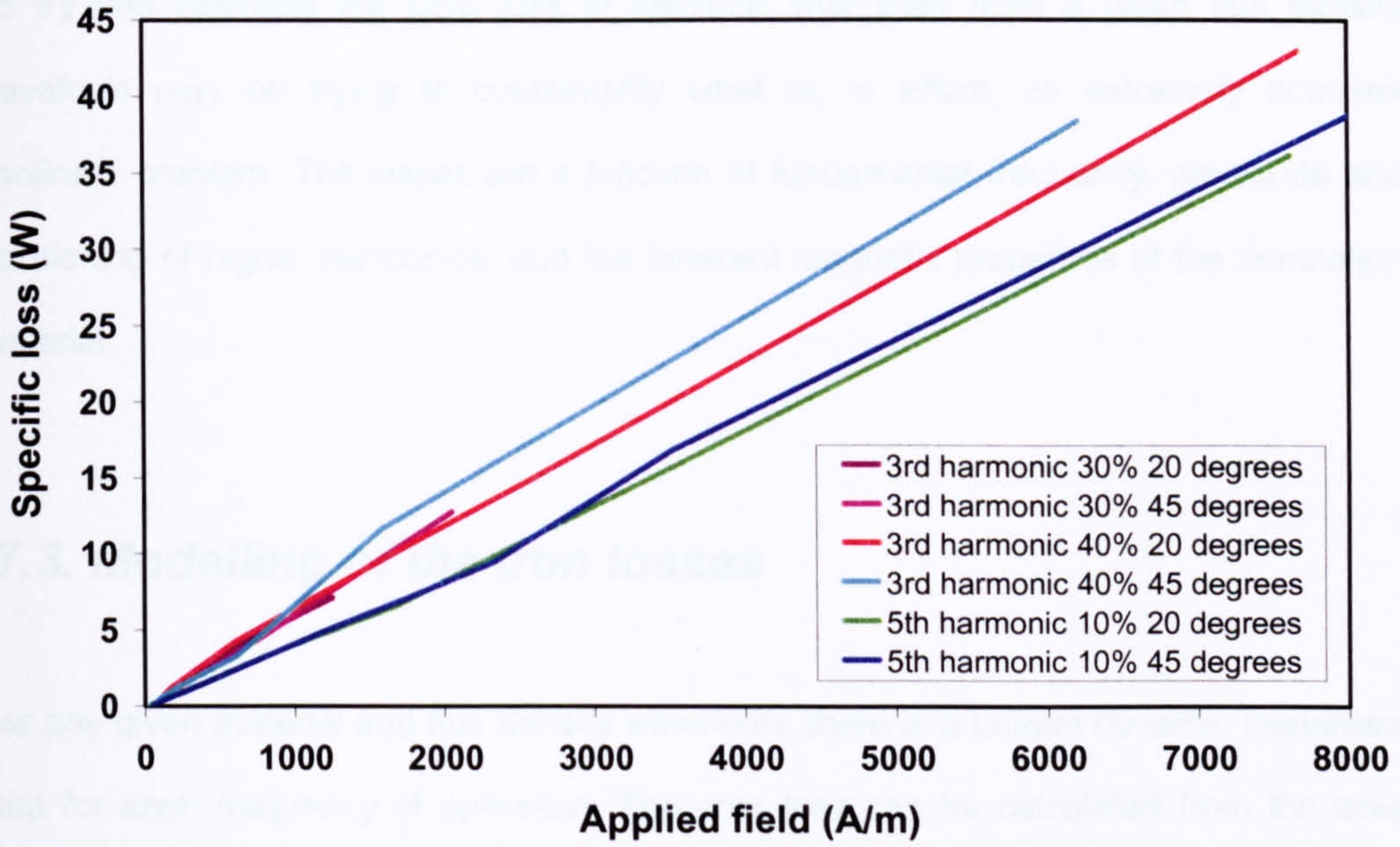

Fig. 7.23. Comparison of measured losses at 52.08 Hz

The losses, as expected, are significantly increased when the frequency of the fundamental component of the flux density is increased. As the frequency of the major hysteresis loop is increased, the ratio of minor loop frequency to major loop frequency increases, so that in addition to the increased losses due the increase in major loop frequency, there is an extra increase in loss due to the increased minor loop relative frequency. As such, the relationship between core loss and frequency is much more complex for hysteresis loops containing minor loops that for the simple major loop that results from a sinusoidal flux density waveform.

To characterise the core losses as a function of either the peak or rate-of-change of flux density, as is common in methods such as those based on the Steinmetz equations, or as a function of the applied field, which has been shown here to be an approximately linear relationship, can give good results for tests with sinusoidal flux densities. However, when the flux density waveform includes higher frequency components (such as the 3^{rd} or 5^{th} harmonics shown above, or combinations of many higher harmonics), the losses are a complex function of a number of variables and characterisation is made more difficult.

To try and calculate the core loss in electrical machines from a given flux density waveform may be trying to oversimplify what is, in effect, an extremely complex nonlinear problem. The losses are a function of fundamental frequency, amplitude and positioning of higher harmonics, and the inherent magnetic properties of the lamination material.

7.3. Modelling of the iron losses

For any given material and flux density waveform, there is a unique dynamic hysteresis loop for each frequency of operation. The core loss can be calculated from the area enclosed by the hysteresis loop. It therefore follows that the most accurate way of predicting the iron loss of a material for a given flux density waveform is to determine the corresponding, unique applied magnetic field waveform, from which the dynamic hysteresis loop can be plotted and the loss calculated from the enclosed area.

It may be suggested that instead of focusing on models to characterise the relationship between flux density and specific loss (or indeed, applied field and specific loss), systems should be developed to model the relationship between flux density and applied field at any given instant. Of course, the relationship between flux density and applied field is easily measured in terms of the virgin or normal magnetisation curves of a material, but such data is taken from the peaks of each measured loop (rather than the instantaneous values which occur at intermediate points around the hysteresis trajectory) and only characterises the *B-H* relationship under specific conditions. The relationship between the applied magnetic field and the flux density depends on the magnetisation history of the material and the rate of change of magnetisation.

The applied field and flux density can be related through either the relative permeability:

$$B = \mu_0 \mu_r H \tag{7.16}$$

or through the magnetisation:

$$B = \mu_0 (H + M) \tag{7.17}$$

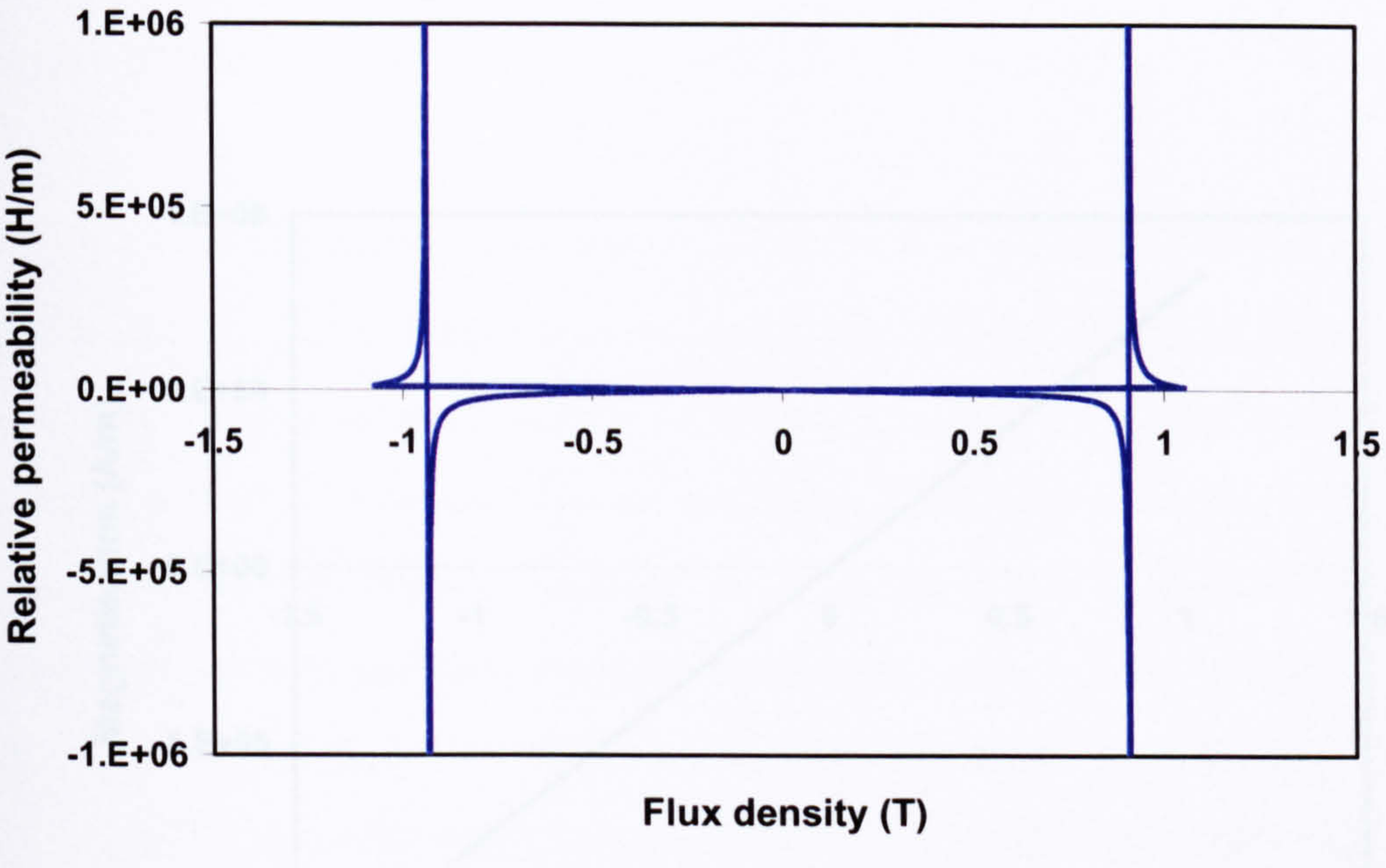

Fig. 7.24. Relative permeability as a function of flux density at 50 Hz

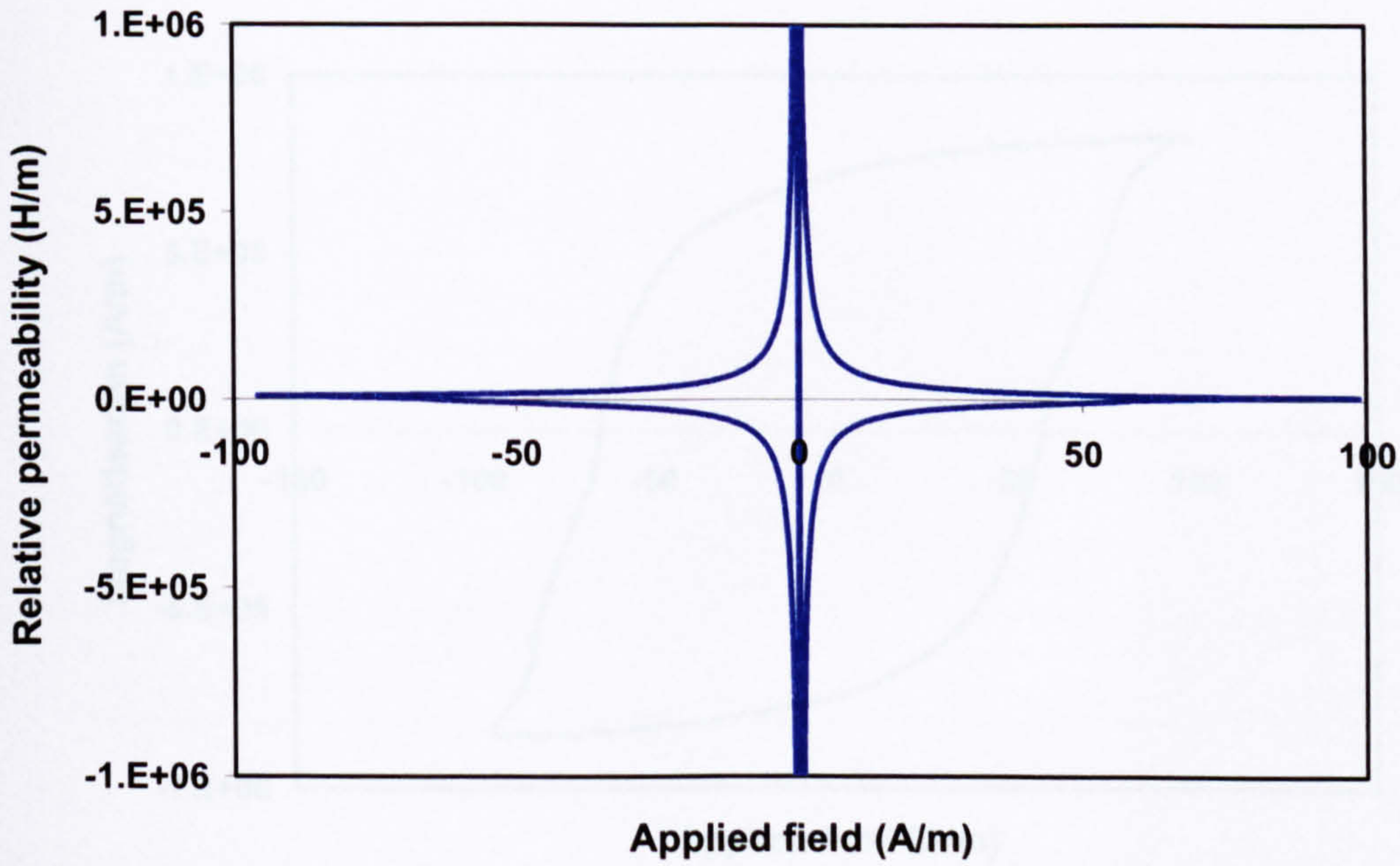

Fig. 7.25. Relative permeability as a function of applied field at 50 Hz

The relative permeability can be plotted as a function of the flux density or the applied field, as shown in Figs. 7.24 and 7.25 for a 50 Hz test point with sinusoidal flux density waveform (no minor loops). Figs. 7.24 and 7.25 show extreme peaks in the relative permeability; these correspond to the points + B_r and – B_r on the major hysteresis loop. The magnetisation M can also be plotted as a function of either the flux density or applied field, as shown in Figs. 7.26 and 7.27.

Fig. 7.26. Magnetisation as a function of flux density at 50 Hz

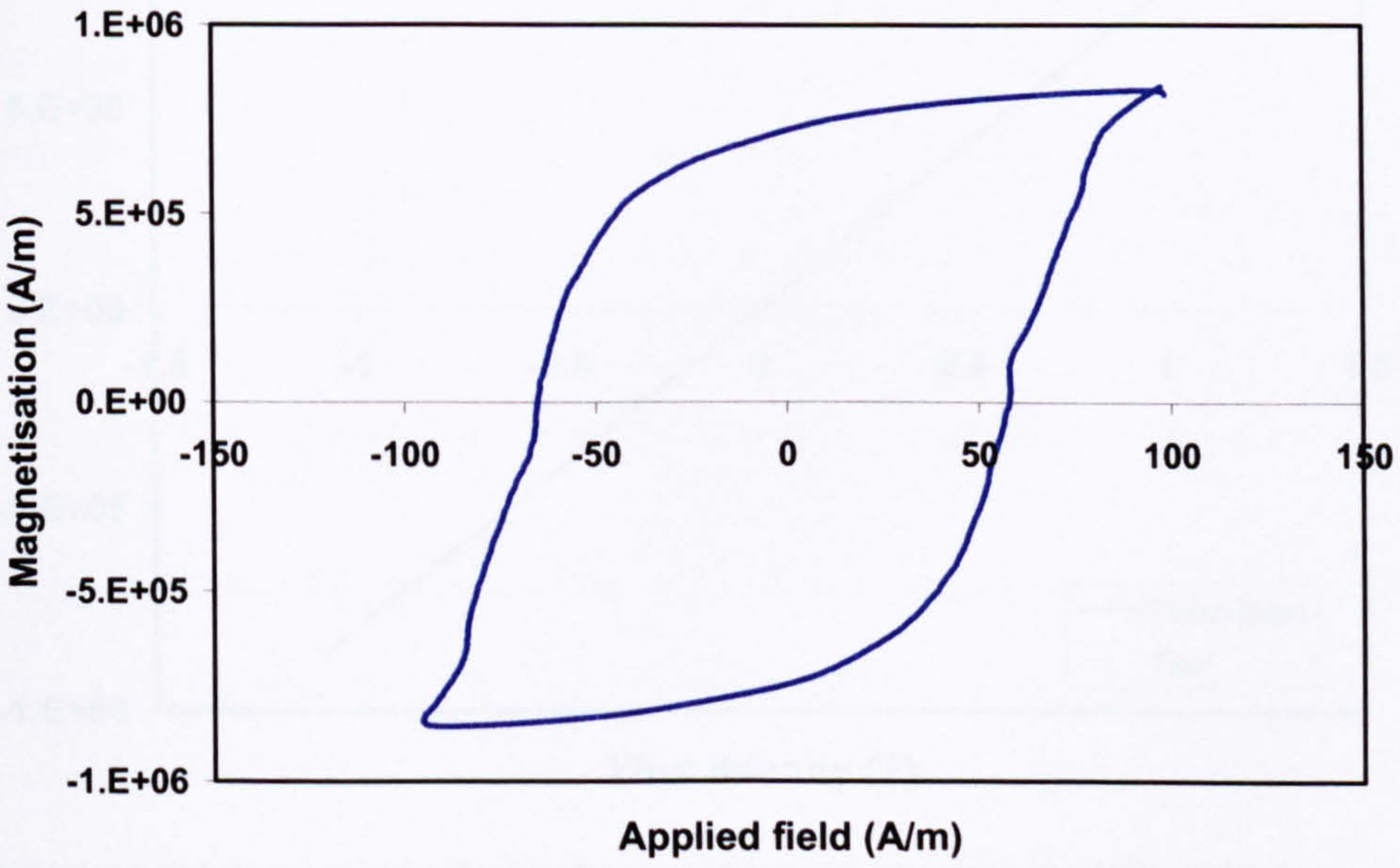

Fig. 7.27. Magnetisation as a function of applied field at 50 Hz

Figs. 7.24, 7.25 and 7.27 all show nonlinear relationships. However, Fig. 7.26 shows that the relationship between magnetisation and flux density is approximately linear. If the magnetisation can be calculated with the required accuracy, it can then be used in a rearranged form of Eq. (7.17) to calculate the applied field, and thus the dynamic hysteresis loop. A linear approximation of the relationship in Fig. 7.26 was found to be

$$M = (795718 \times B) + 1.4835 \tag{7.18}$$

Using this linear approximation, the magnetisation M can be calculated and compared with the magnetisation determined from test results. This is shown in Fig. 7.28. The error in calculated magnetisation was found to be within 5 % for most flux density values, as illustrated in Fig. 7.29. However, when the flux density is very close to zero (as the flux density changes from positive to negative), the percentage error is significantly higher. Although the error in calculated magnetisation is small, when used to calculate the applied field it leads to large errors, as illustrated in the plot of Fig. 7.30, which shows the measured and calculated applied field for each sample of a stored dynamic hysteresis loop.

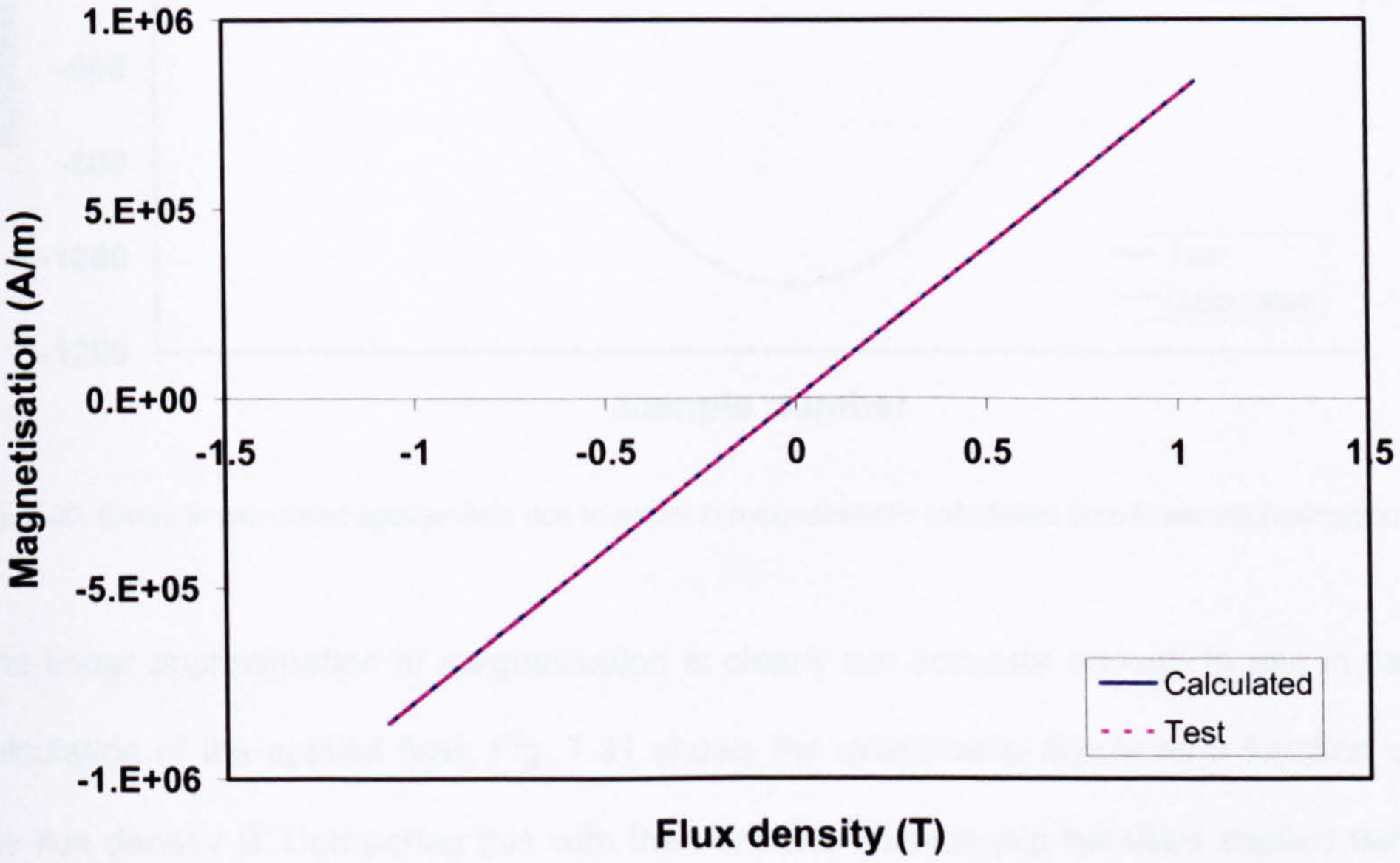

Fig. 7.28. Comparison between calculated magnetisation and magnetisation determined from test data

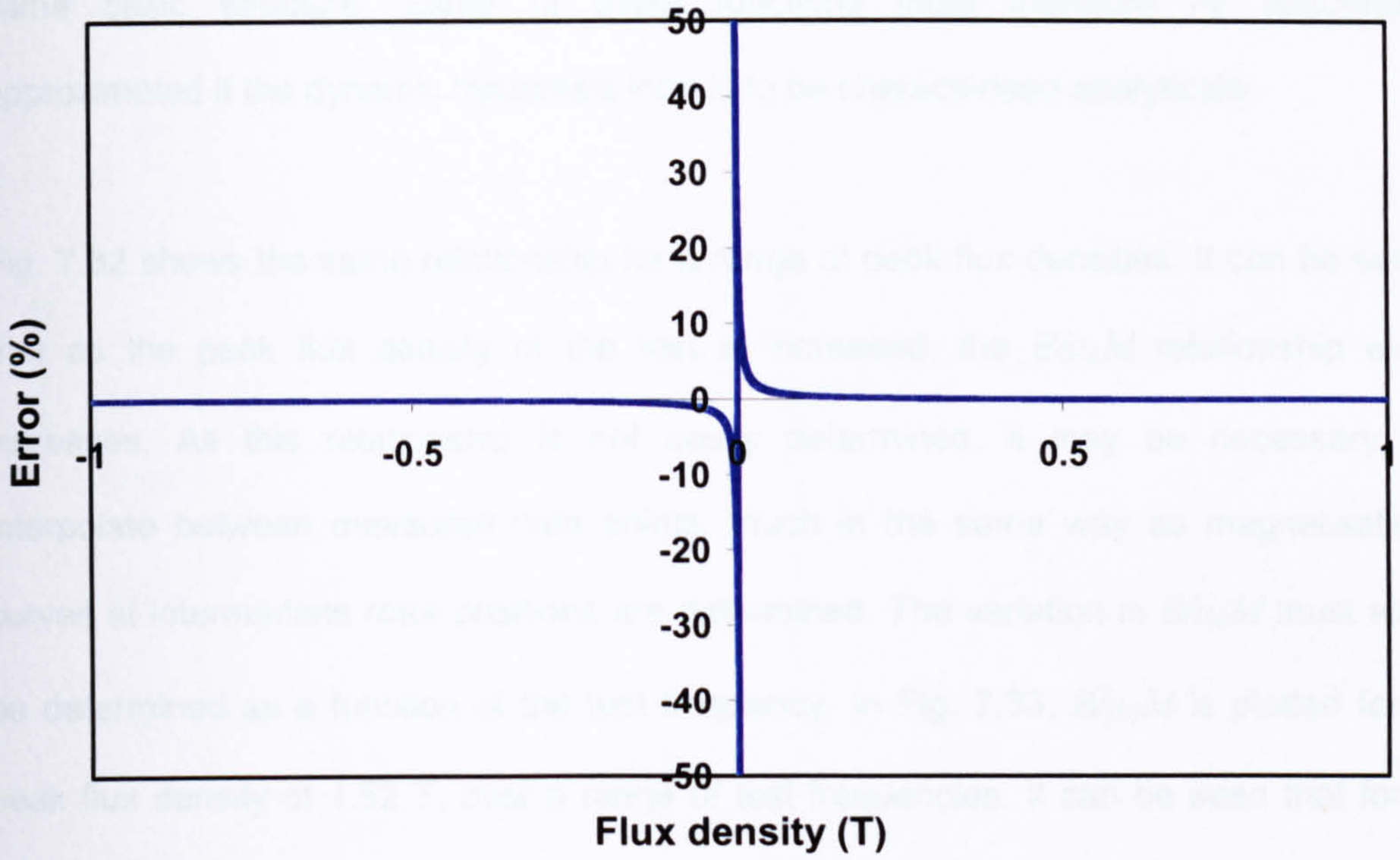

Fig. 7.29. Percentage error in magnetisation calculation, as a function of flux density

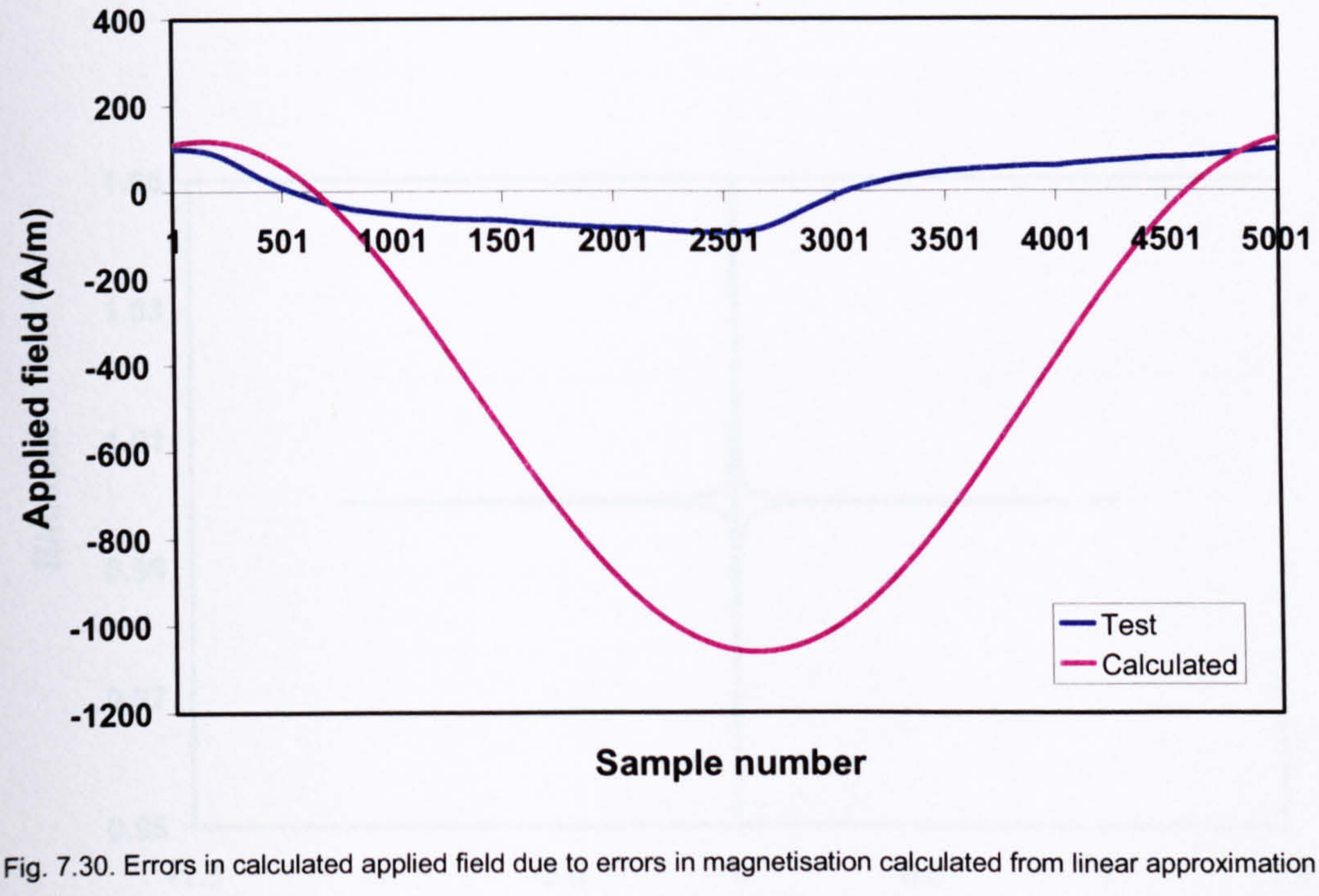

Fig. 7.30. Errors in calculated applied field due to errors in magnetisation calculated from linear approximation

The linear approximation of magnetisation is clearly not accurate enough to use in the calculation of the applied field. Fig. 7.31 shows the relationship $B/\mu_0 M$ as a function of the flux density B. Comparing this with the nonlinear relationship between applied field and relative permeability shown in Fig. 7.25, it can be seen that both functions are of the

same basic structure. Either of these functions must therefore be accurately approximated if the dynamic hysteresis loop is to be characterised analytically.

Fig. 7.32 shows the same relationship for a range of peak flux densities. It can be seen that as the peak flux density of the test is increased, the $B/\mu_0 M$ relationship also increases. As this relationship is not easily determined, it may be necessary to interpolate between measured data points, much in the same way as magnetisation curves at intermediate rotor positions are determined. The variation in $B/\mu_0 M$ must also be determined as a function of the test frequency. In Fig. 7.33, $B/\mu_0 M$ is plotted for a peak flux density of 1.52 T, over a range of test frequencies. It can be seen that for a given peak flux density, the ratio $B/\mu_0 M$ will increase as the test frequency increases. This confirms that the relationship is a function of both peak flux density and test frequency.

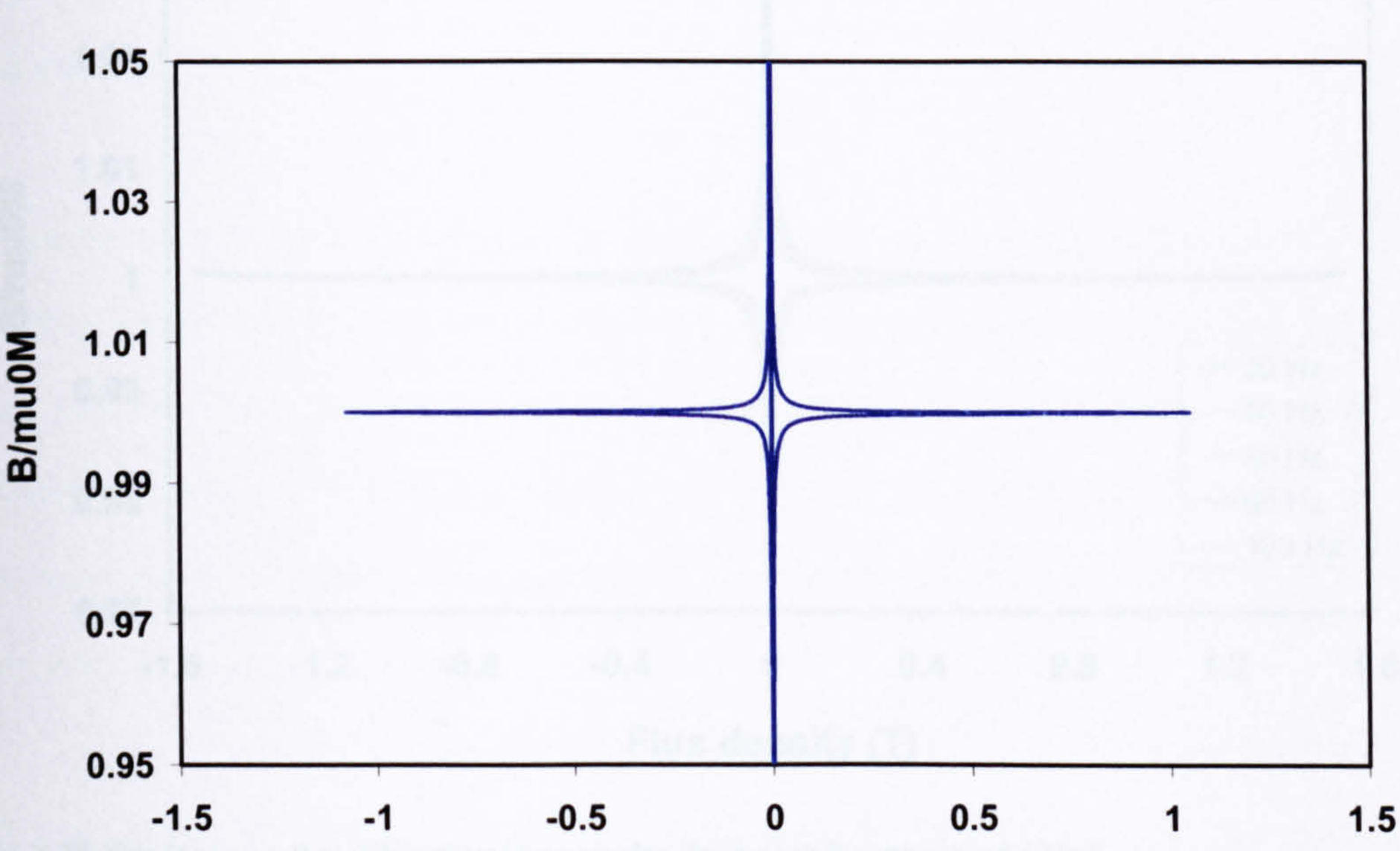

Fig. 7.31. Relationship between $B/\mu_0 M$ and B at 50 Hz

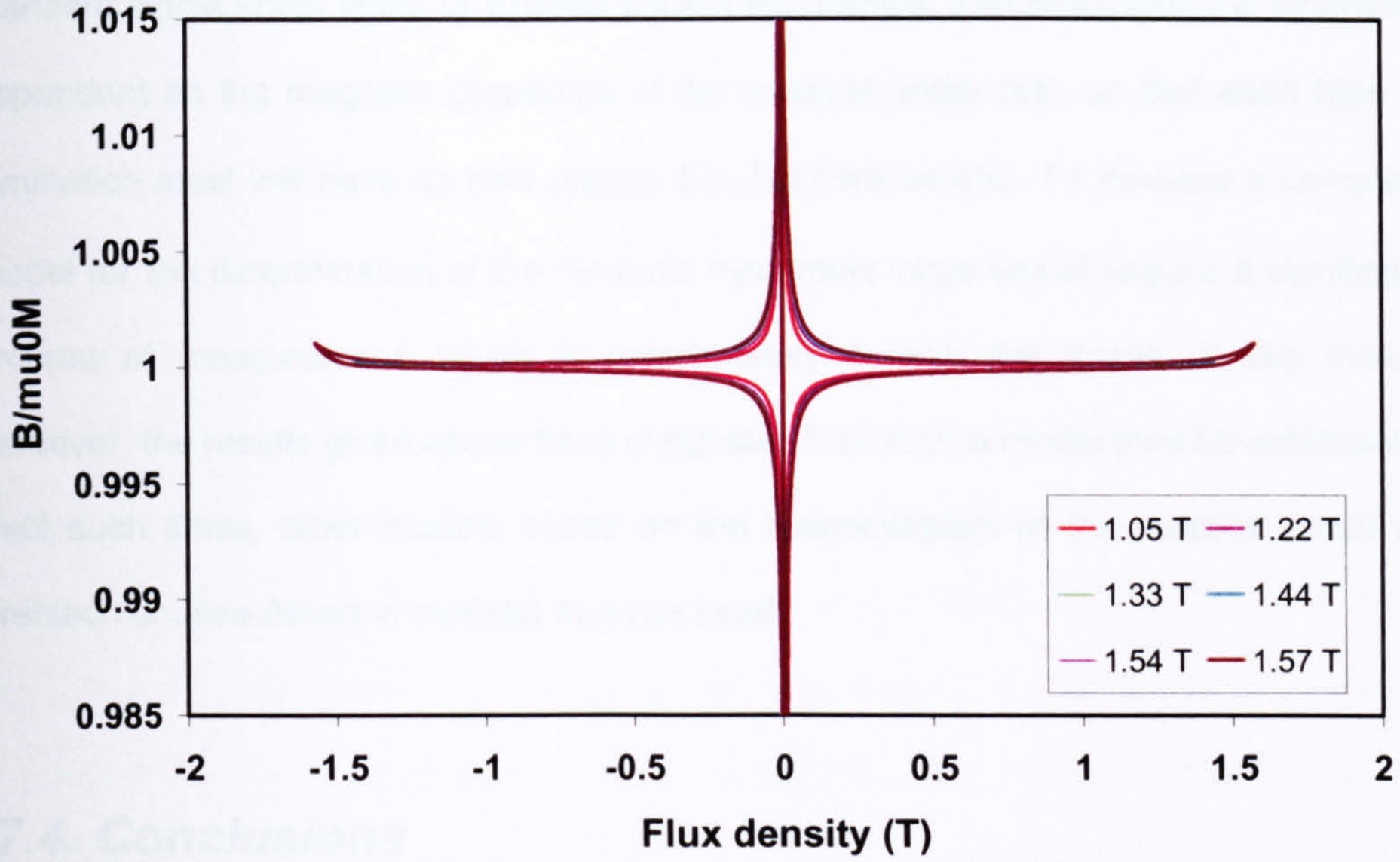

Fig. 7.32. $B/\mu_0 M$ versus B at different peak flux densities, at 50 Hz

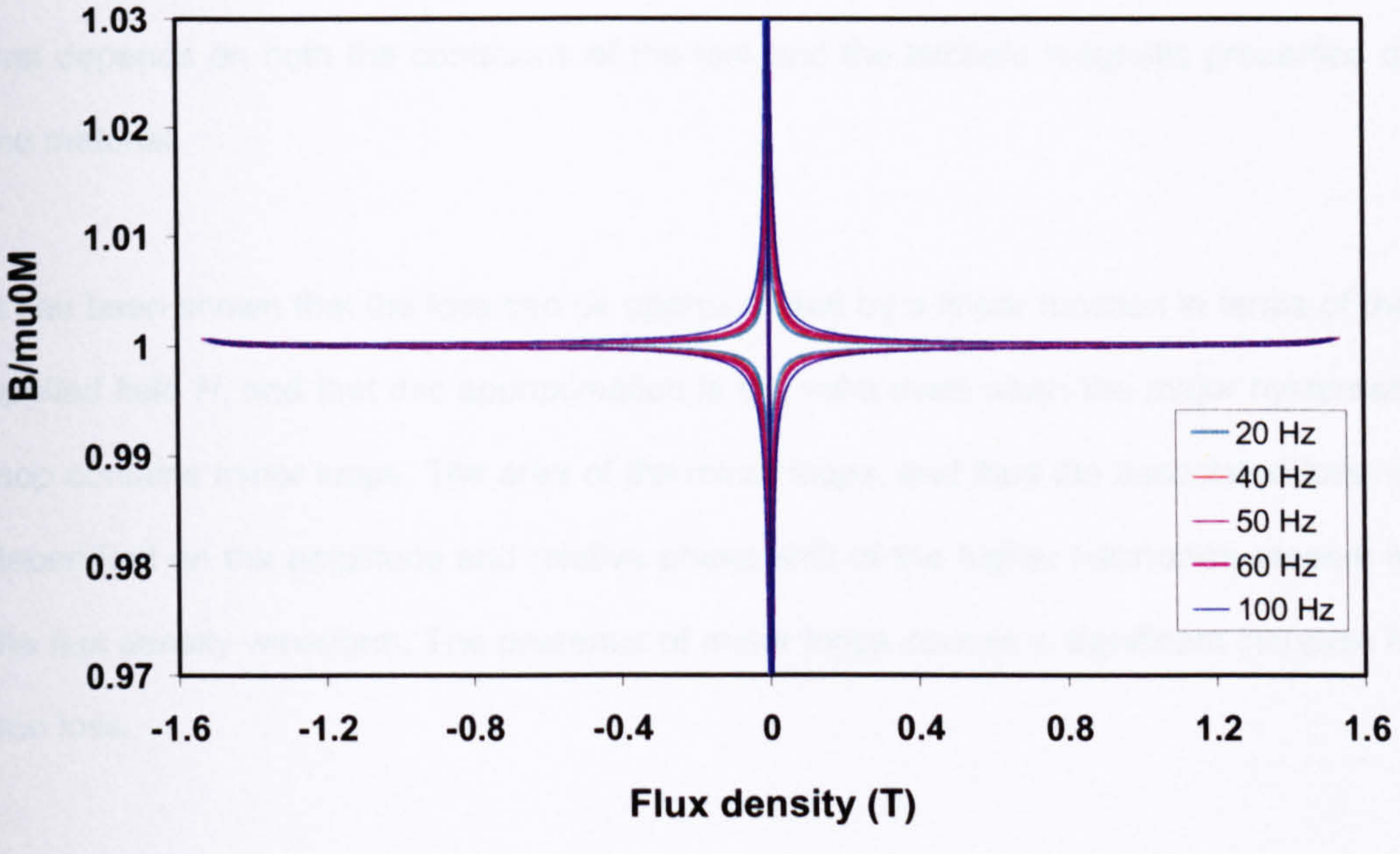

Fig. 7.33. $B/\mu_0 M$ versus B at different test frequencies, for a peak flux density of 1.52 T

It is clear from these preliminary results that to develop a model capable of predicting the dynamic hysteresis loop, the above relationship must be fully characterised in terms of both frequency and peak flux density. All the data required for the determination of the $B/\mu_0 M$ relationship can be found from measurement of B and H carried out on the

standard single sheet tester or Epstein square test frames. The relationship is inherently dependent on the magnetic properties of the material under test, so that each type of lamination steel will have its own unique $B/\mu_0 M$ characteristic. To develop a complete model for the determination of the dynamic hysteresis loops would require a significant amount of measurement, which is unfortunately outwith the scope of this thesis. However, the results given above have suggested that such a model may be achievable. Until such times, other models based on the magnetisation of the material (such as Preisach or Jiles-Atherton models) must be used.

7.4. Conclusions

The measurements given in this chapter have been taken from measurements made on strip samples of electrical steel, using the Epstein square and single sheet tester. The results have shown that the iron losses in electrical sheet steels are a complex function that depends on both the conditions of the test and the intrinsic magnetic properties of the material.

It has been shown that the loss can be approximated by a linear function in terms of the applied field H, and that this approximation is still valid even when the major hysteresis loop contains minor loops. The area of the minor loops, and thus the associated loss, is dependent on the amplitude and relative phase shift of the higher harmonics present in the flux density waveform. The presence of minor loops causes a significant increase in iron loss.

The possibility of modelling the iron losses through determination of the dynamic hysteresis loop has been discussed. Using the results from hysteresis loop measurements, it has been shown that the magnetisation M can be calculated with reasonable accuracy, but that the use of such an approximated function leads to significant errors in the calculation of applied field. To accurately determine the dynamic hysteresis loop, it is necessary to calculate either the relationship between relative

permeability and applied field, or between the function $B/\mu_0 M$ and flux density. These relationships are a function of both the frequency at which the test is carried out, and the maximum flux density.

The measured iron loss characteristics are useful for illustrating the increase in iron losses that will occur when the flux density waveforms include higher harmonic components. Flux density plots calculated from finite element solutions have shown that the flux density waveforms are nonsinusoidal and vary at different points over the rotor and stator cross-sections, as illustrated in Figs. 7.15 to 7.17. To determine the iron loss of a motor, it would be necessary to calculate the loss associated with each section of the motor that exhibits a different flux density characteristic. This is difficult in measurement but much easier to achieve using finite element analysis[7]. Even with such calculations, it is difficult to accurately relate the properties of a material as measured on sheet samples to those of the laminations, due to the effects of punching and annealing.

[7] The iron loss calculation in the SPEED software suite calculates the iron loss from the flux density waveform in each element of the cross-section. A modified Steinmetz equation is used to calculate the iron loss associated with each element, and then the total loss is determined by calculating a weighted average based on the cross-sectional area of each element. This method could be improved by calculating the dynamic hysteresis loop of each element from the flux density waveform, then using the same weighted average approach to determine the total loss.

Chapter 8

Conclusions

This thesis has examined methods of measurement of the magnetisation characteristics of switched-reluctance and interior permanent-magnet machines. The advantages and disadvantages of existing methods have been discussed, and alternative methods presented. A new finite element technique for calculating the magnetisation characteristics has been suggested, with the aim of eliminating many of the ambiguities surrounding existing analysis methods.

The thesis can be split into three sections: the magnetisation of the switched-reluctance machine; the magnetisation of the brushless permanent-magnet machine; and aspects of loss assessment in electrical steels, with emphasis on the effects of nonsinusoidal flux density profiles (which is particularly relevant to both switched-reluctance and permanent-magnet motors).

8.1. Summary of findings

8.1.1. Switched-reluctance Motor

Switched-reluctance Motor Measurements:

The established methods of measuring the static magnetisation curves and i-ψ loop of the switched-reluctance motor were presented and discussed in detail in Chapters 2 and 3. The measurement of the static magnetisation curves showed that the results are susceptible to hysteresis, resulting in different magnetisation curve trajectories for rising and falling currents. The common method of averaging the rising and falling current

trajectories has been proven to be erroneous; measured i-ψ loops will fall outside the boundaries set by such 'averaged' magnetisation curves.

The measurement of i-ψ loops on a dynamometer test rig was shown to be straightforward procedure. The successful measurement of the i-ψ loop requires accurate knowledge of the winding resistance of each phase under test.

Modelling of Switched-reluctance Motor:

The magnetisation characteristics of the SR motor have been modelled using an analytical motor design package, a circuit simulation model and finite element analysis. The magnetisation curves can be calculated from the analytical and finite element design packages, but must be specified in the case of the circuit simulation model. The magnetisation curves are used as an input for further design calculations for both the analytical design package and the circuit simulation model, so it is advisable to use measured magnetisation curve data as an input to the simulations (and to ensure that an adequate number of data points are presented). To include the hysteresis effects seen in the measured magnetisation curve data, a new method has been proposed, whereby both the rising and falling current trajectories are stored, and the trajectory used as the magnetisation curve data at each rotor position depends on the commutation angles of the current pulse.

Modelling of the i-ψ loops has been shown to be possible with all methods. The circuit simulation model and analytical design package showed limited accuracy at rotor positions between the commutation angles. Both methods rely on interpolation between magnetisation curve points to determine the flux-linkage at intermediate rotor positions. It has been shown that the accuracy of the modelled i-ψ loops can be improved by increasing the number of rotor positions for which the magnetisation curve data is stored.

The magnetisation curves and i-ψ loops calculated internally by the analytical design package PC-SRD and finite element software PC-FEA show discrepancies when compared with measurements. This is due, in part, to three-dimensional end-turn effects, which are ignored in the calculations. The results from Chapter 3 show that when the simulation data is adjusted to include end-turn effects, there is much closer correlation with measured data.

Mutual Coupling:

Chapter 4 presents a comprehensive discussion on the effects of mutual coupling on the magnetisation characteristics of the switched-reluctance motor. Mutual coupling effects have been determined from both static and dynamic tests, from static torque and i-ψ loop measurements respectively. From the measurements, it has been shown that the degree of mutual coupling is dependent on the polarity arrangement of the phase coils.

The most significant limitation of both the analytical design package and the circuit simulation model is that mutual coupling effects are not taken into consideration. Modelling of the mutual coupling effects was therefore carried out using 2D finite element analysis. By simulating the test motor with each possible phase polarity arrangement, the coil arrangement which provides maximum phase torque and maximum total torque can be predicted from the resulting i-ψ loops. The polarity of the mutual flux-linkage contributions from each phase can be predicted from the resulting i-ψ loops. The frozen permeability method has been proposed as a means of determining the mutual flux-linkage contributions from each phase, with any number of excited phases.

8.1.2. Permanent-magnet Motor

Permanent-magnet Motor Measurements:

The difficulties in determining the magnetisation characteristics of permanent-magnet motors were discussed in Chapters 2 and 3. The most common method of determining the static magnetisation curves is by addition of the flux-linkage due to current and a magnet flux-linkage determined from open-circuit tests. The assumption of constant magnet flux-linkage has been shown to be invalid.

An alternative method of measuring the magnetisation curves has been proposed, which uses a dynamic test rig to measure the total flux-linkage at each rotor position, using the same method that is employed when measuring the i-ψ loop. Test results have shown that the method is again susceptible to hysteresis effects; the hysteresis effects are dependent on the rate of change of current. A modification to the method, which used trapezoidal current waveforms in place of the common sinusoidal current control waveforms, was shown to result in single-valued magnetisation curves for each rotor position. The test results raise the question of whether the static magnetisation curves provide a suitable representation of the motor characteristics. To obtain single-valued magnetisation curves, it is necessary to eliminate the hysteresis effects caused by the changing current levels in the winding; however, such effects are present when the motor is operating under normal sinusoidal operation.

Measurement of the i-ψ loop of the IPM motor was also discussed in Chapter 3. The i-ψ loops of each phase can be measured separately and simultaneously to determine the effects of mutual coupling.

Methods for measurement of the synchronous reactances were presented in Chapter 5. It is not possible to measure the flux-linkage contribution from the permanent magnets directly under load conditions. An alternative method has been presented, which calculates the permanent-magnet flux by subtraction of the flux-linkage due to current

from the total flux-linkage determined in the magnetisation curve tests. The method shows that the permanent-magnet flux is not fixed at the open-circuit value, but varies under load conditions.

Modelling of Interior Permanent-magnet Motor:

The magnetisation curves of the IPM motor are easily determined from nonlinear two-dimensional finite element analysis. The magnetisation curves are once again modelled for each phase individually, ignoring all mutual coupling effects. The simulated curves also ignore hysteresis effects, which can be considerable for the case of the IPM motor, and are analogous to the magnetisation curves measured on the dynamometer test rig with squarewave current excitation.

The i-ψ loops of each phase of the IPM motor were also calculated using finite element simulations. The i-ψ loop from each phase can be calculated individually (to correspond to the static magnetisation curves), or with multiple excited phases to include the effects of mutual coupling between phases. It has been shown that for phases with unbalanced phase currents (and different numbers of turns per phase), the i-ψ loops for each phase should be translated into flux-MMF loops.

Chapter 5 presented methods for calculating the synchronous reactances and magnet flux-linkage of the IPM motor. Three methods of finite element based synchronous reactance calculation were discussed – calculation from the fundamental component of the airgap flux density distribution, calculations using the total nonlinear flux-linkage solutions, and calculations based on the frozen permeability method. The first two methods rely on the assumption of constant flux-linkage contribution from the permanent magnets, and so were discounted. Frozen permeability simulations have shown that the flux-linkage contribution from the permanent magnets varies under load conditions. The major drawback of the frozen permeability method is that the flux-linkage contributions cannot be directly measured under the same conditions as presented in the simulations, which makes verification of the method difficult.

The frozen permeability method was used to determine the influence of rotor design on the magnetisation characteristics of IPM motors. Simulation results have shown that by introducing rotor bridge sections, the fundamental flux density and total harmonic distortion of the IPM motor design studied are reduced. Using the frozen permeability method, the influence of rotor bridge design on the synchronous reactances has been examined. The frozen permeability simulation results show that the synchronous reactances are strongly influenced by the saturation levels of the bridge sections. The simulation results expand on work by previous authors, who were able to show the influence of the rotor bridge sections, but without the frozen permeability method could not determine the true extent of the variation in synchronous reactances.

8.1.3. Determination of properties of electrical sheet steel

Chapters 6 and 7 looked at the measurement of magnetisation curves and iron losses of electrical sheet steel, using a single sheet tester and Epstein square test frame. Comparison of the magnetisation curves showed discrepancies between the two sets of results, due to different leakage flux compensation methods and the need for calibration of the single sheet test rig to the Epstein square results. Whilst previous literature has recommended that a single calibration value can be used for the effective path length, the results have suggested that the effective path length is a function of both frequency and flux density, and that multiple values should be used depending on the measurement conditions.

All measurements have shown that while the relationship between flux density and iron loss is exponential in nature, the relationship between applied field and measured loss can be approximated by linear functions. The loss can be predicted to within 5% using linear approximations, at all fields over 600 A/m. At lower fields, the relationship between applied field and measured loss is nonlinear. This is the case even when there are minor

loops present in the resultant hysteresis loops (when the flux density waveform contains significant harmonic content).

Measurements of the iron loss associated with nonsinusoidal flux density distributions, where minor loops are present within the main hysteresis loop, have shown that the frequency of the minor hysteresis loop is dependent on the amplitude and phase positions of the higher harmonics present in the waveforms. The minor loop area depends not only on the amplitude and phase shift of the injected harmonics, but also on the frequency of the major hysteresis loop.

The complex relationships between iron loss and frequency, amplitude of applied field and harmonic content of the flux density waveform means that accurate analytical determination of the iron loss is difficult, especially in cases where minor hysteresis loops are present. The properties of a number of iron loss models were discussed in Chapter 6. In Chapter 7, it was proposed that the most accurate method of calculating the iron loss would be to determine the complete dynamic hysteresis loop from a given excitation waveform, or from a specified flux density output waveform (perhaps predicted from finite element simulations). To do this, the relationship between relative permeability and applied field, or between the function $B/\mu_0 M$ and flux density, must be determined. Such a complex nonlinear relationship cannot be characterised easily.

8.2. Future work

Many of the aims of the project, as outlined in Chapter 1, have been met. However, the outcomes of the work contained in the thesis suggest a number of areas of work that should be considered. These have been outlined below.

1. When measured, the magnetisation curves of the switched-reluctance motor were shown to exhibit hysteresis effects. To use measured magnetisation curves as an input to the analytical design software and the circuit simulation model, a different

data file had to be constructed for each commutation case (so that the correct magnetisation curve trajectory was used before and after the turn-off position). In the future, the models should be developed so that both the magnetisation curve trajectories for rising and falling currents are stored, and the correct magnetisation curve trajectories for each rotor position automatically selected according to the commutation angles specified by the user.

2. The magnetisation curves of both the switched-reluctance and interior permanent-magnet motor are two dimensional; that is the flux-linkage is considered a function of the current in the phase under test alone. As such, the magnetisation curves ignore all mutual coupling effects, which may be considerable. To accurately represent the magnetisation characteristics of both motor topologies, the curves should be a function of the current in all excited phases. To achieve this, a multi-dimensional magnetisation curve model should be developed.

3. The magnetisation curves of the interior permanent-magnet motor are static, and do not include time-varying effects caused by the variation of rate-of-change of current. Although single-valued 'static' magnetisation curves can be measured, using the method outlined in Chapters 2 and 3, these assume constant current and so do not accurately represent the magnetic characteristics of the motor under normal operation. This raises the question as to whether static magnetisation curves are, in fact, a suitable representation of the motor properties. The i-ψ loop has been shown to be an excellent method of calculating the electromagnetic torque, and is determined under the normal sinusoidal operating conditions of the motor. As such, models based on the i-ψ loop should be developed as an alterative.

4. Chapter 4 showed that the frozen permeability method can be used to calculate the mutual flux-linkages of the switched-reluctance motor. Using the results obtained from the frozen permeability simulations, it may be possible to adjust the current profiles of each phase to alter the extent of mutual coupling. If this is achieved, the

simulation results could be used as a basis for a current controller, where each phase has a unique current profile. The current profiling can be adjusted to produce the maximum torque per phase, or to balance the torque production in each phase, so as to reduce unbalanced magnetic pull.

5. Further investigation should be made into the verification of the frozen permeability method as a means of calculating the synchronous reactances and flux-linkage contribution from the permanent magnets in the interior permanent-magnet motor. The simulation results presented in Chapter 5 have suggested that the flux-linkage contribution from the permanent magnets varies under load conditions. The difficulties in measuring this flux contribution have been discussed in detail. Further work on the measurement methods suggested in Chapter 5 is needed, to reduce experimental error and to ensure that the controller used in the measurements is capable of maintaining the constant excitation required with minimum current ripple.

6. Iron loss measurements taken on the Epstein square and single sheet tester have been used to determine the calibration factor of the effective magnetic path length, to ensure correlation between both sets of results. The results have a shown a dependence of the magnetic path length on both the frequency and the level of saturation at each test point. Such comparison between the two test frames should be made for samples of other electrical steels, to verify these findings. By examination of results from samples of a number of different materials, it may be possible to determine a relationship between the effective magnetic path length and both the frequency and flux density.

7. The iron loss measurements taken in Chapter 7 have illustrated that the iron losses in electrical steels are a complex function of a number of parameters. Although the results have shown that the losses may be approximated by linear functions in terms of the applied field, the variation of loss with frequency is still undefined, especially in cases where there are minor loops present in the hysteresis loop. This leads to

the conclusion that the most suitable way of determining the iron losses would be from calculation of the dynamic hysteresis loop. Although this has been discussed briefly in Chapter 7, further work is required to develop a model that is capable of producing the dynamic hysteresis loop, given either the flux density waveform or applied field as an input function. Once a model that can accurately determine the dynamic hysteresis loops of electrical sheet steel strips has been produced, it must be expanded for use in the calculation of losses in electric motors. The complex geometry of motor cross-sections, coupled with the effects of lamination punching and annealing, must be taken into consideration.

References

[1] SA Nasar, "D.C.-Switched-reluctance Motor", *Proceedings of the IEE*, vol. 116 n. 6 June 1969 pp1048-1049

[2] BD Bedford, "Compatible permanent magnet or reluctance brushless motors and controlled switched circuits", US patent no. 3678352, July 1972

[3] BD Bedford, "Compatible brushless reluctance motors and controlled switch circuits", US patent no. 3679953, July 1972.

[4] JV Byrne, JB O'Dwyer, "Saturable variable reluctance machine simulation using exponential functions", *Proceedings of the International Conference on Stepping Motors and Systems*, Leeds July 1976, pp. 11-16.

[5] PJ Lawrenson, JM Stephenson, PT Blenkinsop, J Corda, NN Fulton, "Variable speed switched-reluctance motors", *IEE Proceedings*, vol. 127 pt. B n. 4, July 1980, pp. 253-265.

[6] WF Ray, PJ Lawrenson, RM Davis, JM Stephenson, NN Fulton, RJ Blake, "High performance switched-reluctance brushless drives", *IEEE Transactions*, vol. IA-22 no. 4, July/August 1986, pp. 722-730.

[7] B Mecrow, C Wiener, A Clothier, "The modelling of switched-reluctance machines with magnetically coupled windings", *IEEE Transactions on Industry Applications*, vol. 37 n. 6 November 2001 pp1675-1683

[8] TJE Miller, "Optimal design of switched-reluctance motors", *IEEE Transactions on Industrial Electronics*, vol. 49 n. 1, February 2002.

[9] NN Fulton, JM Stephenson, "A review of switched-reluctance machine design", *Proceedings of the International Conference on Electrical Machines*, September 1988, vol. 1 pp423-428.

[10] JR Hendershot, TJE Miller, "Design of Brushless Permanent-Magnet Motors", Oxford: Magna Physics Publishing and Clarendon Press, 1994.

[11] RM Saunders, RH Weakley, "Design of permanent-magnet alternators", *AIEE Transactions*, vol. 70, 1951, pp1578-1581.

[12] DE Plumb, "Permanent magnet rotor", United States Patent no. 2739253, March 20th 1956.

[13] Braun HJ, "Permanent magnet rotor", United States Patent no. 2836743, May 27th 1958.

[14] Westinghouse Electric Corporation, "Permanent magnet rotor", British Patent Specification 1147917, The Patent Office, January 19th 1968.

[15] KJ Binns, WR Barnard, "Novel design of self-starting synchronous motor", *Proceedings of the IEE*, vol. 118 n. 2, February 1971. pp369-372.

[16] KJ Binns, WR Barnard, MA Jabbar, "Hybrid permanent-magnet synchronous motors", *Proceedings of the IEE*, vol. 125 n. 3, March 1978 pp203-208.

[17] VB Honsinger, "Performance of polyphase permanent magnet machines", *IEEE Transactions on Power Apparatus and Systems*, vol. PAS-99 n. 4, July/August 1980 pp1510-1518.

[18] VB Honsinger, "The fields and parameters of interior type AC permanent magnet machines", *IEEE Transactions on Power Applications and Systems*, vol. PAS-101 n4, April 1982 pp867-875.

[19] JW Park, D-H Koo, J-M Kim, H-G Kim, "Improvement of control characteristics of interior permanent-magnet synchronous motor for electric vehicle", *IEEE Transactions on Industrial Applications*, vol. 37 n. 6 November/December 2001 pp1754-1760.

[20] _____, "Ferromagnetic materials, Vol. 2 (Ed. E.P. Wohlfarth)", Amsterdam: North-Holland Publishing Company, 1980.

[21] JMD Coey, "Rare-earth permanent magnets", Oxford: Clarendon Press, 1996.

[22] _____, "Handbook of advanced magnetic materials, Vol. 3: Advanced magnetic materials: Fabrication and processing (Ed. Yi Liu, DJ Sellmyer, D Shindo)", New York: Springer.

[23] HC Lovatt, JM Stephenson, "Measurement of magnetisation characteristics of switched-reluctance motors", *International Conference on Electrical Machines ICEM 1992*, pp465-469.

[24] C Cossar, TJE Miller, "Electromagnetic testing of switched-reluctance motors", *International Conference on Electrical Machines ICEM 1992*, vol. 2 pp470-474.

[25] N Ertugrul, A Cheok, "Automated method for determination of magnetisation characteristics of switched-reluctance machines", *Australasian Universities' Power Engineering Conference AUPEC 1999*, Darwin, 26-69th September 1999, pp17-22.

[26] DWJ Pulle, "New database for switched-reluctance drive simulation", *IEE Proceedings-B*, vol. 138 n. 6 November 1991.

[27] DG Manzer, M Varghese, JS Thorp, "Variable reluctance motor characterisation", *IEEE Transactions on Industry Applications*, vol. 36 n. 1 February 1989.

[28] JM Stephenson, J Corda, "Computation of torque and current in doubly salient reluctance motors from nonlinear magnetization data", *Proceedings of the Institution of Electrical Engineers*, vol. 126 n. 5 May 1979 pp393-396.

[29] TJE Miller, M McGilp, "Nonlinear theory of the switched-reluctance motor for rapid computer-aided design", *IEE Proceedings B*, vol. 137 n. 6, November 1990, pp337-346.

[30] JA Walker, D Dorrell, C Cossar, "Flux-linkage calculation in permanent-magnet motors using the *frozen permeabilities* method", *IEEE Transactions on Magnetics*, vol. 41 n. 10 October 2005 pp3946-3948.

[31] TJE Miller, JA Walker, C Cossar, "Measurement and application of flux-linkage and inductance in a permanent-magnet synchronous machine", *Power Electronics Machines and Drives Conference PEMD 2004*, Edinburgh, 31 March – 2 April 2004, vol. 2 pp674-678.

[32] TJE Miller, M McGilp, M Olaru, "Finite elements applied to synchronous and switched-reluctance motors", *IEE Seminar on current trends in the use of finite elements (FE) in electromechanical analysis and design*, Friday 14 January 2000, London.

[33] DA Staton, RP Deodhar, WL Soong, TJE Miller, "Torque prediction using the flux-MMF diagram in AC, DC and reluctance motors", *IEEE Transactions on Industry Applications*, vol. 32, n. 1 January/ February 1996, pp180-188.

[34] RP Deodhar, "The flux-MMF diagram technique and its applications in analysis and comparative evaluation of electrical machines", PhD Thesis, University of Glasgow October 1996.

[35] DA Staton, WL Soong, C Cossar, TJE Miller, "Unified theory of torque production in AC, DC and reluctance motors", *Conference record of the IEEE Industry Applications Society Annual Meeting 1994*, vol. 1 pp149-156.

[36] N Bianchi, S Bolognani, "Magnetic models of saturated interior permanent magnet motors based on finite element analysis", *Proceedings of the 33rd IEEE Industry Applications Society Annual Meeting*, 12-15 October 1998 , vol. 1 pp27-34.

[37] TJE Miller, M McGilp, PC-SRD Version 8.5 User's Manual, SPEED Laboratory, 25th July 2004.

[38] AM Michaelides, C Pollock, "Effect of end core flux on the performance of the switched-reluctance motor", *IEE Proceedings on Electrical Power Applications*, vol. 141 n. 6 November 1994 pp308-316.

[39] S Williamson, AA Sharkh, "Three dimensional effects in λ/i diagrams for switched-reluctance motors", *International Conference on Electrical Machines ICEM 1992*, vol. 2 pp489-493.

[40] TJE Miller, M McGilp, "SPEED's Electric Motors", SPEED Laboratory, 2005.

[41] TJE Miller, M Popescu, C Cossar, M McGilp, JA Walker, "Calculating the interior permanent-magnet motor", *IEEE International Electric Machines and Drives Conference IEMDC 2003*, 1-4 June 2003, vol. 2 pp1181-1187.

[42] AM Michaelides, C Pollock, "Modelling and design of switched-reluctance motors with two phases simultaneously excited", *IEE Proceedings on Electrical Power Applications*, vol. 143 n. 5 September 1996 pp361-370.

[43] PC Kjaer, "High Performance Control of Switched-reluctance Motors", Doctoral Thesis, University of Glasgow, Glasgow, July 1997.

[44] D Panda, V Ramanarayanan, "Effect of mutual inductance on steady-state performance and position estimation of switched-reluctance motor drive", *Conference Record of the IEEE Industry Applications Society Annual Meeting 1999*, 3-7 October 1999, vol. 4 pp2227-2234.

[45] AK Jain, N Mohan, "Modelling and experimental characterisation of SRMs for simultaneous two phase excitation", *29th Annual conference of the IEEE Industrial Applications Society IECON 2003*, 2-6 November 2003, vol. 2 pp1027-1032.

[46] PP de Paula, WM da Silva, JR Cardoso, SI Nabeta, "Assessment of the influences of the mutual inductances on switched-reluctance machine performance", *IEEE International Electric Machines and Drives Conference IEMDC 2003*, 1-4 June 2003, vol. 3 pp1732-1738.

[47] S Cao, KJ Tseng, "Evaluation of neighbouring phase coupling effects of switched-reluctance motors with dynamic modelling approach", *Proceedings of the Third International Power electronics and motion control conference PIEMC 2000*, 15-18 August 2000, vol. 2 pp881-886.

[48] I Husain, M Ehsani, "Rotor position sensing in switched-reluctance motor drives by measuring mutually induced voltages", *IEEE Transactions on Industry Applications*, vol. 30 n. 32 pp665-67, May/June 1994.

[49] HP Chi, TJ Liang, CL Chu, JF Chen, MT Chang, "Improved mutual voltage technique of indirect rotor position sensing in switched-reluctance motor", *IEEE 33rd Annual Power Electronics Specialist Conference PESC 2002*, 23-27 June 2002, vol. 1 pp271-275.

[50] J Corda, S Masic, JM Stephenson, "Computation and experimental determination of running torque waveforms in switched-reluctance motors", *IEE Proceedings B*, vol. 140, n. 6, November 1993 pp387-392.

[51] RH Park, "Two reaction theory of synchronous machines: Part 2", *Transactions of the American Institute of Electrical Engineers*, vol. 33 n. 22 June 1933 pp 352-355.

[52] B Adkins, "The general theory of electrical machines", London: Chapman and Hall, 1957.

[53] MJ Kamper, AF Volschenk, "Effect of rotor dimensions and cross magnetisation on L_d and L_q inductances of reluctance synchronous machines with cageless flux barrier rotor", *IEE Proceedings – Electrical Power Applications,* vol. 141 n4. July 1994 pp213-220.

[54] PH Mellor, FB Chaaban, KJ Binns, "Estimation of parameters and performance of rare-earth permanent-magnet motors avoiding measurement of load angle", *IEE Proc-B*, vol. 138 n. 6 November 1991, pp322-330.

[55] TJE Miller, "Methods for testing permanent magnet polyphase AC motors", *IEEE Industry Applications Society Winter Meeting 1981*, pp494-499.

[56] P Zhou, MA Rahman, MA Jabbar, "Field circuit analysis of permanent magnet synchronous motors", *IEEE Transactions on Magnetics*, vol. 30 n.4 July 1994.

[57] CV Jones, "The Unified Theory of Electrical Machines", London: Butterworths 1967.

[58] JC Prescott, AK El-Kharashi, "A method of measuring self-inductances applicable to large electrical machines", *Proceedings of the IEE*, vol. 106 Part A April 1959, pp169-173.

[59] JA Walker, C Cossar, TJE Miller, "Simulation and analysis of magnetisation characteristics of interior permanent magnet motors", *Acta Polytechnica Journal of Advanced Engineering*, vol. 45 n. 4/2005 pp25-32.

[60] B Štumberger, G Štumberger, D Dolinar, A Hamler, M Trlep, "Evaluation of saturation and cross-magnetisation effects in interior permanent-magnet synchronous motor", *IEEE Transactions on Industry Applications*, vol. 39 n. 5 September 2003 pp1264-1271.

[61] HP Nee, L Lefevre, P Thelin, J Soulard, "Determination of d and q reactances of permanent-magnet synchronous motors without measurement of the rotor position", *IEEE Transactions on Industry Applications*, vol.36 n. 5 September 2000 pp 1330-1335.

[62] JR Hendershot, TJE Miller, "Design of Brushless Permanent-Magnet Motors", Oxford: Magna Physics Publishing and Clarendon Press, 1994.

[63] MW Degner, R Van Maaren, A Fahim, DW Novotny, RD Lorenz, CD Syverson, "A rotor lamination design for surface permanent magnet retention at high speeds", *IEEE Transactions on Industry Applications*, vol. 32 n. 2, March/April 1996 pp380-385.

[64] ECF Lovelace, "Optimisation of a magnetically saturable interior permanent-magnet synchronous machine drive", PhD Thesis, Massachusetts Institute of Technology, June 2000.

[65] K-J Lee, S Kim , S-Y Lim, J Lee, "Bridge design of interior permanent magnet motor for hybrid electric vehicle", *International Journal of Applied Electromagnetics and Mechanics*, vol. 19 n. 1-4, 2000 pp601-606.

[66] www.ee.surrey.ac.uk/Workshop/advice/coils/power_loss.html.

[67] MR Udayagiri, TS Lipo, "Simulation of inverter fed induction motors including core losses", *IEEE Industrial Electronics Society Annual Conference IECON 1989*, vol. 1 pp232-237.

[68] H Akçay, DG Ece, "Modelling of hysteresis and power losses in transformer laminations", *IEEE Transactions on Power Delivery*, vol. 18 n. 2 April 2003 pp487-492.

[69] E Ritchie, "Iron losses and properties of soft magnetic materials for electrical machines", Note to MSc Students, Institute of Energy Technology, University of Aalborg, Denmark

[70] RD Findlay, N Stranges, DK MacKay, "Losses due to rotational flux in three phase induction motors", *IEEE Transactions on Energy Conversion*, vol. 9 n. 3 September 1994

[71] JE Britain JE, "A Steinmetz contribution to the AC power revolution", *Proceedings of the IEEE*, vol. 72 n. 2 February 1984 pp 196-221.

[72] GR Slemon, X Liu, "Core losses in permanent magnet motors", *IEEE Transactions on Magnetics*, vol. 26 n. 5 September 1990 pp 1653-1655.

[73] Y Chen, P Pillay, "An improved formulation for lamination core loss calculation in machines operating with high frequency and high flux density excitation",

Conference record of the IEEE Industry Applications Society Annual Meeting, 13-18 October 2002, vol. 2 pp 759-766.

[74] K Atallah, D Howe, "Calculation of the rotational power loss in electrical steel laminations from measured H and B", *IEEE Transactions on Magnetics,* vol. 29 n. 6 November 1993.

[75] CD Graham Jr., "Physical origin of losses in conducting ferromagnetic materials (invited)", *Journal of Applied Physics*, vol. 53 n. 11 November 1982 pp8276-8280.

[76] J Reinert, A Brockmeyer, RWAA De Doncker, "Calculation of losses in ferro- and ferrimagnetic materials based on the modified Steinmetz equation", *IEEE Transactions on Industry Applications*, vol. 37 n. 4 July 2001.

[77] J Li, T Abdallah, CR Sullivan, "Improved calculation of core loss with nonsinusoidal waveforms", *Conference record of the 36th IEEE Industry Applications Society Annual Meeting*, 30 September – 4 October 2001 vol. 4 pp2203-2210.

[78] K Venkatachalan, CR Sullivan, T Abdallah, H Tacca, "Accurate prediction of ferrite core loss with nonsinusoidal waveforms using only Steinmetz parameters", *Proceedings of the 2002 IEEE Computers in Power Electronics (COMPEL) Workshop*, 3-4 June 2002 pp36-41.

[79] K Atallah, ZQ Zhu, D Howe, "An improved method for predicting iron losses in brushless permanent magnet DC drives", *IEEE Transactions on Magnetics,* vol. 28 n. 5 September 1992.

[80] MA Mueller, S Williamson, TJ Flack, K Atallah, B. Baholo, D. Howe, PH Mellor, "Calculation of iron losses from time-stepped finite-element models of cage induction machines", *7th International Conference on Electrical Machines and Drives,* 11-13 September 1995 pp88-92.

[81] F Preisach, "Über die magnetische Nachwirkung", *Zeitschrift für Physik*, vol. 94 n. 5 2nd April 1935

[82] ID Mayergoyz, "Dynamic Preisach model of hysteresis", *IEEE Transactions on Magnetics*, vol. 24 n. 6 November 1998 pp2925-2927

[83] D Jiles, D Atherton, "Ferromagnetic hysteresis", *IEEE Transactions on Magnetics*, vol. 19 n. 5 September 1983 pp2183-2185.

[84] DC Jiles, DL Atherton, "Theory of ferromagnetic hysteresis (invited)", *Journal of Applied Physics*, vol. 55 n. 6 15th March 1984 pp2115-2120.

[85] D Jiles, "Introduction to magnetism and magnetic materials 1st Ed." Chapman and Hall, London 1991 ISBN 0-412-38640-5.

[86] KH Carpenter, "A differential equation approach to minor loops in the Jiles-Atherton hysteresis model", *IEEE Transactions on Magnetics*, vol. 27 n. 6 November 1991 pp 4404-4406.

[87] D Lederer, H Igarashi, A Kost, T Honma, "On the parameter identification and application of the Jiles-Atherton hysteresis model for numerical modelling of measured characteristics", *IEEE Transactions on Magnetics*, vol. 35 n. 3 May 1999 pp1211-1214.

[88] CE Lin, JB Wei, CL Huang, CJ Huang, "A new method for representation of hysteresis loops", *IEEE Transactions on Power Delivery*, vol. 4 n. 1 January 1989 pp413-420.

[89] VJ Thottuvelil, TG Wilson, HA Owen Jr., "High-frequency measurement techniques for magnetic cores", *IEEE Transactions on Power Electronics*, vol. 5 n. 1 January 1990 pp41-53.

[90] WR Wieserman, GE Schwarze, JM Niedra, "High frequency, high temperature specific core loss and dynamic B-H loop characteristics of soft magnetic alloys", *Proceedings of the 25th Intersociety Energy Conversion Engineering Conference*, 12 – 17 August 1990, vol. 1 pp397-402.

[91] E Carminati, A Ferrero, "A virtual instrument for the measurement of the characteristics of magnetic materials", *Proceedings of the 9th IEEE Instrumentation and Measurement Technology Conference*, 12 – 14 May 1992, pp346-349.

[92] S-C Wang, C-L Chen, "PC-based apparatus for characterising high frequency magnetic cores", *IEE Proceedings Science and Measurement Technology*, vol. 146 n. 6 November 1999 pp304-308.

[93] CE Lin, J-B Wei, C-L Huang, C-J Huang, "A new model for transformer saturation characteristics by including hysteresis loops", *IEEE Transactions on Magnetics*, vol. 25 n. 3 May 1989 pp2706-2712.

[94] S Prusty, MVS Rao, "A novel approach for predetermination of magnetisation characteristics of transformers including hysteresis", *IEEE Transactions on Magnetics*, vol. 20 n. 4 July 1984 pp607-611.

[95] RM Del Vecchio, "The inclusion of hysteresis processes in a special class of electromagnetic finite element calculations", *IEEE Transactions on Magnetics*, vol. 18 n. 1 January 1982 pp275-284.

[96] Crown Audio Incorporated, "MA-5002VZ Power Amplifier Operation Manual", available from http://www.crownaudio.com/pdf/amps/128313.pdf.

[97] R Post, "Iron losses in electrical machines supplied by power electronics", Preliminary PhD Thesis, Institute of Energy Technology, University of Aalborg Denmark, 2000.

[98] ASTM Standard A343-97, "Standard test method for AC magnetic properties of materials at power frequencies using 25cm Epstein square", ASTM International 1997.

[99] IEC Standard 404 Magnetic Materials Part 2, "Methods of measurement of magnetic, electrical and physical properties of magnetic sheet and strip", IEC 1978.

[100] ASTM Standard A804/A804M-99, "Standard test methods for alternating-current magnetic properties of materials at power frequencies using sheet-type test specimens", ASTM International 1999.

[101] IEC Standard 60404 Magnetic Materials Part 3, "Methods of measurement of the magnetic properties of magnetic sheet and strip by means of a single sheet tester", IEC 2002.

[102] AEG Instruction Manual "Elektroblech-Meßeinrichtung mit 25-cm-Epsteinrahmen" AEG GmbH 1962 (in German).

[103] T Nakata, Y Ishihara, M Nakaji, T Todaka, "Comparison between the H-coil method and the magnetising current method for the single sheet tester", *Journal of Magnetism and Magnetic Materials*, Issue 215-216 2000 pp607-610.

[104] J Sievert, "Recent advances in the one- and two-dimensional magnetic measurement technique for electrical sheet steel", *IEEE Transactions on Magnetics*, vol. 26 n. 5 September 1990 pp2553-2558.

[105] ASTM Standard A927/ A927M-99, "Standard test method for alternating-current magnetic properties of toroidal core specimens using the voltmeter-ammeter-wattmeter method", ASTM International 1999.

[106] IEC Standard 60404 Magnetic Materials Part 6, "Methods of measurement of the magnetic properties of magnetically soft metallic and powder materials at frequencies in the range 20 Hz to 20 kHz by the use of ring specimens", IEC 2003.

[107] AC Worley, JM Stephenson, "Measurement and explanation of B/H curves in laminations with impressed flux waveforms over a wide range of frequencies", *International Conference on Electrical Machines ICEM 1992*, vol. 3 pp1177-1181.

[108] AC Worley, JM Stephenson, "Eddy current behaviour in saturating laminations with impressed flux waveforms", *Sixth International Conference on Electrical Machines and Drives*, 8-10 September 1993 pp229-233.

[109] J Sievert, H Ahlers, P Brosien, M Cundeva, J Luedke, "Relationship of Epstein to SST Results for grain-orientated steel", published in "Non-linear electromagnetic systems ISEM '99", IOS Press 2000, ISBN 1-58603-024-8.

[110] M De Wulf, D Makaveev, Y Houbaert, J Melkebeek, "Design and calibration aspects of small single sheet testers", *Journal of Magnetism and Magnetic Materials*, vol. 254-255 January 2003 pp70-72.

[111] R Schiferl, "Design considerations for salient pole permanent magnet synchronous machines in variable speed drive applications", PhD Thesis, University of Wisconsin, Madison USA, 1987.

Appendix 1

Details of Test Motors

Three test motors have been used in this thesis; 2 line-start interior permanent-magnet motors and one switched-reluctance motor. The cross-section of each motor is given below, along with the design specifications.

A1.1. IPM test motor 1

IPM test motor 1 was produced by Electrolux Compressors, Italy. The design is based on a motor currently produced by the company; the rotor was modified to include permanent-magnet pole pieces. Two prototype rotors were produced; one with a squirrel cage to enable line-start operation and one without. The motor specification is given in Table A1.1. The motor cross-section is shown in Fig. A1.1.

Parameter	Value
Rated voltage	220V, 50Hz
Stack length	39 mm
Lamination stacking factor	0.97
Shaft radius	9.5 mm
Rotor outside radius	31.72 mm
Airgap width	0.28 mm
Stator outside radius	64 mm
Number of poles	2
Number of stator slots	24
Number of rotor bars	28
Rotor bridge thickness	Open slots
Number of phases	Split-phase
Winding type	Custom sine-wound
Magnet arc radius	160 °mech
Magnet type	Ferrite
Lamination material	M340-50E

Table A1.1. Design specification of IPM test motor 1.

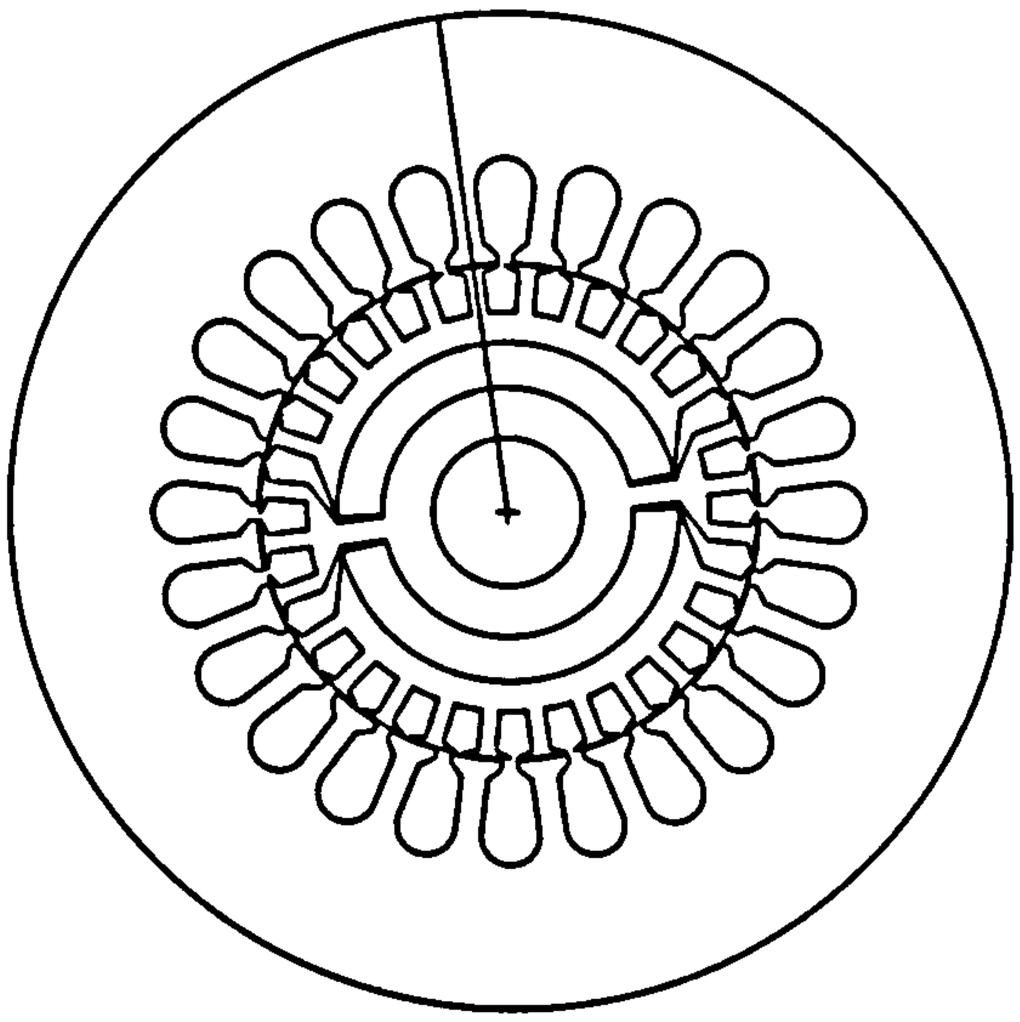

Fig. A1.1. Cross-section of IPM test motor 1.

A1.2. IPM test motor 2

IPM test motor 2 is a commercial motor produced by Rockwell Automation. It was chosen as a test motor because, unlike IPM test motor 1, it has closed rotor slots. In the comparison tests of Chapter 5, the thickness of the rotor bridges is modified. In the original design, the bridge thickness is 0.51 mm. The design specification is given in Table A1.2. The motor cross-section is shown in Fig. A1.2. Details of the lamination material can be found in Ref. [111].

Parameter	Value
Rated voltage	230V, 60Hz
Stack length	95.25 mm
Lamination stacking factor	0.93
Shaft radius	15.75 mm
Rotor outside radius	46.4 mm
Airgap width	0.32 mm
Stator outside radius	77.22 mm
Number of poles	4
Number of stator slots	36
Number of rotor bars	44
Rotor bridge thickness	0.51 mm
Number of phases	3
Winding type	Lap
Magnet width	32.31 mm
Magnet type	Samarium cobalt

Table A1.2. Design specification of IPM test motor 2.

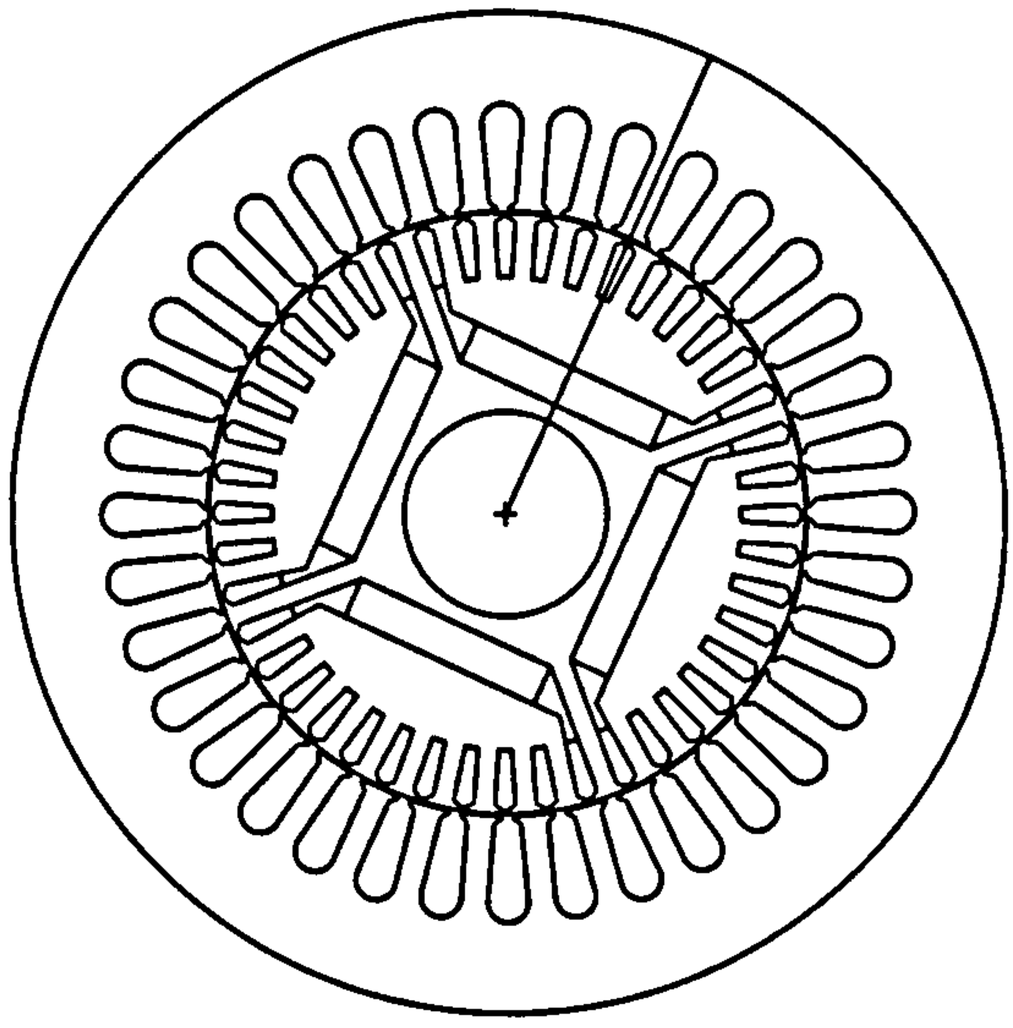

Fig. A1.2. Cross-section of IPM test motor 2.

A1.3. SR test motor 1.

The switched-reluctance test motor used in the thesis was designed by Lucas Aerospace and the SPEED Laboratory, for use in aeroplane landing gear. The motor was chosen as it has been extensively tested in the SPEED Laboratory and both the mechanical and electrical properties of the motor are well known. The motor cross-section is shown in Fig. A1.3. The design specification of the motor is given in Table A1.3.

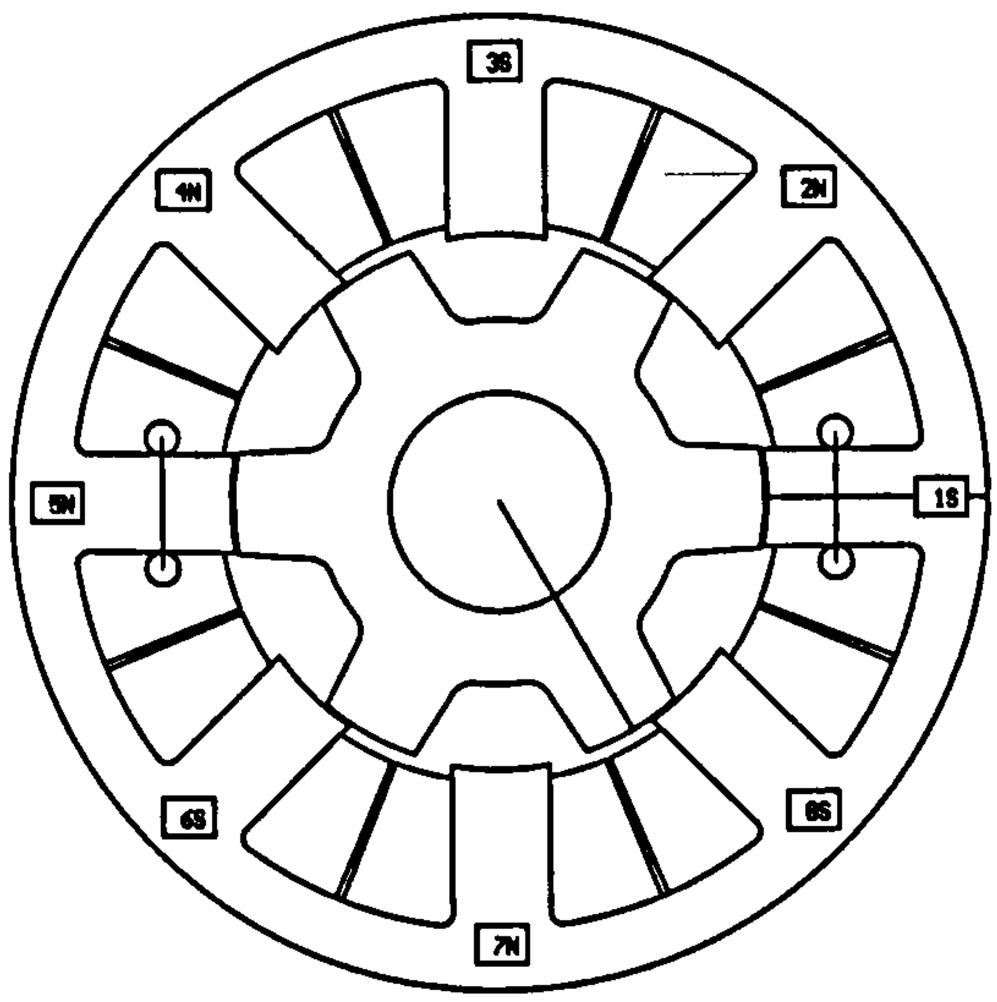

Fig. A1.3. Cross-section of SR test motor 1.

Parameter	Value
Rated voltage	100V, 50Hz
Stack length	70 mm
Lamination stacking factor	0.97
Shaft radius	9 mm
Rotor outside radius	21.8 mm
Rotor back iron thickness	6 mm
Airgap width	0.2 mm
Stator outside radius	40 mm
Stator back iron thickness	5 mm
Number of stator poles	8
Number of rotor poles	6
Number of phases	4
Winding type	Fully pitched
Lamination material	Rotalloy 0.35mm

Table A1.3. Design specification of SR test motor 1.

Appendix 2

Simulink Model of Switched-Reluctance Test Motor

A model of the SR motor was developed in Simulink to help establish whether the error lay in the simulation or in the measurements. A schematic of the Simulink model is shown in Fig. A2.1. The model works by determining the current at a given point from a look-up table, constructed using data taken from measured static magnetisation curves. The voltage drop due to the phase resistance is then calculated and the integral of the resulting voltage is computed, to give a new value of flux-linkage to be passed into the look-up table. The duration of the simulation, the supply voltage and turn-on and turn-off angles are specified by the user in an input file.

From initial simulations, the i-ψ loop calculated by the Simulink model showed much greater current levels than in the measured loop. The phase current is calculated in Simulink using a method to similar to that of the PC-SRD model; the currents are calculated from information on the rotor position and the flux-linkage (which in turn is dependent on the input voltage waveform). Thus, to reduce the currents produced, the supply voltage had to be decreased in the Simulink model. A voltage drop of 2 V was found to be sufficient. It would not be uncommon to see a voltage drop of this magnitude across the devices controlling the motor. Indeed, examination of the voltage waveforms used in the simulation show the voltage amplitude decreases over the duration of the pulse, and that the peak amplitude is slightly less than 100 V.

Although reducing the amplitude of the voltage brought the peak phase current in line with measured levels, it also had the effect of reducing the flux-linkage levels. If the flux-linkage values are too low, it suggests that the current is not flowing for a sufficient length of time to allow the flux-linkage to build. All simulations were run with the same

settings as had been used in the controller during testing (turn-on = 35°, turn-off = 50°). However, when the Flux-MMF loop for the measured data was plotted alongside the measured magnetisation curves, the point of commutation appeared to be greater than 50°. Increasing the turn-off angle in the simulations to 50.5° increased the flux-linkage values to the desired level.

The i-ψ loop predicted by the Simulink model is given in Fig. A2.2, with the measured i-ψ loop and magnetisation curves given for reference. There was good agreement in the torque levels determined from the i-ψ loops computed with the above adjustments. However, the simulated loops still differed from the measured test points. As in the PC-SRD simulated loop, the Simulink loops are rippled until the turn-off angle is reached. The rippling in the loops once again occurs because the current is limited to a set value at the points that lie on the magnetisation curves. Between the magnetisation curves, however, the Simulink model uses linear interpolation to calculate the phase current (in reality, the variation of current with respect to flux-linkage and rotor position is nonlinear). As with the PC-SRD model, the accuracy could be increased by measuring the magnetisation curves at smaller rotor position intervals (thus increasing the amount of data stored in the look-up table).

The design of the model causes some anomalies to arise that limit its usefulness. The most important of these is that the flux-linkage waveform always returns to zero, regardless of the value of phase resistance used. The resistance value to be used in the simulations must be estimated from the original measured test data.

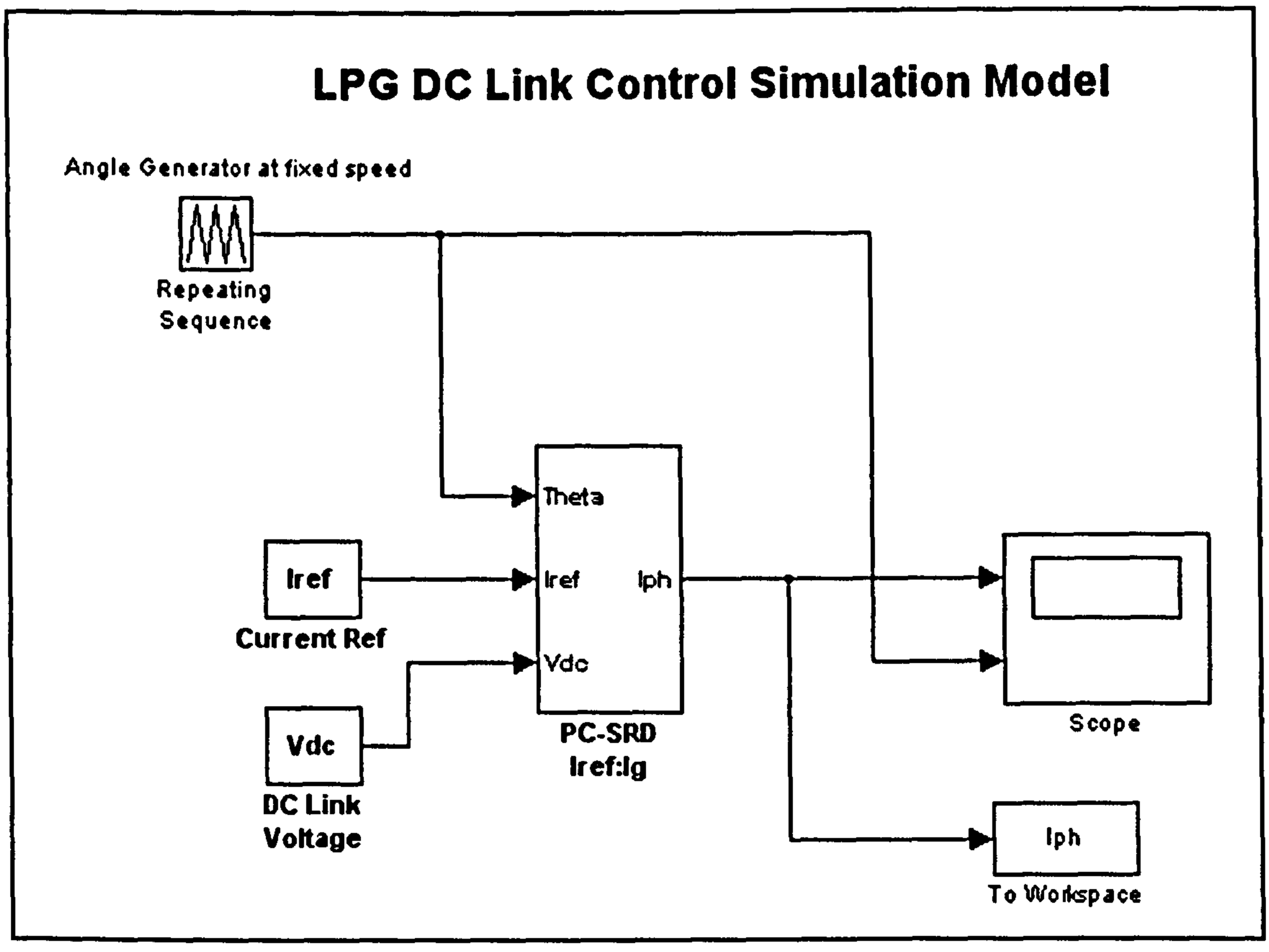

Level 1

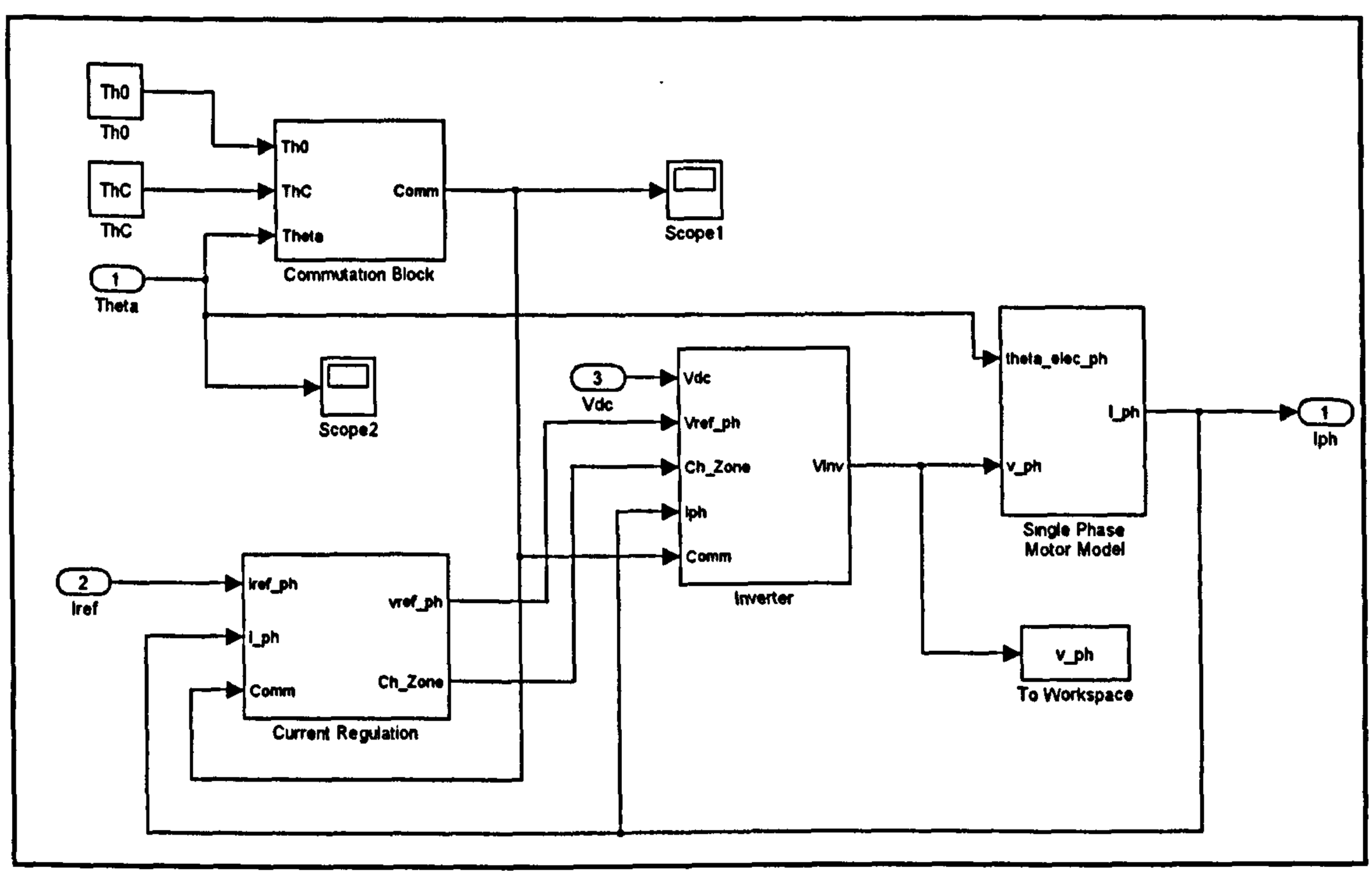

Level 2

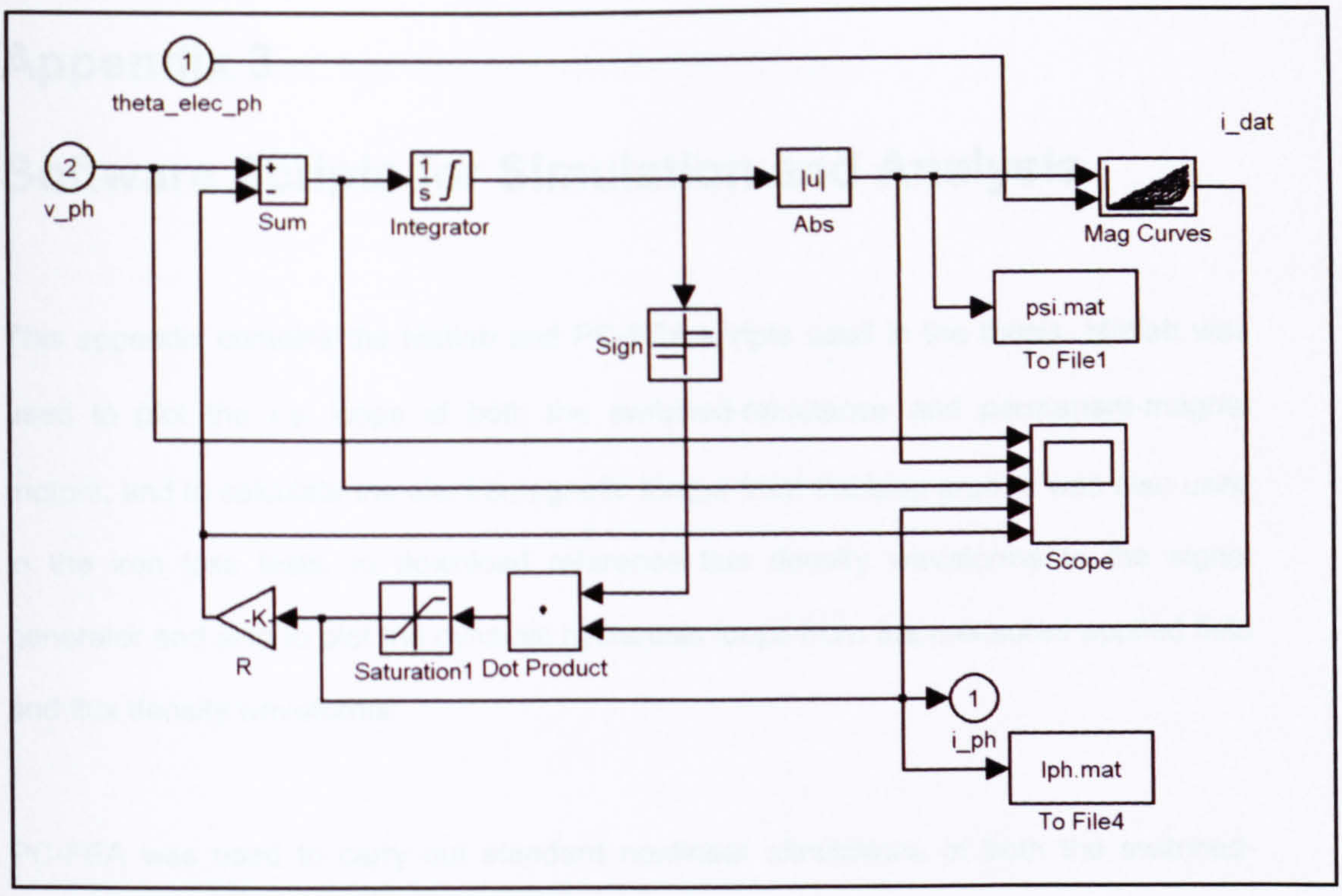

Level 3

Fig. A2.1. Schematic of Simulink model showing nested levels of model

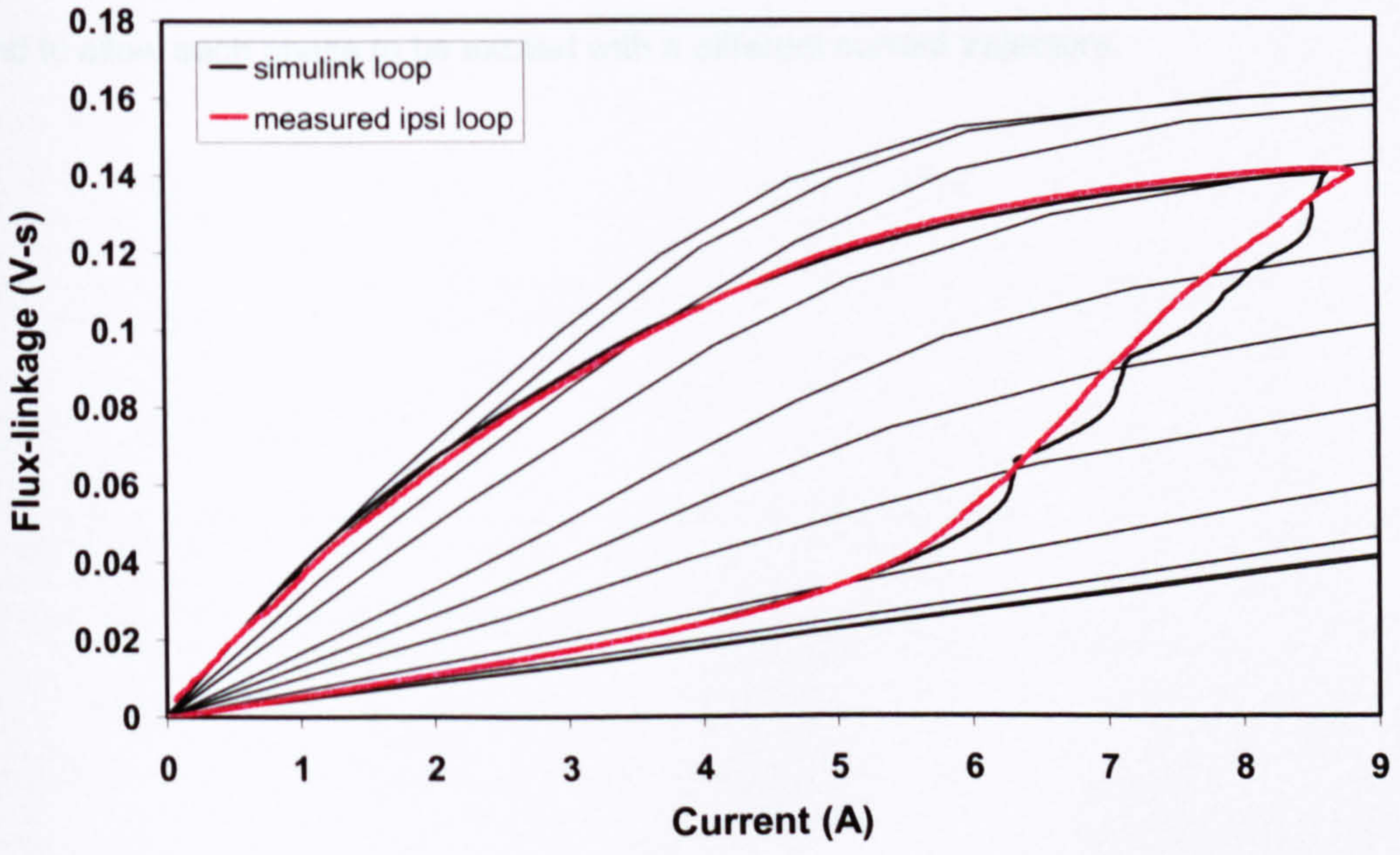

Fig. A2.2. Simulink-generated and measured *i*-ψ loops.

Appendix 3

Software Scripts for Simulation and Analysis

This appendix contains the Matlab and PC-FEA scripts used in the thesis. Matlab was used to plot the i-ψ loops of both the switched-reluctance and permanent-magnet motors, and to calculate the electromagnetic torque from the loop area. It was also used in the iron loss tests, to download reference flux density waveforms to the signal generator and also to plot the dynamic hysteresis loops from the measured applied field and flux density waveforms.

PC-FEA was used to carry out standard nonlinear simulations of both the switched-reluctance and permanent-magnet motors, using the scripting routines automatically generated by the SPEED Finite Element GoFER. The standard finite element routines were modified to enable frozen permeability simulations. In addition, the switched-reluctance motor script was modified to enable the input of specific current waveforms, and to allow each phase to be excited with a different current trajectory.

A3.1. Matlab script for SR motor *i-ψ* loop

```
% calculation of flux MMF diagram for switched-reluctance motor
% comparison between measured data for 1st test and pc-srd results
% turn-on angle = 35 degrees
% turn-off angle = 50 degrees
% speed = 1500

%define some constants needed for each input file
deltaT = 1E-6;                          % time difference between each sample
curr = 'tp11ph_curr.dat'                % data input file
volt = 'tp11ph_volt.dat'
R = 1.9                                 % resistance
Nturns = 70                             % number of turns
c_scale = 200                           % scaling factor for current
v_scale = 20                            % scaling factor for voltage
c_offset = 1.5                          % current offset
v_offset = 3.5                          % voltage offset
ph = 4                                  % number of phases
Nr = 6                                   % number of rotor poles

% file is comma delimited. miss out file header
c_data = dlmread(curr,',',[4250 0 7650 1]);    % read in data values
v_data = dlmread(volt,',',[4250 0 7650 1]);
time  = c_data(:,1);                            % time in seconds
voltage = v_data(:,2)*v_scale;                  % voltage
current = c_data(:,2)*c_scale;                  % current
voltage = voltage + v_offset;
current = current - c_offset;
f_voltage = sgolayfilt(voltage,1,101);
f_current = sgolayfilt(current,1,101);

iR = f_current*R;
[m n] = size(voltage);

accumulate = zeros(m,1);                 % generate new array with same no.
accumulate(1) = 0;                       % set initial value for flux-linkage
for j = 2:m
accumulate(j) = accumulate(j-1)+(((f_voltage(j)-iR(j))*deltaT));
end

figure

plot(f_current,accumulate);              % plot i-psi diagram
xlabel('current');
ylabel('flux-linkage');
inductance = (accumulate(500)-accumulate(100))/(current(500)-current(100))
title(['inductance = 'num2str(inductance)])     % display inductance value


flux_1 = accumulate/Nturns
MMF_1 = f_current*Nturns
figure
plot(MMF_1,flux_1,'m--');                % plot flux-MMF diagram
xlabel('MMF');
ylabel('flux');
title('Flux-MMF diagram for test point 1');
a_1 = polyarea(MMF_1,flux_1);       % calculate area enclosed (torque)
x_1 = max(MMF_1);
y_1 = max(flux_1);
torque_1 = (ph*Nr*a_1)/(2*pi);
text(0.1*x_1,0.9*y_1,['measured torque =' num2str(torque_1)])
% display torque value
hold on

% calculation of flux MMF diagram for switched-reluctance motor - pc-srd results
%define some constants needed for each input file
fin2 = 'pcsrd_t1.dat';                                  % data input file
data_2 = dlmread(fin2,' ',[1 0 219 2]);                 % read in data values
angle_2 = data_2(:,1);                                  % angle in mechanical degrees
current_2 = data_2(:,2);                                % current
flux_link = data_2(:,3);                                % flux-linkage
flux_2 = flux_link/Nturns;
MMF_2 = current_2*Nturns;
```

```
plot(MMF_2,flux_2);                                    % plot flux-MMF diagram
xlabel('MMF');
ylabel('flux');
a_2 = polyarea(MMF_2,flux_2);                          % calculate area enclosed
(torque)
x_2 = max(MMF_2);
y_2 = max(flux_2);
torque_2 = (ph*Nr*a_2)/(2*pi);
text(0.1*x_1,0.95*y_1,['pc-srd torque =' num2str(torque_2)])
% display torque value

plot(angle_2,current_2);
xlabel('angle (mech. deg.)');
ylabel('current');
title('pc-srd current waveform for test point 1');
time = (0:deltaT:(deltaT*(m-1)))';
plot(time,f_current);
xlabel('time');
ylabel('current');
title('measured current waveform for test point 1');
max_measured_I = max(f_current)
max_measured_psi = max(accumulate)
measured_torque = max(torque_1)
measured_loop_area = a_1
max_pc_srd_I = max(current_2)
max_pc_srd_psi = max(flux_link)
pc_srd_torque = max(torque_2)
pc_srd_loop_area = a_2
```

A3.2. Matlab script for IPM motor *i-ψ* loop

```
% electrolux IPM motor
% ipsi loop for phase 1 at 500 rpm, 167V DC, 20 ms/div.
% P control

%define some constants needed for each input file
deltaT = 10E-8;                 % time difference between each sample
volt = 'v_main.txt';            % data taken from oscilloscope
curr = 'i_main.txt';
R = 19.12                       % resistance adjusted for t = 24 degrees
Nturns = 970                    % number of turns
c_scale = 100                   % scaling factor for current
v_scale = 1                     % scaling factor for voltage
ph = 1                          % calculate each phase separately
Nr = 2                          % number of rotor poles

% file is comma delimited. miss out file header
voltage = dlmread(volt,',',[2 0 600002 0]);
current = dlmread(curr,',',[2 0 600002 0]);
voltage = voltage(:,1)*v_scale;
current = current(:,1)*c_scale;
f_current = sgolayfilt(current,1,101);
c_offset = mean(f_current);
f_current = f_current - c_offset;
v_offset = mean(voltage);
voltage = voltage - v_offset;

iR = f_current*R;
[m n] = size(f_current);
accumulate = zeros(m,1);    % set up new array for flux-linkage data
accumulate(1) = 0;
for j = 2:m
accumulate(j) = accumulate(j-1)+(((voltage(j)-iR(j))*deltaT));      % calculate
flux-linkage
end
figure
plot(f_current,accumulate,'m');       % plot i-ψ loop



flux_main = accumulate/Nturns;        % calculate flux and MMF
MMF_main = f_current*Nturns;
f_offset = mean(flux_main);
flux_main = flux_main - f_offset;
figure

plot(MMF_main,flux_main,'k')        % plot flux-MMF loop
xlabel('MMF');
ylabel('flux');
title('Flux-MMF diagram');
a_1 = polyarea(MMF_main,flux_main);
x_1 = max(MMF_main);
y_1 = max(flux_main);
torque_1 = (ph*a_1)/(2*pi);
text(0.1*x_1,0.9*y_1,['measured torque =' num2str(torque_1)])

save 'gamma45_main',MMF_main;
save 'gamma45_main',flux_main;
```

A3.3. Matlab script for IPM motor *i-ψ* loop using fundamental components of waveforms

```
deltaT = 10E-8;                 % time difference between each sample
volt = 'v_main.txt';            % data taken from oscilloscope
curr = 'i_main.txt';
R = 19.12                       % resistance
Nturns = 672                    % number of turns
c_scale = 100                   % scaling factor for current
v_scale = 1                     % scaling factor for voltage
ph = 1                          % calculate each phase separately
Nr = 2                          % number of rotor poles

% file is comma delimited. miss out file header
voltage = dlmread(volt,',',[2 0 600002 0]);
current = dlmread(curr,',',[2 0 600002 0]);
voltage = voltage(:,1)*v_scale;
current = current(:,1)*c_scale;
f_current = sgolayfilt(current,1,101);
c_offset = mean(f_current);
f_current = f_current - c_offset;
v_offset = mean(voltage);
voltage = voltage - v_offset;

% fourier algorithm
a1 = 0;
b1 = 0;
fund = 0;
q = 2*pi/600001
k = zeros(600001,1);
a1 = 0;
b1 = 0;
for k = 1:600001
    x = k*q;
    a1 = a1 + f_current(k)*cos(x);
    b1 = b1 + f_current(k)*sin(x);
end
a2 = 2*a1/600001
b2 = 2*b1/600001
fund = sqrt((a2*a2)+(b2*b2))
phase = atan2(b2,a2)*180/pi
curr_fund = zeros(600001,1);
for k = 1:600001
    x = k*q;
    curr_fund(k) = a2*cos(x) + b2*sin(x);
end
a1 = 0;
b1 = 0;
fund = 0;
q = 2*pi/600001;
k = zeros(600001,1);
a1 = 0;
b1 = 0;
for k = 1:600001
    x = k*q;
    a1 = a1 + voltage(k)*cos(x);
    b1 = b1 + voltage(k)*sin(x);
end
a2 = 2*a1/600001
b2 = 2*b1/600001
fund = sqrt((a2*a2)+(b2*b2))
phase = atan2(b2,a2)*180/pi
volt_fund = zeros(600001,1);
for k = 1:600001
    x = k*q;
    volt_fund(k) = a2*cos(x) + b2*sin(x);
end

iR = curr_fund*R;
[m n] = size(curr_fund);
accumulate = zeros(m,1);
accumulate(1) = 0;
for j = 2:m
```

```
accumulate(j) = accumulate(j-1)+(((volt_fund(j)-iR(j))*deltaT));
% calculate flux-linkage
end

figure
plot(curr_fund,accumulate,'m')                          %plot ipsi loop


flux_fund_main= accumulate/Nturns;                      % calculate flux and MMF
MMF_fund_main = curr_fund*Nturns;
f_offset = mean(flux_fund_main);

flux_fund_main = flux_fund_main - f_offset;
figure

plot(MMF_fund_main,flux_fund_main,'m')                  % plot flux-MMF loop
xlabel('MMF');
ylabel('flux');
title('Flux-MMF diagram');
a_1 = polyarea(MMF_fund_main,flux_fund_main);           % get area of loop
x_1 = max(MMF_fund_main);
y_1 = max(flux_fund_main);
torque_5 = (ph*a_1)/(2*pi);                         % calculate torque from area of loop
text(0.1*x_1,0.9*y_1,['measured torque =' num2str(torque_5)])

save 'gamma45_main_fund',MMF_fund_main;
save 'gamma45_main_fund',flux_fund_main;
```

A3.4. Matlab script to determine reference flux density waveform

```
% The m-file generates a B-waveform and a dBdt-waveform
% with a specified higher harmonic of certain phase shift and downloads it to the
function generator

close all
clear all

periods = 1;
f_sample = input('sample-frequency [kHz] = ');                    % sample frequency
f = input('Desired frequency [Hz] = ');                           % frequency of input
waveform
points = 64;
f_generator = f_sample * 1e3 * periods / points;
while f_generator > f
   f_generator = f_sample * 1e3 * periods / (points);
   points = points + 64;
end

% display possible frequency and ask user to choose
disp(['Choose f = 1) ',num2str(f_sample*1e3*periods/(points-64*2),12),' or 2)
',num2str(f_sample*1e3*periods/(points-64),12)])
svar = input('? = ');
fid = fopen('f_awg.dat','w');
if svar == 1
   f_awg = f_sample*1e3*periods/(points-64*2);
   points = points-64*2;
else
   f_awg = f_sample*1e3*periods/(points-64);
   points = points-64;
end

dum=['f_awg = ', num2str(f_awg,12)];
disp(dum)
dum=['points = ', num2str(points,12)];
disp(dum)
fprintf(fid,'%e\n',f_awg);
fclose('all');
clear fid;
points = -1;
while (points < 1) | (points > 16000)
   points = input('Number of points (max 16000) = ');
end

n=1:points;
waveform = sin(2*pi/points*n);
%

harm = 'y';                                                       % do you want a higher
harmonic injected?
while harm == 'y'
   m = input('Harmonic number = ');                               % pick a harmonic to
inject
   amplitude = input(['Amplitude for ',num2str(m), ' harmonic (% of 1-harm) =
']);  % decide amplitude?
   amplitude = amplitude/100;
   phi = input('Phase (degrees) = ');                             % decide phase angle?
   phi = phi/180*pi;
   waveform = waveform + amplitude*sin(m*2*pi/points*n + phi);
   dum = 'another harmonic? (y/n)';                               % more hamonics required?
   disp(dum)
   harm = input('?','s');
end

subplot(2,1,1)
plot(1:points,waveform)
axis tight
zoom on
grid on
drawnow
```

```
waveform = waveform/max(waveform);
d_waveform = diff(waveform);
d_waveform = d_waveform*0.99/max(d_waveform);

subplot(2,1,2)
plot(1:length(waveform),waveform,1:length(d_waveform),d_waveform)
legend('B_R_E_F','dBdt_R_E_F')
title('Waveform')
grid on
zoom on

harmonics = 200;
a_n = fft(waveform)*2/length(waveform);
a_n = a_n(1:length(a_n)/2);
a_n = a_n(1+periods:periods:length(a_n));
f_FFT = f_awg:f_awg:length(a_n)*f_awg;
M_B = abs(a_n);

% find THD
THD = sqrt(sum((M_B(2:length(M_B))/M_B(1)).^2))*100

cd ..
cd matlab_to_gpib2
fid1 = fopen('download.dat','w');
fid2 = fopen('f_size.dat','w');

% For download setup
download_lines = 0;
dum = 'OUTP:LOAD INF';
fprintf(fid1,'%s%s\n',dum,13);
download_lines = download_lines + 1;
fprintf(fid1,'FREQ %f%s\n',f_awg,13);
download_lines = download_lines + 1;
fprintf(fid2,'%i%s\n',download_lines,13);
download_lines = 0;
dum = 'DATA VOLATILE, ';
download_lines = download_lines + 1;
fprintf(fid1,'%s%s\n',dum,13);
fprintf(fid2,'%i%s\n',download_lines,13);
download_lines = 0;
for n=1:length(d_waveform),
   if n == 1
      fprintf(fid1,'%f%s\n',d_waveform(n),13);
   else
      fprintf(fid1,',%f%s\n',d_waveform(n),13);
   end
   download_lines = download_lines + 1;
end
fprintf(fid2,'%i%s\n',download_lines,13);
fclose(fid1);
fclose(fid2);
!gpib.exe
cd ..
cd harmonic
```

A3.5. Matlab script to download reference waveform to signal generator via GPIB interface

```
function download = f(waveform,frekvens,v_pp);

%!del download.dat
%!del f_size.dat
%!del frekvens.dat
%!del volt.dat

fid1 = fopen('download.dat','w');
fid2 = fopen('f_size.dat','w');
fid3 = fopen('frequency.dat','w');
fid4 = fopen('volt.dat','w');

% Før download setup
download_lines = 0;
dum = 'OUTP:LOAD INF';
download_lines = download_lines + 1;
fprintf(fid1,'%s%s\n',dum,13);
fprintf(fid2,'%i%s\n',download_lines,13);
download_lines = 0;
dum = 'DATA VOLATILE, ';
download_lines = download_lines + 1;
fprintf(fid1,'%s%s\n',dum,13);
fprintf(fid2,'%i%s\n',download_lines,13);
download_lines = 0;
for n=1:length(waveform),
   if n == 1
      fprintf(fid1,'%f%s\n',waveform(n),13);
   else
      fprintf(fid1,',%f%s\n',waveform(n),13);
   end
   download_lines = download_lines + 1;
end
fprintf(fid2,'%i%s\n',download_lines,13);

fprintf(fid3,'%f%s\n',frequency,13);
fprintf(fid4,'%f%s\n',v_pp,13);
fclose(fid1);
fclose(fid2);
fclose(fid3);
fclose(fid4);

!gpib.exe
download =1;
```

A3.6. Excerpt from PC-FEA script for frozen permeability calculations of IPM motor

The following code is taken from the PC-FEA file used to determine frozen permeability flux-linkage solutions for each field source in the IPM motor. Each field source can be turned off as required, by setting the phase currents to zero or by setting the remnant flux density of the permanent magnets (B_m, B_{tt}) to very low values.

```
Parameters RotorStep=[$R]
  Do Times:[NumI]
    Let IPh:=IValues([$R0])
    Parameters IStep=[$R]
    Do Times:[NumGamma]
      Let Gamma:=GammaValues([$R0])
      Parameters GammaStep=[$R]
// Set currents here depending on rotor pos...
// AC control
      Let AngBeta:=Gamma + 90 + RotAngElec
      Let Ia:=Iph      // Initial solution with phase A = Iph
      // * cos(AngBeta)
      Let Ib:=Iph      // phase B current = Iph
      //IPh * cos(AngBeta - 90)
      Region Slot_24 J_Val:(([CLV124]*Ia) + ([CLV224]*Ib))/SlotArea/[PPaths]
      Region Slot_1 J_Val:(([CLV11]*Ia) + ([CLV21]*Ib))/SlotArea/[PPaths]
      Region Slot_2 J_Val:(([CLV12]*Ia) + ([CLV22]*Ib))/SlotArea/[PPaths]
      Region Slot_3 J_Val:(([CLV13]*Ia) + ([CLV23]*Ib))/SlotArea/[PPaths]
      Region Slot_4 J_Val:(([CLV14]*Ia) + ([CLV24]*Ib))/SlotArea/[PPaths]
      Region Slot_5 J_Val:(([CLV15]*Ia) + ([CLV25]*Ib))/SlotArea/[PPaths]
      Region Slot_6 J_Val:(([CLV16]*Ia) + ([CLV26]*Ib))/SlotArea/[PPaths]
      Region Slot_7 J_Val:(([CLV17]*Ia) + ([CLV27]*Ib))/SlotArea/[PPaths]
      Region Slot_8 J_Val:(([CLV18]*Ia) + ([CLV28]*Ib))/SlotArea/[PPaths]
      Region Slot_9 J_Val:(([CLV19]*Ia) + ([CLV29]*Ib))/SlotArea/[PPaths]
      Region Slot_10 J_Val:(([CLV110]*Ia) + ([CLV210]*Ib))/SlotArea/[PPaths]
      Region Slot_11 J_Val:(([CLV111]*Ia) + ([CLV211]*Ib))/SlotArea/[PPaths]
      Region Slot_12 J_Val:(([CLV112]*Ia) + ([CLV212]*Ib))/SlotArea/[PPaths]
      Region Magnet_1 subdom:3,29 PM_val:(Brr,Btt) center:0.000,0.000 miur:1.08
      Output [RefFile]_R[RotorStep]_[Istep]_[GammaStep].mes solution:New
      Compute
      Input [RefFile]_R[RotorStep]_[Istep]_[GammaStep].mes solution:Last
      Let Ia:=0        // Phase A current turned off
      Let Ib:=Iph
      Region Slot_24 J_Val:(([CLV124]*Ia) + ([CLV224]*Ib))/SlotArea/[PPaths]
      Region Slot_1 J_Val:(([CLV11]*Ia) + ([CLV21]*Ib))/SlotArea/[PPaths]
      Region Slot_2 J_Val:(([CLV12]*Ia) + ([CLV22]*Ib))/SlotArea/[PPaths]
      Region Slot_3 J_Val:(([CLV13]*Ia) + ([CLV23]*Ib))/SlotArea/[PPaths]
      Region Slot_4 J_Val:(([CLV14]*Ia) + ([CLV24]*Ib))/SlotArea/[PPaths]
      Region Slot_5 J_Val:(([CLV15]*Ia) + ([CLV25]*Ib))/SlotArea/[PPaths]
      Region Slot_6 J_Val:(([CLV16]*Ia) + ([CLV26]*Ib))/SlotArea/[PPaths]
      Region Slot_7 J_Val:(([CLV17]*Ia) + ([CLV27]*Ib))/SlotArea/[PPaths]
      Region Slot_8 J_Val:(([CLV18]*Ia) + ([CLV28]*Ib))/SlotArea/[PPaths]
      Region Slot_9 J_Val:(([CLV19]*Ia) + ([CLV29]*Ib))/SlotArea/[PPaths]
      Region Slot_10 J_Val:(([CLV110]*Ia) + ([CLV210]*Ib))/SlotArea/[PPaths]
      Region Slot_11 J_Val:(([CLV111]*Ia) + ([CLV211]*Ib))/SlotArea/[PPaths]
      Region Slot_12 J_Val:(([CLV112]*Ia) + ([CLV212]*Ib))/SlotArea/[PPaths]
      Region Magnet_1 subdom:3,29 PM_val:0.0000001,0 center:0.000,0.000 miur:1.08
       // PMs 'turned off'
      // Region Magnet_1 subdom:3,29 PM_val:(Brr,Btt) center:0.0,0.0 miur: 1.08
      // Region Magnet_1 subdom:3,29 bh_code:4 miur:1.08 spline:0
      Problem Cont_Lin XY_Plane
      Output [RefFile]_R[RotorStep]_[Istep]_[GammaStep]FP.mes solution:New
      Compute
      Input [RefFile]_R[RotorStep]_[Istep]_[GammaStep].mes solution:Last
      Problem Cont_Non_Lin XY_Plane
      EndDo
    EndDo
EndDo
```

A3.7. PC-FEA script for frozen permeability calculations of SR motor

The following code is taken from the PC-FEA file used to determine frozen permeability flux-linkage solutions for each field of the switched-reluctance motor. Again, the current in each phase can be turned off as required, by setting the phase currents to zero. In addition, the script has been altered so that the currents in each phase can be separately defined, allowing individual current profiles and switching angles.

```
//Pre-calculation of currents
Do Times:[Nph]
 Parameters m=[$R]
  if ( [m] = 1 )
  Parameters Iph[m]=0..([RotSteps]-1)
  Let Iph[m]:=
(0,0,0,0,0,0,2.8,6.8,9.5,11.3,12,12,12,12,12,12,12,12,12,12,12,12,12,5.4,5.4,5
.4,3.7,2.5,1.2,0.6,0,0,0,0,0,0,0,0,0,0,0,0,0,0,0,0,0,0,0,0,0,0,0,0,0,0,0,0,0)
  endif
  if ( [m] = 2 )
  Parameters Iph[m]=0..([RotSteps]-1)
  Let Iph[m]:=
(12,12,12,12,12,12,12,12,12,12,12,5.4,3.7,2.5,1.2,0.6,0,0,0,0,0,0,0,0,0,0,0,0,0
,0,0,0,0,0,0,0,0,0,0,0,0,0,0,0,0,0,0,0,0,0,0,0,0,0,0,0,0,2.8,6.8,9.5,11.3,12,12,12,12,12,12)
  endif
  if ([m] = 3)
  Parameters Iph[m]=0..([RotSteps]-1)
  Let Iph[m]:=
(0.6,0,0,0,0,0,0,0,0,0,0,0,0,0,0,0,0,0,0,0,0,0,0,0,0,0,0,0,0,0,0,0,0,0,0,2.8,6.
8,9.5,11.3,12,12,12,12,12,12,12,12,12,12,12,12,12,12,12,12,5.4,3.7,2.5,1.2,0.6)
  endif
  if ( [m] = 4 )
  Parameters Iph[m]=0..([RotSteps]-1)
  Let Iph[m]:=
(0,0,0,0,0,0,0,0,0,0,0,0,0,0,0,0,0,0,0,0,0,0,0,0,0,0,0,0,0,0,0,0,0,0,0,2.8,6.8,9.5,11.3,12,12,12,12,12,12,12,
12,12,12,12,12,12,12,12,12,12,12,5.4,3.7,2.5,1.2,0.6,0,0,0,0,0,0,0,0,0,0,0,0,0,0,0,0)
  endif
  enddo

  Region Coil_1 J_Val:(-[Np]*Iph1([$R0])/CoilSideArea/[Paths])
  Region Coil_2 J_Val:(-[Np]*Iph2([$R0])/CoilSideArea/[Paths])
  Region Coil_3 J_Val:([Np]*Iph2([$R0])/CoilSideArea/[Paths])
  Region Coil_4 J_Val:([Np]*Iph3([$R0])/CoilSideArea/[Paths])
  Region Coil_5 J_Val:(-[Np]*Iph3([$R0])/CoilSideArea/[Paths])
  Region Coil_6 J_Val:(-[Np]*Iph4([$R0])/CoilSideArea/[Paths])
  Region Coil_7 J_Val:([Np]*Iph4([$R0])/CoilSideArea/[Paths])
  Region Coil_8 J_Val:(-[Np]*Iph1([$R0])/CoilSideArea/[Paths])
  Problem Cont_Non_Lin XY_Plane
  Output [RefFile]_R[$R0].mes solution:New
  Compute

  Input [RefFile]_R[$R0].mes solution:Last
Do Times:[Nph]
 Parameters m=[$R]
  if ( [m] = 1 )
  Parameters Iph[m]=0..([RotSteps]-1)
  Let Iph[m]:=
(0,0,0,0,0,0,2.8,6.8,9.5,11.3,12,12,12,12,12,12,12,12,12,12,12,12,12,5.4,5.4,5
.4,3.7,2.5,1.2,0.6,0,0,0,0,0,0,0,0,0,0,0,0,0,0,0,0,0,0,0,0,0,0,0,0,0,0,0,0,0)
  endif
  if ( [m] = 2 )
  Parameters Iph[m]=0..([RotSteps]-1)
```

```
  Let Iph[m]:=
(0,0,0,0,0,0,0,0,0,0,0,0,0,0,0,0,0,0,0,0,0,0,0,0,0,0,0,0,0,0,0,0,0,0,0,0,0,0,0,
0,0,0,0,0,0,0,0,0,0,0,0,0,0,0,0,0,0,0,0,0,0,0,0,0,0,0,0,0,0,0,0,0,0,0,0,0,0,0)
  endif
  if ([m] = 3)
  Parameters Iph[m]=0..([RotSteps]-1)
  Let Iph[m]:=
(0,0,0,0,0,0,0,0,0,0,0,0,0,0,0,0,0,0,0,0,0,0,0,0,0,0,0,0,0,0,0,0,0,0,0,0,0,0,0,
0,0,0,0,0,0,0,0,0,0,0,0,0,0,0,0,0,0,0,0,0,0,0,0,0,0,0,0,0,0,0,0,0,0,0,0,0,0,0)
  endif
  if ( [m] = 4 )
  Parameters Iph[m]=0..([RotSteps]-1)
  Let Iph[m]:=
(0,0,0,0,0,0,0,0,0,0,0,0,0,0,0,0,0,0,0,0,0,0,0,0,0,0,0,0,0,0,0,0,0,0,0,0,0,0,0,
0,0,0,0,0,0,0,0,0,0,0,0,0,0,0,0,0,0,0,0,0,0,0,0,0,0,0,0,0,0,0,0,0,0,0,0,0,0,0)
  endif
  enddo

  Region Coil_1 J_Val:(-[Np]*Iph1([$R0])/CoilSideArea/[Paths])
  Region Coil_2 J_Val:(-[Np]*Iph2([$R0])/CoilSideArea/[Paths])
  Region Coil_3 J_Val:([Np]*Iph2([$R0])/CoilSideArea/[Paths])

  Region Coil_4 J_Val:([Np]*Iph3([$R0])/CoilSideArea/[Paths])
  Region Coil_5 J_Val:(-[Np]*Iph3([$R0])/CoilSideArea/[Paths])
  Region Coil_6 J_Val:(-[Np]*Iph4([$R0])/CoilSideArea/[Paths])
  Region Coil_7 J_Val:([Np]*Iph4([$R0])/CoilSideArea/[Paths])
  Region Coil_8 J_Val:(-[Np]*Iph1([$R0])/CoilSideArea/[Paths])
  Problem Cont_Lin XY_Plane
  Output [RefFile]_R[$R0]_FP.mes solution:New
  Compute
//  Input [RefFile]_R[$R0].mes solution:Last
//  Problem Cont_Non_Lin XY_Plane
  EndDo
```

Appendix 4

Bridge Circuit for Static Inductance Measurements

A4.1 Self-inductance measurements

Fig. A4.1 shows a simple inductance bridge circuit that can be used in a static test to determine the change in flux-linkage due to the switching of the phase current. R_M and L_M represent the winding under test. A variable resistor R_{VAR} allows the bridge to be balanced, so that no residual voltage is seen across the digital storage oscilloscope. Resistors R_1 and R_2 are fixed and have equal value. The circuit is fed with a DC voltage, producing a current I in the inductor. At time t = 0 the switch is opened, causing the current in the inductor to fall to zero. As the level of current falls to zero, the bridge is no longer balanced and so a voltage v is recorder across the centre of the bridge by the oscilloscope.

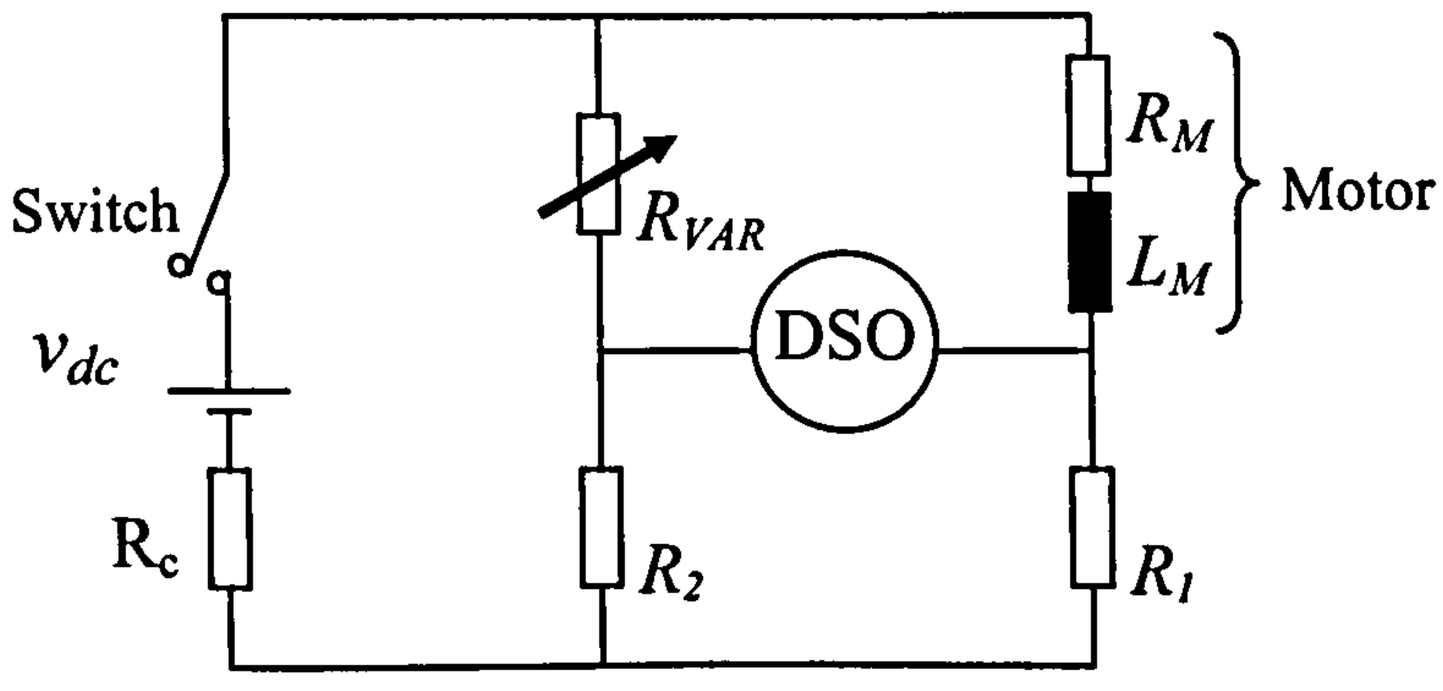

Fig. A4.1. Example of bridge circuit for measuring synchronous inductance.

The instantaneous voltage across resistor R_2 is given by:

$$V_{R_2} = \left[\frac{R_2}{(R_2 + R_{VAR})}\right] v \qquad \text{(A4.1)}$$

and the voltage drop across R_1 is given by:

$$V_{R_1} = \left[\frac{R_1}{(R_M + R_1)}\right] v - \left[\frac{R_1}{(R_M + R_1)}\right] L \frac{di}{dt} \qquad \text{(A4.2)}$$

Due to the choice of resistance values, $R_1/R_M = R_2/ R_{var}$ and so the voltage across the detector can be determined from:

$$v_\Psi = -\left[\frac{R_1}{R_1 + R_2}\right] L \frac{di}{dt} \qquad \text{(A4.3)}$$

The flux-linkage is proportional to the time integral Ψ of the voltage across the centre of the bridge:

$$\Psi = \left[\frac{R_1}{R_M + R_1}\right] LI \qquad \text{(A4.4)}$$

and so the self-inductance of the circuit can be found from the relationship:

$$L = \left[\frac{R_M + R_1}{R_1}\right] \frac{\Psi}{I} \qquad \text{(A4.5)}$$

A4.2 Mutual inductance measurements

Measurement of mutual inductances is also possible, if the bridge circuit is modified slightly to include a second excited winding. An example of the modified circuit proposed by Jones in [57] is given in Fig. A4.2. The circuit measures the mutual inductance between two coils when the second coil is carrying direct current. The bridge is balanced

while there is direct current in the secondary winding and the current in the first winding has been set to the required level. When the current in the first winding is switched off, the voltage induced in the secondary winding is $M_L(di/dt)$. Following the same derivation as was given for the self-inductance calculation, the mutual inductance can be calculated using Eq. (A4.6). It should be noted that the mutual inductance is proportional only to the current in the primary winding, and not the second excited phase.

$$M_L = \frac{(R_M + R_2)\psi}{R_2 I_1} \tag{A4.6}$$

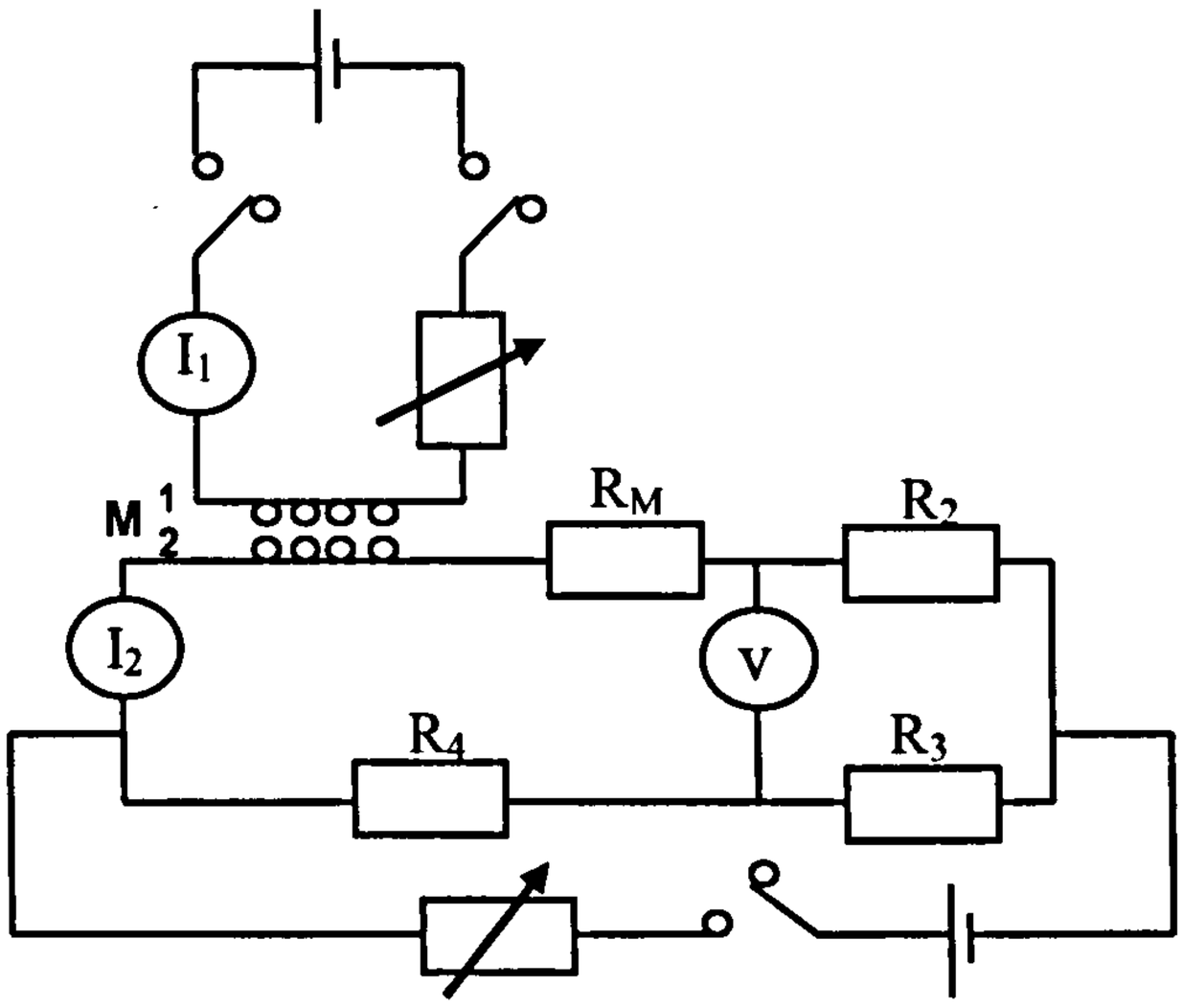

Fig. A4.2. Inductance bridge circuit modified to measure mutual coupling between phases.

Appendix 5

Synchronous Reactance Results

A5.1 Flux-linkages calculated from fundamental flux density

A5.1.1 IPM test motor 1

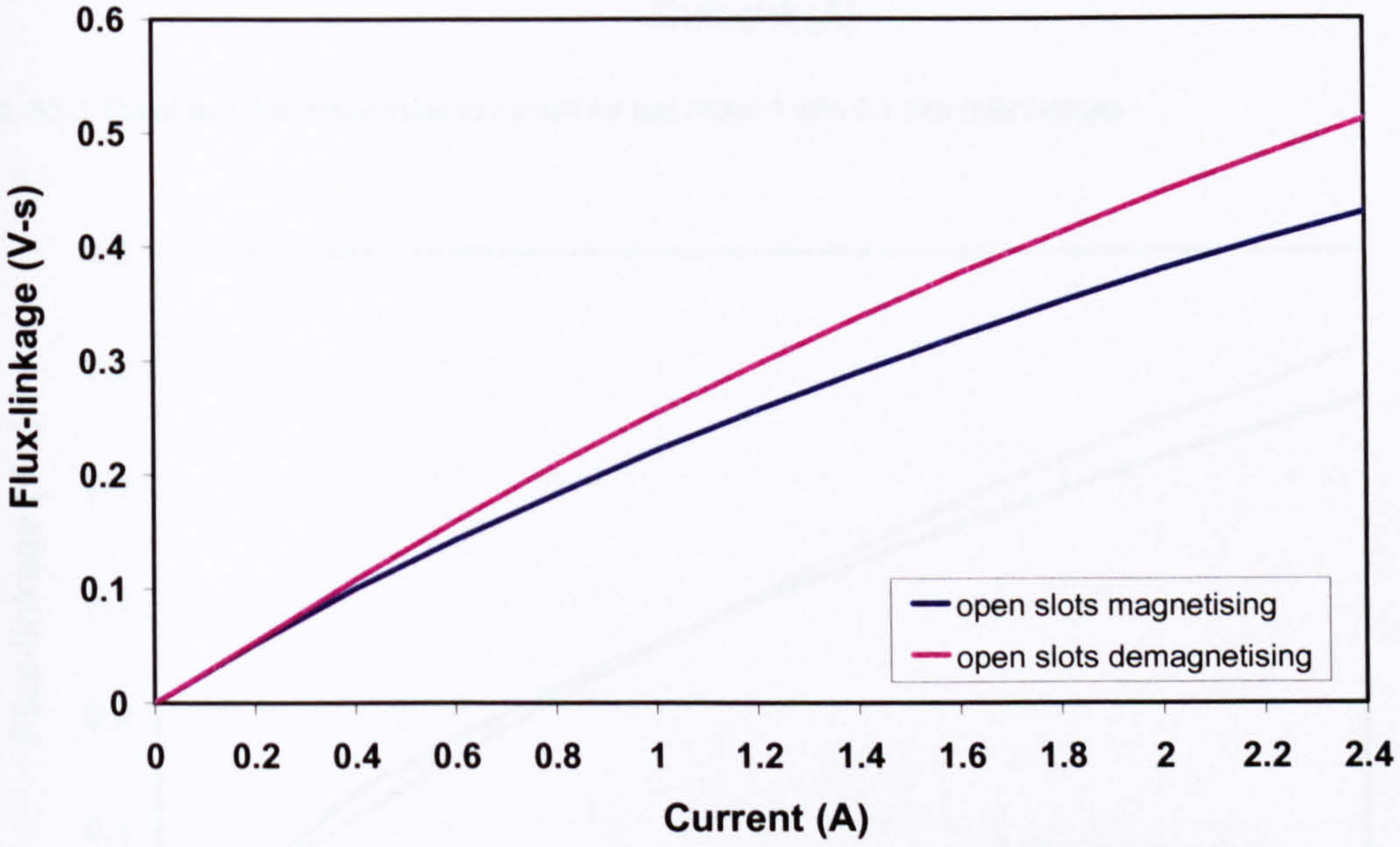

Fig. A5.1. Direct axis flux-linkage due to current for test motor 1 with open rotor slots

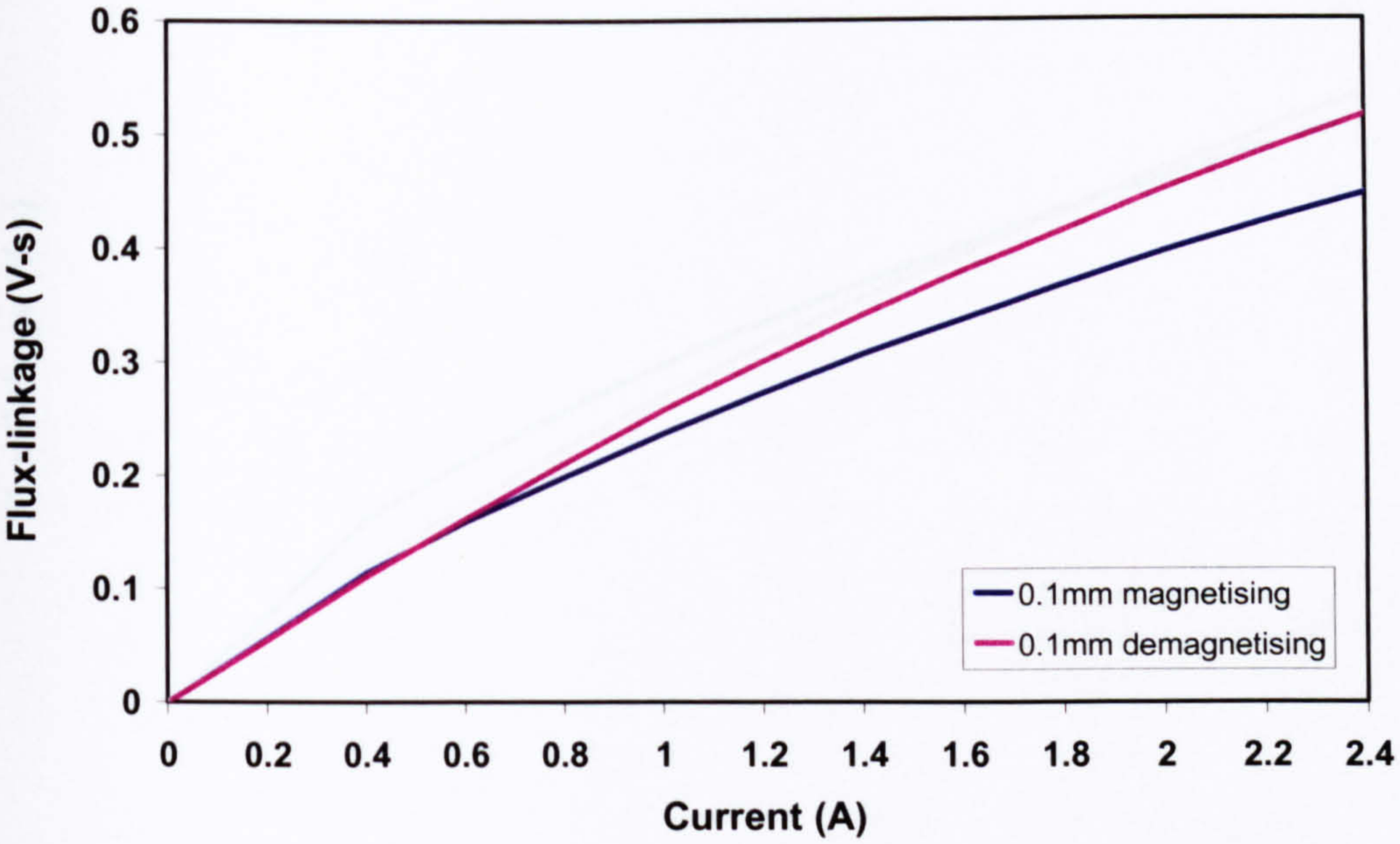

Fig. A5.2. Direct axis flux-linkage due to current for test motor 1 with 0.1 mm rotor bridges

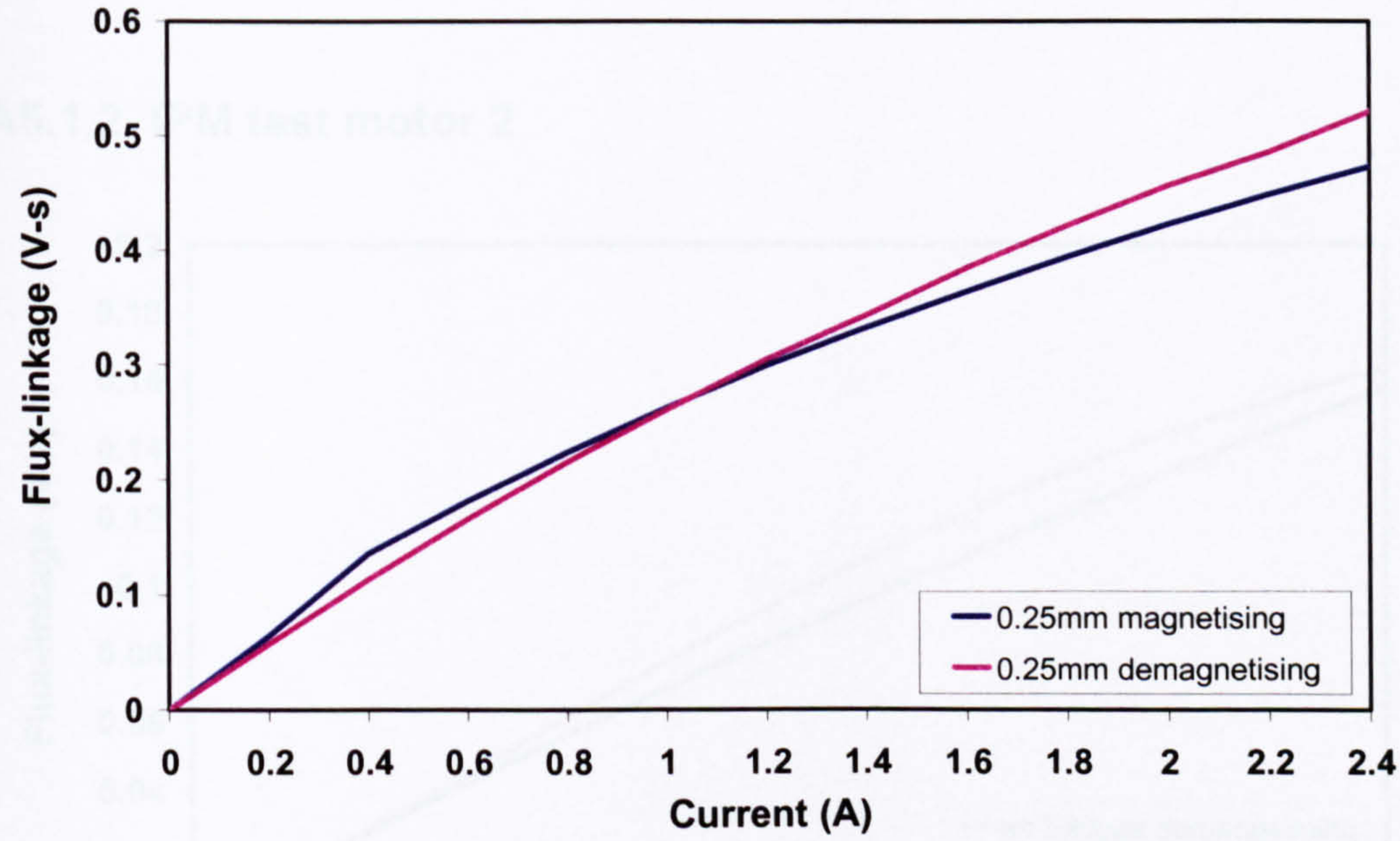

Fig. A5.3. Direct axis flux-linkage due to current for test motor 1 with 0.25 mm rotor bridges

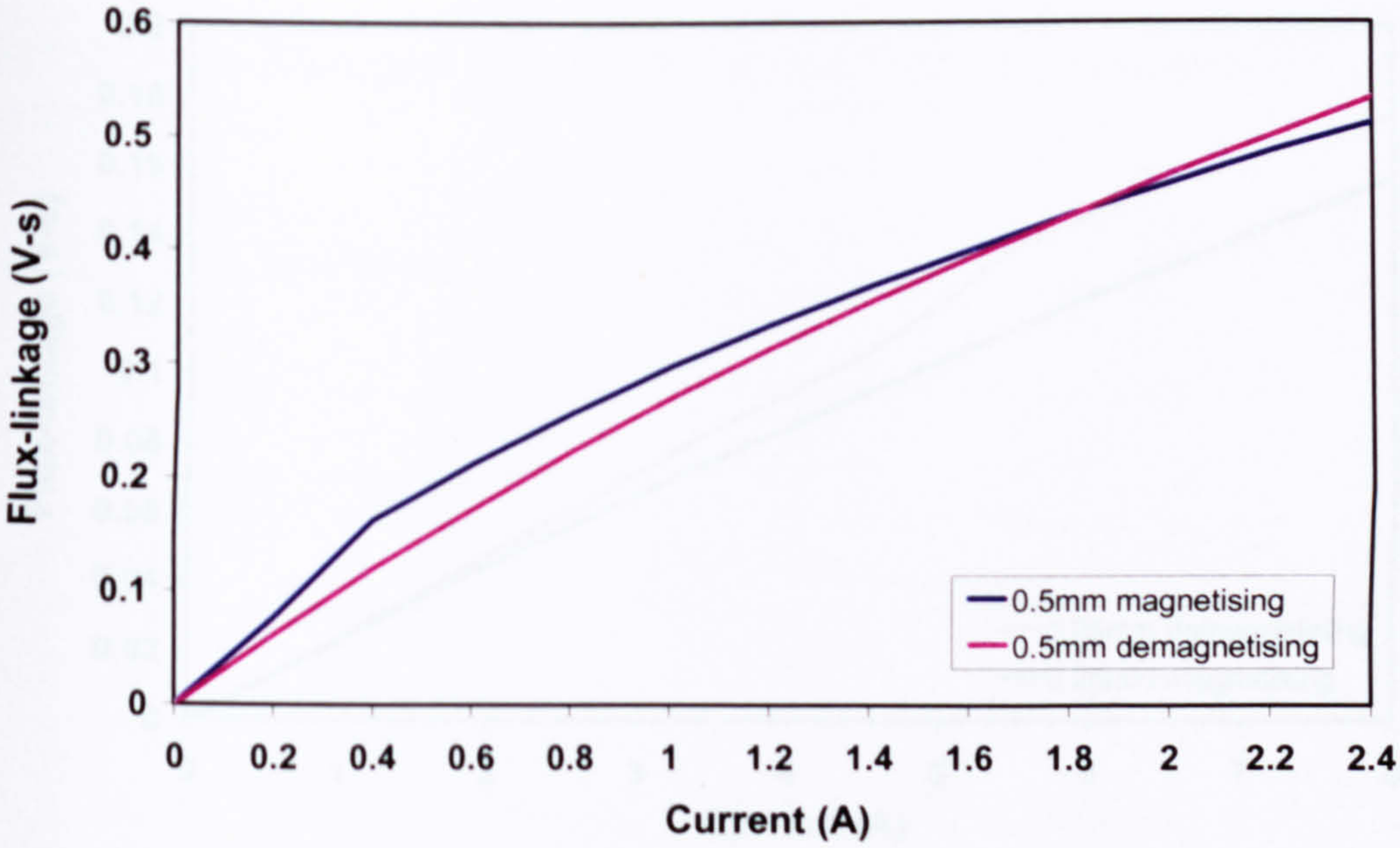

Fig. A5.4. Direct axis flux-linkage due to current for test motor 1 with 0.5 mm rotor bridges

A5.1.2. IPM test motor 2

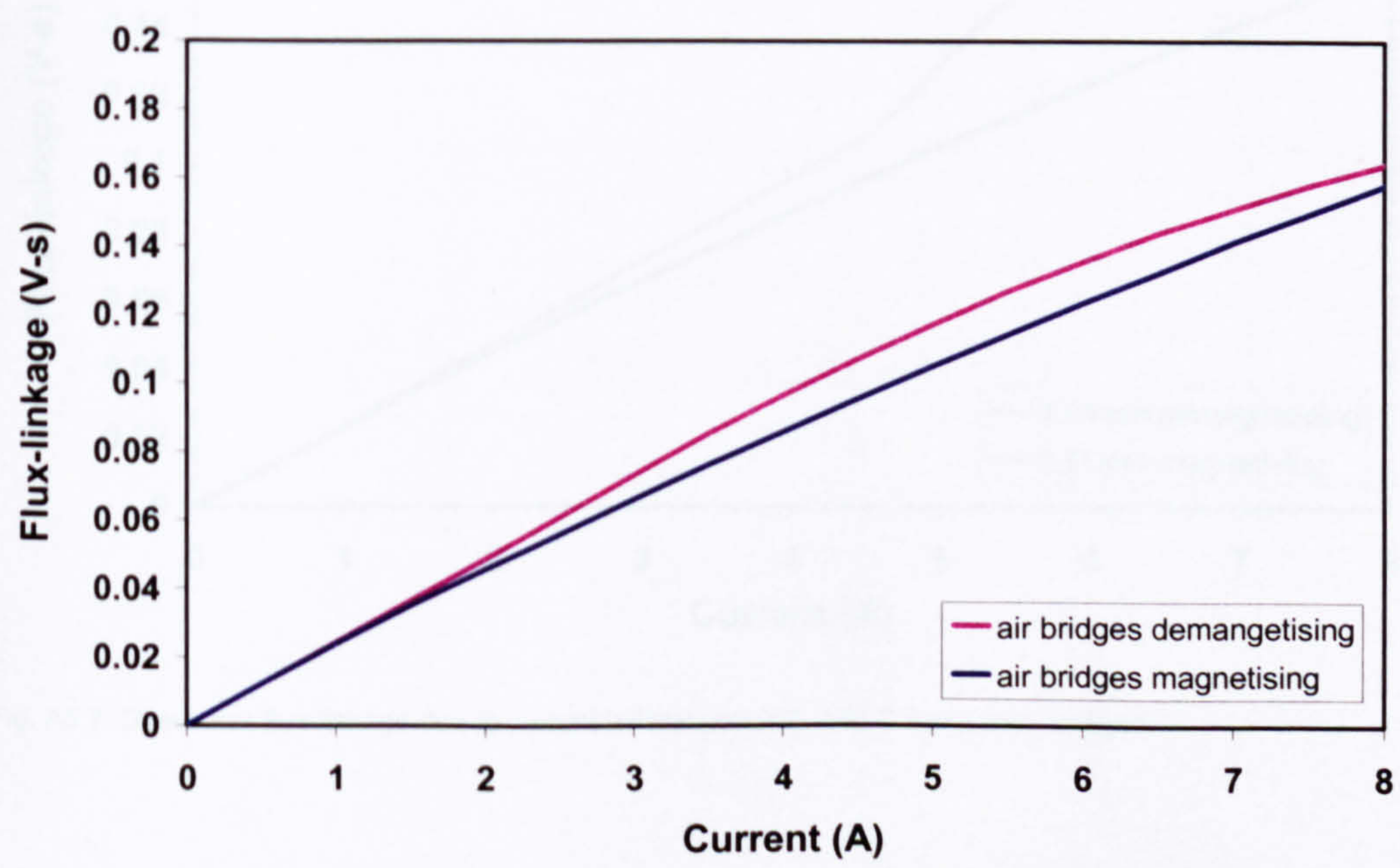

Fig. A5.5. Direct axis flux-linkage due to current for test motor 2, with open rotor slots

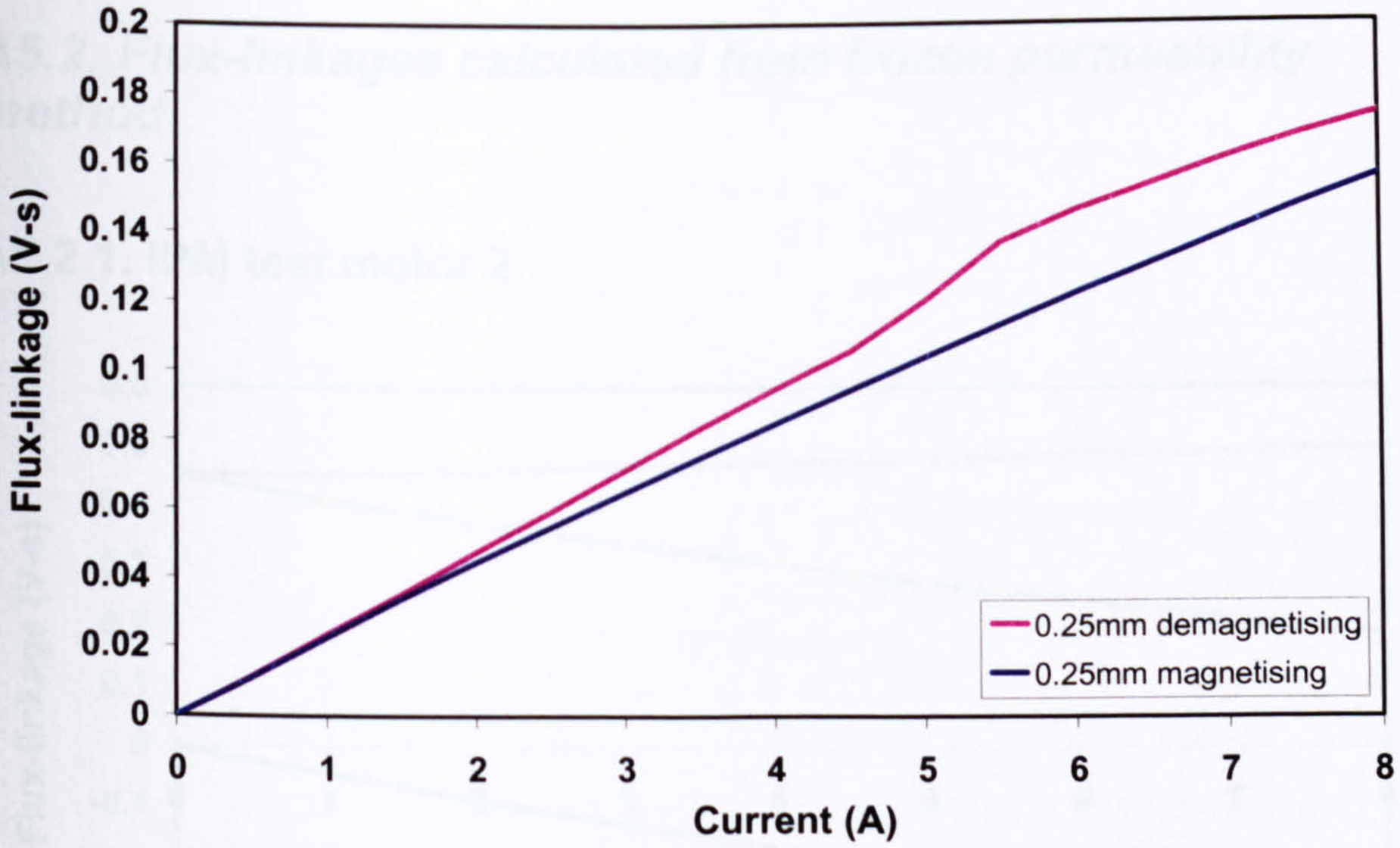

Fig. A5.6. Direct axis flux-linkage due to current for test motor 2, with 0.25 mm rotor bridges

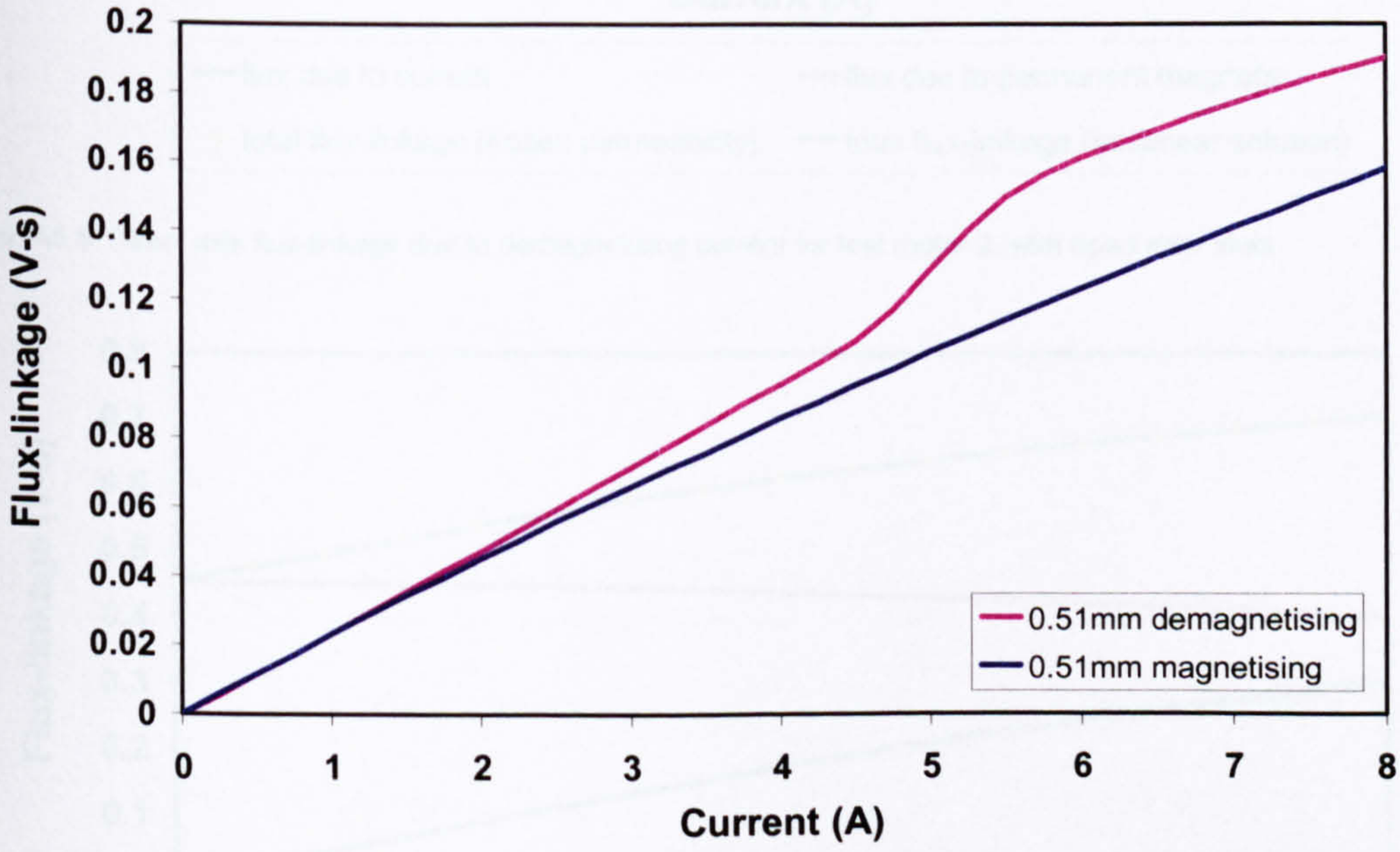

Fig. A5.7. Direct axis flux-linkage due to current for test motor 2, with 0.5 mm rotor bridges

A5.2. Flux-linkages calculated from frozen permeability method

A5.2.1. IPM test motor 2

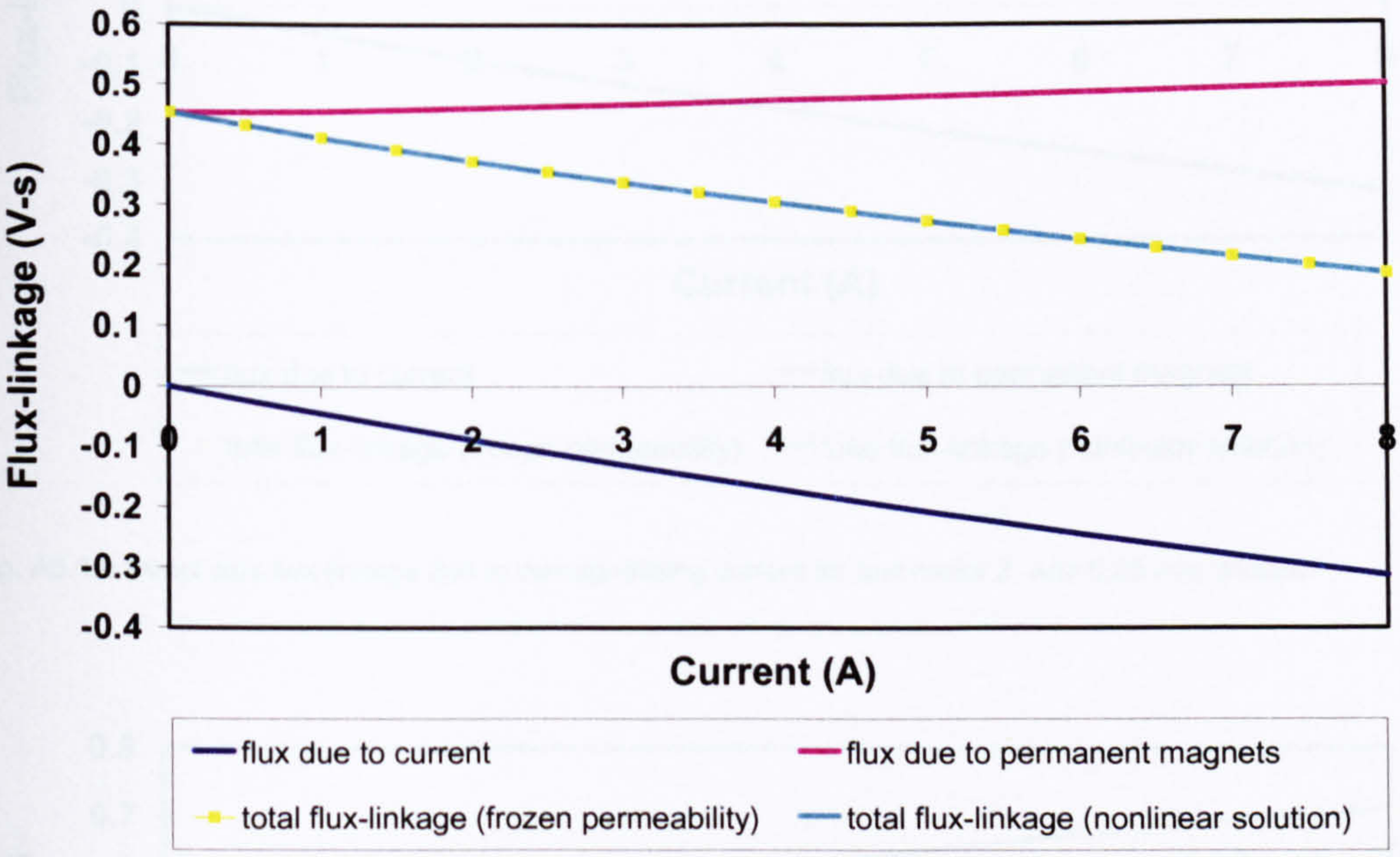

Fig. A5.8. Direct axis flux-linkage due to demagnetising current for test motor 2, with open rotor slots

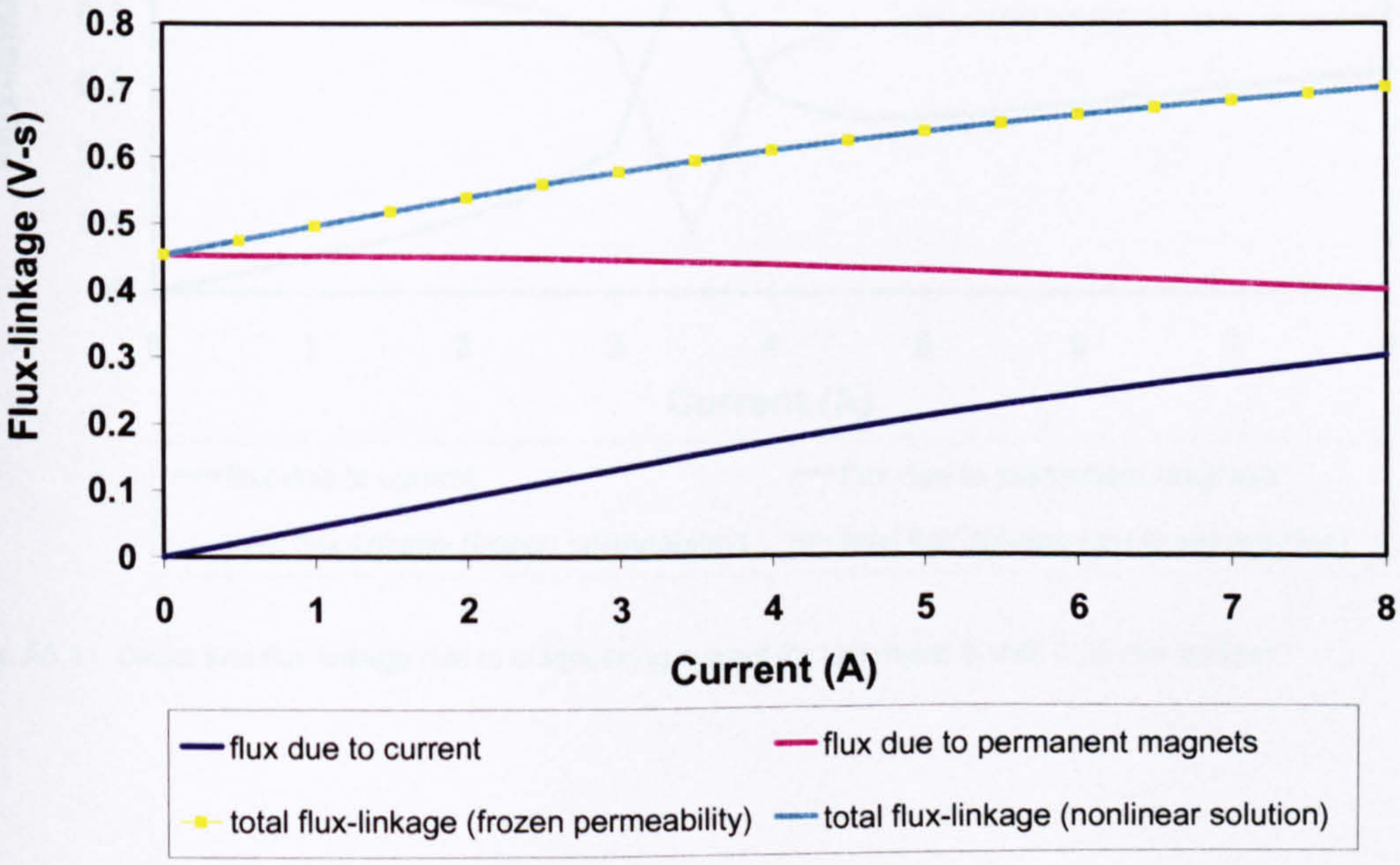

Fig. A5.9. Direct axis flux-linkage due to magnetising current for test motor 2, with open rotor slots

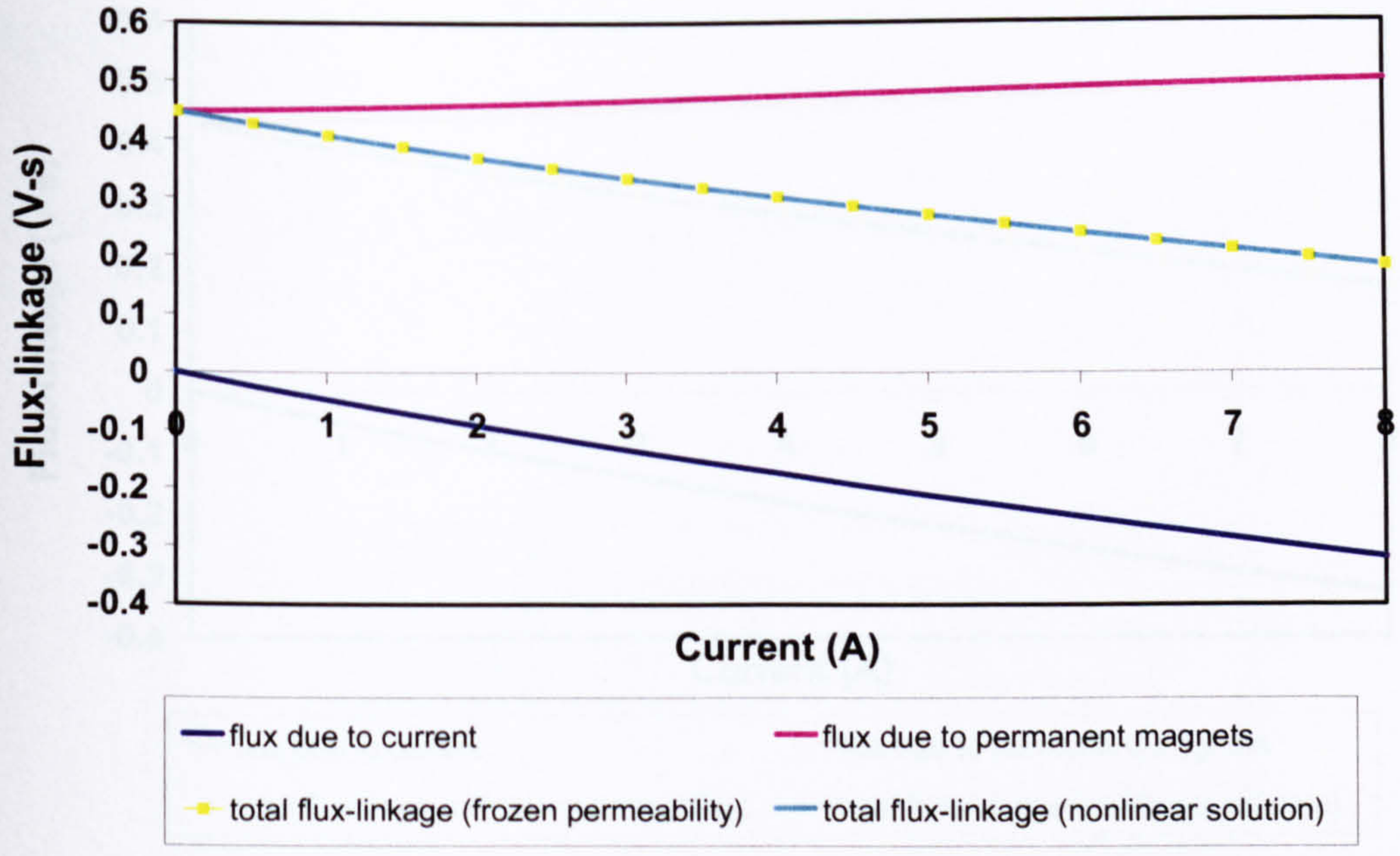

Fig. A5.10. Direct axis flux-linkage due to demagnetising current for test motor 2, with 0.25 mm bridges

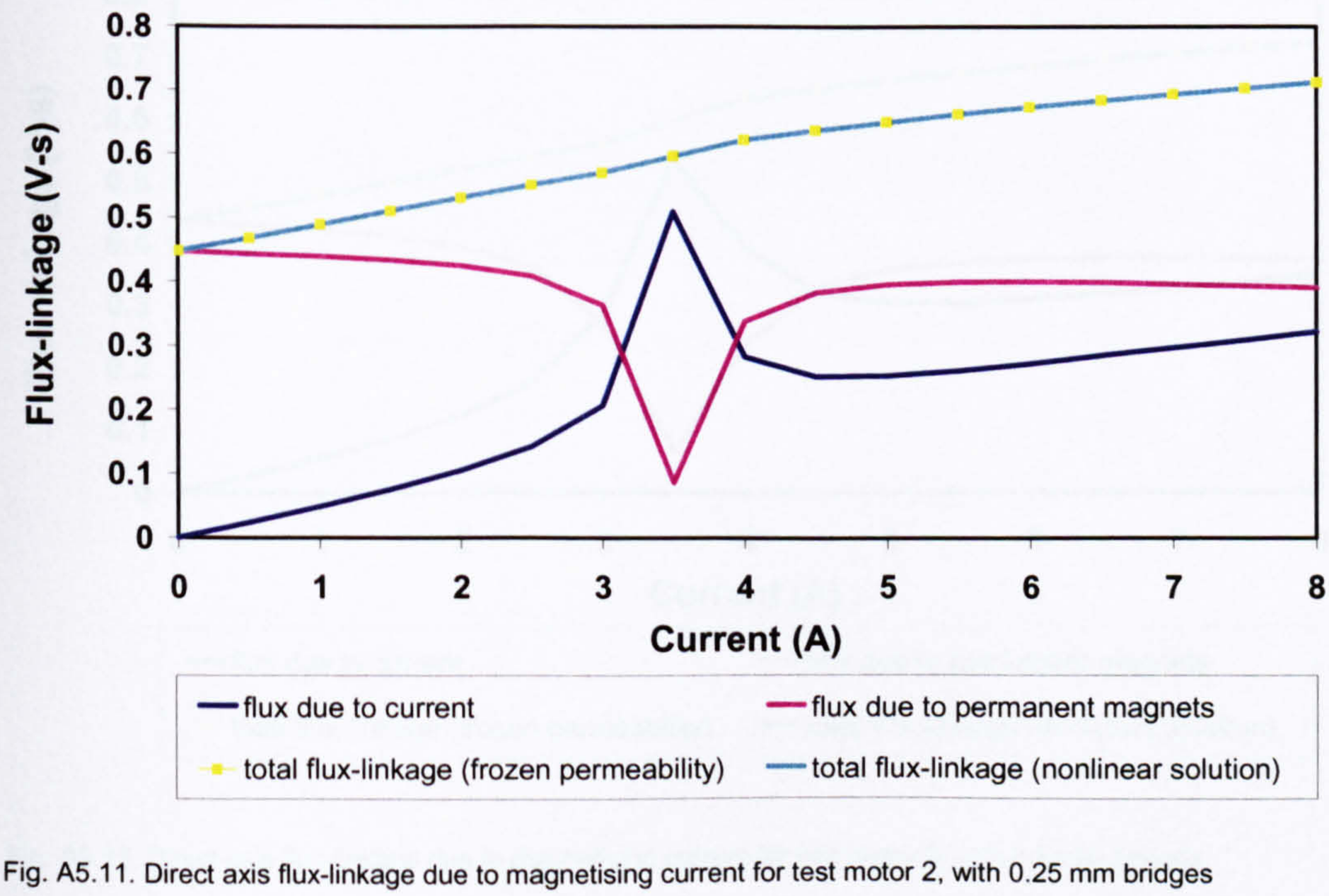

Fig. A5.11. Direct axis flux-linkage due to magnetising current for test motor 2, with 0.25 mm bridges

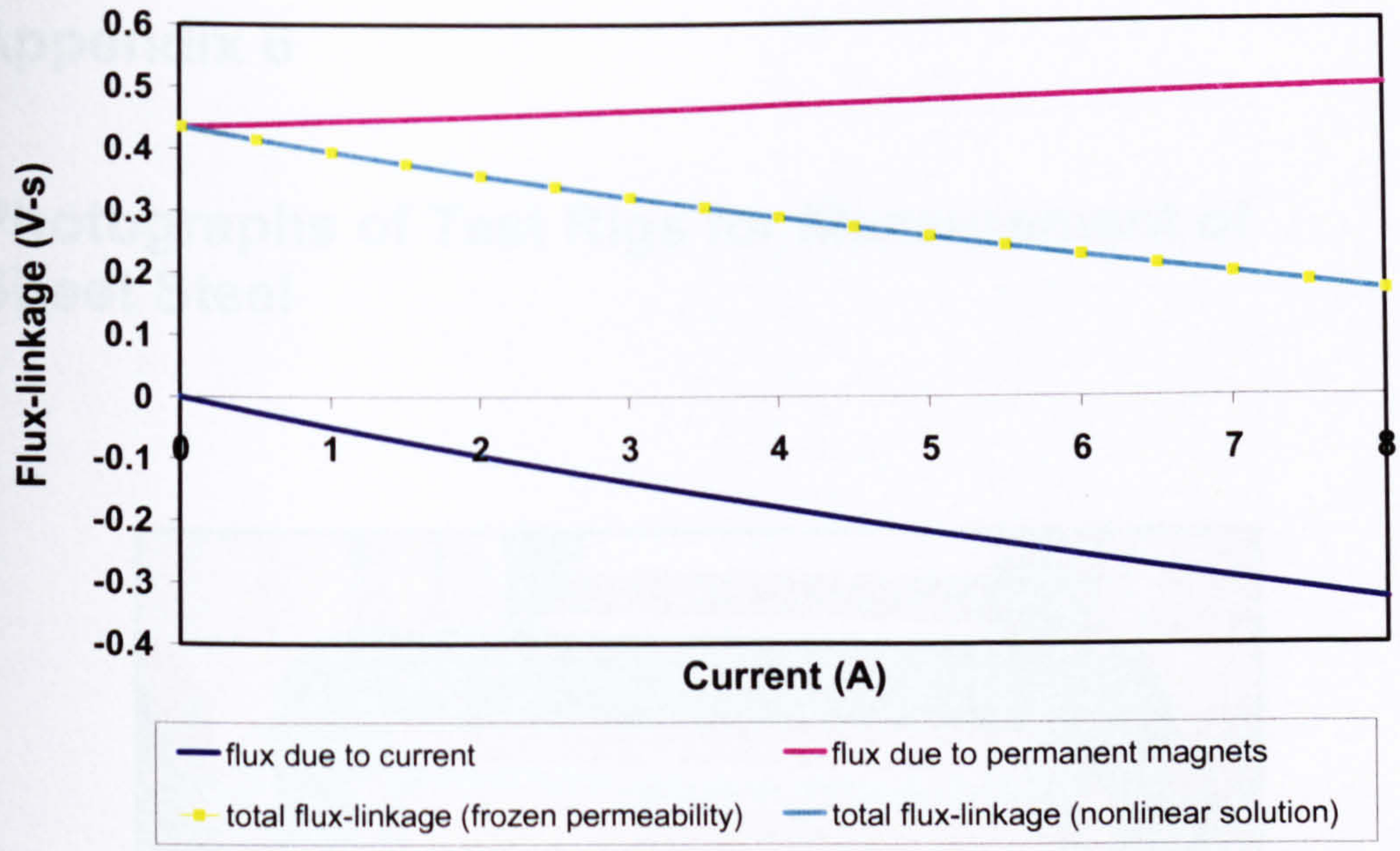

Fig. A5.12. Direct axis flux-linkage due to demagnetising current for test motor 2, with 0.5 mm bridges

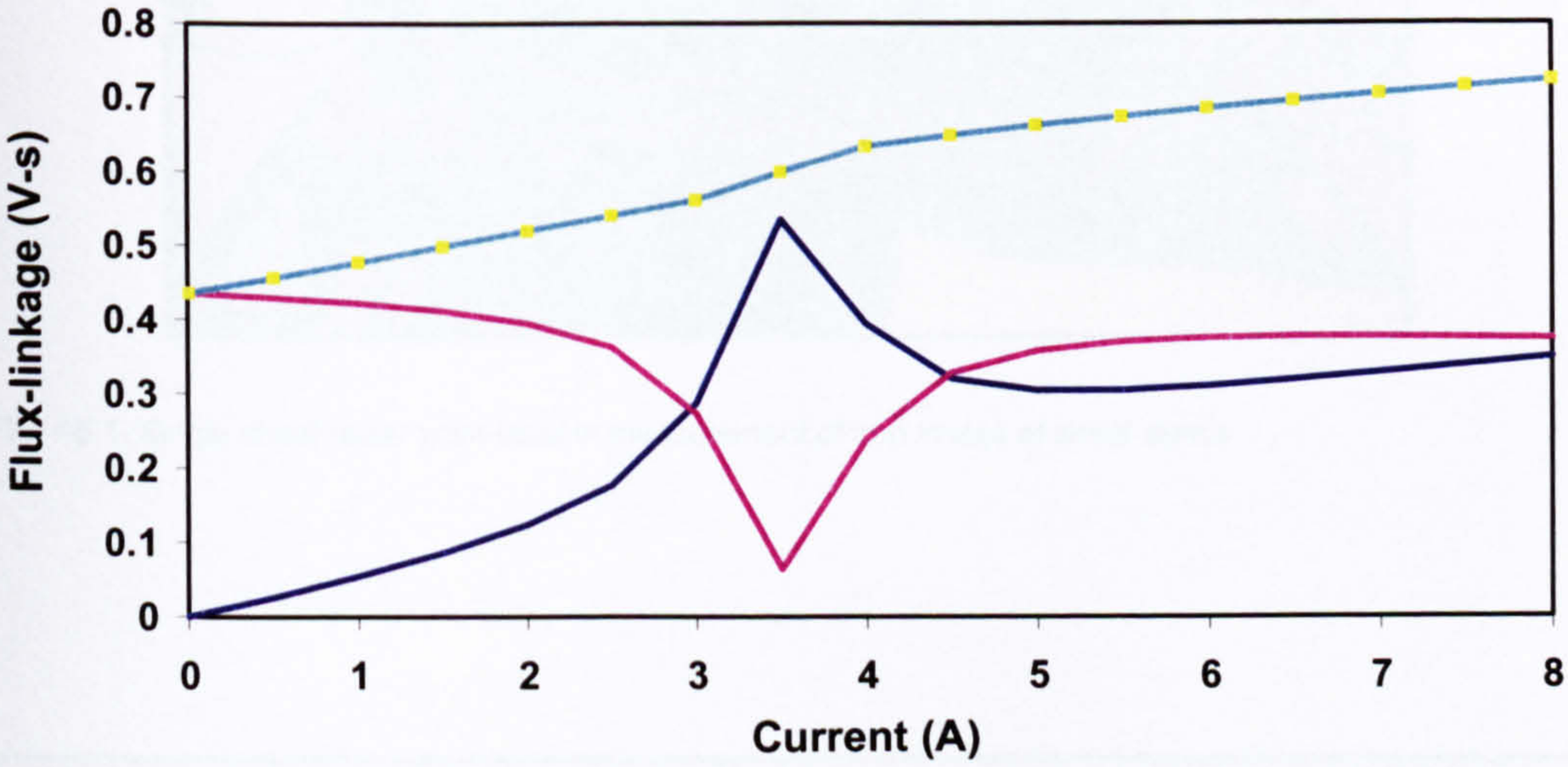

Fig. A5.13. Direct axis flux-linkage due to magnetising current for test motor 2, with 0.5 mm bridges

Appendix 6

Photographs of Test Rigs for Measurement of Sheet Steel

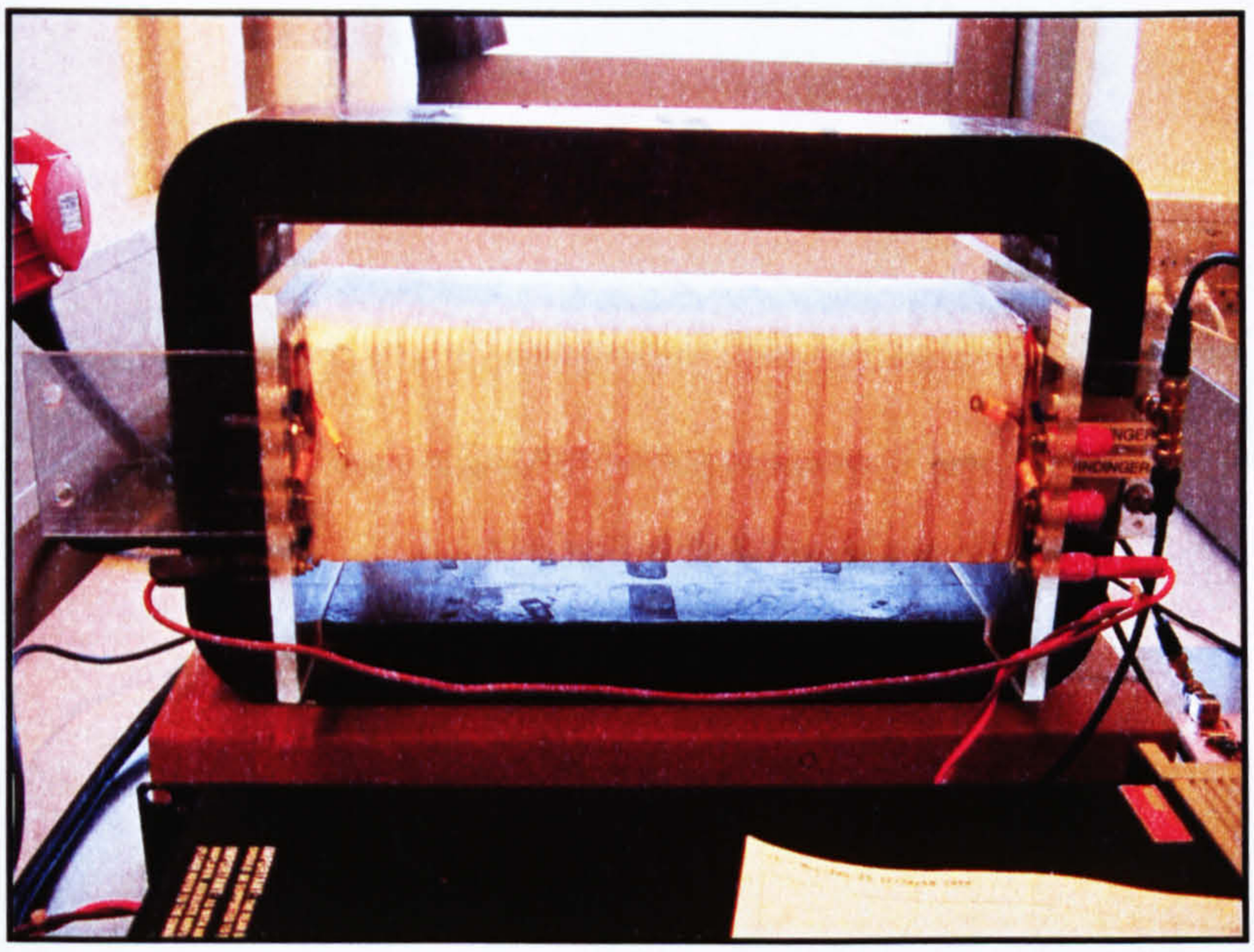

Fig. A6.1. Single sheet tester yoke used in measurement of iron losses of sheet steels

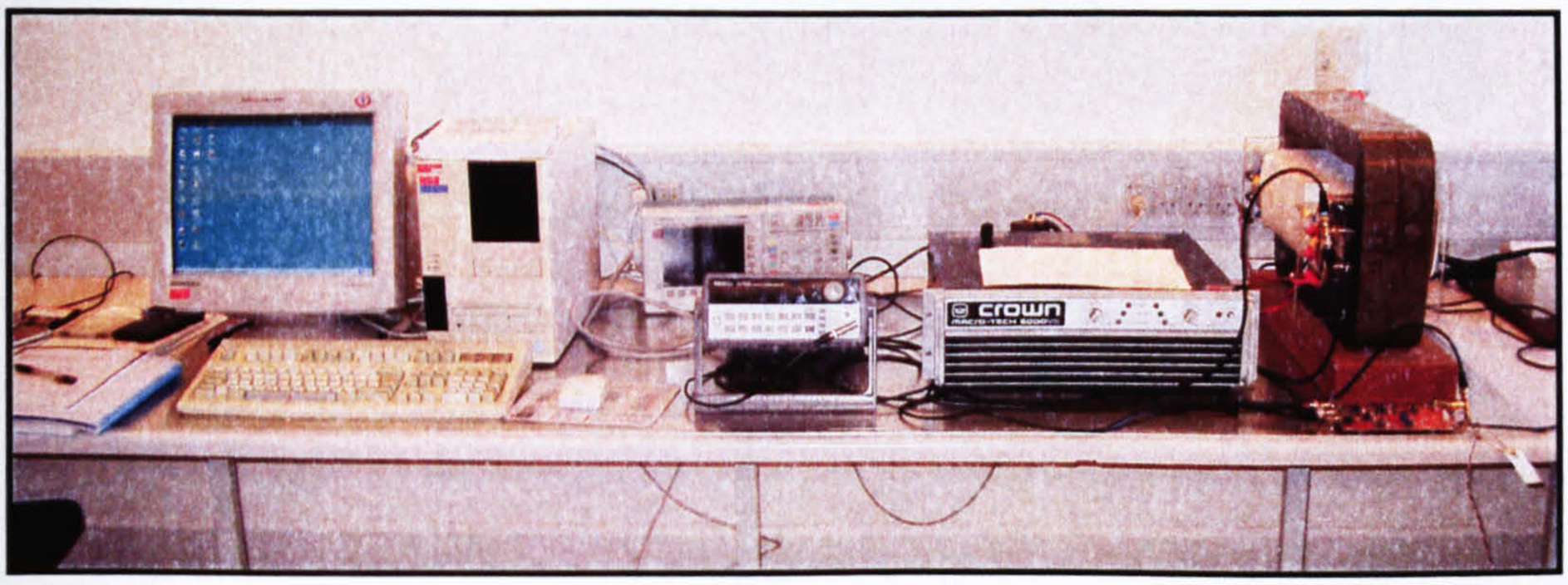

Fig. A6.2. Complete single sheet tester test set-up

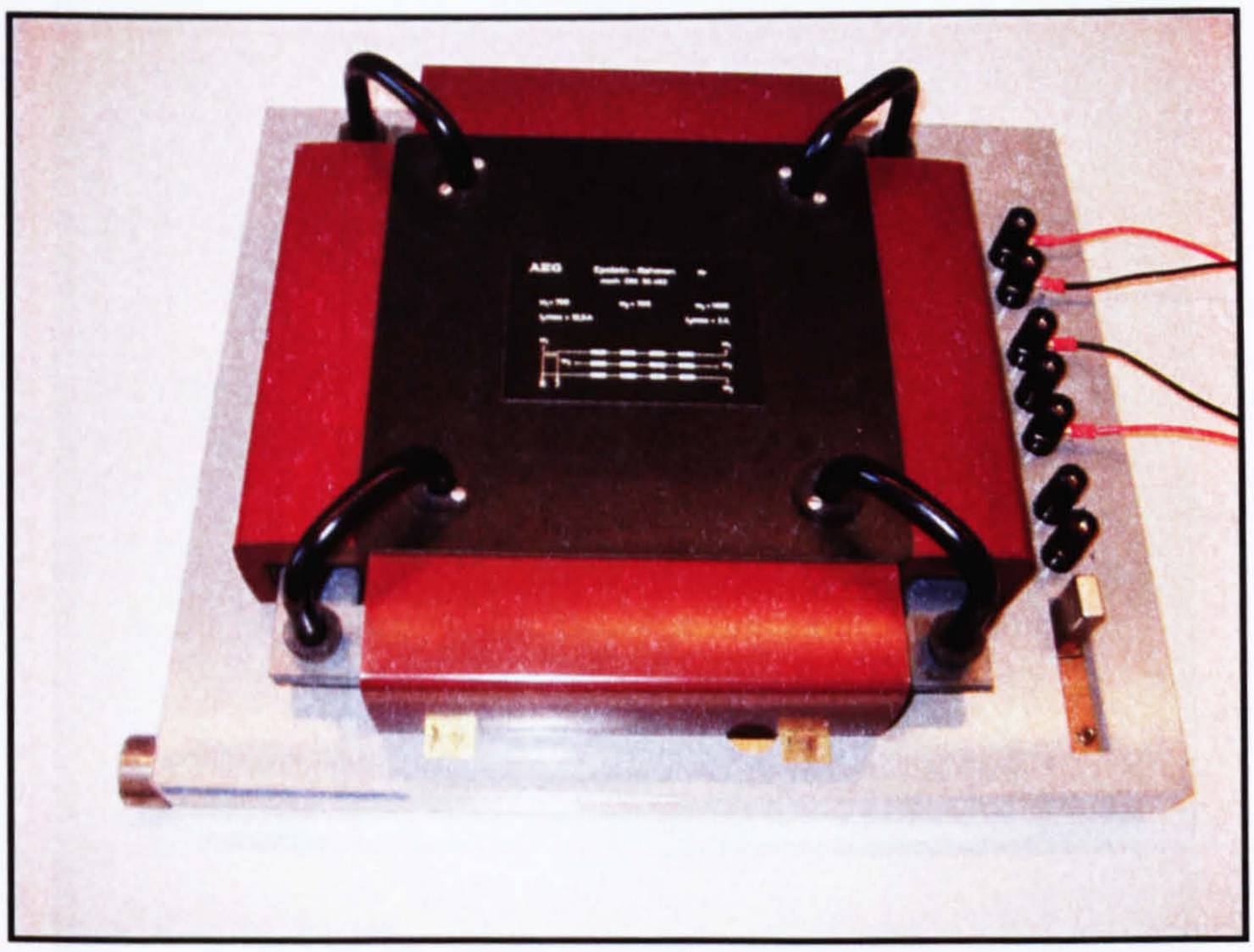

Fig. A6.3. Epstein square test yoke used in measurement of iron losses of sheet steels

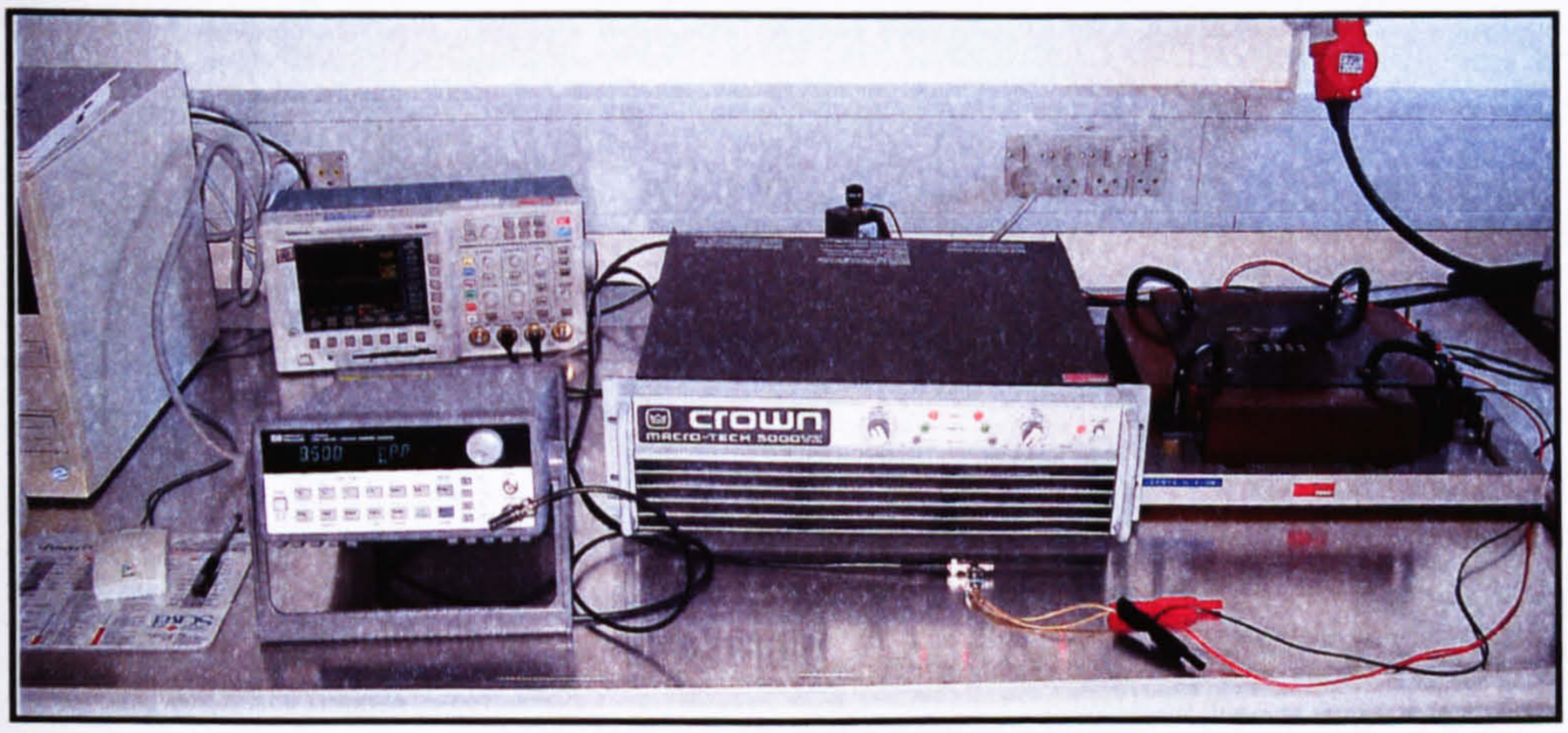

Fig. A6.4. Complete Epstein square test set-up

Fig. A6.5. Toroid ring sample for use in iron loss tests

Appendix 7

Measured Material Data

A7.1. Nested hysteresis loops

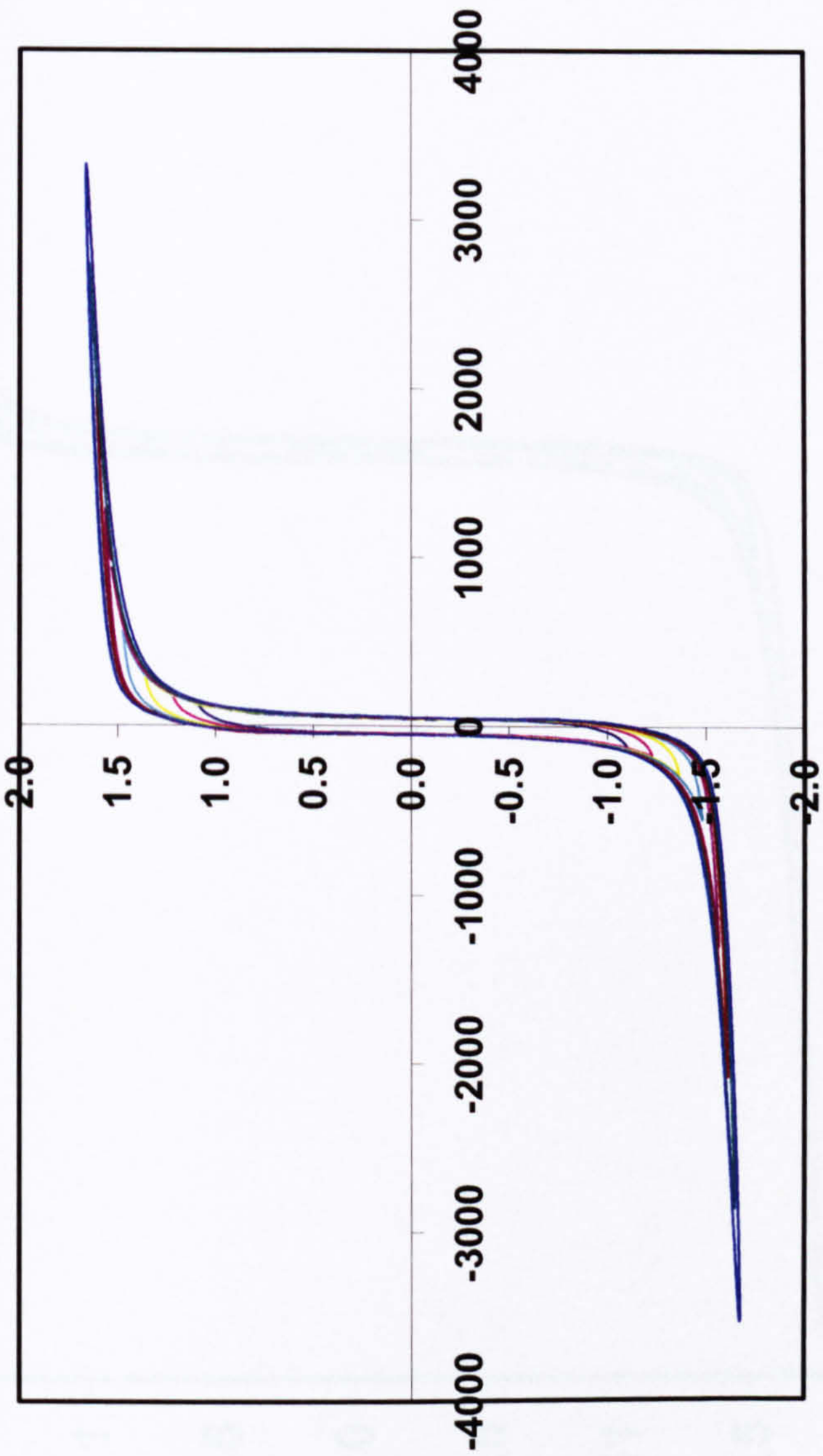

Fig. A7.1. Hysteresis loops measured at 5 Hz on single sheet tester

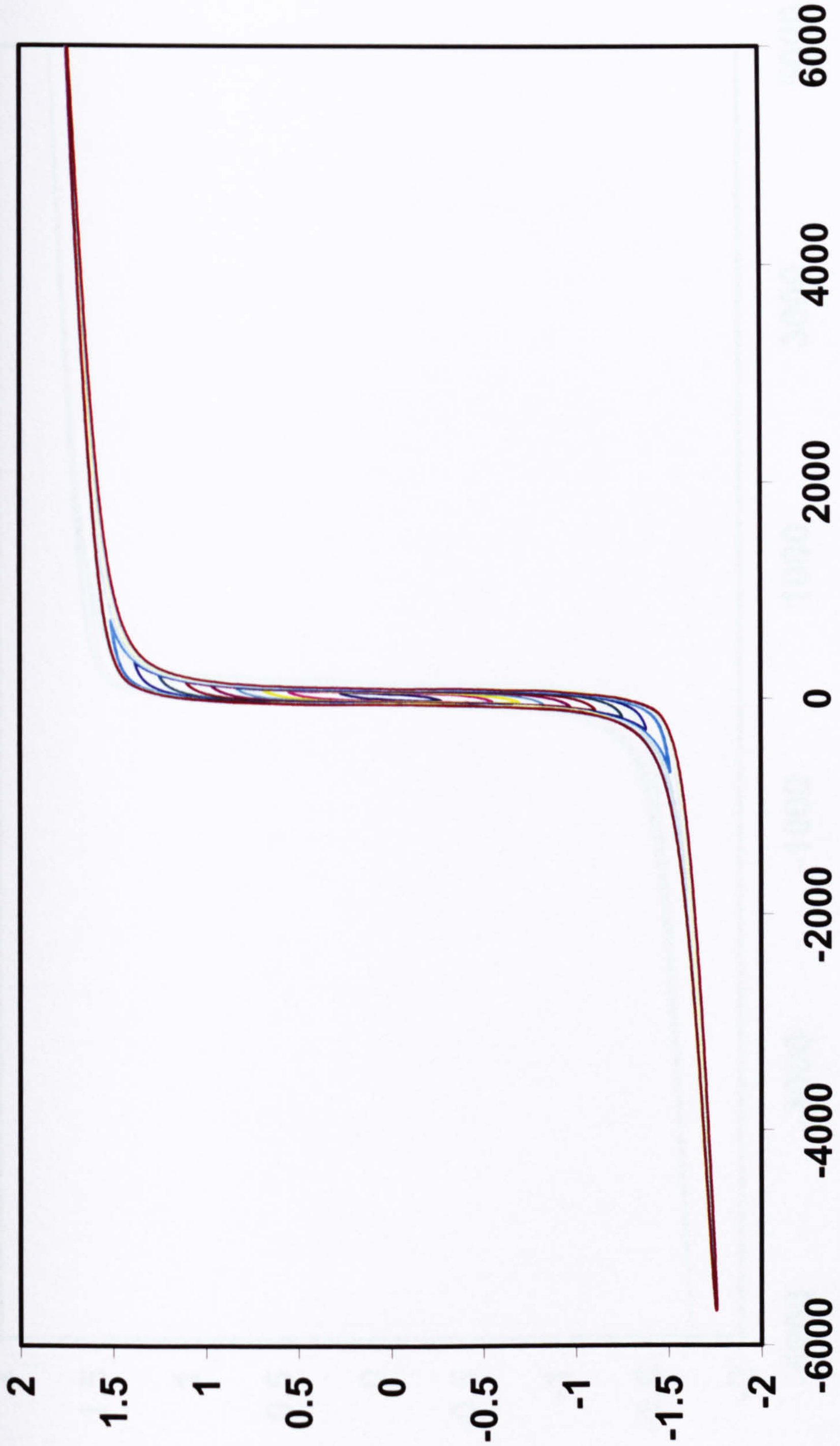

Fig. A7.2. Hysteresis loops measured at 20 Hz on single sheet tester

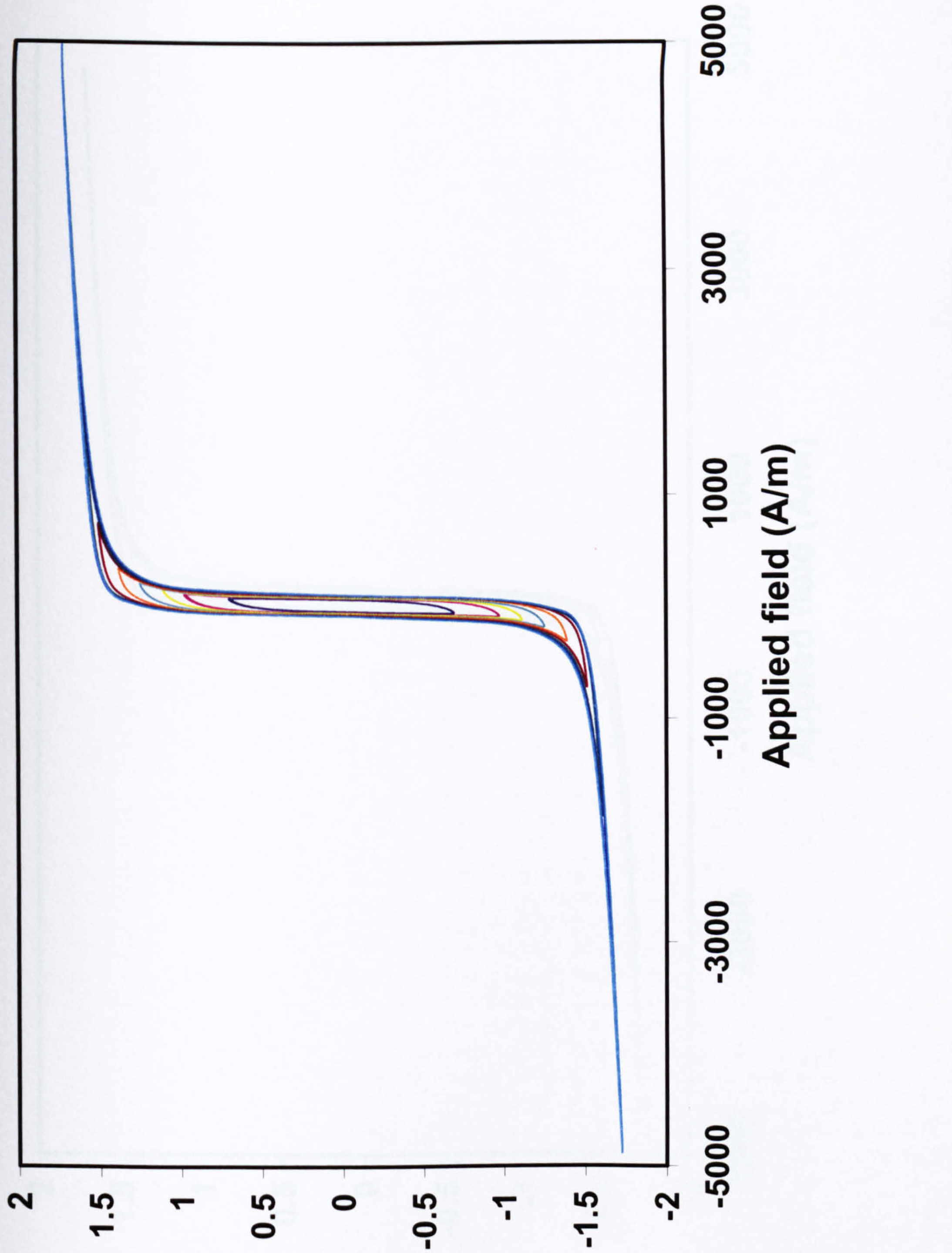

Fig. A7.3. Hysteresis loops measured at 40 Hz on single sheet tester

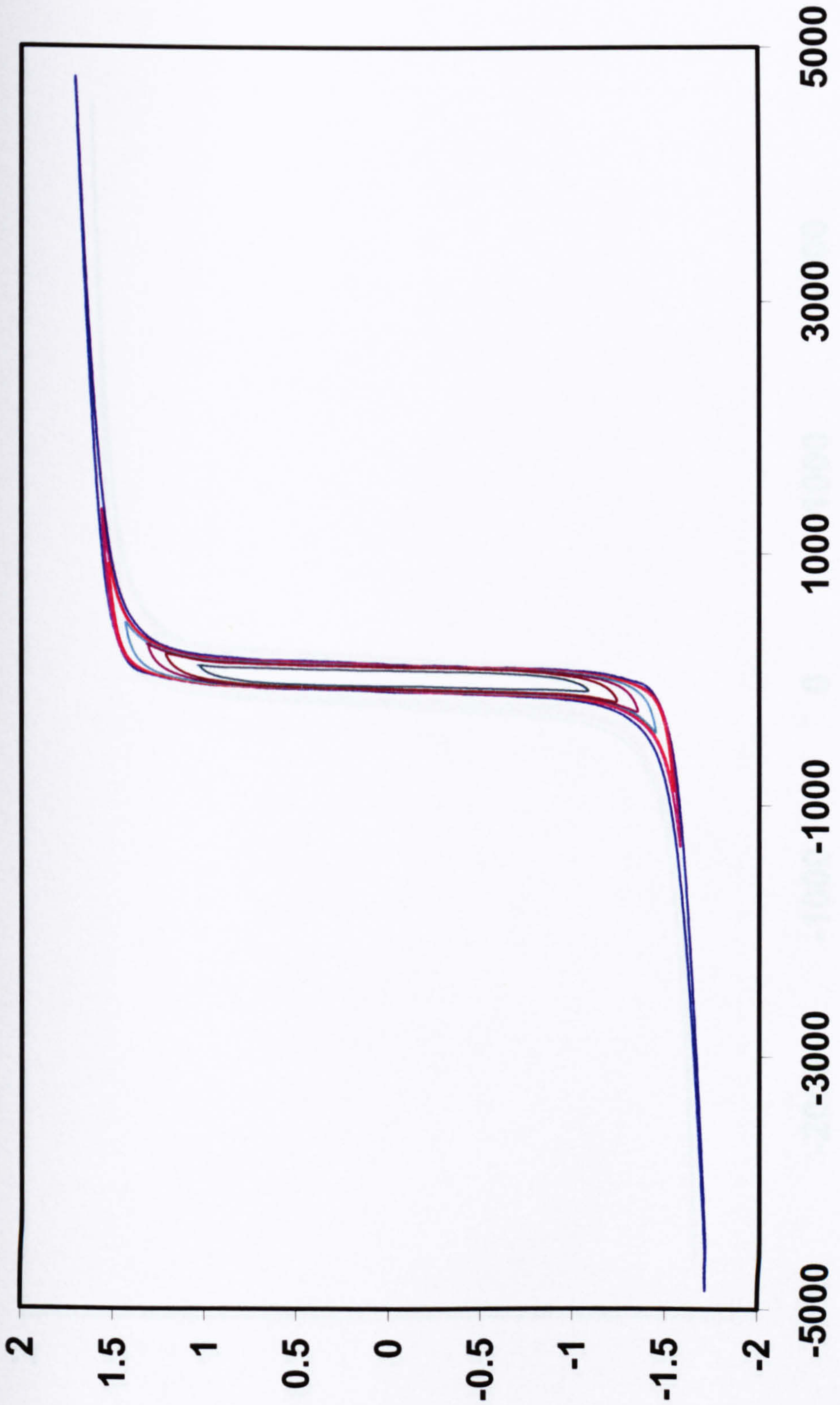

Fig. A7.4. Hysteresis loops measured at 50 Hz on single sheet tester

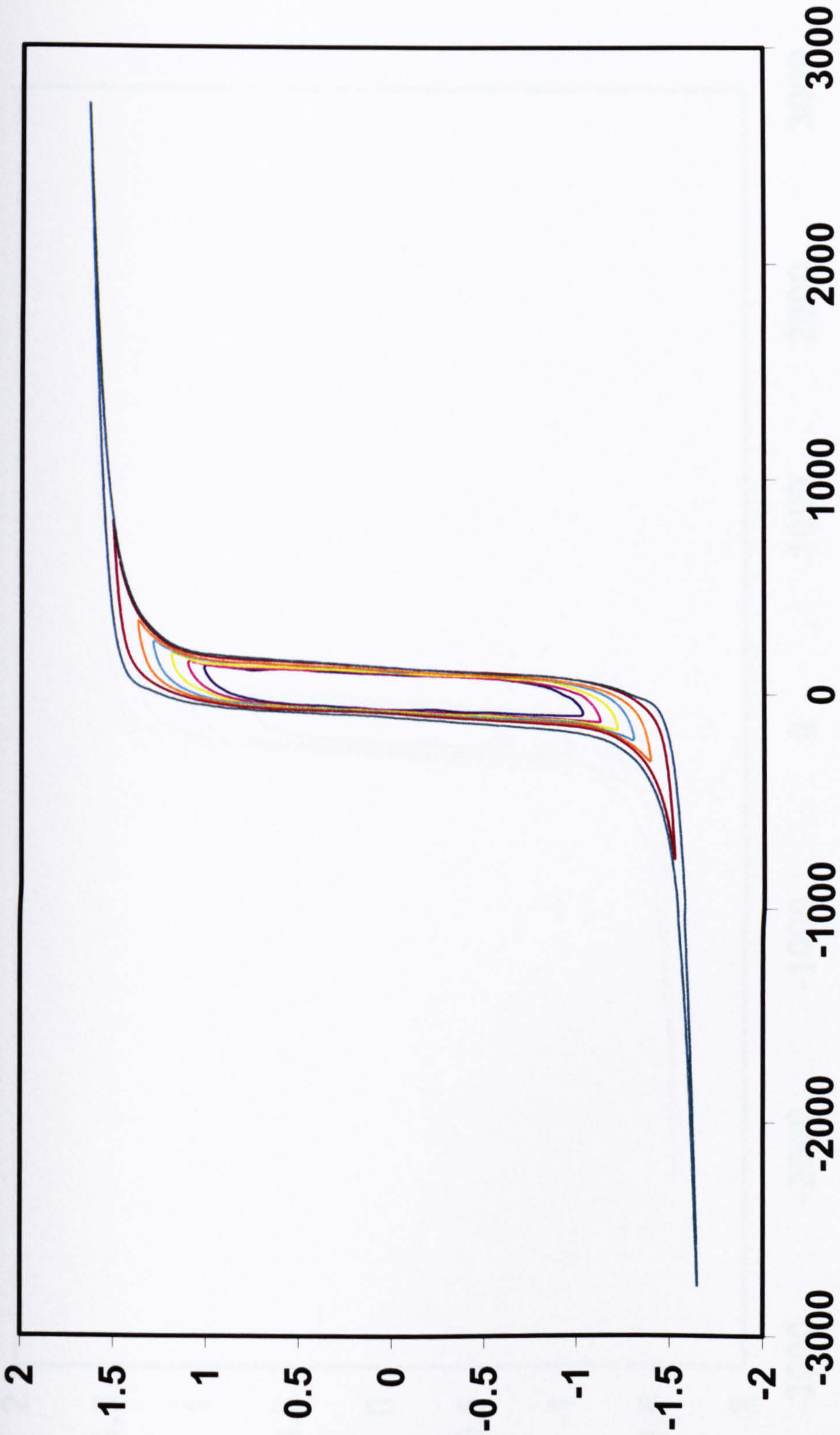

Fig. A7.5. Hysteresis loops measured at 60 Hz on single sheet tester

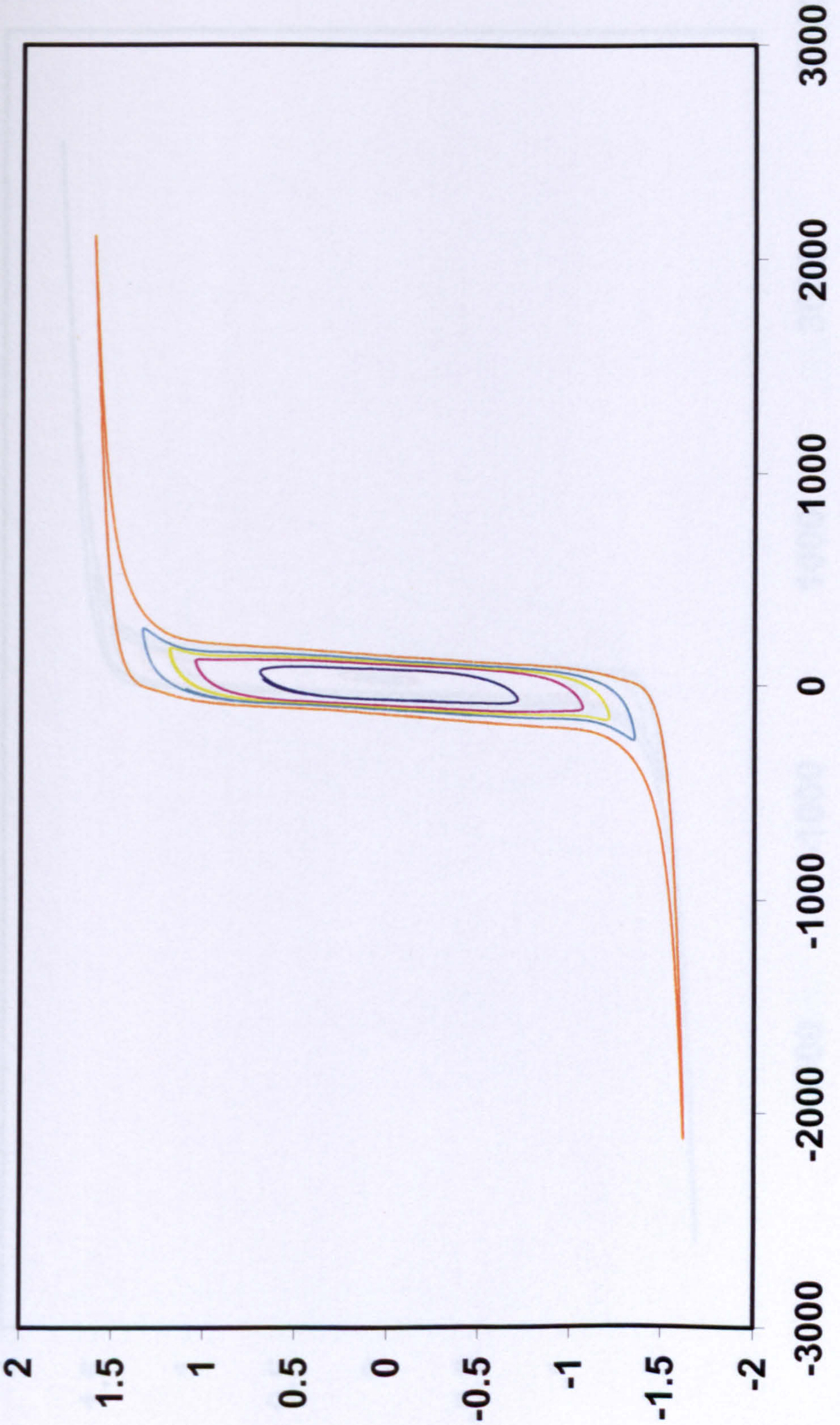

Fig. A7.6. Hysteresis loops measured at 80 Hz on single sheet tester

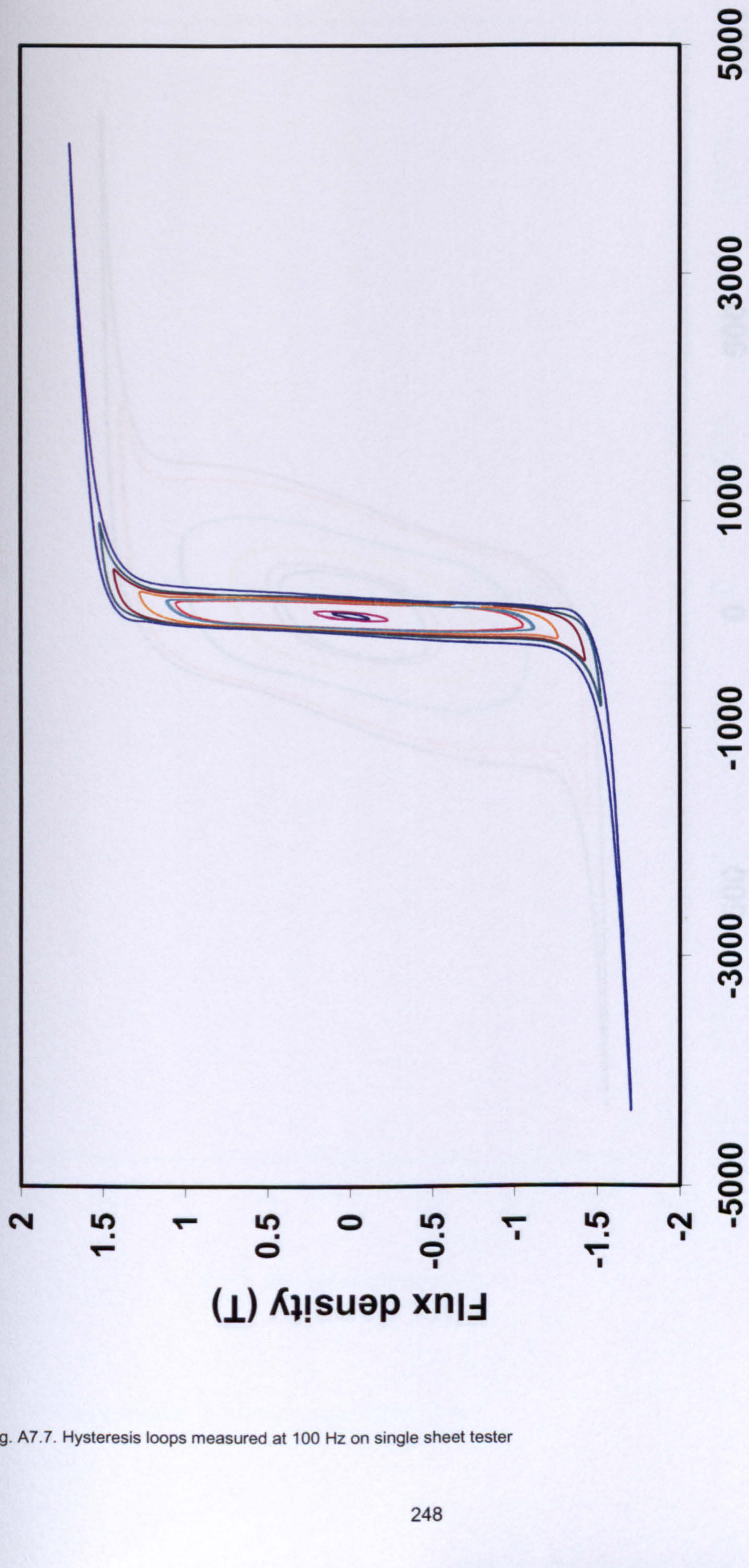

Fig. A7.7. Hysteresis loops measured at 100 Hz on single sheet tester

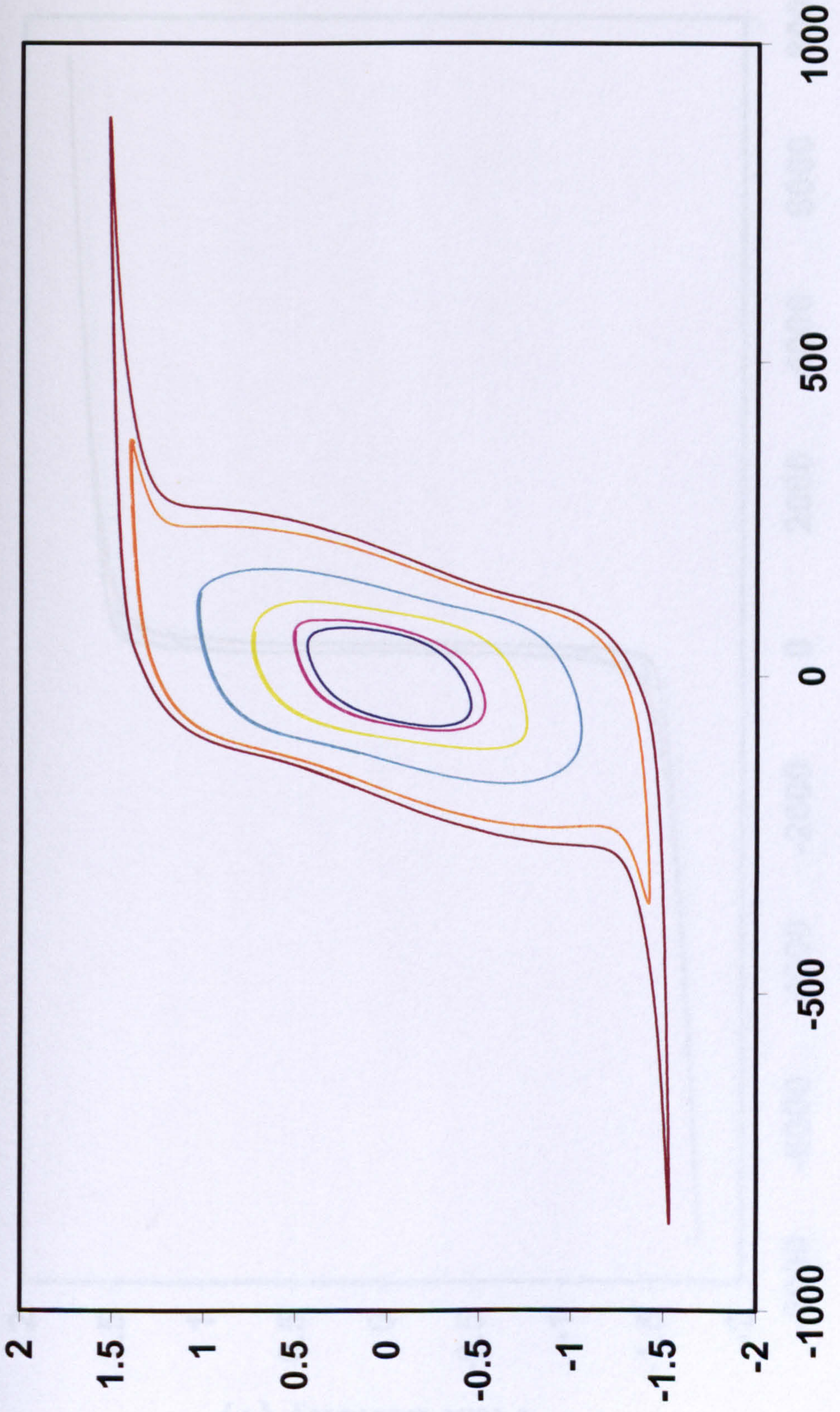

Fig. A7.8. Hysteresis loops measured at 150 Hz on single sheet tester

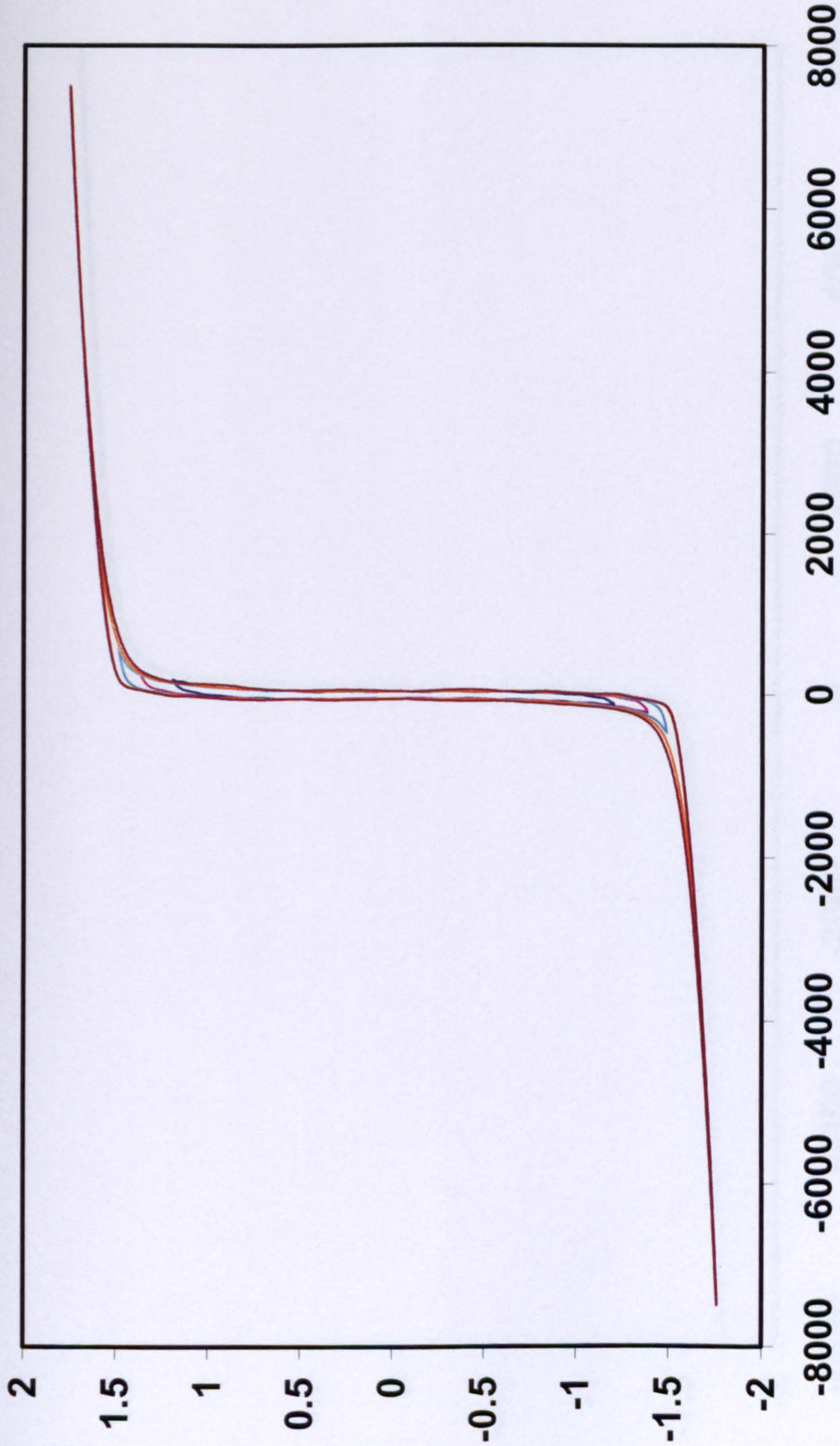

Fig. A7.9. Hysteresis loops at 6 Hz measured on Epstein square

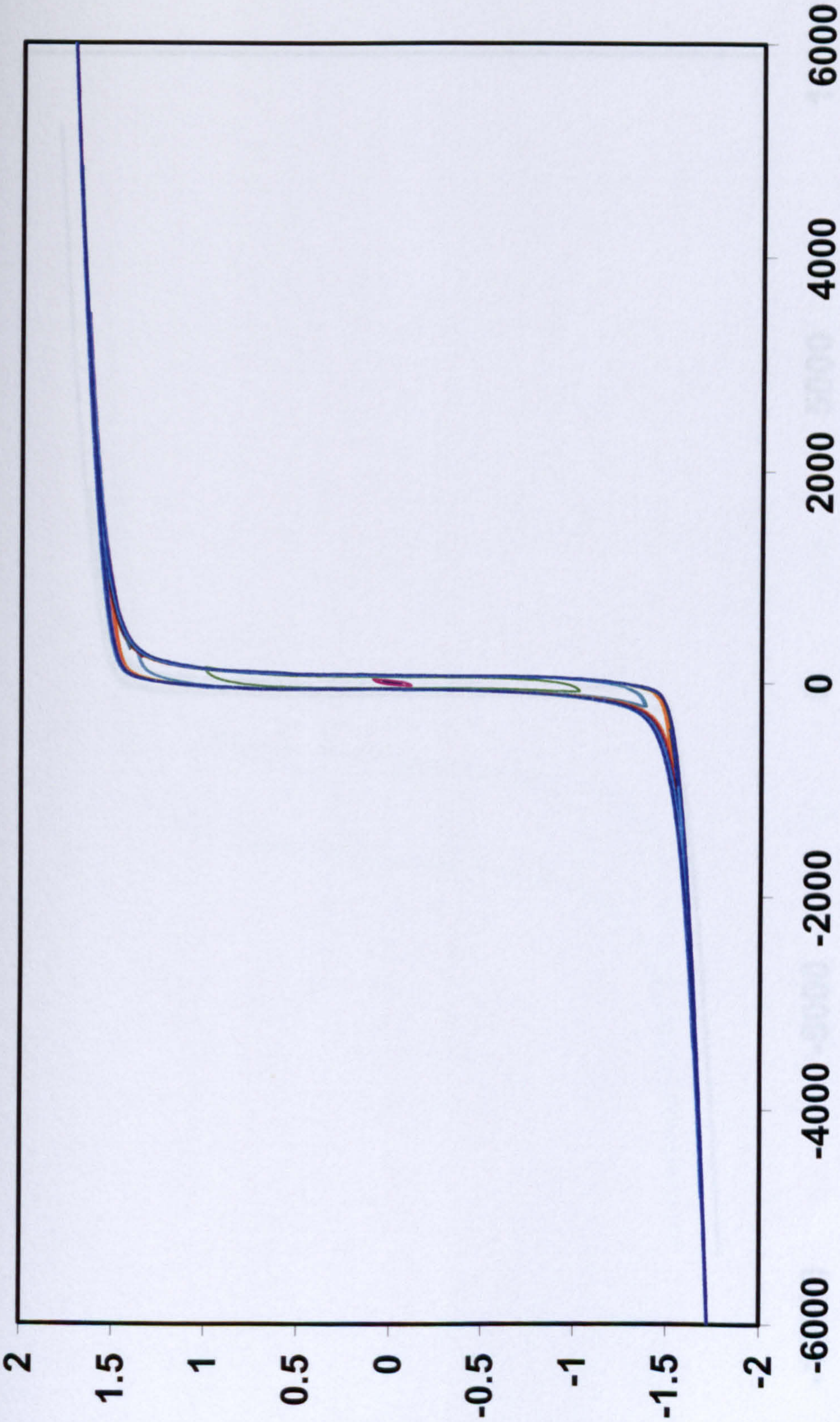

Fig. A7.10. Hysteresis loops at 20 Hz measured on Epstein square

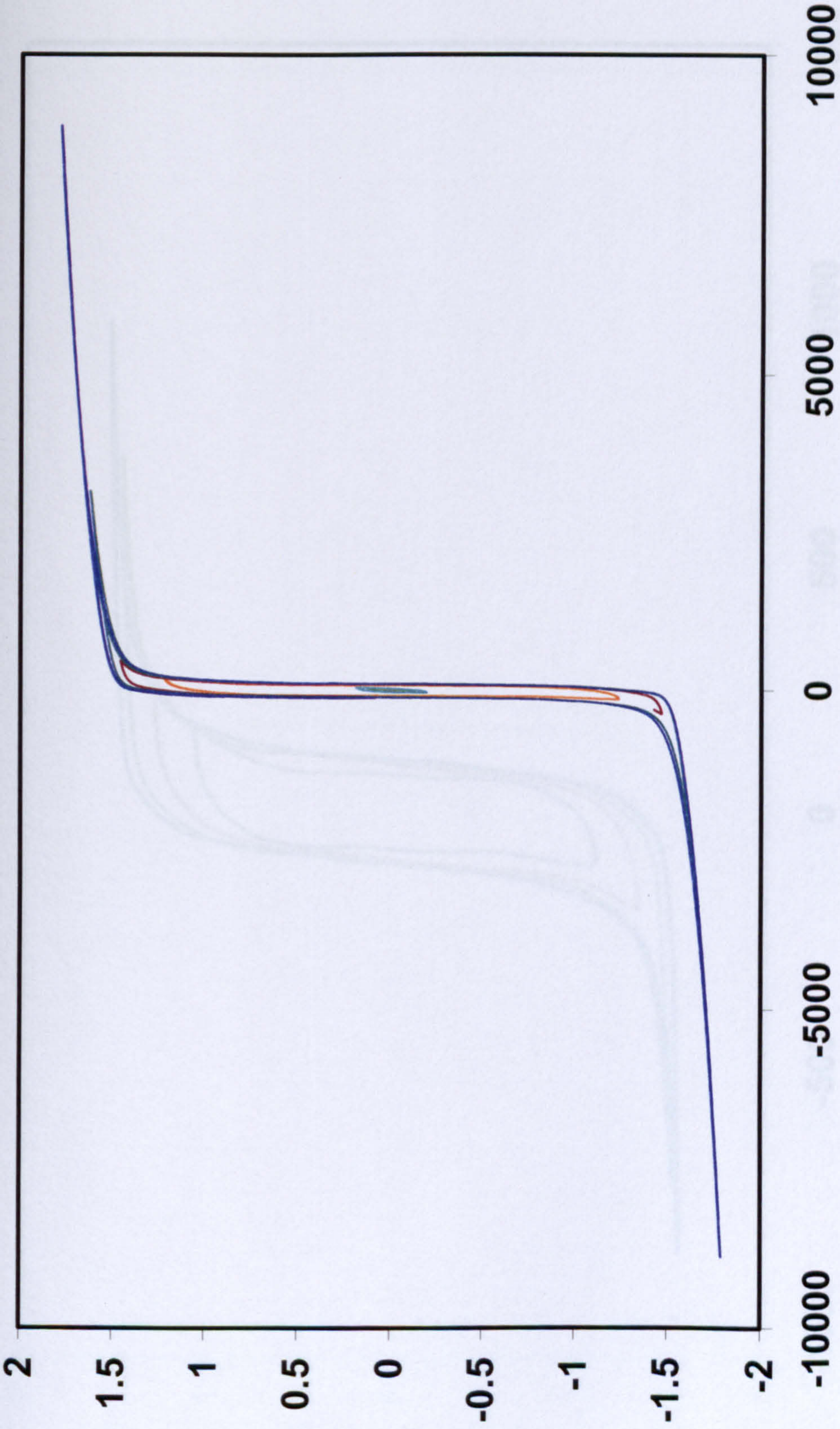

Fig. A7.11. Hysteresis loops at 40 Hz measured on Epstein square

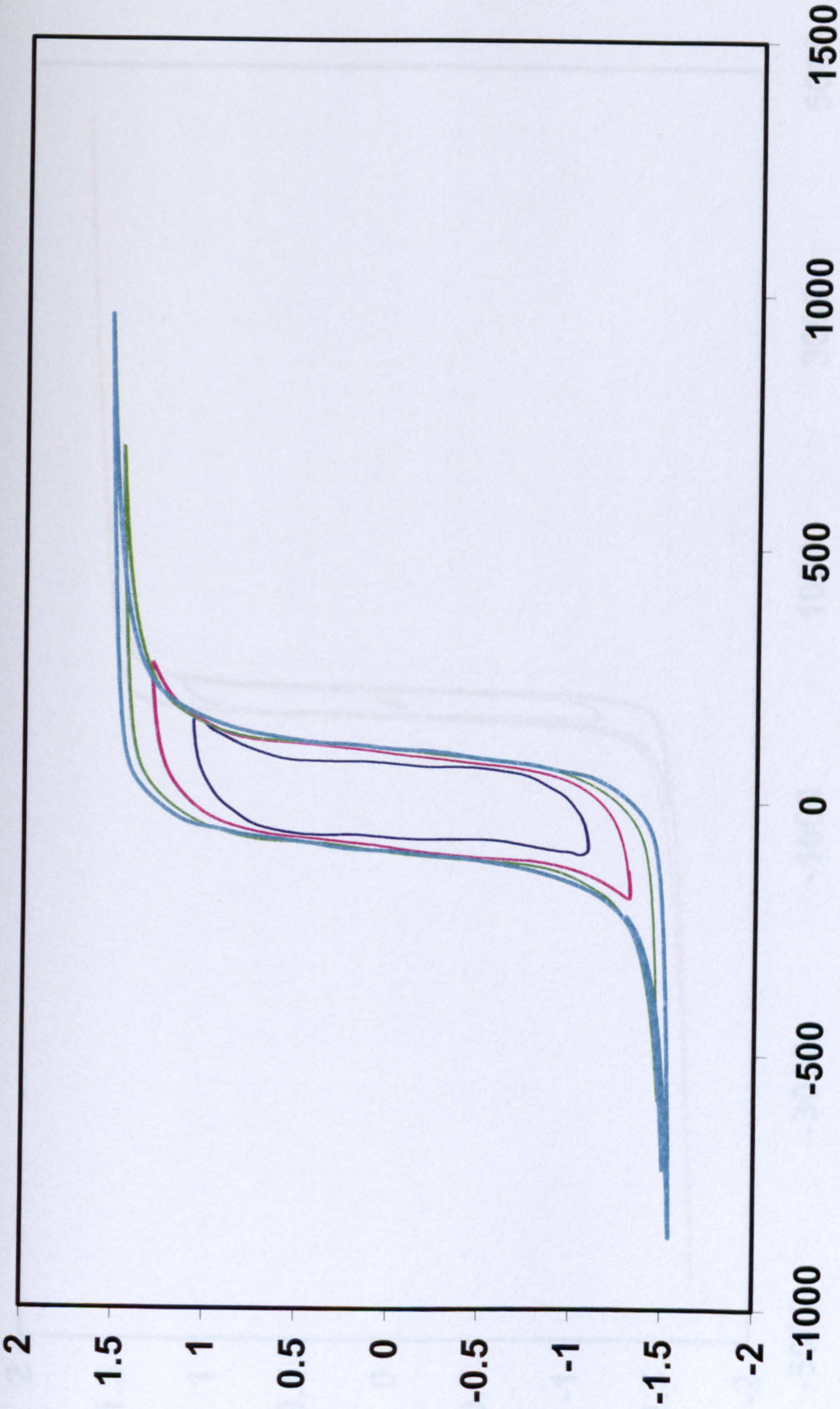

Fig. A7.12. Hysteresis loops at 50 Hz measured on Epstein square

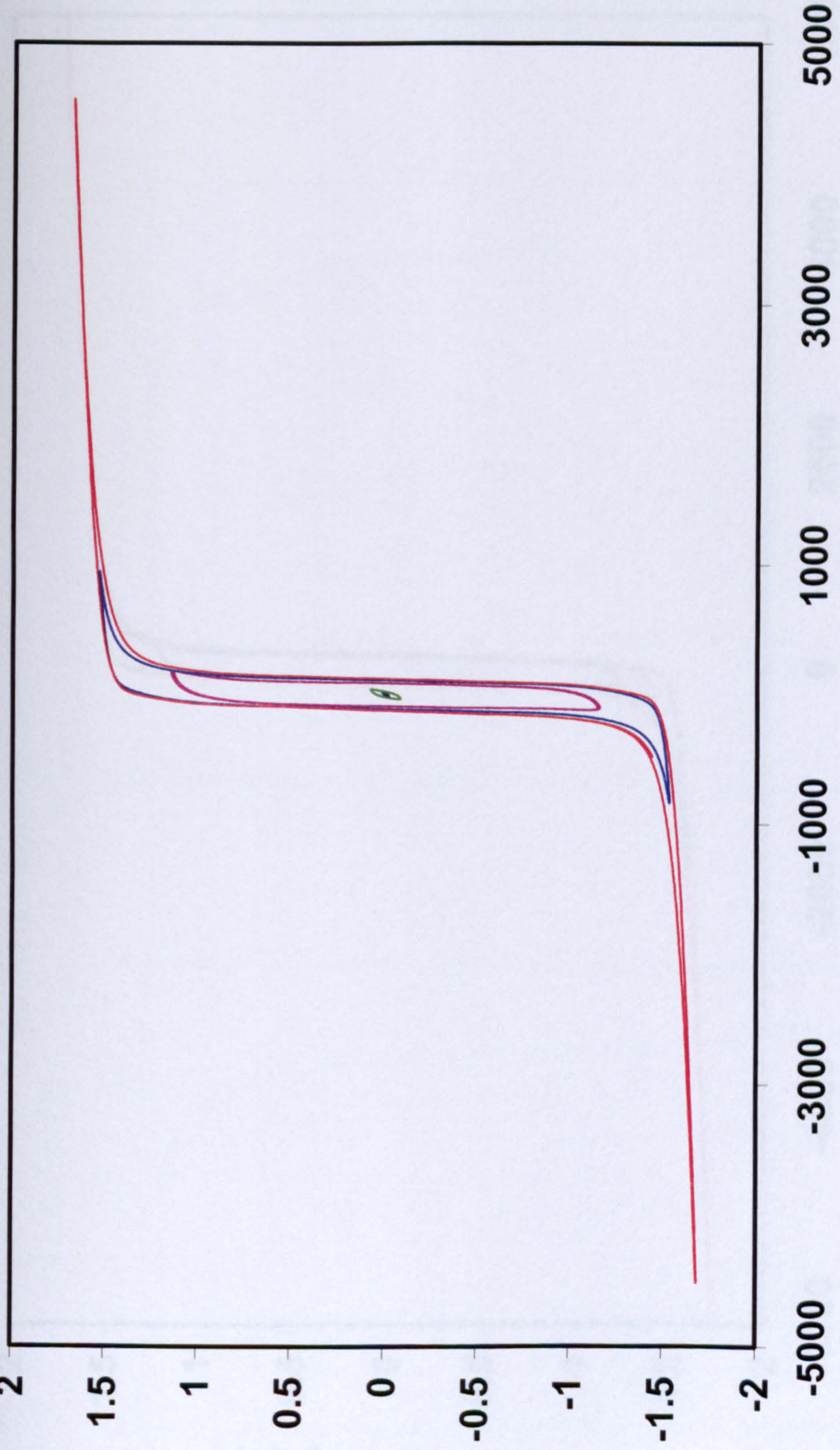

Fig. A7.13. Hysteresis loops measured at 60 Hz on Epstein square

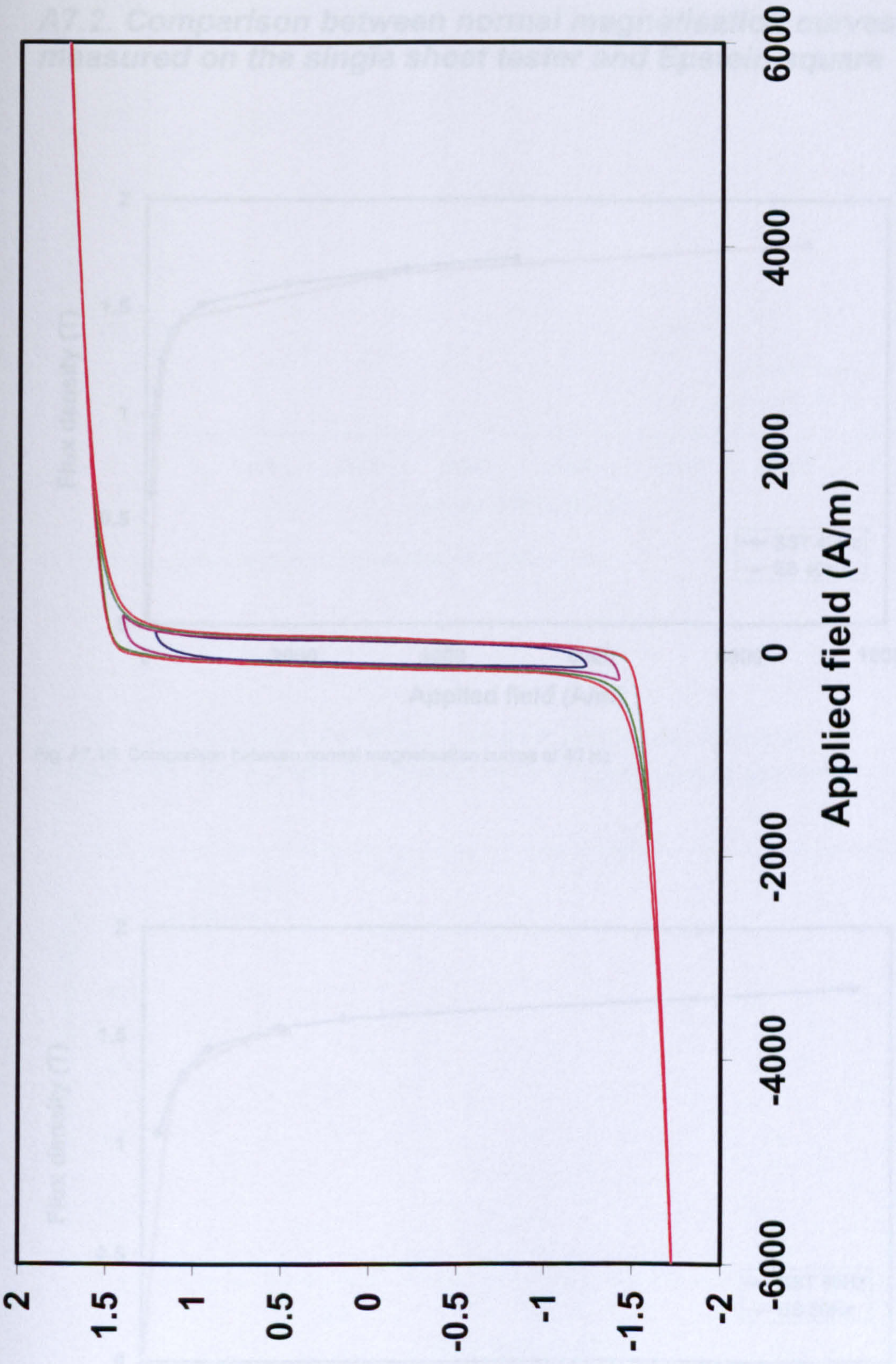

Fig. A7.14. Hysteresis loops measured at 80 Hz on Epstein square

A7.2. Comparison between normal magnetisation curves measured on the single sheet tester and Epstein square

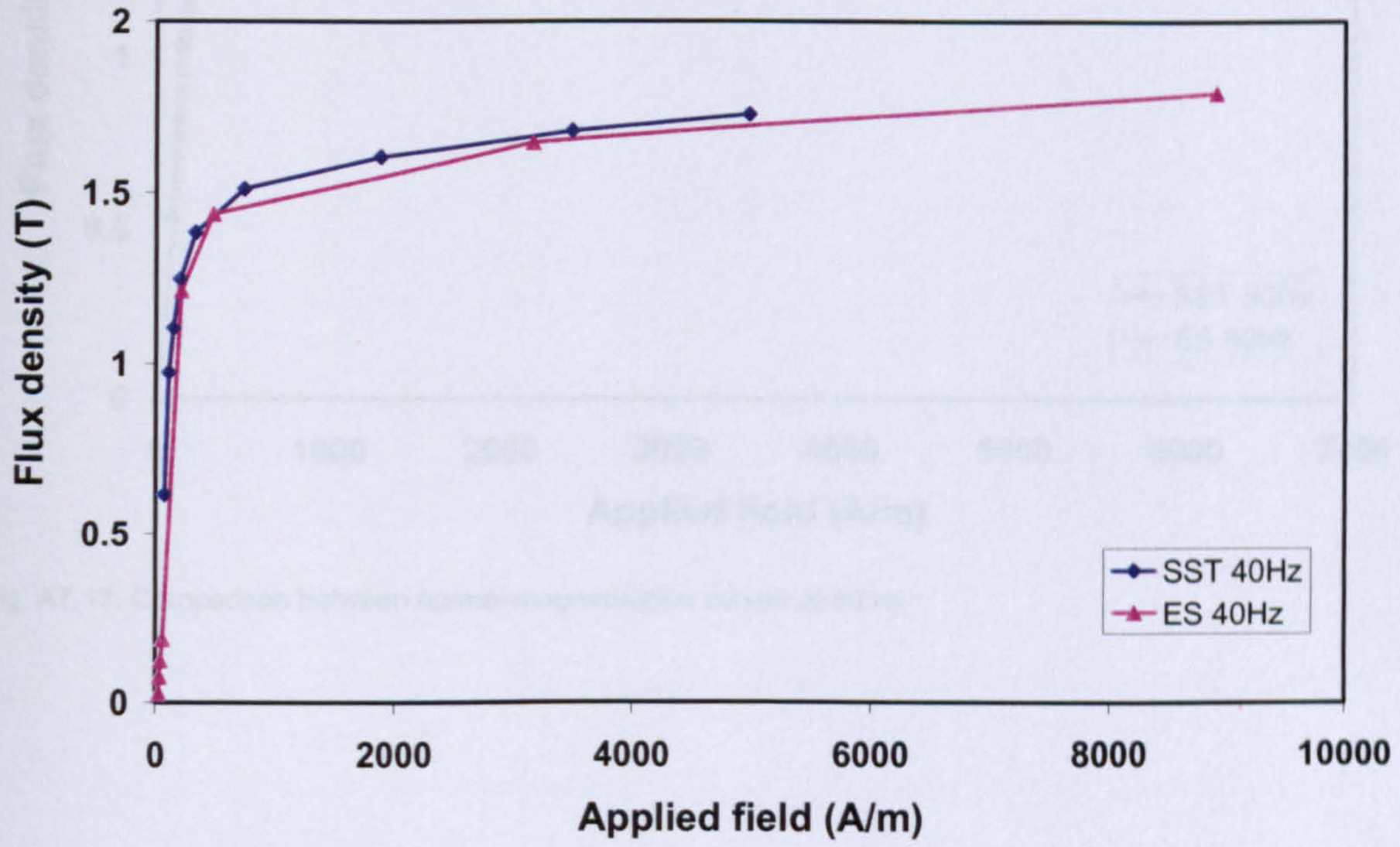

Fig. A7.15. Comparison between normal magnetisation curves at 40 Hz

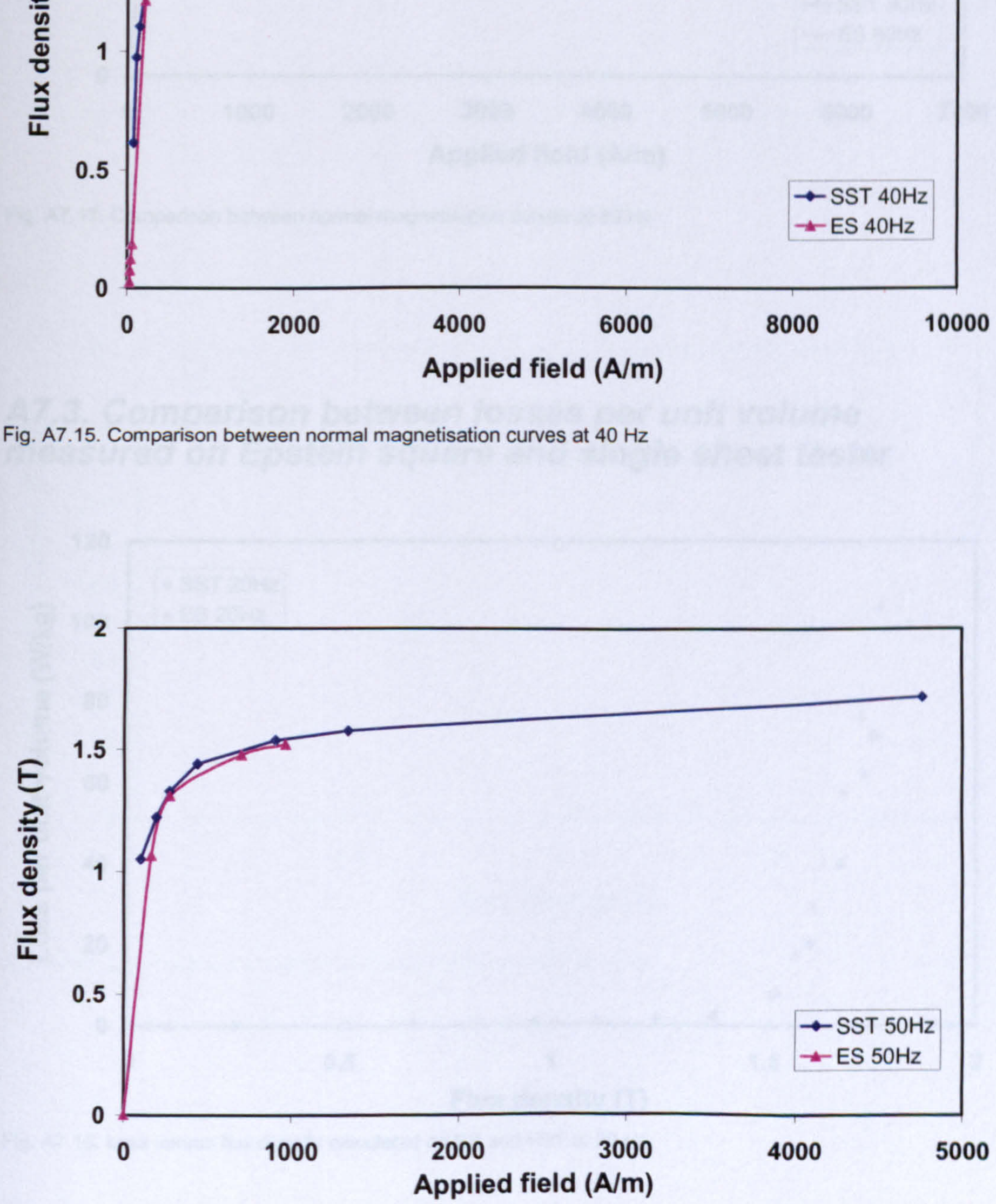

Fig. A7.16. Comparison between normal magnetisation curves at 50 Hz

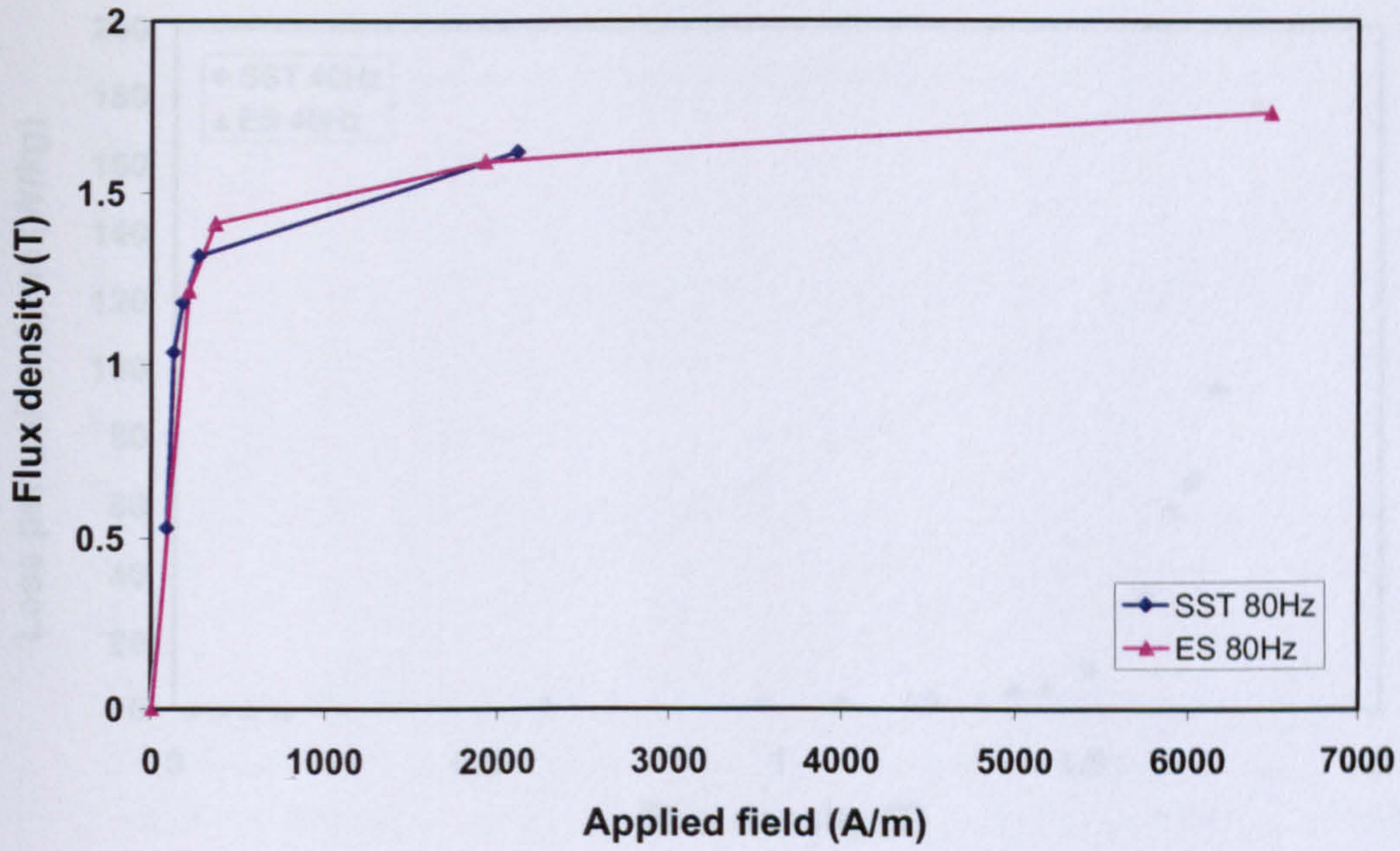

Fig. A7.17. Comparison between normal magnetisation curves at 80 Hz

A7.3. Comparison between losses per unit volume measured on Epstein square and single sheet tester

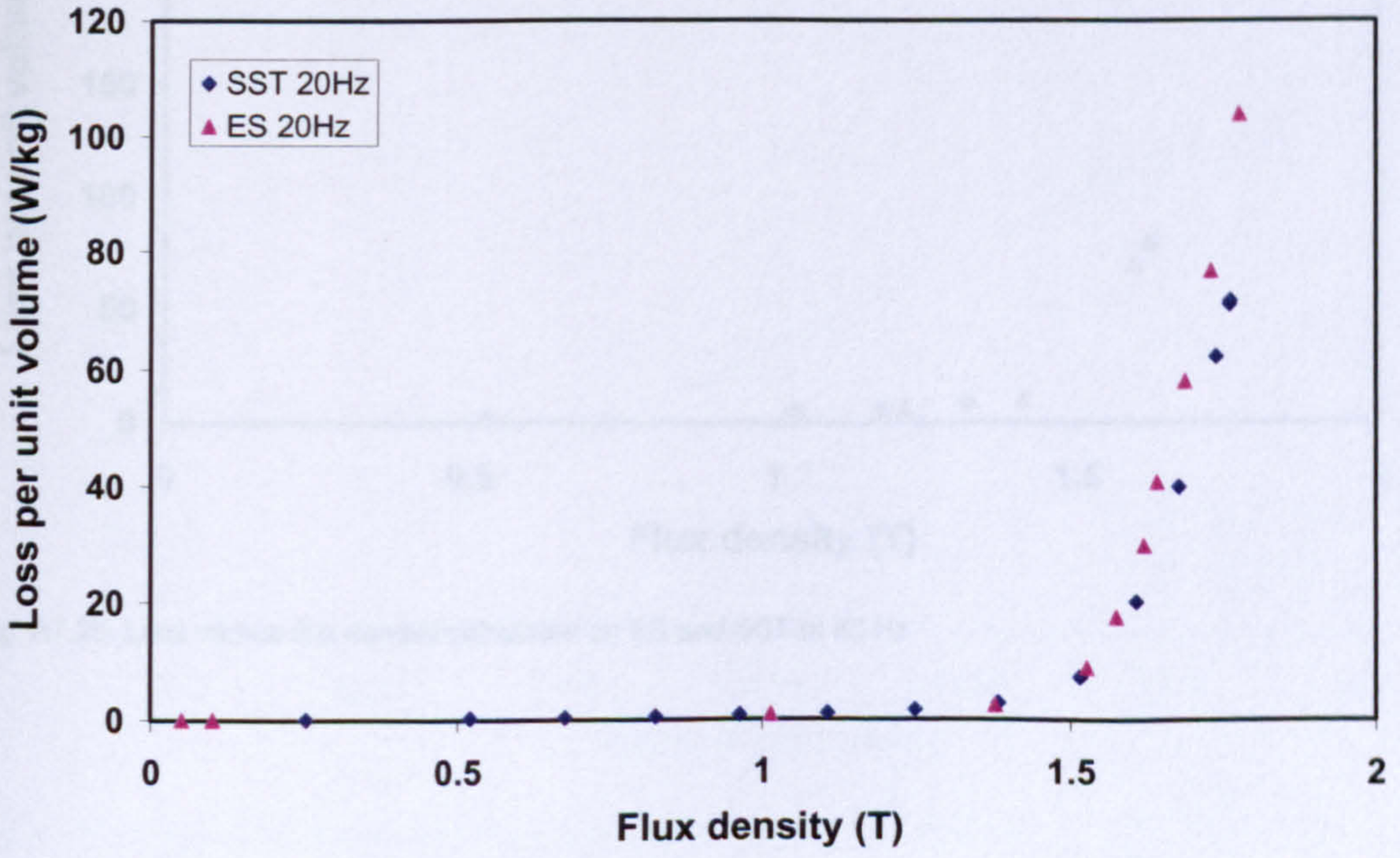

Fig. A7.18. Loss versus flux density calculated on ES and SST at 20 Hz

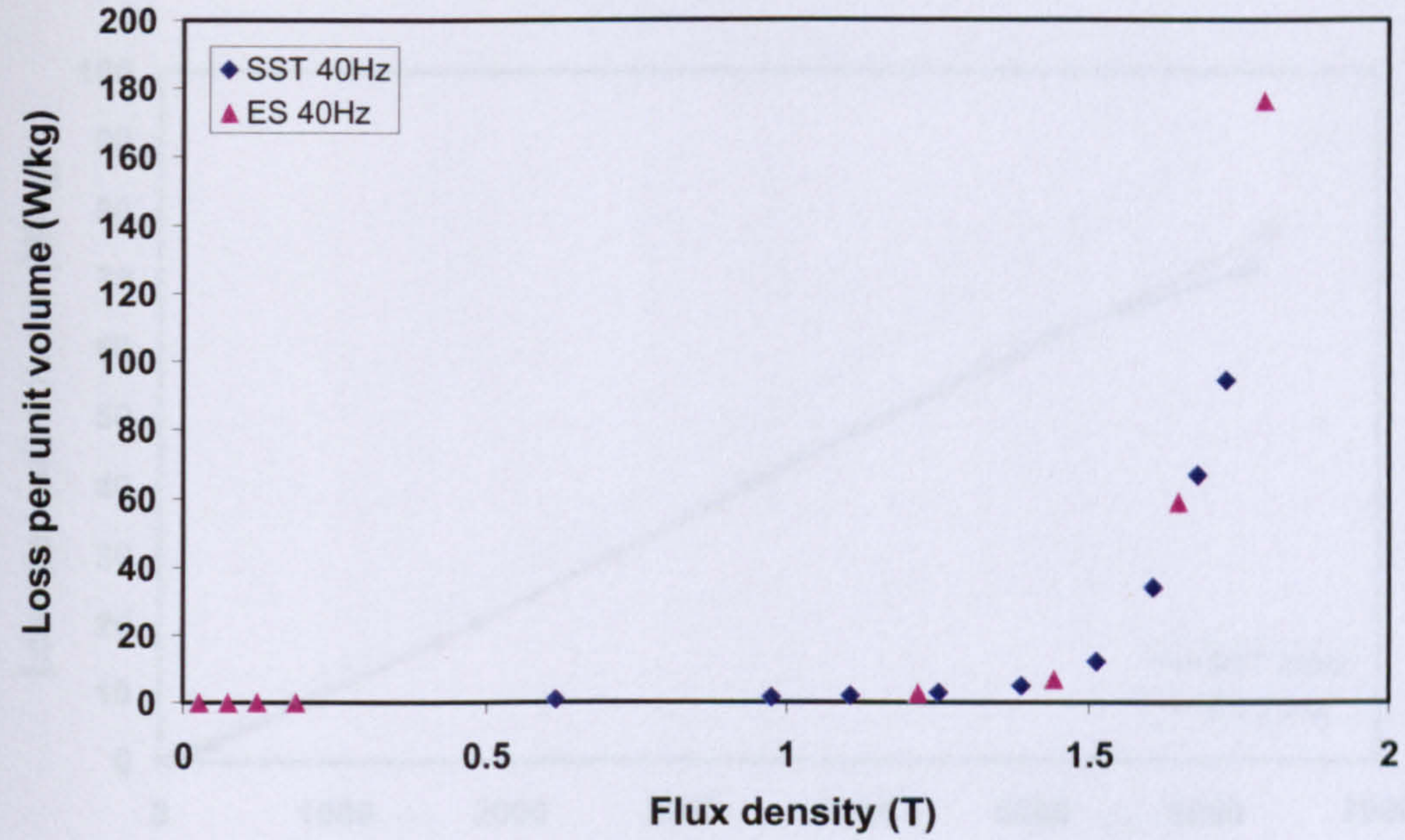

Fig. A7.19. Loss versus flux density calculated on ES and SST at 40 Hz

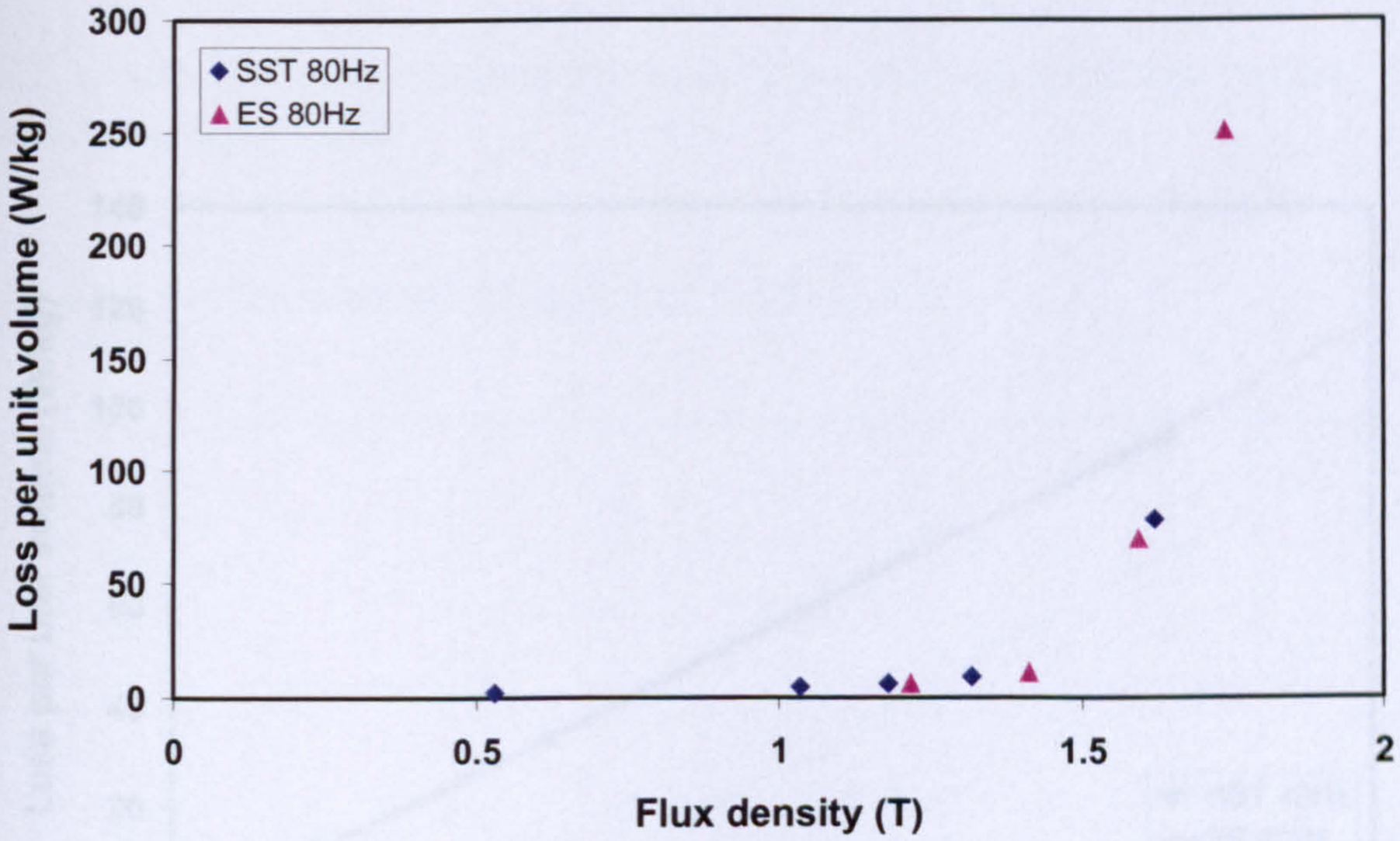

Fig. A7.20. Loss versus flux density calculated on ES and SST at 80 Hz

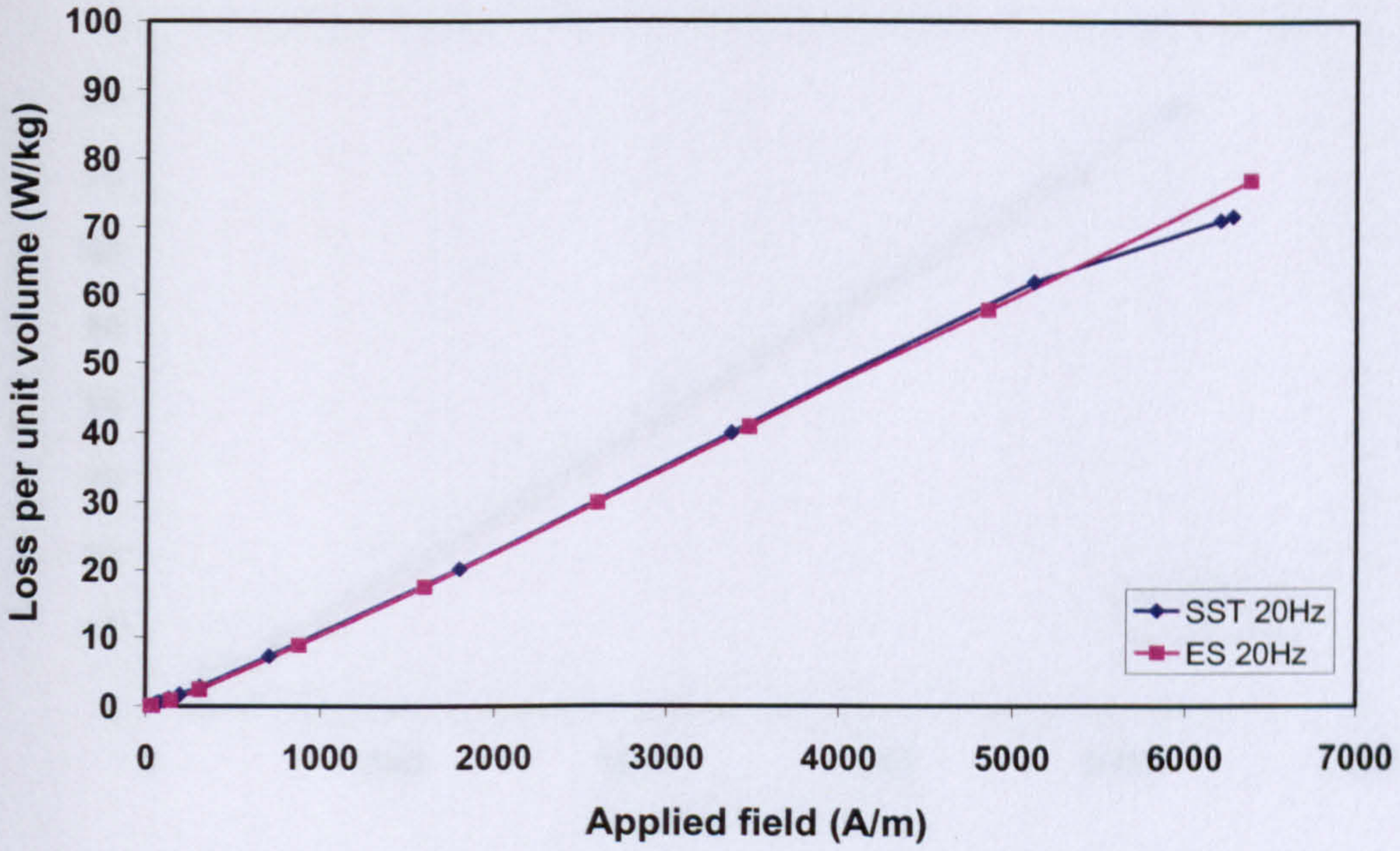

Fig. A7.21. Specific loss versus applied field calculated on ES and SST at 20 Hz

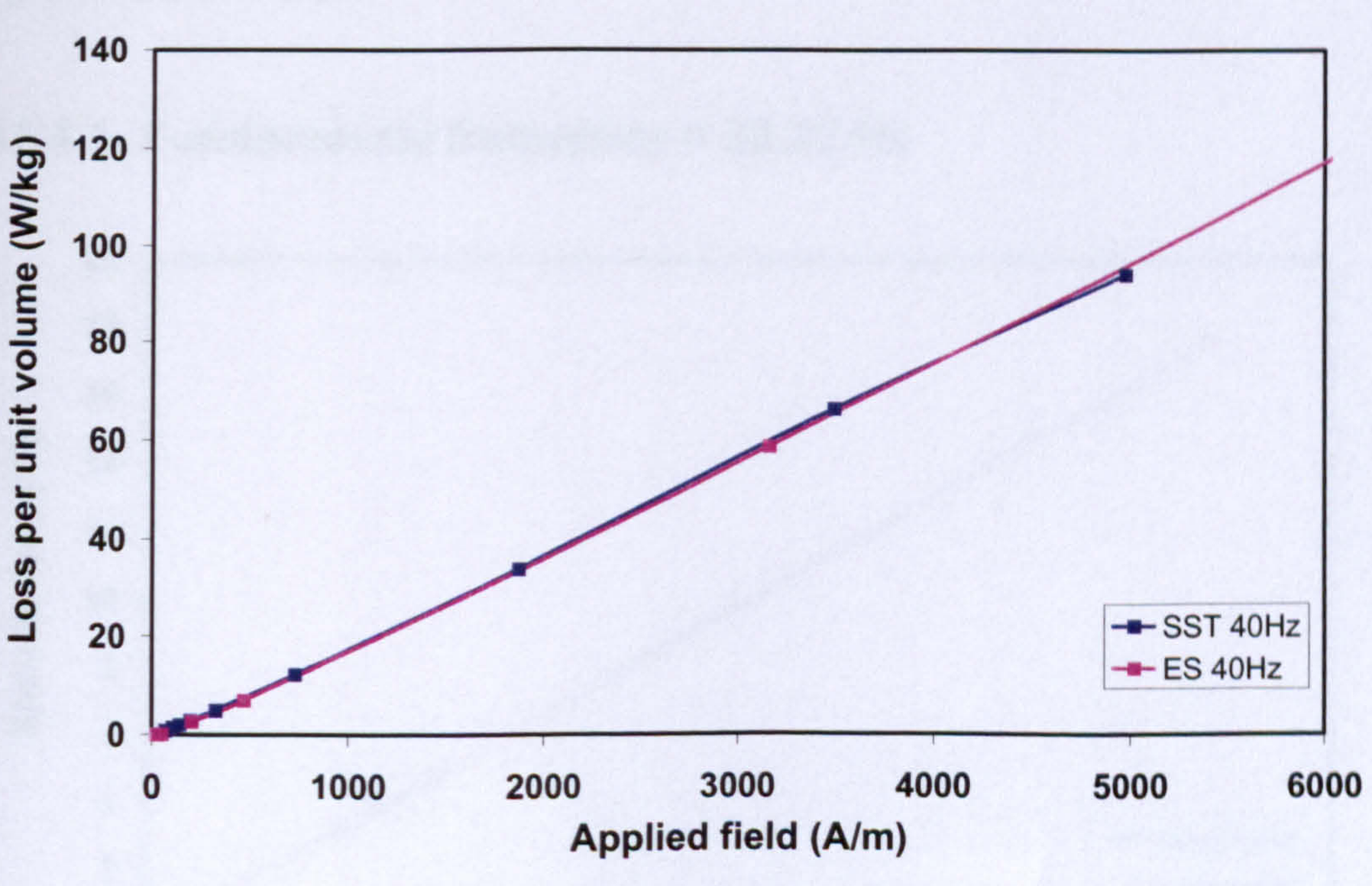

Fig. A7.22. Specific loss versus applied field calculated on ES and SST at 40 Hz

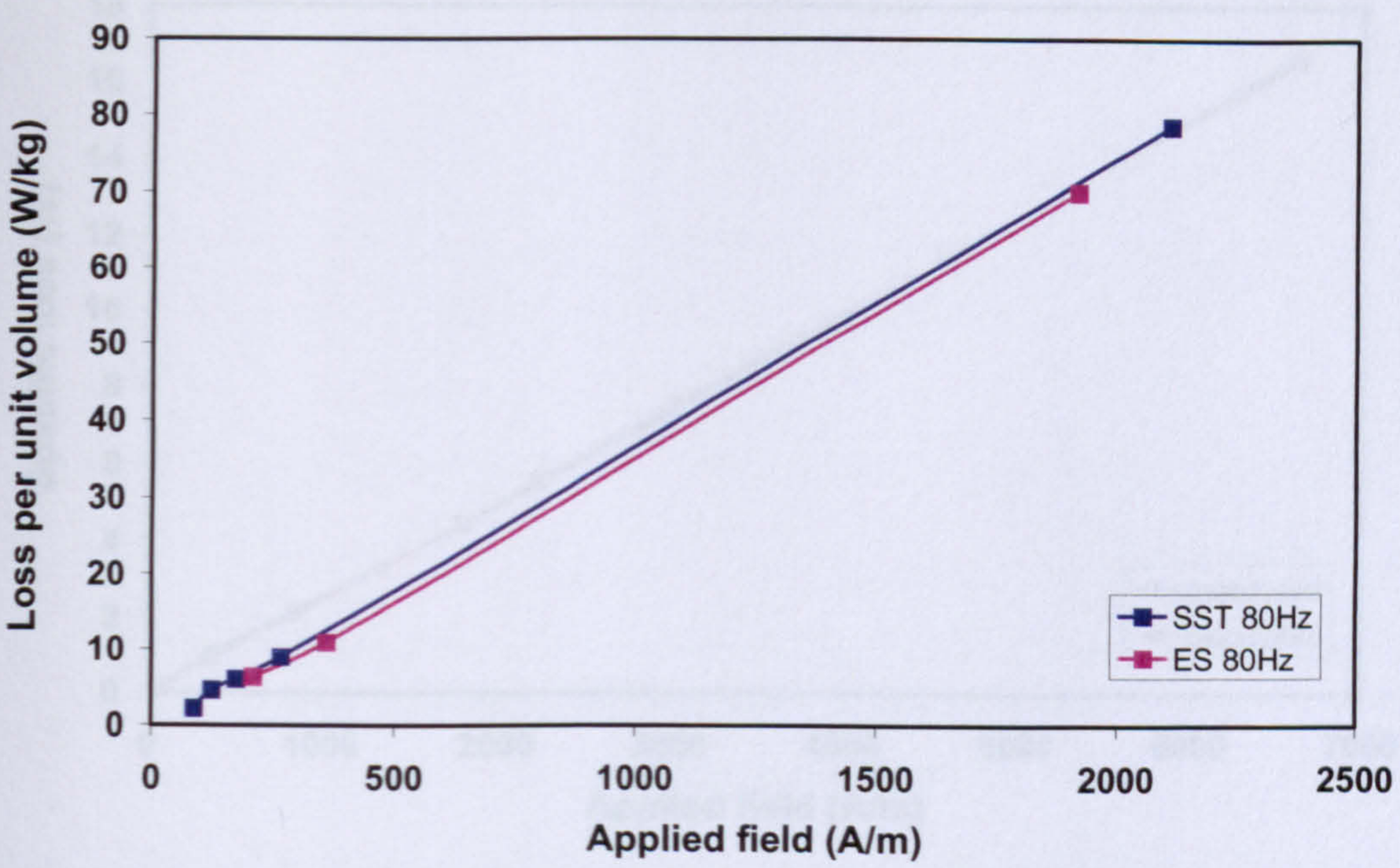

Fig. A7.23. Specific loss versus applied field calculated on ES and SST at 80 Hz

A7.4. Linear approximations of specific losses for minor hysteresis loops

A7.4.1. Fundamental frequency = 22.32 Hz

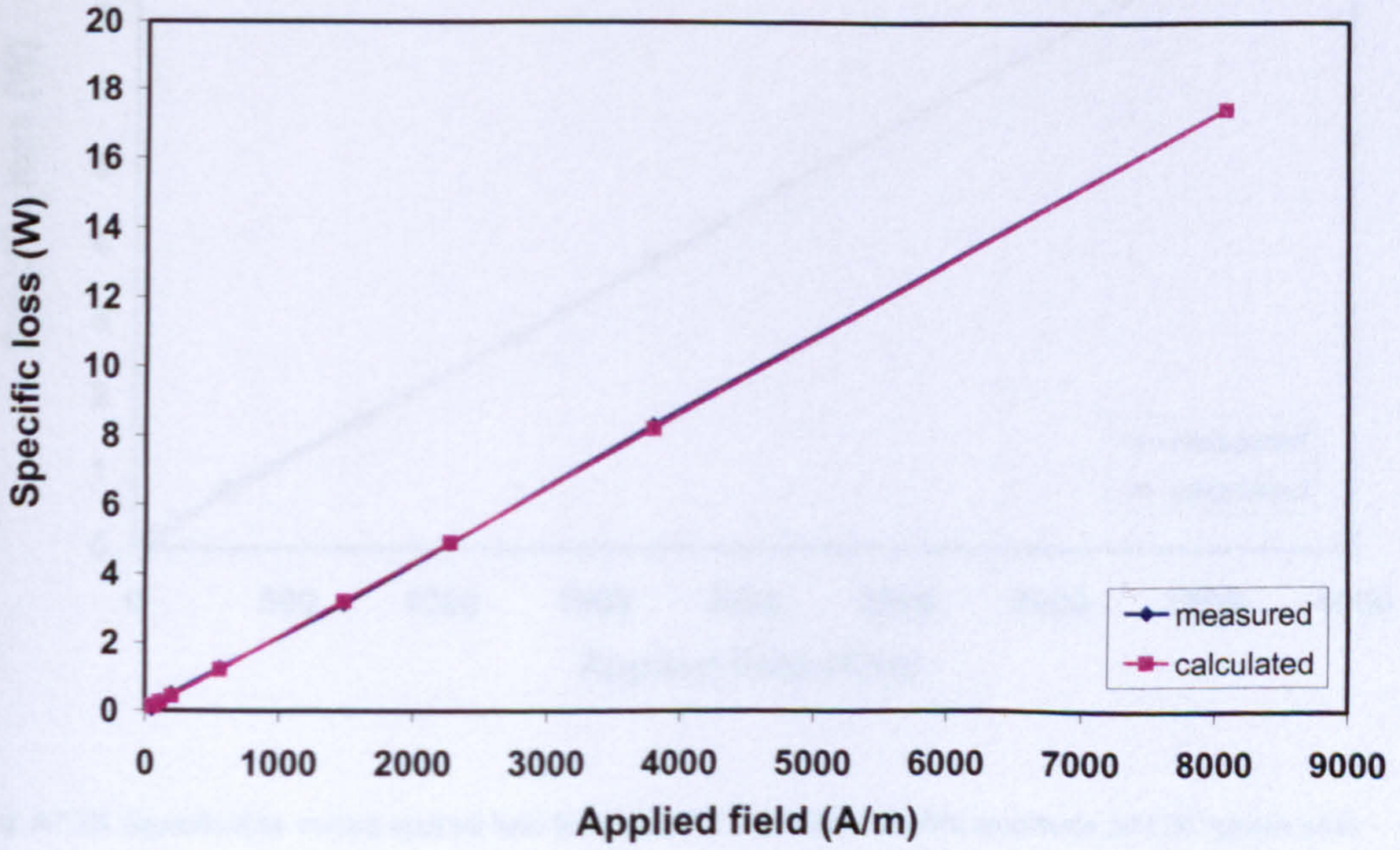

Fig. A7.24. Specific loss versus applied field for injected 3rd harmonic of 30% amplitude and 20° phase shift

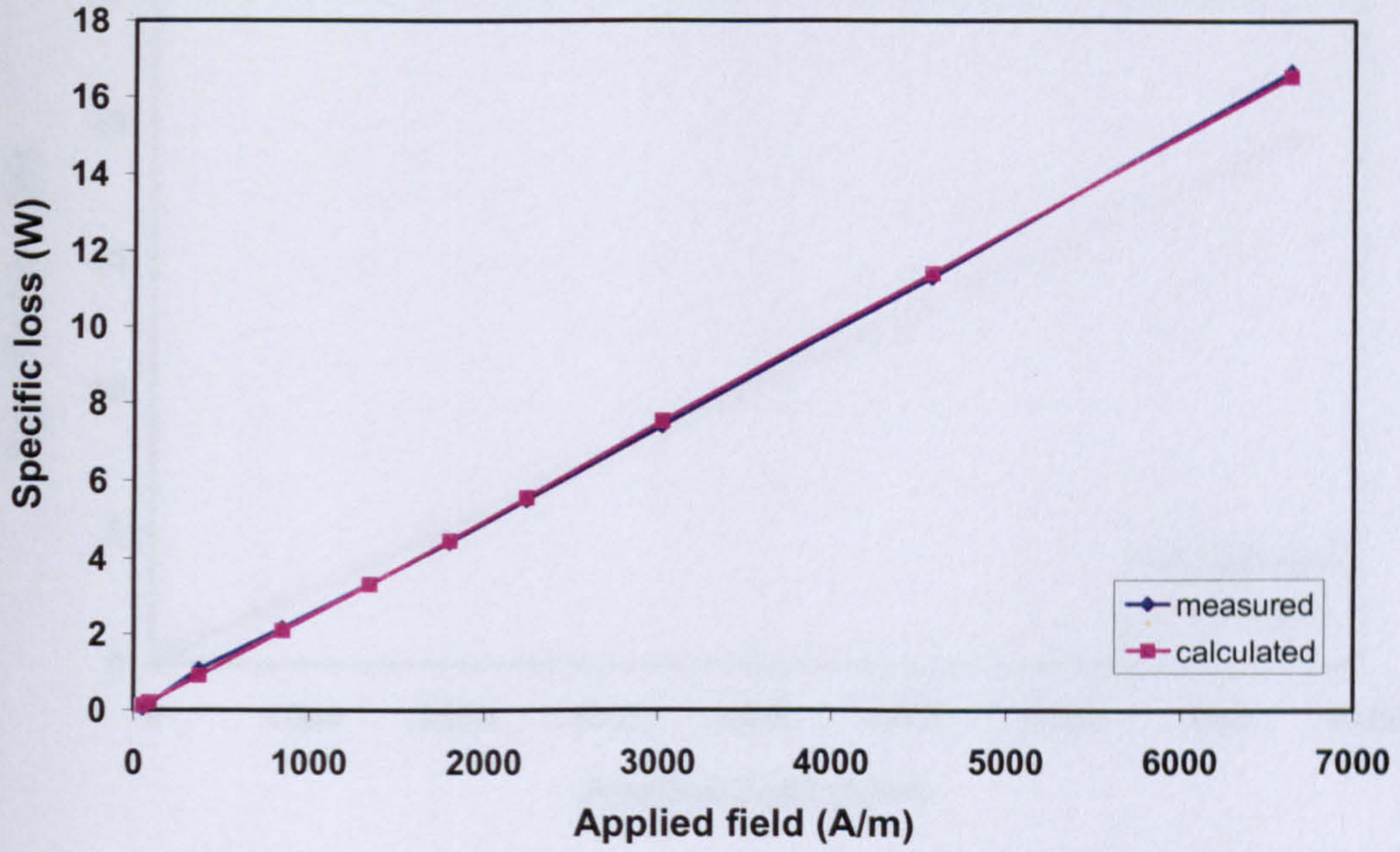

Fig. A7.25. Specific loss versus applied field for injected 3rd harmonic of 30% amplitude and 45° phase shift

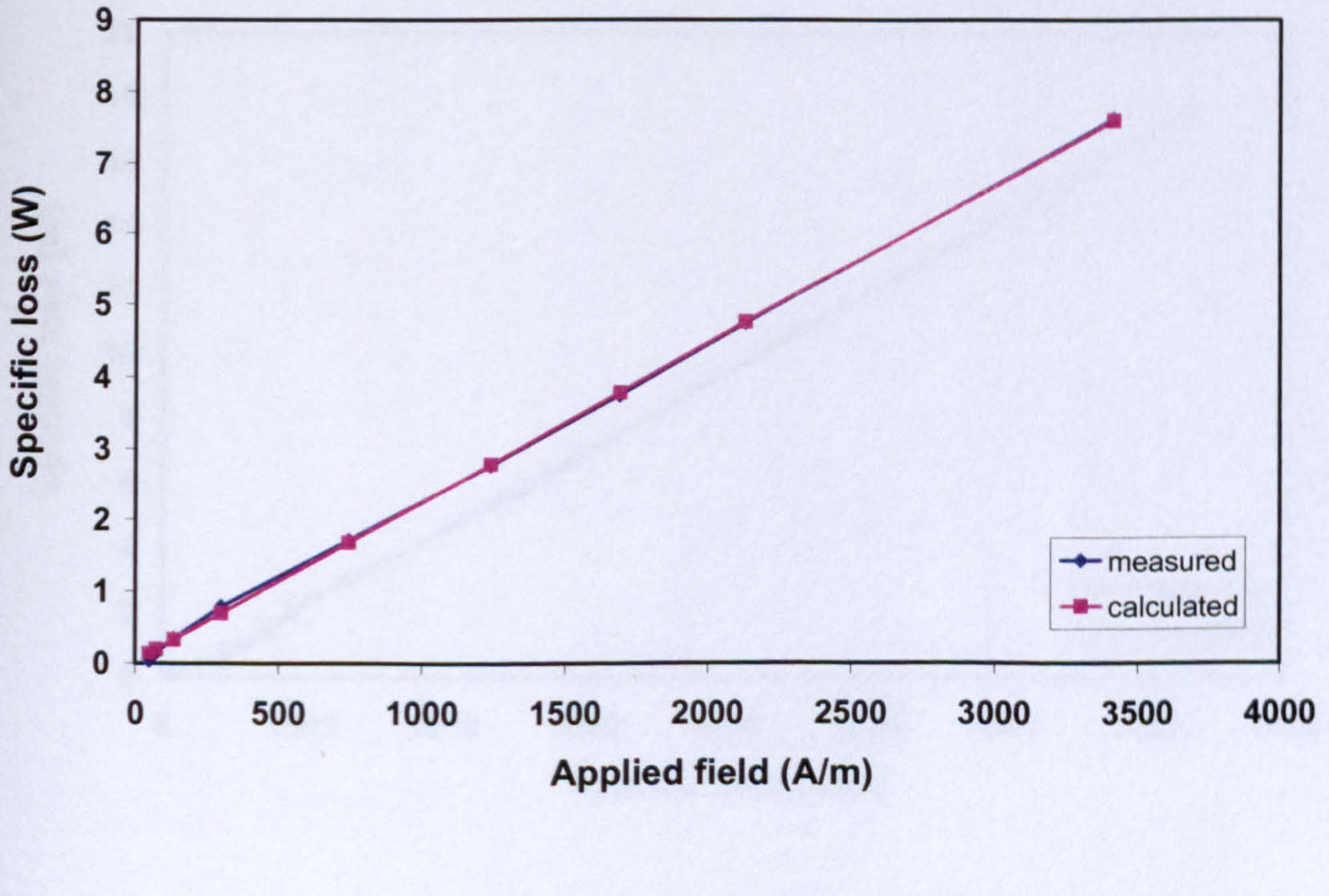

Fig. A7.26. Specific loss versus applied field for injected 3rd harmonic of 40% amplitude and 20° phase shift

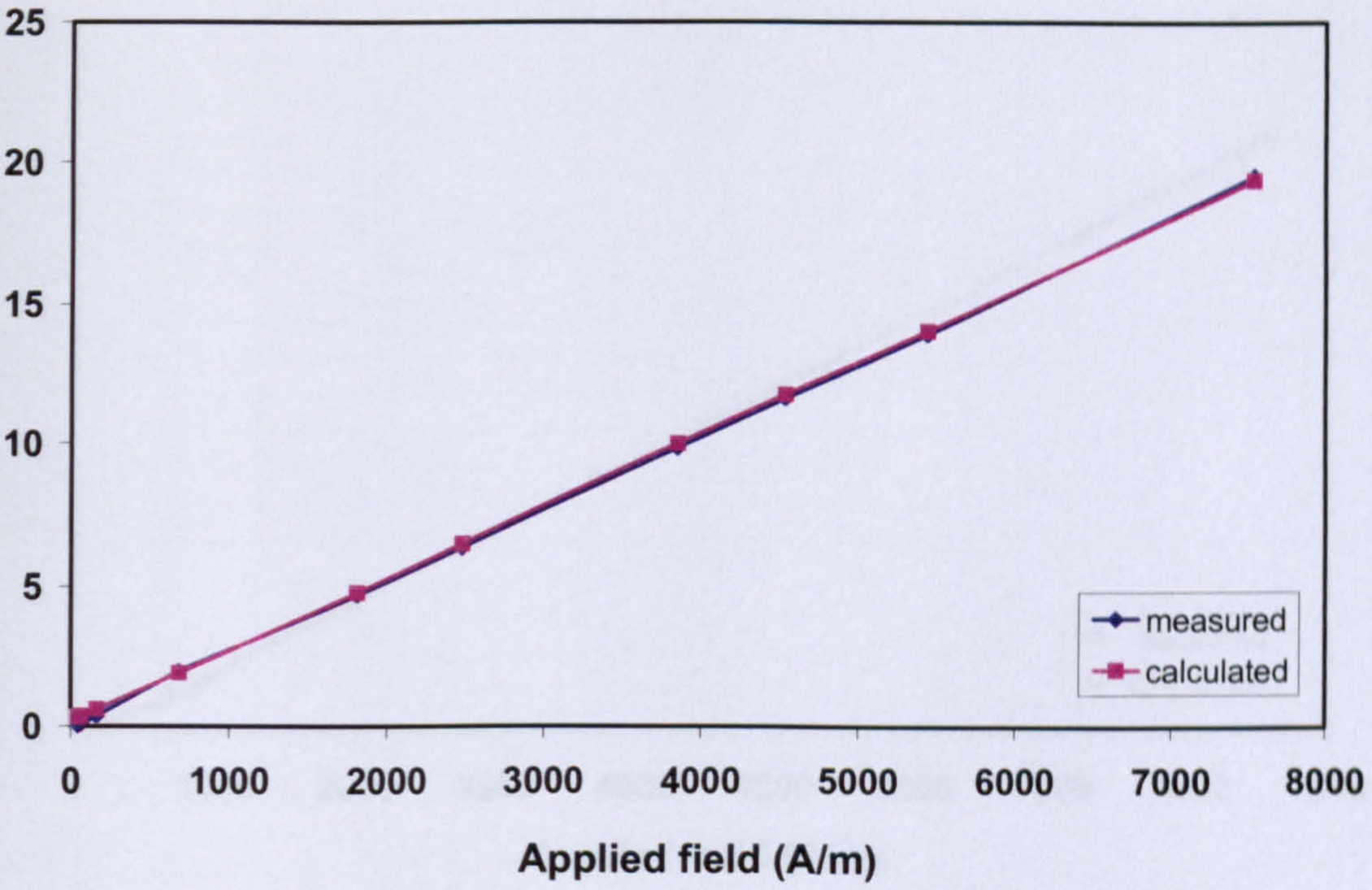

Fig. A7.27. Specific loss versus applied field for injected 3rd harmonic of 40% amplitude and 45° phase shift

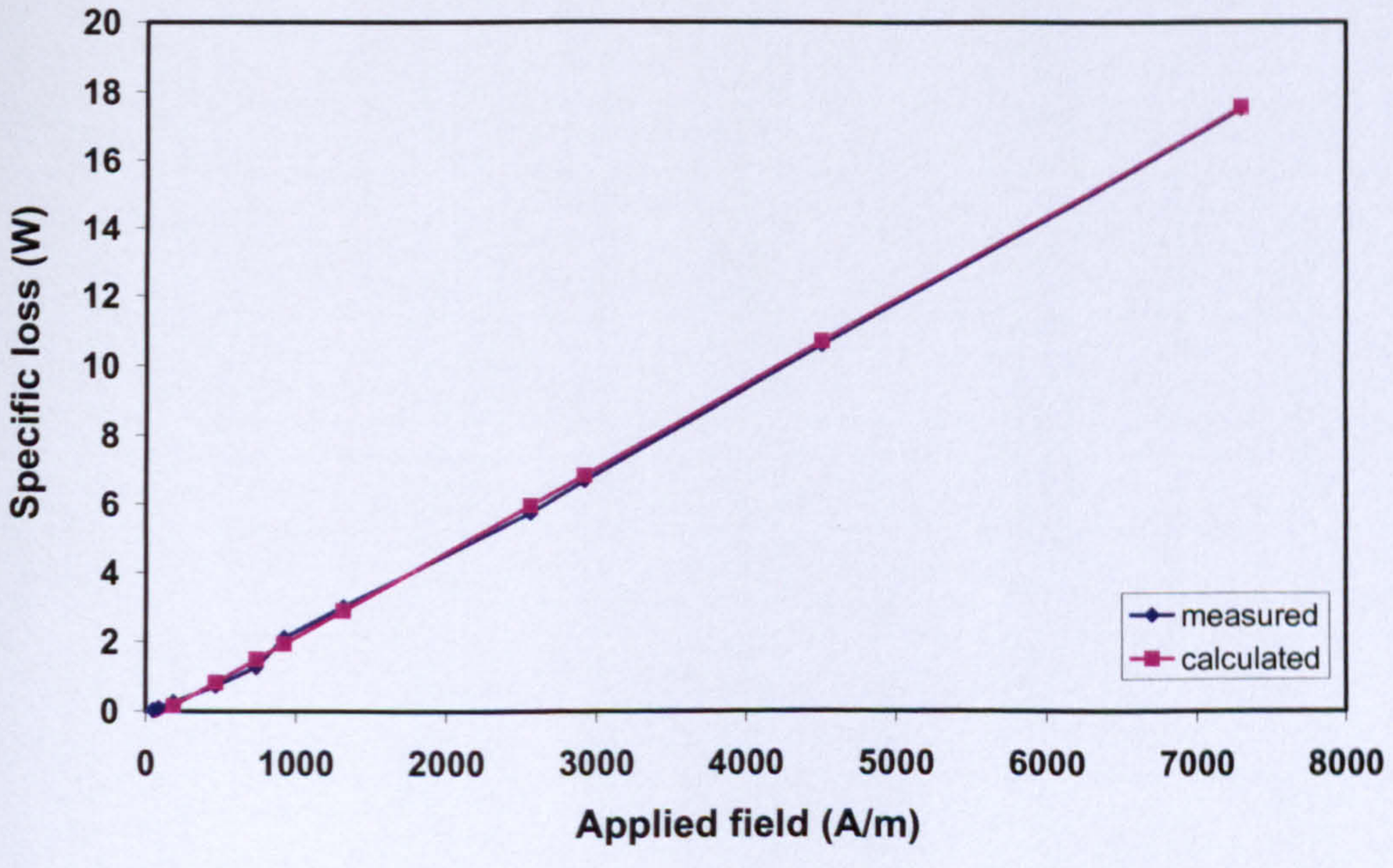

Fig. A7.28. Specific loss versus applied field for injected 5th harmonic of 10% amplitude and 20° phase shift

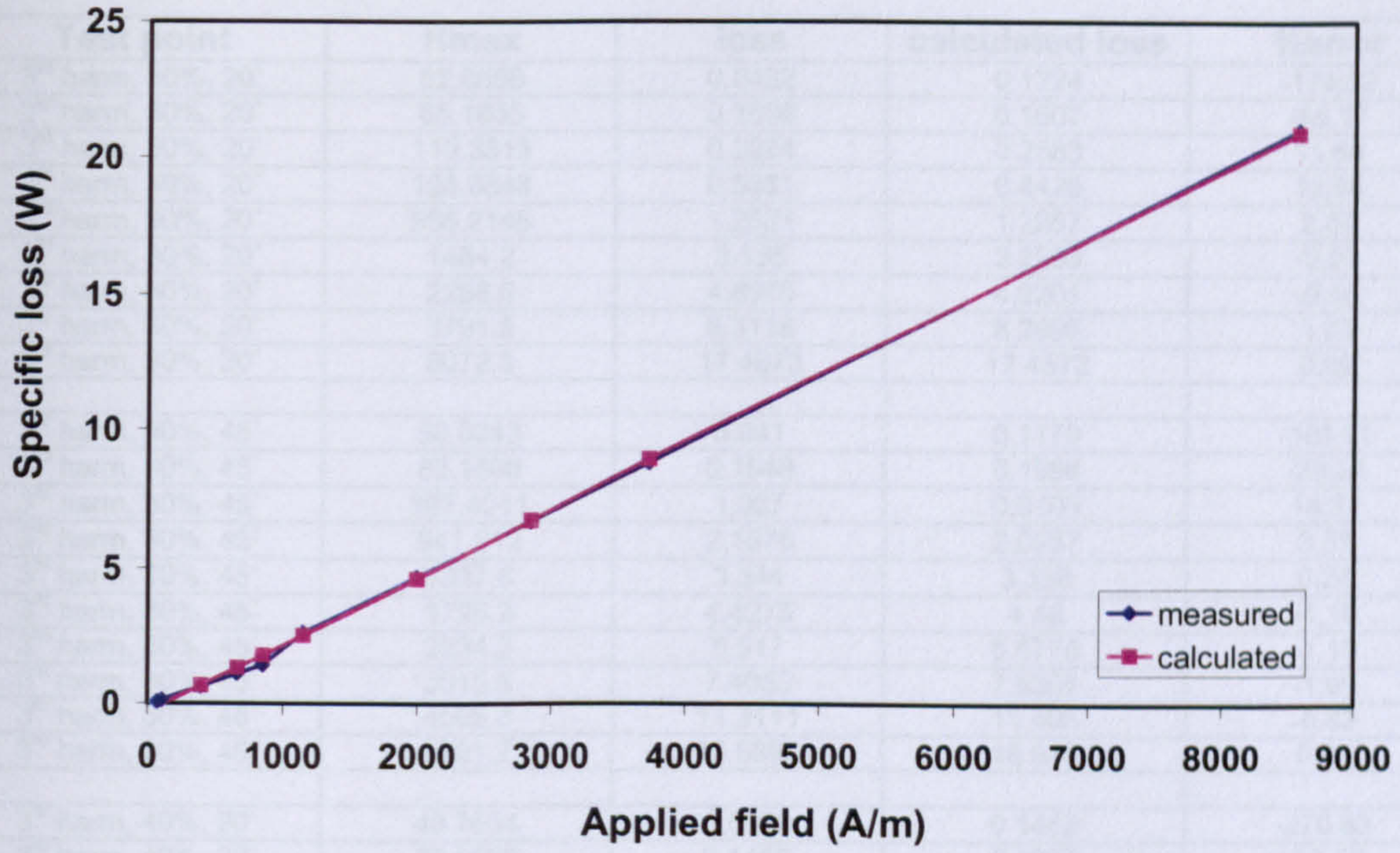

Fig. A7.29. Specific loss versus applied field for injected 5th harmonic of 10% amplitude and 45° phase shift

Test point	Hmax	loss	calculated loss	%error
3rd harm, 30%, 20°	52.0658	0.0482	0.1324	-174.82
3rd harm, 30%, 20°	65.1635	0.1036	0.1607	-55.17
3rd harm, 30%, 20°	110.3518	0.2924	0.2583	11.64
3rd harm, 30%, 20°	195.6848	0.5081	0.4426	12.88
3rd harm, 30%, 20°	558.2146	1.2621	1.2257	2.88
3rd harm, 30%, 20°	1484.2	3.135	3.2258	-2.89
3rd harm, 30%, 20°	2268.6	4.8976	4.9201	-0.46
3rd harm, 30%, 20°	3791.5	8.3118	8.2096	1.23
3rd harm, 30%, 20°	8072.8	17.4673	17.4572	0.06
3rd harm, 30%, 45°	50.0243	0.041	0.1170	-185.51
3rd harm, 30%, 45°	83.1508	0.1549	0.1998	-29.04
3rd harm, 30%, 45°	367.4011	1.067	0.9105	14.67
3rd harm, 30%, 45°	841.512	2.1675	2.0957	3.31
3rd harm, 30%, 45°	1337.6	3.344	3.336	0.24
3rd harm, 30%, 45°	1795.2	4.4273	4.48	-1.19
3rd harm, 30%, 45°	2234.2	5.517	5.5775	-1.10
3rd harm, 30%, 45°	3015.5	7.4052	7.5307	-1.69
3rd harm, 30%, 45°	4565.3	11.3111	11.405	-0.83
3rd harm, 30%, 45°	6621.2	16.6895	16.545	0.87
3rd harm, 40%, 20°	48.7634	0.0389	0.1442	-270.83
3rd harm, 40%, 20°	72.1868	0.1468	0.1962	-33.69
3rd harm, 40%, 20°	134.172	0.3471	0.3338	3.81
3rd harm, 40%, 20°	299.1017	0.7857	0.7	10.91
3rd harm, 40%, 20°	744.0024	1.72	1.6876	1.88
3rd harm, 40%, 20°	1236.7	2.7687	2.7814	-0.46
3rd harm, 40%, 20°	1687.2	3.7495	3.7815	-0.86
3rd harm, 40%, 20°	2125.6	4.7364	4.7548	-0.39
3rd harm, 40%, 20°	3410.2	7.6272	7.6066	0.27
3rd harm, 40%, 45°	42.5464	0.0251	0.3084	-1129.06
3rd harm, 40%, 45°	62.9219	0.0919	0.3604	-292.22
3rd harm, 40%, 45°	158.5507	0.3632	0.6043	-66.38
3rd harm, 40%, 45°	678.7896	1.9846	1.9309	2.71
3rd harm, 40%, 45°	1804.1	4.71	4.8004	-1.92
3rd harm, 40%, 45°	2472.3	6.3753	6.5043	-2.02
3rd harm, 40%, 45°	3845.1	9.8465	10.005	-1.61
3rd harm, 40%, 45°	4533.1	11.6199	11.7594	-1.20
3rd harm, 40%, 45°	5432.7	13.931	14.0533	-0.88
3rd harm, 40%, 45°	7526	19.5364	19.3913	0.74
5th harm, 10%, 20°	50.5879	0.0274	-0.1760	742.55
5th harm, 10%, 20°	87.0709	0.0965	-0.0866	189.82
5th harm, 10%, 20°	185.9854	0.2661	0.1556	41.50
5th harm, 10%, 20°	465.4995	0.7412	0.8404	-13.39
5th harm, 10%, 20°	735.8366	1.2863	1.5027	-16.83
5th harm, 10%, 20°	919.3351	2.1237	1.9523	8.07
5th harm, 10%, 20°	1311.8	3.0232	2.9139	3.62
5th harm, 10%, 20°	2556.6	5.7518	5.9636	-3.68
5th harm, 10%, 20°	2915.6	6.7018	6.8432	-2.11
5th harm, 10%, 20°	4491.4	10.5898	10.7039	-1.08
5th harm, 10%, 20°	7290.7	17.5133	17.5622	-0.28
5th harm, 10%, 45°	66.5005	0.0553	-0.1350	344.27
5th harm, 10%, 45°	100.4331	0.1186	-0.0509	142.94
5th harm, 10%, 45°	388.127	0.62	0.6625	-6.86
5th harm, 10%, 45°	654.7279	1.0954	1.3237	-20.84
5th harm, 10%, 45°	843.1116	1.4293	1.7909	-25.30
5th harm, 10%, 45°	1143.8	2.6443	2.5366	4.07
5th harm, 10%, 45°	1986.1	4.683	4.6255	1.23
5th harm, 10%, 45°	2836.9	6.6914	6.7355	-0.66
5th harm, 10%, 45°	3723	8.7964	8.9330	-1.55
5th harm, 10%, 45°	8561.1	21.0624	20.9315	0.62

Table A7.1. Summary of calculated losses for 22.32 Hz tests

A7.4.2. Fundamental frequency = 52.08 Hz

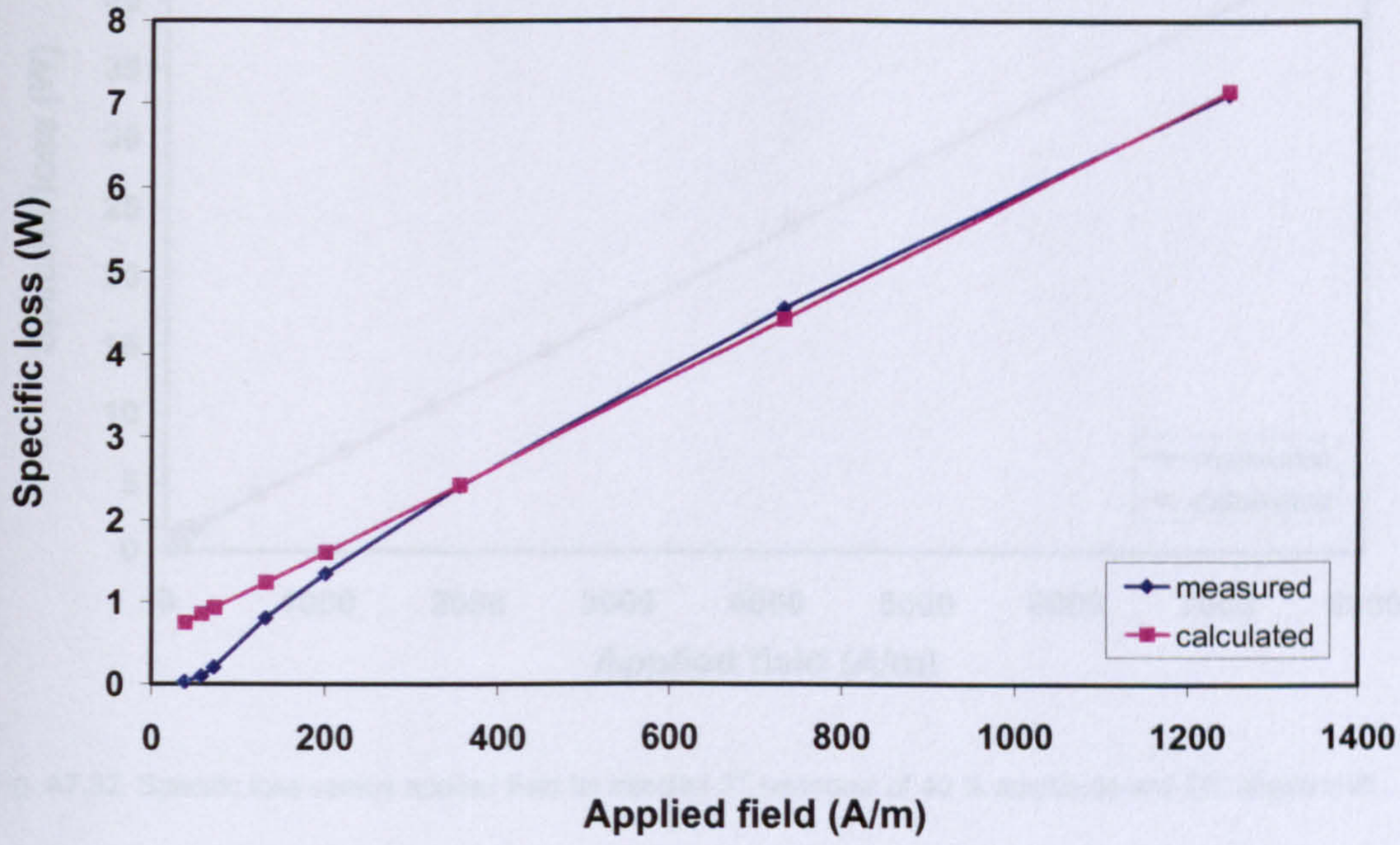

Fig. A7.30. Specific loss versus applied field for injected 3rd harmonic of 30 % amplitude and 20° phase shift

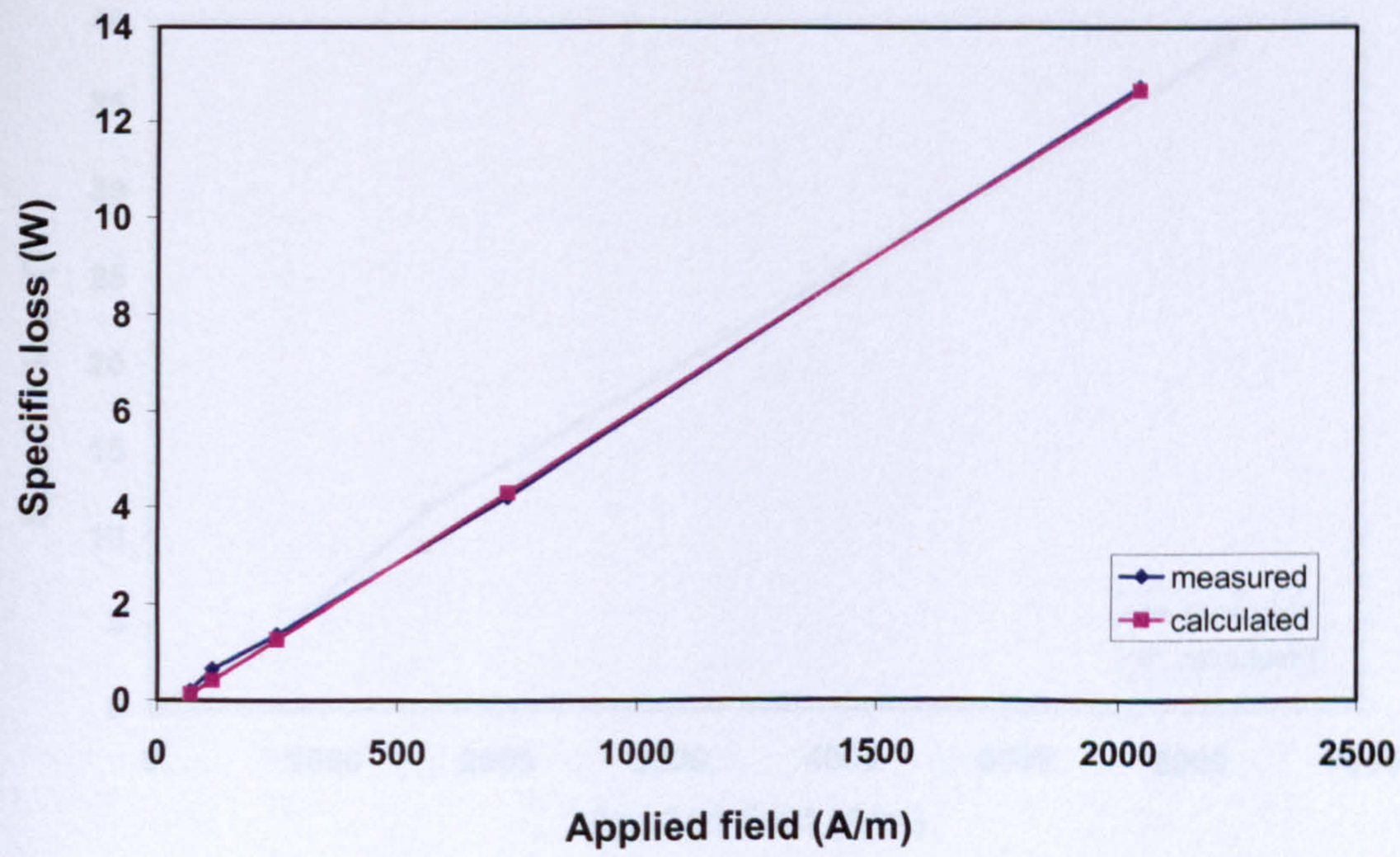

Fig. A7.31. Specific loss versus applied field for injected 3rd harmonic of 30 % amplitude and 45° phase shift

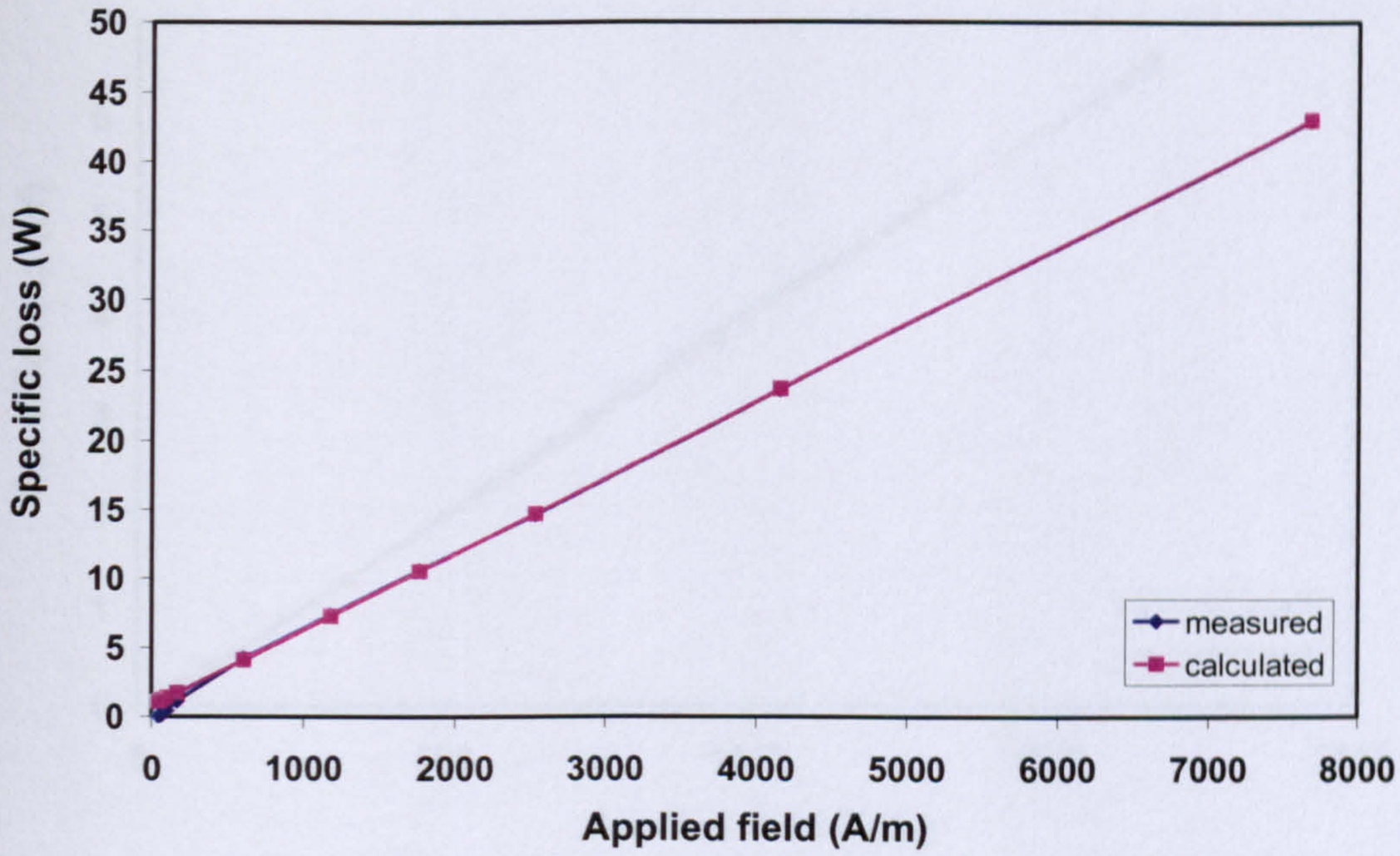

Fig. A7.32. Specific loss versus applied field for injected 3rd harmonic of 40 % amplitude and 20° phase shift

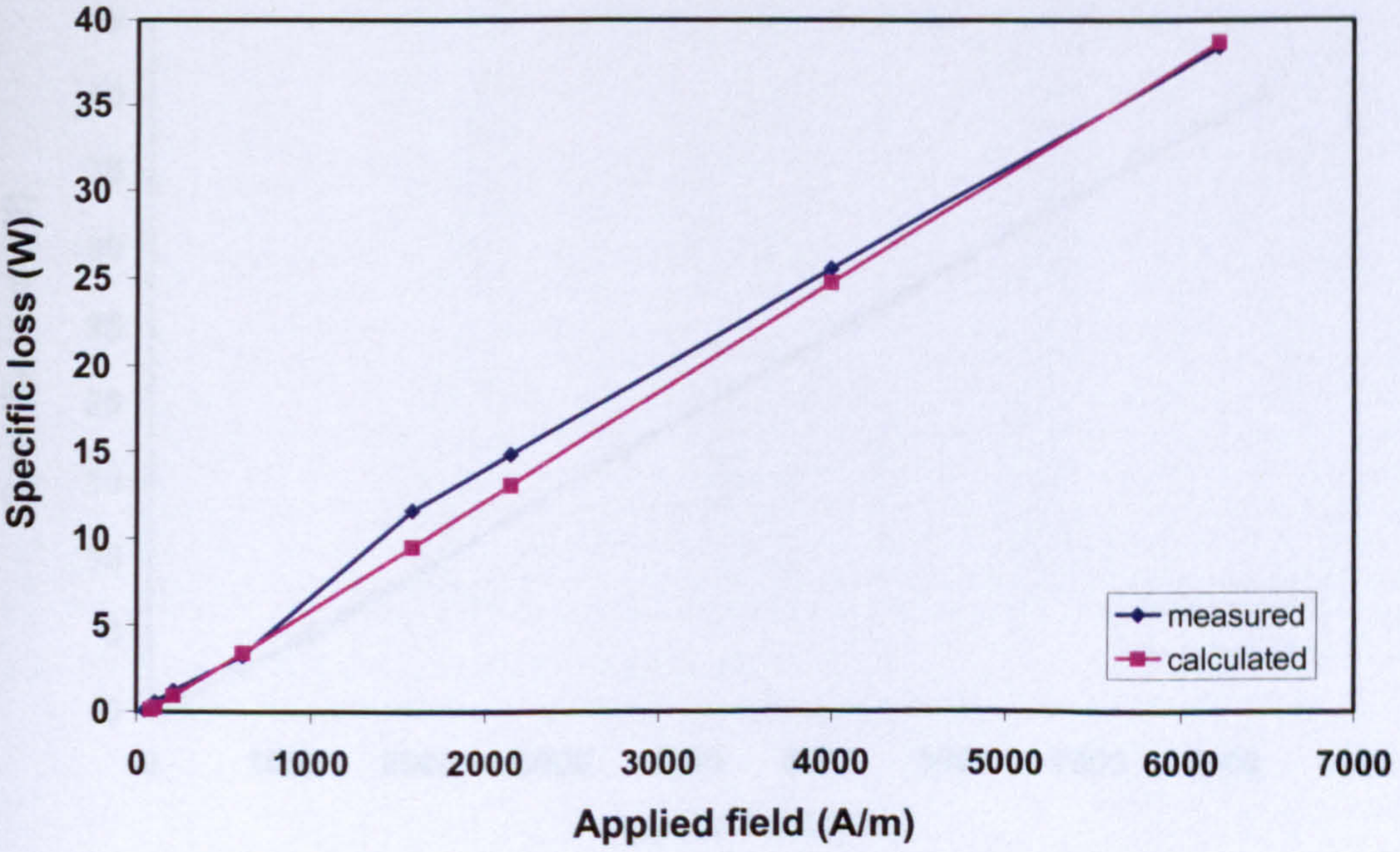

Fig. A7.33. Specific loss versus applied field for injected 3rd harmonic of 40 % amplitude and 45° phase shift

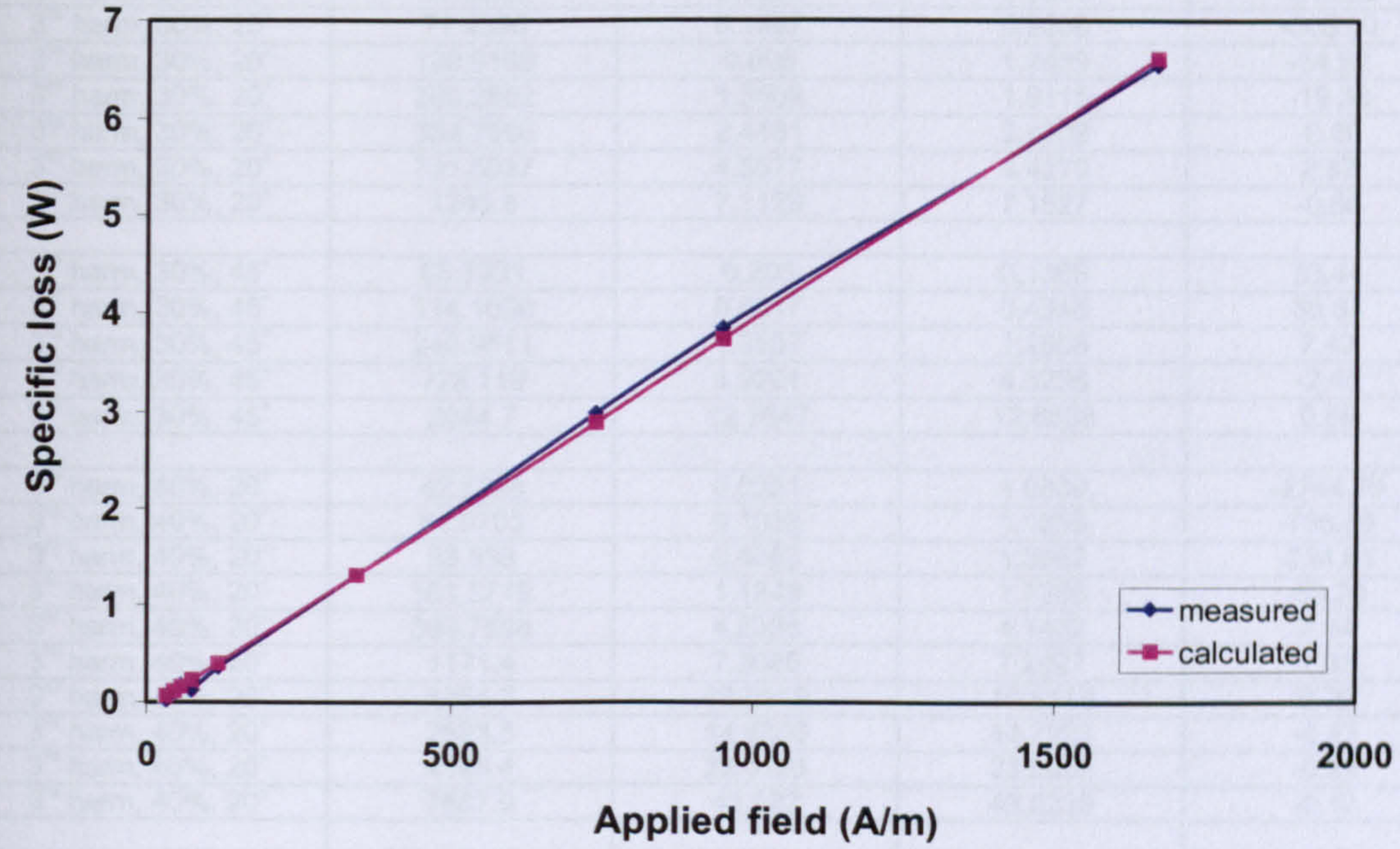

Fig. A7.34. Specific loss versus applied field for injected 5th harmonic of 10% amplitude and 20° phase shift

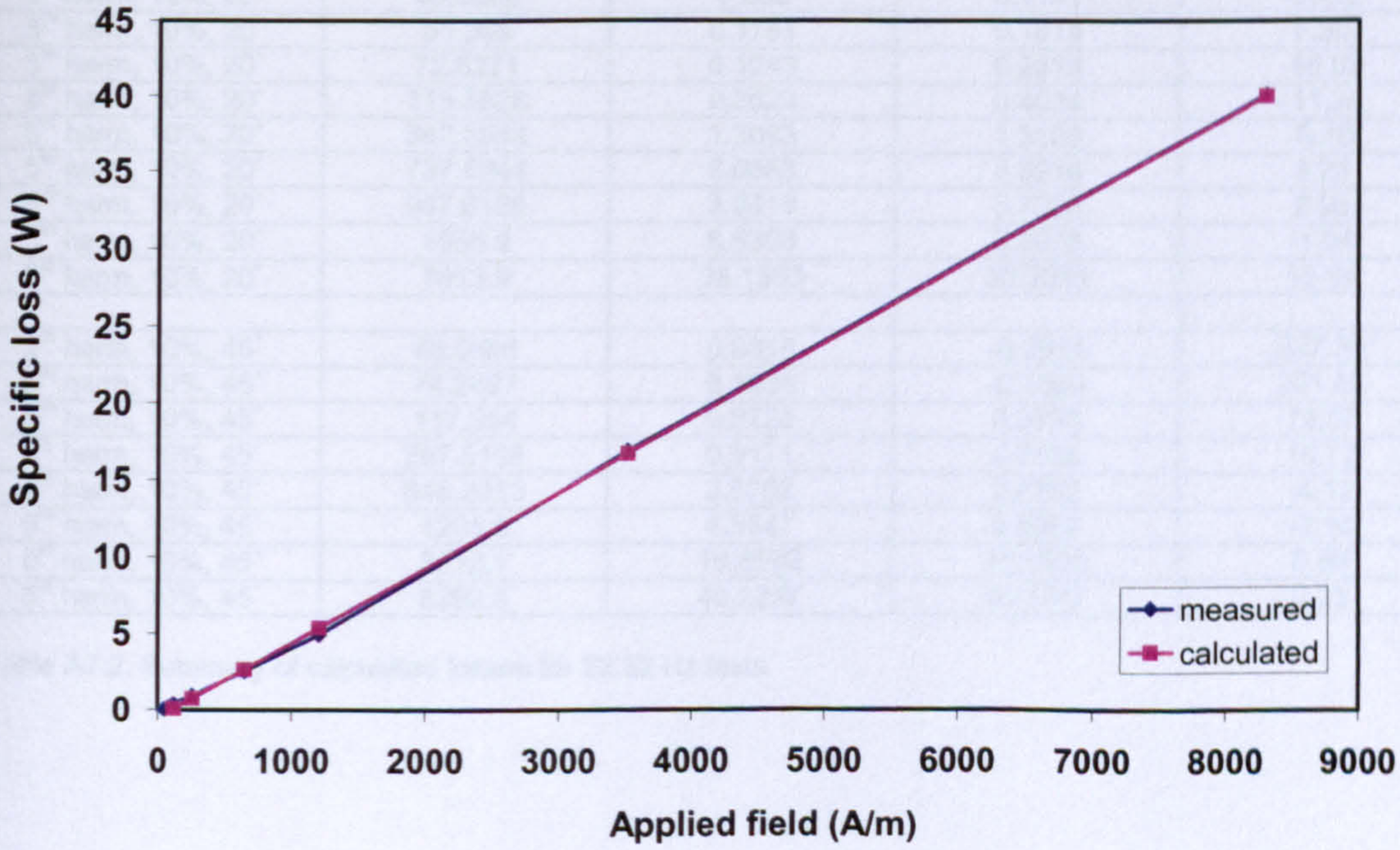

Fig. A7.35. Specific loss versus applied field for injected 5th harmonic of 10% amplitude and 45° phase shift

Test point	Hmax	loss	calculated loss	%error
3rd harm, 30%, 20°	37.9087	0.0248	0.7509	-2927.89
3rd harm, 30%, 20°	57.2259	0.0928	0.8533	-819.50
3rd harm, 30%, 20°	71.4356	0.1997	0.9286	-365.00
3rd harm, 30%, 20°	130.9169	0.805	1.2439	-54.52
3rd harm, 30%, 20°	200.2802	1.3508	1.6115	-19.30
3rd harm, 30%, 20°	354.7596	2.4181	2.4302	-0.50
3rd harm, 30%, 20°	731.5037	4.5577	4.4270	2.87
3rd harm, 30%, 20°	1245.8	7.1129	7.1527	-0.56
3rd harm, 30%, 45°	68.7331	0.205	0.1365	33.44
3rd harm, 30%, 45°	114.1036	0.6617	0.4246	35.84
3rd harm, 30%, 45°	248.9511	1.3837	1.2808	7.43
3rd harm, 30%, 45°	728.119	4.2201	4.3236	-2.45
3rd harm, 30%, 45°	2044.7	12.7547	12.6838	0.56
3rd harm, 40%, 20°	42.5208	0.0381	1.0839	-2744.79
3rd harm, 40%, 20°	61.0703	0.1368	1.1859	-766.88
3rd harm, 40%, 20°	93.858	0.4083	1.3662	-234.61
3rd harm, 40%, 20°	161.5719	1.1349	1.7386	-53.20
3rd harm, 40%, 20°	598.7556	4.2338	4.1432	2.14
3rd harm, 40%, 20°	1171.4	7.3685	7.2927	1.03
3rd harm, 40%, 20°	1756.7	10.5919	10.5119	0.76
3rd harm, 40%, 20°	2523.5	14.6606	14.7293	-0.47
3rd harm, 40%, 20°	4148.4	23.6125	23.6662	-0.23
3rd harm, 40%, 20°	7667.9	42.982	43.0235	-0.10
3rd harm, 40%, 45°	48.79	0.0526	-0.0926	276.09
3rd harm, 40%, 45°	57.7018	0.1152	-0.0365	131.67
3rd harm, 40%, 45°	79.9152	0.299	0.1035	65.40
3rd harm, 40%, 45°	105.2193	0.543	0.2629	51.59
3rd harm, 40%, 45°	210.7015	1.2172	0.9274	23.81
3rd harm, 40%, 45°	608.2667	3.268	3.4321	-5.02
3rd harm, 40%, 45°	1578.4	11.6177	9.5439	17.85
3rd harm, 40%, 45°	2142.8	14.8563	13.0996	11.82
3rd harm, 40%, 45°	3986	25.4928	24.7118	3.06
3rd harm, 40%, 45°	6212.3	38.4302	38.7375	-0.80
5th harm, 10%, 20°	31.0959	0.0217	0.0644	-196.70
5th harm, 10%, 20°	43.5268	0.082	0.1141	-39.16
5th harm, 10%, 20°	55.359	0.1751	0.1614	7.80
5th harm, 10%, 20°	72.8271	0.1243	0.2313	-86.09
5th harm, 10%, 20°	115.8528	0.3623	0.4034	-11.35
5th harm, 10%, 20°	342.6544	1.3093	1.3106	-0.10
5th harm, 10%, 20°	737.8944	2.9883	2.8916	3.24
5th harm, 10%, 20°	947.6126	3.8419	3.7305	2.90
5th harm, 10%, 20°	1666.9	6.5393	6.6076	-1.04
5th harm, 10%, 20°	7613.9	36.1583	30.3956	15.94
5th harm, 10%, 45°	48.6886	0.0316	-0.2614	927.30
5th harm, 10%, 45°	74.2827	0.1338	-0.1360	201.66
5th harm, 10%, 45°	117.354	0.3728	0.0750	79.87
5th harm, 10%, 45°	257.9195	0.9171	0.7638	16.72
5th harm, 10%, 45°	648.2013	2.5702	2.6762	-4.12
5th harm, 10%, 45°	1205.8	4.9547	5.4084	-9.16
5th harm, 10%, 45°	3512.1	16.8592	16.7093	0.89
5th harm, 10%, 45°	8292.8	40.2257	40.1347	0.23

Table A7.2 Summary of calculated losses for 22.32 Hz tests

Appendix 8

Loss Measurements Made on Single Sheet Tester and Epstein Square

In Tables A8.1 and A8.2, results from iron loss measurements with sinusoidal flux density waveforms are presented, for the single sheet tester and Epstein square respectively. In Table A8.2, both the magnetic polarisation J and the flux density B have been given for reference.

The loss characteristics can be approximated by linear functions of applied field H. Comparisons between the losses calculated using the linear approximations and the measured losses are presented in Tables A8.3 and A8.4, for the single sheet tester and the Epstein square respectively.

f (Hz)	Hmax (A/m)	Bmax (T)	Specific loss (W/kg)
5	134.8971	1.0957	0.0317
5	186.2202	1.2235	0.0465
5	290.3953	1.3595	0.0804
5	557.6857	1.4756	0.1733
5	1287	1.5696	0.4511
5	2027.6	1.6121	0.7538
5	2739.2	1.6512	1.058
5	3328.17	1.668312	1.3085
5	3934.6	1.7083	1.5798
5	4456.3	1.7135	1.8246
5	5329.2	1.7425	2.1551
20	38.1582	0.2529	0.0109
20	52.4244	0.521	0.0355
20	69.733	0.6763	0.0526
20	73.25	0.8249	0.0706
20	102.9556	0.9631	0.0964
20	132.8294	1.1066	0.1337
20	192.6681	1.2488	0.2074
20	308.4259	1.3831	0.3603
20	703.6574	1.5146	0.9292
20	1797.1	1.6051	2.6063
20	3368.5	1.6754	5.1537
20	5115.2	1.7364	8.0037
20	6193.9	1.7581	9.1727
20	6266.5	1.7597	9.2527
40	67.8872	0.615	0.104
40	104.3136	0.9742	0.1893
40	139.9349	1.1052	0.2527
40	195.5093	1.2505	0.3673
40	322.7293	1.3866	0.635
40	728.0318	1.5115	1.5726
40	1868.6	1.6041	4.3816
40	3482.3	1.6776	8.555
40	4971.5	1.7247	12.1524
60	121.8702	0.964	0.286
60	142.6838	1.0832	0.3419
60	176.0759	1.1942	0.4333
60	232.58	1.2909	0.5424
60	325.7972	1.3848	0.7531
60	793.9553	1.5154	1.9572
60	2734.4	1.6482	7.4879
80	85.6022	0.5294	0.2806
80	122.0094	1.0353	0.594
80	172.3238	1.1807	0.7763
80	264.2752	1.3181	1.152
80	2106.2	1.6185	10.1476
100	29.0377	0.0995	0.0157
100	42.6756	0.1728	0.0591
100	134.4834	0.764	1.0352
100	143.3299	0.7687	1.1515
100	209.6604	1.2332	1.5742
100	405.2902	1.436	2.8856
100	811.0653	1.5218	5.8193
100	4148	1.7032	32.74
150	75.4831	0.262	0.2858
150	88.0777	0.3639	0.3757
150	116.9521	0.4683	0.7395
150	169.7016	0.674	1.4491
150	374.7398	1.414	3.3094
150	883.5881	1.5295	7.4291

Table A8.1. Specific loss data for samples of M340-50E, as measured on single sheet tester

frequency	Hmax (A/m)	Jval (T)	Bval (T)	Specific loss (W/kg)
6	192.0801	1.1952	1.1969	0.0309
6	299.5896	1.3751	1.3762	0.0538
6	568.9109	1.4886	1.4893	0.12
6	1457.2	1.5719	1.5737	0.3676
6	2783.8	1.6324	1.6359	0.7489
6	7500.2	1.7587	1.7682	2.1384
20	23.4339	0.0501	0.0512	0.0008814
20	34.6191	0.1008	0.1035	0.0028
20	142.4482	1.0136	1.0163	0.1114
20	303.2315	1.378	1.3794	0.3088
20	874.1014	1.5251	1.5262	1.1404
20	1593.6	1.5725	1.5776	2.267
20	2595.1	1.617	1.6236	3.8618
20	3470.5	1.6387	1.6583	5.2623
20	4848	1.6846	1.7020	7.4665
20	6369.4	1.7275	1.7397	9.9216
20	8522.9	1.7732	1.7885	13.4361
40	21.9061	0.025	0.0251	0.0005719
40	26.2685	0.0729	0.0761	0.0033
40	34.6328	0.1205	0.1276	0.0068
40	50.1914	0.184	0.1924	0.0137
40	203.0349	1.2156	1.2283	0.3396
40	467.1905	1.44	1.4618	0.8907
40	3149.3	1.6445	1.6484	7.5704
40	8886.7	1.7878	1.7990	22.7368
50	161.2136	1.0674	1.0826	0.0609
50	269.4965	1.3124	1.3148	0.7248
50	696.7598	1.4789	1.4799	2.2179
50	958.8023	1.5219	1.5431	3.2354
60	18.9126	0.0183	0.0182	0.0007594
60	42.1185	0.0795	0.0809	0.01
60	176.0732	1.1288	1.1512	0.7009
60	262.9143	1.3394	1.3436	1.0793
60	938.2108	1.5303	1.5381	4.6014
60	4573.1	1.6992	1.7050	25.4001
60	7899.9	1.7764	1.7863	45.1002
80	206.5164	1.2167	1.2265	0.8165
80	357.2373	1.412	1.4139	1.4084
80	1914.7	1.5915	1.5939	9.0379
80	6477	1.7331	1.7427	32.484

Table A8.2. Specific loss data for samples of M340-50E, as measured on Epstein square

Appendix 8: Loss measurements made on Single Sheet Tester and Epstein Square

f (Hz)	Hmax (A/m)	Measured loss (W/kg)	Calculated loss (W/kg)	Percentage error
5	134.8971	0.0317	0.03	-7.13
5	186.2202	0.0465	0.05	-17.18
5	290.3953	0.0804	0.10	-19.60
5	557.6857	0.1733	0.20	-17.18
5	1287	0.4511	0.49	-9.69
5	2027.6	0.7538	0.79	-4.94
5	2739.2	1.058	1.08	-1.67
5	3328.17	1.3085	1.31	-0.21
5	3934.6	1.5798	1.55	1.64
5	4456.3	1.8246	1.76	3.40
5	5329.2	2.1551	2.11	2.01
20	38.1582	0.0109	-0.12	1191.26
20	52.4244	0.0355	-0.10	370.76
20	69.733	0.0526	-0.07	230.09
20	73.25	0.0706	-0.06	188.95
20	102.9556	0.0964	-0.02	115.84
20	132.8294	0.1337	0.03	75.67
20	192.6681	0.2074	0.13	38.15
20	308.4259	0.3603	0.31	12.99
20	703.6574	0.9292	0.95	-1.79
20	1797.1	2.6063	2.70	-3.42
20	3368.5	5.1537	5.21	-1.08
20	5115.2	8.0037	8.00	-0.01
20	6193.9	9.1727	9.73	-6.08
20	6266.5	9.2527	9.85	-6.42
40	67.8872	0.104	0.03	74.69
40	104.3136	0.1893	0.12	38.95
40	139.9349	0.2527	0.20	19.73
40	195.5093	0.3673	0.34	7.71
40	322.7293	0.635	0.65	-2.47
40	728.0318	1.5726	1.64	-4.52
40	1868.6	4.3816	4.44	-1.29
40	3482.3	8.555	8.39	1.91
40	4971.5	12.1524	12.04	0.92
50	37.7	0.0312	-0.18	674.36
50	69.3	0.1483	-0.05	135.60
50	98.7	0.3119	0.06	79.22
50	189.9	0.576	0.43	25.42
50	268.1	0.5761	0.74	-28.87
50	434.9	1.4004	1.41	-0.66
50	900.7	3.1179	3.27	-4.97
50	1333.9	4.7763	5.01	-4.80
50	4759.4	18.601	18.71	-0.57
80	85.6022	0.2806	0.29	-3.15
80	122.0094	0.594	0.47	21.24
80	172.3238	0.7763	0.71	7.98
80	264.2752	1.152	1.16	-1.12
80	2106.2	10.1476	10.19	-0.42
100	29.0377	0.0157	-0.12	849.67
100	42.6756	0.0591	-0.01	114.54
100	134.4834	1.0352	0.73	29.88
100	143.3299	1.1515	0.80	30.82
100	209.6604	1.5742	1.33	15.69
100	405.2902	2.8856	2.89	-0.23
100	811.0653	5.8193	6.14	-5.49
100	4148	32.74	32.83	-0.29
150	75.4831	0.2858	0.78	-171.70
150	88.0777	0.3757	0.88	-134.51
150	116.9521	0.7395	1.12	-51.55
150	169.7016	1.4491	1.56	-7.55
150	374.7398	3.3094	3.26	1.48
150	883.5881	7.4291	7.48	-0.74

Table A8.3. Comparison between calculated and measured losses on single sheet tester at 20 Hz

Appendix 8: Loss measurements made on Single Sheet Tester and Epstein Square

frequency	Hmax	Measured loss (W/kg)	Calculated loss (W/kg)	Percentage error
6	192.0801	0.0309	0.00	96.48
6	299.5896	0.0538	0.03	39.63
6	568.9109	0.12	0.11	7.40
6	1457.2	0.3676	0.37	-0.79
6	2783.8	0.7489	0.76	-1.20
6	7500.2	2.1384	2.14	0.16
20	23.4339	0.0008814	-0.19	21940.91
20	34.6191	0.0028	-0.17	6336.05
20	142.4482	0.1114	0.00	101.87
20	303.2315	0.3088	0.26	17.37
20	874.1014	1.1404	1.17	-2.47
20	1593.6	2.267	2.32	-2.33
20	2595.1	3.8618	3.92	-1.56
20	3470.5	5.2623	5.32	-1.15
20	4848	7.4665	7.53	-0.81
20	6369.4	9.9216	9.96	-0.40
20	8522.9	13.4361	13.41	0.22
40	21.9061	0.0005719	-0.39	68787.72
40	26.2685	0.0033	-0.38	11658.76
40	34.6328	0.0068	-0.36	5388.36
40	50.1914	0.0137	-0.32	2428.47
40	203.0349	0.3396	0.08	76.47
40	467.1905	0.8907	0.77	13.62
40	3149.3	7.5704	7.77	-2.63
40	8886.7	22.7368	22.74	-0.03
50	161.2136	0.0609	0.33	-442.48
50	269.4965	0.7248	0.72	0.64
50	696.7598	2.2179	2.26	-1.82
50	958.8023	3.2354	3.20	1.04
60	18.9126	0.0007594	-0.31	41211.16
60	42.1185	0.01	-0.18	1899.25
60	176.0732	0.7009	0.58	16.73
60	262.9143	1.0793	1.08	0.06
60	938.2108	4.6014	4.93	-7.09
60	4573.1	25.4001	25.65	-0.97
60	7899.9	45.1002	44.61	1.09
80	206.5164	0.8165	0.60	26.12
80	357.2373	1.4084	1.37	2.59
80	1914.7	9.0379	9.31	-3.07
80	6477	32.484	32.58	-0.30

Table A8.4. Comparison between calculated and measured losses on Epstein square at 20 Hz

Appendix 9

Author's Publications

The following publications have arisen from the work carried out during the PhD studies.

The paper published in *Acta Polytechnica* was first presented at the 2004 Advanced Engineering Design Conference (AED 2004) in Glasgow, Scotland. The paper published in the *IEEE Transactions on Magnetics* was first presented at the 2005 International Magnetics Conference (INTERMAG 2005) in Nagoya, Japan. The results published in the *Journal of Applied Physics* were originally presented at the 2005 Magnetism and Magnetic Materials Conference (MMM 2005) in San Jose, California.

Miller TJE, Popescu M, Cossar C, McGilp M, Walker JA, Calculating the interior permanent-magnet motor, IEEE International Electric Machines and Drives Conference IEMDC 2003, 1-4 June 2003, vol. 2 pp1181-1187.

Miller TJE, Walker JA, Cossar C, Measurement and application of flux-linkage and inductance in a permanent-magnet synchronous machine, Power Electronics Machines and Drives Conference PEMD 2004, 31 March – 2 April 2004, vol. 2 pp674-678.

Walker JA, Cossar C, Miller TJE, Simulation and analysis of magnetisation characteristics of interior permanent magnet motors, Acta Polytechnica Journal of Advanced Engineering, vol. 45 n. 4/2005 pp25-32.

Walker JA, Dorrell D, Cossar C, Flux-linkage calculation in permanent-magnet motors using the *frozen permeabilities* method, IEEE Transactions on Magnetics vol. 41 n. 10 October 2005 pp3946-3948.

Walker JA, Dorrell DG, Cossar C, Effect of mutual coupling on torque production in switched-reluctance motors, Accepted for the Journal of Applied Physics.

Calculating the interior permanent-magnet motor

T.J.E. Miller, M. Popescu, C. Cossar, M. McGilp, J.A. Walker

SPEED Laboratory, Glasgow G12 8LT, UK

Abstract **- This paper describes the calculation of torque in a brushless permanent-magnet line-start a.c. motor by means of the flux-MMF diagram in combination with the finite-element method. Results are compared with measured flux-MMF diagrams, with shaft torque measurements, and with torque calculated using the classical phasor diagram.**

I. Introduction

The interior permanent-magnet motor (IPM) is a hybrid permanent-magnet/reluctance synchronous brushless motor that is being developed for several applications such as servo motors, elevator drive motors, and electric vehicle traction motors, [1-6,10,12]. Line-start IPM motors are also used for compressors and other applications requiring a high-efficiency alternative to the induction motor; these are often capacitor motors fed from a single-phase supply, as is the motor in Fig. 1, [8]. In many cases the windings are not sine-distributed and the current and EMF waveforms may be non-sinusoidal.

Saturation of the magnetic circuit is particularly complex in these motors: different sections of the machine saturate independently, causing large and sometimes time-varying changes in equivalent-circuit parameters such as inductances and EMF. Unfortunately these are the parameters used in classical methods for calculating torque, current, and voltage.

It therefore becomes unclear to what extent it is safe to rely on classical methods based on equivalent circuits and (in the case of sinewave machines) on phasors and *dq*-axis theory.

The finite-element method is capable of calculating the electromagnetic behavior, but it is rather slow, and it has no *a priori* relationship with the classical theory of operation of the machine.

Funding for this work was provided by the companies of the *SPEED* Consortium. J.A. Walker is partially supported by the U.K. Engineering and Physical Sciences Research Council, by the *SPEED* Consortium, and by Robert Bosch GmbH. Test motors were kindly provided by Electrolux Compressors, Italy; see [8].

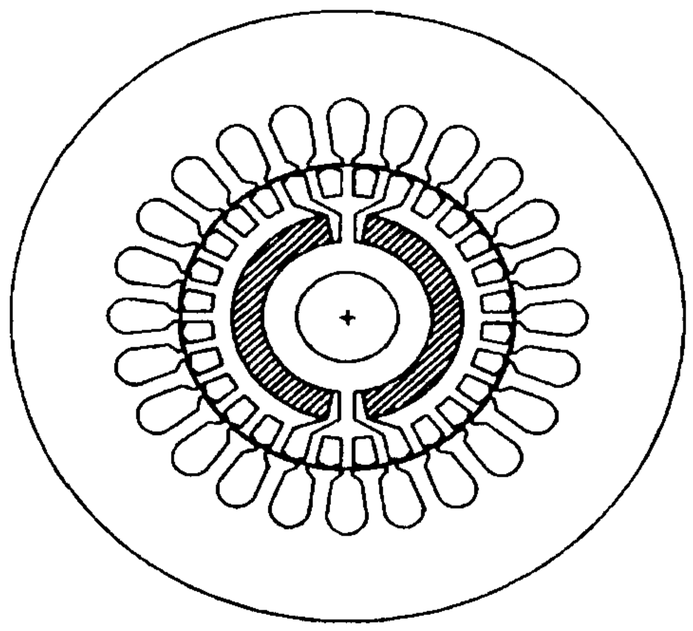

Fig. 1. Cross-section of the 2-pole capacitor motor analyzed. The arc-shaped ferrite magnets are shaded.

This paper shows that for "sinewound" machines, which have sinusoidally distributed stator ampere-conductors, the elliptical flux-MMF diagram [2,11] calculated by classical theory can be readily compared with the same diagram computed by the finite-element method. The comparison provides the link between the finite-element method and the classical theory.

The comparisons throw considerable light on the effect of saturation on the *d*- and *q*-axis parameters, particularly the synchronous reactances X_d and X_q. Because of the difficulty of calculating unambiguous saturated values of X_d and X_q, it is argued that the flux-MMF diagram should be routinely used, especially as its calculation is straightforward using the finite-element method.

The flux-MMF diagram can be measured directly using a digital recording oscilloscope, and the torque calculated from its enclosed area can be compared with the shaft torque obtained from dynamometer tests. These results are presented as experimental validation of the flux-MMF diagram.

0-7803-7817-2/03/$17.00 ©2003 IEEE

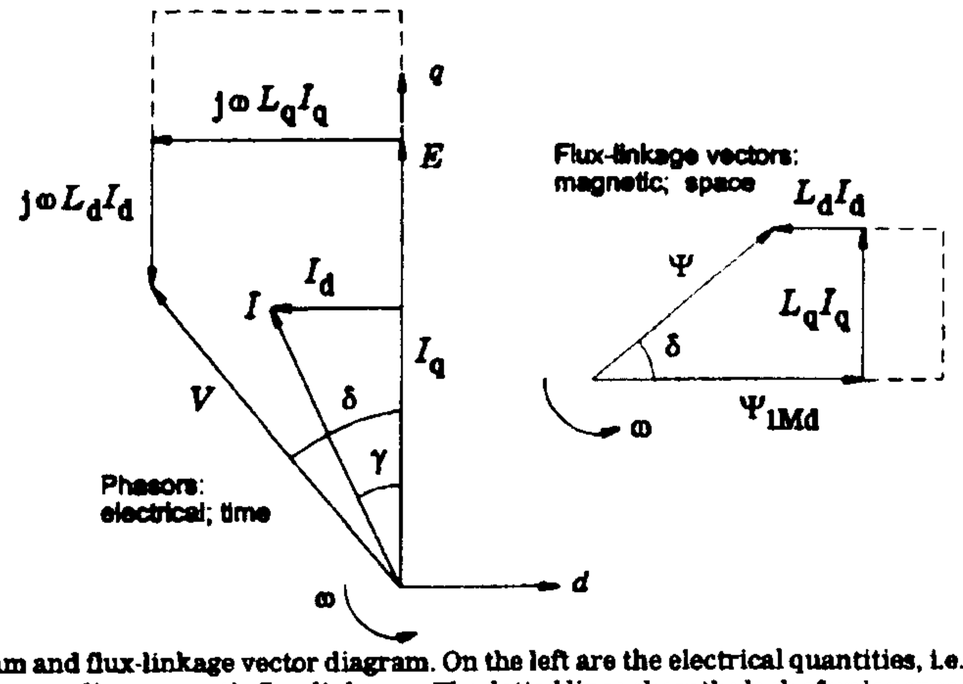

Fig. 2. Phasor diagram and flux-linkage vector diagram. On the left are the electrical quantities, i.e., voltages and currents. On the right are the corresponding magnetic flux-linkages. The dotted lines show the lack of uniqueness in the saturated values of X_d and E. For simplicity, resistance is neglected in this diagram, but normally it must be included.

II. Theory

A. Phasor Diagram for Sinewave Operation

The phasor diagram (Fig. 2) is drawn for one phase of a motor operating with balanced sinusoidal currents so that only the positive sequence field exists. It is assumed that the windings produce a sinusoidal distribution of ampere-conductors around the periphery of a smooth cylindrical stator bore (apart from slotting). The EMF and terminal voltage waveforms are also sinusoidal in time.

The phasor diagram is not only useful in understanding how the torque is limited by the voltage and current available from the drive, but it is also the basis of the circle diagram which is useful for understanding the effect of changes in speed and load, [1,2]. The electromagnetic torque T_e is given in terms of the rms current components I_d and I_q and the synchronous reactances X_d and X_q by

$$T_e = \frac{mp}{\omega}[EI_q + I_d I_q(X_d - X_q)]. \quad (1)$$

where m is the number of phases, p is the number of pole-pairs, ω is the radian frequency, and E is the rms fundamental open-circuit EMF per phase. In terms of the fundamental d- and q-axis flux-linkage components Ψ_d and Ψ_q, the equation for T_e can be expressed as

$$T_e = mp(\Psi_d I_q - \Psi_q I_d) \quad (2)$$

B. Effect of Saturation

Equations (1) and (2) remain valid for the fundamental components even under saturated conditions. Recognizing this, many engineers try to work with "saturated values of X_d and X_q", [1-8]. However, it is not often stated that the saturated value of X_d is not unique. The equation

$$\Psi_d = \frac{1}{\omega}[E + X_d I_d] \quad (3)$$

shows that for any value of d-axis current I_d there is an infinite number of pairs of values of E and X_d that will produce the d-axis flux-linkage Ψ_d that is actually present in the winding.

The lack of uniqueness in the saturated values of E and X_d is illustrated in Fig. 2, where the dotted line construction produces the same value of airgap flux (and flux-linkage Ψ) as the solid lines. It means that the actual airgap flux cannot be uniquely apportioned to the magnet and the armature MMF.

Many estimates of the "saturated value" of X_d tacitly assume that E is constant. For example, in finite-element analysis the permeability in every element of the mesh may be "frozen" at the open-circuit value: the additional flux-linkage due to stator current is computed with these permeabilities, and its ratio to the current that is causing it is taken as a measure of the synchronous inductance.

No matter whether the total flux-linkage is used to derive "total inductance", or whether the additional flux-linkage is used to define "incremental inductance", the process of freezing permeabilities is arbitrary, and can lead to confusion as to which value should be used in equations such as (1). Difficulties can arise in the interpretation of the results of this method, such as discontinuities in the graph of X_d vs. I_d when I_d changes from positive to negative; (see Fig. 13).

Equation (2) suggests that apportionment of q-axis voltage (or d-axis flux-linkage) between E and $X_d I_d$ is actually unnecessary, not only for calculating the torque but even for solving the voltage equations of the circuit, which in the steady state are

$$\begin{aligned} V_d &= R_a I_d - j\omega \Psi_q; \\ V_q &= R_a I_q + j\omega \Psi_d. \end{aligned} \tag{4}$$

If V_d and V_q are known, these equations can be solved for I_d and I_q provided that the relationships between I_d and Ψ_d and between I_q and Ψ_q are known. The functions $\Psi_d(I_d)$ and $\Psi_q(I_q)$ are known as the *magnetization curves* in the d and q axes, and they can be pre-computed by the finite-element method without any ambiguity as to how much flux is attributed to the magnet and how much to the current. Where there is significant cross-saturation, the flux-linkages can be made functions of both currents, i.e. $\Psi_d(I_d, I_q)$ and $\Psi_q(I_d, I_q)$.

C. The Flux-MMF Diagram

The flux-MMF diagram is the locus of a point whose coordinates are flux and MMF, or more conveniently, flux-*linkage* ψ and current i in each phase of the machine, [11]. Over one cycle the area W enclosed within this locus is equal to the electromechanical energy conversion in that phase. If the induced voltage (i.e., the terminal voltage minus the resistance voltage drop) and the current are both sinusoidal, the flux-MMF diagram is elliptical as shown in Fig. 3(a).

In a brushless motor with squarewave current drive and trapezoidal EMF, the diagram is composed approximately of two parallelograms as in Fig. 3(b).

If the phases are balanced, the average electromagnetic torque is derived from the variation of co-energy with rotor position over one cycle:

$$T_e = m \frac{W}{2\pi}. \tag{5}$$

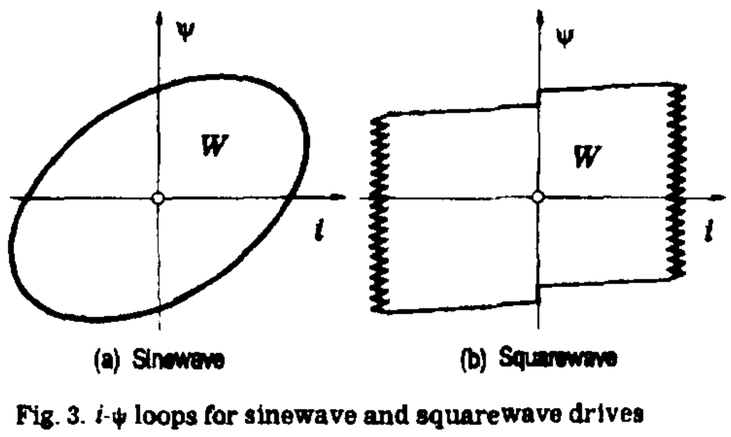

Fig. 3. i-ψ loops for sinewave and squarewave drives

The torque equation (2) is a special case of (5) in which W is the area of the ellipse whose dimensions in the current and flux-linkage axes are defined by I and Ψ respectively. The simplicity of (2) follows from the simple elliptical shape of Fig. 3(a).

The flux-MMF diagram is completely general. It works for *any* waveforms of current and flux-linkage, and does not require sinusoidally distributed windings or sinusoidal time-waveforms of voltage or current. Since the EMF in each phase is equal to $d\psi/dt$, it works for motors having *any* EMF waveform. It also includes cogging torque.

The simple classical form of the torque equation such as (2) arises only under special ideal conditions characterized by the simple geometric shape of the flux-MMF diagram. In the general case these ideal conditions are not met.

D. Calculation of the Flux-MMF Diagram

In classical theory the time-waveforms of flux-linkage and current are expressed by (6) with phase angles and amplitudes as in Fig. 2:

$$\begin{aligned} i(\omega t) &= i_1 \cos \omega t \\ \text{and } \psi(\omega t) &= \psi_1 \cos [\omega t + (\delta - \gamma - \pi/2] \end{aligned} \tag{6}$$

where ψ_1 is derived from the phasor diagram using relationships such as (4). Then the flux-MMF diagram follows directly in a plot of ψ vs. i.

In the finite-element method, the waveform $i(\omega t)$ is applied to the conductor distribution at each of a series of rotor positions such as the one shown in Fig. 4. Simultaneously the appropriate current waveforms are applied to the conductors of the other phases. The flux-linkage ψ of each phase is computed from the weighted summation of vector potentials over the respective conductor areas within the stator slots. Then, as in the classical method, the flux-MMF diagram follows directly in a plot of ψ vs. i.

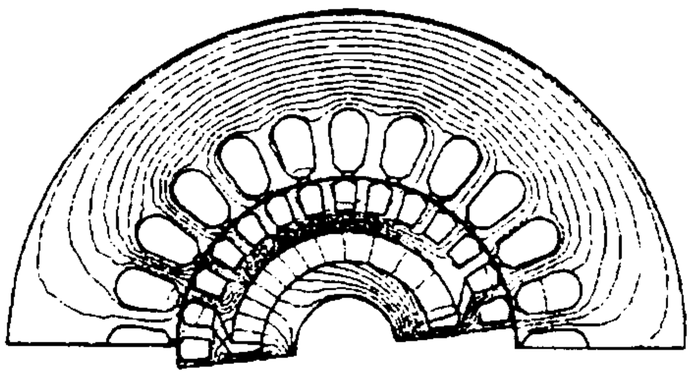

Fig. 4. Finite-element calculation

The flux-MMF diagram obtained in this way includes all flux-linkage components except the end-turn leakage. In particular, slot-leakage is included.

Examples of ψ–i diagrams obtained by both methods are compared with test data in Section III.

E. Extracting E, X_d and X_q from finite-element data

As suggested earlier, the equivalent circuit and the phasor diagram with E, X_d, X_q are not needed for calculating the torque, if the finite-element method is available to be used with the flux-MMF diagram or the Maxwell stress method. However, the finite-element method has no quick means of calculating how much current will flow for a given applied voltage, or *vice-versa*. For this reason it is desirable to correlate the finite-element method with the equivalent-circuit calculation. For sinewave motors it is convenient to do this by extracting values of E, X_d and X_q from the finite-element results.

One way to do this is to use the finite-element method to calculate the self- and mutual inductances of the phase windings directly, as a function of rotor position, since the reactances X_d and X_q can be derived from these. As mentioned earlier, permeabilities are often "frozen" at their open-circuit values, while E is regarded as constant; but because of the ambiguities that arise as a result of the nonlinearity of the magnetic circuit, this method is to be avoided.

Another method is to extract B_1, the fundamental component of the airgap flux-density distribution around the stator bore, by Fourier analysis of the calculated distribution: see Fig. 5. From B_1 the fundamental airgap flux/pole can be calculated, and then the peak flux-linkage per phase is given by (7), where D is the stator bore diameter, L_{stk} the stack length, k_{w1} the fundamental winding factor, and T_{ph} the number of turns in series per phase:

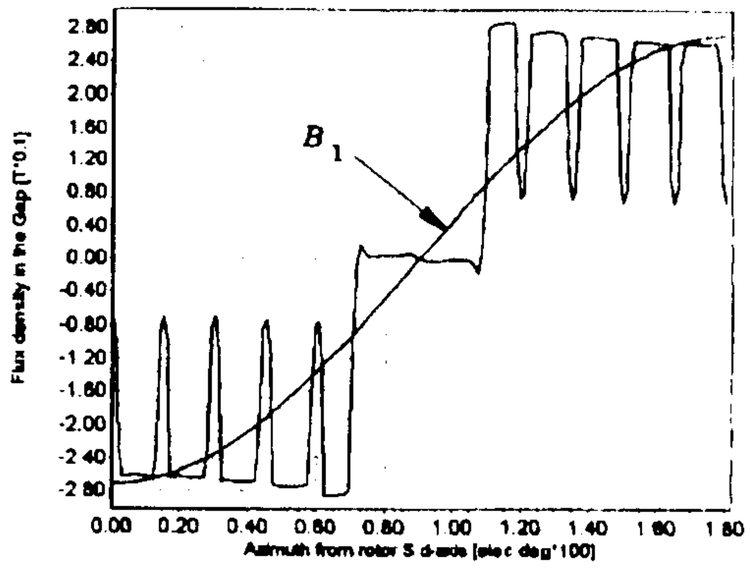

Fig. 5. Finite-element calculation of open-circuit flux-density around the airgap, over two half-poles. The fundamental component B_1 is also shown.

$$\Psi_1 = \frac{B_1 D L_{stk}}{p} \times k_{w1} T_{ph} \quad \text{V-s}. \tag{7}$$

The rms voltage induced in the phase winding by this flux-linkage is

$$V = \frac{\omega \Psi_1}{\sqrt{2}}. \tag{8}$$

If Ψ_1 is calculated for the open-circuit condition, this equation gives E, while (7) gives Ψ_{1Md}, the open-circuit flux-linkage due to the magnet. Under load, it gives the phase voltage V shown in Fig. 2.

When the fundamental distribution $B_1(\theta)$ is obtained, its phase angle can be used as a measure of δ (see Fig. 2), so that if E is assumed constant the reactances X_d and X_q can be extracted by setting $R_a = 0$ and using (4) with

$$\Psi_d = \Psi_1 \cos\delta = \Psi_{1Md} + \frac{L_d}{\omega} I_d$$
$$\text{and} \quad \Psi_q = \Psi_1 \sin\delta = \frac{L_q}{\omega} I_q. \tag{9}$$

The values of $X_d = \omega L_d$ and $X_q = \omega L_q$ obtained in this way from the airgap B distribution do not include the slot-leakage reactance or the end-turn leakage reactance. The only simple way to add these elements is by estimating them with classical design formulas, [1].

III. Measuring the Flux-MMF Diagram

The flux-MMF diagram is measured during normal load-test conditions on a dynamometer as shown in Figs. 6 and 7.

The phase terminal voltage v and current i are recorded digitally and the flux-linkage waveform is obtained from the integral

$$\psi = \int (v - Ri)\,dt, \qquad (10)$$

where R is the phase resistance.

The test motor analyzed in this paper is a 230-V, 50-Hz, 2-pole single-phase capacitor motor with main and auxiliary phases whose winding axes are displaced by 90°. Both windings have 5 concentric coils per pole with approximately sinusoidal distribution of turns; see Fig. 8.

Dynamometer load tests are conducted with approximately sinusoidal currents supplied by a two-phase DSP-controlled PWM inverter. The amplitudes of the main and auxiliary phase currents are controlled to be in the inverse ratio of the effective turns in each winding, so that operation is balanced. The phase orientation of the current is also controlled by the inverter, using shaft position feedback from an optical encoder.

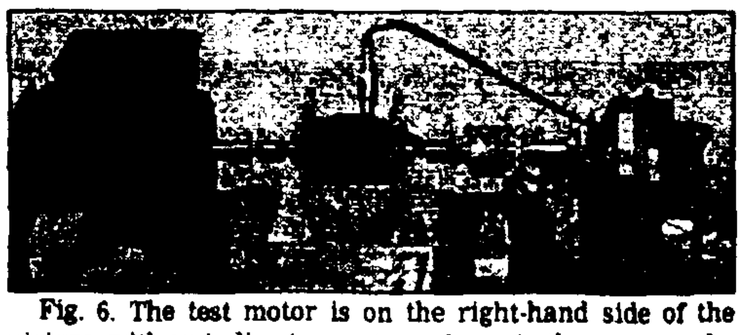

Fig. 6. The test motor is on the right-hand side of the picture, with an in-line torque transducer in the center and a brake machine on the left. Rotor position is measured by an in-line optical encoder.

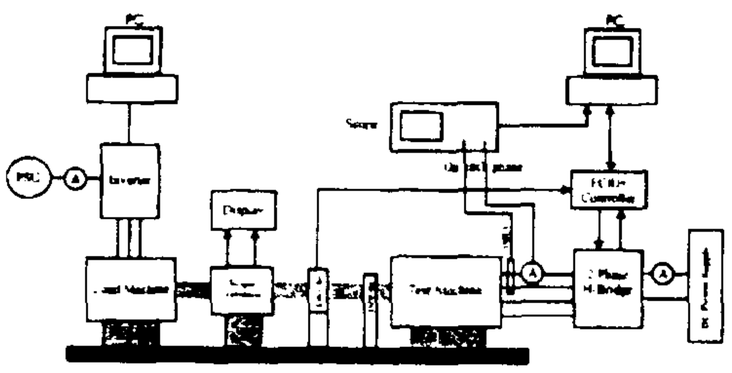

Fig. 7. Dynamometer and test configuration

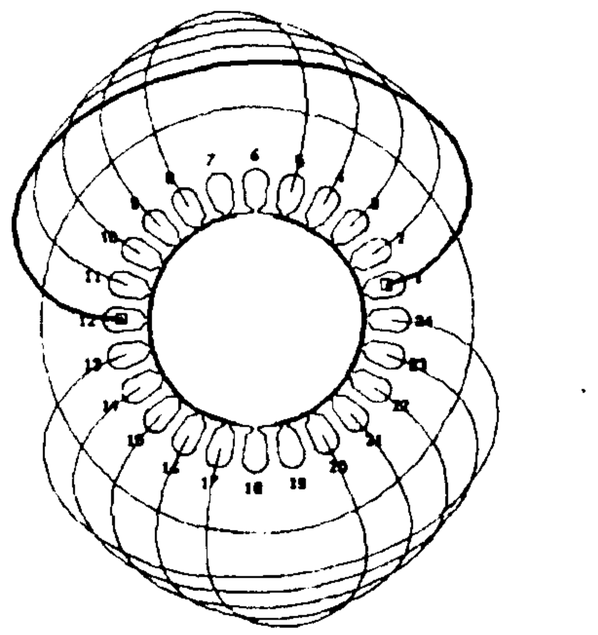

Fig. 8. Main phase winding of test motor.

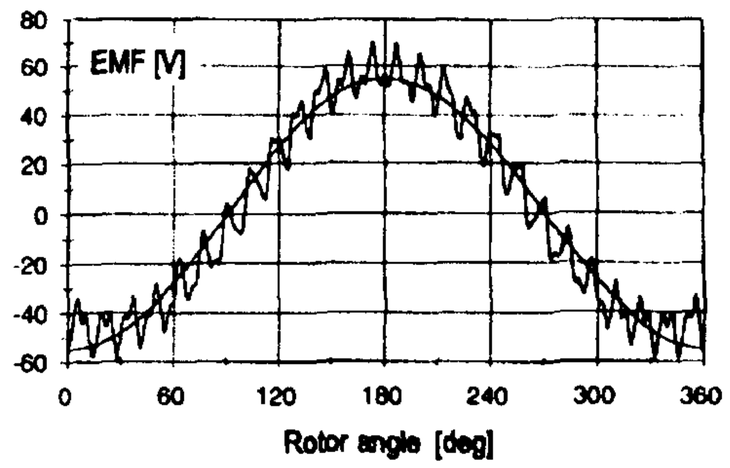

Fig. 9. Measured open-circuit EMF waveform of main phase winding at 1000 rpm. Magnet temperature = 25°C.

The measured open-circuit EMF waveform of the main phase at 1,000 rpm is shown in Fig. 9, together with its fundamental component, $E = 38.9$ V rms.

The test motor has no skew, so the EMF shows considerable ripple arising from the slotting on both the rotor and the stator. The open-circuit flux distribution in the airgap is far from sinusoidal, as shown by the finite-element calculation in Fig. 5.

It is very important to measure or estimate the magnet temperature at every test point, so that the correct remanent flux-density can be used in calculations. The same is true of the winding temperature, so that the phase resistances can be correctly calculated.

IV. Test Results

A. *Measured Flux-MMF Diagram*

Fig. 10 shows the flux-MMF diagram at a typical test point, with a sinusoidal current of 2.0 A (peak) at an angle $\gamma = +40°$ meaning that the current phasor leads the EMF phasor by 40°.

The torque calculated by (5) from the loop areas in Fig. 10 is 1.30 Nm. This includes the contributions from both the main and auxiliary phases, which are almost equal. Also shown is the i-ψ loop computed by the finite-element method without end-turn leakage correction. Without this correction the measured and calculated loops differ slightly, and further deviations arise from the PWM harmonics in the measured loops. However, the loop areas are remarkably close.

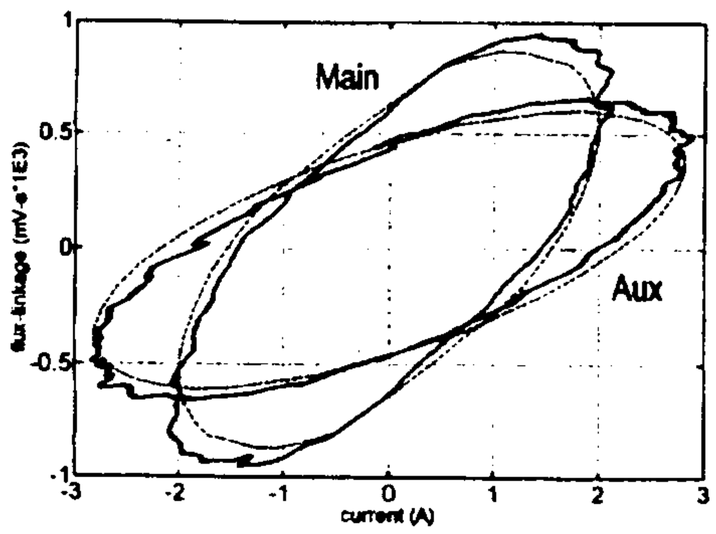

Fig. 10. Measured i-ψ loops for the main and auxiliary phase windings. The dotted lines show the loops derived from the finite-element method driven by the fundamental component of current.

Fig. 11 shows the torque vs. γ over a range from -40° to +40°, with constant current of 2 A peak at 1000 rpm. This current is close to the safe maximum of the motor. Close agreement is obtained between torque values from the i-ψ loops obtained by direct measurement and finite-element calculation, over the whole range. The shaft torque is about 0.1 Nm less than the loop torque, probably owing to a combination of friction and windage and a drag torque caused by iron loss.

Fig. 11 also shows the torque calculated by (1) after adjusting X_d and X_q to match the i-ψ loop obtained by the finite-element method at $\gamma = 40°$ and 2 A, with E = 38.9 V rms, the test value. At other values of γ the "phasor" method deviates because of variations in X_d and X_q caused by saturation.

B. *Variation of X_d and X_q*

Fig. 11 gives little information about the variation of X_d and X_q with current. Accordingly two series of finite-element calculations were carried out, one with current only in the d-axis and the other with current only in the q-axis. For each solution, X_d and X_q were obtained using (7-9). The result is given in Fig. 12, which expresses X_d as a function of I_d with $I_q = 0$, and X_q as a function of I_q with $I_d = 0$. In all cases it is assumed that E is constant, as in [8].

Fig. 12 shows a huge variation of 6:1 in X_q and almost 2:1 in X_d.

Calculations with current flowing simultaneously in both axes show that X_d is affected by I_q, being increased when $I_d < 0$ and decreased when $I_d > 0$, with $I_q > 0$. An example is shown in Fig. 13 which is computed for I_q = 2.0 A (peak), and varying I_d.

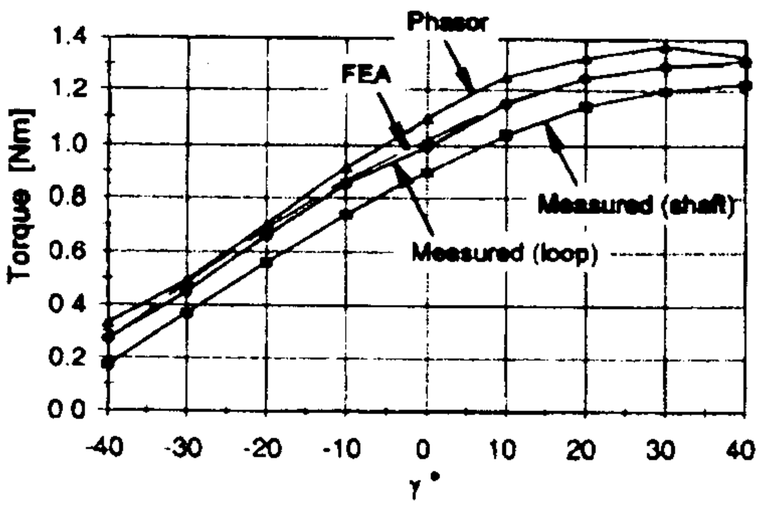

Fig. 11. Torque vs. γ obtained by measurement and calculation. Sinusoidal current, peak value 2.0 A.

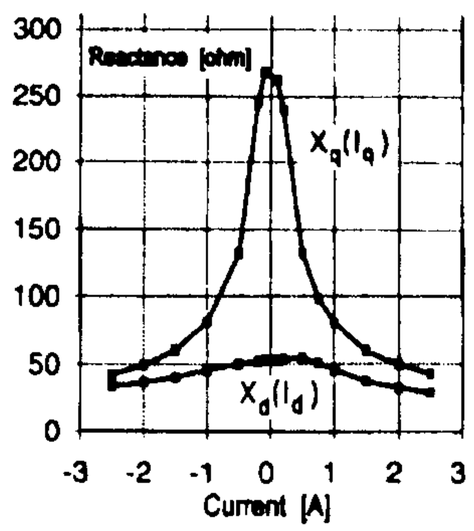

Fig. 12. Variation of X_d vs. I_d with $I_q = 0$, and of X_q vs. I_q with $I_d = 0$, calculated using (7-9) from finite-element data with constant E.

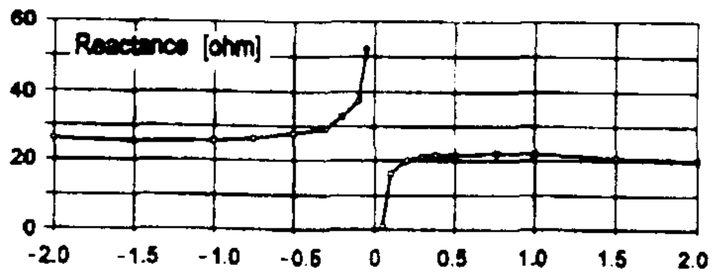

Fig. 13. X_d vs. I_d with I_q = 2.0 A (peak).

The discontinuity at $I_d = 0$ was mentioned earlier in connection with the "frozen permeability" method. It can be attributed to an error or variation ΔE from the open-circuit value E_0:

$$X_d = \frac{V_q - (E_0 + \Delta E)}{I_d} = \frac{V_q - E_0}{I_d} - \frac{\Delta E}{I_d}. \quad (11)$$

If E is assumed constant and equal to E_0, the value of X_d that will be inferred by using only the first term of (11) is in error by $\Delta E/I_d$, which is indefinite when $I_d = 0$.[a] Evidently the effect of cross-saturation is that E depends on the current components I_d and I_q as do X_d and X_q.

V. Conclusion

Experimental validation of the flux-MMF diagram for torque calculation has been given in the form of measured energy conversion loops and shaft torque measurements. The flux-MMF diagram is convenient to calculate by the finite-element method, and if the current waveform is known *a priori*, the terminal voltage can be calculated from $Ri + d\psi/dt$ directly, providing valuable information for drive design.

In contrast, the classical phasor-diagram method is only as accurate as the values of E, X_d and X_q at every load point. X_d and especially X_q vary widely as a function of current, and cross-saturation effects complicate these functions: for example, if E is assumed constant the variation of X_d with I_d can be discontinuous around $I_d = 0$. Since there is no practical means of calculating X_d and X_q accurately other than the finite-element method, it is hard to escape the conclusion that the classical method has little more than symbolic value and that the finite-element method should be used routinely instead. The phasor diagram is still useful as a guide, but inadequate as a model.

Although the finite-element method can be used to calculate E, X_d and X_q for use in the phasor diagram, this method applies only to motors that have sine-distributed windings and sinusoidal waveforms of EMF, current, and terminal voltage. The flux-MMF diagram method, on the other hand, is completely general and applies to motors that do not have these ideal properties.

VI. References

1. Hendershot JR and Miller TJE [1994] *Design of brushless permanent-magnet motors*, Magna Physics Publishing.

2. Miller TJE [1989] *Brushless permanent-magnet and reluctance motor drives*. Oxford University Press.

3. Jahns TM [1987] *Flux-weakening regime operation of an interior permanent-magnet synchronous motor drive*, IEEE Trans. IA-23, No. 4, July/August 1987, pp. 681-689.

4. Bianchi N and Bolognani S [1998] *Unified approach to the analysis and design of an AC motor drive for flux-weakening operation*, Conf. Rec. IEEE Industry Applications Society 33rd Annual Meeting, St. Louis, MO, USA, 12-15 October 1998, pp. 95-102.

5. Bianchi N and Bolognani S [1998] *Magnetic models of saturated interior permanent magnet motors based on finite-element analysis*, Conf. Rec. IEEE Industry Applications Society 33rd Annual Meeting, St. Louis, MO, USA, 12-15 October 1998, pp. 27-34.

6. Honda Y., Higaki T., Morimoto S. and Takeda Y [1998] *Rotor design optimisation of a multi-layer interior permanent-magnet synchronous motor*, IEE Proceedings, Electric Power Applications, 145, No. 2, March 1998, pp. 119-124.

7. Nee H.-P., Lefevre L, Thelin P, Soulard J. [2000] *Determination of d and q reactances of permanent-magnet synchronous motors without measurements of the rotor position*, IEEE Trans. Industry Applications, IA-36, No. 5 , September/October 2000, pp. 1330-1335.

8. Popescu M, Miller TJE, McGilp MI, Strappazzon G, Trivillin N, Santarossa R [2002] *Line Start Permanent Magnet Motor: Single Phase Starting Performance Analysis*, Conf. Rec. IEEE Industry Applications Society, 37th Annual Meeting, Pittsburgh, USA, 13-18 October 2002, pp. 2499-2506.

9. Miller TJE [1981] *Methods for testing permanent-magnet AC motors*. IEEE Industry Applications Society Annual Meeting (IAS), Toronto, October 1981, pp. 494-499.

10. Ionel DM, Eastham JF, Miller TJE and Demeter E. [1998] *Design Considerations for permanent magnet synchronous motors for flux weakening applications*, IEE Proceedings, Electr. Power Appl., Vol. 145, No.5, September 1998, pp. 435-440.

11. Staton DA, Soong, WL, Deodhar RP and Miller TJE [1995] Torque prediction using the flux-MMF diagram in AC, DC and reluctance motors, IEEE Transactions Industry Applications, Vol.32, No.1, Jan-Feb. 1996, pp. 180-188.

12. Soong WL, Staton DA and Miller TJE [1994] *Design of a new axially-laminated interior permanent-magnet motor*. IEEE Trans., Vol.31, No.2, March/April 1995, pp.358 367.

[a] This explanation was originally suggested to one of the authors by R.J. Krefta.

MEASUREMENT AND APPLICATION OF FLUX-LINKAGE AND INDUCTANCE IN A PERMANENT-MAGNET SYNCHRONOUS MACHINE

TJE Miller, J.A. Walker, and C. Cossar

SPEED Laboratory, University of Glasgow, Glasgow G12 8LT.

Keywords: Permanent-magnet machines, magnetic fields, flux-linkage measurement.

Abstract

This paper describes the experimental measurement of flux-linkage/current curves for a permanent-magnet brushless synchronous motor, using a combination of physical rotations and electrical switching operations to determine the static flux-linkages of the windings. A theoretical model is described which uses the resulting magnetization curves to solve "voltage-driven" performance calculations very rapidly, even when the motor is heavily saturated.

1 Introduction

Modern permanent-magnet synchronous brushless machines often have magnetic circuits in which the patterns of saturation are complex and vary with the position of the rotor, Fig. 1. The classical theory of operation relies on such assumptions as the sinusoidal distribution of windings and sinusoidal variation of inductance with rotor position, and has no natural means of representing the strong but localised nonlinear effects that arise in different operating states, [2].

In almost all the literature that deals with the modelling of these machines, the magnet flux (represented by the open-circuit voltage E) is treated as constant, while saturation is represented by current-dependent inductances. Although this model is useful as a basis for circuit simulation, it cannot be completely verified experimentally because the magnet flux cannot be measured or isolated when current is flowing, and so there is no way of telling whether it varies under load. Likewise, a finite-element calculation determines only the total flux and cannot resolve it into separate contributions from the magnet and the current without resorting to superposition, which is not valid in a nonlinear magnetic circuit except over very small ranges of current and rotor position.

This paper presents a model of the PM brushless machine based on static magnetization curves of flux-linkage versus current and rotor position. The magnetization curves are suitable for circuit simulation with a suitable nonlinear algorithm, an example of which is given in the paper. The ultimate objective is a circuit simulation that is capable of solving "voltage-driven" problems which frequently arise when these motors are used with power electronic drives. (The finite-element method is generally too slow for time-stepping problems, although it is invaluable for computing the static magnetization curves).

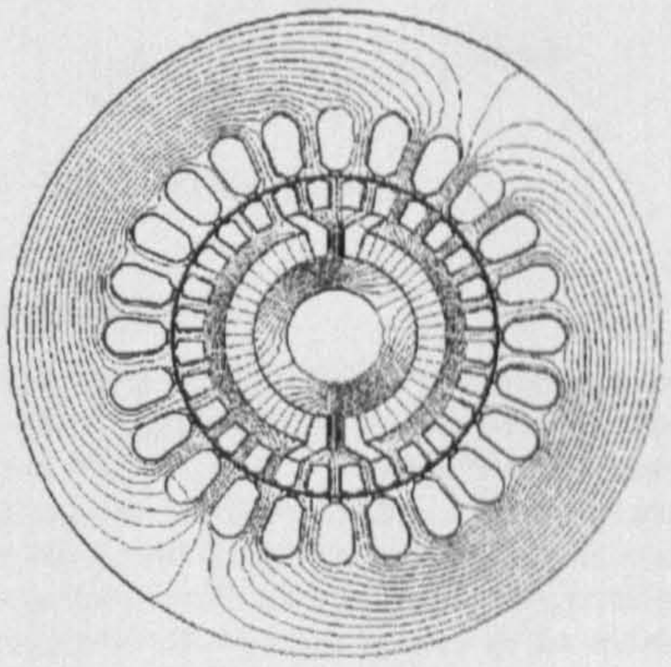

Fig. 1 Finite-element flux-plot of the tested motor, which is a 2-pole line-start split-phase motor having orthogonal main and auxiliary windings.

The model has two important features:

(i) It does not rely on the assumption that the open-circuit voltage (i.e., magnet flux) is constant under load, but deals with the total flux-linkages in the windings.

(ii) It is based on static magnetization curves that can be directly measured.

The paper concerns itself with these two aspects in detail.

2 Theory

Fig. 2 shows a set of magnetization curves for one phase of the motor shown in Fig. 1. The d curve is obtained when the magnet axis (d-axis) is aligned with the phase axis, and the q curve when the rotor interpolar axis is aligned with the phase axis.

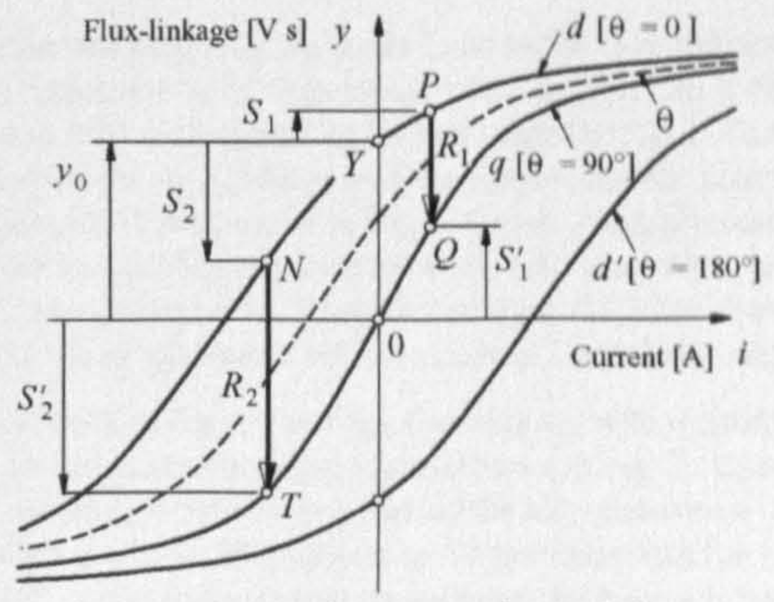

Fig. 2 Static magnetization curves d, q and d'

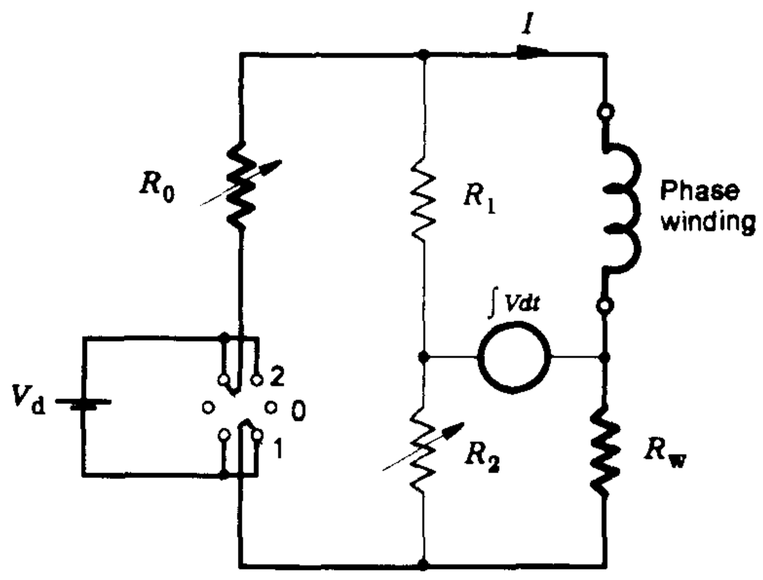

Fig. 3 Inductance bridge circuit described by Jones [1].

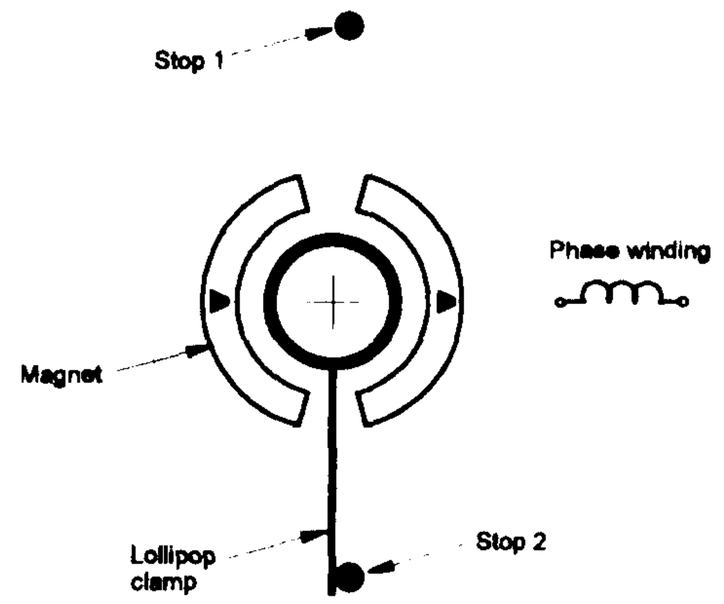

Fig. 4 Rotational test method

The q curve is rather similar to the aligned magnetization curve of a switched reluctance machine, but the d curve has no parallel in the reluctance machine, [3]. The PM machine has an open-circuit flux-linkage, y_0. Along the d curve, magnetizing current is positive, and increases the flux-linkage, but demagnetizing current is negative and decreases it. As the rotor rotates, the magnetization curve transforms itself to intermediate forms such as the one shown dotted.

Although all points in Fig. 2 can be computed by finite-elements, the question arises how to measure these curves for verification. The method used here relies on direct measurement of flux-linkage by integrating the balance voltage in the inductance bridge of Fig. 3, as described in [1] and [4]. The effect of the winding current is independently controlled by switching the direct current in Fig. 3 with a reversing switch to produce a "switching transition", S. The effect of the magnets is independently controlled by rotating the magnets briskly through a predefined angle using a "lollipop" clamp fixed to the shaft (Fig. 4), while the current is held constant. This produces a "rotational transition", R. The inductance bridge eliminates the effects of transient changes in current (including induced currents in the rotor cage) which are inevitable during the transition between the two balanced DC conditions at the start and end.

The measurement of a set of curves as in Fig. 2 is based on a series of combinations of S and R transitions which "walk" the operating state from point to point. A simplified example is explained here, with reference to Fig. 2.

Point P has a magnetizing current and a quadrature (90°) rotation would produce a transition R_1 from P to Q. The flux-linkage change is $|R_1| = y_0 + S_1 - S_1'$, and since $S_1' > S_1$ this is *less* than the open-circuit magnet flux-linkage y_0. Point N has a demagnetizing current and a quadrature rotation would produce a transition R_2 from N to P. The flux-linkage change is $|R_2| = y_0 - S_2 + S_2'$, and since $S_2' > S_2$ this is *greater* than y_0. In general the flux-linkage change produced by a quadrature rotation is not equal to y_0, even when the current is constant.

To verify the form of the magnetization curves it is necessary to make a suitable sequence of S or R transitions to be able to "walk" the operating state at will to any point on Fig. 2, with repeatable and accurate measurements. Examples of such measurements are given in the next section.

3 Measurements

Fig. 5 shows a direct example of the $P'Q$ transition measured in two ways: one is a plain rotation R_1, and the other is a pair of switching transitions S_1 and S_1'. It shows that any point on the magnetization curves can be reached by independent paths of R and S transitions, even though not all states can be reached by S transitions alone or by R transitions alone. This establishes the expected uniqueness of the states and proves that the entire set of curves can be verified by measurement.

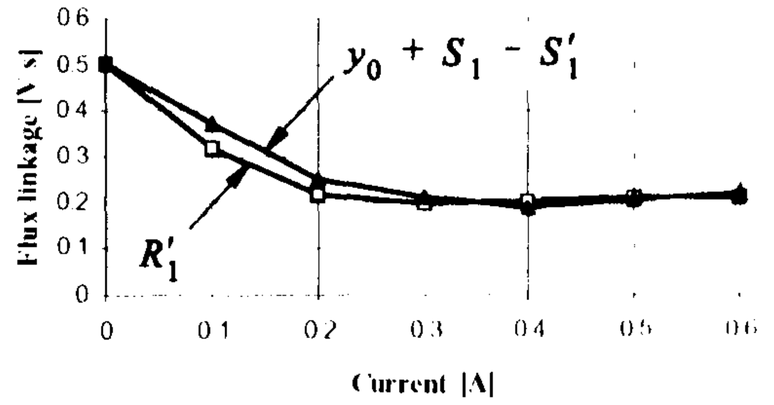

Fig. 5 Direct measurement of R_1 in Fig. 2 by separate rotation and switching transitions.

A more complete set of measurements is shown in Figs. 6 and 7, which again show the comparison of curves obtained by sequences of R and S transitions between the d and q axes, for the separate main and auxiliary windings.

In the main winding (Fig. 6), curve 1 shows the flux-linkage vs. current measured by S transitions with the rotor in a fixed position at 180° corresponding to the d' curve in Fig. 2. Curves 2 and 3 show the flux-linkage with the rotor in the 90° position, corresponding to the q curve in Fig. 2. Curve 2 was obtained by R transitions (rotating the rotor between 180° and 90°), while curve 3 was obtained by S transitions with the rotor fixed at 90°. The close agreement between curves 2 and 3 is noted.

Curves 4 and 5 in Fig. 6 show the flux-linkage with the rotor in the 0° position corresponding to the d curve in Fig. 2. Curve 4 was obtained by R transitions (rotating the rotor between 0° and 90°), while curve 5 was obtained by S transitions with the rotor fixed at 0°. The close agreement between the curves is noted.

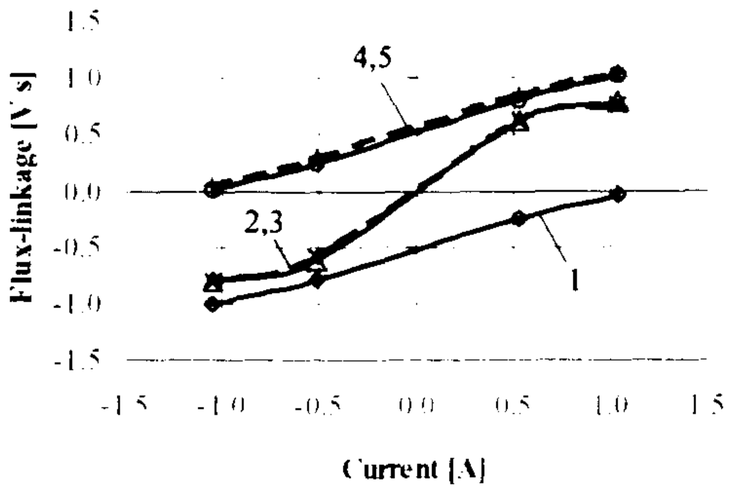

Fig. 6 Magnetization curves measured for the main winding by *R* and *S* transitions

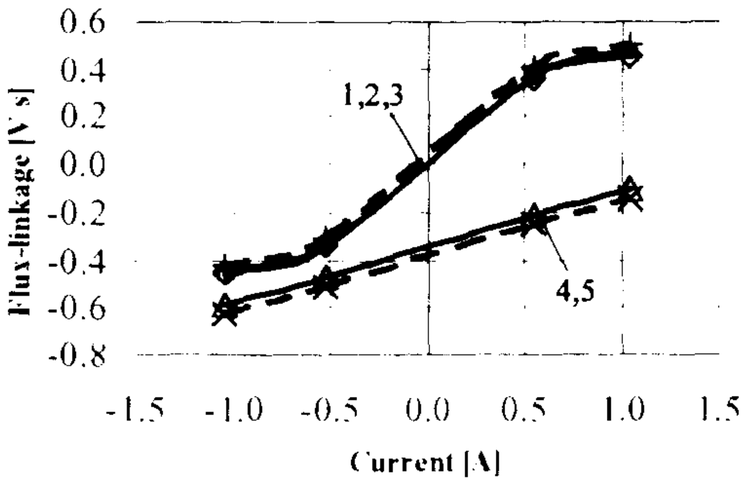

Fig. 7 Magnetization curves measured for the auxiliary winding by *R* and *S* transitions

For the auxiliary winding there is no direct correspondence with Fig. 2 because the *d* and *q* axis positions would be interchanged and the *y* axis would be scaled by the turns ratio. Even so the magnetization curves of the auxiliary winding have exactly the same general form as those of the main winding.

In the auxiliary winding (Fig. 7), curve 1 shows the flux-linkage vs. current measured by *S* transitions with the rotor in a fixed position at 0°. Curves 2 and 3 show the flux-linkage with the rotor in the 180° position. Curve 2 was obtained by *R* transitions (rotating the rotor between 0° and 90°), while curve 3 was obtained by *S* transitions with the rotor fixed at 0°. The close agreement between curves 1, 2 and 3 is noted.

Curves 4 and 5 in Fig. 7 show the flux-linkage of the auxiliary winding with the rotor in the 90° position. Curve 4 was obtained by *R* transitions (rotating the rotor between 0° and 90°), while curve 5 was obtained by *S* transitions with the rotor fixed at 90°. The agreement between the curves is again noted.

The process described in relation to Figs. 4-7 can be continued to cover the entire family of magnetization curves and not just the ones for the *d* and *q* aligned curves.

The curves can also be computed by the finite-element method, and examples are shown in Fig. 8 for comparison with measured curves. A surprising feature of both the computed and measured curves is that the maximum flux-linkage does not occur at the "aligned" position (0° or 180°), but with the rotor considerably displaced (up to 50° or 60°). While this is not fully understood, it is thought to be due partly to the saturation unsaturation of bridges in the rotor, and partly to the non-sinusoidal distribution of airgap flux; (see Fig. 9).

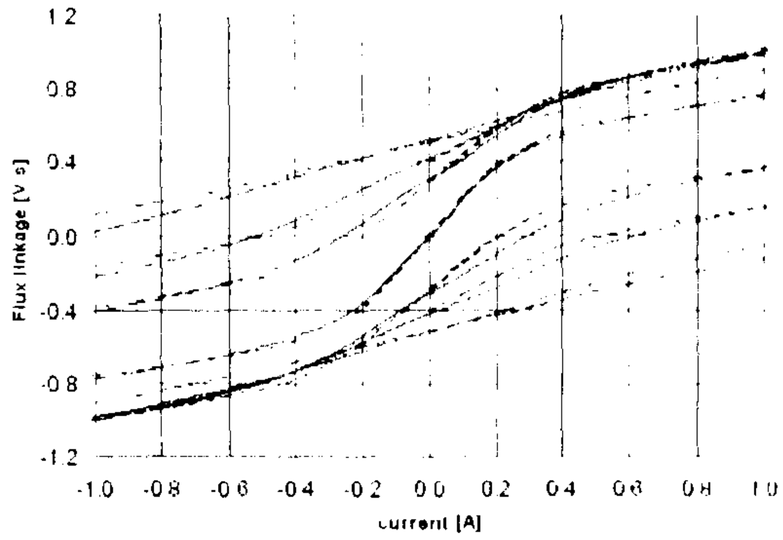

Fig. 8 Static magnetization curves computed by finite elements, compared with measured curves

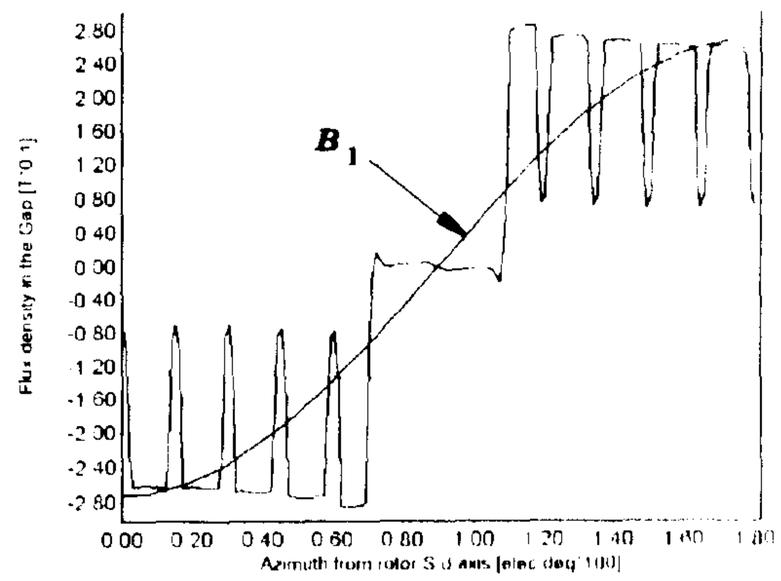

Fig. 9 Airgap flux-density distribution computed by finite-elements

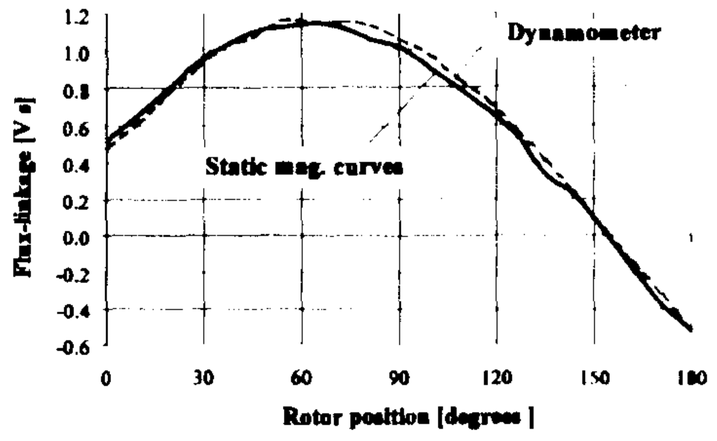

Fig. 10 Flux-linkage waveforms

Finally, Fig. 10 shows a dynamic waveform of flux-linkage measured during a dynamometer test, compared with the same waveform reconstructed from the static magnetization curves. The dynamic waveform was obtained from a continuous integral of $(v - Ri)$ with respect to time. The agreement between these curves provides further confirmation that the method described in the next section is suitable for circuit simulation and the calculation of torque by means of the flux-MMF diagram technique described in [2], which relies on computed waveforms of flux-linkage (as in Fig. 10) and current.

4 Application to a circuit simulation model

The magnetization curves in Fig. 2 are for one phase only, and do not show the effect of cross-saturation, that is, the distortion created by current in the second phase. For *sine-wound* machines a simplified theory can be used, as follows, to express the magnetization curves in a form that does not require multi-dimensional curve-fitting, and is therefore suitable for fast calculation. It relies on the definition of a current space vector, which is possible only if the windings are sine-wound. The two phase currents and the effects of their ampere-conductor distributions can then be represented by the magnitude and spatial orientation of the current space vector.

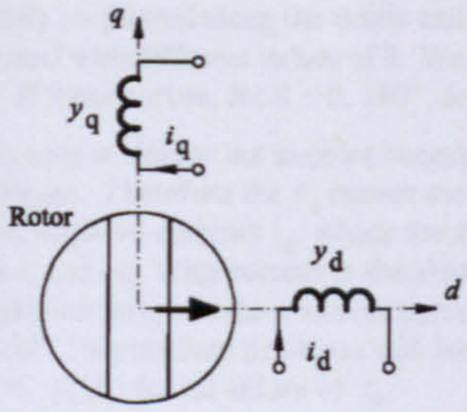

Fig. 11 *dq*-axis model

The synchronous machine theory in *dq* axes has the following relationships between the flux-linkages y_d, y_q and currents i_d, i_q

$$y_d = y_0 + L_d(i_d,i_q)\,i_d; \quad y_q = L_q(i_d,i_q)\,i_q. \quad (1)$$

The coils *d* and *q* are stationary with respect to the rotor, as shown in Fig. 11, and eqns. (1) are in the rotor reference frame. It is common to assume that y_0 is constant while the synchronous inductances L_d and L_q vary with current, but a more general form is

$$y_d = y_d(i_d,i_q); \quad y_q = y_q(i_d,i_q). \quad (2)$$

When multiplied by the frequency jω, eqn. (1) gives

$$\begin{aligned} V_q &= j\omega y_d = E + X_d I_d; \\ V_d &= j\omega y_q = X_q I_q \end{aligned} \quad (3)$$

in which X_d and X_q vary with current but E is constant. On the other hand, the "circuit" counterpart of eqn. (2) does not discriminate between E and $X_d I_d$, but uses V_q directly.

These relationships are represented in Fig. 12. If $i_q = 0$, and $i_d > 0$, L_d is given by the slope of the line *ED*. If $i_d = 0$ and $i_q > 0$, L_q is given by the slope of the line *OQ*. y_0 is the open-circuit flux-linkage in the *d* coil. If L_d and L_q were constant, the curves for y_d and y_q would consist of the lines *ED* and *OQ* produced in both directions as necessary.

In practice L_d and L_q both depend on both i_d and i_q. The analysis is in terms of the values y_d and y_q directly, rather than the slopes of the curves L_d and L_q.

d-axis — The variation of y_d with i_d is subject to saturation. The magnet premagnetizes the magnetic circuit so that positive magnetizing current $i_d > 0$ increases the level of saturation and the slope of *ED* (i.e. L_d) decreases as i_d increases.

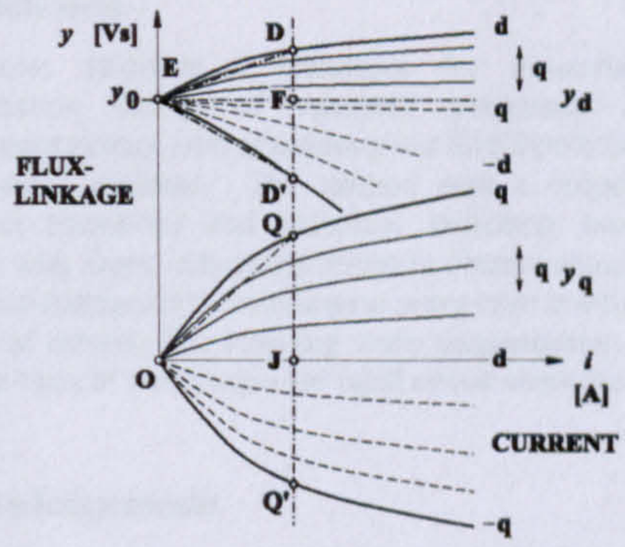

Fig. 12 Static magnetization curves for two axes

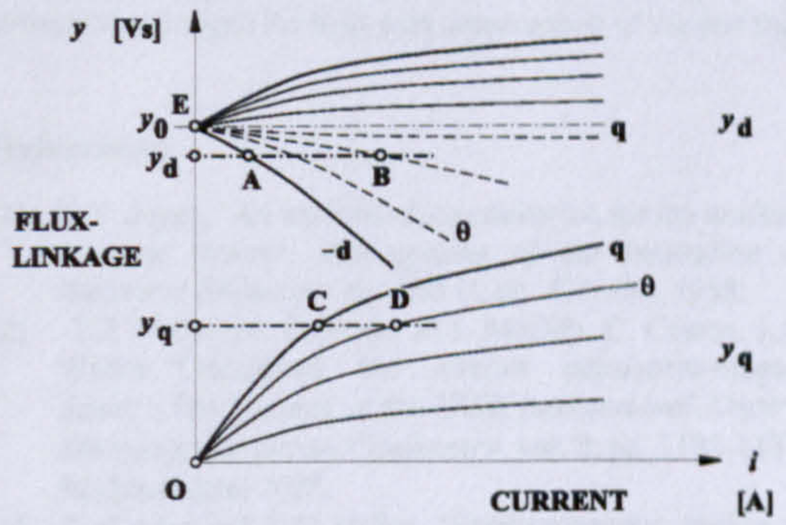

Fig. 13 Solution of flux-linkage / current relationship

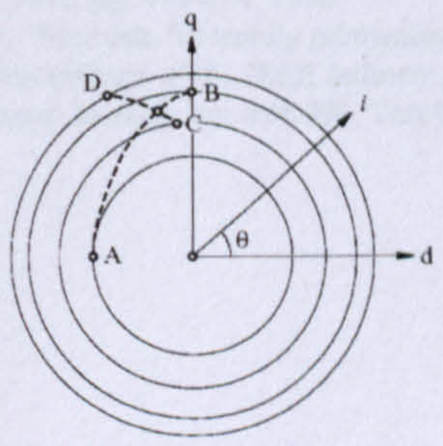

Fig. 14 Solution for both currents

With $i_d < 0$ the current is demagnetizing. In Fig. 12 this is not shown in the left-half plane but as a positive current applied at an angle of 180°, i.e., along the negative *d*-axis labelled -*d* in Fig. 12. It is expected that at first, negative values of i_d will relieve the saturation of the main magnetic circuit so that the slope of *ED'* will be steeper than that of *ED* until the current reaches a sufficiently high value to saturate the magnetic circuit in the reverse direction.

The curves *d* and -*d* for y_d in Fig. 12 are both drawn for $i_q = 0$. With current in the *q*-coil but not in the *d*-coil, it is often assumed that y_d remains constant at y_0, as represented by the line *EF*. However, because of cross-saturation, i_q does affect y_d. Evidently i_q in either direction will decrease y_d, for any i_d.

It makes no difference whether i_q is positive or negative, because the addition of current i_q will only increase the level of saturation above that which is obtained with any value of i_d. Therefore the line q in the y_d curves in Fig. 11 is not along EF but slightly below it.

In general current is flowing in both the d and q coils and we can define a current space-vector

$$\mathbf{i} = i e^{j\theta} = i_d + \mathrm{j} i_q, \quad \text{where } i_d = i \cos\theta \text{ and } i_q = i \sin\theta. \tag{4}$$

This makes it possible to represent the variation of y_d with *both* i_d and i_q as shown in the y_d curves in Fig. 11, in which the current magnitude i is plotted along the x-axis and the different curves are obtained with different values of θ. We have already examined four of these curves, for $\theta = 0$, 180°, and $\pm 90^\circ$.

q-axis — The q-axis is similar but simpler because there is no magnet flux-linkage. Therefore the y_q curves are symmetrical for positive and negative currents i_q, which are shown by the curves labelled q and -q. With current in the d-axis and $i_q = 0$ we expect no variation in y_q and therefore the curves for $i e^{j\pm 180^\circ}$ both lie along OJ. Intermediate positions will have symmetry in that $y_q(-i_q) = -y_q(i_q)$ for all values of i_d.

Solution—In performance calculations the differential circuit equations are integrated and new values of y_d and y_q are computed at every time-step, and i_d and i_q — or i and θ — have to be determined from the magnetization. curves. The algorithm for this is shown in shown in Figs. 13 and 14.

New values of y_d and y_q arising at the end of any integration step are shown in Fig. 13. The value of i indicated by y_d must lie between A and B on the horizontal line AB, and between C and D on the horizontal line CD. Fig. 14 plots the current **i** in the complex dq plane. The lines AB and CD in Fig. 13 are mapped on to this diagram, and their intersection defines the solution.

5 Conclusion

The paper describes a technique for measuring the magnetization curves of saturated permanent magnet synchronous motors, with examples given for a 2-pole line-start interior-rotor machine. The method uses a sequence of rotational transitions and electrical switching transitions together with Jones' inductance bridge to obtain unique values of the flux-linkages in the windings at every rotor position over a range of current. The resulting static magnetization curves form the basis of a technique for rapid circuit simulation.

Acknowledgements

The authors acknowledge the support of the *SPEED* Consortium. J.A. Walker is part-funded by the UK Engineering and Physical Sciences Research Council, Robert Bosch GmbH, and the *SPEED* Laboratory. Test motors were provided by Electrolux Compressors, Italy. Thanks to Jimmy Kelly and Wilson MacDougall for help with construction of the test rigs.

References

[1] C.V. Jones, "An analysis of commutation for the unified-machine theory", *Monographs of the Institution of Electrical Engineers*, no. 302 U, pp. 476-488, 1958.

[2] TJE Miller, M. Popescu, M.I. McGilp, C. Cossar, J.A. Walker."Calculating the interior permanent-magnet motor", *Proceedings of the IEEE International Electric Machines and Drives Conference*, **vol. 2**, pp. 1181-1187, Madison, June 2003.

[3] C. Cossar and TJE Miller, "Electromagnetic testing of switched reluctance motors". International Conference on Electrical Machines (ICEM) Manchester, 15-17 September 1992, pp. 470-474, 1992.

[4] TJE Miller, "Methods for testing permanent-magnet AC motors", *Proceedings of the IEEE Industry Applications Society Annual Meeting*, pp. 494-499, Toronto, 1981.

SIMULATION AND ANALYSIS OF MAGNETISATION CHARACTERISTICS OF INTERIOR PERMANENT MAGNET MOTORS

Jill Alison Walker, Calum Cossar, TJE Miller
SPEED Laboratory, University of Glasgow
Rankine Building
Oakfield Avenue
Glasgow G12 8LT
Scotland, UK

ABSTRACT

Modern permanent magnet (PM) synchronous brushless machines often have magnetic circuits in which the patterns of saturation are complex and highly variable with the position of the rotor. The classical phasor diagram theory of operation relies on the assumption of sinusoidal variation of flux-linkage with rotor position, and neglects the non-linear effects that arise in different operating states. The finite element method is a useful tool for detailed magnetic analysis, but it is important to verify simulation results by direct measurement of the magnetic characteristics of the motor, in terms of "magnetisation curves" of current and flux-linkage. This paper presents results from finite element simulations to determine the magnetisation in a split-phase interior permanent magnet (IPM) motor. Investigation has been made to determine the effects of the rotor geometry on the synchronous reactances and airgap flux distribution. Comparisons are made with a second IPM motor with a different rotor configuration.

Keywords: permanent magnet, finite element method, flux-linkage measurement, rotor bridges

NOTATION AND UNITS

E	voltage associated with the permanent magnets	[V]
E_0	open circuit magnet voltage	[V]
Ψ_1	fundamental flux-linkage associated with B_1	[V-s]
B_1	peak value of fundamental airgap flux density	[T]
D	bore diameter	[m]
L_{stk}	stack length	[m]
N_{ph}	number of phases	
k_{w1}	fundamental winding factor	
p	number of pole pairs	
X_q	quadrature axis synchronous reactance	[Ω]
X_d	direct axis synchronous reactance	[Ω]
R	phase resistance	[Ω]
ω	angular frequency	[rad/sec]
I	phase current	[A]
i	instantaneous current	[A]
I_q	quadrature axis current component	[A]
I_d	direct axis current component	[A]
$R_{A,B}$	non-inductive resistance	[Ω]
R_{VAR}	variable resistance	[Ω]
R_M	winding resistance	[Ω]
L_M	winding inductance	[H]
Ψ	flux-linkage due to current, from Wheatstone bridge	[V-s]

INTRODUCTION

The permanent magnet synchronous motor (PMSM) has risen in prominence owing to its comparably high efficiency and torque per volume ratio. The motor is salient-pole and highly saturable. The rotor may have interior rather than surface-mounted magnets, and may include a cage for starting. The saturation of the magnetic circuit varies with rotor position, resulting in localised effects. The operation of the motor can be analysed using the phasor diagram method, which transforms the phase currents and flux-linkages into direct (polar) and quadrature (interpolar) axis components. The direct axis (d-axis) flux-linkage can be split into two contributions, one from the current and one from the permanent magnets. The EMF associated with the magnets is denoted by the resultant EMF, E. There is no flux-linkage contribution from the permanent magnets on the quadrature axis (q-axis). It is not possible to measure the EMF associated with the magnets with current flowing in the winding and so it is necessary to assume that it remains constant at the open circuit value E_0, irrespective of loading.

As the diagram is based on phasor quantities, it can only be used to calculate sine-wound motors driven by sinusoidal voltages and currents. In cases where the winding distribution is non-sinusoidal, or where the excitation waveforms are non-sinusoidal, it is useful to analyse the motor using Finite Element (FE) software. It is not possible to separate the total flux-linkage calculated using finite elements without resorting to superposition, which cannot be considered valid in the case of non-linear magnetic circuits. Regardless of the method used, it is important to verify the results by measurement. The amount of magnet flux crossing the airgap is heavily dependent on the rotor design. The rotor slots are sometimes fully enclosed by bridge sections, which lowers the noise or harmonic content in the airgap flux distribution. The bridges quickly saturate and create magnetic short circuits within the rotor, contributing significantly to the levels of leakage flux and thus reducing the amount of flux crossing the airgap. The rotor slots can be designed so as to provide lower harmonic content in the flux density whilst limiting leakage flux.

SIMULATION OF MAGNETIC CHARACTERISTICS USING FINITE ELEMENTS

The motor cross sections can be modelled by finite elements, as shown in Figure 1 [1]. Single load point simulations can be run to determine the airgap flux density distribution when the phase axis is aligned with the direct and quadrature axis rotor positions, for increasing load current. The direct and quadrature axis synchronous reactances are calculated from the fundamental component of the airgap flux density. The peak fundamental flux-linkage is given by (1) and then the RMS synchronous reactances can be calculated from (2) and (3).

$$\Psi_1 = \frac{B_1 D L_{stk} N_{ph} k_{w1}}{p} \quad \text{[V-s]} \quad (1)$$

$$X_d = \left[\frac{\Psi_1 \omega}{\sqrt{2}} - E_0 \right] \Big/ \mathrm{I} \quad [\Omega] \quad (2)$$

$$X_q = \frac{\Psi_1 \omega}{I\sqrt{2}} \quad [\Omega] \quad (3)$$

According to (2), the direct axis synchronous reactance calculation requires separation of the current component of flux-linkage from the magnet component. It is, therefore, once again convenient to assume that the open circuit magnet flux is constant and independent of loading. The properties of the permanent magnets can be matched in the finite element simulations by comparing simulated open circuit back EMF waveforms to experimental results.

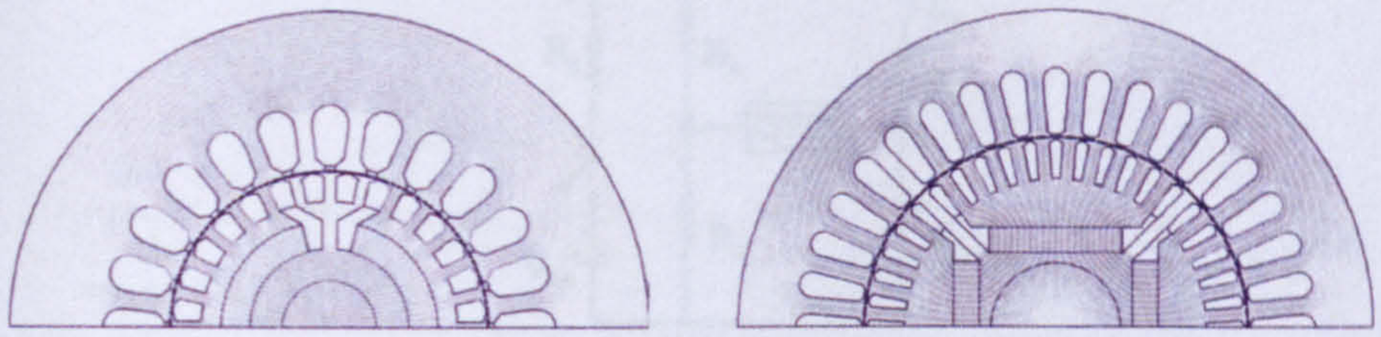

Figure 1. Finite element plots Test Motor 1 (left) and Test Motor 2 (right)

The static magnetisation curves of the motor represent the variation of flux-linkage with current at successive rotor positions and can be represented in terms of either the direct and quadrature axes or phase quantities. By minor alteration of a scripting routine in the finite element software, it is possible to calculate the flux-linkages at incremental rotor positions with constant current in the winding. The flux-linkage is calculated from the magnetic vector potential in each of the stator slots and so the direct axis value includes the flux-linkage contributions from both the direct axis current and the permanent magnets.

VERIFICATION OF SIMULATION RESULTS BY MEASUREMENT

The testing of IPM motors necessarily differs from that of wound-field synchronous machines, due to the permanent excitation resulting from the magnets. For wound-field machines, the synchronous reactances are measured from open circuit saturation tests and short-circuit tests in accordance with IEEE Standard 115-1995 [2]. The method for determining synchronous reactances, independently discovered by Jones and El-Kharashi [3,4], was first applied to permanent magnet motors by Miller [7]. The phase of the motor to be tested is connected into one leg of a Wheatstone bridge circuit, as in Figure 2. The resistance Rm and inductance Lm

represent the winding under test. The variable resistor R_{VAR} is adjusted so that when the switch is open there is no voltage across the centre of the bridge. The switch is initially closed, to allow a DC current I_{DC} to flow through the bridge circuit. When the switch is then opened, the current through the inductor decays from I_{DC} to zero. During this transient period, the voltage across the centre of the bridge is given by (4). The voltage waveform is stored in a digital storage oscilloscope (DSO). By integrating this voltage with respect to time, the flux-linkage for the given level of current can be found. If the bridge is balanced and the resistor ratios have been selected such that $R_A = R_B$, then the inductance of the winding is given by (5). From this, the synchronous reactances can be determined (6). The synchronous reactances will vary as a function of load.

$$v = v_{R_B} - v_{R_{var}} = -\left(\frac{R_{\text{var}}}{R_{\text{var}} + R_{\text{M}}}\right) L_M \frac{di}{dt} \quad [\text{v}] \qquad (4)$$

$$L_M = \frac{2\Psi}{I_{\text{DC}}} \quad [\text{H}] \qquad (5)$$

$$X = \omega L_M \quad [\Omega] \qquad (6)$$

The direct measurement of magnetisation curves in switched reluctance motors using locked rotor tests with pulsed voltage waveforms is described by Miller, [5]. The bridge circuit used for measurement of the synchronous reactances can be incorporated into the locked rotor test rig. However, the flux-linkage calculated by integration of the instantaneous voltage is due to winding current only and does not include any contribution from the permanent magnets. It is commonly assumed that the flux-linkage contribution from the permanent magnets is independent of current and varies only with rotor position. Under this assumption, the contribution from the magnets can be calculated from integration of the open circuit back EMF waveform. An indirect method of verifying the magnet flux-linkage with current in the winding, combining the Wheatstone bridge circuit and a rotational test, has been discussed by Miller et al. [6]. The rotor is locked into position and the flux-linkage due to current measured as for the synchronous reactance measurements. The rotor is then rotated through a predetermined angle and the change in flux-linkage added to the flux-linkage from the Wheatstone bridge measurement. The result will be the total flux-linkage at the new rotor position. The flux-linkage due to current at the new rotor position is easily measured using the bridge circuit. Subtraction of this value from the total flux-linkage leaves the magnet flux-linkage contribution at the new rotor position, which if the magnet flux is independent of current, will equal the open circuit magnet flux-linkage at that rotor angle.

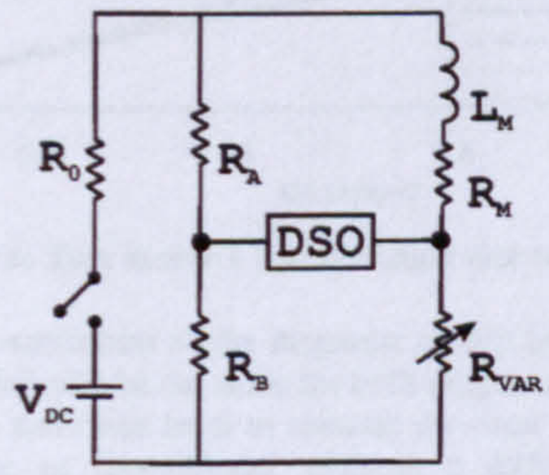

Figure 2. Wheatstone bridge circuit for measurement of synchronous reactances.

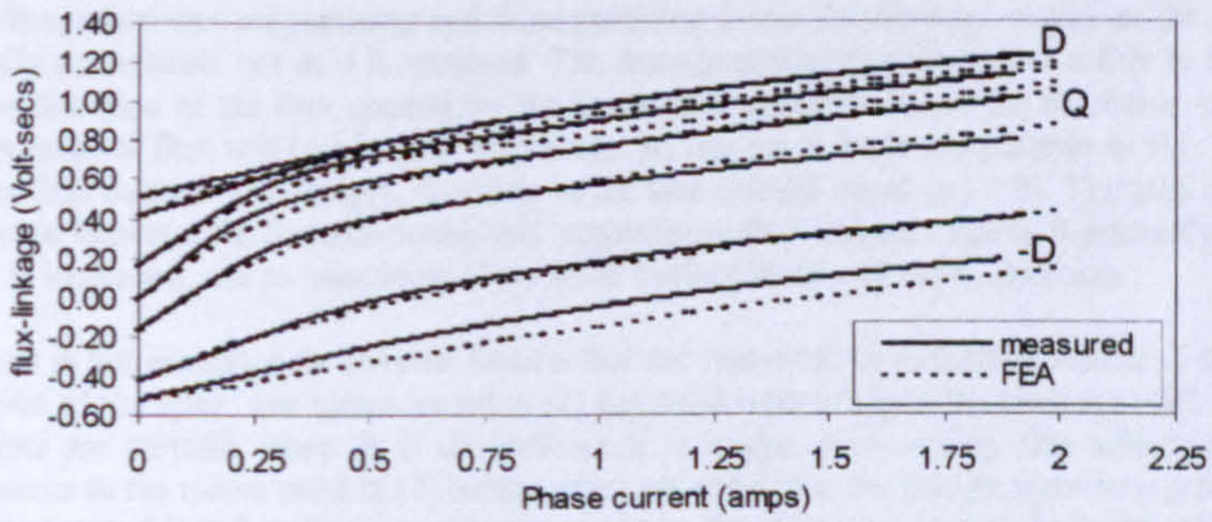

Figure 3. Comparison between measured and FE-simulated magnetisation curves.

Taking the starting point for the measurements as the quadrature axis, there will be no flux-linkage contribution from the permanent magnets and so the q-axis magnetisation curve can be determined solely from the Wheatstone bridge circuit. Using the rotational test method, the total flux-linkage at each successive rotor position will be the sum of the flux-linkage at the previous rotor position and the change in flux-linkage measured during rotation. In this way, the complete set of magnetisation curves can be measured without any assumption of the magnet flux-linkage. Measured magnetisation curves for test motor 1 have been compared with simulated results, shown as dashed lines, in Figure 3.

ANALYSIS OF MAGNETISATION CHARACTERISTICS

Simulations have been run on two test motors. Parameter information is given in Appendix 1. Simulation results from the first test motor have been compared with measured values for verification. The flux-linkages due to current of motor 1, a split-phase, 2 pole IPM motor are shown in Figure 4. The quadrature axis synchronous reactance is higher than that of the direct axis, due to presaturation of the direct axis from the permanent magnets. There is greater variation in the quadrature axis synchronous reactance because the slope of the magnetisation curve is steeper in the q-axis operating region than in the d-axis region.

There is a difference in the direct axis static inductance levels between magnetising and demagnetising currents, caused by presaturation of the magnetic circuit by the permanent magnets. The operating point of the motor is shifted high up the linear region of the material saturation characteristic, so that the introduction of magnetising current will shift the operating point into saturation. A demagnetising current produces magnetic flux in opposition to that of the permanent magnets, shifting the operating point further down the linear region of the curve. Because the slope in the linear region is steeper than in the saturation region, the demagnetising synchronous reactance will be larger for a given current magnitude. The permanent magnets have no effect on the quadrature axis saturation levels. The synchronous reactance is the same for both magnetising and demagnetising current.

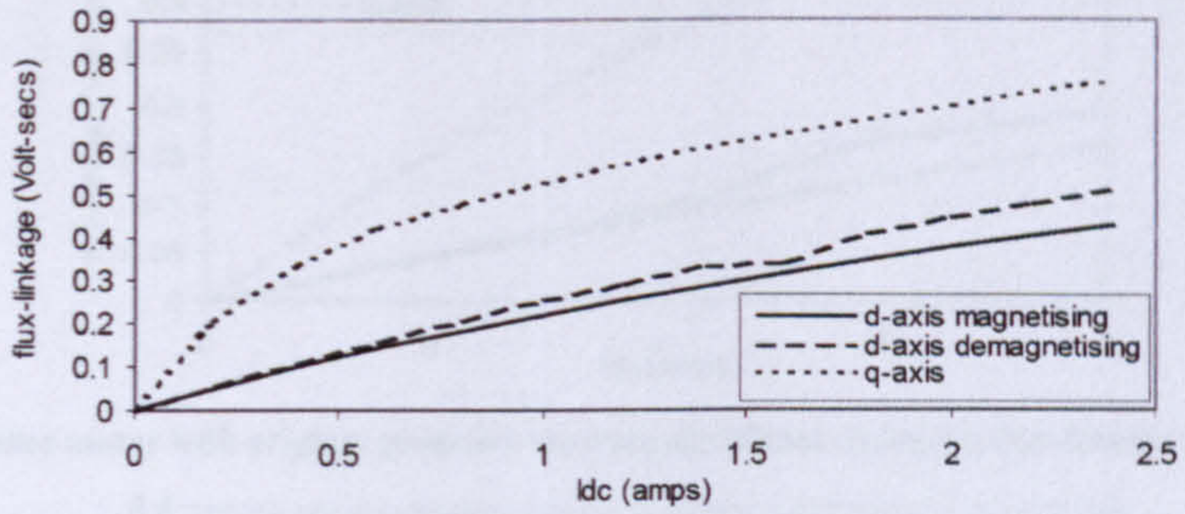

Figure 4: Test motor 1 flux-linkages due to current

A number of papers discuss the pre-saturation of the magnetic circuit by the permanent magnets. [7] suggests that the direct axis flux-linkage will initially be the same for both magnetising and demagnetising currents. When the demagnetising current reaches a sufficient level to saturate the rotor bridge areas in the opposite direction, there will then be a step increase in flux-linkage, creating a difference between the magnetising and demagnetising flux-linkages that will remain as the current increases further. The explanation given in [7] is specific to the geometry of the rotor tested and the true nature of the synchronous reactances is, in fact, slightly different. The change between magnetising and demagnetising d-axis flux-linkage occurs as the saturation of the bridges is initially neutralised, not as it is reversed. The demagnetising current creates a flux in the rotor bridges that opposes the direction of the flux created by the permanent magnets. When the current is sufficiently high, these two components of flux will be of equal magnitude. At this point, both components of flux will flow across the airgap rather than through the bridges, resulting in the step change noted in [7, 8]. The step change results in an initial difference between the demagnetising and magnetising flux-linkages that will gradually decrease as the level of current is increased, due to saturation of the rotor bridges in the opposing direction.

This phenomenon is not immediately obvious from either the measured or simulated results of test motor 1, due to the construction of the rotor. The motor tested in [7] has solid rotor bridges; the slots are fully enclosed. In test motor 1, the slots are partially open. It is the difference in bridge permeability that affects the synchronous reactances. Whereas in the motor used in [7] bridge areas are saturated, the bridge areas in test motor 1 act as an extension of the airgap. Most flux flows across the airgap to the stator rather than between adjacent rotor bars and the difference in synchronous reactances is gradual rather than a step change. Test motor 1 was remodelled

with the rotor bridges specified as the same material as the bars; the width of the bridges is such that there is a significant amount of leakage flux. The resulting flux-linkages are shown in Figure 5. A second test motor, similar to that used in [7], has also been simulated. Figure 6 shows the simulated values of flux-linkage due to current for the original geometry. When the bridges are removed to create open rotor slots, there is no longer a significant change in the flux-linkage, as shown in Figure 7. The initial level of saturation in the bridges is decreased if the width is increased, thereby reducing the difference in flux-linkage levels for positive and negative currents.

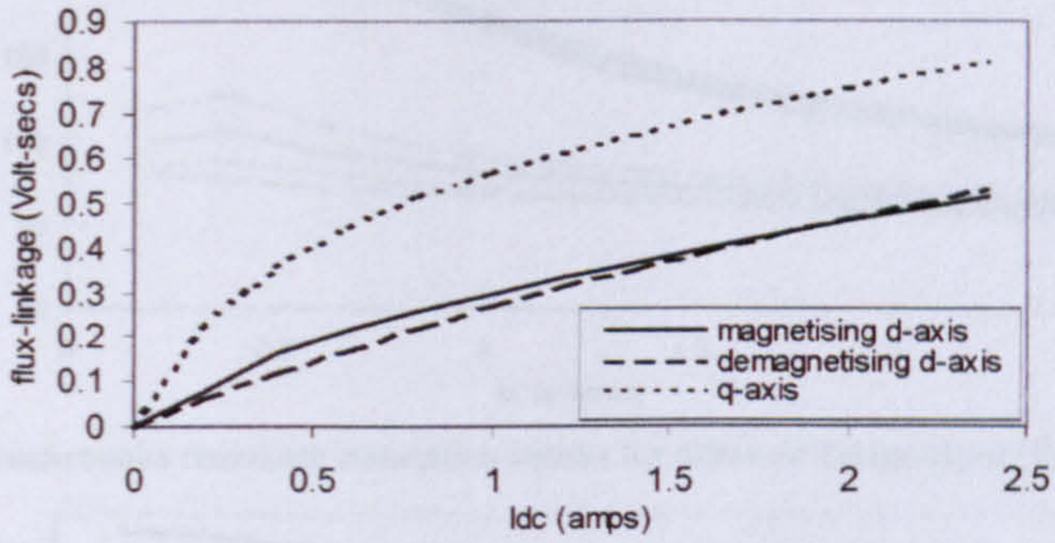

Figure 5. Results of flux-linkage simulations for test motor 1 with remodelled rotor bridges.

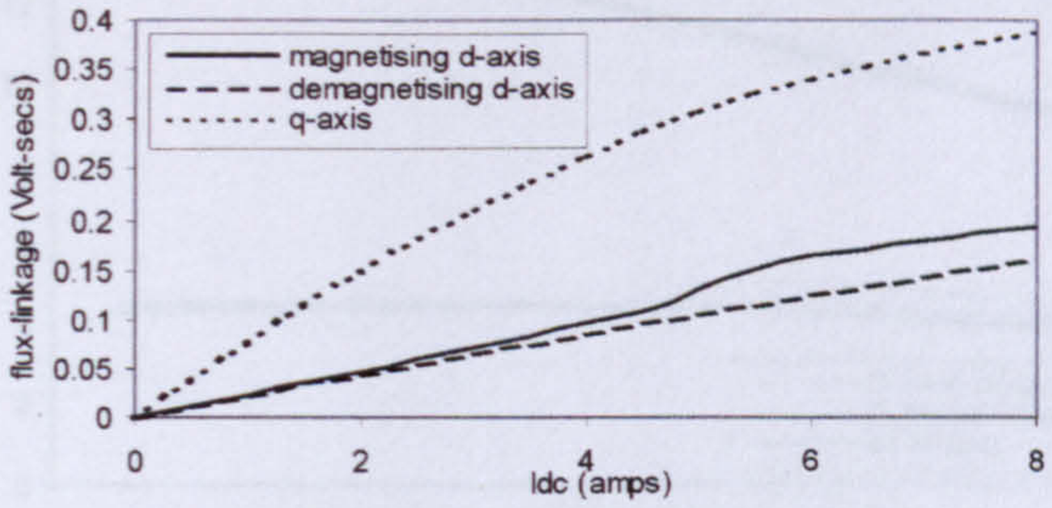

Figure 6. Reliance motor with original geometry showing significant change in flux-linkage due to current

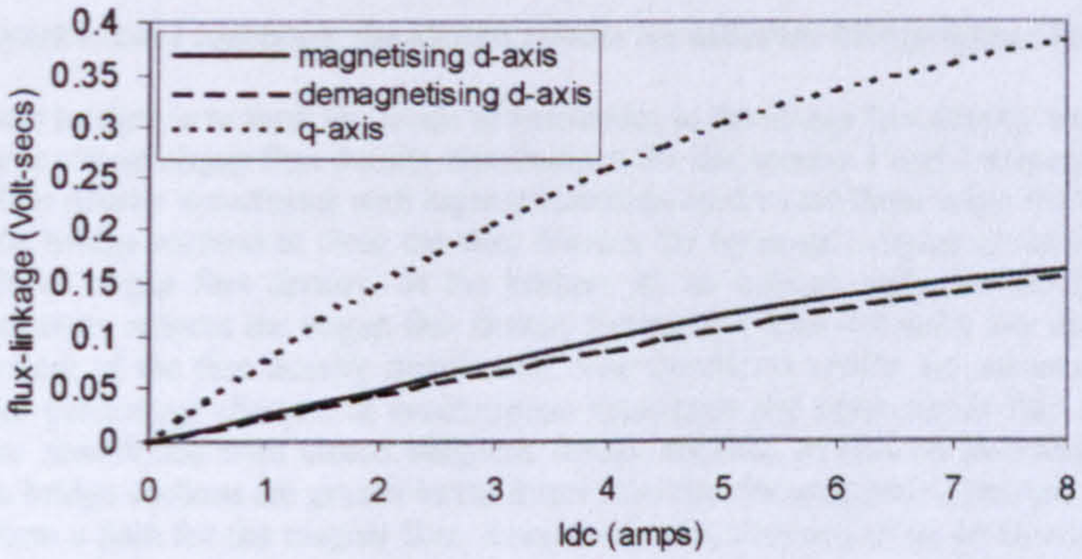

Figure 7. Reliance motor with remodelled geometry showing no step change in flux-linkage due to current

DEPENDENCE OF MAGNETISATION CHARACTERISTICS ON ROTOR BRIDGE DESIGN

Fuller investigation into the effects of the rotor bridges has been carried out using the FE software. Test motor 1 has been modelled with four different bridge configurations: with the original open rotor slots (bridge areas are air) and with three different thicknesses of bridges with the same material as the rotor bars. Figure 8 shows the results of synchronous reactance simulations for each configuration. Test motor 2 has been modelled with the original rotor design (rotor bridges are the same material as the rotor bars), with the bridges at half the original thickness and with open rotor slots. The synchronous reactance simulation results are shown in Figure 9.

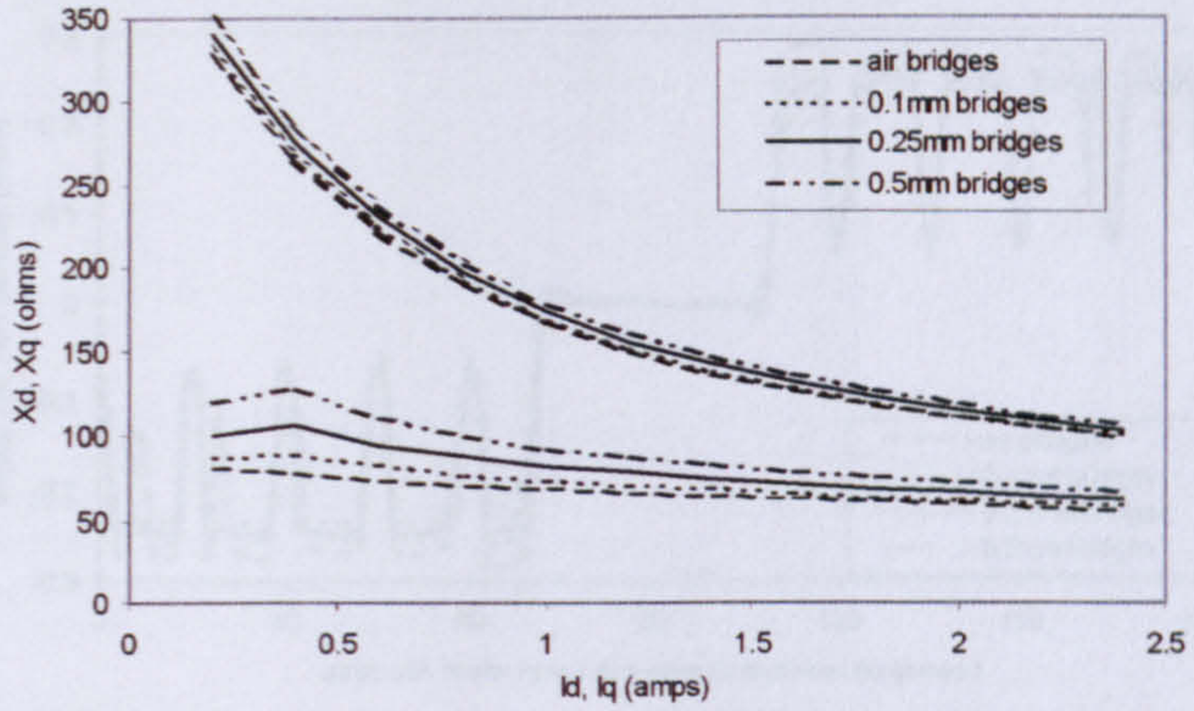

Figure 8. Synchronous reactance simulation results for different bridge types (Test Motor 1)

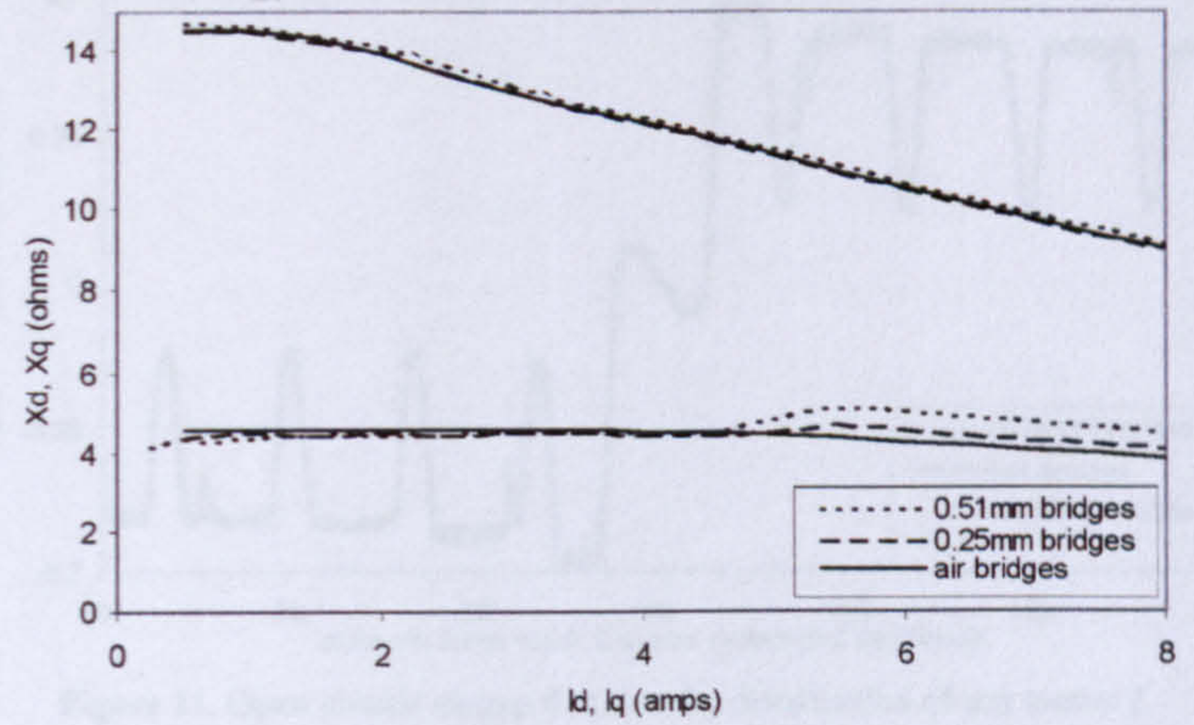

Figure 9. Synchronous reactance simulation results for different bridge types (Test Motor 2)

The effect of the rotor bridges is to limit the levels of harmonics in the airgap flux density waveform. Figures 10 and 11 show the open circuit airgap flux density distributions for test motors 1 and 2 respectively. For both test motors, the airgap flux density waveforms with highest harmonic content are those when the rotor slots are open. Introducing magnetic bridge sections to close the slots reduces the harmonic content of the waveforms, but also decreases the levels of airgap flux density, as the bridges act as leakage paths for the flux. Increasing the thickness of these sections reduces the airgap flux density further, but does not make any discernible difference to the harmonic content of the flux density distribution. The simulation results are summarised in Table 1. It shows the maximum percentage changes in synchronous reactances and open circuit flux density waveforms, when open slots are remodelled with closed magnetic bridge sections of various thicknesses. The effects of adding the magnetic bridge sections are greater in the direct axis than the quadrature, because the rotor bars lying on the direct axis form a path for the magnet flux, whereas there is assumed to be no flux-linkage contribution from the magnet flux on the quadrature axis.

Parameter	Test Motor 1			Test Motor 2	
	0.1mm	0.25mm	0.5mm	0.25mm	0.51mm
Xq	**+2 %**	**+4 %**	**+8 %**	**+0.7 %**	**+1.3 %**
Xd	**+14 %**	**+36 %**	**+63 %**	**+8 %**	**+19 %**
Bgap (OC)	**-9 %**	**-13 %**	**-17 %**	**-2 %**	**-4 %**

Table 1. Comparison between partially open and fully closed rotor slots, showing significant increases in d-axis reactance and decreases in airgap flux density when bridge thickness is increased.

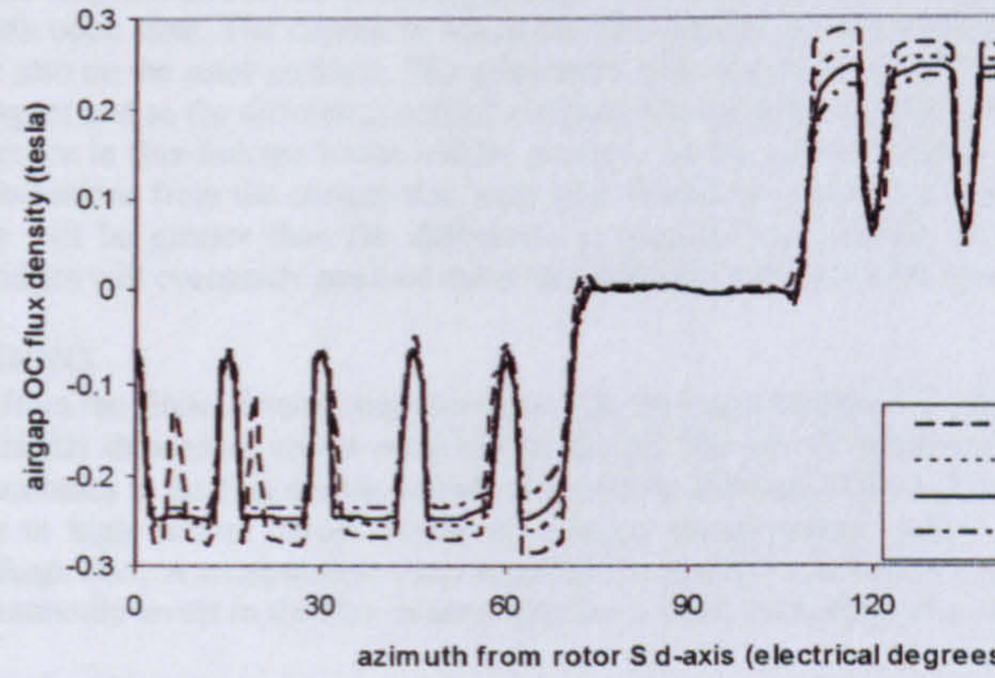

Figure 10. Open circuit airgap flux density distribution of test motor 1

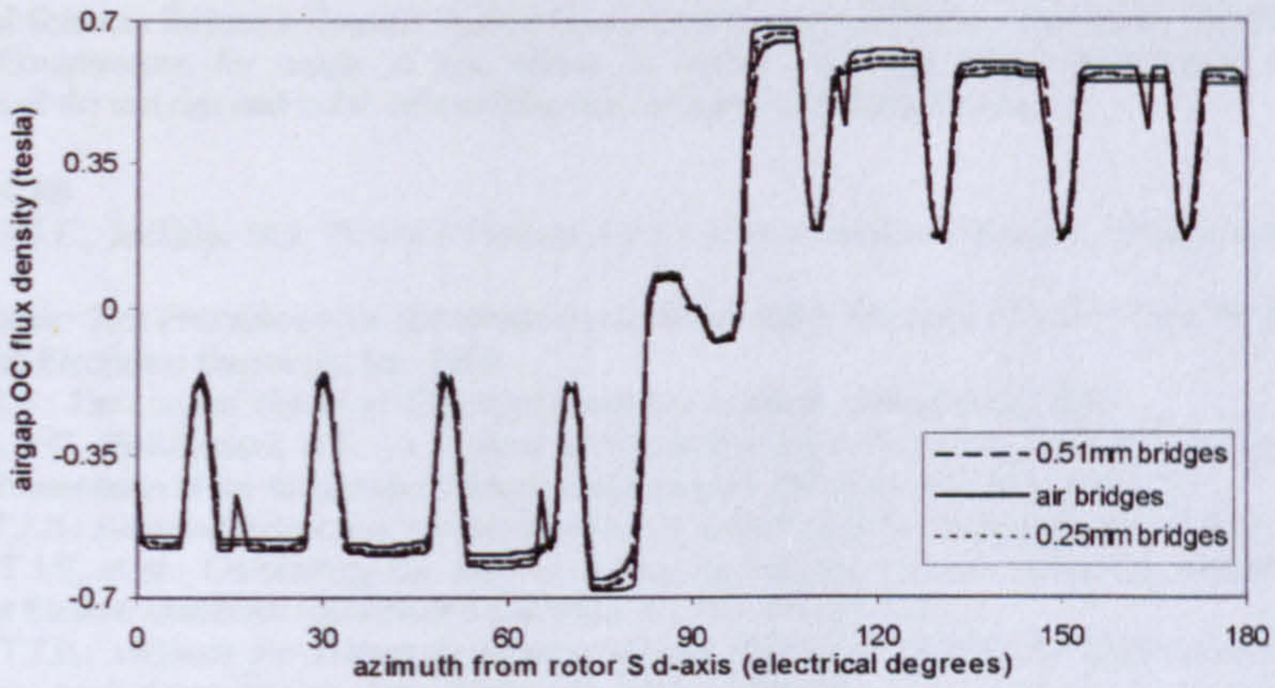

Figure 11. Open circuit airgap flux density distribution of test motor 2

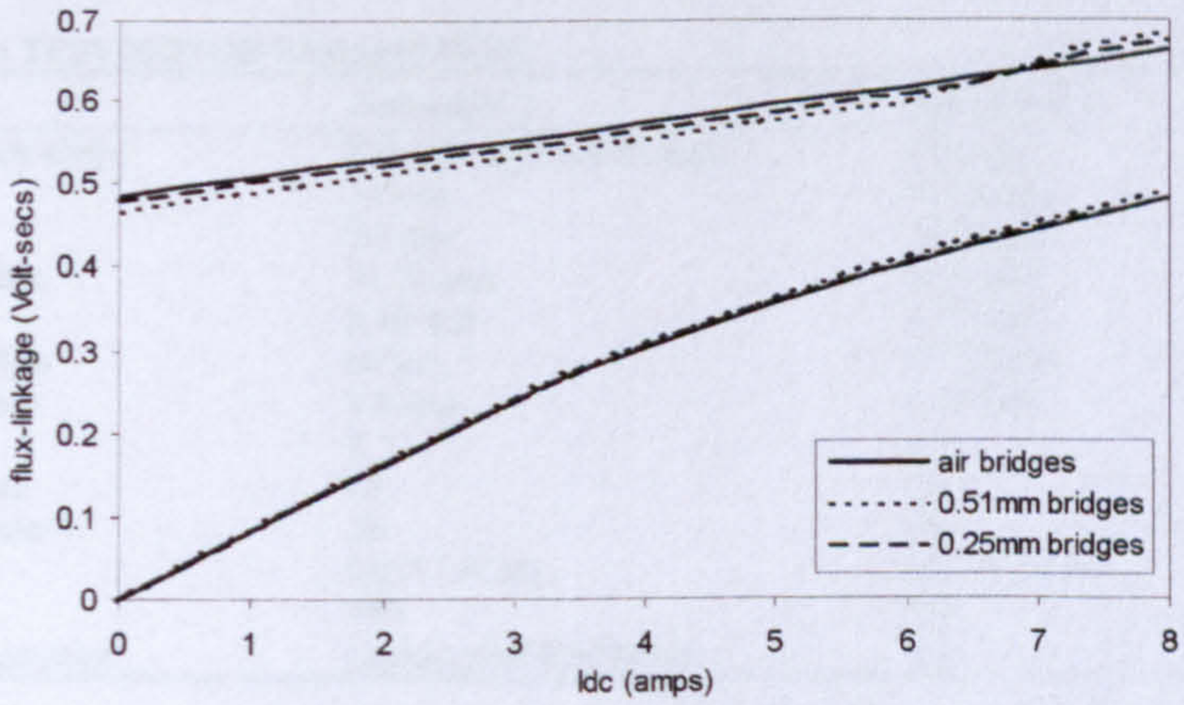

Figure 12. Direct and quadrature axis magnetisation curves for one phase of test motor 2

The effects of closing the rotor slots with magnetic bridge material can also been seen in the magnetisation curves of the test motors. At low current levels, the magnetic circuit is dominated by the flux contribution from

the permanent magnets and so the total flux-linkage will be less for the rotor designs with magnetic bridges than for those with open slots. The degree to which the flux-linkage is reduced is dependent on the thickness of the bridges, but also on the rotor position. The quadrature axis magnetisation curve has no flux-linkage contribution from the magnet and so the difference will be minimal. On the direct axis the magnet contribution is greatest and so the difference in flux-linkage levels will be greatest. As the level of current increases, the difference in flux-linkage contributions from the current also increases. When the current reaches a certain level, the difference in flux-linkage will be greater than the difference in magnet flux crossing the airgap, and so the rotors with magnetic bridges will eventually produce more flux-linkage than those with open slots, as in Figure 12.

CONCLUSIONS

The results from the finite element analysis show that the magnetisation characteristics of the permanent magnet motors are highly dependent on the rotor bridge design. The use of magnetic rotor bridges is advantageous in reducing harmonics in the flux density distribution and the addition of the bridge sections can lead to increases in flux-linkage at high current levels. However, designs incorporating closed rotor slots have been shown to increase leakage flux. A compromise must therefore be reached whereby the dimensions of the bridge sections reduce the harmonic levels in the flux density distribution and the leakage flux is kept to a reasonable level.

ACKNOWLEDGEMENTS

The authors acknowledge the support of the SPEED Consortium. J. A. Walker is funded by the UK Engineering and Physical Sciences Research Council, Robert Bosch GmbH and the SPEED Consortium. Thanks are given to Electrolux Compressors, for supply of test motors, to Jimmy Kelly and Wilson MacDougall for help with construction of the test rigs and to Dr. Mircea Popescu for many useful discussions.

REFERENCES

[1] Miller, T.J.E., McGilp, M.I: *PC-FEA Version 3.0/5.0 User's Manual.* Glasgow: SPEED Laboratory May 2002 .

[2] *IEEE Guide: Test Procedures for Synchronous Machines.* IEEE Standard 115-1995 New York: Institute of Electrical and Electronic Engineers, Inc. 1995.

[3] Jones, C.V.: *The Unified Theory of Electrical Machines.* London: Butterworths, 1967.

[4] Prescott, J.C., El-Kharashi, A.K.: *A Method of Measuring Self-inductances Applicable to Large Electrical Machines.* Proceedings of the Institution of Electrical Engineers **106** (Part A), 1959, p.169-173.

[5] Miller, T.J.E.: *Switched Reluctance Motors and Their Control.* Oxford: Clarendon Press, 1993.

[6] Miller, T.J.E. et al.: *Calculating the Interior Permanent-Magnet Motor.* Conference Record of the IEEE International Electric Machines and Drives Conference **2**, 2003, p.1181-1187.

[7] Miller, T.J.E.: *Methods for Testing Permanent Magnet Polyphase AC Motors.* Conference Record of the IEEE Industry Applications Society Annual Meeting, 1981, p.494-499.

[8] Rahman, M.A., Zhou, P.: *Analysis of Brushless Permanent Magnet Synchronous Motors.* IEEE Transactions on Industrial Electronics **43** 1996, p.256-267.

APPENDIX 1: TEST MOTOR PARAMETERS

Parameter	*Test motor 1*	*Test motor 2*
Stator lamination shape	Circular, chamfered edges	Circular
Stack length	39 mm	95.25 mm
Shaft radius	9.5 mm	15.75 mm
Rotor outer radius	31.72 mm	46.4 mm
Airgap length	0.28 mm	0.32 mm
Stator outer radius	64 mm	77.22 mm
Magnet thickness	5.8 mm	6.35 mm
No. of poles	2	4
No. of rotor bars	28	44
No. of stator slots	24	36
Rated voltage	220 V, 50 Hz	230 V, 60 Hz
Turns/ Phase	970	168
Winding configuration	Custom sine-distributed	Lap

Flux-Linkage Calculation in Permanent-Magnet Motors Using the Frozen Permeabilities Method

Jill Alison Walker, *Student Member, IEEE*, David G. Dorrell, *Member, IEEE*, and Calum Cossar

SPEED Laboratory, Department of Electronics and Electrical Engineering, University of Glasgow, Glasgow G12 8LT

Finite-element analysis can be used to determine the magnetization characteristics in terms of curves of flux-linkage against current or rotor position. The "frozen permeabilities" technique is presented as a method of apportioning flux-linkage contributions to the phase currents and permanent magnets, and for inductance calculations. Results from a split-phase interior permanent magnet motor are presented and compared with experimental data. Drawbacks to the method are discussed.

Index Terms—**Electric machines, finite-element (FE) calculations, permanent magnets, time-dependent magnetic fields.**

I. Introduction

IN PERMANENT-MAGNET (PM) motors, the excitation is provided by two sources: the armature current, which can be removed, and the PMs, which provide a constant source of excitation. In the design process it can be desirable to calculate the individual flux contributions from the currents and the PMs. Methods such as the phasor diagram rely on superposition to extract the individual flux-linkage contributions, which are then used to calculate the direct and quadrature axis inductances. Such methods assume the magnet flux remains constant at the open-circuit value when in fact it varies according to load.

In finite-element (FE) simulations, it is possible to split the flux-linkage into individual components by freezing the permeabilities. Verification of the results by measurement is complicated by the constant excitation of the PMs. The method presented here uses a combination of static and dynamic tests to measure the flux-linkage contribution from the PMs. Frozen permeability simulation results from a commercial FE package are verified using the proposed measurement techniques.

II. Frozen Permeability Method

The *frozen permeability* technique is a method for separating the total flux-linkage into contributions from the current and PMs in FE simulations. The flux-linkage is determined from the magnetic vector potential. An initial nonlinear solution is calculated for the given rotor position and load current and the resulting permeabilities in each element of the FE mesh stored. Using these permeabilities, one field source can be "turned off" and a new linear solution calculated, to determine the flux-linkage contribution from the remaining source. For example, to calculate the flux-linkage due to the PMs, the phase currents would be set to zero. To calculate the flux-linkage contribution from the phase currents, the remanent flux of the PMs (Br, Bt) would be set to zero. The sum of the two individual components will equal the total flux-linkage as calculated in the original nonlinear solution. Flux plots corresponding to the separate frozen permeability solutions are shown in Figs. 1 and 2.

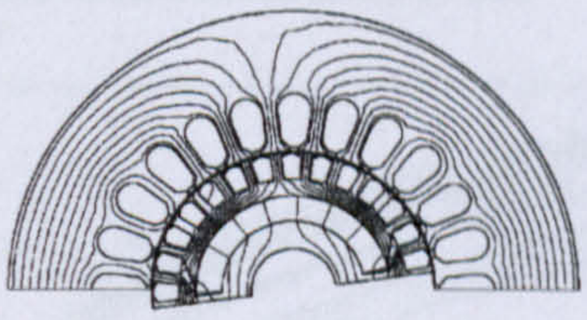

Fig. 1. Flux plot showing frozen permeability solution with currents only.

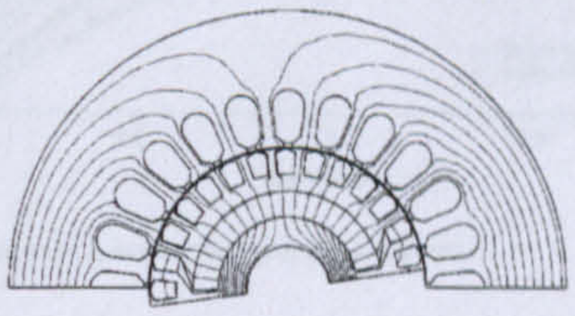

Fig. 2. Flux plot showing frozen permeability solution with magnets only.

The method was used by Bianchi *et al.* to calculate the parameters of a PM synchronous motor [1] and is included as a feature in a number of software packages [2], [3]. There is little mention of the method in literature and, in particular, there is a lack of experimental data to substantiate whether the method is in fact valid. Although the sum of the individual contributions equals the total flux-linkage from the nonlinear solution, the weighting of the flux-linkage due to current and magnet flux-linkage contributions may be wrong. Without experimental verification, there is no way of knowing if the solutions determined by the frozen permeability method are correct. The flux-linkage due to the PMs can be measured on open-circuit, but there is no way of measuring it directly under load conditions. The magnet flux-linkage must, therefore, be found by subtraction of the current contribution from the total flux-linkage, taken from the motor magnetization curves.

III. Measurement of Magnetization Curves

The magnetization curves for the motor are presented in the form of flux-linkage versus current for successive rotor positions. Previously the magnetization curves may have been constructed by adding the flux-linkage due to current (as calculated from the locked-rotor tests) to the value of open-circuit magnet

Digital Object Identifier 10.1109/TMAG.2005.854973

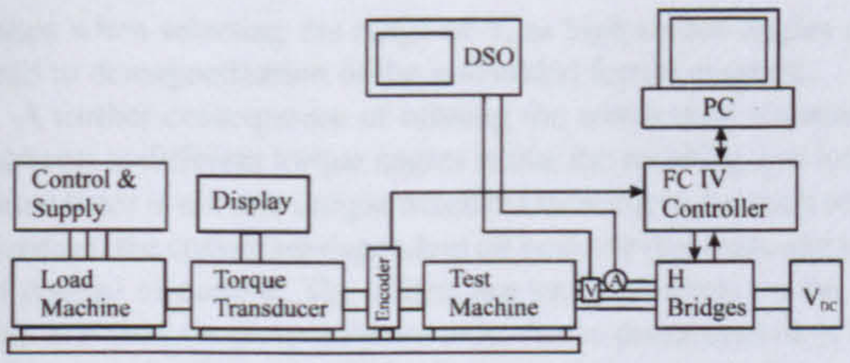

Fig. 3. Dynamometer test setup.

flux-linkage at the given rotor position [determined by integration of the open-circuit back electromotive force (EMF) waveform]. This method cannot be considered accurate as it assumes the magnet flux remains constant at the open-circuit value.

A dynamic test is required to measure the total flux-linkage under load conditions. To include the flux-linkage contributions from the PMs, the rotor must be rotated so that the magnets pass under the phase winding. With constant current in the phase winding, it is possible to determine the *change in total flux-linkage* between successive rotor positions, but not the absolute value of flux-linkage at each position. To determine the absolute value and measure the magnetization curves, it is necessary to have a reference point whereby at one rotor position the total flux-linkage is already known. If there was no cross-saturation of the magnetic flux paths, no flux-linkage contribution from the PMs would be seen on the quadrature axis, but to assume this is no more valid than the assumption that the magnet flux is independent of load.

The solution is to calculate the total flux-linkage from the i-ψ (*ipsi*) loop. Detailed information can be found in [4], [5]. The i-ψ loop is used to determine the average electromagnetic torque from the change in coenergy over one electromagnetic cycle. The change in coenergy is equal to the area enclosed by the current versus flux-linkage trajectory. Because the current used to drive the motor is periodic, and for the brushless synchronous motor is sinusoidal, for every revolution there will be two points where the phase current is zero. The flux-linkage on open-circuit can be calculated from the back EMF waveform, and so the locus of the *ipsi* loop can be calculated with respect to the two open-circuit points. If rotor position sensing is included in the *ipsi* loop measurement, the total flux-linkage at each rotor position can be determined. The dynamometer setup is shown in Fig. 3.

IV. Experimental Results

Results are presented for a split-phase, two-pole interior PM motor with sinusoidally distributed motor winding, Fig. 2. For each rotational test, the phase voltage, phase current, and position information are stored. The data is then manipulated using MATLAB [7] into tables of total flux-linkage versus current at each rotor position. Fig. 4 shows the magnetization curves for the main phase of the motor. The measured curves are represented by solid lines; dashed lines represent total flux-linkages calculated in FE from the magnetic vector potential. The direct and quadrature axis curves are labeled for reference. The measured flux-linkage contributions from the currents and the PMs

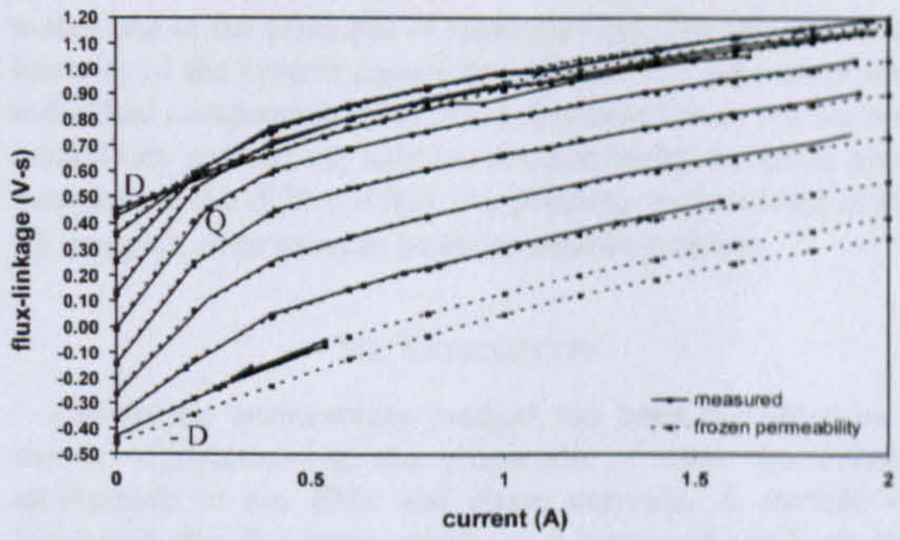

Fig. 4. Magnetization curves for main phase of test motor.

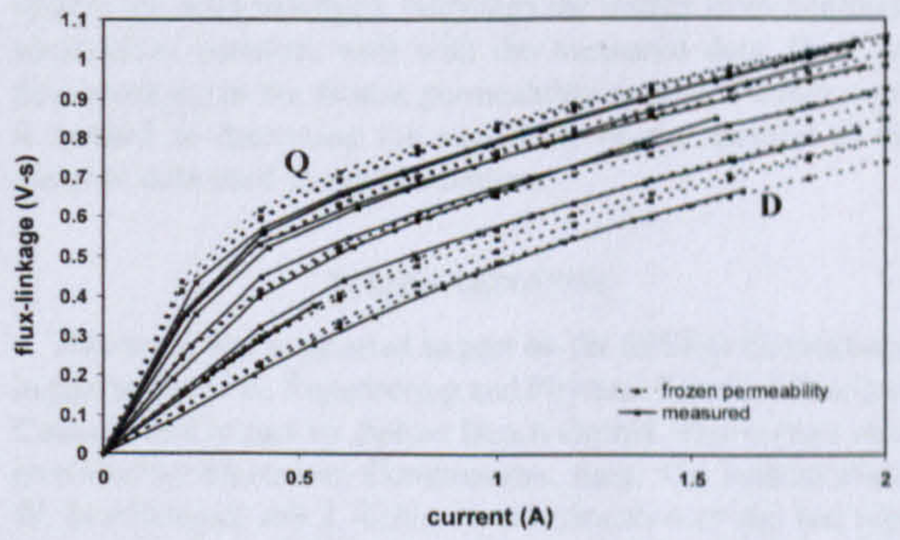

Fig. 5. Flux-linkage contribution from phase current.

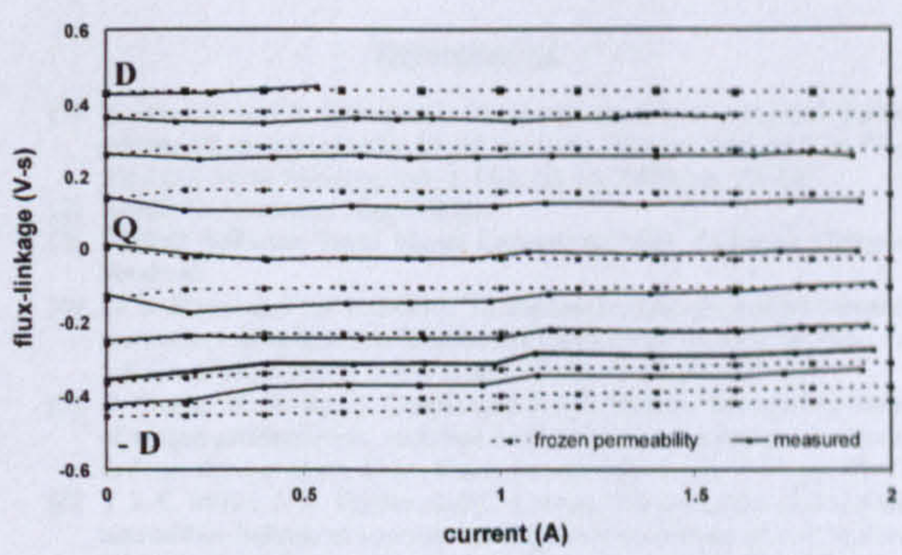

Fig. 6. Flux-linkage contribution from PMs.

are shown in Figs. 5 and 6, respectively, along with results from the two-dimensional FE simulations.

V. Discussion

The dynamic tests used to calculate the i-ψ loops were originally driven with sinusoidal current, producing elliptical ipsi loops. However, a number of problems arise from using a sinusoidal current waveform. The sinusoidal variation in current means that to achieve the required current levels at each rotor position, the motor must either be run at currents higher than the rated currents, or with large torque angles γ. Care must be

taken when selecting the range of γ, as high torque angles can lead to demagnetization of the embedded ferrite magnets.

A further consequence of running the motor with sinusoidal currents at different torque angles is that the resulting *ipsi* loops show there is not one unique magnetization curve for each rotor position; the curves are dependent on both the direction and rate of change of current. The effects are less prominent on the direct axis than on the quadrature axis, due to presaturation of the magnetic circuit by the PMs. Running the motor with square wave rather than sinusoidal currents reduces the range of gamma values required and also limits the rate-of-change effects. The resulting magnetization curves are single-valued and equivalent to static magnetization curves. The single-valued magnetization curves correlate well with the results from the nonlinear FE simulations. The magnetization curves generated from the sinusoidal i-ψ loops showed considerable hysteresis effects, which are neglected in the FE simulations.

Although the two sets of magnetization curves show close correlation, there are discrepancies between the measured current and magnet flux-linkage contributions and those calculated from the frozen permeabilities method. However, both sets of results show that the PM flux-linkage varies with load conditions.

Variation between the individual components may be due in part to the representation of the motor materials in the FE software. The magnet information was taken from manufacturers' data sheets. Under the sinusoidal ipsi loop test conditions, the ferrite magnets were demagnetised slightly. Although the remanent flux B_r has been adjusted accordingly, the demagnetization may not be uniform across the magnet cross-section. For the purposes of the simulations, the magnets are assumed to have a remanent flux of 0.32 and a recoil permeability of 1.08. The rotor and stator laminations have a complicated geometry and although the materials are represented by measured B-H curves, the magnetic properties will vary from a single sheet tester sample, due to rotational fluxes and the effects of punching and stamping. Slight changes in the material data were found to have an effect on the separation into individual flux components by the proposed method. A number of possible combinations of steel B-H curve and magnet data may exist which correlate well with the measured magnetization curves, but provide different results when the separation of the fluxes by the frozen permeability method is carried out.

The difficulty in verification of the method arises because we cannot measure the exact quantities that are calculated in the frozen permeability method. The locked-rotor tests measure a change in flux-linkage due to an applied current, but we cannot measure the magnet flux-linkage under this applied current directly. Although a value for the magnet flux can be derived, it makes use of the principle of superposition. The inherent nonlinearity of the system cannot be ignored. The separation into individual components by the FE software is linear, but the permeabilities used in the solution are nonlinear. Accurate measurement of the different flux components, as calculated in the FE analysis, does seem to be an intractable problem.

VI. Conclusion

The frozen permeability method has been discussed as a means of determining the proportion of total flux-linkage attributable to the PMs and phase currents. A method of measuring the flux components, as a means of verifying the frozen permeability results, has been suggested. The difficulties in measuring the individual components in the nonlinear system are acknowledged. Although the results from nonlinear simulations correlate well with the measured data, there are discrepancies in the frozen permeability results. Further work is needed to determine the sensitivity of the method to the material data used in the simulations.

Acknowledgment

This work was supported in part by the SPEED Consortium, in part by the U.K. Engineering and Physical Sciences Research Council, and in part by Robert Bosch GmbH. Test motors were provided by Electrolux Compressors, Italy. The authors thank W. MacDougall and J. Kelly for construction of the test rigs. They also thank Dr. M. Popescu for help with the PC-FEA scripting.

References

[1] N. Bianchi and S. Bolognani, "Magnetic models of saturated interior permanent magnet motors based on finite element analysis," in *Proc. 33rd IAS Annu. Meeting*, vol. 1, Oct. 12–15, 1998, pp. 27–34.
[2] Ansoft Corporation, Maxwell 2D.
[3] SPEED Software Suite, Speed Laboratory, Univ. Glasgow, Glasgow, Scotland.
[4] M. R. Harris and T. J. E. Miller, "Comparison of design and performance parameters in switched reluctance and inductance motors," in *Proc. 4th Int. Conf. Elect. Mach. Drives*, Sep. 13–15, 1989, pp. 303–307.
[5] D. Staton, W. Soong, C. Cossar, and T. J. E. Miller, "The unified theory of torque production in switched and synchronous reluctance motors," in *Proc. 6th Int. Conf. Elect. Mach. Drives*, Sep. 8–10, 1993, pp. 67–72.
[6] T. J. E. Miller, J. A. Walker, and C. Cossar, "Measurement and application of flux-linkage in a permanent magnet synchronous motor," in *Proc. 2nd Int. Conf. Power Electron., Mach. Drives*, vol. 2, Mar. 31–Apr. 2 2004, pp. 674–678.
[7] Matlab, The Mathworks, Inc..

Manuscript received February 7, 2005.

JOURNAL OF APPLIED PHYSICS 99, 08R304 (2006)

Effect of mutual coupling on torque production in switched reluctance motors

Jill A. Walker,[a] David G. Dorrell, and Calum Cossar
SPEED Laboratory, Department of Electronics and Electrical Engineering, University of Glasgow, Rankine Building, Oakfield Avenue, Glasgow, Lanarkshire G12 8LT, United Kingdom

(Presented on 3 November 2005; published online 18 April 2006)

In many cases, the normal operation of switched reluctance machines requires excitation of two or more phases simultaneously. When multiple phases are conducting simultaneously, the flux paths from each phase will overlap, which may lead to localized saturation. In such cases, the flux linkage must be considered a function not just of the current in the test winding but of all excited windings. The degree of mutual coupling between phases influences the per-phase magnetization curves and torque characteristics. In machines with even phase numbers, the degree of mutual coupling between phases varies due to discontinuities in the phase polarity arrangement. From nonlinear finite element simulations, it is possible to compare the i-ψ loop diagrams under single-phase and multiphase excitations, and hence the torque produced. The mutual flux linkage from each phase can be calculated separately for each rotor position using the frozen permeability method, to further analyze the mutual coupling effects. For a given excitation current profile, the torque can be maximized by careful arrangement of the phase polarities. © *2006 American Institute of Physics.*
[DOI: 10.1063/1.2162822]

I. INTRODUCTION

The magnetization characteristics of the switched reluctance motor are normally represented by per-phase static magnetization curves or i-ψ loops.[1] The torque produced by each phase can be calculated from the area enclosed by the current/flux linkage or $i-\psi$ trajectory. Such characteristics are normally measured with only one phase excited and so mutual coupling between phases is ignored.

In the switched reluctance motor, the currents in each phase are switched in sequence. In the ideal case, they are square wave, with instantaneous rise and fall times. In reality, it can take several degrees of rotation for the current to rise or fall. This can lead to overlap between adjacent phase currents. In some cases, the switching angle may be advanced to increase torque production; this also results in overlapping current (and flux-linkage) profiles.

When two or more phases are conducting simultaneously, the flux paths from each phase share sections of the laminations, leading to saturation and lower permeabilities in localized regions of the steel, or conversely to reduction in flux density in the steel and increased permeability. When the phases share saturated regions of steel, the phase flux linkage and torque are functions of the currents in all excited phases. In such cases, it is necessary to take mutual coupling between phases into account to accurately predict the magnetization curves or i-ψ loop of each phase.

The degree of mutual coupling is dependent on the polarity arrangement of the phase—in particular, whether the adjacent phases are of the same or opposite polarities.[2] Figure 1 shows the cross section of an 8/6, four-phase motor with two phases of same polarity conducting. For three-quarters of the stator back iron, the fluxes are additive. In these sections of the back iron, the steel is most likely to saturate. This leads to reduced localized permeabilities and lower flux linkage per phase for a given input current. In the remaining quarter of the back iron, the fluxes flow in opposing directions, so saturation is unlikely. Figure 2 shows the same motor, with adjacent phases of opposite polarities. In this case, there are only additive fluxes for one-quarter of the stator back iron. As such, the case where the phases are of opposite polarities would be expected to show less prominent mutual coupling effects. The degree of mutual coupling can be minimized by careful design of the motor cross section.[3]

II. FINITE ELEMENT MODELING OF MUTUAL COUPLING

The effects of mutual coupling can be seen in the shape of the i-ψ trajectory. The i-ψ trajectories can be calculated during normal operation (with each phase being switched in

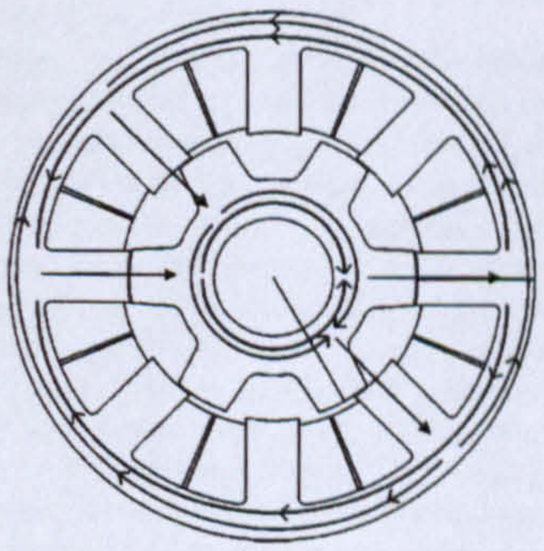

FIG. 1. Flux plots NN polarities.

[a]Electronic mail: jwalker@elec.gla.ac.uk

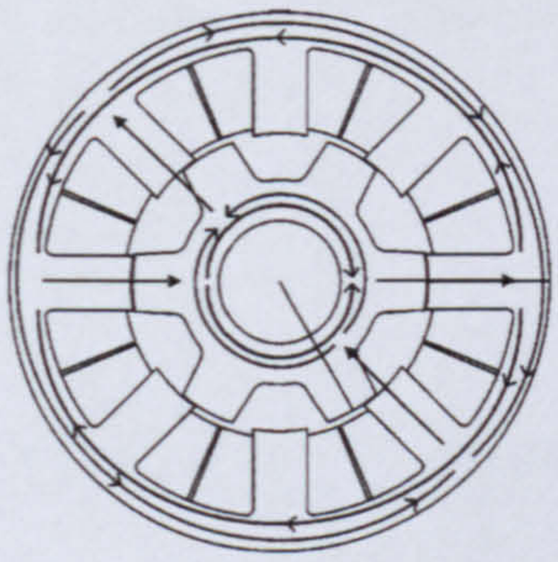

FIG. 2. Flux plots NS polarities.

turn) and for each phase singly excited. Any differences between the resulting i-ψ loops are due to the mutual interaction between the phases. The change in total flux linkage in each phase, due to the other excited phases, is easily determined from nonlinear finite element simulations.

Figure 3 shows the i-ψ loop for one phase of the four phase 8/6 motor for three cases—when the phase is singly excited, when all phases are excited in sequence (phase currents overlap at switching regions) and the polarity of the next phase in the sequence is the same, and when there is current overlap and the polarity of the next phase is opposite. The current trajectories are the same in all three cases (the control system operates in current-control mode with fixed turn-on and turn-off times).

Figure 3 clearly shows that the arrangement of the phase polarities will have a significant effect on the shape of the $i-\psi$ loop and the area enclosed. The area of the i-ψ loop is greater when the adjacent phases are of opposite polarities. In motors with odd phase numbers, this would be the standard configuration. However, for motors with even phase numbers there will always be a discontinuity in the phase polarity arrangement, whereby two adjacent poles must have the same polarity. For example, in the 4 phase test motor, the original winding configuration leads to a N-S-N-S-S-N-S-N

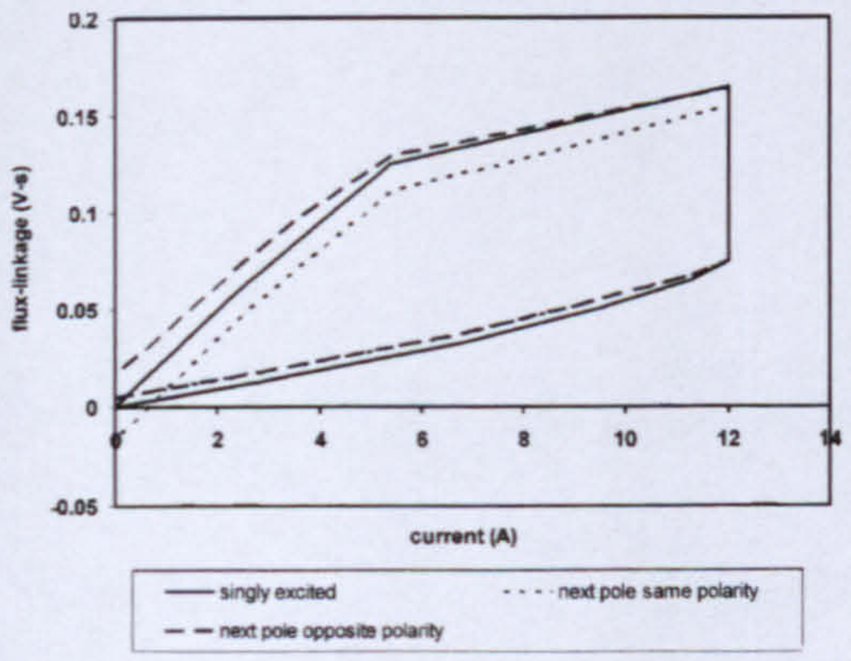

FIG. 3. i-ψ loops for three different cases.

TABLE I. Loop torque for different phase polarity combinations.

Phase combination (previous/current/next)	Torque produced (N m)
NSS or SNN	0.6927
NNN or SSS	0.8321
NSN or SNS	0.9197
NNS or SSN	1.0585

pole arrangement (adjacent poles of phases 4 and 1 have same polarity). From nonlinear solutions with all phases excited, the per-phase torque for each combination of phase polarities can be calculated. The per-phase average torque over one cycle, as calculated from the area of the i-ψ loop, is given in Table I for each possible polarity combination.

From Table I, it can be seen that the phase torques will be unbalanced for the same current excitation, due to differences in the pole combinations for each phase. The maximum torque will occur in phase 4 of the test motor, and the minimum torque will occur in phase 1. Phases 2 and 3 produce the same level of torque.

The arrangement of phase polarities also affects the amount of ripple in the complete torque wave form under normal operation. When the two adjacent conducting phases are of the same polarity, the peak instantaneous torque is higher than when the phases are of opposite polarities. The difference in minimum torque between the two cases is much smaller than the difference in peak torque, resulting in a significantly higher torque ripple (>25%) for the case when the adjacent phases are of opposite polarities. In any complete cycle of operation, the ripple will vary, due to discontinuity in the phase polarity arrangement.

The effect of phase polarity arrangement on the efficiency of the motor is also significant. The input current wave form is the same regardless of the phase polarity arrangement, so that the copper losses are the same for all cases. There will be a small difference in the iron losses between different polarity arrangements; the iron losses themselves account for only a small percentage of the total losses. As such, the polarity combination that gives the greatest torque (NNS or SSN) will result in a higher efficiency than other polarity combinations.

Although the nonlinear finite element simulations prove that the phase torques are heavily dependent on the winding polarity arrangements, they give no indication as to what proportion of the total flux linkage is due to self-flux-linkage and what proportion is due to mutual flux linkage. The induced mutual flux linkages in all phases can be determined by running frozen permeability finite element simulations for each phase in turn.[4,5] The mutual, self-, and total flux linkages for phases 1 and 4 (determined from a combination of nonlinear and frozen permeability solutions), for windings polarities of N-S-N-S are given in Figs. 4 and 5, respectively.

Figure 4 shows that the mutual flux linkage from phase 2 seen in phase 1 is positive, creating a positive total flux linkage before phase 1 has been excited. As the rotor changes position, phase 1 itself is excited, which increases the positive flux linkage. As the current in phase 1 is switched off, phase 4 turns on. The mutual flux linkage created by phase 4

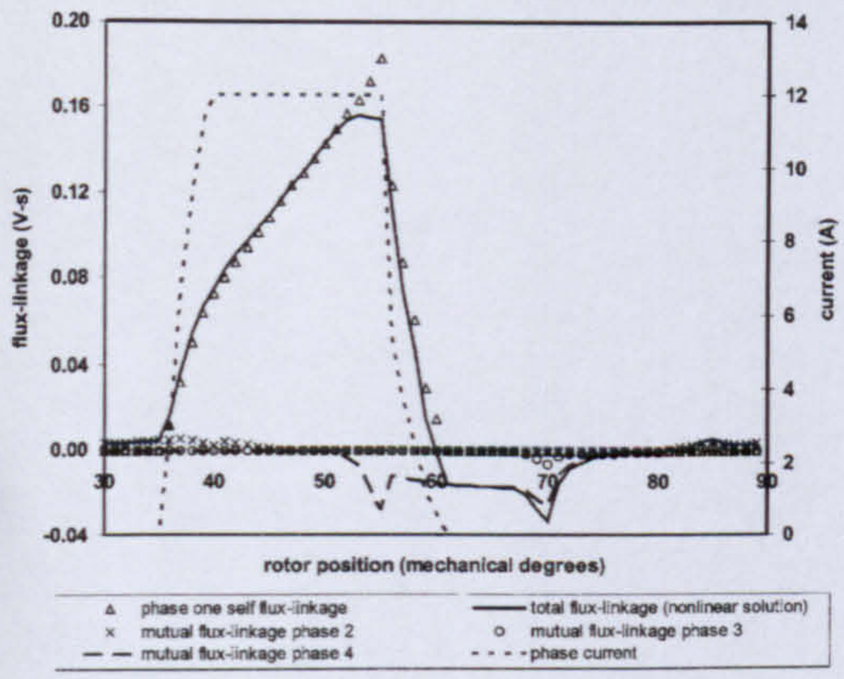

FIG. 4. Flux linkages of phase 1 from finite element solutions.

is negative. As the current in phase 1 decreases, the mutual flux linkage becomes more dominant, until the total flux linkage becomes negative. There is no significant mutual flux linkage from phase 3, as it is not adjacent to phase 1. Figure 4 clearly illustrates that the cause of the crossover seen in the $i-\psi$ loop is the combination of positive mutual flux linkage from the preceding phase in the sequence and negative mutual flux linkage from the next phase.

Figure 5 shows the self- and mutual flux linkages for phase 4. The mutual flux linkage from phase 1 is shown to be negative, resulting in a negative total flux linkage at zero current in phase 4. As the excitation of phase 4 increases, the total flux linkage becomes positive. When the current from phase 4 decreases, the current in phase 3 is introduced, creating a positive mutual flux linkage. This results in a positive total flux linkage for zero current in phase 4. Once again, there is no significant mutual coupling between the remaining nonadjacent phase (phase 2). The combination of negative mutual flux linkage at the beginning and positive mutual flux linkage at the end of the i-ψ loop results in the maximum possible phase torque for the given excitation wave forms.

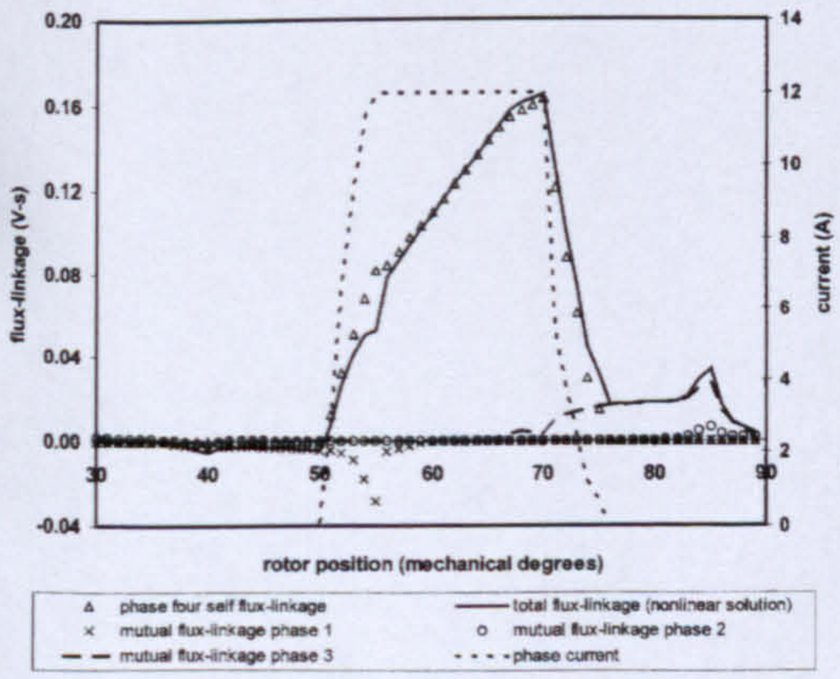

FIG. 5. Flux linkages of phase 4 from finite element solutions.

III. DISCUSSION

In the presented results, the mutual flux linkage created by the previous phase in the sequence is shown to be much smaller than that created by the next excited phase in the sequence (e.g., $M_{21} \ll M_{41}$), regardless of the phase polarities. The next phase in the sequence has the greatest effect on the shape of the i-ψ loop and thus the torque produced.

To maximize the torque in phase 1 of the motor, the total flux linkage when the current is switched off should be positive. This cannot be achieved with balanced excitation wave forms, due to the negative mutual flux linkage from phase 4. With certain control systems, it may be possible to excite the motor with different current wave forms in each phase. In such cases, the current wave forms of phases 4 and 1 can be modified to increase the total flux linkage during the overlap periods. There is a trade-off between reduction of the mutual flux linkage (due to phase 4) in phase 1 and reduction of the self-flux-linkage of phase 4. Frozen permeability finite element simulations can be used to estimate the reduction in both the mutual flux linkage in phase 1 and self-flux-linkage in phase 4.

In general, there are two courses of action that can be taken to reduce the effect of mutual flux linkage from the next phase in the sequence. Firstly, the turn-off angle of the current phase can be delayed, to ensure that the self-flux-linkage of the phase is greater than the negative mutual flux linkage created by the next phase in the sequence, thus canceling out the mutual flux linkage. Secondly, the turn-on angle of current from the next phase in the sequence can be delayed or reduced.

IV. CONCLUSIONS

This paper has shown the influence of mutual coupling on the per-phase magnetization characteristics of the switched reluctance motor. The magnitudes of the mutual flux linkages are shown to be strongly dependent on the polarity arrangement of the phases. The mutual coupling effects from each phase can be calculated using the finite element frozen permeability method. Further work shall investigate the finite element optimization of current excitation wave forms to reduce the influence of mutual coupling, using the frozen permeability method.

ACKNOWLEDGMENTS

The authors acknowledge the support of the SPEED Consortium. One of the authors (J. W.) is funded by the UK Engineering and Physical Sciences Research Consul, the SPEED Consortium, and Robert Bosch GmbH.

[1]T. J. E. Miller, *Switched Reluctance Motors and Their Control* (Magna Physics, Oxford, 1993).
[2]D. Panda and V. Ramanarayanan, IEEE Industry Applications Conference 1999, Phoenix, Arizona, 3–7 October 1999, Vol. 4, pp. 2227–2234.
[3]A. M. Michaelides and C. Pollock, IEE Proc.: Electr. Power Appl. **143**, 361 (1996).
[4]N. Bianchi and S. Bolognani, IEEE Industry Applications Conference 1998, St. Louis, Missouri, 12–15 October 1998, Vol. 1, pp. 27–34.
[5]J. A. Walker, D. Dorrell, and C. Cossar, IEEE Trans. Magn. **41**, 3946 (2005).